Materials Horizons: From Nature to Nanomaterials

Bibhu Prasad Swain *Editor*

Advances in Nanostructured Materials

Springer

Materials Horizons: From Nature to Nanomaterials

Series Editor

Vijay Kumar Thakur, School of Aerospace, Transport and Manufacturing, Cranfield University, Cranfield, UK

Materials are an indispensable part of human civilization since the inception of life on earth. With the passage of time, innumerable new materials have been explored as well as developed and the search for new innovative materials continues briskly. Keeping in mind the immense perspectives of various classes of materials, this series aims at providing a comprehensive collection of works across the breadth of materials research at cutting-edge interface of materials science with physics, chemistry, biology and engineering.

This series covers a galaxy of materials ranging from natural materials to nanomaterials. Some of the topics include but not limited to: biological materials, biomimetic materials, ceramics, composites, coatings, functional materials, glasses, inorganic materials, inorganic-organic hybrids, metals, membranes, magnetic materials, manufacturing of materials, nanomaterials, organic materials and pigments to name a few. The series provides most timely and comprehensive information on advanced synthesis, processing, characterization, manufacturing and applications in a broad range of interdisciplinary fields in science, engineering and technology.

This series accepts both authored and edited works, including textbooks, monographs, reference works, and professional books. The books in this series will provide a deep insight into the state-of-art of Materials Horizons and serve students, academic, government and industrial scientists involved in all aspects of materials research.

More information about this series at https://link.springer.com/bookseries/16122

Bibhu Prasad Swain
Editor

Advances in Nanostructured Materials

Springer

Editor
Bibhu Prasad Swain
Department of Physics
National Institute of Technology Manipur
Imphal, India

ISSN 2524-5384 ISSN 2524-5392 (electronic)
Materials Horizons: From Nature to Nanomaterials
ISBN 978-981-16-8390-9 ISBN 978-981-16-8391-6 (eBook)
https://doi.org/10.1007/978-981-16-8391-6

Preface

The field of nanomaterials consists of building nanometric structures, which are made up of a limited number of atoms in the miniaturized world. Organic flexible electronics represent a highly promising technology that provides increased functionality and the potential to meet future challenges of scalability, flexibility, low power consumption, lightweight, and reduced cost. These materials may find wide scope due to their utilization with curved surfaces and incorporated into several products that could not support traditional electronics. This book covers device physics, processing and manufacturing technologies, circuits and packaging, metrology and diagnostic tools, architectures, and system engineering. The first unit (Chaps. 1–7) covered organic semiconducting nanomaterials and conducting polymers. Highlighting emerging organic and polymeric optoelectronic materials and devices, it presents the fundamentals, principal mechanisms, representatives. This second unit (Chaps. 8–15) describes various applications on water treatment, photovoltaic materials, energy storage applications. Magnetic nanomaterials and polymeric nanomaterials are important materials in daily life. The third unit (Chaps. 16–21) of this book emphasizes materials and their uses in water treatment, induced heat generation, tissue engineering, sensor, and energy applications. The third unit describes ferroelectric and piezoelectric materials and their applications in various fields. This is a guided tour of the discovery of the nanoworld which we hope will arouse the reader's curiosity so that they will engage more profoundly with the subject. In many different fields, we can observe a tidal wave of new products, which are directly linked to nanosciences.

We have entered the nano era: progress in the domains of electronics, information technology, and telecommunications allows us to bring together once separate fields. Microelectronics, which is covered in Chap. 1, has merged with methylammonium lead bromide perovskite films and their applications to optoelectronic devices. Chapter 2 will introduce this convergence and the impressive new perspectives that it opens up. Silicon nanowires for hybrid solar cells. Chapter 3 deals with a start-of-the-art for green energy storage using lead-free dielectrics. The nanostructures exhibit excellent material characteristics, including high carrier mobility and radiative recombination rate as well as long-term stability, good optical transparency,

mechanical flexibility, and electrical characteristics. Hence, Chap. 4 deals with nanostructure semiconductor materials for device applications. Silicon nanowires (SiNWs) have been widely studied as light-harvesting antennas in photocatalysts due to their ability to absorb broad-spectrum solar radiation, but they are typically limited by poor photoelectrochemical stability. Hence, Chap. 5 emphasizes reduced graphene oxide/SiNWs heterojunction for photovoltaic application. Controlling the morphology of high bandgap zinc oxide nanostructured materials is critical for their use in technological applications including in sensing, electronics, and energy harvesting. Hence, Chap. 6 focuses on chemical bath deposited zinc oxide nanostructured thin films and their applications. Supercapacitors are energy storage devices that will replace or boost batteries in multiple applications for their widespread utilization and commercialization, Moreover, it has many technological challenges dealing with stability of electrode, flexibility, and corrosion issues. Chapter 7 will deal with recent trends and research challenges on supercapacitors. Industrial wastewater is generated with anthropogenic activities and is the most environmental threat that needs remediation to overcome the environmental damages, thereby reducing human risks. Currently, wastewater treatment techniques are applied, and the utilization of nanomaterials for pollutant removal is an emerging technology. Chapter 8 deals with magnetic nanoparticles in wastewater treatment, supercapacitor, and biomedical applications. The study of the magnetohydrodynamic flow of a nanoparticle suspension under the influence of varied magnetic and electric fields has been the focus of research in contemporary times. Chapter 9 deals with the effects of viscosity on magnetically induced heat generation. A shape-controlled synthesis of nanoparticles by regulating chemical diffusion and reaction kinetics. Chapter 10 deals with the morphology-controlled synthesis and morphology-induced structures of different nanoparticles. Ionic liquids are structurally heterogeneous on the nanoscale; the features of this structure are highly variable, but controllable through polar/apolar structure and composition, charge density, and H-bonding capacity of the cation and anion. Chapter 11 deals with nanostructures in ionic liquid. The recent efforts and key research challenges regarding natural, synthetic, and hybrid polymers both with and without organic and inorganic fillers are employed for various applications. Chapter 12 deals with recent advances in nanostructured polymers. In recent years, polymer nanocomposites (PNCs) have attracted the attention of scientists and technologists in water purification due to improved processability, surface area, stability, tunable properties, and cost-effectiveness. Chapter 13 deals with polymer nanocomposite for water remediation. Heavy metals like mercury (Hg), cadmium (Cd), arsenic (As), lead (Pb), and chromium (Cr) are highly poisonous and hazardous to human health due to their non-biodegradability and highly toxic properties, even at trace levels. Thus, efficient, low-cost, and environmentally friendly methodologies of removal are needed. These removal needs to require fast detection, quantification, and remediation to have heavy metal-free water. Nanostructures emerged as a powerful tool capable to detect, quantify, and remove these contaminants. Chapter 14 gives information on low-dimensional nanostructured materials for the sustainable generation of water and energy. Insufficiently stable and sensitive processing conditions of heterojunction addressed the development of core/shell quantum dots (QDs),

which incorporate a shell of wider bandgap semiconductor materials around the QD cores. Chapter 15 deals with X-ray probing for the structural and functional studies of CdSe-CdS nanoparticles for detector application. Piezoelectric materials and devices have drawn extensive attention for energy harvesting due to their excellent electromechanical conversion properties. With increasing concerns about environmental problems in traditional lead-based piezoelectric materials, it is imperative to develop lead-free piezoelectric alternatives. Chapter 16 deals with lead-free piezoelectric nanostructures and their applications. Barium titanate materials displaying a positive temperature coefficient of resistivity are ubiquitously employed as thermistors in electrical current and voltage control systems, as well as in gas and thermal sensing applications. Chapter 17 deals with barium titanate-based lead-free ferroelectrics ceramics: and their past, present, and future. Nanoferrites were tested in three different photoreactor configurations. The rate of hydrogen evolution by nanoferrite was significantly influenced by the photoreactor configuration. Chapter 18 deals with recent advances in nanoferrite materials for photocatalysts and electrocatalysts for water splitting. Lead-based perovskites, predominantly $Pb(Zr,Ti)O_3$ (PZT)-based ceramics are with excellent electromechanical properties, with wider research and industrial use. Chapter 19 deals with polycrystalline alkali niobate piezoelectric ceramics sintered by microwave technique.

Imphal, India Bibhu Prasad Swain

Contents

Part I Nanomaterials for Devices

1 Methyl Ammonium Lead Bromide Perovskite Films and Their Applications to Optoelectronic Devices 3
Bhabani Sankar Swain

2 Silicon Nanowires: A Magic Material for Hybrid Solar Cells 21
Rabina Bhujel, Sadhna Rai, Utpal Deka, Joydeep Biswas, and Bibhu P. Swain

3 Lead-Free Dielectrics: A State-Of-The-Art for Green Energy Storage 37
Swetapadma Praharaj and Dibyaranjan Rout

4 Nanostructure Semiconductor Materials for Device Applications 57
Mahdie Kamalabadi, Kheibar Dashtian, Abbas Afkhami, Tayyebeh Madrakian, and Arash Ghoorchian

5 Reduced Graphene Oxide/Silicon Nanowire Heterojunction-Fabrication and Photovoltaic Application 87
Sadhna Rai, Rabina Bhujel, Joydeep Biswas, and Bibhu P. Swain

6 Chemical Bath Deposited Zinc Oxide Nanostructured Thin Films and Their Applications 99
Sumitra Nongthombam and Bibhu Prasad Swain

7 Recent Trends and Research Challenges on Supercapacitor 115
Pukhrambam Sushma Devi and Bibhu Prasad Swain

Part II Magnetic Nanomaterials and Nanostructured Polymers

8 Magnetic Nanoparticles in Wastewater Treatment, Supercapacitor, and Biomedical Applications 131
N. Joseph Singh, Boris Wareppam, and L. Herojit Singh

9 Effects of Viscosity on the Magnetic-Induced Heat Generation 145
Y. Haripriya Devi, L. Herojit Singh, and Boris Wareppam

10 Morphology-Controlled Synthesis and Morphology-Induce Structures of Different Nanoparticles 163
Heikham Farida Devi

11 Nanostructures in Ionic Liquid 181
Somas Singh Urikhinbam and Lenin S. Shagolsem

12 Recent Advances in Nanostructured Polymers 199
Thoudam Vilip Singh and Lenin S. Shagolsem

13 Polymer Nanocomposite Membranes for Water Remediation 227
Divyansh Upreti and T. Umasankar Patro

14 Low-Dimensional Nanostructured Materials for Sustainable Generation of Water and Energy 281
Jackson Pame and Lenin S. Shagolsem

15 X-Ray Probing for the Structural and Functional Studies of CdSe-CdS Nanoparticle for Detector Application 297
S. R. Patra and B. Mallick

Part III Ferroelectric Nanomaterials

16 Magnetism in Nanostructured Spinel Ferrites with Recent Advances in Processing, Characterization, and Applications 317
Elangbam Chitra Devi and Shougaijam Dorendrajit Singh

17 Lead-Free Piezoelectric Nanostructures and Their Applications 343
Huidrom Surjalata Devi and Mamata Maisnam

18 Lead-Free Ferroelectrics: Barium Titanate Based Ceramics: Past, Present, and Future 359
Devidas Gulwade

19 Recent Advances on Ferrites Nanomaterial's as Photocatalyst for Environment 381
Promod Kumar, Gajendra Kumar Inwati, Mohan Chandra Mathpal, Jero Maze, and H. C. Swart

20 Polycrystalline Alkali Niobate Piezoelectric Ceramics Sintered by Microwave Technique 411
Irom Monika Aniz and Mamata Maisnam

21 Electrical Characterization of Sol–GelDerived Nanostructured Li–Ni–Co Ferrites 431
Nandeibam Nilima, Sumitra Phanjoubam, and Mamata Maisnam

About the Editor

Dr. Bibhu Prasad Swain is currently an associate professor and HOD at the Department of physics, National Institute of Technology Manipur, Langol, Imphal. He obtained his B.Sc. Physics (Hons.) from Utkal University, Bhubaneswar, and M.Sc. (Physics), M.Tech (Materials Science) and Ph.D. from the National Institute of Technology Rourkela, Barkatullah University, and Indian Institute of Technology, Bombay, respectively. His major areas of research interests include high bandgap semiconductors thin films for device applications, biocompatibility coating for artificial heart valve coating and stent applications, silicon and carbon-based alloys of nanostructured materials and titanium nitride-based mechanical hard coating applications. He has published more than 100 papers in reputed international journals. Dr. Swain received the Japan Society of Promotion of the Science (JSPS) Fellow at the National Institute of Advanced Industrial Science and Technology (AIST) Japan; National Research Foundation (NRF), Fellowship, at University of Cape Town; and Brain Korea 21 Fellowship at Seoul National University. He also served in various administrative posts such as Dean academic and IIC president in NIT Manipur. Currently, he is a reviewer of more than 25 international journals and editorial board member of Nanoscience and Nanotechnology Asia.

Part I
Nanomaterials for Devices

Chapter 1
Methyl Ammonium Lead Bromide Perovskite Films and Their Applications to Optoelectronic Devices

Bhabani Sankar Swain

1 Introduction

Methylammonium lead halide perovskite ($MAPbX_3$, X = I, Br, Cl) have been a material of interest to scientists and researchers due to their versatile optoelectronic properties. Especially, Methylammonium lead bromide ($MAPbBr_3$), which has a larger direct bandgap (2.3 eV) with balanced change diffusion length, exciton binding energy enables its application to the solar cell, photodiode, light-emitting diode, laser, x-ray scintillator, etc. [1–11]. Due to its large bandgap, the solar cell based on $MAPbBr_3$ provides a short circuit current (J_{sc}) of approximately 9 mA/cm^2 and an open-circuit voltage (V_{oc}) of 1.5–1.6 V. Results show the UV–vis absorption band cut off and the PL intensity appeared at 532 nm shows $MAPbBr_3$ is the possible candidate of green LED. Device-based on $CH_3NH_3PbBr_3$ with higher lower unoccupied molecular orbital (LUMO = -3.4 eV) and deeper higher occupied molecular orbital (HOMO = -5.6 eV) level can achieve high V_{oc} and be semi-transparent which is a suitable candidate to be used as a top cell of all tandem solar cells.

In this chapter, some basic properties of $MAPbBr_3$ perovskite films including crystal structure, bandgap, and some of the optoelectronic properties will be discussed. We will discuss different fabrication methods to fabricate $MAPbBr_3$ perovskite films. Finally, some possible applications of $MAPbBr_3$perovskite film including solar cell, photodiode, laser, and x-ray scintillator to be discussed.

B. S. Swain (✉)
Department of Materials Science and Engineering, Kookmin University, Seoul, Republic of Korea
e-mail: bsswain@kookmin.ac.kr

B. P. Swain (ed.), *Advances in Nanostructured Materials*, Materials Horizons:
From Nature to Nanomaterials, https://doi.org/10.1007/978-981-16-8391-6_1

2 Fabrication Methods of $MAPbBr_3$ Perovskite Films

$MAPbBr_3$ films can be fabricated by different deposition methods including one-step process, two-step process ((dipping (static) as well as spinning (dynamic)), thermal evaporation process, and an anion exchange reaction method. In a one-step process, the equimolar concentration of lead bromide ($PbBr_2$) and methylammonium bromide (MABr) were dissolved in a suitable solvent such as dimethylformamide (DMF), Dimethyl sulfoxide (DMSO), or γ-butyrolactone and spin-coated at optimum condition (spinning rate and spinning time) to achieve the desired thickness of $MAPbBr_3$. In the two-step process, $PbBr_2$ is to be deposited first and then $PbBr_2$ film to be either dip casting or spin-cast by the MABr solution. In the thermal evaporation process, $PbBr_2$ and MABr to be co-evaporated to achieve the desired thickness of $MAPbBr_3$ film. Each method has its advantage and disadvantage. In the later section, each method will be discussed extensively.

2.1 One-Step Deposition Process

In earlier research in perovskite materials, the researcher fabricated perovskite films by one-step deposition method. This is a very easy method to fabricate highly crystalline $MAPbBr_3$ Perovskite film for device application. In this method, the equimolar concentration of $PbBr_2$ and MABr is to be dissolved in suitable solvents or solvent mixture, spin-coated on the substrate. Many groups have extensively used this method to fabricate highly compact and pinhole-free $MAPbBr_3$ film with desired thickness [1–11]. Colloidal ethylammonium methylammonium lead bromide ($EA_xMA_{1-x}PbBr_3$) nanocrystals (NCs) were synthesized by a mixture of ethylammonium bromide and methylammonium bromide (0.04) [12]. In this method, a total of 0.04 mmol of a mixture of ethylammonium bromide and methylammonium bromide, octyl ammonium bromide (12.6 mg, 0.06 mmol), and $PbBr_2$ (36.7 mg, 0.1 mmol) were dissolved in 400 μL DMF. The resulted solution again dispersed in γ-butyrolactone under stirring condition results in $MAPbBr_3$ [12].

When a mixture of MABr and medium/long-chain alkyl ammonium bromide was reacted with $PbBr_2$ in the presence of oleic acid and octadecene, highly stable $MAPbBr_3$ was obtained [13]. The main role of longer chain alkyl ammonium cation which only fits the periphery of octahedral sites of $PbBr_6$ inhibits the 3D growth of the nanoparticles. This strategy produces intrinsic perovskite nanoparticles stabilized by the long alkyl chains [13]. Single crystal $MAPbBr_3$ perovskite was synthesized by the inverse temperature crystallization method [14]. In this method, the equal molar concentration of $PbBr_2$ and MABr in DMF was taken in DMF and placed at 100 C in an oil bath. This process was repeatedly done and washed by anhydrous ether to fabricate a larger single crystal. The different cycle of deposition processes gives rise to different crystal planes. The study shows that the first cycle of the deposition process gives $MAPbBr_3$ single crystal grown along (200) plane. However,

the $MAPbBr_3$ crystal grown after the third cycle leads to polycrystalline in nature [14]. By using hot methylamine (CH_3NH_3) gas injection onto $MAPbBr_3$ films, a comparatively larger single crystal was fabricated by Ye et al. [15]. As a result, the recrystallization process converts the $MAPbBr_3$ polycrystalline films to single-crystal $MAPbBr_3$ film, which was confirmed by the XRD spectra. The schematics of their process are presented in Fig. 1.

The size and shape of $MAPbBr_3$ nanocrystals were modified by adding the $MAPbBr_3$ solution into 1,2,4-trichlorobenzene (TCB) and also further size and shape were controlled by adding cyclohexane of different ratios to TCB [16]. Ligand free synthesis method commonly provides surface passivation to $MAPbBr_3$ nanocrystal without the cover of ligands. By choosing a proper solvent for dispersion that is not miscible by the nanocrystals promotes the recrystallization process. This leads to dispersion of nanocrystal in the immiscible solvent to synthesize dispersed $MAPbBr_3$ nanocrystal [16]. Similarly, Kirakosyan et al. varied the TCB and Cyclohexane ratio to fabricate different sizes of $MAPbBr_3$ nanocrystals and studied their optical properties. To fabricate cube-shaped $MAPbBr_3$ crystals with tuning different sizes were synthesized by the ligand-free precipitation method [17]. Cyclohexane was miscible with TCB but poorly miscible with DMF. Thus, an addition of cyclohexane to TCB retarded diffusion of the injected droplets of DMF solution for re-precipitation of

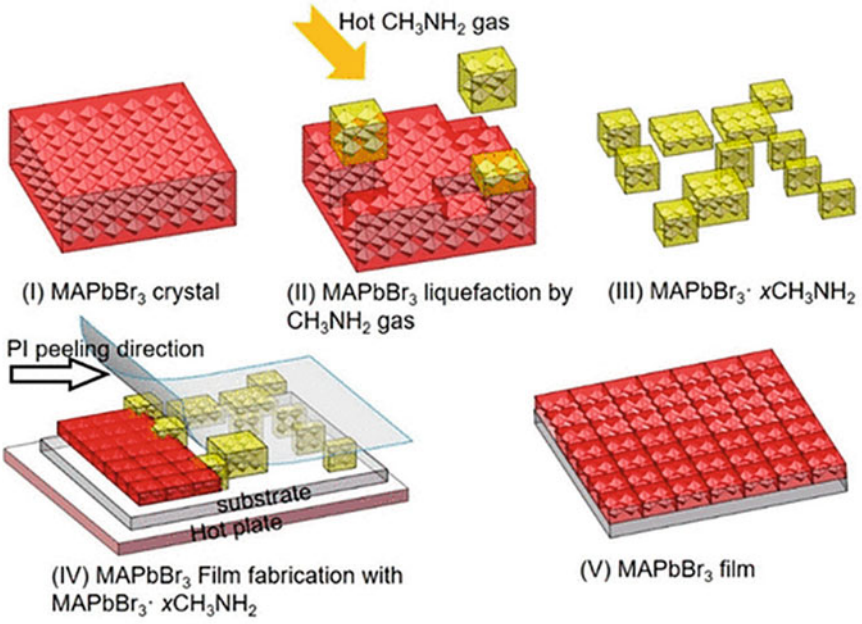

Fig. 1 Schematic diagrams for $MAPbBr_3 \cdot xCH_3NH_2$ precursor preparation and $MAPbBr_3$ formation by pressure-assisted soft-cover deposition (I) $MAPbBr_3$ crystal; (II) $MAPbBr_3$ single crystal liquefied by hot CH_3NH_2 gas; (III) $MAPbBr_3 \cdot xCH_3NH_2$ precursor; (IV) $MAPbBr_3$ film fabrication by pressure-assisted soft-cover deposition; (V) $MAPbBr_3$ film [15]

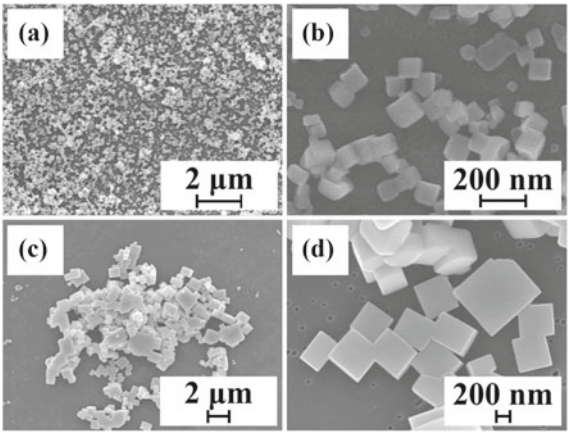

Fig. 2 SEM image of $MAPbBr_3$ fine crystals. (**a**, **b**) using the TCB and (**c**, **d**) using the TCB-Cyclohexane mixed solvent as a poor medium [16]

$MAPbBr_3$. So, a mixture of good and poor solvents retarded the recrystallization process, results in a small number of nuclei and their growth to large size (Figs. 2, 3).

In a similar method of fabrication, different groups fabricated $MAPbBr_3$ by the LARP method. A mixture of 0.4 mmol $PbBr_2$ and 0.32 mmol CH_3NH_3Br was added to 10 ml of chlorobenzene (CB) mixed with 40 µl of n-octylamine and 1 ml of oleic acid. After ultra-sonification for 30 min changed the solution color from transparent to orange, confirmed $MAPbBr_3$ quantum dots. Further ultra-sonification and centrifuge result in bright yellow-green $MAPbBr_3$ QDs colloid solution with strong green emission was observed. The concentration of PeQDs solution is estimated to be 0.6 mg/ml in CB. PMMA was dissolved in the colloidal solution at a concentration of 10 mg/ml to form the PeQDs-PMMA precursor solution for device fabrication [18].

2.2 Two-Step Deposition Process

The two-step processed perovskite film was fabricated by Mitzi et al. and others [7–10]. It was observed that the two-step processed $MAPbI_3$ perovskite film has comparatively better microstructure, structural and optical properties, which results in higher PCE contrast to 1-step processed perovskite films. However, in earlier research, the researcher focused only on a one-step process due to the solubility issue of MABr in isopropyl alcohol. In the two-step process, $PbBr_2$ was spin-coated at a typical condition and MABr was either dipped in MABr or spin-coated of MABr at a typical process condition. Wu et al., fabricated $MAPbBr_3$ films by two-step spinning process. In this process, $PbBr_2$/DMF was spin-coated onto ETL and then

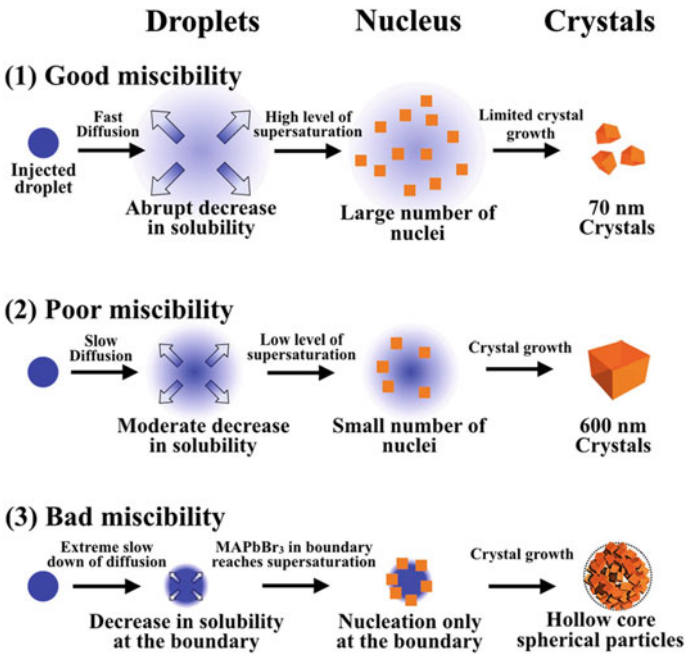

Fig. 3 Schematic illustrations of proposed mechanisms for $MAPbBr_3$ fine crystals. (1) 70 nm $MAPbBr_3$ NCs, (2) 600 nm $MAPbBr_3$ Crystals, and (3) $MAPbBr_3$ crystals with hollow spherical structures [16]

MABr/IPA was spin-coated on to $PbBr_2$ film. The advantage of spin coating deposition is, its dynamic process provides better control of conditions such as spinning rate, spinning time, reaction time, solvent evaporation. They have also observed post solvent annealing of $MAPbBr_3$ films improved the surface morphology of $MAPbBr_3$.

In a 2-step processed $MAPbBr_3$, Swain et al. fabricated $MAPbBr_3$ nanocube arrays by both solution engineering [20] and solvent engineering [21]. The main issue is the solubility issue of MABr in IPA. Ethanol and methanol can be alternative solvents to dissolve MABr. It should be noted here that the maximum solubility of MABr in IPA is about 10 mg/mL. However, MABr has much higher solubility (~90 mg/mL) in ethanol and methanol. The concentration of MABr in ethanol/methanol leads to different shapes and sizes of $MAPbBr_3$ nano/micro cubes.

The most common solvent to prepare PbX_2 is DMF. DMSO, and GBL or mixer of these solvents. Different microstructures were realized by using DMF and DMSO as solvents. A uniform, dense, compact sub-micron size perovskite nanocube arrays perovskite film was fabricated using DMF as solvent. However, nanorod and microplate perovskite films were fabricated when DMSO was used as the solvent. Moreover, Post-treatment of DMF and DMSO with MABr/ethanol improved the

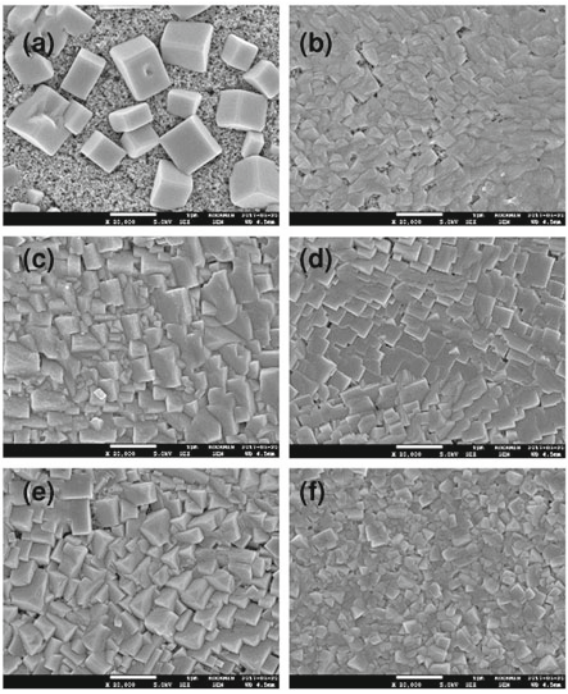

Fig. 4 Microstructure evolution of $MAPbBr_3$ film deposited by 2-step spin coating process using different MABr concentration in ethanol; (**a**) 5 mg/ml, (**b**) 15 mg/ml, (**c**) 30 mg/ml, (**d**) 45 mg/ml, (**e**) 60 mg/ml, and (**f**) 75 mg/ml [20]

microstructure [21]. It was also observed that the absorbance of $MAPbBr_3$ fabricated using DMF as solvent is more than that of MAPbBr3 fabricated using DMSO [21] (Figs. 4, 5, 6, 7, 8).

2.3 Ligand Mediated Growth of $MAPbBr_3$

Different shapes and sizes of $MAPbBr_3$ nanocube, nanowire, and nanosheet of nanocrystals could be achieved ligand assisted by control of thermodynamic (surface ligands) and kinetic (aging time, feed rate, and concentration) parameters for optimized design of optoelectronic properties and device application [22]. In a typical synthesis, $MAPbBr_3$ was prepared by adding 0.2 mmol of $PbBr_2$ and 0.2 mmol of MABr in 0.5 mL of oleic acid, and 20 μL of oleylamine or octylamine into a 5 mL DMF solution (Fig. 9). The resultant solution of 1 mL was dispersed in 10 mL of anhydrous toluene or other organic solvents to induce the precipitation $MAPbBr_3$ nanocrystal. In addition, a further variation of concentration of octylamine ligand (10 μL, 50 μL, 75 μL) tuned the $MAPbBr_3$ microstructure (Fig. 10) [22].

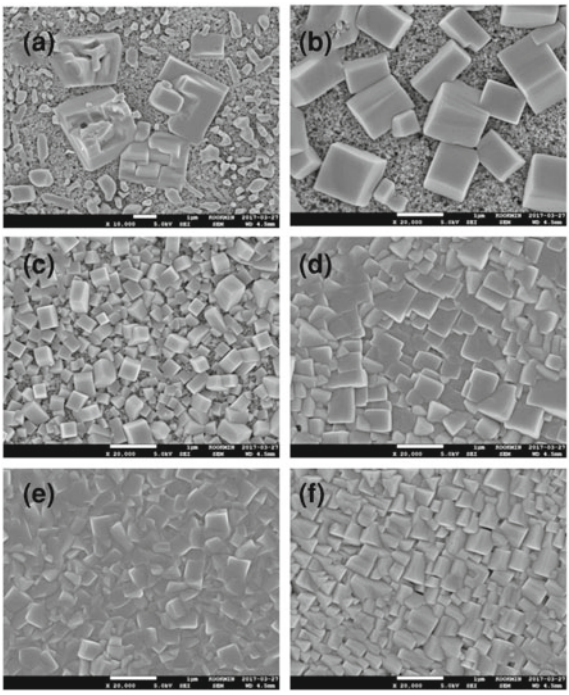

Fig. 5 Microstructure evolution of $MAPbBr_3$ film deposited by 2-step spin coating process using different MABr concentration in methanol; (**a**) 5 mg/ ml, (**b**) 15 mg/ml, (**c**) 30 mg/ml, (**d**) 45 mg/ml, (**e**) 60 mg/ml, and (**f**) 75 mg/ml [20]

3 Properties of $MAPbBr_3$ Perovskite Films

3.1 Structural Properties

Figure 11 shows the typical X-ray diffraction patterns of $MAPbBr_3$ single-crystal and polycrystalline film, respectively. The peaks appeared at 14.98°, 21.20°, 25.36°, 30.17°, 33.87°, 43.26°, 46.02°, and 53.59° corresponds to the diffraction plane (001), (110), (111), (002), (210), (211), (220), and (003) of polycrystalline $MAPbBr_3$ respectively. The crystal structure of MAPbBr3 nanocrystals belongs to the space group of $Pm\bar{3}m$ with a lattice spacing, a = 5.9896 Å. The crystalline nature of the perovskite films $MAPbBr_3$ depends on the deposition method which surely has different morphology, thickness, and quality of films. The crystallinity of $MAPbBr_3$ depends upon the surface properties of substrates, the molar concentration of precursor and types of solvent used, processing condition (spinning rate, reaction time), annealing temperature, and annealing time.

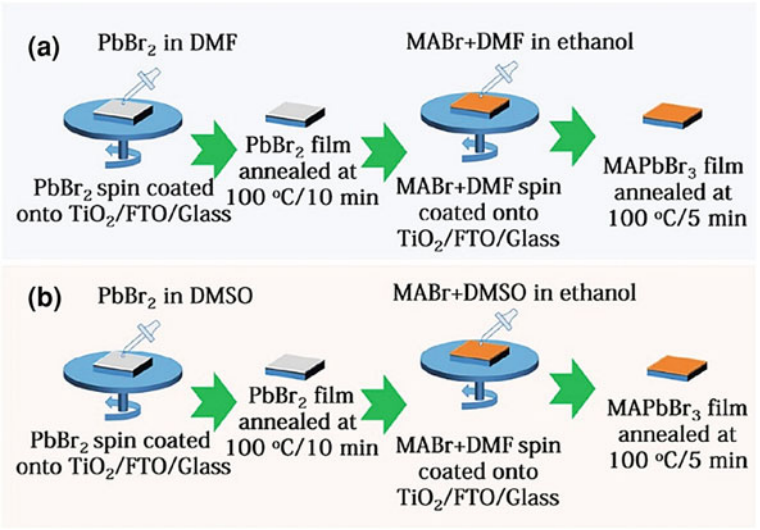

Fig. 6 A schematic illustration of the fabrication process of $MAPbBr_3$ perovskite films fabricated by two steps spin coating (using DMF). $PbBr_2$/DMF was spin-coated on TiO_2/glass substrate at typical condition (3000 rpm/30 s) and annealed at 100 °C for 5 min 50 μL of DMF was added to 30 mg MABr/ethanol and the solution was spin-coated on to $PbBr_2$ film at 1500 rpm/30 s and annealed at 100 °C for 5 min (Expt. 1), **b** the same experiment was performed using DMSO as solvents (Expt.2) [21]

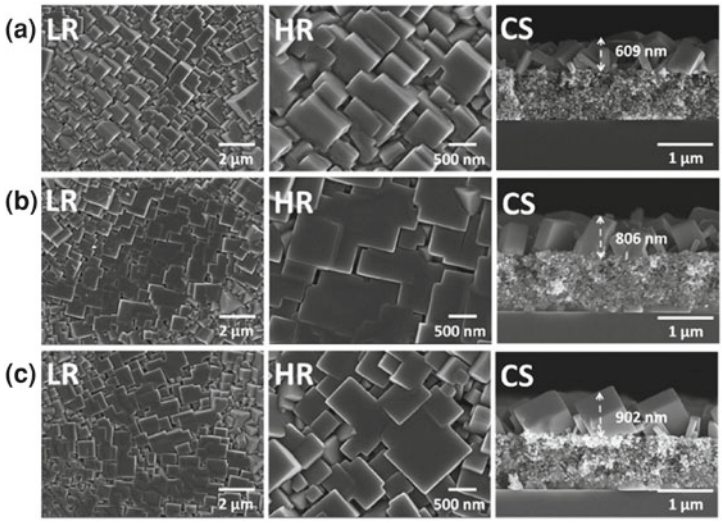

Fig. 7 The low resolution (LR) and high resolution (HR) SEM images of $MAPbBr_3$ perovskite films were fabricated by using DMF after different reaction times; **a** 1 min, **b** 3 min, and **c** 5 min. The reaction time means the time allowed the DMF/MABr/ethanol solution on the $PbBr_2$ before spinning starts [21]

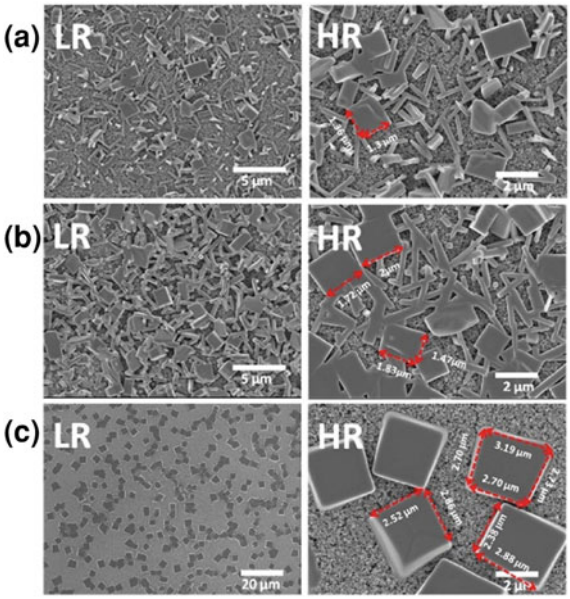

Fig. 8 The LR- and HR-SEM images of $MAPbBr_3$ perovskite films were fabricated by using DMSO after different reaction times; **a** 1 min, **b** 3 min, and **c** 5 min [21]

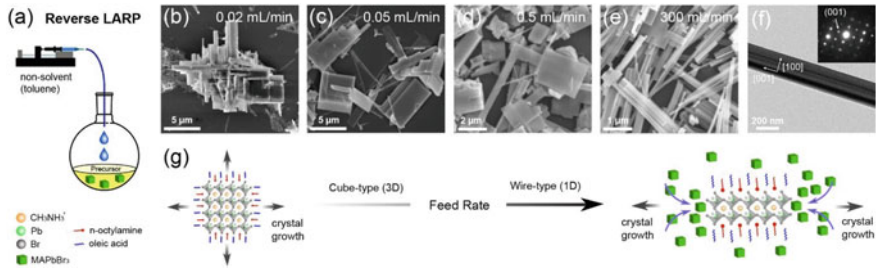

Fig. 9 **a** Schematic illustration of the experimental setup where toluene was added into the precursor solution (MABr: PbBr2: octylamine: oleic acid = 1: 1.25: 1.1: 8.8) at a constant feed rate (0.02–300 mL/min). SEM images of MAPbBr3 crystals synthesized at the feed rate of **b** 0.02, **c** 0.05, **d** 0.5, and **e** 300 mL/min, respectively. **f** TEM image and diffraction pattern (inset) of a single MAPbBr3 NW **g** Scheme show a crystal shape determined by the preferential growth process depending on the feed rate [22]

3.2 Optical Properties

The size and microstructure-dependent optical properties were studied by Droseros et al. [24]. They studied three different types of polycrystalline, microcrystals $MAPbBr_3$ films. A blue shift of absorption onset and PL bands was observed with decreasing crystal size. They have also confirmed that additive passivation of

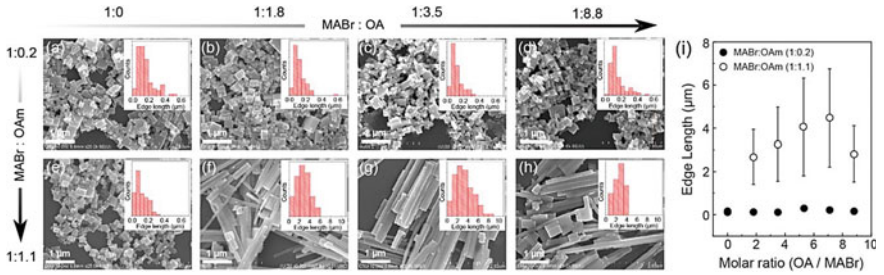

Fig. 10 **a-h** SEM images and **i** the characteristic length of MAPbBr3 crystals aged for 1 day depending on the amount of n-octylamine (0.03 and 0.18 mmol; MABr:OAm = 1:0.2 and 1:1.1) and oleic acid (0.28, 0.57, and 1.41 mmol; MABr:OA = 1:1.8, 1:1.35, and 1:8.8) at the feed rate of 300 mL/min. The insets show the distribution of average particle size [22]

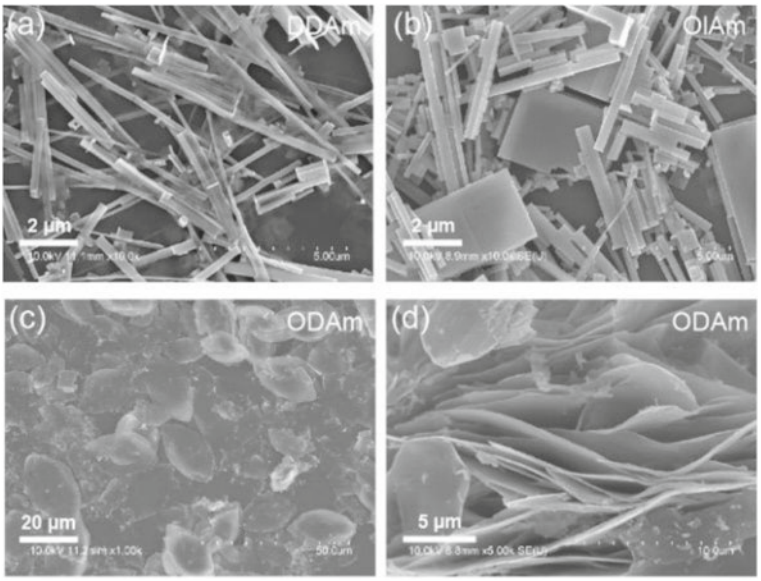

Fig. 11 SEM images of MAPbBr3 crystals synthesized in the presence of **a** dodecylamine (DDAm), **b** oleylamine (OlAm), and **c**, **d** octadecylamine (ODAm) [22]

nanocrystals reduced the surface trapping. The blue shift of PL peak of $MAPbBr_3$ film was observed with increasing of annealing of temperature 70 to 110 °C a blue shift was observed. They explained the phenomena by the formation of unordered crystals as well as a low crystallinity of the material [24] (Fig. 12).

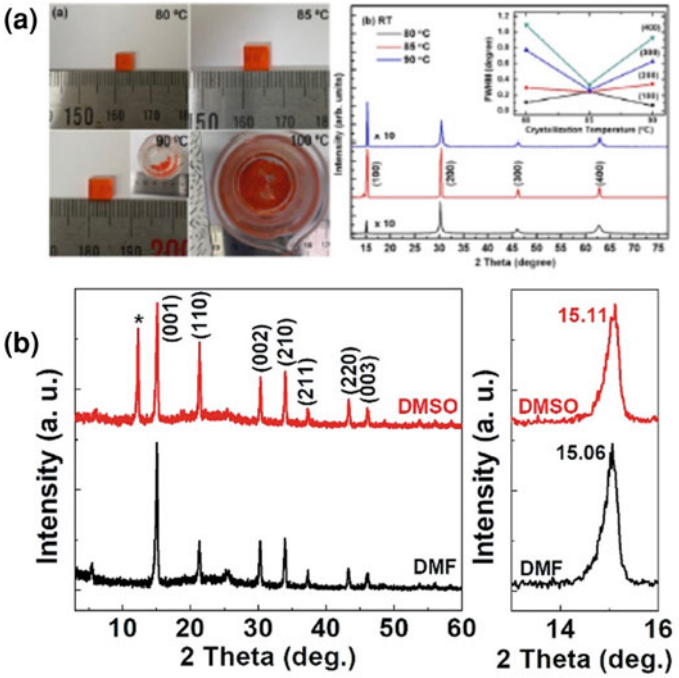

Fig. 12 **a** MAPbBr3 single-crystal images at different crystallization temperatures. X-ray diffraction patterns at room temperature. The inset shows the full width at half maximum (FWHM) of (100), (200), (300), and (400) planes [23] and **b** comparison of XRD spectra of the polycrystalline film deposited by two-step method using DMF and DMSO as solvent [21]

4 Applications of $MAPbBr_3$ Perovskite Films

4.1 Solar Cells

$MAPbBr_3$ as an active layer with conventional (p-i-n) and inverted solar cell (n-i-p) was realized by choosing suitable electron transport layer (ETL) and hole transport layer (HTL) matching with lowest unoccupied molecular orbital (LUMO) and highest occupied molecular orbital (HOMO) of $MAPbBr_3$. Ultraviolet photoelectron spectroscopy (UPS) studies show the HOMO and LUMO of $MAPbBr_3$ were 3.8 and 5.7 eV, respectively, and the UV–Vis spectroscopy confirmed the bandgap of $MAPbBr_3$ is about 2.3 eV. This energy level of $MAPbBr_3$ allows many ETL and HTL to match with the energy level of $MAPbBr_3$ for solar cell application. The most common ETL used for $MAPbBr_3$ solar cells is TiO_2 because of the simple method to fabricate by spin coating of commercially available mesoporous anatase TiO_2 nanoparticles. As we know, the solar cell requires each layer to be a dense, pinhole-free, and compact layer. So, the microstructure of the $MAPbBr_3$

mainly decides the PCE of solar cells by minimizing series resistance and providing high shunt resistance. HTL, as well as ETL-free $MAPbBr_3$ perovskite active layer, was realized by Peng et al. [25]. The device shows an excellent efficiency of 5.49% without any transport materials [25] (Table 1). ICBA (1′,1″,4′,4″-Tetrahydro-di[1,4]metha-nonaphthaleno[1,2:2′,3′,56,60:2″,3″][5,6] fullerene-C60) has a higher LUMO level compared to PCBM (phenyl-C61-butyric acid methyl ester) used as ETL in perovskite solar cell to improve the Voc and FF [19].

4.2 Light-Emitting Diodes

So far, several groups fabricated $MAPbBr_3$-based LED using different electron injection layers (EIL) and hole injection layers (HIL) concerning HOMO and LUMO levels of $MAPbBr_3$ [28–33]. With a device architecture of ITO/ poly(N-vinyl carbazole) (PVK)/$MAPbBr_3$/TPBI/LiF/Al, the external quantum efficiency of 9.3% was achieved by n-butyl ammonium bromide additive into $MAPbBr_3$ solution, which results in a delay in the growth of $MAPbBr_3$ crystal results smooth, dense and pinhole-free film with the roughness of 1 nm [28]. In another approach, mixing of precursor solutions ($PbBr_2$ + MABr and $Pb(Ac)_2$-$3H_2O$ + MABr) which can efficient passive micrometer crystal by nanometer crystal, Qin et al. demonstrated self-passivating $MAPbBr_3$ films toward very stable electroluminescence of 49,119 cd/m^2 with EQE = 11.31%. The device shows a lower turn-on bias (1.9 V) which is comparatively lower than the bandgap of $MAPbBr_3$ (Eg = 2.25 V) in an LED architecture of ITO/PEDOT: PSS/$MAPbBr_3$/TPBi/LiF/Ag [29]. Zhang et al. improved the surface morphologies as well as passivate the $MAPbBr_3$ film by introducing phenethylamine (PEA) into the MAPBr3 solution. They observed that the addition of PEA suppresses the exciton quenching at the ETL/perovskite and perovskite/HTL interface, which results in maximum current efficiency of 9.81 cd/A^{-1} in ITO/LiF/$MAPbBr_3$/LiF/Bphen/LiF/Al [30]. Using a π-Conjugated Ligand (4-aminobenzonitrile(ABN)) ligand, MAPbBr3 film with nanosized with reduced trap density was achieved [31]. In this unique approach, furthermore, a maximum luminance of 3350 cd/m^2 with an external quantum efficiency of 8.85% was achieved by using an LED architecture of ITO/PEDOT:PSS/PVK/$MAPbBr_3$-ABN improved the performance of methylammonium lead bromide (MAPbBr3)-based PeLEDs by reducing the $MAPbBr_3$ crystal size to the nanoscale and reducing the trap density.

4.3 X-ray Scintillators

$MAPbBr_3$ can also use in x/γ detection for medical imaging, industrial inspection, and astronomical telescopes. An enhanced X-ray sensitivity ~529 $\mu C \cdot Gy_{air}^{-1}$ cm^{-2}

Table 1 Solar cell efficiency with $MAPbBr_3$ as an active layer

Device architecture	J_{sc} (mA/cm^2)	V_{oc} (V)	FF	PCE (%)	References
FTO/TiO2/$MAPbBr_3$/Spiro-OMETAD/Au	9.35	1.05	0.58	5.70	[20]
FTO/TiO2/MAPbBr3/Spiro-OMETAD/Au	5.37	1.37	0.80	5.87	[21]
FTO/TiO2/MAPbBr3/Spiro-OMETAD/Au	5.24	1.30	0.44	3.02	[21]
ITO/PEDOT:PSS/$CH_3NH_3PbBr_3$/ICBA/Ca/Al	6.04	1.61	0.77	7.50	[19]
FTO/m-TiO_2/$MAPbBr_3$/PCBTDPP/Au	4.47	1.16	0.59	3.04	[26]
FTO/m-TiO_2/$MAPbBr_3$/P3HT/Au	2.98	0.50	0.51	0.76	[26]
FTO/bl-TiO_2/mp-TiO_2/$MAPbBr_3$/PTAA/Au	6.6	1.29	0.70	5.9	[27]
FTO/bl-TiO_2/mp-TiO_2/$MAPbBr_3$/PF8-TAA/Au	6.3	1.36	0.70	6.0	[27]
FTO/bl-TiO_2/mp-TiO_2/$MAPbBr_3$/PIF8-TAA/Au	6.1	1.40	0.79	6.7	[27]
FTO/bl-TiO2/$CH_3NH_3PbBr_3$\P3HT/Au	8.5	1.09	0.79	7.3	[4]
FTO/bl-TiO2/$CH_3NH_3PbBr_3$\P-TAA/Au	8.4	1.35	0.82	9.3	[4]
FTO/bl-TiO2/$CH_3NH_3PbBr_3$\PIF8-TAA/Au	8.4	1.51	0.82	10.4	[4]
FTO/bl-TiO_2/m-TiO_2/$CH_3NH_3PbBr_3$/Spiro-OMeTAD/Au	11.68	0.95	0.69	7.66	[3]
FTO/bl-TiO_2/m-TiO_2/$CH_3NH_3PbBr_3$/PTAA/Au	12.31	1.097	0.69	9.31	[3]

was achieved under 80 kVp X-ray at an electric field of 50 V·cm^{-1} using aluminum zinc oxide (AZO)/$MAPbBr_3$ p–n junction structure [5] (Figs. 13, 14).

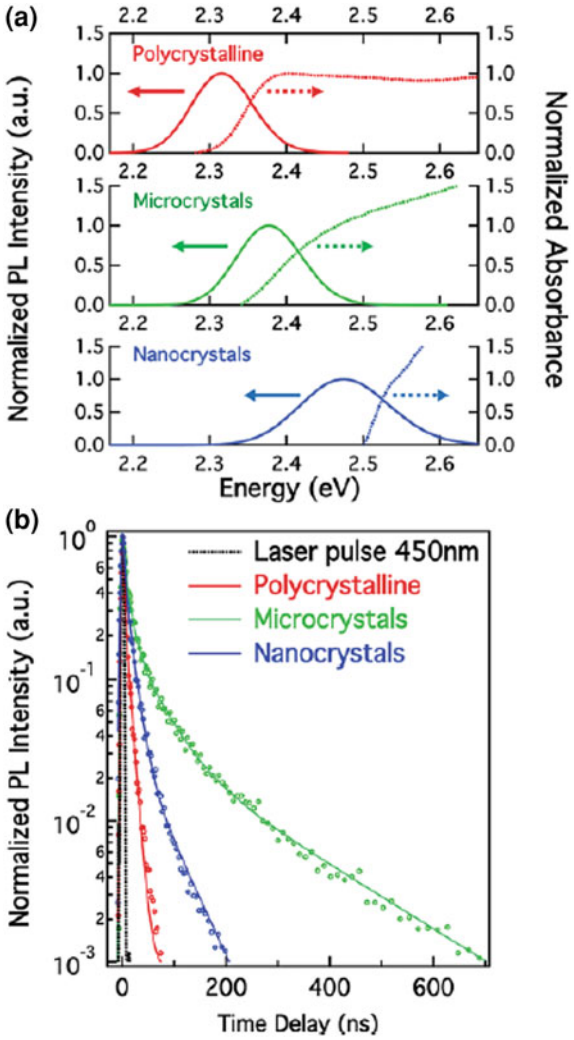

Fig. 13 **a** Steady-state PL (left) and absorption spectra (right) and **b** TRPL dynamics of the three samples, recorded with excitation at 450 nm with 3 ns duration pulses and a repetition rate of 10 Hz at a common carrier density of ∼1016 cm − 3. The detection is at the wavelength of the maximum PL intensity [24]

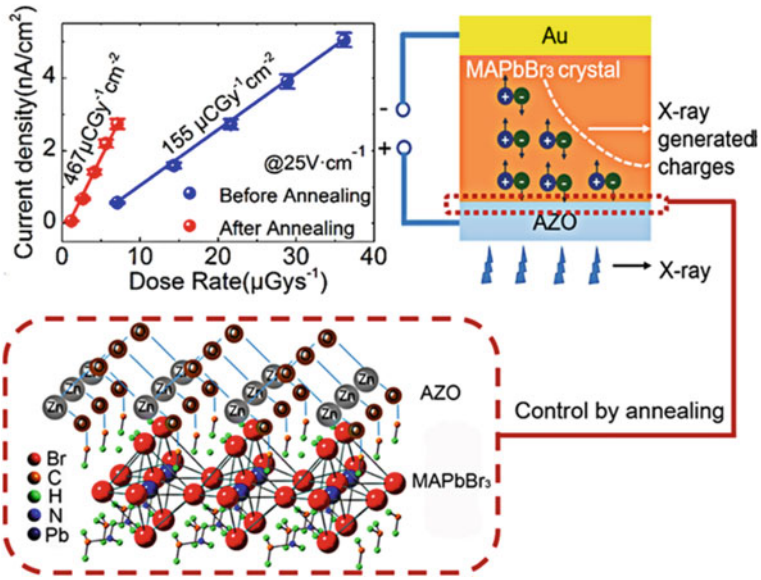

Fig. 14 The current density of MAPbBr3 layer with Au and AZO contacts with different X-ray dose to optimize the performance of MAPbBr3 detectors, which have many potential applications in medical and security detection with low radiation dose brought to the human body [5]

5 Summary/Conclusion

In summary, we have discussed the various synthesis and deposition methods of $MAPbBr_3$ perovskite films for different applications. The preparation methods presented here can be helpful to fabricate highly stable and high performances optoelectronics devices in the future.

References

1. Heo JH, Im SH (2016) $CH_3NH_3PbBr_3$-$CH_3NH_3PbI_3$ perovskite–perovskite tandem solar cells with exceeding 2.2 V open-circuit voltage. Adv Mater 28:5121
2. Kedem N, Brenner TM, Kulbak M, Schaefer N, Levcenko S, Levine I, Abou-Ras D, Hodes G, Cahen D (2015) Light-induced increase of electron diffusion length in a p–n junction type $CH_3NH_3PbBr_3$ perovskite solar cell. J Phys Chem Lett 6:2469
3. Mali SS, Shim CS, Hong CK (2015) Highly stable and efficient solid-state solar cells based on methylammonium lead bromide ($CH_3NH_3PbBr_3$) perovskite quantum dots. NPG Asia Mater 7:208
4. Heo H, Song DH, Im SH (2014) Planar $CH_3NH_3PbBr_3$ hybrid solar cells with 10.4% power conversion efficiency, fabricated by controlled crystallization in the spin-coating process. Adv Mater 26:8179

5. Li L, Liu X, Zhang H, Zhang B, Jie W, Sellin PJ, Hu C, Zeng G, Xu Y (2019) Enhanced X-ray sensitivity of $MAPbBr_3$ detector by tailoring the interface-states density. ACS Appl Mater Interf 11:7522–7528
6. Bouanani LE, Keating SE, Avila-Avendano C, Reyes-Banda CG, Pintor-Monroy MI, Singh V, Murillo BL, Higgins M, Quevedo-Lopez MA (2021) Solid-state neutron detection based on methylammonium lead bromide perovskite single crystals. ACS Appl Mater Interf 13:28049–28056
7. Liang K, Mitzi DB, Prikas MT (1998) Synthesis and characterization of organic−inorganic perovskite thin films prepared using a versatile two-step dipping technique. Chem Mater 10:403
8. Burschka J, Pellet N, Moon S-J, Humphry-Baker R, Gao P, Nazeeruddin MK, Grätzel M (2013) Sequential deposition as a route to high-performance perovskite-sensitized solar cells. Nature 499:316
9. Im J-H, Kim H-S, Park N-G (2014) Morphology-photovoltaic property correlation in perovskite solar cells: one-step versus two-step deposition of $CH_3NH_3PbI_3$. APL Mater 2:081510
10. Im J-H, Jang I-H, Pellet N, Grätzel M, Park N-G (2014) Growth of $CH_3NH_3PbI_3$ cuboids with controlled size for high-efficiency perovskite solar cells. Nat Nanotechnol 9:927
11. Liu Y, Zhang Y, Yang Z, Feng J, Xu Z, Li Q, Hu M, Ye H, Zhang X, Liu M, Zhao K, Liu SF (2019) Low-temperature-gradient crystallization for multi-inch high-quality perovskite single crystals for record performance photodetectors Mater. Today 22:67–75
12. Mittal M, Jana A, Sarkar S, Mahadevan P, Sapra S (2016) Size of the organic cation tunes the band gap of colloidal organolead bromide perovskite nanocrystals. J Phys Chem Lett 7:3270–3277
13. Gonzalez-Carrero S, Galian RE, Pérez-Prieto J (2015) Approaching the top of the emissive properties of $CH_3NH_3PbBr_3$ perovskite nanoparticles. J Mater Chem A 3:9187−9193
14. Chen L-C, Lee K-L, Lin S-E (2018) Observation of hybrid $MAPbBr_3$ perovskite bulk crystals grown by repeated crystallizations crystals, vol 8, pp 260
15. Ye F, Wu H, Qin M, Yang S, Niu G, Lu X, Wang J, Mitzi DB, Choy WC (2020) H: high-quality MAPbBr 3 cuboid film with promising optoelectronic properties prepared by a hot methylamine precursor approach. ACS Appl Mater Interfaces 12:24498–24504
16. Umemoto K, Pu Y-J, Yumusak C, Scharber MC, White MS, Sariciftci NC, Yoshida T, Matsui J, Uji H, Masuhara A (2018) Size control of $CH3NH3PbBr_3$ perovskite cuboid fine crystals synthesized by ligand-free re-precipitation method. Micros Techno 24:619–623
17. Kirakosyan A, Yun S, Kim D, Choi J (2018) Formation of $CH_3NH_3PbBr_3$ perovskite nanocubes without surfactant and their optical properties. J Korean Inst Surf Eng 51:1
18. Yang K, Lia F, Veeramalai CP, Guo T (2017) A facile synthesis of $CH_3NH_3PbBr_3$ perovskite quantum dots and their application in flexible nonvolatile memory. Appl Phys Lett 110:083102
19. Wu C-G, Chiang C-H, Chang S-H (2016) Moderate temperature processed solar cell with record-high-V_{oc} of 1.61 V and FF of 0.77 based on solvent annealed $CH_3NH_3PbBr_3$/ICBA active layer. Nanoscale 8:4077–4085
20. Swain BS, Sheik MAK, Singh S, Rahim A, Jeong D, Lee L (2018) $CH_3NH_3PbBr_3$ nanocubes-array for solar cell application. Mater Sci Semicond Process 74:361–368
21. Swain BS, Lee J (2021) Tailoring methyl-ammonium lead bromide nanostructure by solvent engineering and their application to high open circuit voltage solar cells. Physica E 126:114420–114427
22. Kirakosyan A, Jeon KG, Kim C-Y, Kim Y, Choi J (2021) Binary ligands-mediated morphological evolution of methylammonium lead bromide nanocrystals cryst. Eng Comm 23:4434–4438
23. Oh, Jaewon (2020) Won Yeob Jeong, Seo Yun Lee, Bom Lee, and Mee-Yi Ryu, influence of crystallization temperature on the optical properties of MAPbBr 3 single crystals. Appl Sci Converg Technol 29(1):19–22
24. Droseros N, Longo G, Brauer JC, Sessolo M, Bolink HJ, Banerji N (2018) Origin of the enhanced photoluminescence quantum yield in MAPbBr 3 perovskite with reduced crystal size. ACS Energy Lett 3(6):1458–1466
25. Peng W, Wang L, Murali B, Ho K-T, Bera A, Cho N, Kang C-F, Burlakov VM, Pan J, Sinatra L, Ma C, Xu W, Shi D, Alarousu E, Goriely A, He J-H, Mohammed OF, Wu T, Bakr OM (2016)

Solution-grown monocrystalline hybrid perovskite films for hole-transporter-free solar cells. Adv Mater 28:3383–3390
26. Cai B, Xing Y, Yang Z, Zhang W-H, Qiu J (2013) High-performance hybrid solar cells sensitized by organolead halide perovskites. Energy Environ Sci 6:1480
27. Ryu S, Noh JH, Jeon NJ, Kim YC, Yang WS, Seo J, Seok SI (2014) Voltage output of efficient perovskite solar cells with high open-circuit voltage and fill factor. Energy Environ Sci 7:2614–2618
28. Xiao Z, Kerner RA, Zhao L, Tran NL, Lee KM, Koh T-W, Scholes GD, Rand BP (2017) Efficient perovskite light-emitting diodes featuring nanometre-sized crystallites. Nat Photonics 11:108–115
29. Qin J, Zhang J, Bai Y, Ma S, Wang M, Xu H, Loyd M, Zhan Y, Hou X, Hu B (2019) Enabling self-passivation by attaching small grains on surfaces of large grains toward high-performance perovskite LEDs. iScience 19:378–387
30. Zhang M, Yuan F, Zhao W, Jiao B, Ran C, Zhang W, Wu Z (2018) High-performance organo-lead halide perovskite light-emitting diodes via surface passivation of phenethylamine. Org Elect 60:57–63
31. Jung K, Choi H, Kim H, Park YC, Lee M-J (2020) Highly luminescent and stable CH3NH3PbBr3 quantum dots with 91.7% photoluminescence quantum yield: Role of guanidinium bromide dopants. J Alloys Comp 832:154990
32. An HJ, Kim YC, Kim DH, Myoung J-M (2020) High-performance green light-emitting diodes based on $MAPbBr_3$ with π-conjugated ligand. ACS Appl Mater Interf 12:16726–16735
33. Cho H, Jeong S-H, Park M-H, Kim Y-H, Wolf C, Lee C-L, Heo J-H, Sadhanala A, Myoung NS, Yoo S, Im SH, Friend RH, Lee T-W (2015) Overcoming the electroluminescence efficiency limitations of perovskite light-emitting diodes 350:1222−1225

Chapter 2
Silicon Nanowires: A Magic Material for Hybrid Solar Cells

Rabina Bhujel, Sadhna Rai, Utpal Deka, Joydeep Biswas, and Bibhu P. Swain

1 Introduction

Crystalline Si has served an essential purpose in different solar cells due to its outstanding optical and electrical properties to improve the power conversion efficiency (PCE) of the solar cells. But, at the same time, the methods applied for the preparation of crystalline Si solar cells require a high-temperature diffusion process which is expensive at the same time. Therefore, it is complicated to reduce the price of crystalline Si solar cells for its commercial applications. The cost of conventional p–n junction can be reduced to some extent using a Schottky junction, which mainly contains a metal-Si contact. However, the use of a thick Si absorbing layer in the Schottky junction limits the PCE of the solar cell. The past studies show that the replacement of bulk Si with SiNWs in the different Schottky junction solar cells including the hybrid solar cell improves the PCE to the solar cell. SiNWs are one of the most extensively studied materials by researchers all over the globe due to their wide application in the fields of optoelectronics [1], photonics [2], and photovoltaic's [3]. It has also been an important material used in sensors [4], light-emitting diodes [5] as well as in transistors [6]. The excellent light-absorbing properties of SiNWs and their low cost make it an essential material in different types of hybrid solar cells.

R. Bhujel (✉) · S. Rai
Centre for Materials Science and Nanotechnology, Sikkim Manipal Institute of Technology, Sikkim Manipal University, Majhitar, East Sikkim, Rangpo 737136, India

U. Deka
Department of Physics, Sikkim Manipal Institute of Technology, Sikkim Manipal University, Majhitar, East Sikkim, Rangpo 737136, India

J. Biswas
Department of Chemistry, Sikkim Manipal Institute of Technology, Sikkim Manipal University, Majhitar, East Sikkim, Rangpo 737136, India

B. P. Swain
Department of Physics, National Institute of Technology, Manipur, Langol, India

B. P. Swain (ed.), *Advances in Nanostructured Materials*, Materials Horizons: From Nature to Nanomaterials, https://doi.org/10.1007/978-981-16-8391-6_2

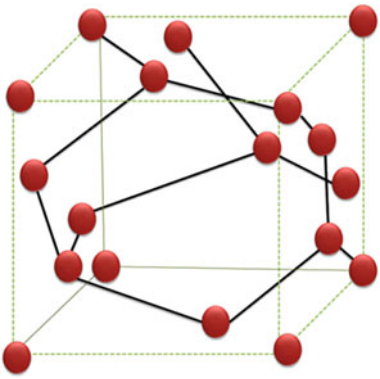

Fig. 1 Structure of Si

The synthesis procedure of SiNWs is very simple and cost-effective well-known as electroless metal-assisted chemical etching (EMACE). Therefore, this book chapter aims to study the importance of SiNWs in different hybrid solar cells.

2 Silicon and Its Structure

Silicon is a nonmetallic semiconducting element that belongs to the carbon family in the periodic table. The atomic number of Si is 14 and is therefore tetravalent with the electronic configuration of [Ne] $3s^2 3p^2$. Si covers approximately 27.7% of the earth's crust; therefore, it is the second most abundant element on the earth. Silicon in its purest form exists as a hard dark grey solid with a metallic luster. It has an octahedral crystalline structure as shown in Fig. 1. The bandgap of Si is 1.12 eV and is indirect.

3 Silicon Nanostructures

To reduce the excessive consumption of Si and to develop the properties of devices, different structures of Si were produced like porous silicon, nanotubes, Si nanowires (SiNWs), Si pyramids, Si quantum dots, etc. These nanostructures of Si have unique properties which boost the device properties as compared to its bulk counterpart (Fig. 2).

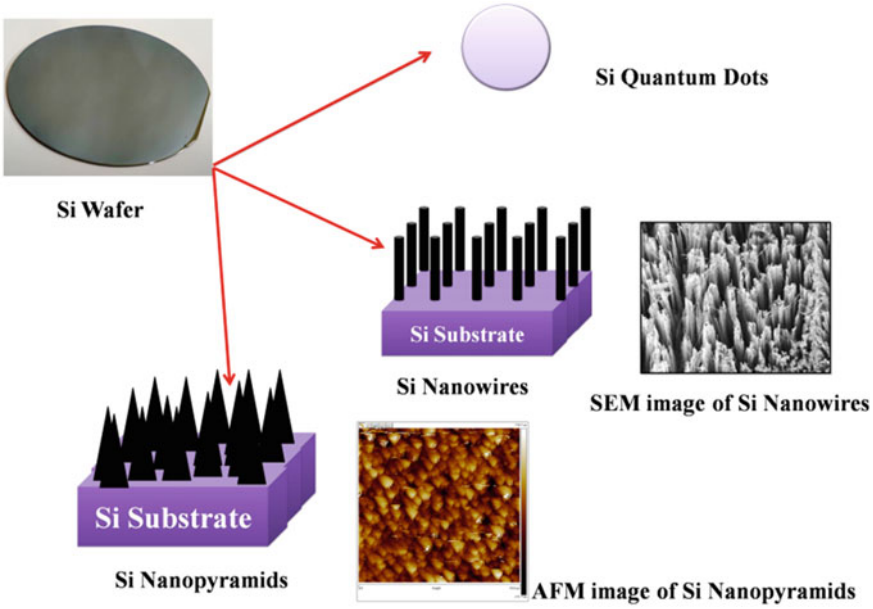

Fig. 2 Different nanostructures of Si

3.1 Silicon Quantum Dots

The zero-dimensional structure of semiconducting Si is known as quantum dots where the size of the nanoparticles lies in the range of 1–10 nm. SiQDs hold great applicative potential in various devices such as light-emitting diodes, biosensors, fluorescent biomarking agents, solar cells, etc. Depending upon the requirement the optical as well as the electrical behavior, properties of SIQDs can be controlled by varying the nanoparticle size, crystalline nature, and also by the doping of foreign materials. The band-gap of crystalline Si in its bulk form has indirect nature which yet gets converted into the direct form in the case of SiQDs where the size is less than 5 nm.

3.2 Si Nanopyramids

Si Nanopyramids (both upright and inverted) have attracted research interests, due to their excellent light trapping properties. Generally, Si pyramids are formed by the alkaline etching of Si wafers or by the laser processes. The excellent antireflection properties and a small surface area increase (1.7 times than the flat surface) resulted in higher efficiency toward the Si solar cells.

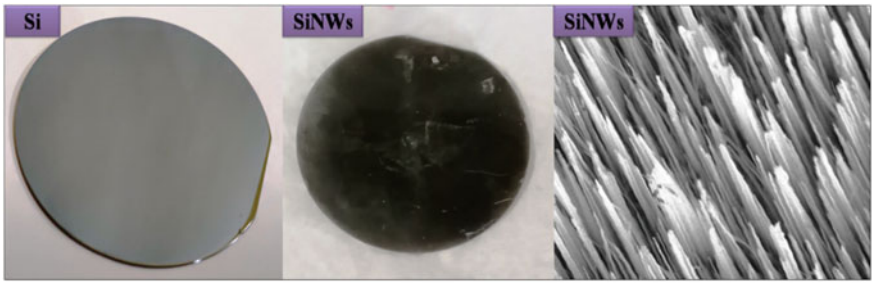

Fig. 3 Optical and SEM images of Si and SiNWs

3.3 Si Nanowires

Silicon Nanowires (SiNWs) is a one-dimensional structure of Si generally formed by the etching of Si precursor or vapor–liquid phase growth on a substrate using different catalysts like gold, silver, etc. The properties of Silicon nanowires are quite different as compared to their bulk counterpart due to their unusual quasi-one-dimensional electronic structure. Because of its one-dimensional nature, light trapping by SiNWs is many folds greater as compared to bulk Si. The reflectance in SiNWs is as low as 3% within the wavelength range of 400–1100 nm. The use of SiNWs over Si favors a reduction in material cost as well as increases the PCE of the solar cell, owing to its extremely good electrical as well as optical properties. Over the other SiNWs structure, SiNWs are highly favored because of their low cost synthesis procedure and excellent light-harvesting properties. SiNWs also improve the electron mobility path from the active interface to the electrodes for carriers. They also offer a large contact area between two different materials (Fig. 3).

4 Techniques Utilized for the Growth of SiNWs

4.1 Electroless Metal Assisted Chemical Etching Method (EMACE)

This is the easiest and cost-effective way for the production of SiNWs. The procedure includes two main steps which are deposition of metal nanoparticles (Ag/Au/Pt/Ni) on Si surface followed by the etching of the Si surface to get the desired product. Both types of SiNWs (n & p) can be grown on Si wafers by using this technique. The synthesis of SiNWs was started in 2002 when Peng et al. showed the large-scale synthesis of SiNW arrays by the simple one-step etching of the Si wafer using a solution containing HF and $AgNO_3$ at room temperature. Since then various modifications have been done to produce SiNWs in the best easy and cost-effective way

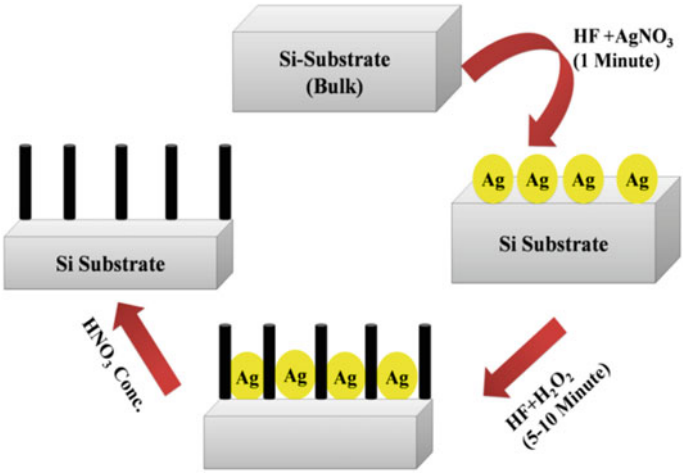

Fig. 4 Synthesis of SiNWs via EMACE method

through this solution-based method. SiNWs with varying diameters and lengths can be obtained by just changing the parameters of the materials used. The optimization of the dimensions of SiNWs is possible for obtaining better performance regarding the absorption of solar radiation (Fig. 4).

Studies have been made to understand the importance of metal catalysts such as Ag, Au, Pt, and Cu on the growth of SiNWs by maintaining the reaction temperature at 50 °C. As studied Ag and Au's catalyst was extremely good for obtaining highly dense arrays of SiNWs [7]. Furthermore, the reflectance spectra of SiNWs grown using Ag catalyst showed an extremely low average reflectance of 1.6% in the wavelengths region of 300 to 1000 nm [8]. The SEM studies revealed that the SiNWs obtained from EMACE are highly dense and agglomerated on the tip. This might affect the properties of SiNWs. To overcome this problem Gong et al. [9] came up with a new idea of tapering SiNWs in a 30% NaOH solution. The SiNWs obtained after NaOH tapering had needle-like structures. The main motive of this tapering was to avoid the tip agglomeration such that the polymers get well dispersed on the SiNWs surface. SiNWs can also be prepared using Sn as the metal catalyst [10]. The obtained SiNWs have reflectance lower than 5% in the wavelength region of 500 nm (Fig. 5).

4.2 Lithography Followed by Etching

This is one of the oldest techniques of depositing different metal nanoparticles on Si surface which then acts as a catalyst for the growth of SiNWs. This technique is mainly used for the large-scale manufacture of SiNWs. As reported earlier by Peng et al. [7] colloidal Si particles were deposited first by lithography which was further

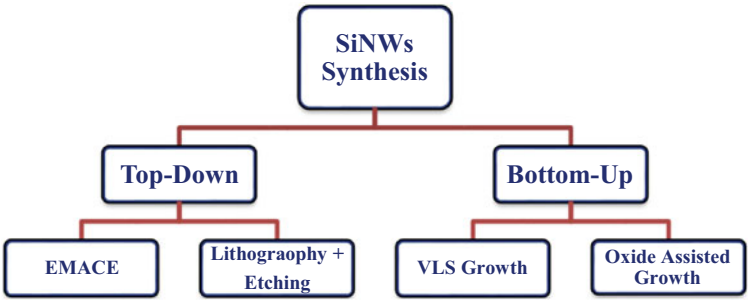

Fig. 5 Techniques utilized for SiNWs synthesis

etched to produce the desired SiNWs.They also reported that the change in the size of colloidal silica crystals affects the diameter and density of the SiNWs. Moreover, Si nanopillars were obtained using this technique where at first Ag colloidal particles were deposited on the Si surface which mainly acts as a catalyst [11]. The Ag patterned Si wafer was then wet etched to produce the nanopillar arrays (NPAs). The length of NPAs was 2.2 μm and the diameter was 180–325 nm. The other method utilized the use of gold nanomesh which acts as a mask to etch the Si substrate. Fedja et al. studied that the length and diameter can also vary with the etching rate [12].

4.3 Vapor–Liquid-Solid (VLS) Technique

This technique includes the growth of high-quality SiNWs as they are prepared inside a CVD reactor. The other quality includes the dense and crystalline structure of SiNWs. VLS technique also prefers using catalysts such as Ag, Au, Cu, Sn, or Al metal nanoparticles. The commonly used precursor gases are Silane or Si tetrachloride. Inside the reaction chamber of the CVD instrument, various reactions between the reactor material and the precursor gas take place which results in the growth of a thin layer of vertically aligned SiNWs. The CVD reactor used can either be an atmospheric pressure chemical vapor deposition (APCVD) or a plasma-enhanced chemical vapor deposition (PECVD) instrument. The past studies revealed that the growth velocity affects the SiNWs parameter. When that was taken in the range of 10^{-2}-10^{3} nm min^{-1} SiNWs with different diameters and lengths were obtained. VLS technique can be separated into several categories depending on the reaction conditions and the precursor used. Later on, it was studied that hetero-structural NiS/SiO_2 nanowire/nanotubes (NW/NTs) can be prepared using an APCVD reactor. The average diameter of the obtained nanostructure was 50 nm while the length was 10 mm [13]. Swain et al. [14] reported the synthesis of SiNWs by sputtering Au on Si substrate. The deposition of Au was then executed at a temperature of 700 °C for about 1–3 h in an APCVD reactor. The deposition of SiNWs was further executed using a low-pressure chemical vapor deposition (LPCVD) reactor. The diameter of

the SiNWs was less than 3 nm. The precursor and the carrier gas used for the growth of SiNWs are mostly SiH_4 and H_2 respectively [15]. Yu et al. showed that the production of SiNWs is also possible by using Bi as the catalyst. They also studied that parameters like the length and diameter of SiNWs are completely dependent on the size of Bi particles [16].

4.4 Oxide Assisted (OA) Growth of SiNWs

This technique utilizes the growth of SiNWs using oxides and not the costly metal catalysts. The SiNWs obtained are pure and free from metal impurities. It is a method used to grow pure SiNWs using oxides instead of metals as a catalyst. In this technique, oxide plays a key role and permits the large-area growth of SiNWs with controlled dimensions. The carbothermal evaporation OAG method was used by Hutagalung et al. [17] to obtain SiNWs with a diameter in the range of 10–90 nm. The reaction was performed at a furnace temperature of 110 °C for about 6 h. The obtained SiNWs were vertically aligned and had crooked structures. Mainly, inside the reactor, the Si substrate and the source material are placed at least 12 cm away. Davenas et al. [18] produced SiNWs with a diameter of < 20 nm and length of 10 μm using an OAG technique. The mechanism of SiNWs growth was dependent on a dismutation reaction of silicon monoxide at 1200 °C. No catalyst was used in this procedure.

5 SiNWs Hybrid Solar Cell -Basic Principle

The essential components of SiNWs hybrid solar cell are n-type SiNWs, the inorganic component of the solar cell, and conducting polymers consisting of the organic part. When the sunlight of a particular wavelength is incident on the SiNWs hybrid solar cell, the electron excitation takes place from the valence shell to the conduction band (CB) and becomes free. These highly energetic electrons then diffuse and some of them reach the junction where they get accelerated by an inbuilt Galvanic potential. This process generates electromotive force due to which the light energy gets converted into electrical energy. The electron that reaches the CB of SiNWs is being injected by the electrons present in the LUMO of organic conducting polymers. Thus, the energy level matching of the organic conducting polymers and the semiconductor is essential. It is considered that the lowest occupied energy level (LUMO) of the organic conducting polymers has to be at least 0.16 eV higher than the CB of the n-type semiconductor to facilitate electron transfer to the CB from the LUMO.

The generation of photocurrent mainly includes four steps as illustrated in Fig. 6 (1) absorption of solar radiation, (2) electron hole-pair generation and its separation in a p–n junction, (3) diffusion of charge carriers (holes and electrons) in an n-type l

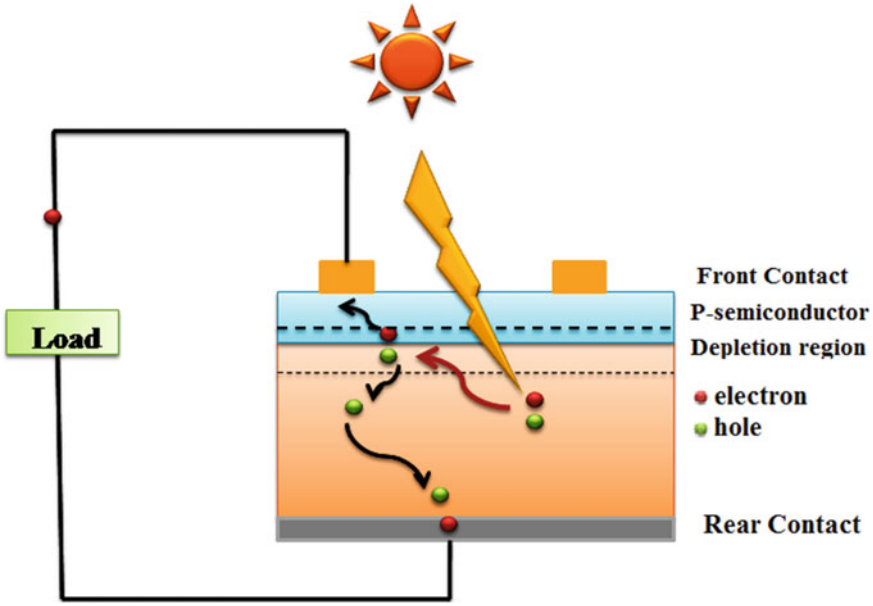

Fig. 6 The basic structure of *a* solar cell

and p-type semi-conduction material and finally (4) circuit completion at rear contact. Among the above four steps, step 1 and step 2 are important where light absorption and electron–hole pair generation occur in the p–n junction [4].

The expression showing the relationship between current density and the applied voltage is given by

$$J = J_{ph} - J_0\left[exp\left\{\frac{q(V + JR_s)}{nK_BT}\right\} - 1\right] - \frac{V + JR_s}{R_{sh}} \tag{1}$$

where J_{ph} is photocurrent density which depends upon various factors such as properties of the materials used, device structure, the power of incident light, etc., J_0 stands for reverse saturation current density, q corresponds to the electronic charge, V is applied voltage, K_B stands for Boltzman's constant, R_s is series resistance, T is absolute temperature, and R_{sh} is the shunt resistance. The practically studied solar cell model shows J contains both series and shunt resistance as shown by the equivalent circuit model with resistance. From this circuit diagram, it is clear that the diode is connected in parallel with J_{ph} and R_{sh} and is connected in series with R_{sh}. The last term in the equation is called shunt current, which depends on the values of both of the resistances (Fig. 7).

The open-circuit voltage (V_{oc}) of the solar cell is described as the voltage without the current flow ($J = 0$). Again V_{oc} is obtained as given below [19]

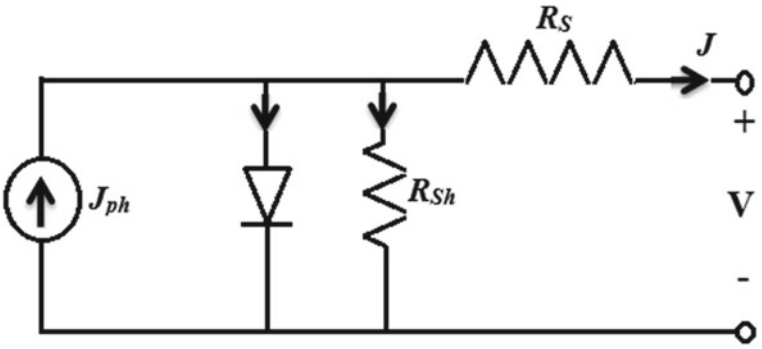

Fig. 7 Circuit diagram of a photovoltaic device

$$V_{oc} = \frac{K_B T}{q} \ln\left(\frac{J_{ph}}{J_0} + 1\right) \tag{2}$$

Finally, the fill factor (FF) of the solar cell is obtained as given below

$$FF = \frac{P_{Max}}{V_{oc} \times J_{sc}} \tag{3}$$

It can be defined as the ratio of P_{Max} to the product of V_{oc} and J_{sc}. P_{Max} is the maximum power generated from the solar cell. The FF is highly affected by the value of the resistance. FF increases proportionally with the increase in the value of R_{sh} while decreases with the rise in the value of R_s.

Finally, the power conversion efficiency of a solar cell can be obtained by the equation given below

$$Efficiency(\eta)\% = \frac{V_{oc} \times J_{sc} \times FF}{P_{in}} \tag{4}$$

where J_{sc} is short circuit current density and P_{in} is the power input. The schematic of the J-V characteristic curve of a solar cell is shown in Fig. 8. It has been observed from Eq. (4) that the efficiency of a solar cell is directly related to FF, V_{oc} and J_{sc}.

6 Recombination Loses

The generated electron–hole pair remains separated and mobile for a very short period after which they return to the lowest energy state by the process called recombination. During the recombination process, the separated electrons and holes again recombine by emitting some amount of energy in terms of photons or phonons. The

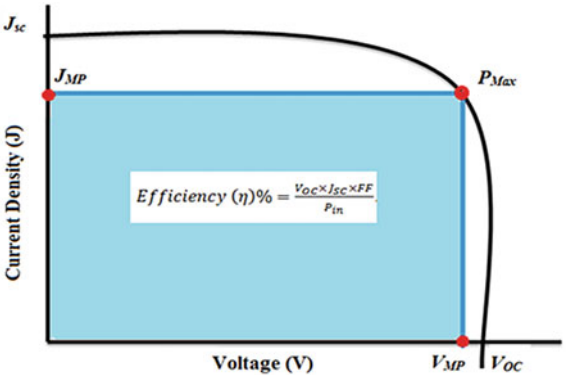

Fig. 8 J-V characteristic curve of a solar cell

process of recombination is further divided into three main categories: (i) Radiative recombination, (ii) Auger recombination, and (iii) Shockley–Read–Hall (SRH) recombination. The different types of recombination processes are shown in Fig. 9

In the radiative recombination process band to band, recombination takes place. The electrons residing in the CB and the holes in the VB combine and emit a photon. This type of recombination process takes place mostly in the direct bandgap semiconductors.

The Auger recombination process contains three carriers. In this process, the energy emitted by the recombination of the charge carriers is captured by the third carrier. This type of recombination is responsible for reducing the lifetime and efficiency of a solar cell device and only takes place in impure and defective materials. The SRH recombination process takes place in two different steps. In the first step, the electrons or holes are trapped in the forbidden energy level introduced due to the defects present in the crystal system. In the next step, the hole or electron gets excited to the same energy levels just before the electrons get thermally re-emitted

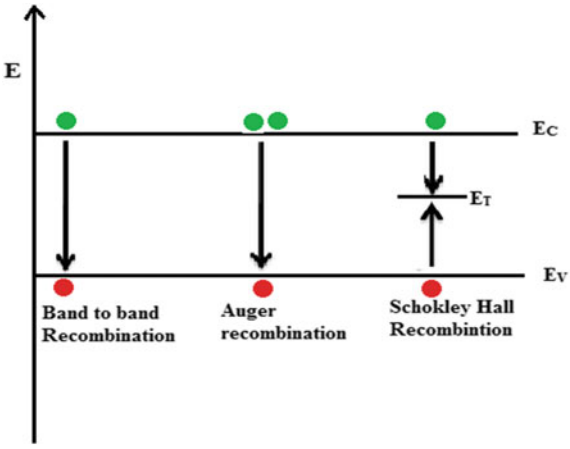

Fig. 9 Types of recombination that takes place in a solar cell

into the conduction band and then the recombination occurs. All of the recombination processes explained above limit the lifetime of charge carriers. The generated electron–hole pair is lost due to these recombination processes and hence no power is generated by the solar cell device.

7 SiNWS Hybrid Solar Cell State of Art

The excellent electrical optical and physical properties of SiNWs make it an important material for different types of solar cells. As reported by the earlier research, SiNWs Hybrid solar cells are mainly separated into two classes based on the type of junction (i.e. axial and radial). In the radial junction solar cells, the charge travels radially from the center of the SiNWs to the surrounding of the solar cell, while in axial junction SiNWs hybrid solar cell the charge progresses longitudinally along the SiNWs. Solar cells are mainly designed in a way to separate the charge carriers as much as possible, but thermalization forces the electrons and holes to recombine and thus fails to collect the charges at the opposite ends of the solar cell. The minority charge carrier collection capability of the solar cells depends on the diameter of the NWs. The diameter of the SiNWs is as small as the diffusion length where the charge separation and collection takes place such that more minority carriers can be collected. If compared the radial junction with the axial junction hybrid solar cell then in radial junction hybrid solar cell the charge carrier collection distance is less and compared to the diffusion length of minority carriers. Therefore, the radial junction is more favored over the axial junction in solar cells. The excellent properties of the radial junction solar cell include excellent charge separation, low reflection, relaxation in interfacial strain, and above all the minimum reflectivity (Fig. 10).

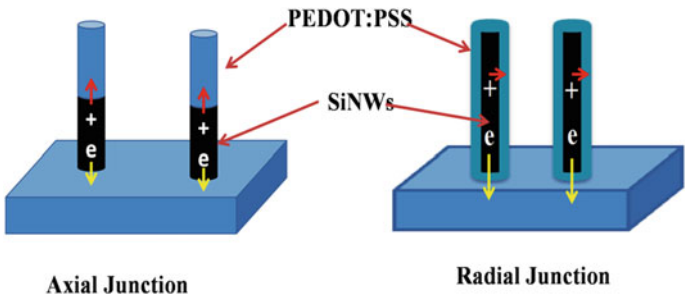

Fig. 10 Different types of SiNWs/organic heterojunction

8 Inorganic Heterojunction SiNWs Solar Cells

Heterojunction SiNWs solar cell is prepared by combining another inorganic material with SiNWs such that the overall solar cell efficiency is improved. These types of structures can either be obtained by growing SiNWs on bulk Si substrate or by passivation of some inorganic layer on the SiNWs by CVD technique. The incorporation of SiNWs in the solar cell increases the surface area so as the recombination rate. Therefore the surface of the SiNWs should be passivated evenly by the proper coating of the Si–H layer.

Leontis et al. [20] reported the fabrication of n-type SiNWs for its application in c-Si solar cells. The reflectivity of the SiNWs was comparatively lower than the random Si nanopyramids used in other conventional c-Si solar cells. They have also shown a comparative study between the bulk Si solar cell and SiNWs solar cell. It was observed that SiNWs solar cell obtained a 45% increase in efficiency than the bulk Si solar cell. Jia et al. fabricated core–shell TCO/a-Si/Si nanowires (SiNWs) heterojunction solar cells and obtained an efficiency of 7.29% at AM1.5 [21]. The improvement of the solar cell efficiency was attributed to the formation of a-Si/Si nanowires radial heterojunction and also the use of a three-step cleaning procedure of SiNWs which might deteriorate the performance of the solar cell.

9 Organic/Inorganic SiNWs Hybrid Solar Cells

9.1 SiNWs/PEDOT:PSS Hybrid Solar Cell

A combination of inorganic and organic parts consisting of a p–n junction is called a hybrid solar cell. In the SiNWs/PEDOT:PSS hybrid solar cell the inorganic part is composed of thin and vertically aligned SiNWs, while the organic part consists of PEDOT:PSS. The excellent light trapping of SiNWs reduces the cost of solar cells by using a very thin absorber layer of bulk Si. Although the current research shows the highest efficiency of 17.4% for the bulk Si/PEDOT:PSS it is not practical to use a large piece of bulk that leads toward the high cost of hybrid solar cells [22]. Therefore SiNWs are a brilliant replacement of bulk in a hybrid solar cell that claims to obtain higher efficiency at a very reasonable cost. The efficiency of hybrid solar cells can reach up to 13.11% using SiNWs in SiNWs/PEDOT:PSS solar cell Yu et al. [23]. It was also analyzed that compared to the pristine SiNWs, the SiNWs with the lowest reflectivity showed better performance. Recently, various attempts have been made by researchers across the globe to achieve better solar cell efficiency for the SiNWs/PEDOT:PSS hybrid solar cells. A better-performance and cost-effective hybrid radial junction solar cell were fabricated using *n*-type SiNWs and PEDOT:PSS [24]. The hybrid solar cell with the NWs length of 0.57 mm showed the best cell performance having a PCE of 9.3%. The incorporation of AgNPs in SiNWs also showed some improvement toward the solar cell performance, due to the plasmonic

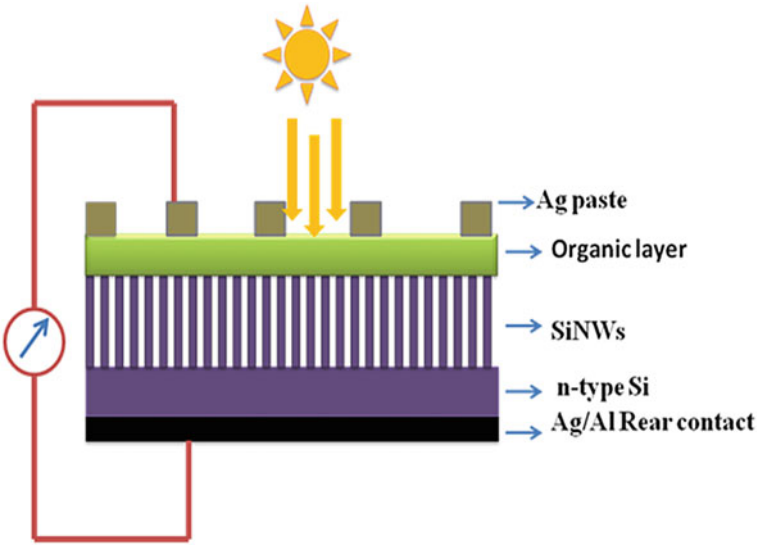

Fig. 11 SiNWs hybrid solar cell

backscattering effects of AgNPs on the back surface, leading to an overall improvement in PCE compared to similar devices with SiNWs without AgNPs [25]. Furthermore the incorporation of rGO in the SiNWs/PEDOT:PSS hybrid solar effectively increases the PCE. The excellent properties of rGO combined with PEDOT:PSS help an easy movement of the charge carriers [26] (Fig. 11).

9.2 SiNWs/P_3HT:PCBM Hybrid Solar Cell

In this type of SiNWs hybrid solar cell, the organic conduction material is poly(3-hexylthiophene:phenyl-C61-butyric acid methyl ester (P3HT:PCBM) and the inorganic part is SiNWs. It has been observed by the past studies that SiNWs combined with P_3HT:PCBM conducting polymer obtained an efficiency of 1.21 to 1.91% with the current densities of 7.17 to 11.61 mA/cm^2 [27]. Eisenhawer et al. fabricated a hybrid solar cell with SiNWs/P_3HT:PCBM heterojunction. The solar cell showed a very good efficiency of 4.2%. In this case, the SiNWs were produced by the VLS growth technique using Au catalyst in a UHV CVD reactor [28]. This solar cell obtained an improvement of 10% as compared to that of the pristine solar cells without nanowires. The improvement in solar cell performance was the result of an enhanced electron transport mechanism forced by silicon nanowires. The effect of SiNWs purity on hybrid solar cell performance was also studied. Jeon et al. reported that after performing the HF and HCl treatment on SiNWs the efficiency of the SiNWs/P_3HT:PCBM hybrid solar cell was improved from 0.35 to 1.5%. The result

shows the significance of acid treatment on SiNWs for obtaining better solar cell efficiency [29].

9.3 SiNWs/Other Polymer Heterojunction Solar Cells

To obtain better efficiency, various types of organic conducting polymers were combined with SiNWs to fabricate a hybrid solar cell. These attempts made by different groups only helped to improve the result. Different types of inorganic and organic heterojunctions were prepared like PEDOT:PSS/P_3HT: SiNWs by Devenasa et al. SiNWs in this case were grown by VLS technique without using a catalyst. The as-obtained solar cell showed an open-circuit voltage of 0.68 V [18]. The other combinations include PEDOT:PSS/SiNWs:PVK and PEDOT:PSS/SiNWs:MEH-PPV. Dkhil et al. studied the photovoltaic effect of the above-mentioned solar cells and found that SiNWs:PVK nanocomposite solar cells showed better results than MEH-PPV solar cells [30]. Later on He et al. reported the fabrication of a hybrid solar cell based on silicon nanorods (SiNRs) and an organic semiconductor named Spiro-OMeTAD [31]. The device showed an efficiency of 10.3% with an area of 1 cm^2. The length of the SiNWs was 0.35 μm. Chehata et al. combined the MEH-PPV polymer matrix with SiNWs to produce a hybrid heterojunction solar cell [15]. The optimization of the SiNWs amount was done for obtaining better solar cell performance. The optimum composition of MEH-PPV: SiNWs was 1:2 to obtain a PCE of 5.6%.

10 Conclusion

SiNWs are one of the most widely studied materials in hybrid solar cells owing to their exceptional electrical and optical properties. The one-dimensional nature of SiNWs improves the electron mobility pathway due to the confinement of electrons in a particular direction. SiNWs are reported to have an excellent light-harvesting property which is beneficial for solar cells. Moreover, by changing the length and diameter of SiNWs, it is possible to tune the bandgap, which is another advantage for solar cells. Considering the cost, hybrid solar cells prepared by SiNWs are far more cost-effective than Si solar cells. In Si solar cells thick wafer of Si is used which makes it costly, while in SiNWs solar cells a small Si wafer is required to produce the same amount of PCE to the solar cells. Therefore, it is logical that SiNWs are a magic material for solar cells.

References

1. Dixit S, Shukla AK (2018) Optical properties of lonsdaleite silicon nanowires: a promising material for optoelectronic applications. J Appl Phys 123:224301
2. Brönstrup G, Jahr N, Leiterer C, Csäki A, Fritzsche W, Christiansen S (2010) Optical properties of individual silicon nanowires for photonic devices. ACS Nano 4:7113–7122
3. Peng KQ, Lee ST (2011) Silicon nanowires for photovoltaic solar energy conversion. Adv Mater 23:198–215
4. Park I, Li Z, Pisano AP, Williams RS (2010) Top-down fabricated silicon nanowire sensors for real-time chemical detection. Nanotechnology 21
5. Katiyar AK, Sinha AK, Manna S, Ray SK (2014) Fabrication of Si/ZnS radial nanowire heterojunction arrays for white light-emitting devices on Si substrates. ACS Appl Mater Interf 6:15007–15014
6. Cui Y, Zhong Z, Wang D, Wang WU, Lieber CM (2003) High-performance silicon nanowire field-effect transistors. Nano Lett 3:149–152
7. Peng K, Zhang M, Lu A, Wong NB, Zhang R, Lee ST (2007) Ordered silicon nanowire arrays via nanosphere lithography and metal-induced etching. Appl Phys Lett 90:28–31
8. Bai F, Li M, Huang R, Li Y, Trevor M, Musselman KP (2014) A one-step template-free approach to achieve tapered silicon nanowire arrays with controllable filling ratios for solar cell applications. RSC Adv 4:1794–1798
9. Moiz SA, Alahmadi ANM, Aljohani AJ (2020) Design of silicon nanowire array for PEDOT: PSS-silicon nanowire-based hybrid solar cell. Energies 13:3797
10. Jeon M, Kamisako K (2009) Synthesis and characterization of silicon nanowires using tin catalyst for solar cells application. Mater Lett 63:777–779
11. Wang HP, Lai KY, Lin YR, Lin CA, He JH (2010) Periodic Si nanopillar arrays fabricated by colloidal lithography and catalytic etching for broadband and omnidirectional elimination of fresnel reflection. Langmuir 26:12855–12858
12. Wendisch FJ, Rey M, Vogel N, Bourret GR (2020) Large-scale synthesis of highly uniform silicon nanowire arrays using metal-assisted chemical etching. Chem Mater
13. Ge JP, Wang J, Zhang HX, Li YD (2004) A general atmospheric pressure chemical vapor deposition synthesis and crystallographic study of transition-metal sulfide one-dimensional nanostructures. Chem A Eur J 10:3525–3530
14. Swain BS, Swain BP, Hwang NM (2010) Investigation of electronic configuration and plasmon loss spectra in Au-catalyzed silicon nanowire networks. J Appl Phys 108:1–7
15. Chehata N, Ltaief A, Ilahi B, Salam B, Bouazizi A, Maaref H, Beyou E (2014) Improved photovoltaic performance of silicon nanowires/conjugated polymer hybrid solar cells. Synth Met 191:6–11
16. Yu L, Fortuna F, O'Donnell B, Jeon T, Foldyna M, Picardi G, Roca I Cabarrocas P (2012) Bismuth-catalyzed and doped silicon nanowires for one-pump-down fabrication of radial junction solar cells. Nano Lett 12:4153–4158
17. Hutagalung SD, Yaacob KA, Aziz AFA (2007) Oxide-assisted growth of silicon nanowires by carbothermal evaporation. Appl Surf Sci 254:633–637
18. Davenas J, Ben DS, Cornu D, Rybak A (2012) Silicon nanowire /P3HT hybrid solar cells: effect of the electron localization at wire nanodiameters. Energy Proc 31:136–143
19. Fonash SJ (2010) Solar cell device physics. Sol Cell Device Phys. https://doi.org/10.1016/C2009-0-19749-0
20. Leontis I, Botzakaki MA, Georga SN, Nassiopoulou AG (2018) Study of Si nanowires produced by metal-assisted chemical etching as a light-trapping material in n - type c - Si solar cells. ACS Omega 3:10898–10906
21. Jia G, Steglich M, Sill I, Falk F (2012) Solar energy materials & solar cells core—shell heterojunction solar cells on silicon nanowire arrays. Sol Energy Mater Sol Cells 96:226–230
22. Zielke D, Niehaves C, Lövenich W, Elschner A, Hörteis M, Schmidt J (2015) Organic-silicon solar cells exceeding 20% efficiency. Energy Proc 77:331–339

23. Liu Z, Wang H, Fung M, Lee C (2013) Low-cost solar cell based on a composite of silicon nanowires and a highly conductive nonphotoactive polymer. Chem Eur J, 17273–17276
24. Sato K, Dutta M, Fukata N (2014) Inorganic/organic hybrid solar cells: optimal carrier transport in vertically aligned silicon nanowire. Nanoscale 11:6092–6101
25. Sharma M, Pudasaini PR, Ruiz-zepeda F, Elam D, Ayon Ultrathin AA (2014) Flexible organic—inorganic hybrid solar cells based on silicon nanowires and PEDOT : PSS. ACS Appl Mater Interf 6:4–11
26. Bhujel R, Rai S, Deka U, Sarkar G, Biswas J (2021) Bandgap engineering of PEDOT : PSS / rGO a hole transport layer for SiNWs hybrid solar cells. Bull Mater Sci 0123456789
27. Huang J, Hsiao CS Chao, Lin C (2009) Well-aligned single-crystalline silicon nanowire hybrid solar cells on glass. Sol Energy Mater Sol Cells 93:621–624. https://doi.org/10.1016/j.solmat.2008.12.016
28. Eisenhawer B, Sensfuss S, Sivakov V, Pietsch M, Andr G (2011) Increasing the efficiency of polymer solar cells by silicon nanowires, pp 315401. https://doi.org/10.1088/0957-4484/22/31/315401.
29. Jeon T, Geffroy B, Tondelier D, Yu L, Jegou P, Jousselme B, Palacin S, Roca P, Bonnassieux Y (2012) Solar energy materials & solar cells effects of acid-treated silicon nanowires on hybrid solar cells performance. Sol Energy Mater Sol Cells 1–6
30. Ben DS, Bourguiga R, Davenas J, Cornu D (2012) Influence of the polymer matrix on the efficiency of hybrid solar cells based on silicon nanowires. Mater Sci Eng B 177:173–179
31. He L, Jiang C, Lai DH, He L, Jiang C, Lai D, Wang H (2011) Highly efficient Si-nanorods/organic hybrid core-sheath heterojunction solar cells Highly efficient Si-nanorods/organic hybrid core-sheath heterojunction solar cells. Appl Phys Lett 021104:2011–2014

Chapter 3
Lead-Free Dielectrics: A State-Of-The-Art for Green Energy Storage

Swetapadma Praharaj and Dibyaranjan Rout

1 Introduction

With greater advancements in science and technology, the lifestyle and lifespan of the human race are improving which has lead to problems like overpopulation and excessive use of energy. A survey speaks that the global energy consumption has increased from 54,207 TWh in 1973 to 111,125 TWh in 2016 [1] and is expected to increase much more in the future. The present demands for energy probably arise from higher living standards, reduction in poverty, and decreasing mortality rates. As per a review published by Robert Rapier in Forbes magazine in June 2020, fossil fuels including coal, natural gas, and petroleum cater to at least 84% of world energy needs [2]. Not only it is creating global warming and air pollution but also leading to the fast depletion of fossil fuels. Hence there is an urgent surge to shift our energy dependence from fossil fuels to cleaner and greener renewable sources such as solar, wind, tidal, geothermal, etc. However, most of the renewable sources are intermittent which poses challenges in harnessing them as and when needed. Conversion of renewable energy into other reliable forms (usually electricity) might be one of the feasible solutions to overcome the above-mentioned insecurities by implementing efficient and reliable electrical energy storage systems. Several energy storage technologies such as batteries, solid oxide fuel cells (SOFC), electrochemical capacitors (ECs), flywheels, superconducting magnetic energy storage (SMES), and electrostatic/dielectric capacitors have brought a path-breaking revolution in this area of interest. Though all of these systems are quite efficient, none of them fulfill the conditions of both high energy density and power density simultaneously. Ragone

S. Praharaj · D. Rout (✉)
Department of Physics, School of Applied Sciences, KIIT Deemed to be University, Bhubaneswar 751024, Odisha, India
e-mail: droutfpy@kiit.ac.in

S. Praharaj
e-mail: spraharajfpy@kiit.ac.in

B. P. Swain (ed.), *Advances in Nanostructured Materials*, Materials Horizons: From Nature to Nanomaterials, https://doi.org/10.1007/978-981-16-8391-6_3

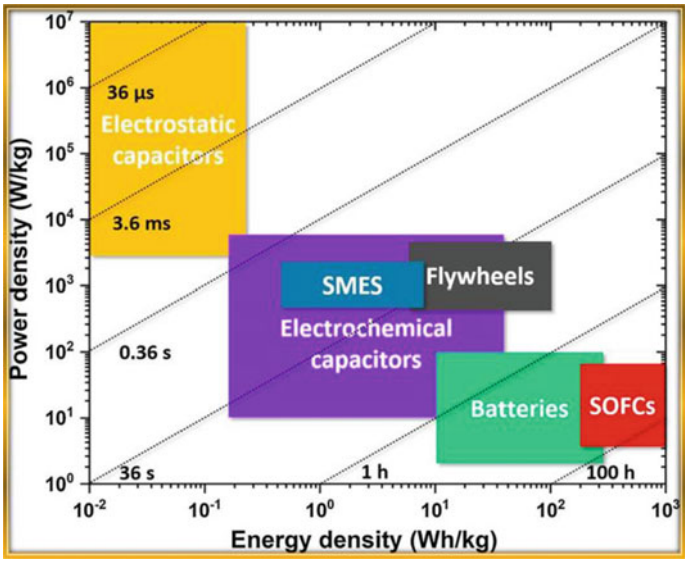

Fig. 1 Ragone plot comparing different energy storage devices: electrostatic capacitors, superconducting magnetic energy storage systems (SMES), electrochemical capacitors, flywheels, batteries, and solid oxide fuel cells (SOFCs) [3]

plot (Fig. 1) seems to be useful and is widely used in benchmarking the performance of the presently known energy storage devices based on a relative graph between energy density and power density.

While batteries and fuel cells demonstrate high energy density and low power density, dielectric capacitors exhibit contrasting features. Meanwhile, ECs possess medium energy and power density but suffer from large leakage current (~mA), low operating voltage (<3 V) and involves a high cost (9500 USD/kWh) [4, 5]. Dielectric capacitors are found to be most suitable for cost-effective, high voltage, and large-scale applications with their unique properties of faster charge–discharge rates (~ns) and fairly good power density (up to 10^8 W/kg). Such unique properties make them appropriate for super high power electronic systems such as medical defibrillators, electrical weapons, spacecraft, satellites, hybrid electric vehicles as shown in Fig. 2. They occupy almost 25% of the volume and weight of portable and power electronics as well as pulsed power systems.

One of the disadvantages of the dielectric capacitors is relatively low energy density as shown in Fig. 1. Thus it is very important to elevate the energy density of the dielectric materials used in capacitors as it will enhance the volumetric efficiency of the devices benefitting the miniaturization and easy integration of consumer electronics. For most of these applications, we rely on lead-based materials due to their unsurpassed performances which have inevitably invited environmental concerns. Blindly addressing the energy issues by neglecting lead emission would be accompanied by secondary damage to the mother earth. To plausibly elevate the energy

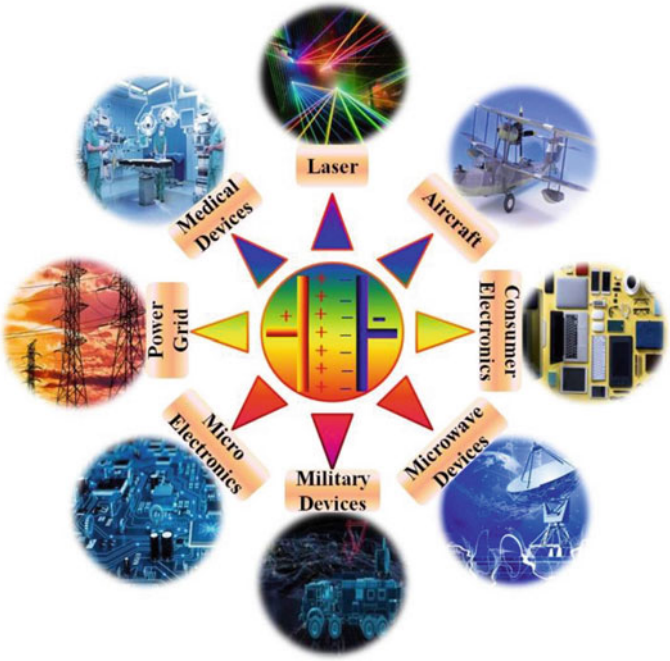

Fig. 2 Various applications of dielectric capacitors as energy storage devices

crisis without secondary Pb pollution, lead-free dielectric could be possibly the best solution for energy storage capacitors. In this chapter, we would draw the attention of the readers to the importance of lead-free dielectric materials from a capacitor point of view and record the probable measures of enhancing their storage performance.

2 Fundamentals of Dielectric Energy Storage in Capacitors

A typical dielectric capacitor is designed by sandwiching a dielectric layer between two conductive metal plates (e.g., Ag, Au, or Pt) as electrodes. The energy storage capability of the dielectric layer is determined in terms of capacitance given by the basic equation:

$$C = \frac{\varepsilon_0 \varepsilon_r A}{d}, \tag{1}$$

where ε_0 is the dielectric permittivity of free space (8.85 X 10^{-12} F/m); ε_r is the relative permittivity (or dielectric constant) of the dielectric material; A denotes the overlapping area of both the electrodes, and d is the thickness of the layer. The

capacitance is independent of the potential difference between the plates and charges stored on it but depends only on the geometry of the capacitor and the permittivity of the dielectric layer.

On applying an external voltage V, positive and negative charges start accumulating on the plates which are conventionally known as the charging process. Charging creates an internal electric field that is opposite in direction to the externally applied field. Piling up of the charges on the capacitor plates leads to an increase in the internal field and finally this process ends up when the internal electric field comes at par with the applied field. Supposing that charges $+Q$ reside on the capacitor plate, then the capacitance is given by Q/V. Many a time it is found that the relative permittivity of the dielectrics is affected by the external bais which in turn alters the capacitance. In such cases, capacitance may be expressed in terms of incremental variation:

$$C = \frac{dq}{dv} \tag{2}$$

During the charging process, work is done by the applied field in moving the charges and hence electrostatic energy is stored is dielectric and can be calculated as

$$W = \int_0^{Q_{\max}} V dq, \tag{3}$$

where Q_{max} is the maximum stored charge and dq is the incremental change in charge stored.

One of the salient figures of merit for energy storage dielectric capacitors is the total energy density (J) defined as energy stored per unit volume and is expressed as

$$J = \frac{W}{Ad} = \frac{\int_0^{Q_{\max}} V dq}{Ad} = \int_0^{D_{\max}} E dD, \tag{4}$$

where D refers to the electric displacement in the dielectric layer under the corresponding electric field E. In the case of dielectrics with high relative permittivity, the electric displacement $D(= \varepsilon_0 \varepsilon_r E)$ is very close to the polarization P. Hence Eq. (4) may be rewritten as

$$J = \int_0^{P_{\max}} E dP = \int_0^{E_{\max}} \varepsilon_0 \varepsilon_r E dE \tag{5}$$

Here E_{max} is the maximum electric field induced by the charges accumulated during the charging process.

The actual charge stored is usually determined by J_{res} (recoverable energy density) rather than J and is illustrated as

$$J_{rec} = \int_{P_r}^{P_{\max}} E\,dP \tag{6}$$

The energy storage efficiency for the dielectric material can be calculated as

$$\eta = \frac{J_{rec}}{J} \tag{7}$$

The above equations signify that both J and J_{rec} can be derived from polarization versus electric field ($P - E$) loops [6] as shown in Fig. 3a-f.

In the figure, we highlight four types of dielectric materials. The first category is linear dielectric in which the permittivity is independent of electricity due to the absence of domain structure. Hence Eq. (5) reduces to

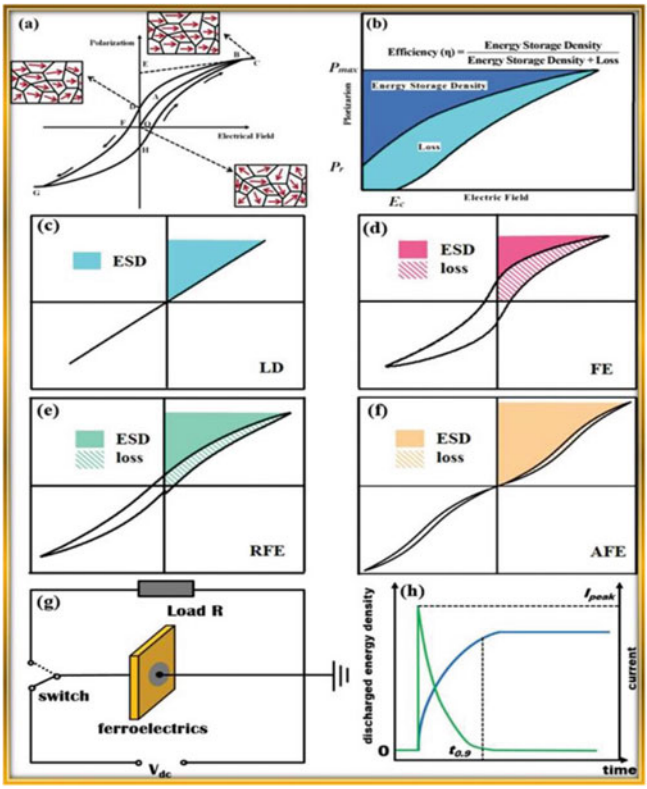

Fig. 3 **a** Switching of ferroelectric domains during the charge–discharge cycle; **b** Schematic of energy storage density (ESD) and efficiency (η) shown in P–E loop; **c-f** Schematic of ESD and loss in linear dielectric (LD), ferroelectrics (FE), relaxor ferroelectrics (RFE) and antiferroelectrics (AFE) respectively; **g** Basic circuit for measuring discharge energy density; **h** Discharge energy density and current as a function of time [7]

$$J = \frac{1}{2}\varepsilon_0 \varepsilon_r E^2 \tag{8}$$

The second group refers to the ferroelectric materials (FE) which have a well-defined domain structure. The most typical feature of this group of materials is the existence of a non-linear relationship between polarization and electric field giving rise to a square hysteresis loop. This is caused by the switching of the domain polarization direction with the direction and magnitude of the applied field. As such growth, disappearance, and domain wall displacements greatly influence the structure and electrical properties of ferroelectric materials, the third and fourth categories consisting of relaxor ferroelectrics (RFE) and antiferroelectrics (AFE) are both subgroups of FEs. Relaxor ferroelectrics containing polar nano regions (PNRs) show the ease of domain/domain wall motion leading to slimmer *P–E* loops and enhanced energy storage density. RFEs exhibit a unique feature of diffuse phase transition which ensures better thermal stability [8]. On the contrary, in the case of AFEs polarization and electric field follow a linear relationship below a certain critical electric field Ec. However, the loop becomes non-linear above Ec. The existence of two sets of lattice structures with opposite polarization directions in antiferroelectric leads to double *P–E* loops. Such a peculiarity is responsible for high energy storage density for AFEs.

The above-discussed methodology of ascertaining the energy storage density is often referred to the as quasistatic method. There is yet another approach to measuring the storage density called the dynamic method. In this procedure, the discharged energy density is derived from charge–discharge measurements. At first, a capacitor with the sample dielectric is charged by the applied external bias, and charges are stored on the capacitor plates. Then the same capacitor is allowed to discharge through an appropriate load resistor R_L. All this is carried out in a simple switching circuit (MOSFET is used as the electronic switch) as shown in Fig. 3g. If $I(t)$ and $V(t)$ are the voltage and currently recorded in R_L at any instant of time t during the discharging process, then the discharged energy density is (J_{dis}) is given by

$$J_{dis} = \frac{\int R_L I^2(t)dt}{V_{vol}} = \frac{\int V^2(t)dt}{R_L V_{vol}}, \tag{9}$$

where V_{vol} refers to capacitor volume. It is important to note that $R_L >>$ equivalent series resistor of the capacitor so that maximum stored energy can be delivered to the load resistor and the estimated discharge energy density is almost equal to the stored energy density [9]. Nevertheless, the energy density (in the dynamic method) is determined by calculating the integrated area in the *P–E* loop and is often more than that obtained by the charge–discharge method [10, 11]. Such kind of inconsistency may be ascribed to diverse mechanisms of *P–E* loops and dynamic discharge current at different frequencies [11, 12]. It is a usual practice to measure the *P–E* loops under low frequencies, i.e., on a scale of milliseconds. On the other hand, charge–discharge measurements are carried out on a microsecond scale. At higher frequencies of an electric field, domains/domain walls are clamped due to which their switching is

hindered leading to more energy loss. This phenomenon is more pronounced in the case of materials with macro-sized domain structure, i.e., FE and AFE. However curbing the domain size to nano-level (as in the case of RFE) facilitates faster and easier domain wall motion reducing the energy loss to a greater degree [13]. Hence the charge–discharge method is more suitable for assessing the performance of capacitors used in pulse power applications where they need to release the stored energy in the shortest possible time. Maximum current I_{peak} during the discharging process and $t_{0.9}$ (Fig. 3h) representing the 90% of discharge time are generally employed to characterize the energy storage capabilities of capacitors for high power and pulse power applications under a given load resistor [13–15]. Besides, *P–E* loop method is appropriate for estimating the performance of the material itself since the domains can switch their polarization direction fairly well under low-frequency measurements.

Apart from energy density, there are few other application-oriented figures of merit for capacitor materials include power density and dielectric breakdown strength (for high pulse power capacitors); ripple current capability, equivalent series resistance, and RC constant (for coupling capacitors).

3 Energy Storage in Lead-Free Materials: Bulk to Nano

3.1 Ferroelectrics

Ferroelectrics are materials featured by a finite polarization even in the absence of an external electric field. This polarization switches reversibly between two stable states depending on the direction of an applied field. These localizations of different polarization co-exist inside the FE materials are conventionally known as FE domains [16]. The switching behavior of the ferroelectric domains is studied experimentally with the help of *P–E* loops giving rise to the fingerprint square hysteresis loop. FEs with high dielectric permittivity are often associated with high dielectric loss and large remnant polarization yielding low values of recoverable energy density and dielectric breakdown strength. Thus it can be said that conventional ferroelectrics are not quite appropriate for energy storage. However, in recent times, many modifications have been proposed by different researchers to improve the energy storage capability of classical ferroelectrics. Some of the potential lead-free candidates identified in this regard include $BaTiO_3$ (BT), $SrTiO_3$ (ST), $Na_{0.5}Bi_{0.5}TiO_3$ (NBT), and $BaTiO_3$-$BiMeO_3$ (BT-BMe) based systems.

Barium titanate (BT) is one of the typical perovskite materials exhibiting an optimum dielectric permittivity along with outstanding ferroelectric properties. At the same time, it possesses a low Curie temperature and substantial remnant polarization which are not beneficial from an energy storage point of view. Efforts have been made in the past by some researchers to augment the properties of BT by using other ions as dopants. Substitution of Ca^{2+} at the A-site of the perovskite ($Ba_{0.7}Ca_{0.3}TiO_3$) gives a comparatively higher recoverable energy density of 1.41 J/cm^3 which is 40%

greater than pristine BT and moderate energy efficiency of 61% [17]. Similarly, the substitution of Zr^{4+} (existing only in one valance state) at the B-site which is already occupied by multivalent Ti ions (Ti^{3+} and Ti^{4+}) reduces the loss factor to a great extent by minimizing the electron hopping conduction between Ti^{3+} and Ti^{4+} [18]. Materials considered to be ideal for energy storage are often expected to be associated with high dielectric breakdown strength. Reducing the porosity and grain size with uniform grain size distribution may prove to be advantageous in such cases. In one of the research works, $Ba_{0.4}Sr_{0.6}TiO_3$ (a derivative of BT) was sintered in O_2 atmosphere to reduce the grain size down to 0.44 μm. sintering in O_2 forbids the creation of oxygen vacancies inhibiting grain growth. Breakdown strength of 16.72 kV/mm, the energy storage density of 1.0081 J/cm^3, and efficiency of 73.78% were achieved under this condition [19]. Sodium bismuth titanate or $Na_{0.5}Bi_{0.5}TiO_3$ (NBT) is another potential ferroelectric but a high remnant polarization (~39 μC/cm^2) and large leakage current hinder its energy storage performance. Several investigations have been focused on the development of NBT-based solid solutions and composites to improve their storage capability. Yao et al. [20] improved the storage properties of $0.9(0.94NBT\text{-}0.06BT)\text{-}0.1NaNbO_3$ by introducing ZnO as a dopant. Zn^{2+} ions in the B-site greatly boosted the dielectric constant (3218 at room temperature and 1 kHz) and increased the difference between remnant polarization and maximum polarization due to the local distortions of the perovskite unit cell.

3.2 Relaxor Ferroelectrics

Grain size, crystallite size, domain width, and defect structures are some crucial parameters to decide the storage properties of the materials. Conventional ferroelectrics even after modifications could attain a maximum energy storage efficiency of 50–60% owing to micrometer grain sizes and sub-micrometer domain widths. Domain wall mobility or switching which has a major contribution in determining the polarization behavior provides much less output in the case of optimized ferroelectric materials. An appropriate extension to the nanoworld is dispensed by relaxor ferroelectrics with nanoscale polarization disorders giving rise to natural nanometer-size polar structures even in bulk materials. These polar structures of polar nano regions (PNRs) are highly mobile and can dynamically change over several orders in response to external stimuli, e.g., electric field [21]. Being very small in feature size, these PNRs can flip easily on changing the direction of the applied electric field giving rise to slim $P-E$ loops, large maximum polarization, small remnant polarization, and moderate dielectric breakdown strength. Moreover, RFEs often exhibit fairly good temperature stability of energy storage properties due to their unique characteristic of diffuse phase transitions with temperature [22]. Few cases will be elaborated on here. Zhao et al. [23] modified BT (a known ferroelectric) by introducing $Bi(Ni_{2/3}Ta_{1/3})O_3$ as the end component which disrupted the long-range ferroelectric order of the parent compound into nano-sized PNRs. They noticed a crossover from FE to RFE with the

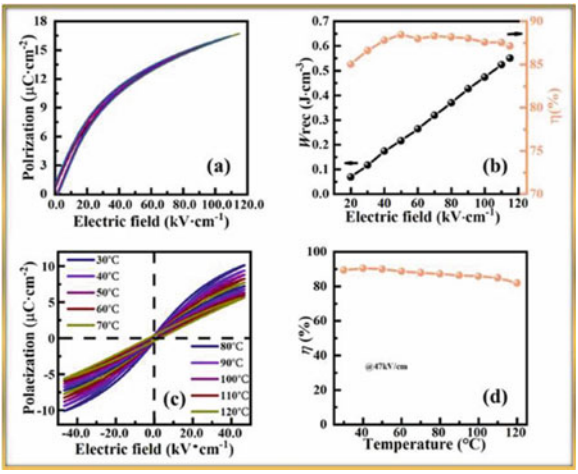

Fig. 4 **a** *P–E* loops **b** Recoverable energy density (W_{rec}) and η of $0.95BaTiO_3$-$0.05Bi_{0.5}Na_{0.5}TiO_3$ under different test electric fields; **c** *P–E* loops **d** η of $0.95BaTiO_3$-$0.05Bi_{0.5}Na_{0.5}TiO_3$ at 47 kV/cm in the temperature range 30 – 120 °C [23]

appearance of slim polarization hysteresis loops and extremely low remnant polarization. The composition with $0.05Bi(Ni_{2/3}Ta_{1/3})O_3$ demonstrated a recoverable energy density of 0.55 J/cm^3 with an efficiency of 87.15% at 117 kV/cm. In addition to that, the same composition also showed excellent temperature stability of energy storage properties (Fig. 4). Superior energy storage performance was observed in relaxor NBT-xBaZrO$_3$ compositional series with a slim polarization hysteresis loop and small remnant polarization. Besides, the replacement of Na^+ with higher valent Ba^{2+} reduces the grain size of the system gradually resulting in improved breakdown strength. With added advantages of excellent temperature stability and fatigue resistance, 0.75NBT-0.25BaZrO$_3$ displays a recoverable energy density of 1.56 J/cm^3 and high efficiency of 80.56% [24]. Similar studies have been conducted on NBT based systems to revamp the storage properties. In a ternary system based on NBT ((1-x)0.65NBT-0.35$Bi_{0.2}Sr_{0.7}TiO_3$)-xBaSnO$_3$), the addition of BaSnO$_3$ as an end member not only boosted the energy storage performance but also exhibited a thermally stable high dielectric constant. For 0.2 BaSnO$_3$, recoverable energy as high as 3.75 J/cm^3, efficiency 84.8%, and an outstanding power density of 38.73 MW/cm^3 could be achieved making it promising for pulsed power capacitor applications [25].

3.3 Antiferroelectrics

Antiferroelectrics is named so due to the presence anti parallel dipole moments and a zero net polarization, unlike ferroelectrics. Under substantially high electric field (AFE-FE phase switching field E_F), these antiparallel dipoles reorient themselves to form a ferroelectric phase producing macroscopic polarization. In most cases, it is a reversible transition since the FE phase again switches back to the AFE phase on reducing the applied field below E_A (field corresponding to FE-AFE transition).

Hence this unique category of materials posses double hystereses loop with almost a remnant polarization very close to zero and is very crucial in obtaining high recoverable energy and efficiency. Pb-based antiferroelectrics have been very attractive in this regard as they offer appreciable energy storage properties for practical applications [26]. However, research is in progress in full swing to find a suitable lead-free material at par with the pb-based materials. One of the lead-free antiferroelectric materials which owe much potential is $AgNO_3$. In 2016, undoped and Mn-doped $AgNO_3$ were reported to possess a high energy density > 2 J/cm^3 [27, 28]. Thereafter, Gao et al. [29] enhanced the AFE phase stability of this compound by La-doping. As expected, they could discover a very high energy density of 4.4 J/cm^3 and a moderate efficiency of 70% along with improved breakdown strength in 2 mol% La-doped $AgNO_3$. Similar modifications were also made by Zhao et al. and Han et al. [30, 31] (Fig. 5). Apart from that, NBT based systems when modified with some niobates also

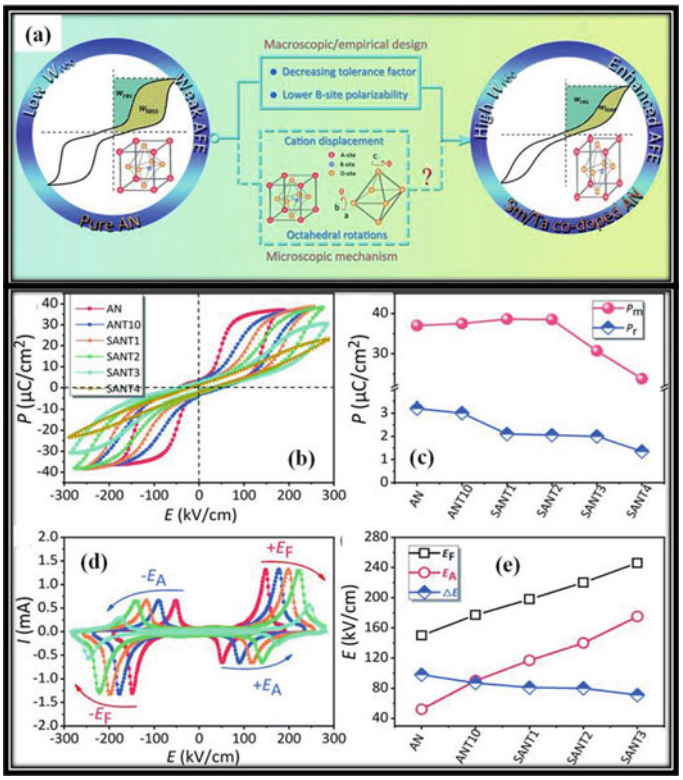

Fig. 5 **a** Representative diagram showing a strategy to improve recoverable energy in antiferroelectrics **b** polarization hysteresis loops **c** maximum and remnant polarization (P_m and P_r) **d** current (I) vs electric field **e** E_F, E_A and ΔE of AN, ANT10, SANT1, SANT2, SANT3 and SANT4 respectively.(Abbbriviations: $AgNbO_3$ (AN), $AgNb_{0.9}Ta_{0.1}O_3$ (ANT10) and $(Sm_xAg_{1-3x})(Nb_{0.9}Ta_{0.1})O_3$ (SANT1, SANT2, SANT3 for $x = 1, 2, 3, 4$ mol% respectively)) [31]

demonstrate fair energy storage properties. NBT-BT-KNN and NBT-$Ba_{0.5}K_{0.5}TiO_3$-KNN systems [32, 33] exhibit antiferroelectric-like behavior and adequate storage properties. But the energy storage performance is less appealing than $AgNO_3$ based systems. Nevertheless, adding $NaNbO_3$ (NN) as an end member to NBT showcased giant recoverable energy (W) of 7.02 J/cm^3 and efficiency (η) of 85%. In addition, NBT-0.22NN could maintain an optimum W > 3.5 J/cm^3 and η > 88% in the range 25–250 °C and 0.1–100 Hz making it a potential candidate for future pulsed power applications [34]. This may be attributed to the crossover of RFE of NBT to AFE relaxor phase with an increase in NN concentration making the AFE polarization loops slimmer and increasing the energy storage performance.

3.4 Glass–Ceramics

Though the energy storage density could be strengthened in FEs, RFEs, and AFEs by suitable modifications improving the dielectric breakdown strength (BDS) remains an issue, the lead-free materials (ceramics in particular) have a high concentration of defects which limits the BDS of the above-discussed ceramics. Factors such as porosity, grain size, charge transport, interfacial polarization, and the presence of secondary phases greatly influence the dielectric breakdown strength of the materials. Finer grain size with very little porosity is advantageous for obtaining high BDS. Some of the studies point out that introducing an appropriate amount of glass to the ceramics can substantially improve the BDS and thus maximizing the difference between maximum polarization and remnant polarization. Adding such glasses generates liquid phase sintering leading to grain refinement and large BDS. It is observed that B_2O_3-SiO_2 based glasses possess optimum electric durability and wettability due to which it acts as an effective additive for improving the performance of the parent composition [35]. Incorporation of 20 vol % of BaO-SiO_2-B_2O_3 glass into $Ba_{0.4}Sr_{0.6}TiO_3$ increased the dielectric breakdown strength of pristine ceramic from 12.1 to 23.9 kV/mm [36].

Wang et al. [37] made a detailed investigation on the effect of BaO-SrO-TiO_2-Al_2O_3-SiO_2-BaF_2 glass on grain size and BDS on barium titanate. They also noticed that BDS was related to charging transport across the grain boundaries in the space charge depletion region and was inversely proportional to the average field strength E_{GB} in the grain boundary space charge layer and is given by

$$E_{GB} = E\left(\frac{d_B}{d_{GB}}\right) \tag{10}$$

Here, E represents the externally applied electric field to the specimen; d_B and d_{GB} refer to the grain size and width of grain boundary space charge layer respectively. In yet another report, 0.5NBT-0.5ST ceramic was modified with glass addition (B_2O_3-Bi_2O_3-ZnO-SiO_2). With a glass content of 1wt, the energy density reached 1.67 J/cm^3 under a field strength of 200 kV/cm. The grain size was refined from 3.07 μmm to

0.98 μm without changing the phase structure and almost doubling the dielectric breakdown strength [38].

From the above discussions, it is now very clear that the dielectric and energy storage properties are largely dependent on the grain size of the ceramics/materials. The multilayer energy storage ceramic capacitors (MLESCC) which are widely preferred in the present time comprise hundreds of thin dielectric layers arranged in parallel with alternating interlayer metal electrodes. Usually, these dielectric layers are constructed from ceramics with high dielectric permittivity such a BT. Commercially available MLESCCs employ ~1 μm thick dielectric layers which require grain size of the order of 50–150 nm to meet the temperature stability and ensure reliable performance [39]. So, nanoscience or nanotechnology plays a vital role in this regard due to their unique properties as compared to the bulk. In the early stages single component nanomaterials were studied extensively but with rapid progress in technology, multi-component nanomaterials such as nanocomposites, thin films, core–shell structure, etc. due to diverse structure and composition. We will discuss a few of them here.

3.5 Core–Shell Structure

Core–shell structured materials have attracted the attention of the research community due to their extraordinary physical and chemical properties. Such structures are fabricated to overcome the hazards of densification in the case of nanomaterials. Considering the example of $BaTiO_3$, its nanocrystalline form (~30 nm) exhibits a slim and nearly linear *P–E* loop along with postponed saturation polarization and high dielectric breakdown strength dedicated to its fine grain size. On the other hand, it is very difficult to obtain high-density BT with a grain size maintained at the nanoscale (<100 nm) owing to easier grain growth in nanoparticles. Various synthesis techniques have been explored in the past to address this issue, e.g., spark plasma sintering, hot isostatic pressing, two-step sintering, etc. These listed methods accrue huge equipment costs, or the starting materials are monodisperse particles with sizes not greater than 10 nm. One of the alternatives adopted by Su et al. [40] was the introduction of a low melting glass as a coating on $BaTiO_3$ nanoparticles. The glass $65Bi_2O_3$-$20B_2O_3$-$15SiO_2$ forms a thin layer on commercially available BT nanoparticles forming a core–shell structure. The glass coating layer thickness could be adjusted by precursor concentrations and at an optimum loading of 26 vol% of borosilicate glass, no noticeable grain growth was obtained. This corroborates the fact that the coating acts as an effective grain growth inhibitor during the sintering process. The overall core–shell structure exhibited postponed saturation polarization and high dielectric breakdown strength of $\geq$ 1000 kV/cm. It also demonstrated a very high energy density of ~10 J/cm^3 which is much greater than bulk ceramics (Fig. 6).

In another study, $BaTiO_3$ nanoparticles were encapsulated in the FeO layer by the sol precipitation method. The FeO coating and secondary phase are crucial in impeding grain growth during sintering by infusing an effective diffusion

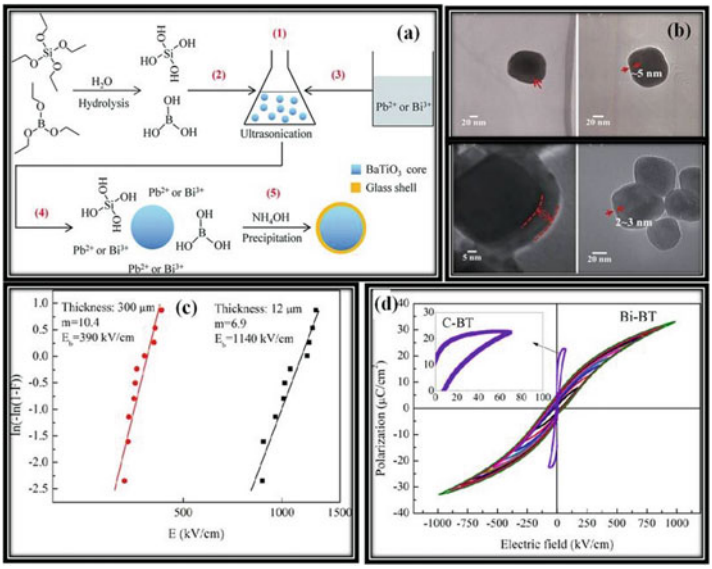

Fig. 6 **a** Representative diagram showing the formation of $BaTiO_3$/65Bi_2O_3-20B_2O_3-15SiO_2 glass core–shell structure **b** TEM micrographs indicating the thickness of the coating layer on the as-prepared nanoparticles **c** dielectric breakdown strength of the composite structure at two different thicknesses of 300 μm and 12 μm respectively **d** comparison of P – E loops for coarse-grained $BaTiO_3$ (C-BT) and glass coated composite (Bi-BT) [40]

layer. $BaTiO_3$@3%FeO nanoceramics displayed a high discharge energy density of 1.5 J/cm^3 at 300 kV/cm (8 times more than pristine BT), fast discharge features ($\tau_{0.9}$<1.5 μsec), excellent temperature (25–120 °C), and cyclic (up to 1 × 10^5 times) stability [41]. Similar work was performed by Huang et al. [42] in which they used SiO_2 to coat $Ba_{0.4}Sr_{0.6}TiO_3$ by wet-chemical process and then dense ceramics were fabricated out of the core–shell nanoparticles by spark plasma sintering. It was remarkable to note that the polarization decreased monotonously on increasing the amount of SiO_2 coating while the dielectric breakdown strength increased. $Ba_{0.4}Sr_{0.6}TiO_3$ ceramics with 8 mol% of SiO_2 exhibited a maximum energy storage density of 1.6 J/cm^3 at 400 kV/cm with an extremely high efficiency of 90.9%.

3.6 *Thick/Thin Films*

Another effective way of exploring the potential of nanotechnology is to incorporate the prospective nanoparticles as fillers in polymers to form thick/thin films. Such films have lesser defects as compared to their bulk counterparts and hence possess a high breakdown strength and energy storage density. For example, an

extraordinarily high recoverable energy density of 27 J/cm^3 in addition to breakdown strength of 1894 kV/cm was attained in Mn-doped 0.7NBT-0.3ST relaxor thin films grown on Pt/Ti/SiO_2/Si substrates synthesized through the sol–gel method [43]. $Sr_{0.6}(Na_{0.5}Bi_{0.5})_{0.4}Ti_{0.99}Mn_{0.01}O_3$ RFE thin films grown on the same substrate yield recoverable energy of 33.58 J/cm^3 along with appealing breakdown strength of 3134.3 kV/cm owing to less no. of oxygen vacancies [44]. Cheng et al. [45] observed ultra-high recyclable energy density in $Ba(Zr_{0.2}Ti_{0.8})O_3$ (BZT) ferroelectric films up to 166 J/cm^3 and efficiency up to 83% on reducing the film thickness to few nanometers. This is quite different from the typical FEs in the sense that the films show much-delayed saturation polarization which increases continuously from almost zero at remnant in a multipolar state to a substantial value under maximum applied field. Such a particular behavior may be attributed to the creation of an adaptive nanodomain structure in the perovskite films via phase engineering and strain tuning (Fig. 7). The reported film in this study is suitable for dielectric capacitors in energy storage, conditioning, and conversion. Films fabricated using physical methods ensure better crystalline quality and higher breakdown strength. One of the best examples is the attainment of a recoverable energy density of 154 J/cm^3 (applied field of 3500 kV/cm) in $(Bi_{1/2}Na_{1/2})_{0.9118}La_{0.02}Ba_{0.0582}(Ti_{0.97}Zr_{0.03})O_3$ epitaxial thin films deposited by pulsed laser deposition technique [46]. High epitaxial quality, optimum dielectric breakdown strength, and excellent relaxor dispersion are responsible for ultrahigh-energy storage in these thin films.

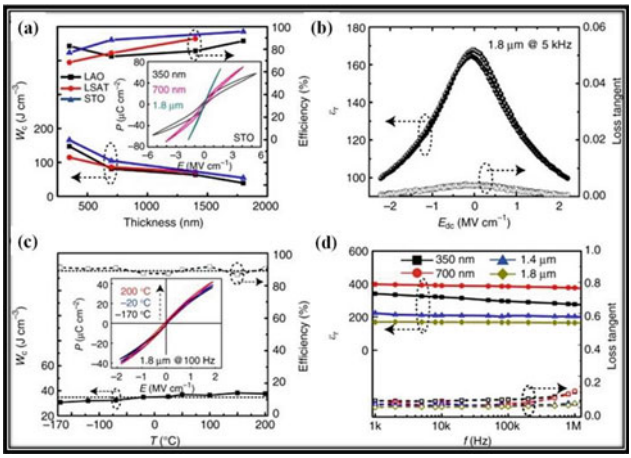

Fig. 7 **a** Variation of energy density (W_c), η and P – E loops with a thickness of BZT films grown on different substrates **b** room temperature variation of dielectric constant (ε_r) and loss tangent **c** (W_c), η and temperature-dependent P – E loops of 1.8 μm BZT film on LAO substrate **d** variation of ε_r and loss at the different thicknesses of BZT films grown on LAO [45]. (Abbreviations: $LaAlO_3$ (LAO), (La,Sr)(Al,Ta)O_3 (LSAT) and $SrTiO_3$ (STO))

3.7 Polymer Nanocomposites

Polymers are another category of materials that can give a tough competition to bulk and films in energy storage with an added advantage of wearability. Biaxial polypropylene (BOPP), polyphenylene sulfide (PPS), and polycarbonate (PC) are polymers that are already explored for commercial production. Despite that bottleneck for energy storage density is encountered and the problem of low permittivity, the inferior temperature stability of macromolecules has choked the pathway to practical applications. Hence, polymer nanocomposites with ceramics in the form of nanoparticles, nanofibers, and nanorods as fillers are more attractive as next-generation energy storage materials. Few instances describing the potential of polymer-ceramic nanocomposites as energy storage materials are cited here. It is a common observation that when ceramics nanofillers are incorporated into polymer matrix for building 0–3 or 1–3 structures; an improvement in permittivity and fairly better thermal stability may be expected. Boron nitride nanosheets (BNNSs) in P(VDF-TrFE-CFE) provide an insulating barrier to reduce the leakage current and lead to an enhancement in breakdown strength. The highest energy density and efficiency derived from this system were 20.3 J/cm^3 and 78% respectively. Further, its ternary counterparts with BT and BST were designed to achieve up gradation in dielectric breakdown strength by blocking electrical trees' development. Energy storage density of 21.1 J/cm^3 and η of 78% was achieved in P(VDF-CTFE)/12 wt% BNNS/15 wt% BT while for P(VDF-CTFE)/12 wt% BNNS/5 wt% BST, the featured values were 24.4 J/cm^3 and 76% respectively [47–49]. Hao et al. [50] in their work mentioned ultimate sized ferroelectric nanofillers, i.e., BT nanocrystals (prepared by TEG-sol method) in PVDF-co-hexafluro propylene (PVDF-HFP) matrix to enhance the breakdown strength and storage performance. They noticed highly enhanced breakdown strength (380 kV/mm) and maximal discharge energy density of 9.7 J/cm^3 at 30 vol% loadings of BT nanoparticles which were significantly higher than composites with coarse BT fillers (Fig. 8).

Nevertheless, the polymer-ceramic nanocomposites often suffer from poor interfacial compatibility and agglomeration of fillers which may affect the energy storage capacity. Surface modification and functionalization of the fillers are the most feasible solution to mitigate these issues. In a report by Gao et al. [51], BT nanoparticles were hydroxylated by H_2O_2 followed by a surface modification with DN-101 (a titanate coupling agent). They could notice an improvement in maximum polarization, breakdown strength, and discharge energy density in the treated nanocomposites as compared to the untreated ones. In another investigation, polydopamine (PDA) was employed to modify the surface of $BaSrTiO_3$ (BST) nanoparticles to increase the compatibility of ceramic fillers with polymer matrices. This technique remarkably elevated the dielectric breakdown strength of the nanocomposites to 466 MV/m, and at the same time, recoverable energy density was increased to 11 J/cm^3 which was almost 160% more than composites with unmodified BST [52]. Recently, sandwich nanocomposite structures have gained importance as they offer better performance features as compared to single-layer composites. Shen et al. [53]

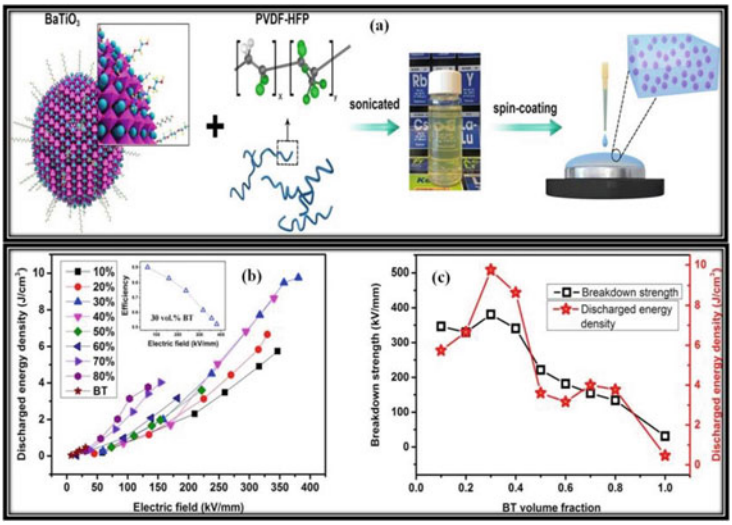

Fig. 8 **a** Representative diagram for the formation of BT/PVDF-HFP nanocomposite film **b** discharged energy density vs electric field at different vol% of BT **c** variation of breakdown strength and discharged energy density with vol% of BT [50]

implemented a comprehensive phase model to evaluate the breakdown strength of sandwich composite structures under electrostatic stimuli in this regard. Basing on the high-throughput results, they modeled a PVDF/BT nanocomposite sandwich with upper and lower layers filled with parallel nanosheets and middle layer filled with vertical nanofibers and obtained an energy density 2.44 times higher than virgin PVDF polymer (Fig. 9).

4 Summary

With the growing demands of modern society and the urgent need for securing our environment, lead-free energy storage devices have become indispensible. Nevertheless, research is rapidly progressing in this direction and it is expected that within few years lead-free materials to uproot the Pb-based in-framing energy storage devices. One of the most important figures of merit identified to strengthen the storage performance is these materials is recoverable/discharge energy density. As per the fundamental principles involved, enhancing the dielectric breakdown strength is the most effective way to improve the energy density. In addition to it, some of the applications require that the employed material should maintain its storage capacity in harsh conditions such as high temperature, and hence thermal stability is of utmost importance. So, in this chapter, we list the energy storage performance of different categories of prospective materials, oxides in particular, and their evolution from bulk to nanoscale.

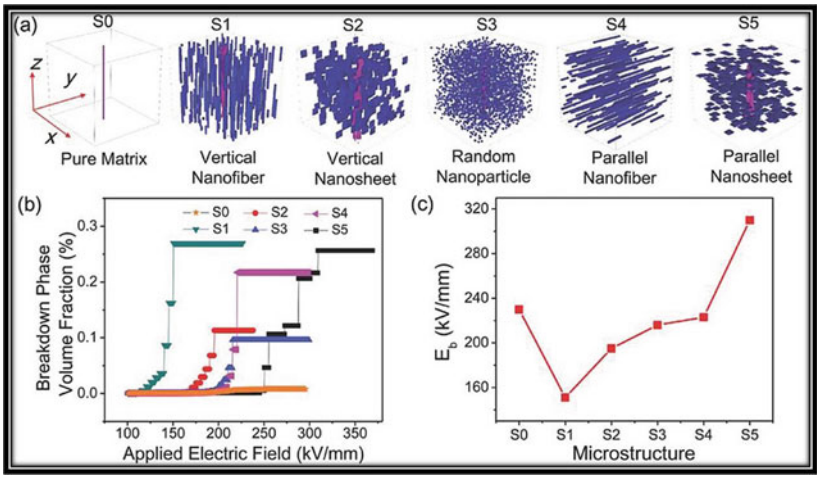

Fig. 9 **a** 3-D simulations of breakdown phase morphology in nanocomposites with different microstructures **b** evolution of breakdown phase volume fraction (10% except pure matrix) at applied electric fields **c** extracted breakdown strengths for corresponding nanocomposites [53]

Further, different methodologies which have proven to be achieving success in this context are also discussed. The first among them is domain engineering by inducing defects in both bulk and thin films suitable for polarization augmentation, particularly in the case of RFEs and AFEs. Another attempt that is of much importance is interfacial engineering employed in layered composites or core–shell structures and is essential to build stronger interfacial bonds for superior storage capabilities. The next one is downsizing the coarse grains into fine-grained structures which put a positive on the dielectric breakdown strength and indirectly on energy storage density. Moving ahead, we elaborated how the materials in their nano form exhibit exotic properties as compared to bulk due to minimal defects and surface properties. Ultra high energy densities, thermal stability, and breakdown strength could be achieved with core–shell structures and thin films. Sandwich polymer nanocomposites with optimum features are worthwhile for use in flexible electronics. Besides, phase-field simulation and first-principle calculations also provide evidence for experimental data and can give a projection for new generation energy storage materials. Thus, constant research efforts of the feature refining by implementation different synthesis techniques and utilization of computer simulation going hand in hand will sure give birth to more prospective and progressive materials to cater our future energy needs.

References

1. Key world energy statistics (2018) International Energy Agency
2. Rapier R (2020) Fossil Fuels Still Supply 84 Percent Of World Energy, June 2020— And

Other Eye Openers From BP's Annual Review. https://www.forbes.com/sites/rrapier/2020/06/20/bp-review-new-highs-in-global-energy-consumption-and-carbon-emissions-in-2019/?sh=4e2e94cf66a1
3. Yang L, Kong X, Li F, Hao H, Cheng Z, Liu H, Li JF, Zhang S (2019) Perovskite lead-free dielectrics for energy storage applications. Prog Mater Sci 102:72–108
4. Kusko A, DeDad J (2007) Stored energy-Short-term and long-term energy storage methods. IEEE Ind Appl Mag 13:66–72
5. Yao K, Chen S, Rahimabady M, Mirshekarloo MS, Yu S, Tay FEH, Sritharan T, Lu L (2011) Nonlinear dielectric thin films for high-power electric storage with energy density comparable with electrochemical supercapacitors. IEEE Trans Ultrason Ferroelectr Freq control 58:1968–1974
6. Jaffe B (1961) Antiferroelectric ceramics with field-enforced transitions: a new nonlinear circuit element. Proc IRE 49:1264–1267
7. Sun Z, Wang Z, Tian Y, Wang G, Wang W, Yang M, Wang X, Zhang F, Pu Y (2020) Progress, outlook, and challenges in lead-free energy-storage ferroelectrics. Adv Electron Mater 6:190069
8. Jin L, Li F, Zhang S (2014) Decoding the fingerprint of ferroelectric loops: Comprehension of the material properties and structures. J Am Ceram Soc 97:1–27
9. Chu BJ, Zhou X, Neese B, Zhang QM, Bauer F (2006) Relaxor ferroelectric poly(vinylidene fluoride-trifluoroethylene-chlorofluoroethylene) terpolymer for high energy density storage capacitors. IEEE Trans Dielectr Electr Insul 13:1162–1169
10. Hao X (2013) A review on the dielectric materials for high energy-storage application. J Adv Dielectr 3:1330001
11. Love GR (1990) Energy storage in ceramic dielectrics. J Am Ceram Soc 73:323–328
12. Li F, Yang K, Liu X, Zou J, Zhai J, Shen B, Li P, Shen J, Liu B, Chen P, Zhao K (2017) Temperature induced high charge–discharge performances in lead-free $Bi_{0.5}Na_{0.5}TiO_3$-based ergodic relaxor ferroelectric ceramics. Scr Mater 141:15–19
13. Tang H, Lin Y, Sodano HA (2013) Synthesis of high aspect ratio $BaTiO_3$ nanowires for high energy density nanocomposite capacitors. Adv Energy Mater 3:451–456
14. Chen X, Zhang H, Cao F, Wang G, Dong X, Gu Y, He H, Liu Y (2009) Charge-discharge properties of lead zirconate stannate titanate ceramics. J Appl Phys 106:034105
15. Xu C, Liu Z, Chen X, Yan S, Cao F, Dong X, Wang G (2016) High charge-discharge performance of $Pb_{0.98}La_{0.02}(Zr_{0.35}Sn_{0.55}Ti_{0.10})_{0.995}O_3$ antiferroelectric ceramics. J Appl Phys 120:074107
16. Ulrich R, Schaper L, Nelms D, Leftwich M (2000) Comparison of paraeletric and ferroelectric materials for applications as dielectrics in thin film integrated capacitors. Int J Microcircuits Electron Packag 23:172–181
17. Puli VS, Pradhan DK, Riggs BC, Chrisey DB, Katiyar RS (2014) Structure, ferroelectric, dielectric and energy storage studies of $Ba_{0.70}Ca_{0.30}TiO_3$, $Ba(Zr_{0.20}Ti_{0.80})O_3$ ceramic capacitors. Integr Ferroelectr 157:139–146
18. Eoh YJ, Kim E (2015) Dependence of dielectric properties on microstructural characteristics of $(Ba_{0.7}Sr_{0.25}Ca_{0.05})(Ti_{0.9}Zr_{0.1})O_3$ ceramics. Ceram Int 41:S2–S8
19. Jin Q, Pu YP, Wang C, Gao ZY, Zheng HY (2017) Enhanced energy storage performance of $Ba_{0.4}Sr_{0.6}TiO_3$ ceramics: influence of sintering atmosphere. Ceram Int 43:S232–S238
20. Yao Y, Li Y, Sun N, Du J, Li X, Zhang L, Zhang Q, Hao X (2018) Enhanced dielectric and energy-storage properties in ZnO-doped $0.9(0.94Na_{0.5}Bi_{0.5}TiO_3-0.06BaTiO_3)-0.1NaNbO_3$ ceramics. Ceram Int 44:5961–5966
21. Shvartsman VV, Lupascu DC (2012) Lead-free relaxor ferroelectrics. J Am Ceram Soc 95:1–26
22. Zheng DG, Zuo RZ, Zhang DS, Li Y (2015) Novel $BiFeO_3$-$BaTiO_3$-$Ba(Mg_{1/3}Nb_{2/3})O_3$ lead-free relaxor ferroelectric ceramics for energy-storage capacitors. J Am Ceram Soc 98:2692–2695
23. Zhao H, Yang X, Pang D, Long X (2021) Enhanced energy storage efficiency by modulating field-induced strain in $BaTiO_3$-Bi $(Ni_{2/3}Ta_{1/3})$ O_3 lead-free ceramics. Ceram Int
24. Yu Y, Zhang Y, Zhang Y, Li H, Zhang Q, Lu Y, He Y (2020) High-temperature energy storage performances in $(1-x)(Na_{0.50}Bi_{0.50}TiO_3)$-$xBaZrO_3$ lead-free relaxor ceramics. Ceram Int 46:28652–28658

25. Shi P, Zhu X, Lou X, Yang B, Guo X, He L, Liu Q, Yang S, Zhang X (2021) $Bi_{0.5}Na_{0.5}TiO_3$-based lead-free ceramics with superior energy storage properties at high temperatures. Compos B Eng 215:108815
26. Zhang Y, Liu P, Shen M, Li W, Ma W, Qin Y, Zhang H, Zhang G, Wang Q, Jiang S (2020) High energy storage density of tetragonal PBLZST antiferroelectric ceramics with enhanced dielectric breakdown strength. Ceram Int 46:3921–3926
27. Tian Y, Jin L, Zhang H, Xu Z, Wei X, Politova ED, Stefanovich SY, Tarakina NV, Abrahams I, Yan H (2016) High energy density in silver niobate ceramics. J Mater Chem A 4:17279–17287
28. Zhao L, Liu Q, Zhang S, Li JF (2016) Lead-free $AgNbO_3$ anti-ferroelectric ceramics with an enhanced energy storage performance using MnO_2 modification. J Mater Chem C 4:8380–8384
29. Gao J, Zhang Y, Zhao L, Lee KY, Liu Q, Studer A, Hinterstein M, Zhang S, Li JF (2019) Enhanced antiferroelectric phase stability in La-doped $AgNbO_3$: perspectives from the microstructure to energy storage properties. J Mater Chem A 7:2225–2232
30. Zhao L, Gao J, Liu Q, Zhang S, Li JF (2018) Silver niobate lead-free antiferroelectric ceramics: enhancing energy storage density by B-site doping. ACS Appl Mater Interfaces 10:819–826
31. Han K, Luo N, Mao S, Zhuo F, Liu L, Peng B, Chen X, Hu C, Zhou H, Wei Y (2019) Ultrahigh energy-storage density in A-/B-site co-doped $AgNbO_2$ lead-free antiferroelectric ceramics: insight into the origin of antiferroelectricity. J Mater Chem A 7:26293–26301
32. Ding J, Liu Y, Lu Y, Qian H, Gao H, Chen H, Ma C (2014) Enhanced energy-storage properties of 0.89 $Bi_{0.5}Na_{0.5}TiO_3$–0.06$BaTiO_3$–0.05$K_{0.5}Na_{0.5}NbO_3$ lead-free anti-ferroelectric ceramics by two-step sintering method. Mater Lett 114:107–110
33. Hao J, Xu Z, Chu R., Li W, Juan D, Peng F (2015) Enhanced energy-storage properties of $(1-x)[(1-y)(Bi_{0.5}Na_{0.5})TiO_3$–$y(Bi_{0.5}K_{0.5})TiO_3]$–$x(K_{0.5}Na_{0.5})NbO_3$ lead-free ceramics. Solid State Commun 204:19–22
34. Qi H, Zuo R (2019) Linear-like lead-free relaxor antiferroelectric $(Bi_{0.5}Na_{0.5})TiO_3$–$NaNbO_3$ with giant energy-storage density/effiffifficiency and super stability against temperature and frequency. J Mater Chem A 7:3971–3978
35. Divya PV, Kumar V (2007) Crystallization studies and properties of $(Ba_{1-x}Sr_x)TiO_3$ in borosilicate glass. J Am Ceram Soc 90:472–476
36. Zhang QM, Wang L, Luo J, Tang Q, Du J (2009) Improved energy storage density in barium strontium titanate by addition of BaO-SiO_2-B_2O_3 glass. J Am Ceram Soc 92:1871–1873
37. Wang XR, Zhang Y, Song XZ, Yuan ZB, Ma T, Zhang Q, Deng CS, Liang TX (2012) Glass additive in barium titanate ceramics and its influence on electrical breakdown strength in relation with energy storage properties. J Eur Ceram Soc 32:559–567
38. Liu G, Wang Y, Han G, Gao J, Yu L, Tang M, Li Y, Hu J, Jin L, Yan Y (2020) Enhanced electrical properties and energy storage performances of NBT-ST Pb-free ceramics through glass modification. J Alloys Compd 836:154961
39. Cai Z, Wang X, Hong W, Luo B, Zhao Q, Li L (2018) Grain-size–dependent dielectric properties in nanograin ferroelectrics. J Am Ceram Soc 101:5487–5496
40. Su X, Riggs BC, Tomozawa M, Nelson JK, Chrisey DB (2014) Preparation of $BaTiO_3$/low melting glass core–shell nanoparticles for energy storage capacitor applications. J Mater Chem A 2:18087–18096
41. Wang H, Cao M, Tao C, Hao H, Yao Z, Liu H (2021) Tuning the microstructure of $BaTiO_3$@FeO core-shell nanoparticles with low temperatures sintering dense nanocrystalline ceramics for high energy storage capability and stability. J Alloys Compd 864:158644
42. Huang YH, Wu YJ, Liu B, Yang TN, Wang JJ, Li J, Chen LQ, Chen XM (2018) From core–shell $Ba_{0.4}Sr_{0.6}TiO_3$@SiO_2 particles to dense ceramics with high energy storage performance by spark plasma sintering. J Mater Chem A 6:4477–4484
43. Zhang YL, Li WL, Cao WP, Feng Y, Qiao YL, Zhang TD, Fei WD (2017) Mn doping to enhance energy storage performance of lead-free 0.7NBT-0.3ST thin films with weak oxygen vacancies. Appl Phys Lett 110:243901
44. Zhang YL, Li WL, Qiao YL, Zhao Y, Wang ZY, Yu Y, Xia HT, Li Z, Fei WD (2018) 0.6ST-0.4NBT thin film with low level Mn doping as a lead-free ferroelectric capacitor with high energy storage performance. Appl Phys Lett 112:093902

45. Cheng H, Ouyang J, Zhang YX, Ascienzo D, Li Y, Zhao YY, Ren Y (2017) Demonstration of ultra-high recyclable energy densities in domain-engineered ferroelectric films. Nat Commun 8:1–7
46. Peng B, Zhang Q, Li X, Sun T, Fan H, Ke S, Ye M, Wang Y, Lu W, Niu H, Scott JF (2015) Giant electric energy density in epitaxial lead-free thin films with coexistence of ferroelectrics and antiferroelectrics. Adv Electr Mater 1:1500052
47. Li Q, Zhang G, Liu F, Han K, Gadinski MR, Xiong C, Wang Q (2015) Solution-processed ferroelectric terpolymer nanocomposites with high breakdown strength and energy density utilizing boron nitride nanosheets. Energy Environ Sci 8:922–931
48. Wang G, Li J, Zhang X, Fan Z, Yang F, Feteira A, Zhou D, Sinclair DC, Ma T, Tan X, Wang D (2019) Ultrahigh energy storage density lead-free multilayers by controlled electrical homogeneity. Energy Environ Sci 12:582–588
49. Liu F, Li Q, Li Z, Dong L, Xiong C, Wang Q (2018) Ternary PVDF-based terpolymer nanocomposites with enhanced energy density and high power density. Compos Part A: Appl Sci Manuf 109:597–603
50. Hao Y, Wang X, Bi K, Zhang J, Huang Y, Wu L, Zhao P, Xu K, Lei M, Li L (2017) Significantly enhanced energy storage performance promoted by ultimate sized ferroelectric $BaTiO_3$ fillers in nanocomposite films. Nano Energy 31:49–56
51. Gao L, He JL, Hu J, Li Y (2014) Large enhancement in polarization response and energy storage properties of poly(vinylidene fluoride) by improving the interface effect in nanocomposites. J Phys Chem C 118:831–838
52. Xie YC, Jiang WR, Fu T, Liu JJ, Zhang ZC, Wang SN (2018) Achieving high energy density and low loss in PVDF/BST nanodielectrics with enhanced structural homogeneity. ACS Appl Mater Interfaces 10:29038–29047
53. Shen ZH, Wang JJ, Lin YH, Nan CW, Chen LQ, Shen Y (2018) High-throughput phase-field design of high-energy-density polymer nanocomposites. Adv Mater 30:1704380

Chapter 4
Nanostructure Semiconductor Materials for Device Applications

Mahdie Kamalabadi, Kheibar Dashtian, Abbas Afkhami, Tayyebeh Madrakian, and Arash Ghoorchian

1 Introduction

Nanostructure semiconductors as highly applicable materials are receiving significant interest for various devices ranging from electronic devices to solar cells (SCs). These nanomaterials are a class of electrical and electronic materials, whose band gap ($0 - 4$ eV) lies between insulators and metals. The energy gap for organic materials denotes the distance between the highest occupied molecular orbital (HOMO) and lowest unoccupied molecular orbital (LUMO) levels that governs the charge transport in the materials. While energy gap for inorganic materials is defined as the distance between the conduction and valence states, other characteristics of these materials are electrical conductivity, light sensitivity, satisfactory surface area, adjustable morphology, adjustable bandgap, and rectifying effects. Semiconductors possess a negative coefficient of purification conductivity, and their conductivity increases with temperature [1].

M. Kamalabadi · A. Afkhami (✉) · T. Madrakian (✉) · A. Ghoorchian (✉)
Faculty of Chemistry, Bu-Ali Sina University, Hamedan, Iran
e-mail: afkhami@basu.ac.ir

T. Madrakian
e-mail: madrakian@basu.ac.ir

A. Ghoorchian
e-mail: a.ghoorchian@che.basu.ac.ir

K. Dashtian
Chemistry Department, Yasouj University, Yasouj, Iran

A. Afkhami
D-8 International University, Hamedan, Iran

T. Madrakian
Autophagy Research Center, Shiraz University of Medical Sciences, Shiraz, Iran

B. P. Swain (ed.), *Advances in Nanostructured Materials*, Materials Horizons: From Nature to Nanomaterials, https://doi.org/10.1007/978-981-16-8391-6_4

The major property of semiconductors for use in device applications is the control ability of their conductivity over a wide temperature range by engineering their surface, bulk, and interfaces. The surface engineering by the introduction of dopants in semiconducting materials can considerably change the existing characters or generate new characters [2]. Dopants are classified into two types, donors and acceptors, in which donor dopants release electrons and lead to the n-type conductivity, while acceptors provide holes or positive carriers, and cause the p-type conductivity [3]. Semiconductor junction-based interface engineering can be created with the careful selection of narrow gap materials [4, 5]. The behavior of electrons and holes as charge carriers at these junctions is the basis of most modern electronic devices.

Other essential demands on the semiconductors are sufficiently large band gap and high mobilities of the free carriers. Since the electrical properties of semiconductors are influenced by temperature, light, doping, and voltage, these materials-based devices can be used for energy conversion and amplification [1].

In this chapter, we classify nanostructure semiconductor materials into three types, including organic semiconductors (OSCs), inorganic semiconductors (ISCs), and organic–inorganic semiconductors (OISCs), and present an overview of their optical and electrical properties and device applications.

2 Organic Semiconductors

The OSC term refers to organic compounds that possess the remarkable capability to transport charge carriers (electrons and holes) [6]. The OSCs belong to two main classes of small molecules or π-conjugated oligomers, and conjugated polymers that are used in device applications like SCs, energy storage devices, organic light-emitting diodes (OLED), organic field-effect transistors (OFET), sensors, etc. [7]. Significant advances in organic chemistry and the design of π-conjugated molecular systems have fueled revolutionary changes in device development based on OSCs [8].

2.1 Solar Cells

The ability of Si-based semiconductors for the fabrication of photovoltaic (PV) cells has extensively been investigated, owing to their high efficiency. However, their high production cost is the major obstacle to market success [9]. Hence, the introduction of new materials is still attractive in device applications. OSCs have appeared as a promising category of PV materials in recent years because of their low-cost fabrication and ease of scale-up. In these devices, energy from sunlight is converted to electrical power using OSCs through the PV effect [10]. The charge carriers pass through the interfaces of OSC and electrode. Thus, the overall efficiency of developed devices is governed by the electronic structure of the used material.

Organic SCs are generally categorized into five main categories: (i) single layer, (ii) multilayer, (iii) bulk heterojunction architecture, (iv) dye-sensitized, and (v) tandem SC [11].

A single layer of organic SC is made up of a thin active layer of OSC, sandwiched between two electrodes (cathode and anode). A layer of high work function indium tin oxide (ITO) is commonly employed as the anode, while different metallic electrodes with a low work function (calcium, magnesium, or aluminum) can be employed as the cathode. The difference in the electrode work function is insufficient to overcome the exciton binding energy, which is approximately 0.5 eV in OSCs. This fact limits the employment of single-layer organic SCs in device applications. Unfortunately, very low quantum efficiency in the order of 1% was reported for single-layer PV cells [12].

The multilayer PV cell, also known as planar donor–acceptor heterojunction, contains two distinct layers: an electron acceptor layer with relatively high electron affinity, and an electron donor layer with lower electron affinity. Since there is a difference in the ionization energy and electron affinity values of these two layers, electrostatic forces can be generated across the interface between the layers [13]. A precise selection of OSCs to be used is necessary to make the differences large enough. The excitons in OSCs have intrinsically short exciton diffusion length; hence, a decrease in the power-conversion efficiencies (PCE) is occurred compared to inorganic-based SCs. One efficient candidate for overcoming this limitation in PV technology is the use of C60 fullerene and its derivatives as the n-type material. C60 derivatives have become more and more prominent in PV technology because of their excellent electronegativity and electron mobility. For example, a multilayer SC was presented by Brendel et al. based on the zinc phthalocyanine/C60 [14]. In another effort, Geiser et al. reported a poly(3-hexylthiophene)/C60 bilayer heterojunction system [15]. They indicated that electrons were collected at the polymer, while C60 excitation occurred at the anode. The solar-to-electrical power efficiency of 2.6% was achieved on the completed device.

In multilayer PV devices, the low surface area between the acceptor and donor electrodes increases the lifetime of the devices. The researchers address the issue by using bulk heterojunction configuration, which consists of blending acceptor and donor compounds to form an active layer [16]. As a result, the excitons migrate short distances, and the donor–acceptor interface is increased significantly. In 2020, a copolymer comprising an electron-rich unit 4,9-bis-(2-ethylhexyloxy)naphtho[1,2-b:5,6-b']dithiophene (zNDT) and two-electron acceptor units of benzodiathiazole (BT) and thieno[3,4-c]pyrrole-4,6-dione (TPD) (abbreviated as P(zNDT-TPDBT)) was synthesized [17], as shown in Fig. 1. The bulk heterojunction blend consisted of P(zNDT-TPDBT) and [6]-phenyl-C71-butyric acid methyl ester (PC71BM) demonstrates a promising efficiency of 2.4% with fill factor (FF) of 47%, and open-circuit voltage (VOC) of 0.91 V.

A dye-sensitized architecture consists of two optically transparent conducting electrodes and a redox electrolyte. A light-absorbing sensitizer was coated on the working electrode surface. An organic electrolyte containing a redox probe, like I^-/I_3^- mediator in an acetonitrile solution, is placed in between two electrodes. The

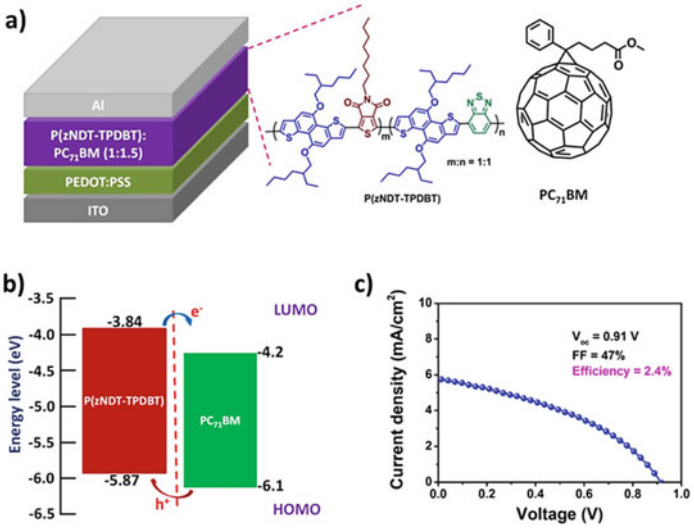

Fig. 1 **a** Schematic overview of the developed device; **b** Energy level diagram of PC71BM and P(zNDT-TPDBT); and **c** J–V characteristics of an as-prepared cell under an illumination (100 mW/cm2). Reproduced from [17] with permission

redox reaction is accelerated at the counter electrode [18]. Porphyrin sensitizers are one the most popular OSCs for the construction of efficient dye-sensitized based PV cells [19]. They show high PCEs of approximately 10%. Recently, researchers have demonstrated that the aromatic ring fusion to a porphyrin core is a promising methodology to enhance the performance of these SCs [20, 21]. It should be pointed out that the best efficiency achieved for this type of SCs in the laboratory is approximately 13%, which is higher than that in large-area modules (about 8%) [22].

In the tandem configuration, a series of connected p-n junctions of dissimilar semiconductors are used. The presence of each semiconductor enables the absorbance of a wide range of light wavelengths, leading to the enhanced PCEs. For instance, an organic-based tandem SC is fabricated, where a polymer: fullerene active layer and a small molecule were employed as bottom and top sub-cells, respectively [23]. The interface between two active layers allows efficient charge transport across. A short-circuit current density of 8.48 mA/cm^2, a good PCE of 6.26%, and a VOC of 1.46 V are obtained for the as-fabricated device.

2.2 Organic Light-Emitting Diodes

OLEDs have been considered as one promising candidate for light-source technologies, which are being presented in many display technologies. OLEDs can be divided into two distinct categories: small molecule-based light-emitting diodes (SMLEDs)

and semiconducting polymer-based light-emitting diodes (PLEDs). Generally, traditional evaporation techniques are used to manufacture SMLEDs. Therefore, given the low cost of production, PLEDs are more preferred in display applications, compared to SMLEDs [24].

Common strategies for the fabrication of OLEDs are illustrated in Fig. 2. A single-layer OLED is designed by sandwiching an emitting layer (EL) between two the anode and cathode electrodes. The EL should have two basic characters: (i) good electron and hole transport and (ii) high quantum efficiency. The EL is an OSC with high color purity and high efficiency. A two-layer OLED is another cell structure that takes advantage of two different organic layers. The hole transport layer (HTL) and the electron transport layer (ETL) are used respectively as hole and electron transport. In the three-layer structure, an additional organic active layer can be sandwiched between the transport layers (HTL and ETL) to create a site of the hole–electron recombination. In a multi-layer cell structure, in addition to the three layers, a hole injection layer (HIL) is also introduced. The exciton quenching and charge carrier leakage are eliminated in multi-layer OLEDs, leading to improve efficiency.

The roles and features of anode and cathode in OLED devices are similar to those of SCs. Transporting holes and blocking electrons are performed at the HTL. However, ETL provides electron-transporting and hole blocking abilities in OLEDs. The materials used in the HIL should be having high electron blocking capacity and high mobility.

OLEDs compete with other display technologies (e.g., liquid crystal displays and inorganic light-emitting diodes) because they have the following benefits: low power consumption, high resolution, improved color variation, brightness, low weight, and low cost. Developing new organic light-emitting materials with both narrow emission lines and high quantum efficiencies is of great interest for industry [25]. A substantial challenge in the era of OLEDs is the construction of an efficient diode with sufficient color purity and a narrow emission line.

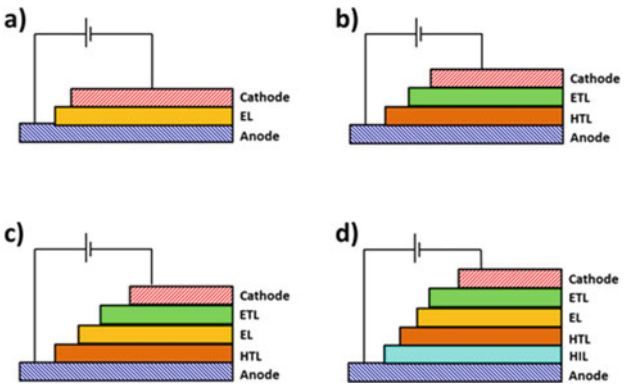

Fig. 2 Different cell structures of OLEDs: **a** single-layer, **b** two-layer, **c** three-layer, and **d** multi-layer

In this context, a pure-blue device with narrow emission of 19 nm and high external quantum efficiency of 32% at 1000 cd m^{-2} was fabricated based on the 2,3,5,6-tetrafluoro-5′-phenyl-[1,1′:3′,1″-terphenyl]-4-carbonitrile as an emitter [26].

Also, organic complexes can be employed as emitting active layers in the field of OLEDs with various emission wavelengths. For example, in 2011, the efficient novel yellow phosphorescent iridium complexes, $Ir(PPOHC)_3$ and $(PPOHC)_2Ir(acac)$ (PPOHC: 3-(5-(4-(pyridine-2-yl)phenyl)-1,3,4-oxadiazol-2-yl)-9-hexyl-9H-carbazole), were prepared [27]. The authors report that Ir(III) complexes with a carbazole–oxadiazole unit can be used as promising materials in electroluminescent devices. In this work, white and yellow PLEDs exhibited an efficiency of 16.4 cd A^{-1} and 15.3 cd A^{-1}, respectively. Furthermore, Zink et al. synthesized a series of highly luminescent complexes based on the two triphenylphosphines, a bridging P-N ligand, and Cu(I) ion [28]. Emission colors can be easily adjusted between deep blue and yellow by changing functional groups of the bridging ligand.

2.3 Organic Field-Effect Transistors

In a transistor or field-effect transistor (FET) device, the flow of electrons is modulated using a small potential applied. These electronic systems can have coated wide range and areas on the flexible supports. These devices have received accelerating consideration in the last decades because they provide some instruction that falsehood beyond those easily addressed via wafer-based electronics and cusses to enormous revolute in the electronics industry. OFETs are one of the fundamental elements for the next generation of electronics, which have wide applications. The OFET consists of the following components: drain, gate, source electrodes, an OSC, and an insulator.

The coating of a semiconducting layer is a critical step in the fabrication of OFETs. To characterize the performance of OFETs, the following parameters are investigated: field-effect mobility (the ratio of the velocity to the electric field), minimum gate voltage, and on/off current ratio [29].

The application of OSCs for the construction of these devices is attractive thanks to their flexibility, transparency, tunability of properties, and light-weight compared to traditional Si-based transistors [30]. Pentacene has historically been considered an OSC in the field of OFETs. However, pentacene has limitations, including instability under the solution process and insufficient device properties; developing novel OSCs is the most concern topic for future applications in organic electronics. Significant efforts have been focused on the presentation of new OFETs devices [31–34]. For example, to increase the π-system conjugation, the anthracene core can be modified with arenes such as naphthalene, thiophene, bithiophene, and diphenyl [34]. In 2015, Liu and co-workers found thin-film field-effect transistors based on 2,6-diphenyl anthracene, having dense molecule packing and high stability [35]. The as-fabricated OFETs device exhibited maximum mobility of 14.8 cm^2 V^{-1} s^{-1} due to the use of layer-by-layer structures.

OFET devices have also been utilized as the sensing layer to manufacture electrochemical sensors, gas sensors, and biosensors. The selectivity of OFET-based sensors can be controlled with the modification of the used OSC. For instance, Bayn et al. utilized polycyclic aromatic hydrocarbons (PAHs) as a p-type semiconducting material to detect different volatile organic compounds in the presence of humidity [36]. Interestingly, the as-fabricated PAH-based FET array sensor can distinguish aromatic and non-aromatic analytes. In another work, an electrolyte gated OFET (EGOFET) as an ultrasensitive immune-sensor was fabricated for the determination of the primary inflammatory cytokine TNFα [37]. A gold electrode modified with anti-TNFα antibody is considered as the gate electrode. The EGOFET channel is prepared by a thick film of pentacene via high vacuum sublimation. The developed OFET biosensor responds to the analyte concentration with a detection limit of 100 pM.

2.4 Other Applications

The OSCs are also exploited in other applications, e.g., sensing, energy storage, and electrochromic devices.

Advances in OSCs over recent decades have yielded a wide variety of sensing devices that can effectively be used in analytical applications. The chemiresistive gas sensors promise to fabricate electronic noses due to their low cost and a simple readout circuit. The interdigital electrodes (IDEs) design, a planar substrate comprising of two parallel conductive electrodes, is utilized to fabricate the chemiresistive gas sensors. The OSC, as a sensing active layer, is coated on the surface of IDEs, as illustrated in Fig. 3. In these devices, changes in the electrical resistance of the active layer due to the exposure of analyte vapors are recorded via a simple digital multimeter [38]. The conducting polymers, e.g., polypyrrole [39, 40], polythiophene [41], and polyaniline [42, 43], are considered good candidate materials for the construction of chemiresistive gas sensors. Hien et al. [42] presented a sensitive chemiresistive NH_3 gas sensor based on polyaniline nanowires and palladium nanoparticles. The sensing active layer is coated on the Pt-IDEs. The authors reported that the chemiresistor sensor has a rapid response time, high sensitivity, and good selectivity to ammonia gas.

As one of the most important types of supercapacitors, the pseudocapacitors provide an applicable device to store energy because of the high power density and energy density compared to electrochemical double-layer capacitors. The pseudocapacitors store energy based on a faradic process. The semiconducting polymers have been extensively employed as pseudocapacitors because of their redox properties [44].

Another interesting application of nanostructure OSCs is the fabrication of electrochromic devices (ECDs). These are a potentially exciting class of optoelectronic devices with reversible optical changes due to an electrical stimulus. Several types of conjugated polymers and their derivatives have been successfully employed to

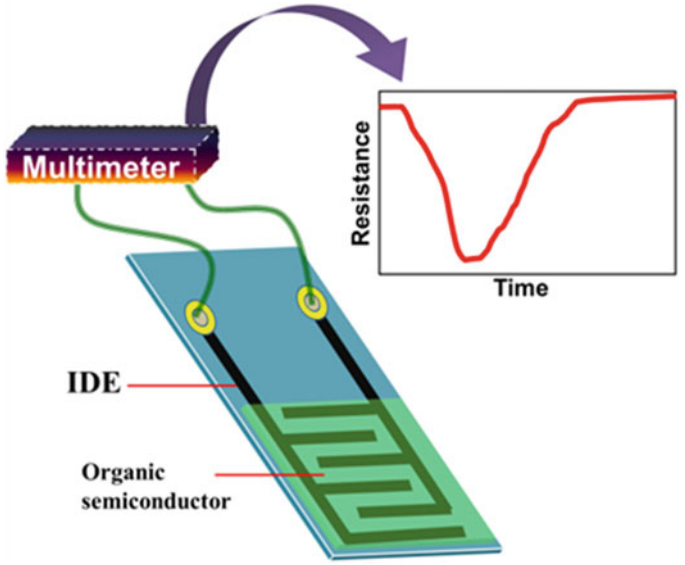

Fig. 3 A schematic illustration of a typical chemiresistive gas sensor

demonstrate electrochromic behavior. They present high coloration efficiency and rapid response time [45]. For instance, a series of nanostructured polymer-based semiconductors comprising triphenylamine and thiadiazole units were synthesized and investigated as novel ECDs [46]. In another attempt, Ghoorchian and co-workers [47] introduced modified poly(thionine) (PTH) and poly(methylene blue) (PMB) as nanostructure electrochromic materials (See Fig. 4). In this work, the color of PTH and PMB films is reversibly changed from colorless to pale purple and blue, respectively, during the oxidation.

3 Inorganic Semiconductors

ISCs are semiconducting materials made from a non-carbon-based material [48]. Among metal oxides, metal chalcogenides, metal phosphides, metal phosphates, metal halides, and oxyhalides have emerged as trending materials for device applications [49]. In a device design, optoelectronic characteristics of ISCs such as optical behavior, energy gap, work function, electron–hole separation, electron lifetime, and excited-state conductivity are vitally important [48, 50]. Generally, a comparison between ISCs and OSCs-based optoelectronics and sensing devices is that, in the OSCs, molecular matters are adhered together through the Van der Waals interactions, while intramolecular bonds are covalent, respectively [51]. Hence, the interactions between molecules are loose, and the permissible mean route for charge carriers moving in the semiconductors is approximately balanced to the intermolecular space.

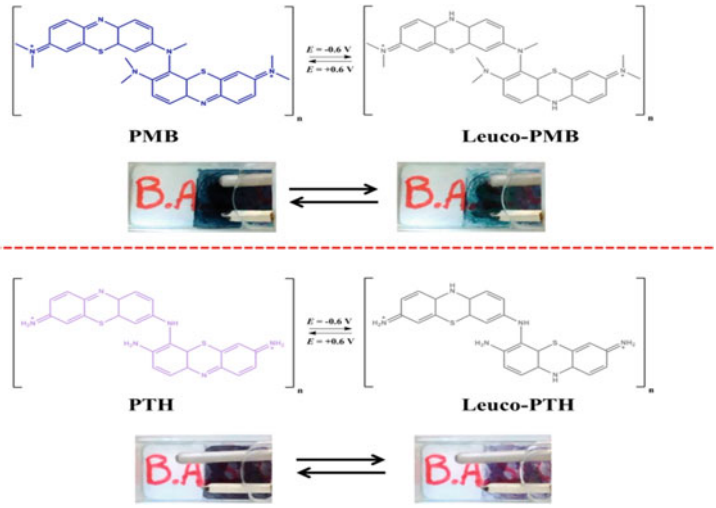

Fig. 4 The electrochromic behavior of modified PMB and PTH films. Reproduced from [47] with permission

Consequently, the energy band structure of OSCs is localized and not delocalized on the overall structure [51]. Therefore, charge separation transfers are incoherent in OSCs. Generally, every transfer site is localized due to energetic and local disorders that are considerably higher than the coordinated structure [52]. Hence, conductivities in OSCs stand far lower than in ISCs.

In addition to the ISCs themselves, the supports act a consequential behavior in the design of the ISCs-based devices because of their surface roughness and smoothness, surface charge density and zeta potential, flexibility and rigidity, transparency and turbidity, work function and ionization energy, surface area, structure and reactivity, surface activation energy and reaction rate, and fully semiconducting properties [53]. For example, in SC application, transparency and the characterizations of the support are of a priority in which ITO has been mostly applied, while in electronics devices flexibility is very important [54, 55]. Since this section investigates several classes of ISCs that can be applied to construction high-performance devices in the following, some semiconductors and their device applications will be examined.

3.1 Solar Cells

Some traditional types of SCs are amorphous silicon SCs, copper indium gallium selenide SCs, dye-sensitized SCs, luminescent solar concentrator cells, organic SCs, perovskite SCs, quantum dot SCs, etc. [56–58]. Since dye-sensitized SC, quantum dot SC, and perovskite SC have engrossed the consideration of many technologists from the photo-voltaic field. Its efficiency is considered when it comes to PCE,

which consecutively is subordinate to the electron transfer rate. They are introduced to be influenced by changes in electronic, optical, and mechanical characters accompanied by crystallinity, morphology, specific surface area, and aspect ratios of the semiconductors. The fascinating physico-chemical properties of semiconductors and long-distance instinctive energy migration assemble them sensational candidates as efficient charge transporters, impressive routes for electron transfer and superior surface area for dye absorption, photosensitizers for SCs [54]. The structure of a PV device is the assembling tandem cell of 5.0 independent thin-film layers (see Fig. 5). Two current collectors as an important and indispensable constituent of PVs that at least one are high conductivity along with high visible light transparency and constructed by n-type counterpart semiconductors (ITO, FTO, TiO_2, Nb_2O_5, SnO_2, WO_3, $SrTiO_3$, and Zn_2SnO_4), as well as to no extent p-type semiconductors are in each particular manufacturing application [59]. Then two barrier layers, commonly one accountable for the hindering of electromigration, and another one (on the contrary direction) for the hindering of the hole forwarding (TiO_2, PbI_2) [60, 61]. Finally, the operational layer is accountable for the light and energy harvesting and the comprehensive significant agent of the PVs device [55, 62]. So it can be said that ISCs based metal oxides, metal halides, metal chalcogenides in quantum dot shape and perovskite structure can be used in designing many parts of the SC device.

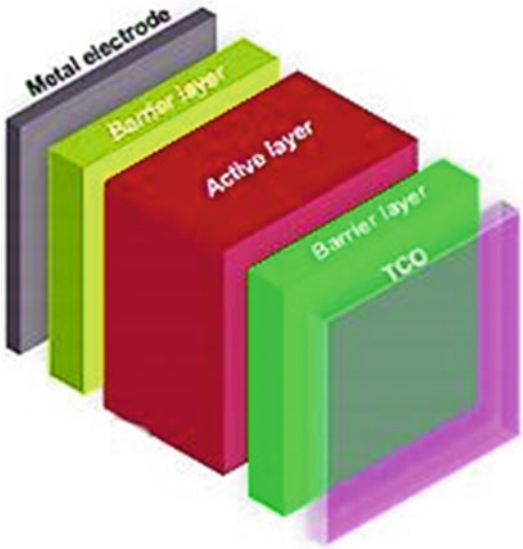

Fig. 5 Essential arrangement structure of next-generation SC devices (generally the operational layer introduces the SC type)

3.2 ISC-Based OFETs

Mounting ISCs as the functional agents onto flexible supports obtains many benefits such as being bendable, scalable, portable, and lightweight in an extensive application's scope such as flexible displays, electronic textiles, medical image sensors, active antennas, smart wearable devices, sensory skins, and large-area e-papers to name a few. In the design of these systems, integrating ISCs with plastic as attractive flexible substrates for as-mentioned applications, necessitate processing temperatures under the glass-transition temperatures of the plastics supports have been a major challenge in the development of these systems. To create cost-effective and reproducible methods such as the printing of functional inks comprising ISCs progressively the consideration and started from transition metal chalcogenides (TMCs) and metal oxides for a good deal of potential applications.

Furthermore, one of the most applicable electronic-based ISCs is LEDs which include progressively deposited electron-injection-booster, hole transport as appropriate definitive hosts, high multiplet energy electron transport hosts, critical hole-transport (organic monomolecular) layers, hole-injection layers which act as remarkable agents in the modification of the electron/hole injection to achieve transport balance of charge carriers in the single emission layer of LEDs with electron-transporting host, and support (e.g., ITO, FTO) anode layers, assimilated straightly with the thin films FETs.

In this regard, John Rogers et al. deeply focused on the appearance of promising, efficiency and applicable materials for stretchable and flexible inorganic LEDs, which can provide the fundamentals for a wide range of convincing, untraditional systems, through deformable presentations, battery-free device prototype lighting provenances to wearable, biomechanics, skin-mounted, non-invasive, and implantable bioelectronics with diagnostic and therapeutic applications [63–65]. They in NeuroLux company have a lot of research on interdisciplinary developments in material preparation strategy, device designs and constructions, mechanical lineaments, and arrangement strategies over the soft, smooth, flexible, and fully implantable inorganic LEDs with considerable operating properties even under inordinate faces of mechanical transformation [66, 67]. An example of their research work is given in Fig. 6. which revealed a multifunctional, fully implantable, and wireless optoelectronic device, in a tilted detonated perspective arrangement demonstrating various components (see Fig. 6a), a digital image of a remotely powered, as-proposed flexible hierarchical control implementation and integrated system, accentuation the four blue-emitting micro-inorganic LEDs at the head surface (see Fig. 6b) and a healthy, disease freely moving the mouse (a long time after the as-proposed device inserting) (see Fig. 6c) [68, 69].

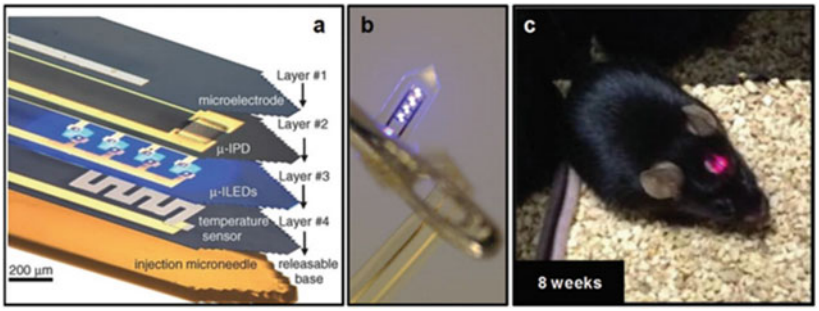

Fig. 6 A typical micro inorganic LED **a**, a photograph of this flexible integrated system **b**, and this device implantation in a healthy, freely moving mouse **c**. Adopts from [63–65]

3.3 Gas Sensors

The ISC-based gas sensors have an extensive range of applications in safety and health, environmental monitoring and analysis, agriculture, indoor and mine air quality, and medical diagnosis and treatment [70]. Therefore, here we introduced the fundamentals type and the emerging assessments and technologies applied in ISC-based gas sensing devices. Overlay, as-mentioned devices operate by recording a physical character changed by adsorption/desorption behaviors, recognition, and physicochemical reactions over ISCs based sensing species and solid-state support. The investigation of some parameters of ISCs and the exploration of principles, which prospectively applied through material choosing for gas sensing applications, were the special platforms of this section [71]. Additionally, highlight such ISC-based gas sensors as a headlight for promising applications.

The ISC gas sensors are devices that are constructed of ISCs which are applied for measurement of the concentration of a target gas by the record of the changes in electrical resistance, electrochemical signals (amperometric and potentiometric), optical signals, mass sensitive, and thermoelectric [72]. Generally, commercial ISC gas sensors operate on the axiom of reversible gas (volatile organic compounds and industrial gas) adsorption procedure at the ISC surface [73, 74]. Adsorption or diffusion of the target gas on the ISC surface followed by catalytic oxidation or reduction cusses to change in the electrical resistance, optical properties, and electrochemical characters of the ISC-based gas sensing devices, which are then attributed to the target gas type (oxidative or reductive) and its concentration (see Fig. 7).

Due to the demands of commercial low-power, cost-effective, and portable sensing devices, installing a heater under solid-state for metal oxide-based gas sensors has created many important challenges (metal oxides are activated at 100–500 °C) [75–77]. The advent of new semiconductors (metal chalcogenides and metal halides), as well as the doping of some materials into the metal oxides structure, has been removed this limitation, and a wider range for the use of these devices has emerged

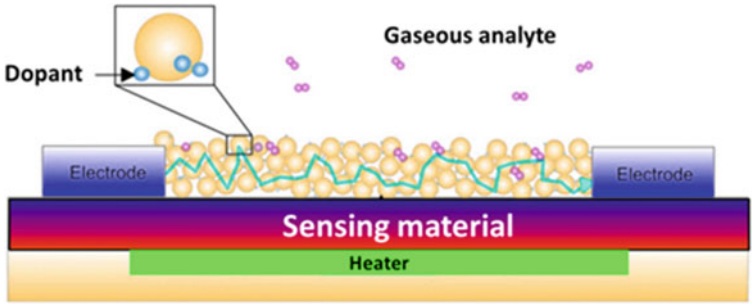

Fig. 7 Typical ISC-based gas sensor

[78–81]. Additionally, typical 3S factors of ISC-based gas sensors that are sensitivity, selectivity, and stability of ISCs are challenged which the use of different methods to improve them has been examined as follows:

(1) Design and construction of single and multi-heterojunctions between ISCs [82–84]
(2) Design and construction of Schottky junction between ISCs and metals [83, 85, 86]
(3) Design and construction of ohmic junction between ISCs and metals [87, 88]
(4) Bulk engineering of the ISCs (surface modifications, morphology controlling, co-catalyst loading, etc.) [89, 90]
(5) Surface engineering of the ISCs (crystal phase controlling and size/thickness controlling) [91, 92]
(6) ISCs derived from metal–organic frameworks (MOFs) and analogues (Prussian blue) [92–94]

However, there are still challenges in selectivity and stability, which have greatly improved with the advent of composites of porous materials such as organic–inorganic polymers and organic polymers (COFs, graphene, polyaniline, and polypyrrole) with ISCs [95–98]. In this case, organic and porous materials are used as capturing and recognizing gases, and semiconductor materials are used as sensitizers. However, in many cases, noble metal has been used as a sensitizer in these systems [98–100].

The nanostructured metal oxide (NMO) as well-known semiconductor materials-based gas sensors technologies has the adequate physisorption of O_2 with a negative charge (O_2^-, O^-, and O^{2-}) and create the electron-depletion zone as an insulating region on the surface of n-type semiconductors and hole-accumulation and inversion layers on the surface of p-type NMO semiconductors [101]. The reducing or hydrogen-rich gases, such as ethanol, methanol, acetone, NH_3, CH_4, CO, and H_2S, are oxidized via interactions with as-mentioned negatively charged O_2 followed by injection of electrons into the electron-depletion layer (in n-type) or hole-accumulation layer (in p-type) NMOs, which causes to declines or enlarges the sensor resistance, respectively. Antithetically, oxidizing or oxygen-rich gases such as nitrogen oxides

(e.g., NO, NO_2), halogen gases, and O_3 are adsorbed on the surfaces of metal oxide semiconductors can eliminate additional surface adsorbed electrons and enlarges or declines sensor response in p-type and n-type NMOs semiconductors, respectively [80, 102–107]. Thus, the mechanism of NMOs-based gas sensing devices can be administrated by reactions of the reducing gas and the negatively charged surfaces O_2, and the adsorption of oxidizing gases with O_2^-, O^-, and O^{2-} [104, 108].

The wide applied of TMCs such as CdS, WS_2, and MoS_2 based semiconductors in gas sensing fields is attributed to their robust spin–orbit effect, an exceptional integration of two-dimensional atomic-scale thickness, promising optoelectronic, physical, and mechanical characters, and general direct bandgap configuration [106, 109]. TMCs in thin films form generally constructed by vacuum deposition techniques, bulk exfoliation methods, chemical synthesis approach, and mechanical cleavage assays to strip bulk materials [110, 111]. The mechanism of TMCs based gas sensors is similar to NMOs which the initial disposal to the air of p-type TMCs promotes the capturing of O_2 on their surface, expropriation several electrons from the VB outstanding to the formation of O_2^-, O^-, and O^{2-} which makes an enhance in the hole concentration and a decrement in the resistance [112, 113]. The disposal of oxidizing or oxygen riches gas to subsequently excited electrons from the VB and outstanding to an enhance in intrinsic hole carrier concentration and accumulation, consequential in the creation of the hole layer on the p-type ISCs surface and makes the p-type TMC more conductive. Regarding a reducing or hydrogen-rich gas, the conflict will happen [114, 115].

Although fabrication of Au sensitized SnO_2, TiO_2, CuO, Co_3O_4, Al_2O_3, ZnO, and WO_3 chemiresistive type gas sensor has been developed for industrials and mines application [116, 117]. But also, highly sensitive, wearable, and breath analyzer gas sensors for the monitoring of human health risk be allowed to expeditiously grow commercially available [118–120]. In the case of wearable sensors, the sensor implement is an advancement on prevailing wearable sensors due to a self-heating mechanism that cusses to increases sensitivity [119, 121]. In this regard, hand and arm showing sensor can be applied to inner write with mobile phone-sized read beside it.

In the breath analysis cases, the sensing and recognizing of biomarker gases from human exhaled breath utilizing semiconductors type chemiresistors has fascinated major consideration due to it prepared robust, non-invasive, comfortable, economical, portable, or point of care, safe, and quick disease diagnosis [122, 123]. Especially, the exhaled ammonia and acetone are thought out as prospective biomarkers to analyses renal diseases during hemodialysis and diabetes, respectively [101, 124]. Since the gas chromatography or ion mobility spectrometry as conventional high-technology equipment to measure the accurate breath ammonia and acetone concentrations are expensive, bulky, and need sampling and pre-conditioning which hinders the real-time breath analysis [101]. Thus the desired ISCs via superior catalytic activities and combinatorial strategies can prospect for the progress of sensing systems that monitor less-reactive macromolecules and capable screening, respectively [122, 123]. In this regard, Kalidoss et al. report an overview on the exponential development of the non-invasive diagnosis of diabetes mellitus from exhaled breath by NMOs chemiresistive

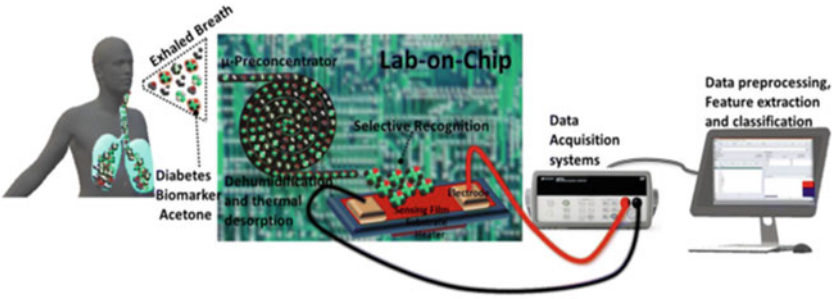

Fig. 8 A typical metal oxide-based metal oxide chemiresistive gas sensor. Adapted from [125]

gas sensors and μ-preconcentration (see Fig. 8) [125]. The amazing factors from these conventional gas sensors, preconcentration, and collection of breath samples challenges the breath-based diagnosis, which breath analysis utilizing ISC-based chemiresistors via ultralow energy usage conjunct to the Internet of Things (IOTs) will concrete new strategy to overcome these challenges and robust disease and patient diagnosis [101, 126–128]. In this regard, Yoon et al. [101] report NMOs, carbon-based materials, and TMC semiconductors-based chemiresistors IoT sensors intended for breath analysis on a miniaturized device for disease diagnosis [101].

4 Organic–Inorganic Semiconductors

OISCs represent an exciting family of semiconductors, which are fabricated from hybrid organic and inorganic semiconductor materials [3]. Although organic and inorganic semiconductor materials have unique properties, they have many obstacles in their non-hybrid form. However, their hybridization with each other surmounts these obstacles. Also, the combination of the advantageous properties of organic semiconductors with inorganic semiconductors offers superior potentials in diverse applications, such as environmental, sensors, electronic devices, SCs, and biomedical applications. With the development of science and technology, the demand for electronic devices has been increased. Although these devices have improved the human life quality, they suffer from some practical problems, such as the need for novel materials to boost the performance of devices. The OISCs open a new window for the development of high-performance electronic devices because these materials benefit from the synergy between the intrinsic advantages of organic materials and those of inorganic materials. In this section, some examples of different applications of the OISCs in electronic devices are described.

4.1 Polymer Composites with Nanoparticles

In recent years, nanoparticle–polymer composite materials have attracted intense attention in scientific fields because these organic–inorganic nanocomposites possess a combination of excellent properties of each component. Composites based on semiconductor nanoparticles and polymers are very attractive for electronic applications, like flexible electronics, SCs, and light-emitting displays [129–131].

The properties of nanocomposites have strongly dependent on their preparation strategies. The in-situ polymerization and melt blending are the most routes employed for the preparation of semiconductor nanocomposites [132]. Melt blending is considered as the simple, cost-effective, and optimum strategy for the preparation of composites of semiconductor nanoparticles with various polymers. In this method, a solution containing inorganic nanoparticles dispersed in the polymer matrix is prepared, and then nanocomposites are accessed through extrusion [133]. The in-situ polymerization is based on the dispersion of semiconductor nanoparticles in the monomeric solution before a polymerization process [134]. In terms of the large-scale production of nanocomposites, the greatest challenge is the lack of low-cost methods to control the dispersion of the inorganic nanoparticles in the polymer matrix. The nanoparticles typically aggregate, negating the benefits of the nano-dimensions [135]. To prevent the aggregation of nanoparticles in the polymeric matrix and enhance the interaction between the components, several methods are used (1) the surface functionalization of nanoparticles with ligands, active monomers, or coupling agents; (2) the modification of polymers with the polar groups; and (3) the utilization of a compatibilizing agent that led to the improvement incompatibility between nanofillers and polymer matrix [136–138].

The family of quantum dots (QDs) represents a particular class of inorganic semiconductor nanoparticles, revealing unique properties, including size-tunable optical, electronic, and catalytic properties [139, 140]. Hybrid composites based on QDs and conjugated polymers have recently gained much attention in device applications. The SCs based on these composites are gained popularity today because of their low cost, flexibility, lightweight, good electron mobility, spectral tunability, and high dielectric constant [141, 142]. The performance of these SCs critically depends on the shape and size of nanoparticles [143]. Many studies have provided the performance improvement of hybrid devices comprising polymer and QDs of different sizes. Roghabadi et al. [142] used CdSe crosslinking by m-phenylenediamine to improve the performance of polymer/QDs hybrid SCs. The obtained results indicated the device performance on the size of CdSe QD. The SC performance was improved when the size of QDs was increased from 2.3 to 8.3 nm.

Photocatalysts play a pivotal role in pollutants removal or energy storage. ISCs have been considered promising candidates for photocatalysis applications [144]. Currently, TiO_2 is the most used ISC as the photocatalyst in solar energy conversion and environmental remediation. However, the main disadvantages of TiO_2 are the absorption of only ultraviolet light and the high speed of electron–hole recombination, which is attributed to its high bandgap energy [145]. Organic–inorganic

hybrid materials are of scientific interest to improve ISCs performance. Among novel promising photoactive materials, photocatalysts based on the ISCs and some conjugated polymers have seen an explosive growth of interest in photocatalytic systems. These hybrid photoactive materials benefit from the synergy between conjugated polymers and ISCs, leading to improved light absorption, higher surface areas, higher stability to photo-corrosion, and improved photo charge generation. Thanks to their photostability, optoelectronic, and morphological properties, conjugated polymers improve photocatalytic efficiency[146, 147].

In recent years, the development of PLEDs has been of growing concern because of their great applications in wearable electronics and flexible displays [148]. The polymer used in PLEDs should be possessed identical chemical and physical properties, including absorption and emission spectra, molecular weights, charge injection, and transfer stability, as well as thermal stability. Nevertheless, the potential use of PLED devices is ultimately limited by some disadvantages of polymers in terms of high cost, low optoelectronic efficiency, poor stability, and short lifetimes [149]. Recently, numerous efforts have been concentrated on improving the PLEDs efficiency, by employing polymer-inorganic nanocomposites. Since polymer-inorganic nanocomposites possess both advantages of the polymer and inorganic nanoparticles, they increase the flexibility and electroluminescent efficiency of PLEDs [150]. The addition of inorganic components into the polymer matrix can enhance the thermal, electrical, and optical characters of composite material [151, 152]. Sabah et al. [153] studied the role of ZnO, WO_3, V_2O_5, and TiO_2 as ISCs on the optical and electrical properties of the synthesized polyvinyl alcohol (PVA) for the PLED application. The obtained results showed PVA/ZnO and PVA/TiO_2 nanocomposites were the best candidates for the fabrication of PLEDs because of their clear emission bands. In another work, Jamatia et al. [154] mixed prepared $Fe_xZn_{1-x}O$ ($x = 0.01, 0.05, 0.10$) nanoparticles with poly[2-methoxy-5-(2-ethylhexyloxy)-1,4-phenylenevinylene] (MEH-PPV) polymer and used the as-prepared nanocomposite as thin active layer in PLEDs. Figure 9 depicts the scheme of the fabricated device in this study. ITO, Mg, poly(3,4-ethylene dioxythiophene) doped with polystyrene sulfonate (PEDOT:PSS), and $Fe_xZn_{1-x}O$/MEH-PPV were used as the anode, cathode, HTL layer, and active layer, respectively. Holes are introduced from the anode through the PEDOT:PSS layer into $Fe_xZn_{1-x}O$/MEH-PPV. However, the

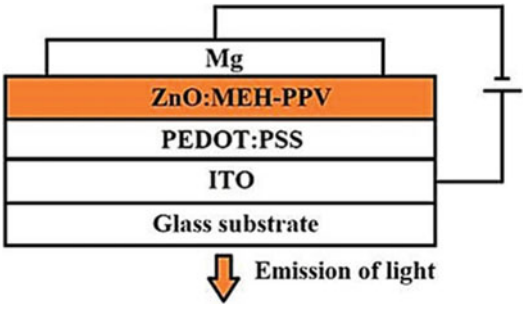

Fig. 9 Schematic diagram of the fabricated PLED using $Fe_xZn_{1-x}O$/MEH-PPV nanocomposite. Reproduced from [154] with permission

cathode injects electrons into the active layer. They showed that the luminance intensity of a PLED based on the as-prepared nanocomposite was significantly increased compared to the PLED based on neat MEH-PPV.

Another application of nanoparticle–polymer composites is in light-dependent resistor (LDR) devices. The LDR device or photoresistor cell is a semiconductor device whose resistance depends on the intensity of the entire light, and its resistance is decreased with the increasing light intensity [155]. LDR devices usually suffer from the high toxicity of the materials used in their manufacture [156]. Hence, the introduction of new, economical, and efficient environmentally friendly materials for LDRs has become an important research area in recent years. Among developed inorganic nanoparticles, ZnO nanostructures have triggered considerable interest in device applications because of their wide direct bandgap, high chemical, and thermal stability, inexpensive preparation, and high mechanical strength [157]. Hybrid ZnO with the conjugated polymers is considered a class of remarkable OISCs due to their synergic effect and nanoscale interaction [158]. Rawal et al. [158] synthesized hybrid polypyrrole-ZnO nanostructures through the chemical oxidation method and investigated the photoconduction behavior of the prepared nanocomposites. The dark conductivity of the nanocomposites decreased with the increasing nanoparticle concentration because of nanoscale interfacial interaction between the ZnO and polypyrrole. The structure of the electronic band of the polymer was altered due to the strong coupling between inorganic nanoparticles and polymer, leading to an improvement in the photosensitivity of nanocomposite. The photo-response of the synthesized nanocomposites was increased with enhancing illumination intensities, making polypyrrole-ZnO nanocomposites ideal candidate materials for the non-toxic LDR devices.

4.2 Metal–organic Frameworks

MOFs are an exciting group of hybrid inorganic–organic crystalline materials comprised of metal ions and organic ligands. Thanks to their unique properties, including abundant accessible active sites, high surface area, high intrinsic porosities as well as complimentary electronic and mechanical characteristics; MOFs have attracted immense research interests in different fields of electronic devices [112, 159–162]. The rapidly growing demand for efficient energy storage devices has motivated researchers to developed electrical energy storage devices, e.g., supercapacitors and batteries. The electrode materials are fundamental elements for these devices. Among employed materials, MOFs have been increasingly utilized in electrical energy storage devices because of their unique properties, including quick electron transfer, large specific surface areas, multiple redox-active sites, and short ion diffusion distance [162]. Hu et al. [163] reported the preparation of Ni- and Mn-based frameworks, named Ni-UMOFNs and MnUMOFNs, and investigated their performance as anode materials in rechargeable lithium batteries. Compared to Ni-UMOFNs, the Mn-UMOFNs showed a more favorable anodic performance, such as a

higher reversible capacity and rate capability. This better performance was attributed to the structural properties of Mn-UMOFNs over Ni-UMOFNs, including larger specific surface areas, the thinner thickness of nanosheets, and smaller ionic radius.

Among electrical energy storage devices, supercapacitors have received particular attention thanks to their excellent power density, good safety, and rapid energy storage function [164]. Porous materials, such as MOFs and/or MOF derivatives, have always been considered as the best candidate for supercapacitor development because they facilitate electron and mass transportation [165, 166]. Jia et al. [167] developed NiCo-MOF nanosheets as the anodic materials in asymmetric supercapacitors (ASCs). The NiCo-MOF nanosheets were prepared through the soaking method. The in-situ growth of nanosheets led to creating more pore structures, which enhances capacitive properties due to its more active sites. The NiCo-MOF nanosheets based ASC device exhibited excellent performance with high specific energy (57.8 Wh kg^{-1}) and 71.40% capacity retention after 6000 cycles.

4.3 Organic–Inorganic Halide Perovskite

Organic–inorganic halide perovskites are an interesting family of semiconductors with exciting applications ranging from SCs to LED devices. These materials follow the ABX3 structure, where A and B are two distinct cations with various ionic sizes, while X is an anion [168]. Recently, perovskites generated enormous interest in photodetection applications because of their remarkable optoelectronic properties, including high mobility [169], ferroelectric polarization [170], low binding energy [171], and dielectric constant [172]. Despite the intrinsic characteristics of perovskite materials, their limited photo-detection or response time (>10 μs) and response range (<800 nm) are considerably challenging to fabricate some high-speed and high-performance optoelectronic devices. However, continuous efforts have been made to surmount these obstacles [173–175]. For example, Geng et al. [176] directly integrated the $CH_3NH_3PbBr_3$ perovskite on a silicon substrate to develop a photodetector with broad-spectrum (405–1064 nm) and high-speed (520 ns).

SCs based on perovskite has received considerable research attention in the past decade due to their PCE, strong solar absorption, inexpensive materials constituents, and ease of fabrication [177, 178]. Various techniques have been employed to prepare perovskite electrode materials, such as one-step and two-step spin coating methods[179, 180], and physical vacuum-based deposition [181]. Fabrication methods affect the PCE by impacting the morphologies of perovskite materials [182].

Among perovskite materials, organometal halide $CH_3NH_3MX_3$ (M = Pb, Sn, X = halogen) has attracted intrinsic attention in SCs. The SC based on $CH_3NH_3MX_3$ was first fabricated in 2009. This SC exhibited a low PCE of about 3–4% [183]. This result led to the development of perovskite SCs with increased PCE. Jung et al. presented a perovskite SC with a PCE of 22.7%. In this work, a layer of poly(3-hexylthiophene) (P3HT) as an HTM was deposited on the perovskite

surface ((FAPbI$_3$)0.95(MAPbBr$_3$)0.05). P3HT is an ideal candidate for use as the HTM because of its excellent advantages, including low cost [184], remarkable optoelectronic properties [185, 186], and ease of fabrication [187, 188].

Thanks to their superb optoelectronic properties, such as external quantum efficiency, narrow emission bandwidth, high photoluminescence quantum efficiency (PLQE), and tunable emission wavelength [189], perovskite materials have been playing a significant role in developing LED devices. In the past several years, perovskite LED devices have undergone significant development to improve their efficiency. Recently, green, red, and near-infrared LED devices based on perovskite materials have been reported to have external quantum efficiency increased up to 21% [190–192]. Despite that blue perovskite LEDs are one of the main parts of lighting and display devices, they suffer from low PLQE because of their relatively large bandgap [193, 194]. To overcome this challenge, much progress has been made in the type of perovskite materials. Sun et al. [195] introduced a new way to increase the efficiency of blue-emitting perovskite nanocrystals. They synthesized composite materials, including CsPb(Cl/Br)$_3$ and Cs$_4$Pb(Cl/Br)$_6$ and then, enhance their efficiency to 90% through a simple anion-exchange reaction. These high-performance materials were used to fabricate blue LED devices and to prepare anti-counterfeiting inks.

5 Conclusion

Semiconducting materials have widely emerged in many device applications related to electronics, optoelectronics, energy storage, and analytical chemistry. These mainly fall into three families: OSCs, ISCs, and IOSCs. We described how diverse semiconductors were utilized as active materials for the design, development, and construction of devices. Advances in the preparation of π-conjugated oligomers, and conjugated polymers, as OSCs, have gained a lot of interest because of their potential in tunability properties, low cost, and flexibility. They are imperative for a range of applications including SCs, energy storage devices, OLEDs, OFETs, sensors, etc. OSCs will be able to decrease the cost of device manufacturing compared to ISCs. Another interesting type of nanostructure semiconducting material is ISC. Several types of metal oxides, metal chalcogenides, metal phosphides, metal phosphates, metal halides, and oxyhalides have been employed to fabricate devices. They present a great potential for the fabrication of chemiresistive gas sensors. Pure OSCs or ISCs are unable to fabricate some devices because their unique properties are insufficient. One of the major strategies to overcome the challenge of fabrication is using IOSCs due to their promising characters such as flexibility, low-cost production, and high efficiency. Furthermore, the hybrid IOSCs can be used to fabricate different devices, especially LED.

References

1. Gupta K, Gupta N (2016) Semiconductor materials: their properties, applications, and recent advances. Adv Semicond Mater Dev, 3–40
2. Pradhan N, Das Adhikari S, Nag A, Sarma D (2017) Luminescence, plasmonic, and magnetic properties of doped semiconductor nanocrystals. Angew Chem Int Ed 56:7038–7054
3. Zhou K, Zhou Y (2021) Introduction to organic-inorganic Heterojunction. Optoelectronic organic-inorganic semiconductor heterojunctions, pp. 1–8
4. Dashtian K, Hajati S, Ghaedi M (2020) L-phenylalanine-imprinted polydopamine-coated CdS/CdSe in type II heterojunction as an ultrasensitive photoelectrochemical biosensor for the PKU monitoring. Biosens. Bioelectron 165:112346
5. Dashtian K, Hajati S, Ghaedi M (2021) Ti-based solid-state imprinted-Cu2O/CuInSe2 heterojunction photoelectrochemical platform for highly selective dopamine monitoring. Sens Actuators B Chem 326:128824
6. Coropceanu V, Cornil J, da Silva Filho DA, Olivier Y, Silbey R, Brédas JL (2007) Charge transport in organic semiconductors. Chem Rev 107:926–952
7. Mishra A, Bäuerle P (2012) Small molecule organic semiconductors on the move: Promises for future solar energy technology. Angew Chem Int Ed 51:2020–2067
8. Jiang W, Li Y, Wang Z (2013) Heteroarenes as high-performance organic semiconductors. Chem Soc Rev 42:6113–6127
9. Li N, Niu X, Chen Q, Zhou H (2020) Towards commercialization: the operational stability of perovskite solar cells. Chem Soc Rev 49:8235–8286
10. Hiszpanski AM, Loo YL (2014) Directing the film structure of organic semiconductors via post-deposition processing for transistor and solar cell applications. Energy Environ Sci 7:592–608
11. Fukuda K, Yu K, Someya T (2020) The future of flexible organic solar cells. Adv Energy Mater 10:2000765
12. Brabec CJ, Sariciftci NS, Hummelen JC (2001) Plastic solar cells. Adv Funct Mater 11:15–26
13. Li G, Zhu R, Yang Y (2012) Polymer solar cells. Nat Photonics 6:153–161
14. Brendel M, Krause S, Steindamm A, Topczak AK, Sundarraj S, Erk P, Höhla S, Fruehauf N, Koch N, Pflaum J (2015) The effect of gradual fluorination on the properties of FnZnPc thin films and FnZnPc/C60 bilayer photovoltaic cells. Adv Funct Mater 25:1565–1573
15. Geiser A, Fan B, Benmansour H, Castro F, Heier J, Keller B, Mayerhofer KE, Nüesch F, Hany R (2008) Poly(3-hexylthiophene)/C60 heterojunction solar cells: implication of morphology on performance and ambipolar charge collection. Sol Energy Mater Sol Cells 92:464–473
16. Dennler G, Scharber MC, Brabec CJ (2009) Polymer-fullerene bulk-heterojunction solar cells. Adv Mater 21:1323–1338
17. Ramachandran M, Raj MR, Azeez UHA, Sorrentino A, Anandan S, Ashokkumar M (2020) Synthesis of random copolymer using Zig-Zag Naphthodithiophene for bulk Heterojunction polymer solar cell applications. J Polym Res 27:1–10
18. Sugathan V, John E, Sudhakar K (2015) Recent improvements in dye-sensitized solar cells: a review. Renew Sustain Energy Rev 52:54–64
19. Duvva N, Prasanthkumar S, Giribabu L (2019) Influence of strong electron-donating nature of phenothiazine on A3B-type porphyrin-based dye-sensitized solar cells. J Sol Energy 184:620–627
20. Mathew S, Yella A, Gao P, Humphry-Baker R, Curchod BF, Ashari-Astani N, Tavernelli I, Rothlisberger U, Nazeeruddin MK, Grätzel M (2014) Dye-sensitized solar cells with 13% efficiency achieved through the molecular engineering of porphyrin sensitizers. Nat Chem 6:242–247
21. Urbani M, Grätzel M, Nazeeruddin MK, Torres T (2014) Meso-substituted porphyrins for dye-sensitized solar cells. Chem Rev 114:12330–12396
22. Kalyanasundaram K (2010) Dye-sensitized solar cells
23. Ka Y, Hwang H, Kim C (2017) Hybrid organic tandem solar cell comprising small-molecule bottom and polymer: fullerene top subcells fabricated by thin-film transfer. Sci Rep 7:1–8

24. Chen Y, Ma D (2012) Organic semiconductor heterojunctions as charge generation layers and their application in tandem organic light-emitting diodes for high power efficiency. J Mater Chem 22:18718–18734
25. Salehi A, Dong C, Shin D-H, Zhu L, Papa C, Bui AT, Castellano FN, So F (2019) Realization of high-efficiency fluorescent organic light-emitting diodes with low driving voltage. Nat Commun 10:1–9
26. Chan C-Y, Tanaka M, Lee Y-T, Wong Y-W, Nakanotani H, Hatakeyama T, Adachi C (2021) Stable pure-blue hyperfluorescence organic light-emitting diodes with high-efficiency and narrow emission. Nat Photonics 15:203–207
27. Tang H, Li Y, Wei C, Chen B, Yang W, Wu H, Cao Y (2011) Novel yellow phosphorescent iridium complexes containing a carbazole–oxadiazole unit used in polymeric light-emitting diodes. Dyes Pigm 91:413–421
28. Zink DM, Volz D, Baumann T, Mydlak M, Flügge H, Friedrichs J, Nieger M, Bräse S (2013) Heteroleptic, dinuclear copper (I) complexes for application in organic light-emitting Diodes. Chem Mater 25:4471–4486
29. Ando M, Kawasaki M, Imazeki S, Sasaki H, Kamata T (2004) Self-aligned self-assembly process for fabricating organic thin-film transistors. Appl Phys 85:1849–1851
30. Sirringhaus H (2014) 25th-anniversary article: organic field-effect transistors: the path beyond amorphous silicon. Adv Mater 26:1319–1335
31. Anthony JE (2006) Functionalized acenes and heteroacenes for organic electronics. Chem Rev 106:5028–5048
32. Takimiya K, Shinamura S, Osaka I, Miyazaki E (2011) Thienoacene-based organic semiconductors. Adv Mater 23:4347–4370
33. Pandey M, Kumari N, Nagamatsu S, Pandey SS (2019) Recent advances in the orientation of conjugated polymers for organic field-effect transistors. J Mater Chem C 7:13323–13351
34. Chen M, Yan L, Zhao Y, Murtaza I, Meng H, Huang W (2018) Anthracene-based semiconductors for organic field-effect transistors. J Mater Chem C 6:7416–7444
35. Liu J, Dong H, Wang Z, Ji D, Cheng C, Geng H, Zhang H, Zhen Y, Jiang L, Fu H (2015) Thin-film field-effect transistors of 2, 6-diphenyl anthracene (DPA). ChemComm 51:11777–11779
36. Bayn A, Feng X, Müllen K, Haick H (2013) Field effect transistors based on polycyclic aromatic hydrocarbons for the detection and classification of volatile organic compounds. ACS Appl Mater Interfaces 5:3431–3440
37. Berto M, Casalini S, Di Lauro M, Marasso SL, Cocuzza M, Perrone D, Pinti M, Cossarizza A, Pirri CF, Simon DT (2016) Biorecognition in organic field-effect transistors biosensors: the role of the density of states of the organic semiconductor. Anal Chem 88:12330–12338
38. Fratoddi I, Venditti I, Cametti C, Russo MV (2015) Chemiresistive polyaniline-based gas sensors: a mini-review. Sens Actuat B Chem 220:534–548
39. Alizadeh N, Ghoorchian A (2014) Catalytic behavior of transition metal cations in electrosynthesis and growth of nanostructure conducting polypyrrole films on/between the passive Cu interdigital electrodes: application in gas sensors. Electroanalysis 26:2644–2654
40. Ghoorchian A, Alizadeh N (2018) Chemiresistor gas sensor based on sulfonated dye-doped modified conducting polypyrrole film for high sensitive detection of 2, 4, 6-trinitrotoluene in air. Sens Actuators B Chem 255:826–835
41. Liao F, Yin S, Toney MF, Subramanian V (2010) Physical discrimination of amine vapor mixtures using polythiophene gas sensor arrays. Sens Actuators B Chem 150:254–263
42. Hien HT, Giang HT, Van Hieu N, Trung T, Van Tuan C (2017) Elaboration of Pd-nanoparticle decorated polyaniline films for room temperature NH3 gas sensors. Sens Actuators B Chem 249:348–356
43. Wu Q, Shen W, Lv D, Chen W, Song W, Tan R (2021) An enhanced flexible room temperature ammonia gas sensor based on GP-PANI/PVDF multi-hierarchical nanocomposite film. Sens Actuators B Chem 334:129630
44. Namsheer K, Rout CS (2021) Conducting polymers: a comprehensive review on recent advances in synthesis, properties and applications. RSC Adv 11:5659–5697

45. Mortimer RJ, Dyer AL, Reynolds JR (2006) Electrochromic organic and polymeric materials for display applications. Displays 27:2–18
46. Ma F, Liu F, Hou Y, Niu H, Wang C (2020) Electrochromic materials based on novel polymers containing triphenylamine units and benzo [c][1, 2, 5] thiadiazole units. Synth Met 259:116235
47. Ghoorchian A, Madrakian T, Afkhami A, Bagheri H (2021) Spectroelectrochemical and electrochromic behavior of poly (methylene blue) and poly (thionine)-modified multi-walled carbon nanotubes. J Solid State Electrochem 25:1217–1229
48. Sun Y, Rogers JA (2007) Inorganic semiconductors for flexible electronics. Adv Mater 19:1897–1916
49. Garlapati SK, Divya M, Breitung B, Kruk R, Hahn H, Dasgupta S (2018) Printed electronics based on inorganic semiconductors: from processes and materials to devices. Adv Mater 30:1707600
50. Jiang Y, Tian B (2018) Inorganic semiconductor biointerfaces. Nat Rev Mater 3:473–490
51. Guo S, Yang D, Zhang S, Dong Q, Li B, Tran N, Li Z, Xiong Y, Zaghloul ME (2019) Development of a cloud-based epidermal MoSe2 device for hazardous gas sensing. Adv Funct Mater 29:1900138
52. Athanasopoulos S, Tscheuschner S, Bässler H, Köhler A (2017) Efficient charge separation of cold charge-transfer states in organic solar cells through incoherent hopping. J Phys Chem Lett 8:2093–2098
53. Petti L, Münzenrieder N, Vogt C, Faber H, Büthe L, Cantarella G, Bottacchi F, Anthopoulos TD, Tröster G (2016) Metal oxide semiconductor thin-film transistors for flexible electronics. Appl Phys Rev 3:021303
54. Boro B, Gogoi B, Rajbongshi B, Ramchiary A (2018) Nano-structured TiO2/ZnO nanocomposite for dye-sensitized solar cells application: a review. Renew Sustain Energy Rev 81:2264–2270
55. Swarnkar A, Mir WJ, Chakraborty R, Jagadeeswararao M, Sheikh T, Nag A (2019) Are chalcogenide perovskites an emerging class of semiconductors for optoelectronic properties and solar cell? Chem Mater 31:565–575
56. Im JS, Lee SK, Lee YS (2011) Cocktail effect of Fe 2 O 3 and TiO 2 semiconductors for a high performance dye-sensitized solar cell. Appl Surf Sci 257:2164–2169
57. Kaur R, Sharma AL, Kim K-H, Deep A (2017) A novel CdTe/Eu-MOF photoanode for application in quantum dot-sensitized solar cell to improve power conversion efficiency. J Ind Eng Chem 53:77–81
58. Spoerke ED, Small LJ, Foster ME, Wheeler J, Ullman AM, Stavila V, Rodriguez M, Allendorf MD (2017) MOF-sensitized solar cells enabled by a pillared porphyrin framework. J Phys Chem C 121:4816–4824
59. Pérez-Tomás A, Mingorance A, Tanenbaum D, Lira-Cantú M (2018) Metal oxides in photovoltaics: all-oxide, ferroic, and perovskite solar cells. The future of semiconductor oxides in next-generation solar cells, pp. 267–356
60. Wei H, Shi J, Xu X, Xiao J, Luo J, Dong J, Lv S, Zhu L, Wu H, Li D (2015) Enhanced charge collection with ultrathin AlO x electron blocking layer for hole-transporting material-free perovskite solar cell. Phys Chem Chem Phys 17:4937–4944
61. Lee H-J, Abe K, Kim JS, Lee M-J (2017) Electron-blocking by the potential barrier originated from the asymmetrical local density of state in the oxide semiconductor. Sci Rep 7:1–8
62. Du J, Shi JJ (2019) 2D Ca3Sn2S7 chalcogenide perovskite: a Graphene-like semiconductor with direct Bandgap 0.5 eV and ultrahigh carrier mobility 6.7× 104 cm2 V− 1 s− 1. Adv Mater 31:1905643
63. Park SI, Brenner DS, Shin G, Morgan CD, Copits BA, Chung HU, Pullen MY, Noh KN, Davidson S, Oh SJ (2015) Soft, stretchable, fully implantable miniaturized optoelectronic systems for wireless optogenetics. Nat Biotechnol 33:1280–1286
64. Gutruf P, Yin RT, Lee KB, Ausra J, Brennan JA, Qiao Y, Xie Z, Peralta R, Talarico O, Murillo A (2019) Wireless, battery-free, fully implantable multimodal and multisite pacemakers for applications in small animal models. Nat Commun 10:1–10

65. Zhang H, Rogers JA (2019) Recent advances in flexible inorganic light-emitting diodes: from materials design to integrated optoelectronic platforms. Adv Opt Mater 7:1800936
66. Zhang Y, Mickle AD, Gutruf P, McIlvried LA, Guo H, Wu Y, Golden JP, Xu Y, Grajales-Reyes JG, Wang X (2019) Battery-free, fully implantable optofluidic cuff system for wireless optogenetic and pharmacological neuromodulation of peripheral nerves. Sci Adv 5:eaaw5296
67. Burton A, Obaid SN, Vázquez-Guardado A, Schmit MB, Stuart T, Cai L, Chen Z, Kandela I, Haney CR, Waters EA (2020) Wireless, battery-free subdermally implantable photometry systems for chronic recording of neural dynamics. PNAS 117:2835–2845
68. Kim T-I, McCall JG, Jung YH, Huang X, Siuda ER, Li Y, Song J, Song YM, Pao HA, Kim R-H (2013) Injectable, cellular-scale optoelectronics with applications for wireless optogenetics. Science 340:211–216
69. Shin G, Gomez AM, Al-Hasani R, Jeong YR, Kim J, Xie Z, Banks A, Lee SM, Han SY, Yoo CJ (2017) Flexible near-field wireless optoelectronics as subdermal implants for broad applications in optogenetics. Neuron 93:509–521. e503
70. Jaaniso R, Tan OK (2013) Semiconductor gas sensors
71. Dasgupta N, Ranjan S, Lichtfouse E (2018) Environmental nanotechnology, vol 2
72. Hagleitner C, Lange D, Hierlemann A, Brand O, Baltes H (2002) CMOS single-chip gas detection system comprising capacitive, calorimetric and mass-sensitive microsensors. IEEE J Solid-State Circuits 37:1867–1878
73. Kim Y, Kwon KC, Kang S, Kim C, Kim TH, Hong S-P, Park SY, Suh JM, Choi M-J, Han S (2019) Two-dimensional NbS2 gas sensors for selective and reversible NO2 detection at room temperature. ACS Sens 4:2395–2402
74. Ou JZ, Ge W, Carey B, Daeneke T, Rotbart A, Shan W, Wang Y, Fu Z, Chrimes AF, Wlodarski W (2015) Physisorption-based charge transfer in two-dimensional SnS2 for selective and reversible NO2 gas sensing. ACS Nano 9:10313–10323
75. Dey A (2018) Semiconductor metal oxide gas sensors: a review. Mater Sci Eng B 229:206–217
76. Han D, Zhai L, Gu F, Wang Z (2018) Highly sensitive NO2 gas sensor of ppb-level detection based on In2O3 nanobricks at low temperature. Sens Actuators B Chem 262:655–663
77. Han B, Liu X, Xing X, Chen N, Xiao X, Liu S, Wang Y (2016) A high response butanol gas sensor based on ZnO hollow spheres. Sens Actuators B Chem 237:423–430
78. Rana C, Bera SR, Saha S (2019) Growth of SnS nanoparticles and its ability as ethanol gas sensor. J Mater Sci Mater Electron 30:2016–2029
79. Zhang L, Li Z, Liu J, Peng Z, Zhou J, Zhang H, Li Y (2020) Optoelectronic gas sensor based on few-layered InSe Nanosheets for NO2 detection with ultrahigh antihumidity ability. Anal Chem 92:11277–11287
80. Parfenov AA, Yamilova OR, Gutsev LG, Sagdullina DK, Novikov AV, Ramachandran BR, Stevenson KJ, Aldoshin SM, Troshin PA (2021) Highly sensitive and selective ammonia gas sensor based on FAPbCl 3 lead halide perovskites. J Mater Chem C 9:2561–2568
81. Nur'aini A, Oh I (2020) Volatile organic compound gas sensors based on methylammonium lead iodide perovskite operating at room temperature. RSC Adv 10:12982–12987
82. Nakate UT, Ahmad R, Patil P, Wang Y, Bhat KS, Mahmoudi T, Yu Y, Suh E-K, Hahn Y-B (2019) Improved selectivity and low concentration hydrogen gas sensor application of Pd sensitized heterojunction n-ZnO/p-NiO nanostructures. J Alloys Compd 797:456–464
83. Ranjbar F, Hajati S, Ghaedi M, Dashtian K, Naderi H, Toth J (2021) Highly selective MXene/V2O5/CuWO4-based ultra-sensitive room temperature ammonia sensor. J Hazard Mater, 126196
84. Naderi H, Hajati S, Ghaedi M, Dashtian K, Sabzehmeidani M (2020) Sensitive, selective and rapid ammonia-sensing by gold nanoparticle-sensitized V2O5/CuWO4 heterojunctions for exhaled breath analysis. Appl Surf Sci 501:144270
85. Tabata H, Sato Y, Oi K, Kubo O, Katayama M (2018) Bias-and gate-tunable gas sensor response originating from modulation in the Schottky barrier height of a graphene/MoS2 van der Waals heterojunction. ACS Appl Mater Interf 10:38387–38393
86. Minh Triet N, Thai Duy L, Hwang B-U, Hanif A, Siddiqui S, Park K-H, Cho C-Y, Lee N-E (2017) High-performance Schottky diode gas sensor based on the heterojunction of

three-dimensional nanohybrids of reduced graphene oxide–vertical ZnO nanorods on an AlGaN/GaN layer. ACS Appl Mater Interf 9:30722–30732
87. Liu J, Zhang L, Cheng B, Fan J, Yu J (2021) A high-response formaldehyde sensor based on fibrous Ag-ZnO/In2O3 with multi-level heterojunctions. J Hazard Mater 413:125352
88. Dinesh V, Sukhananazerin A, Biji P (2017) An emphatic study on role of spill-over sensitization and surface defects on NO2 gas sensor properties of ultralong ZnO@ Au heterojunction NRs. J Alloys Compd 712:811–821
89. Reddeppa M, Mitta SB, Park B-G, Kim S-G, Park SH, Kim M-D (2019) DNA-CTMA functionalized GaN surfaces for NO2 gas sensor at room temperature under UV illumination. Org Electron 65:334–340
90. Hu X, Zhu Z, Li Z, Xie L, Wu Y, Zheng L (2018) Heterostructure of CuO microspheres modified with CuFe2O4 nanoparticles for highly sensitive H2S gas sensor. Sens Actuators B Chem 264:139–149
91. Wang X, Wang T, Si G, Li Y, Zhang S, Deng X, Xu X (2020) Oxygen vacancy defects engineering on Ce-doped α-Fe2O3 gas sensor for reducing gases. Sens Actuators B Chem 302:127165
92. Gao X, Zhang T (2018) An overview: Facet-dependent metal oxide semiconductor gas sensors. Sens Actuat B Chem 277:604–633
93. Jo Y-M, Kim T-H, Lee C-S, Lim K, Na CW, Abdel-Hady F, Wazzan AA, Lee J-H (2018) Metal–organic framework-derived hollow hierarchical Co3O4 nanocages with tunable size and morphology: ultrasensitive and highly selective detection of methylbenzenes. ACS Appl Mater Interf 10:8860–8868
94. Song X-Z, Qiao L, Sun K-M, Tan Z, Ma W, Kang X-L, Sun F-F, Huang T, Wang X-F (2018) Triple-shelled ZnO/ZnFe2O4 heterojunctional hollow microspheres derived from Prussian Blue analogue as high-performance acetone sensors. Sens Actuat B Chem 256:374–382
95. Koo W-T, Choi S-J, Jang J-S, Kim I-D (2017) Metal-organic framework templated synthesis of ultrasmall catalyst loaded ZnO/ZnCo 2 O 4 hollow spheres for enhanced gas sensing properties. Sci Rep 7:1–10
96. Majhi SM, Mirzaei A, Kim HW, Kim SS (2021) Reduced graphene oxide (rGO)-loaded metal-oxide nanofiber gas sensors: an overview. Sens 21:1352
97. Amarnath M, Gurunathan K (2021) Highly selective CO2 gas sensor using stabilized NiO-In2O3 nanospheres coated reduced graphene oxide sensing electrodes at room temperature. J Alloys Compd 857:157584
98. Hwang K, Ahn J, Cho I, Kang K, Kim K, Choi J, Polychronopoulou K, Park I (2020) Microporous elastomer filter coated with metal organic frameworks for improved selectivity and stability of metal oxide gas sensors. ACS Appl Mater Interfaces 12:13338–13347
99. Li S, Liu A, Yang Z, He J, Wang J, Liu F, Lu H, Yan X, Sun P, Liang X (2019) Room temperature gas sensor based on tin dioxide@ polyaniline nanocomposite assembled on flexible substrate: ppb-level detection of NH3. Sens Actuators B Chem 299:126970
100. Zhang Y, Zhang J, Jiang Y, Duan Z, Liu B, Zhao Q, Wang S, Yuan Z, Tai H (2020) Ultrasensitive flexible NH3 gas sensor based on polyaniline/SrGe4O9 nanocomposite with ppt-level detection ability at room temperature. Sens Actuators B Chem 319:128293
101. Yoon J-W, Lee J-H (2017) Toward breath analysis on a chip for disease diagnosis using semiconductor-based chemiresistors: recent progress and future perspectives. Lab Chip 17:3537–3557
102. Gagaoudakis E, Panagiotopoulos A, Maksudov T, Moschogiannaki M, Katerinopoulou D, Kakavelakis G, Kiriakidis G, Binas V, Kymakis E, Petridis K (2020) Self-powered, flexible and room temperature operated solution processed hybrid metal halide p-type sensing element for efficient hydrogen detection. J Phy Mater 3:014010
103. Majhi SM, Naik GK, Lee H-J, Song H-G, Lee C-R, Lee I-H, Yu Y-T (2018) Au@ NiO core-shell nanoparticles as a p-type gas sensor: novel synthesis, characterization, and their gas sensing properties with sensing mechanism. Sens Actuat B Chem 268:223–231
104. Hua Z, Tian C, Huang D, Yuan W, Zhang C, Tian X, Wang M, Li E (2018) Power-law response of metal oxide semiconductor gas sensors to oxygen in presence of reducing gases. Sens Actuat B Chem 267:510–518

105. Ma J, Ren Y, Zhou X, Liu L, Zhu Y, Cheng X, Xu P, Li X, Deng Y, Zhao D (2018) Pt nanoparticles sensitized ordered mesoporous WO3 semiconductor: gas sensing performance and mechanism study. Adv Funct Mater 28:1705268
106. Dun M, Tan J, Tan W, Tang M, Huang X (2019) CdS quantum dots supported by ultrathin porous nanosheets assembled into hollowed-out Co3O4 microspheres: a room-temperature H2S gas sensor with ultra-fast response and recovery. Sens Actuat B Chem 298:126839
107. Wang J, Deng H, Li X, Yang C, Xia Y (2020) Visible-light photocatalysis enhanced room-temperature formaldehyde gas sensing by MoS2/rGO hybrids. Sens Actuat B Chem 304:127317
108. Zhang J, Qin Z, Zeng D, Xie C (2017) Metal-oxide-semiconductor based gas sensors: screening, preparation, and integration. Phys Chem Chem Phys 19:6313–6329
109. Yang Z, Zhang D, Chen H (2019) MOF-derived indium oxide hollow microtubes/MoS2 nanoparticles for NO2 gas sensing. Sens Actuat B Chem 300:127037
110. Schiettecatte P, Rousaki A, Vandenabeele P, Geiregat P, Hens Z (2020) Liquid-phase exfoliation of rhenium disulfide by solubility parameter matching. Langmuir
111. Liu Y, Li R (2020) Study on ultrasound-assisted liquid-phase exfoliation for preparing graphene-like molybdenum disulfide nanosheets. Ultrason. Sonochem 63:104923
112. Jiang H, Cao L, Li Y, Li W, Ye X, Deng W, Jiang X, Wang G, Xu G (2020) Organic "receptor" fully covered few-layer organic–metal chalcogenides for high-performance chemiresistive gas sensing at room temperature. ChemComm 56:5366–5369
113. Jha RK, Bhat N (2020) Recent progress in chemiresistive gas sensing technology based on molybdenum and tungsten chalcogenide nanostructures. Adv Mater Interf 7:1901992
114. Kim J-H, Kim J-Y, Mirzaei A, Kim HW, Kim SS (2021) Synergistic effects of SnO2 and Au nanoparticles decorated on WS2 nanosheets for flexible, room-temperature CO gas sensing. Sens Actuat B Chem 332:129493
115. Kumar S, Pavelyev V, Mishra P, Tripathi N, Sharma P, Calle F (2020) A review on 2D transition metal di-chalcogenides and metal oxide nanostructures based NO2 gas sensors. Mat Sci Semicon Proc 107:104865
116. Xu H, Ju D, Chen Z, Han R, Zhai T, Yu H, Liu C, Wu X, Wang J, Cao B (2018) A novel hetero-structure sensor based on Au/Mg-doped TiO2/SnO2 nanosheets directly grown on Al2O3 ceramic tubes. Sens Actuat B Chem 273:328–335
117. Xu Y, Ma T, Zheng L, Sun L, Liu X, Zhao Y, Zhang J (2019) Rational design of Au/Co3O4-functionalized W18O49 hollow heterostructures with high sensitivity and ultralow limit for triethylamine detection. Sens Actuat B Chem 284:202–212
118. Raghu AV, Karuppanan KK, Nampoothiri J, Pullithadathil B (2019) Wearable, flexible ethanol gas sensor based on TiO2 nanoparticles-grafted 2D-titanium carbide nanosheets. ACS Appl Nano Mater 2:1152–1163
119. Li W, Chen R, Qi W, Cai L, Sun Y, Sun M, Li C, Yang X, Xiang L, Xie D (2019) Reduced graphene oxide/mesoporous ZnO NSs hybrid fibers for flexible, stretchable, twisted, and wearable NO2 E-textile gas sensor. ACS Sens 4:2809–2818
120. Moon HG, Jung Y, Han SD, Shim Y-S, Jung W-S, Lee T, Lee S, Park JH, Baek S-H, Kim J-S (2018) All villi-like metal oxide nanostructures-based chemiresistive electronic nose for an exhaled breath analyzer. Sens Actuat B Chem 257:295–302
121. Yan Q, Gao L, Tang J, Liu H (2019) Flexible and stretchable photodetectors and gas sensors for wearable healthcare based on solution-processable metal chalcogenides. J Semicond 40:111604
122. Gregis G, Sanchez J-B, Bezverkhyy I, Guy W, Berger F, Fierro V, Bellat J-P, Celzard A (2018) Detection and quantification of lung cancer biomarkers by a micro-analytical device using a single metal oxide-based gas sensor. Sens Actuat B Chem 255:391–400
123. Wu T-C, De Luca A, Zhong Q, Zhu X, Ogbeide O, Um D-S, Hu G, Albrow-Owen T, Udrea F, Hasan T (2019) Inkjet-printed CMOS-integrated graphene–metal oxide sensors for breath analysis. NPJ 2D Mater Appl 3:1–10
124. Yang D, Gopal RA, Lkhagvaa T, Choi D (2021) Metal oxide gas sensors for exhaled breath analysis: a review. Meas Sci Technol

125. Kalidoss R, Umapathy S (2020) An overview on the exponential growth of non-invasive diagnosis of diabetes mellitus from exhaled breath by nanostructured metal oxide chemi-resistive gas sensors and μ-preconcentrator. Biomed Microd 22:1–9
126. Salam A (2020) Internet of things for sustainable mining. Int Things Sustain Comm Develop, 243–271
127. Dhingra S, Madda RB, Gandomi AH, Patan R, Daneshmand M (2019) Internet of Things mobile–air pollution monitoring system (IoT-Mobair). IEEE Internet Things J 6:5577–5584
128. Johannessen LN, Grimstad HJ, Skjetne JE, Myklebust IN, Svendsen KVH (2020) Embedded systems and the internet of things: can low-cost gas sensors be used in risk assessment of occupational exposure? J Occup Environ Hyg Indexing 17:495–503
129. Choudhary RB, Nayak D (2021) Tailoring the properties of 2-D rGO-PPy-ZnS nanocomposite as emissive layer for OLEDs. Optik 231:166336
130. Kesavan AV, Ramamurthy PC (2021) Photo-active polymer nanocomposite layer for energy applications. Polymer-based advanced functional composites for optoelectronic and energy applications, pp. 135–156
131. Liao Y, Tian Y, Ma X, Zhao M, Qian J, Wang X (2020) Flexible electronics directly written with an ultrastable ballpoint pen based on a graphene nanosheets/MWCNTs/Carbon Black Nanocomposite. ACS Appl Electron Mater
132. Kalia S, Haldorai Y (2015) Organic-inorganic hybrid nanomaterials, vol 267
133. Sheng X, Zhao Y, Zhang L, Lu X (2019) Properties of two-dimensional Ti3C2 MXene/thermoplastic polyurethane nanocomposites with effective reinforcement via melt blending. Compos Sci Technol 181:107710
134. Abedi S, Abdouss M (2014) A review of clay-supported Ziegler-Natta catalysts for production of polyolefin/clay nanocomposites through in situ polymerization. APPL CATAL A-GEN 475:386–409
135. Balazs AC, Emrick T, Russell TP (2006) Nanoparticle polymer composites: where two small worlds meet. Science 314:1107–1110
136. Boles MA, Ling D, Hyeon T, Talapin DV (2016) The surface science of nanocrystals. Nat Mater 15:141–153
137. Qin S, Hu Y, Tian X, Tian Y, Liu W, Zhao L (2020) Modification of cellulose nanocrystals by self-assembly nucleation agents to improve poly (L-lactide) nanocomposite'properties. Cellulose 27:4337–4353
138. Peng B, Wu H, Bao W, Guo S, Chen Y, Huang H, Chen H, Lai S-Y, Jow J (2011) Effects of ultrasound on the morphology and properties of propylene-based plastomer/nanosilica composites. Polym J 43:91–96
139. Yun HJ, Lim J, Roh J, Neo DCJ, Law M, Klimov VI (2020) Solution-processable integrated CMOS circuits based on colloidal CuInSe 2 quantum dots. Nat Commun 11:1–10
140. Kagan CR, Bassett LC, Murray CB, Thompson SM (2020) Colloidal quantum dots as platforms for quantum information science. Chem Rev 121:3186–3233
141. Roghabadi FA, Aghmiuni KO, Ahmadi V (2016) Optical and electrical simulation of hybrid solar cell based on conjugated polymer and size-tunable CdSe quantum dots: Influence of the QDs size. Org Electron 34:164–171
142. Roghabadi FA, Kokabi M, Ahmadi V, Abaeiani G (2016) Quantum dots crosslinking as a new method for improving charge transport of polymer/quantum dots hybrid solar cells and fabricating solvent-resistant film. Electrochim Acta 222:881–887
143. Li Z, Wang W, Greenham NC, McNeill CR (2014) Influence of nanoparticle shape on charge transport and recombination in polymer/nanocrystal solar cells. Phys Chem Chem Phys 16:25684–25693
144. Liras M, Barawi M, Víctor A (2019) Hybrid materials based on conjugated polymers and inorganic semiconductors as photocatalysts: from environmental to energy applications. Chem Soc Rev 48:5454–5487
145. Schneider J, Matsuoka M, Takeuchi M, Zhang J, Horiuchi Y, Anpo M, Bahnemann DW (2014) Understanding TiO2 photocatalysis: mechanisms and materials. Chem Rev 114:9919–9986

146. Zhang G, Lan ZA, Wang X (2016) Conjugated polymers: catalysts for photocatalytic hydrogen evolution. Angew Chem Int Ed 55:15712–15727
147. Park J (2017) Visible and near infrared light active photocatalysis based on conjugated polymers. J Ind Eng Chem 51:27–43
148. Vij D (2004) Handbook of electroluminescent materials
149. Park JH, Lim YT, Park OO, Kim JK, Yu J-W, Kim YC (2004) Polymer/gold nanoparticle nanocomposite light-emitting diodes: enhancement of electroluminescence stability and quantum efficiency of blue-light-emitting polymers. Chem Mater 16:688–692
150. Dey S, Kar AK (2021) Effect of acceptor concentration in the FRET controlled photoluminescence of PMMA-ZnO nanocomposite for the application of PLED device. Opt Laser Technol 136:106811
151. Colvin VL, Schlamp MC, Alivisatos AP (1994) Light-emitting diodes made from cadmium selenide nanocrystals and a semiconducting polymer. Nature 370:354–357
152. Xiong H-M, Shen W-Z, Wang Z-D, Zhang X, Xia Y-Y (2006) Liquid polymer nanocomposites PEGME− SnO2 and PEGME− TiO2 prepared through solvothermal methods. Chem Mater 18:3850–3854
153. Sabah FA, Razak IA, Kabaa E, Zaini M, Omar A (2020) Characterization of hybrid organic/inorganic semiconductor materials for potential light emitting applications. Opt Mater 107:110117
154. Jamatia T, Skoda D, Urbanek P, Sevcik J, Maslik J, Munster L, Kalina L, Kuritka I (2019) Microwave-assisted synthesis of Fe x Zn 1− x O nanoparticles for use in MEH-PPV nanocomposites and their application in polymer light-emitting diodes. J Mater Sci Mater Electron 30:11269–11281
155. Román-Raya J, Ruiz-García I, Escobedo P, Palma AJ, Guirado D, Carvajal MA (2020) Light-dependent resistors as dosimetric sensors in radiotherapy. Sens 20:1568
156. Luque A, Hegedus S (2003) Photovoltaic science and engineering
157. Pan L, Muhammad T, Ma L, Huang Z-F, Wang S, Wang L, Zou J-J, Zhang X (2016) MOF-derived C-doped ZnO prepared via a two-step calcination for efficient photocatalysis. Appl Catal B 189:181–191
158. Rawal I, Dwivedi N, Tripathi RK, Panwar O, Malik HK (2017) Organic-inorganic hybrid nanomaterials for advanced light dependent resistors. Mater Chem Phys 202:169–176
159. Zhao R, Liang Z, Zou R, Xu Q (2018) Metal-organic frameworks for batteries. Joule 2:2235–2259
160. Xin N, Liu Y, Niu H, Bai H, Shi W (2020) In-situ construction of metal organic frameworks derived Co/Zn–S sandwiched graphene film as free-standing electrodes for ultra-high energy density supercapacitors. J Power Sourc 451:227772
161. Ajdari FB, Kowsari E, Shahrak MN, Ehsani A, Kiaei, Z, Torkzaban H, Ershadi M, Eshkalak SK, Haddadi-Asl V, Chinnappan A (2020) A review on the field patents and recent developments over the application of metal organic frameworks (MOFs) in supercapacitors. Coord Chem Rev 422:213441
162. Zhao W, Peng J, Wang W, Liu S, Zhao Q, Huang W (2018) Ultrathin two-dimensional metal-organic framework nanosheets for functional electronic devices. Coord Chem Rev 377:44–63
163. Li C, Hu X, Tong W, Yan W, Lou X, Shen M, Hu B (2017) Ultrathin manganese-based metal–organic framework nanosheets: low-cost and energy-dense lithium storage anodes with the coexistence of metal and ligand redox activities. ACS Appl Mater Interfaces 9:29829–29838
164. Wang D-G, Liang Z, Gao S, Qu C, Zou R (2020) Metal-organic framework-based materials for hybrid supercapacitor application. Coord Chem Rev 404:213093
165. Li B, Dai F, Xiao Q, Yang L, Shen J, Zhang C, Cai M (2016) Nitrogen-doped activated carbon for a high energy hybrid supercapacitor. Energy Environ Sci 9:102–106
166. Chen S, Zhao L, Wei W, Li Y, Mi L (2020) A novel strategy to synthesize NiCo layered double hydroxide nanotube from metal organic framework composite for high-performance supercapacitor. J Alloys Compd 831:154794
167. Jia R, Zhao C, Huang Z, Liu X, Wang D, Hui Z, Xu X (2020) An in situ growth strategy of NiCo-MOF nanosheets with more activity sites for asymmetric supercapacitors. Ionics 26:6309–6318

168. Qiu L, He S, Ono LK, Qi Y (2020) Progress of surface science studies on ABX3-based metal halide perovskite solar cells. Adv Energy Mater 10:1902726
169. Stranks SD, Snaith HJ (2015) Metal-halide perovskites for photovoltaic and light-emitting devices. Nat Nanotechnol 10:391–402
170. Frost JM, Butler KT, Brivio F, Hendon CH, Van Schilfgaarde M, Walsh A (2014) Atomistic origins of high-performance in hybrid halide perovskite solar cells. Nano Lett 14:2584–2590
171. Miyata A, Mitioglu A, Plochocka P, Portugall O, Wang JT-W, Stranks SD, Snaith HJ, Nicholas RJ (2015) Direct measurement of the exciton binding energy and effective masses for charge carriers in organic–inorganic tri-halide perovskites. Nat Phys 11:582–587
172. Juarez-Perez EJ, Sanchez RS, Badia L, Garcia-Belmonte G, Kang YS, Mora-Sero I, Bisquert J (2014) Photoinduced giant dielectric constant in lead halide perovskite solar cells. J Phys Chem Lett 5:2390–2394
173. Arakawa Y, Nakamura T, Urino Y, Fujita T (2013) Silicon photonics for next generation system integration platform. IEEE Commun Mag 51:72–77
174. Koos C, Vorreau P, Vallaitis T, Dumon P, Bogaerts W, Baets R, Esembeson B, Biaggio I, Michinobu T, Diederich F (2009) All-optical high-speed signal processing with silicon–organic hybrid slot waveguides. Nat Photonics 3:216–219
175. Miller DA (2009) Device requirements for optical interconnects to silicon chips. Proc IEEE 97:1166–1185
176. Geng X, Wang F, Tian H, Feng Q, Zhang H, Liang R, Shen Y, Ju Z, Gou G-Y, Deng N (2020) Ultrafast photodetector by integrating perovskite directly on silicon wafer. ACS Nano 14:2860–2868
177. Zhang L, Zhao Y, Dai Q (2021) Recent progress in perovskite solar cell: fabrication, efficiency, and stability. Devel Solar Cells Theory Exper 1
178. Jung HS, Park NG (2015) Perovskite solar cells: from materials to devices. Small 11:10–25
179. Sun S, Salim T, Mathews N, Duchamp M, Boothroyd C, Xing G, Sum TC, Lam YM (2014) The origin of high efficiency in low-temperature solution-processable bilayer organometal halide hybrid solar cells. Energy Environ Sci 7:399–407
180. Burschka J, Pellet N, Moon S-J, Humphry-Baker R, Gao P, Nazeeruddin MK, Grätzel M (2013) Sequential deposition as a route to high-performance perovskite-sensitized solar cells. Nature 499:316–319
181. Liu M (2013) Johnston, and HJ Snaith. Nature 501:395–398
182. Nguyen MT, Vu TVP, Bui BT, Luong TT, Nguyen MH, Ngoc LHH, Truong TT, Nguyen-Tran T (2016) Optical and structural study of organometal halide materials for applications in perovskite-based solar cells. J Electron Mater 45:2322–2327
183. Kojima A, Teshima K, Shirai Y, Miyasaka T (2009) Organometal halide perovskites as visible-light sensitizers for photovoltaic cells. J Am Chem Soc 131:6050–6051
184. Zhang M, Lyu M, Yu H, Yun JH, Wang Q, Wang L (2015) Stable and low-cost mesoscopic CH3NH3PbI2Br perovskite solar cells by using a thin poly (3-hexylthiophene) layer as a hole transporter. Chem Eur J 21:434–439
185. Ludwigs S (2014) P3HT revisited-from molecular scale to solar cell devices, vol 265
186. Kim Y, Cook S, Tuladhar SM, Choulis SA, Nelson J, Durrant JR, Bradley DD, Giles M, McCulloch I, Ha C-S (2011) A strong regioregularity effect in self-organizing conjugated polymer films and high-efficiency polythiophene: fullerene solar cells. Mater Sustain Energy Collect Peer-Review Res Rev Art Nat Publish Group, pp 63–69
187. Krebs FC, Gevorgyan SA, Alstrup J (2009) A roll-to-roll process to flexible polymer solar cells: model studies, manufacture and operational stability studies. J Mater Chem 19:5442–5451
188. Osaka I, McCullough RD (2008) Advances in molecular design and synthesis of regioregular polythiophenes. Acc Chem Res 41:1202–1214
189. Yang X, Zhang X, Deng J, Chu Z, Jiang Q, Meng J, Wang P, Zhang L, Yin Z, You J (2018) Efficient green light-emitting diodes based on quasi-two-dimensional composition and phase engineered perovskite with surface passivation. Nat Commun 9:1–8

190. Chiba T, Hayashi Y, Ebe H, Hoshi K, Sato J, Sato S, Pu Y-J, Ohisa S, Kido J (2018) Anion-exchange red perovskite quantum dots with ammonium iodine salts for highly efficient light-emitting devices. Nat Photonics 12:681–687
191. Lin K, Xing J, Quan LN, de Arquer FPG, Gong X, Lu J, Xie L, Zhao W, Zhang D, Yan C (2018) Perovskite light-emitting diodes with external quantum efficiency exceeding 20 per cent. Nature 562:245–248
192. Cao Y, Wang N, Tian H, Guo J, Wei Y, Chen H, Miao Y, Zou W, Pan K, He Y (2018) Perovskite light-emitting diodes based on spontaneously formed submicrometre-scale structures. Nature 562:249–253
193. Ahmed GH, El-Demellawi JK, Yin J, Pan J, Velusamy DB, Hedhili MN, Alarousu E, Bakr OM, Alshareef HN, Mohammed OF (2018) Giant photoluminescence enhancement in CsPbCl3 perovskite nanocrystals by simultaneous dual-surface passivation. ACS Energy Lett 3:2301–2307
194. ten Brinck S, Infante I (2016) Surface termination, morphology, and bright photoluminescence of cesium lead halide perovskite nanocrystals. ACS Energy Lett 1:1266–1272
195. Zito J, Infante I (2021) The future of ligand engineering in colloidal semiconductor nanocrystals. Acc Chem Res 54:1555–1564

Chapter 5
Reduced Graphene Oxide/Silicon Nanowire Heterojunction-Fabrication and Photovoltaic Application

Sadhna Rai, Rabina Bhujel, Joydeep Biswas, and Bibhu P. Swain

1 Introduction

The photovoltaics (PV) field has made tremendous advancement in the last decade, with an average compound annual growth rate of more than 35%. Wilson et al., in their article "The 2020 photovoltaic technologies roadmap" reported that "At the end of 2019, the world's cumulative PV capacity was 591 GW with an annual module production capacity of 184 GW and shipments of approximately 125 GW" [1]. PV plays a significant role in the journey of the world's transition to renewable energy because it is environmentally friendly, and there is no carbon emission and is cost-efficient.

The performance of the PV cells depends on their constituent materials. Silicon is widely used in PV cells because of its abundant availability, non-toxic nature. Currently, the maximum efficiency of 24–25% is obtained for laboratory and commercial silicon solar cells under non-concentrated sunlight [2]. Silicon, a semiconductor material, has excellent optical and electronic properties, which are highly beneficial for PV cells. Recently, silicon nanowires (SiNWs) have been thoroughly studied as a material for PV cells. The SiNWs show reduced reflectivity and enhanced light trapping. The bandgap of Si is 1.12 eV [3] which can be tuned due to the quantum confinement effect in SiNWs. The overall electronic and optical properties are enormously improved when planar Si is converted into SiNWs.

S. Rai · R. Bhujel
Centre for Materials Science and Nanotechnology, Sikkim Manipal Institute of Technology, Sikkim Manipal University, Majhitar, East Sikkim 737136, India

J. Biswas
Department of Chemistry, Sikkim Manipal Institute of Technology, Sikkim Manipal University, Majhitar, East Sikkim 737136, India

B. P. Swain (✉)
Department of Physics, National Institute of Technology, Manipur, Manipur Langol-795004, India
e-mail: bpswain@nitmanipur.ac.in

B. P. Swain (ed.), *Advances in Nanostructured Materials*, Materials Horizons: From Nature to Nanomaterials, https://doi.org/10.1007/978-981-16-8391-6_5

Graphene possesses superior electronic and optical properties, which are beneficial for a PV cell, such as transparency, low sheet resistance, large surface area, and excellent conductivity. It possesses extraordinary charge carrier mobility with a value as high as 200,000 cm^2/Vs [4], enabling easy movement of electrons. However, the mass production of pristine graphene is expensive, increasing the overall cost of the solar cell. The alternative to graphene is the chemically synthesized reduced graphene oxide (rGO) [5]. Its properties are similar to pristine graphene with the added benefit of tunable bandgap energy. The bandgap in rGO can be tuned by controlling the extent of reduction. In addition, rGO possesses the ability to be chemically doped (n or p doping).

Schottky junction solar cells have widely been studied because they are easy to assemble, simple, and economically profitable. Researchers use indium tin oxide (ITO) as an alternative to the metal in the Schottky junction. However, indium is a rare element that leads to a high cost of production for ITO. Also, the brittle nature of ITO hinders its application in flexible devices. These limitations can be overcome by the use of graphene or rGO in place of ITO. Li et al. reported the first graphene/Si Schottky junction PV cell in 2010 with an efficiency of 1.5% [6].

The current chapter describes the various generations of solar cells, fabrication techniques for the rGO/SiNWs heterojunctions. Further, the development in the efficiency of these solar cells over the years has also been elaborated.

2 Generations of Solar Cell

Based on the working principle and the types of materials used, solar cells are categorized into four generations.

2.1 First Generation Solar Cells

They are based on the principles of a typical p–n junction diode. The 1st generation solar cells are mainly made up of silicon. They are the most common type of solar cells available in the market and account for about > 80% of solar panels sold around the globe. They are highly efficient with a longer lifetime. First-generation solar cells are still the most cost-efficient commercially available solar cells, as shown in Fig. 1. The first generation solar cell is further divided into two categories.

- **Mono-crystalline Silicon Solar Cells:** In this type of solar cell, the whole wafer is composed of a single crystalline Si. A single cell measures about few inches. Many cells are placed on a grid to form a solar module/panel to increase the output power. They are highly efficient and can give efficiency. To date, the highest efficiency of ~ 26.7% is achieved by Kaneka Corporation [8]. For this type of solar cell, highly pure Si is required. In addition, the process to grow a large single crystal

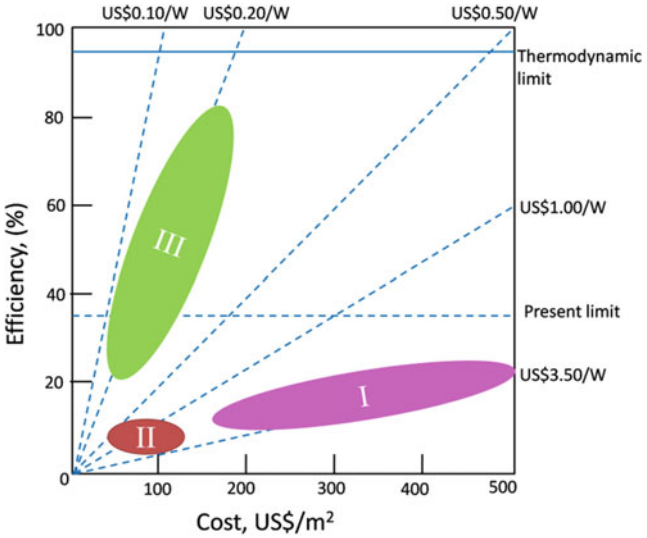

Fig. 1 Cost versus solar cell efficiency [7]

is complex and laborious. This increases the production cost. Hence, though it has high efficiency, it is costly. Furthermore, they lose their efficiency at higher temperatures.

- **Polycrystalline Silicon Solar Cells**: This type of solar cell consists of several crystals of Si. The production of this type of solar cell is less laborious compared to the monocrystalline solar cell. Hence, they are comparatively cheaper. However, on lowering the production cost, the efficiency is compromised. The highest efficiency reported is ~ 24.4% by Jinko Solar [8].

2.2 Second Generation Solar Cells

The second-generation solar cells consist of a thin film of photoactive material on a substrate. The thin-film technology gives it the advantage of reduced mass, which enables it to be integrated into lightweight and flexible devices. Also, the absence of metal fingers in the front allows it to be applied on windows, cars, buildings, smartwatches, etc. They have lower efficiency and cost than first-generation solar cells. They can also work at higher temperatures [9]. They are further divided into the following three categories.

- **Amorphous Si (a-Si) based thin-film solar cells:** They are fabricated using abundantly available raw material called amorphous Si (a-Si). In a-Si, hydrogen atoms are bonded to Si and are called hydrogenated amorphous silicon (a-Si:H). The a-Si:H do not have long-range order like crystalline Si. The a-Si is deposited

on low-cost substrates viz., glass, metal, or plastic foils. The a-Si-based thin-film solar cells are work on the principle of p-i-n or n-i-p diode. The front contact consists of a transparent conductive oxide, and the rear contact is a metal film. The thin film is deposited on the substrate using the plasma-enhanced chemical vapour deposition (PECVD) technique [10]. The highest recorded efficiency is ~ 14% [8]. The efficiency can be improved by the development of cell design and deposition techniques.

- **Cadmium Telluride (CdTe) Thin Film Solar Cells:** CdTe has a direct bandgap value of 1.20 eV and a high absorption coefficient. Due to its excellent electrical and optical properties, it was recognized as a reliable material for thin-film solar cells. The first CdTe solar cells were reported to have an efficiency of ~ 10%. A CdTe solar cell consists of a substrate viz., glass, molybdenum, polyamide, and stainless steel. The front contact is a transparent conducting oxide (TCO) viz., Indium tin oxide (ITO) or Fluorine tin oxide (FTO). The n-type CdS acts as the intermediate layer between TCO and p-type CdTe. The CdTe layer absorbs the maximum visible light. The rear contact is made commonly up of metal or metal alloys [11, 12]. The CdTe thin-film solar cell with the highest efficiency of ~22.1% was manufactured by First Solar, Inc. in 2015[8].
- **Copper Indium Gallium Selenide (CIGS) Thin Film Solar Cells:** In this type of solar cell, a thin film of copper indium gallium selenide is used as the photoactive material. The CIGS thin film is deposited on a substrate mainly soda-lime glass, and a molybdenum layer acts as the back contact. Other substrates such as polymers and metal foils can also make a flexible and lighter device. CdS are deposited on top of the CIGS layer, which acts as a buffer. On the top lies a TCO viz., ITO, or doped ZnO [13]. Nakamura et al. reported the highest efficiency of 23.35% for Cd-free CIGS thin-film solar cells in 2019 [14].

2.3 Third Generation Solar Cells

Third-generation solar cells target high efficiency with minimum cost. In this type of solar cell, semiconductor nanoparticles are used as the photoactive material. The use of semiconductor nanoparticles may help in overcoming the Shockley-Queisser limit ($\eta = 33\%$). Some of the categories of third-generation solar cells are discussed below.

- **Nanocrystal Solar cells:** In this type of solar cell, inorganic nanocrystals are coated on a substrate. The nanocrystals can be synthesized easily in scalable quantities. They have a high absorption coefficient and superior transport properties. Some examples of nanocrystals are Si, CdTe, and CIGS, and those substrates are Si and organic conductors.
- **Polymer-Based Solar cells:** A highly conjugated polymer semiconductor is used in polymer-based solar cells. The polymer is solution-processable, making it feasible to be easily coated on the plastic material using cost-effective and low-energy coating techniques. The simplest polymer-based solar cell consists of a

transparent front electrode, a semiconductor polymer that acts as the active layer, and a back electrode printed on plastic material. The thickness of the active layer lies between 150-200 nm. The most successful type of polymer solar cell is the bulk heterojunction (BHJ). In a single junction BHJ, a transparent back electrode, a hole transport layer, the active layer, a blend of donor polymer/acceptor molecule, and a front metal electrode is layered together [15]. However, in tandem junction BHJ, several single junctions BHJ are stacked together [16]. The highest reported efficiency is 17.3% for a tandem junction BHJ. The manufacturing cost of polymer solar cells is low. The flexibility of the device makes it applicable in portable devices, wearable devices, and buildings.

- **Dye-Sensitized Solar Cells (DSSC):** In a DSSC, the main components are a working electrode (ITO or FTO), a semiconductor material (TiO_2 (anatase), ZnO, Nb_2O_5, SnO_2), a dye, an electrolyte (Iodide), and a counter electrode (Pt, graphene) [17–19]. The semiconductor materials are coated on the working electrode. The dye remains adsorbed on the semiconductor material. The counter electrode is dipped in an electrolyte. The working and the counter electrode are fixed together to prevent the electrolyte from leaking. The highest efficiency reported for DSSC is ~ 12.25% [8].
- **Perovskite Solar Cells:** Perovskites are compounds with the molecular structure of type ABX_3. Organic–inorganic metal halide compounds are used as perovskite materials in solar cells. Perovskites are used as the light-absorbing material and electron/hole transport layer since they have excellent charge mobility and carrier lifetime [20]. The highest efficiency reported for perovskite solar cells is ~29.15% [8].
- **Multi-junction Solar Cells:** Multi-junction solar cells contain a stack of multiple p-n junctions. They are made up of different semiconductor materials having different bandgap energies. The use of multiple p-n junctions allows absorbance of light energy with different wavelengths. This ensures the conversion of the maximum amount of light into electrical energy with minimum loss. The semiconductor materials are stacked so that those with the highest bandgaps are at the top and lowest at the bottom. In 2018 Geisz et al. proposed a solar cell design with six junctions AlGaInP/AlGaAs/GaAs/GaInAs(3) having bandgap energies 2.15/1.72/1.41/1.17/0.96/0.70 eV, which has the potential to exceed 50% efficiency [21].
- **Organic–Inorganic Hybrid Solar Cells:** The organic material is conjugated organic polymers viz., PEDOT:PSS, PVV, P3HT:PCBM, etc. The inorganic material consists of quantum dots or nanoparticles (nanowires, nanorods, or tetrapods). The photoactive material is sandwiched between two electrodes having different work functions. The working is similar to that of polymer solar cells. The inorganic materials have the advantage over organic materials as they are more stable and do not undergo photodegradation. The quantum confinement effect in nanoparticles helps in tuning the bandgap of the inorganic materials. The inorganic quantum dots transfer charge to the organic counterparts faster than the recombination rate [22]. Regardless of the various advantages of the inorganic materials, the efficiency of

this type of solar cell is still low. However, more study and improvements are required to realize the full potential of these solar cells.

3 Reduced Graphene Oxide/silicon Nanowires (rGO/SiNWs) Heterojunction

To make rGO/SiNWs heterojunction, rGO must be deposited on top of the SiNWs. Various methods are used for this purpose, some of which are discussed below.

- **Spin coating:** The spin coating is a standard and easy method for the deposition of rGO on SiNWs. The instrument used for this process is called a spin coater. A dispersion of rGO is made in a solvent. The solvent used is usually volatile, which is quickly evaporated during the spin coating process. The substrate (SiNWs) is placed on the spin coater and is subjected to rotation at high speed. This dispersion is then applied to the centre of the wafer. The rotation is continued till the excess solvent is dried, and a film of desired thickness is obtained. The crucial factors that affect the thickness and uniformity of the film are rotation speed and the concentration of the rGO dispersion.
- **Drop casting:** A dispersion of rGO is made using a volatile solvent and is spread over the SiNWs. It is then dried in suitable conditions (Fig. 2).

The thickness of the film can be varied by varying the volume and concentration of the dispersion. Using this method, rGO can be deposited to a relatively small substrate. The process is a simple, easy, and cost-effective method for the deposition of rGO on SiNWs. However, the film deposited may not be uniform (Fig. 3).

- **Dip coating:** In this process, a solution of rGO is made. The SiNWs are dipped in this solution for a certain amount of time. It is then pulled out of the solution vertically. In this step, the rGO stars coating the SiNWs. The thickness of the film depends on the speed of the withdrawal. The slower the speed, the thinner will be the film. The excess solvent is then drained off and evaporated. After the

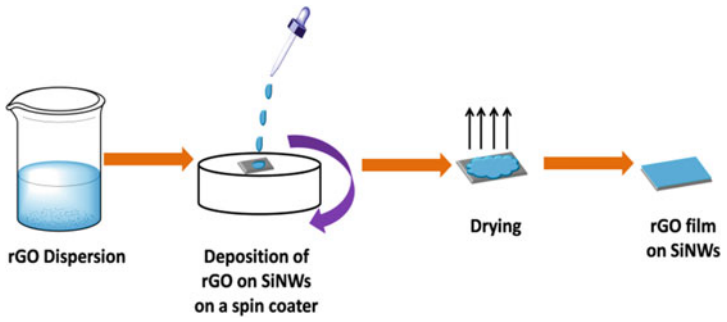

Fig. 2 Schematic for the process of spin coating of rGO on SiNWs

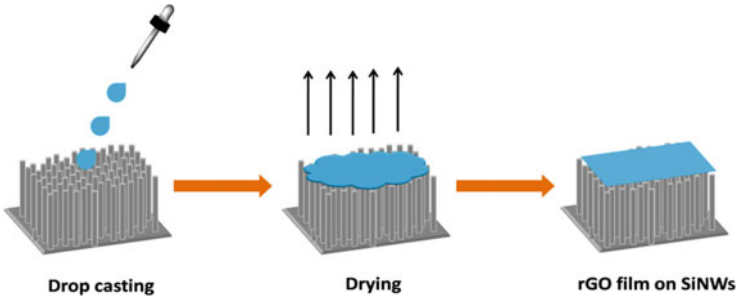

Fig. 3 Schematic for the process of drop-casting of rGO on SiNWs

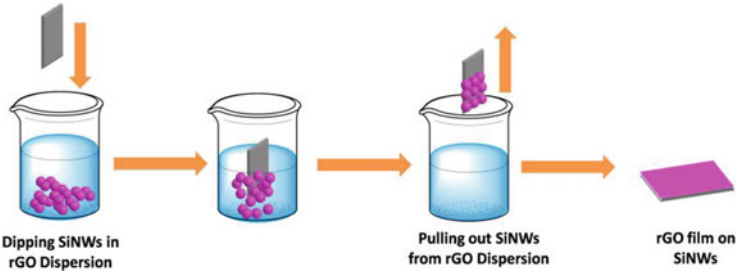

Fig. 4 Schematic for the process of dip coating of rGO on SiNWs

evaporation, a thin film of rGO remains on the surface of SiNWs. Though the process is simple and easy, the thickness and uniformity of the film may not be suitable.

- **Spray coating:** This process is similar to spray painting. The solution of rGO in a solvent with a stabilizer is prepared. This solution is then sprayed on SiNWs using a syringe pump. The SiNWs can be heated during the spraying process or heated after the process is complete. It is also a cost-effective method (Figs. 4, 5).

4 Photovoltaic Application

Nanomaterials have broad applicability because of the possibility of tuning their properties. The properties of the nanomaterials are tailored by controlling their morphology, structure, composition and introducing some impurities. In this section, we will discuss the photovoltaic application of rGO/SiNWs heterojunction. Graphene and its derivatives, mainly GO and rGO, are widely studied for photovoltaic applications. They possess outstanding optical and electronic properties, which makes them suitable for application in photovoltaics, e.g., graphene has a vast theoretical surface area (2630 m^2g^{-1}), high electron mobility (~20,000 cm^2V^{-1} s^{-1}), and thermal conductivity (5000 Wm^{-1} K^{-1}). However, pristine graphene possesses a

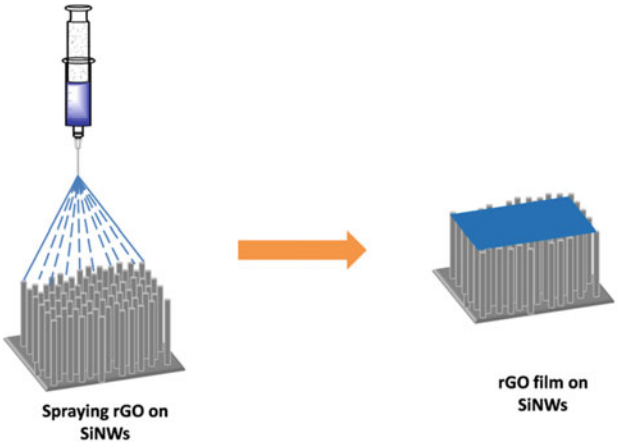

Fig.5 Schematic for the process of spray coating of rGO on SiNWs

zero bandgap [23]. However, the bandgap is essential for photoactive materials. rGO is a solution to this problem. The bandgap in rGO varies with the presence of oxygen and other impurities. The bandgap of rGO can vary from ~1 to 1.69 eV depending upon the percentage of the oxygen moieties present in it [24]. The oxygen functionalities in rGO enable it to form hydrogen bonds with polar protic solvents. Hence, it is stable in these solvents which help in the fabrication of devices. Also, these functionalities open the possibility of doping with other functional groups. The doping leads to interesting optical and electronic properties owing to modification of the work function in rGO. This helps in minimizing the sheet resistance. With the help of modification, their work function can be matched with the HOMO and LUMO of other photoactive materials, leading to decreased potential barriers. It plays a significant role in the performance of the photovoltaic device.

Si is a semiconductor, and it is the most common material used in solar cells. The highest theoretical value of efficiency for Si solar cells is about 29% under non-concentrating sunlight [2]. The improvement in the efficiency of Si solar cells depends upon the device design and fabrication. One of the examples of solar cells using Si is Schottky junction solar cells. They can be easily fabricated at room temperature at minimum cost. The most straightforward design is the coating of graphene on n-type or p-type Si. Graphene/Si Schottky junction solar cells have been currently studied to obtain high-efficiency solar cells. Graphene acts as an antireflective coating to Si. Li et al. first fabricated graphene/Si solar cells in 2010 [6]. They found the reflection to decrease by ~70% in the visible region and ~80% in the infra-red region. The solar cell fabricated by them showed an efficiency of 1.5%. Since then, various research works have been conducted to improve the efficiency of graphene/Si solar cells. Graphene and its derivatives (GO and rGO) have been employed for the same. The efficiency depends on some factors, viz., quality, defect states, and impurity in GO and rGO. The efficiency can also be improved if the problem of high reflectivity in

planar Si can be overcome. For this purpose, SiNWs have emerged as a promising candidates.

SiNWs have the advantage over bulk Si in terms of physical, optical, and electronic properties. SiNWs have excellent light trapping properties, so the reflectivity is low in the visible region. The anti-reflective property can be modified by controlling the length of the nanowires [25]. SiNWs have a unique 1D structure and a higher surface area to volume ratio. Additionally, they have a direct bandgap in contrast to the indirect bandgap of bulk Si. The quantum confinement effect in SiNWs allows the movement of electrons in one direction, thus affecting the bandgap energy of the material. The bandgap energy can be tuned by varying the diameter of the nanowires [26]. Thus, SiNWs are widely used for application in solar cells.

5 Current Density–Voltage (J-V) Characteristics:

The current density–voltage characteristic is essential to determine the efficiency of a solar cell. The efficiency of the rGO/SiNWs Schottky junction solar cell can be calculated using the following equation:

$$Efficiency(\eta)\% = \frac{V_{OC} \times J_{SC} \times FF}{P_{in}}.$$

V_{OC}, J_{SC}, FF, and Pin refer to open-circuit voltage, short circuit current, fill factor, and power input in the above equation, respectively. These values are obtained from the current density versus voltage plot, as shown in Fig. 6.

Xie et al. fabricated a graphene nanoribbon/multiple SiNW Schottky junction solar cell. The values of V_{OC}, J_{SC}, FF, and η for the device were 0.59 V, 11.3 mA/cm^2, 0.221, and 1.47% [27]. Fan et al. compared the efficiency of graphene/SiNW before and after doping. Graphene was doped using thionyl chloride to get an enhanced η value of 2.86%. This value was almost four times greater than that of undoped graphene/SiNW solar cells, i.e., 0.68% [28].

The energy band diagram for p-rGO/SiNW and n-rGO/p-SiNW Schottky junction is shown in Fig. 7. When a potential is applied, the partial carriers in SiNW tend to move towards rGO. At the interface of rGO/SiNW, the energy level will be bend upward (n-SiNW) and downward (p-SiNW), and a depletion region will be formed. When illuminated by light, the charges in the depletion region will be separated. The resultant electron and holes will move in the opposite direction, which generates the photocurrent [4].

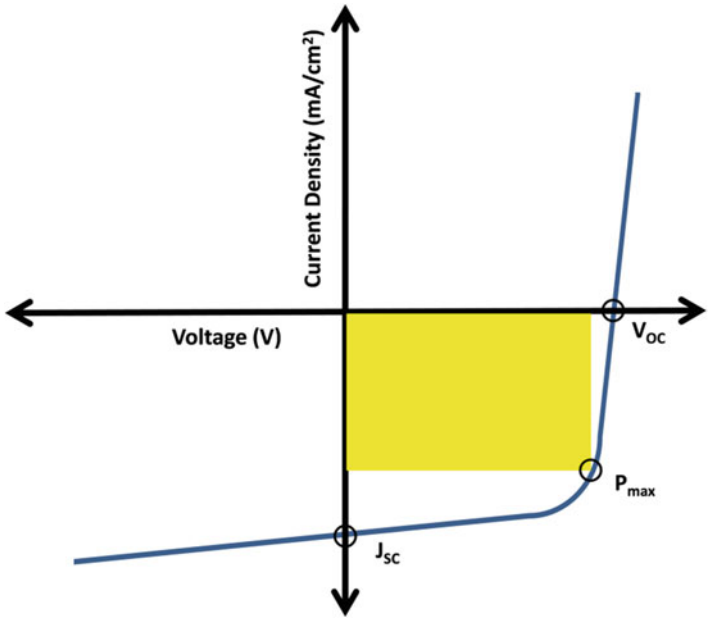

Fig. 6 Current density versus voltage curve for solar cell

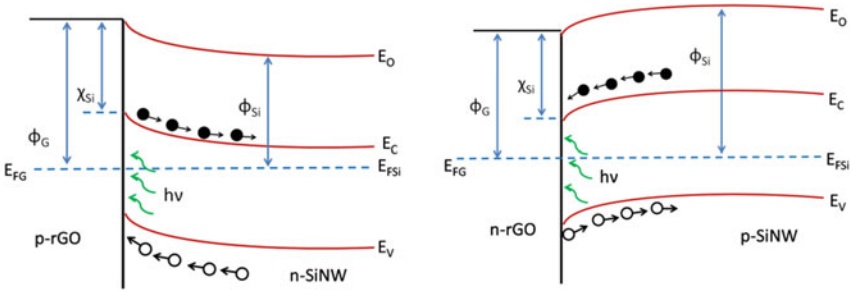

Fig. 7 Energy band diagram for p-rGO/n-SiNW and n-rGO/p-SiNW Schottky junction

6 Summary/Conclusion

The advancement in photovoltaics is essential for providing an alternative energy source to fossil fuels. It can cater to the energy requirements of the ever-demanding society. The efficiency of the solar cells depends on the materials used for the device fabrication. The majority of the existing solar cells are formed of Si. Many studies have been done over the years, and nanomaterials have made a significant contribution to improving the efficiency of solar cells. In this case, the 2D material, particularly

graphene and its derivatives, has been widely used. The extraordinary optical, electronic, and physical properties of graphene contribute to its applicability in solar cells. In addition, SiNWs have also been mainly studied for application in solar cells. They have the advantage of improved light trapping ability over planar Si. The integration of graphene and SiNWs leads to the formation of Schottky junction solar cells. The improvement in the device design, fabrication techniques, and materials' properties would give a solar cell having high efficiency.

Acknowledgements The authors sincerely acknowledge UGC-DAE-CSR Indore (CSR-IC-MSR-07/CRS-215/2017-18/1296) for providing financial support to Miss Sadhna Rai.

References

1. Wilson GM, Al-Jassim M, Metzger WK, Glunz SW, Verlinden P, Xiong G, Mansfield LM, Stanbery BJ, Zhu K, Yan Y et al (2020) The 2020 photovoltaic technologies roadmap. J Phys D Appl Phys 53:493001
2. Blakers A, Zin N, McIntosh KR, Fong K (2013) High-efficiency silicon solar cells. Energy Proc 33:1–10
3. Low J, Kreider M, Pulsifer D, Jones A, Gilani T (2009) Band gap energy in silicon. Am J Undergrad Res 8:27–32
4. Xie C, Lv P, Nie B, Jie J, Zhang X, Wang Z, Jiang P, Hu Z, Luo L, Zhu Z et al (2011) Monolayer graphene film/silicon nanowire array schottky junction solar cells. Appl Phys Lett 99:133113
5. Zhang X, Zhang D, Chen Y, Sun X, Ma Y (2012) Electrochemical reduction of graphene oxide films: preparation, characterization and their electrochemical properties. Chinese Sci Bull 57:3045–3050
6. Li X, Zhu H, Wang K, Cao A, Wei J, Li C, Jia Y, Li Z, Li X, Wu D (2010) Graphene-on-silicon schottky junction solar cells. Adv Mater 22:2743–2748
7. Green MA (2001) Third generation photovoltaics: ultra-high conversion efficiency at low cost. Prog Photovolt Res Appl 135:123–135
8. Green MA, Dunlop E, Hohl-Ebinger J, Yoshita M, Kopidakis N, Hao X (2021) Solar cell efficiency tables (Version 57). Prog Photovoltaics Res Appl 29:3–15
9. Matsui T, Sai H, Saito K, Kondo M (2012) Amorphous-silicon-based thin-film solar cells exhibiting low light-induced degradation. Jpn J Appl Phys 51:10NB04
10. Rech B, Wagner H (1999) Potential of amorphous silicon for solar cells. Appl Phys A Mater Sci Process 69:155–167
11. Basol BM, McCandless B (2014) Brief review of cadmium telluride-based photovoltaic technologies. J Photonics Energy 4:040996
12. Muteri V, Cellura M, Curto D, Franzitta V, Longo S, Mistretta M, Parisi ML (2020) Review on life cycle assessment of solar photovoltaic panels. Energies 13:252
13. Kaelin M, Rudmann D, Tiwari AN (2004) Low-cost processing of CIGS thin film solar cells. Sol Energy 77:749–756
14. Nakamura M, Yamaguchi K, Kimoto Y, Yasaki Y, Kato T, Sugimoto H (2019) Cd-Free Cu(In, Ga)(Se,S) 2 Thin-Film Solar Cell With Record Efficiency of 23.35%. IEEE J Photovoltaics 9:1863–1867
15. Gusain A, Faria RM, Miranda PB (2019) Polymer solar cells—interfacial processes related to performance issues. Front Chem 7:1–25
16. Meng L, Zhang Y, Wan X, Li C, Zhang X, Wang Y, Ke X, Xiao Z, Ding L, Xia R, Yip HL, Cao Y, Chen Y (2018) Organic and solution-processed tandem solar cells with 17.3% efficiency. Science 361:1094–1098

17. Sharma K, Sharma V, Sharma SS (2018) Dye-sensitized solar cells: fundamentals and current status. Nanoscale Res Lett 13:381
18. Nazeeruddin MK, Baranoff E, Grätzel M (2011) Dye-sensitized solar cells: a brief overview. Sol Energy 85:1172–1178
19. Grätzel M (2003) Dye-sensitized solar cells. J Photochem Photobiol C Photochem Rev 4:145–153
20. Zhou D, Zhou T, Tian Y, Zhu X, Tu Y (2018) Perovskite-based solar cells: materials, methods, and future perspectives. J Nanomater 2018:1–15
21. Geisz JF, Steiner MA, Jain N, Schulte KL, France RM, McMahon WE, Perl EE, Friedman DJ (2018) Building a six-junction inverted metamorphic concentrator solar cell. IEEE J Photovoltaics 8:626–632
22. Wright M, Uddin A (2012) Organic-inorganic hybrid solar cells: a comparative review. Sol Energy Mater Sol Cells 107:87–111
23. Ren S, Rong P, Yu Q (2018) Preparations, properties, and applications of graphene in functional devices: a concise review. Ceram Int 44:11940–11955
24. Abid Sehrawat P, Islam SS, Mishra P, Ahmad S. Reduced Graphene Oxide (RGO) based wideband optical sensor and the role of temperature, defect states and quantum efficiency. Sci Rep 8:3537
25. Hasan M, Huq MF, Mahmood ZH (2013) A review on electronic and optical properties of silicon nanowire and its different growth techniques. Springerplus 2:151
26. Hutagalung SD, Fadhali MM, Areshi RA, Tan FD (2017) Optical and electrical characteristics of silicon nanowires prepared by electroless etching. Nanoscale Res Lett 12:425
27. Xie C, Jie J, Nie B, Yan T, Li Q, Lv P, Li F, Wang M, Wu C, Wang L et al (2012) Schottky solar cells based on graphene nanoribbon/multiple silicon nanowires junctions. Appl Phys Lett 100:193103
28. Fan G, Zhu H, Wang K, Wei J, Li X, Shu Q, Guo N, Wu D (2011) Graphene/silicon nanowire schottky junction for enhanced light harvesting. ACS Appl Mater Interfaces 3:721–725

Chapter 6
Chemical Bath Deposited Zinc Oxide Nanostructured Thin Films and Their Applications

Sumitra Nongthombam and Bibhu Prasad Swain

1 Introduction

ZnO nanostructures are promising building blocks for a variety of versatile photonic and electronic applications in energy harvesting such as LEDs, solar cells, photovoltaic, electronic devices including transistors, transparent conducting oxides, flat panel displays, and in chemical sensing, photocatalyst, and so on [1]. In addition, ZnO is known to exist in different morphologies, thanks to its unique physicochemical characteristics owning a wide bandgap (~3.4 eV), and high excitonic energy of 60 meV. Apart from these, ZnO being highly abundant in nature, economical, non-hazardous, and easily processable by many techniques makes it an interesting material for production by various techniques. On the other hand, thin film nanostructures technology advances in material science owing to its unique characteristic defined by its geometry, thickness, and structure [2]. Thin films are grown by three kinds of techniques: (1) Sputtering method, (2) Vapor deposition technique, and (3) solution-based technique [3]. Wet-chemistry techniques are the most economical among the three techniques and are appropriate for processing in any research environment because it does not require large complex instruments and high temperature/high vacuum conditions. Among the wet chemistry techniques, special attention is given to the CBD method favored by its low cost, simple experimental setup, and good potential for scaling up.

CBD is a simple and facile technique to grow thin films over a substrate dipped in a solution of chemical precursors under control parameters. The technique was initially established in 1884 but limited to only PbS and PbSe until when the method began to be utilized extensively in the deposition of selenides, sulfides, and oxides-based thin films in the 1990s [3].

S. Nongthombam · B. P. Swain (✉)
Department of Physics, National Institute of Technology Manipur, Imphal, India
e-mail: sumitra@nitmanipur.ac.in

B. P. Swain (ed.), *Advances in Nanostructured Materials*, Materials Horizons: From Nature to Nanomaterials, https://doi.org/10.1007/978-981-16-8391-6_6

Despite the various advantages of CBD such as easily processible, low-temperature deposition, large area coatings, and reproducibility, the technique is limited to lack of control over growth kinetics thus making it difficult to obtain films of high purity. Herein, the chapter deals with the basic understanding of the CBD method followed by ZnO nanostructured thin films deposited by the CBD method for numerous applications. In addition, the different parameters involved in the CBD process and their influences concerning the growth of ZnO nanostructures by CBD are also addressed.

2 Chemical Bath Deposition

Chemical bath deposition can be defined as a technique to chemically deposit thin films on a suitable substrate using a precursor solution consisting of their constituent compounds. The deposition process of a solid layer on the substrate involves the controlled precipitation of the desired compound from the solution of its constituents. The precipitation can be regulated through the control of the different constraints such as bath temperature, precursor concentration, pH, deposition time, complexing agents, etc. The process simply occurs when a suitable solid substrate is dipped into an aqueous solution containing the metal salts, chalcogenides, and complexing agents to undergo appropriate equilibrium reaction mechanisms.

The basic construction occurring in CBD is shown in Fig. 1 [4]. Initially, the substrate to be used should be carefully cleaned to etched nucleation sites on the surface of the substrate. This helps in the proper adhesion of the solid coating on the substrate surface during deposition. The basic cleaning process can be done by washing the substrate with detergents, followed by rinsing with distilled water and scrubbing with ethanol, and finally dried in a hot air oven. Here, the substrate is immersed in a suitable chemical solution containing metal salts, chalcogenides, and complexing agents. The precursor solution containing the beaker is placed in bath solution and stirred well by using a magnetic stirrer with substrate vertically clamped inside the beaker containing solution. Finally, under control parameters, the precursor solution undergoes a chemical change depositing a thin film over the substrate.

Chalcogenides are usually chemical compounds that consist of one chalcogenide anion and at least one electropositive element. In CBD, commonly thiourea ($N_2H_4(CS)$), selenourea ($N_2H_4(CSe)$), and water are used as sources for sulfides, selenides, and oxides, respectively. Complexing agents are chemical additives used in the preparation of thin films in controlling the concentration of metal ions during the deposition process. Examples of complexing agents include hexamine (HA), hydrazine hydrate, diethanolamine (DEA), triethanolamine (TEA), trisodium citrate, ammonia, malic acid, ethylenediamine tetra-acetate disodium, and hexamethylenetetramine (HMTA) [5].

The basic steps followed in the deposition process by CBD are as follows and taking a simple example of ZnO thin film formation using zinc nitrate, HMTA, the reaction mechanisms occurring are shown along with.

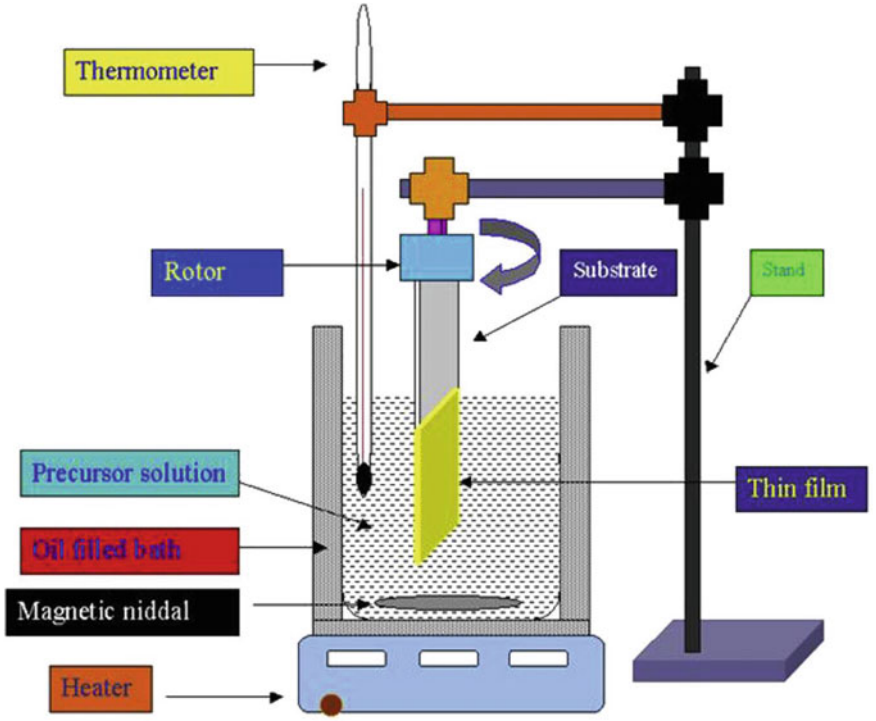

Fig. 1 Schematic diagram of Chemical bath deposition process

(a) Equilibrium hydrolysis reaction between water and the complexing agent.

$$C_6H_{12}N_4 + 6H_2O \leftrightarrow 4NH_3 + 6CH_2O$$

$$NH_3 + H_2O \leftrightarrow NH_4^+ + OH^-$$

(b) Formation of metal-complex ions.

$$Zn^{2+} + C_6H_{12}N_4 \leftrightarrow Zn(C_6H_{12}N_4)^{2+}$$

$$Zn^{2+}4NH_3 \leftrightarrow Zn(NH_3)_4^{2+}$$

(c) Formation of the solid film on the substrate.

$$\mathrm{Zn}(NH_3)_4^{2+} + 2OH^- \rightarrow ZnO + H_2O + C_6H_{12}N_4$$

The kinetics of the growth of thin films is determined by the ion-ion deposition of chalcogenide on the substrate surface. When the metal salts containing compound is mixed with chalcogenides in the form of an aqueous solution, precipitation occurs on the substrate. For deposition of thin film to occur, the value of the ionic product should exceed the solubility product. However, the precipitation formation should be maintained in such a controlled manner that bulk deposition does not happen. To ensure this, the release of the metal and chalcogenide ions should occur in a steady mode to prevent bulk precipitation. This can be done by using appropriate complexing agents for trapping the metal ions while controlling the concentration of the complexants [5]. The strength of the complexing agent should be moderate to prevent bulk deposition or to get desired uniform film without precipitating out.

During the initial phase of the CBD process, nucleation sites are created on the immersed surface from the aqueous solution until which deposition rate of film is almost negligible, and once the nucleation centers are created, film starts to grow rapidly. Usually, a seed layer is made to form on a substrate before deposition of thin films because seeding of the substrate can give a substantial impact on the morphology of nanostructured thin films. The quality of films deposited by CBD, therefore, depends significantly on the seed layer as the seed layer can drop the thermodynamic barrier providing some nucleation centers. Again, the morphology of the CBD synthesized film growth is reliant on the orientation and crystallinity of the seed layer. Rezaie et al. study the impact of seed layers in controlling the physical properties of ZnO nanorods (NRs) via CBD with Al-doped ZnO as the seed layer. The study reveals that the seed layer considerably depends on the morphology and crystallinity of the growth behavior of ZnO NRs thereby promoting the orientation and growth rate of the ZnO NRs. The study also reported that the size of ZnO NRs grown on Al-doped ZnO layers is four percent greater in comparison to those grown on ZnO layers [6]. Terasako et al. studied the effect of seed layer in ZnO NRs grown by CBD and also three different seed layers Au/Ti/Si (100), Au/SiO_2/Si (100), and ZnO: Ga (GZO)/glass films are investigated for their influence on the structural and optical properties of the ZnO NRs grown [7]. The study found that ZnO NRs are grown preferentially oriented in the c-axis regardless of the different substrate used and relative photoluminescence (PL) intensity of near band edge emission to the orange emission increases with more deposition time in the case of ZnO NRs grown on GZO/glass and Au/SiO_2/Si (100) substrate. Further, the average length is estimated to be ~1100, ~1600, and ~2000 nm, respectively, and the average width as ~200, ~400, and ~1000 nm, respectively, for GZO/glass, Au/SiO_2/Si (100), and Au/Ti/Si (100), respectively.

Thus, CBD is a reliable solution-based method that is widely employed due to its numerous advantages. The advantage of CBD over other wet chemistry methods includes lower deposition temperature, large surface area scaling, low-cost, simple and easy processing, and the thin films produced by it are uniform and well adherent. In addition, the controllable characteristics of the film deposited by CBD allow the production of nanostructures with diverse morphologies.

3 ZnO Nanostructures

ZnO is an important semiconductor compound receiving tremendous popularity because of its various interesting intriguing properties having a wide bandgap, high thermal, chemical, and mechanical stability, large exciton binding energy, and high mobility [8]. Its abundance in nature, non-toxicity, biodegradability, and ease in doping despite the above properties makes it a suitable material for diverse applications [9]. In addition, ZnO being a low cost, easily processible by various techniques, and diverse morphology synthesis possibility aids the importance of ZnO nanostructures for versatile applications [10]. ZnO and ZnO-based compounds are advantageous for a vast range of technological applications encompassing gas sensors, solar cells, supercapacitors, photocatalysis, photodetectors, LEDs, etc. In recent years, ZnO nanostructures have been grown by employing various techniques including gas-phase reaction methods such as thermal evaporation, radio frequency magnetron sputtering, spray pyrolysis, epitaxial method, vapor deposition method, etc. [11]. However, the heavy cost of high temperature and high vacuum requirement conditions for such gas-phase reactions limits the large-scale production of this material. In this regard, wet chemistry techniques find a good alternative as it is simple, low cost, and involve low temperature and eco-friendly [12]. In particular, the CBD method is reliable to deposit thin films because of its simple experimental setup, low cost, and low-temperature deposition.

4 Growth Parameters Suitable for Depositing ZnO Nanostructures Based Thin Films by CBD

In the CBD process, pH control is very necessary to find the most suitable growth conditions. For depositing ZnO thin films, maintaining the pH of the precursor solution between 9 to 13 is required as pH plays a pivotal role in the solubility of hydroxides and hydronium ions [13]. Many complexing agents are being studied in recent years in the deposition of nanostructured ZnO thin films. Rakhsha et al. studied the optimum pH conditions of Cu and Ag-doped ZnO nanowires (NWs) through the CBD method [14]. Using concentration pH diagrams, the behavior of Zn and dopant complexes are examined which finds that neither highly acidic nor basic environments are suitable for the growth of ZnO NWs. And, the optimum pH is found at $pH = 10.8$ favoring the morphological conditions by inhibiting the formation of homogenous nucleation. Mwankemwa et al. studied the influence of ammonia in the growth of ZnO NRs and reveal that presence of ammonia can alter the extent of supersaturation of the precursor compounds thereby triggering a notable change in the morphology and thus providing better crystal orientation of the ZnO nanorods while adding definite amounts of ammonia [12]. The degree of supersaturation is of three kinds: (1) low supersaturation, (2) intermediate supersaturation, and (3) high supersaturation. It depends on the chemical precursor solution and pH of the precursor

solution where substrate and precursor solution interfacial is strongly influenced by the reaction temperature with the nature of substrate, solution, and metal ionized salts present [15]. In CBD growth of ZnO nanorods, hexamethylenetetramine (HMTA) is popularly exploited as a complexing agent as it offers favorable morphology and high crystallinity in comparison to other complexing agents [16]. Shi et al. demonstrated that there are two critical factors to be considered for the growth of ZnO nano crystallites-concentration of Zinc ions and pH temperature bath [17]. HMTA plays a dual role in the growth of thin films via CBD. (1) It acts as a buffer pH over a range of chemical precursor concentrations and solutions. (2) It acts as a capping agent promoting anisotropic growth. This is possible by forming a strong steric hindrance effect inhibiting the growth laterally and promoting growth in the vertical alignment [18]. Another important factor to consider in the CBD process is the deposition time. Molefe et al. studied the effects of reaction time on structural, morphological, and optical properties of ZnO nanoflakes prepared by the CBD method [19]. The study found that the structural properties are strongly dependent on the reaction time evidencing a change in the structure of the synthesized ZnO with the reaction time from cubic to hexagonal wurtzite structure. Also, from the optical property study, absorption wavelengths are found to be shifted to higher wavelengths with an increase in reaction time, and the PL intensity is also increased with increasing reaction time where the intensity is maximum for one min.

5 Applications of ZnO Thin Films Prepared by CBD

The growth of nanostructured ZnO thin films prepared by the CBD technique provides usefulness in numerous applications.

5.1 Photocatalysis

The photocatalytic method based on semiconducting nanostructures emerges as a new kind of water decontamination technique that works by the generation of hydroxyl radicals through the use of light irradiated semiconductors [20]. ZnO nanostructures have attracted significant interest in photocatalytic applications owing to their wide bandgap, high exciton binding energy, high stability, and strong emission characteristics [10]. High exciton binding energy allows the possibility of excitonic effects at or even above room temperature which subsequently delivers excellent luminescent properties in the visible and UV region [21]. Although TiO_2 is reported as the most widely used semiconductor for photocatalytic applications, ZnO offers certain advantages over TiO_2. One important factor is its higher overall generation of oxidizing radicals on its surface and higher absorption efficiency across a large fraction of the solid spectrum. The second point is the higher photocatalytic degradation of organic dyes of ZnO than TiO_2 [22].

Cirak et al. reported on the photocatalytic applications of decorated ZnO nano rice via CBD on electrochemically synthesized TiO_2 nanotubes arrays (TZN) to examine photodegradation of Rhodamin B (RhB) under UVA irradiation [20]. The photocatalytic activity of TZN is observed to be improved with eight chemical deposition cycles providing 95% of the RhB photodegradation efficiency for the maximum amount of ZnO deposition in comparison to 65% of bare TiO_2 nanotubes. The reason for the enhanced photocatalytic activity of TZN is asserted to the increased number of OH^- radicals with the decoration of ZnO nano rice, thereby growing the active centers on the TiO_2 arrays.

In another work, Macan et al. synthesized hierarchical ZnO nanostructures by the CBD method for photocatalytic degradation of 2,5-dihydroxybenzoic acid [22]. The investigation of photocatalytic behavior demonstrates that ZnO films are efficient photocatalysts showing photoactive retention of 80% after ten cycles with no significant decrease in activity until the ninth cycle.

5.2 UV Photodetectors

UV Photodetector is an important device widely used for numerous applications such as space communications, water purification systems, ozone layer monitoring, biochemical analysis, flame sensing, etc. Wide bandgap materials such as GaN, TiO2, GaP, and ZnO are suitable for UV photodetector devices as their bandgap lies in the UV region, and their properties featuring good thermal stability and radiation toughness [23]. UV detectors based on ZnO nanostructures are of immense attention for photodetector applications because it affords good absorption layers for UV light owing to its intriguing properties such as wide bandgap, and high exciton binding energy favor with its cost-effectiveness, simple manufacture, and low deposition temperature [24]. Also, the defects created in ZnO nanostructures either by Zinc interstitial or Oxygen vacancies played a significant role in improving its electrical properties [25].

Shaikh et al. demonstrated the fabrication of Ag/ZnO/Ag (MSM) UV photodetector based on ZnO thin films prepared by CBD which observe a maximum photocurrent of 113.83 μA at 5 V bias voltage [23]. The device attains good responsibility with rising time about 9 s and fall time about 21 s suggesting ZnO thin films grown by CBD as potential candidates for UV photodetector applications.

Gu et al. investigated the vertically aligned ZnO NRs grown by CBD for UV photodetector applications which exhibited photosensitivity of 2,348 and signal-to-noise-ratio of 67 dB at 0.5 mol/L concentration which are two important indexes to evaluate the performance of UV detector device [26]. Further, the minimum rise time and fall time of 0.993 s and 2.036 s indicate the excellent performance of the device which is ascribed to the better crystallinity and larger aspect ratio of the ZnO NRs at 0.5 mol/L concentration of the precursor solution. In another work reported by Khazali et al. for studying UV photodetector performance of CBD synthesized ZnO

NRs, photosensitivity of 58% and maximum current gain of 1.52% under UV illumination of 385 nm at a bias voltage of 5 V [27]. Also, in their work, a steady photocurrent is observed after several cycles showing good stability and reproducibility, thus revealing ZnO NRs as potential candidates for UV photodetectors applications.

5.3 Solar Cells

Solar cells are eco-friendly energy harvesting techniques that are enormously utilized in modern technology to meet the energy requirements of humanity sustainably. Oxide semiconducting materials being easy in fabrication and possessing efficient charge collection properties emerge as one of the feasible alternatives for solar cells in replacement for silicon where silicon is the most conventional used material for solar energy technology but limited due to its unbalanced cost and less efficiency. Among them, ZnO nanostructures are one of the promising materials owing to their suitable band gap and good absorption properties. In addition, the diverse morphologies of ZnO nanostructures make it gain more interest for its versatile applications. 1-D ZnO nanostructures such as nanowires, nanorods, nanobelts, nanotubes, etc. draw significant attention for potential applications in dye-sensitized solar cells (DSSCs) which is provided by its morphological advantage inefficient transport of photogenerated excitons [28]. Good alignment, large surface area, and length to diameter ratio are very important for photovoltaic applications [8]. ZnO is also studied as an anti-reflecting coating in solar cells owing to its interesting features such as easy processing, abundance, appropriate refractive index (~1.9), good transparency, and wide bandgap. Anti-reflective coatings are important to enhance light absorption in silicon solar cells. For attaining an anti-reflecting coating effect on a silicon surface, the anti-reflecting materials used should be transparent and its refractive index should be between air and silicon.

Qu et al. reported a study on chemically bath deposited ZnO nanorods as ARC in silicon solar cells [29]. The multiple light scattering of ZnO NRs is induced by its light-trapping structure and thereby decreasing the reflectance of silicon solar cells. Thus, in their work, the photovoltaic conversion efficiency of polycrystalline silicon solar cells while using ZnO NRs as an anti-reflective layer is increased by 170% in comparison to that without ZnO NRs based anti-reflective layer. The reason lies in the effective reduction of optical loss through the decrease in reflection and enhanced photon absorption by the utilization of ZnO-based anti-reflective coating.

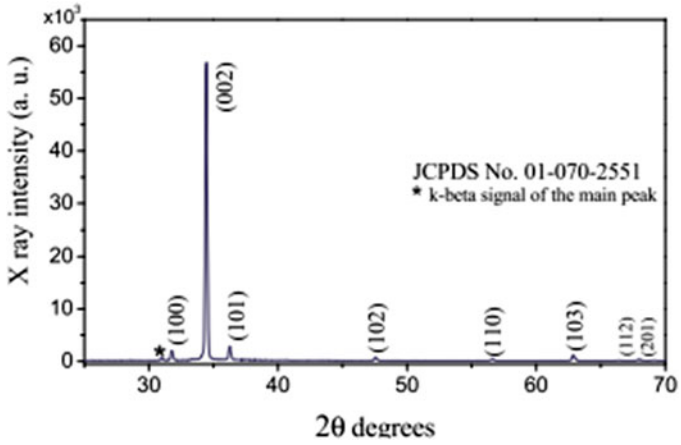

Fig. 2 XRD spectra of ZnO nanocolumns prepared by CBD on a seeded ZnO layer at 400 °C

6 Characterization of ZnO Nanostructures-Based Thin Films Grown by CBD Technique

6.1 XRD Study

Figure 2 shows the XRD pattern of ZnO nanocolumns (NCs) synthesized by CBD from the ZnO seed layer at 400 °C [30]. The XRD spectrum depicts diffraction peaks corresponding to (100), (002), (101), (102), (110), (103), (112), and (201) phases attributing to the hexagonal wurtzite structure which matches well with standard card No. 01–070-2551. The observance of a sharp peak in the XRD spectrum indicates the good crystallinity and the incomparably most intense peak for (002) reflection compared to all the other peaks specifies the preferential orientated growth of ZnO NCs concerning the c-axis.

6.2 SEM Study

SEM images of pH-controlled ZnO NRs deposited on a glass substrate via CBD are shown in Fig. 3 [31]. The morphology of the ZnO NRs for growth conditions at different pHs of 9.5, 10.5, and 11.5 is illustrated in both low- and high-resolution SEM images which evidenced the formation of vertically aligned hexagonal ZnO NRs on the substrate regardless of the different pH control. However, with the increase of pH value, the average size of the ZnO NRs is observed to be larger and the density of the ZnO NRs also increases. At lower pH (pH = 9.5), the observance of non-uniform distribution of the NRs and lack of alignment is due to the homogenous nucleation

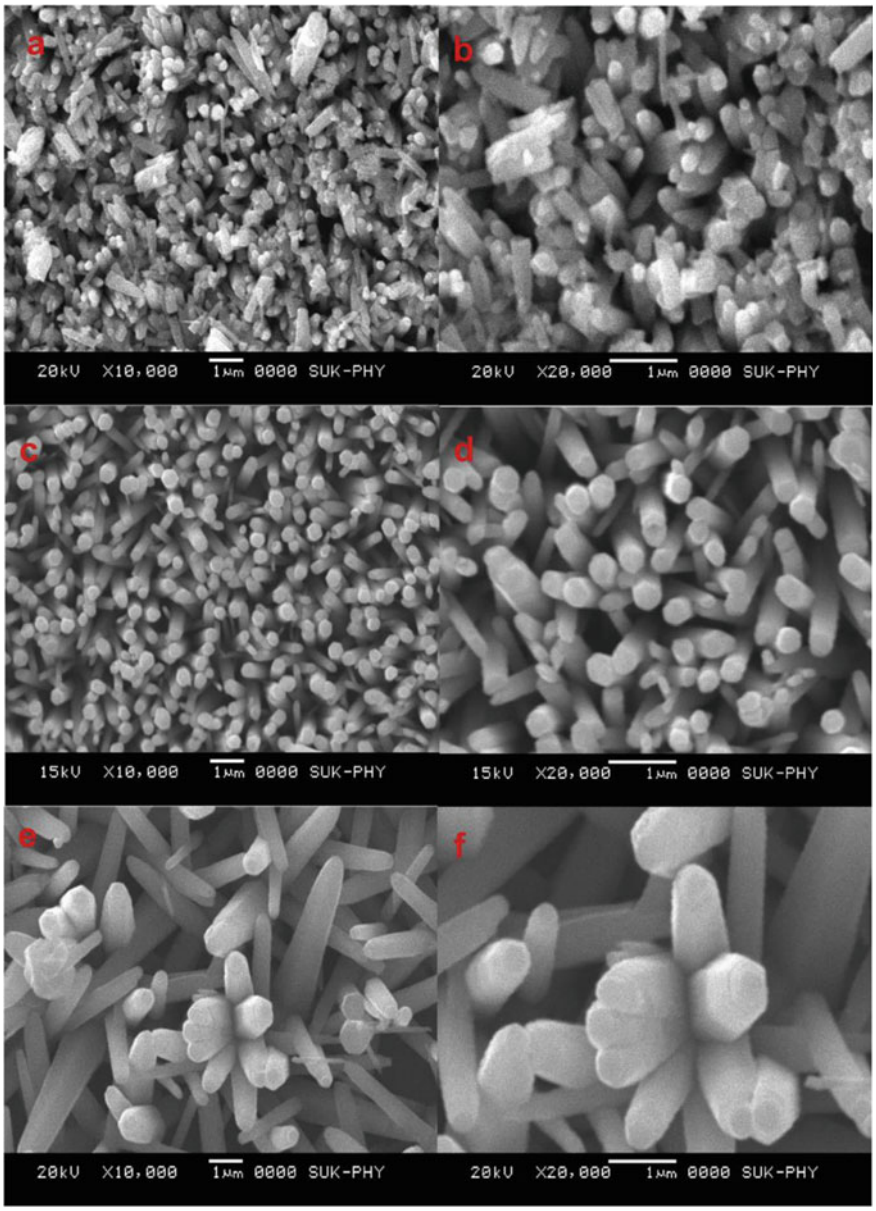

Fig. 3 SEM images of ZnO NRs synthesized via CBD at different pH growth conditions **a**, **c**, **e** lower magnification images at pH = 9.5, 10.5, and 11.5, respectively, **b**, **d**, **f** higher magnification SEM images at pH = 9.5, 10.5, and 11.5, respectively

at the initial stage of growth. At pH = 10.5, heterogenous nucleation begins to dominate over homogenous nucleation promoting the growth on the substrate where the diameter of the NRs is observed to be increased from approximately 264 nm at pH = 9.5 to around 379 nm at pH = 10.5. The maximum diameter of the NRs is estimated to be around 712 nm at pH = 11.5 featuring the most uniform and densely packed NRs among the three pH conditions. The significant increase in diameter of the NRs at pH = 11.5 is ascribed to the heterogeneous nucleation process of ZnO NRs and more release of ammonia affecting the growth ensuring the vertical arrangement of the NRs, thereby suggesting the optimum growth conditions of ZnO NRs at pH = 11.5.

6.3 Raman Study

Raman study: Fig. 3 displays Raman spectrum of ZnO NCs prepared via CBD from ZnO seed layer at 400 °C [30]. As seen from the spectrum, two well-defined vibrational peaks are centered at around 97 and 436 cm^{-1} which corresponds to E_2 low (E_2L) and E_2 high (E_2H). The Raman peaks are further deconvoluted using the Lorentzian function assigning to E_2L, $A_1(TO)$, E_2H, $A_1(LO)$, and linear combinations $2E_1L$, E_2H-E_2L, 2LA, TA + LO. The vibrational modes are ascribed to the hexagonal wurtzite structure of ZnO with the E_2L and E_2H modes corresponding to the Zinc sublattice and Oxygen sublattice, respectively.

6.4 PL Properties

Figure 4 shows the PL spectra of ZnO NRs grown by CBD with different molar precursor concentrations $Zn(NO_3)_2$:$C_6H_{12}N_4$ [21]. The spectra display two kinds of emission peaks-sharp intense emission in the range 370–400 nm corresponding to near band edge emission peak (NBE) and the broad emission at around 500–800 nm range attributing to defect level effects emission (DLE) in all the three different molar precursor concentrations. The exhibition of NBE is due to the recombination of the free excitons and DLE signifies the defect states originating from oxygen vacancies and zinc interstitials. And, the relatively strong PL intensities of NBE as compared to DLE indicates the good crystallinity of ZnO NRs with fewer structural defects. Again, with increasing molar ratio from 1:0.1 to 1:1, the observance of the significant increase in the PL intensity of NBE indicates the better crystallinity of the NRs with more concentration of HMTA, thus showing enhanced optical properties at a 1:1 molar ratio. However, with more increase of HMTA concentration at 1: 2 molar ratios, the relative PL intensity decreases which is probably due to the increase in defect levels.

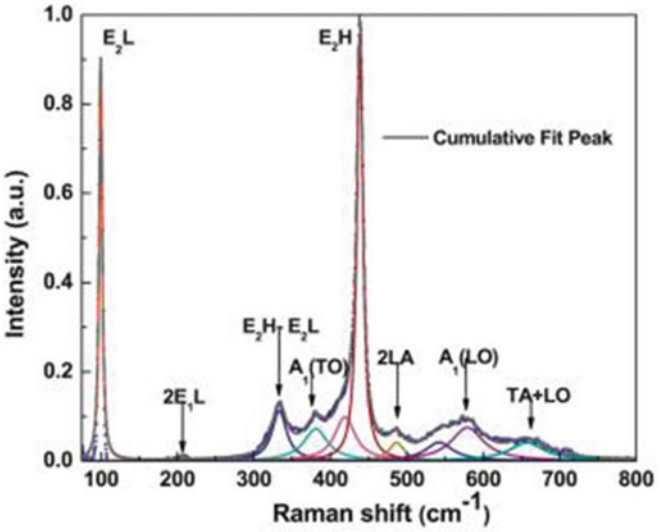

Fig. 4 Raman spectra of ZnO nanocolumns via CBD at 400 °C

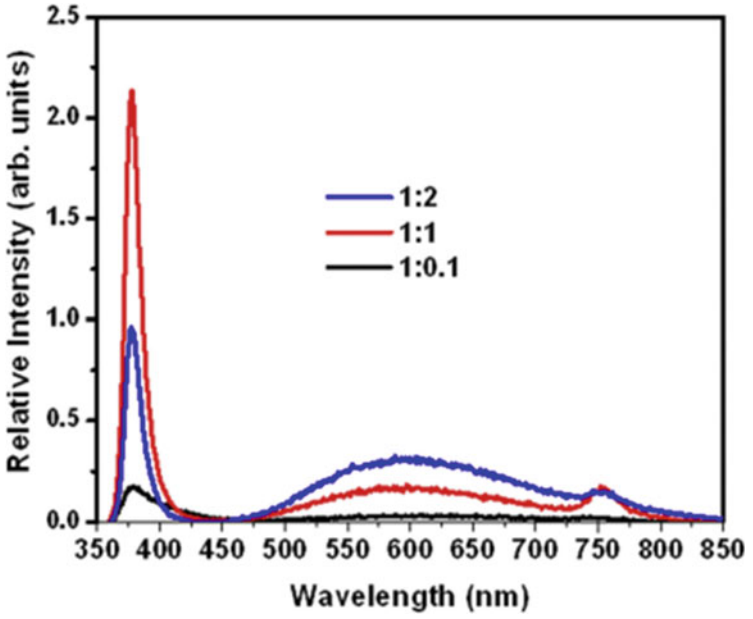

Fig. 5 PL spectra of ZnO NRs at different molar concentrations of $Zn(NO_3)_2$:HMTA

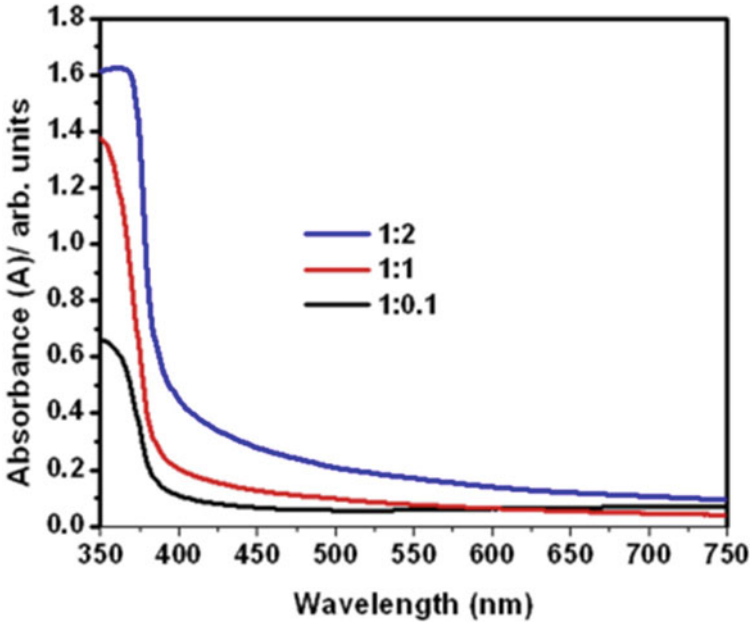

Fig. 6 UV–Vis spectra of ZnO NRs grown by CBD method for different molar ratios of Zn(NO3)2: HMTA

6.5 UV–Visible Study

Figure 6 shows the UV–Visible absorbance spectra of ZnO NRs grown by CBD method varying molar ratios of precursor solutions ($Zn(NO_3)_2$:HMTA [21]. The spectra display the clear observance of absorbance peak located at around 350–380 nm which are the characteristics of ZnO NRs high excitonic energy in all the different molar ratios. However, the observance increases with the increase in molar ratios of $Zn(NO_3)_2$:HMTA. The reason is asserted to the improved surface morphology and crystallinity of the NRs at higher molar ratios.

7 Conclusion

In summary, chemical bath deposition is a reliable technique to grow nanostructured diverse morphologies of ZnO thin films uniformly and well adhered. However, control parameters in the CBD process strongly influenced the growth rate of films. So, it is essential to choose suitable growth conditions like maintaining the pH of the chemical precursor solution, bath temperature, and deposition time primarily. The pH of the chemical bath can be controlled by mixing proportionate ratios of metal salts and complexing agents in the precursor solution to prevent any homogenous

nucleation from occurring on the substrate. This can lead to the better crystallinity and good orientation of the CBD synthesized thin films which are again important factors for ZnO-based thin film applications in photovoltaic, sensing, UV detectors, etc., and has been reviewed in this chapter.

References

1. Ilican S, Gorgun K, Aksoy S, Caglar Y, Caglar M (2018) Fabrication of p-Si/n-ZnO: Al heterojunction diode and determination of electrical parameters. J Mol Struct 1156:675–683
2. Gashaw HF, Abza T (2019) Short review of factors affecting chemical bath deposition method for metal chalcogenide thin films. Int J Thin Fil Sci Tec 8:43–53
3. Ezekoye BA, Offor PO, Ezekoye VA, Ezema FI (2013) Chemical bath deposition technique of thin films: a review. IJSR- Int J Sci Res 2:452–456
4. Pawar SM, Pawar BS, Kim JH, Joo OS, Lokhande CD (2011) Recent status of chemical bath deposited metal chalcogenide and metal oxide thin films. Curr Appl Phys 11:117–161
5. Trejo-Ramos AI, González-Chan IJ, Oliva AI (2020) Physical properties of chemically deposited ZnS thin films: role of the solubility curves and species distribution diagrams. Mater Sci Semicond Process, 118
6. Rezaie MN, Manavizadeh N, Nayeri FD, Bidgoli MM, Nadimi E, Boroumand FA (2018) Effect of seed layers on low-temperature, chemical bath deposited ZnO nanorods-based near UV-OLED performance. Ceram Int 44:4937–4945
7. Terasako T, Obara S, Sakaya S, Tanaka M, Fukuoka R, Yagi M, Nomoto J, Yamamoto T (2019) Morphology-controlled growth of ZnO nanorods by chemical bath deposition and seed layer dependence on their structural and optical properties. Thin Solid Films 669:141–150
8. Hou S, Li C (2016) Aluminum-doped zinc oxide thin film as seeds layer effects on the alignment of zinc oxide nanorods synthesized in the chemical bath deposition. Thin Solid Films 605:37–43
9. Kurbanov SS, Jeon HC, Shaymardanov ZS, Rakhimov RY, Kang TW (2016) Photoluminescence from porous textured ZnO films grown by chemical bath deposition. J Lumin 170:168–173
10. Shimpi NT, Rane YN, Shende DA, Gosavi SR, Ahirrao PB (2020) Synthesis of rod-like ZnO nanostructure: study of its physical properties and visible-light-driven photocatalytic activity. Optik 217:164916
11. Ahmed MAM, Meyer WE, Nel JM (2018) Structural, optical, and electrical properties of a Schottky diode fabricated on Ce doped ZnO nanorods grown using a two-step chemical bath deposition. Mater Sci Semic Proc 87:187–194
12. Mwankemwa BS, Nambala FJ, Kyeyune F, Hlatshwayo TT, Nel JM, Diale M (2017) Influence of ammonia concentration on the microstructure, electrical and raman properties of low-temperature chemical bath deposited ZnO nanorods. Mater Sci Semic Proc 71:209–216
13. Rosado-Mendoza M, Oliva-Avilés AI, Oliva AI (2018) Preferential regions of growth of chemical bath deposited ZnO and Zn(OH)2 thin films at room conditions. Thin Solid Films 645:231–240
14. Rakhsha AH, Abdizadeh H, Pourshaban E, Golobostanfard MR, Mastelaro VR, Montazerian M (2019) Ag and Cu doped ZnO nanowires: a pH-controlled synthesis via chemical bath deposition. Materialia 5:100212
15. Soundarrajan P, Sankarasubramanian K, Logu T, Sethuraman K, Gupta A, Senthil Kumar SM, Jeganathan K, Ramamurthi K (2019) The degree of supersaturation dependent ZnO nano/micro rod arrays thin films growth using chemical bath deposition and hydrothermal methods. Phys E Low-Dimens Syst Nanostruct 106:50–56
16. Son NT, Noh JS, Park S (2016) Role of ZnO thin film in the vertically aligned growth of ZnO nanorods by chemical bath deposition. Appl Surf Sci 379:440–445

17. Shi Z, Walker AV (2016) Zinc oxide chemical bath deposition on functionalized organic thin films: formation of nanorods, nanorockets, and nanoflowers. Thin Solid Films 606:106–112
18. Strano V, Urso RG, Scuderi M, Iwu KO, Simone F, Ciliberto E, Spinella C, Mirabella S (2014) Double role of HMTA in ZnO nanorods grown by chemical bath deposition. J Phys Chem C 118:28189–28195
19. Molefe FV, Koao LF, Dolo JJ, Dejene BF (2014) Effect of reaction time on structural, morphology and optical properties of ZnO nanoflakes prepared by chemical bath deposition method. Physica B Condens Matter 439:185–188
20. Bozkurt ÇB, Caglar B, Kılınç T, Morkoç KS, Erdoğan Y, Kılıç S, Kahveci E, Ercan EA, Çırak Ç (2019) Synthesis and characterization of ZnO nanorice decorated TiO2 nanotubes for enhanced photocatalytic activity. Mater Res Bull 109:160–167
21. Ungula J, Swart HC (2019) Structural, morphological and optical properties of ZnO nanorods grown on a ZnO: Ga seeded thin film: the role of chemical bath deposition precursor concentration at constant and varying II/VI molar ratios. Thin Solid Films 687:137483
22. Macan J, Ivanko M, Bukovčan I, Grčić I, Gajović A (2019) Stable hierarchical ZnO structures for photocatalytic degradation of 2,5-dihydroxybenzoic acid. Mater Sci Semic Proc 97:48–55
23. Shaikh SK, Inamdar SI, Ganbavle VV, Rajpure KY (2016) Chemical bath deposited ZnO thin film based UV photoconductive detector. J Alloys Compd 664:242–249
24. Mohammadi S, Zavvari M (2017) High performance n-ZnO/p-metal-oxides UV detector grown in low-temperature aqueous solution bath. Thin Solid Films 626:173–177
25. Alshamarti HA, Omran Alkhayatt AH (2020) Enhancement characterization of the MSM detector based on Mn doped-ZnO NRS synthesized by microwave assisted chemical bath deposition. Mater Sci Semic Proc 114:105068
26. Gu P, Zhu X, Yang D (2020) Vertically aligned ZnO nanorods arrays grown by chemical bath deposition for ultraviolet photodetectors with high response performance. J Alloys Compd 815:152346
27. Saleh Al-Khazali SM, Al-Salman HS, Hmood A (2020) Low cost flexible ultraviolet photodetector based on ZnO nanorods prepared using chemical bath deposition. Mater Lett 277:128177
28. Boda MA, Bozkurt ÇB, Demir Z, Çırak Ç (2019) Facile synthesis of hybrid ZnO nanostructures by combined electrodeposition and chemical bath deposition for improved performance of the dye-sensitized solar cell. Mater Lett 248:143–145
29. Qu Y, Huang X, Li Y, Lin G, Guo B, Song D, Cheng Q (2017) Chemical bath deposition produced ZnO nanorod arrays as an anti-reflective layer in the polycrystalline Si solar cells. J Alloys Compd 698:719–724
30. Ma B, Rodriguez RD, Ruban A, Pavlov S, Sheremet E (2019) The correlation between electrical conductivity and second-order Raman modes of laser-reduced graphene oxide. Phys Chem Chem Phys 21:10125–10134
31. Gawali SA, Mahadik SA, Pedraza F, Bhosale CH, Pathan HM, Jadkar SR (2017) Synthesis of zinc oxide nanorods from chemical bath deposition at different pH solutions and impact on their surface properties. J Alloys Compd 704:788–794

Chapter 7
Recent Trends and Research Challenges on Supercapacitor

Pukhrambam Sushma Devi and Bibhu Prasad Swain

1 Introduction

Fossil fuel has been a major source of energy since Industrial Revolution. It was estimated that the total world demand for fossil fuel energy was more than 13.5 BTOE (billion tons of oil equivalent) and it will cross more than 18 BTOE by 2035 [1, 2]. There is massive depletion in natural resources which resulted in problems related to the economy and the carbon cycle. Increasing demands for the consumption of energy stimulate the need of developing different variants of energy. Issues were rising in various domains such as generation and storage of power. Researching and developing technology for generating power based on renewable energy has become part of mitigation strategies. Most of the renewable energies are converted in the form of electricity, except for biofuels. As a result of this, the importance of creating a platform for storing electrical energy such as batteries and supercapacitors have evolved [3, 4]. Among other energy-storing devices, the supercapacitor is the most efficient. The gap between ion batteries and conventional capacitors is bridged by supercapacitors. The many advantages of supercapacitors include no pollution, easy maintenance, lower cost, high density of energy and power, fast charging and discharging, long life cycle, and ability to discharge high current instantaneously [5]. In the last few decades, many changes were seen in the field of the development of supercapacitors, mainly the introduction of materials that are nanostructural engineered. Nanostructured materials show comparatively better behavior than bulk materials as they have a high surface area and sufficient active sites for reaction. They also have better chemical properties compared to bulk materials [5].

P. S. Devi (✉) · B. P. Swain
Department of Physics, National Institute of Technology, Lamphelpat, Manipur, India
e-mail: sushmadevi@nitmanipur.ac.in

B. P. Swain (ed.), *Advances in Nanostructured Materials*, Materials Horizons:
From Nature to Nanomaterials, https://doi.org/10.1007/978-981-16-8391-6_7

2 Supercapacitor

Supercapacitors, an electrical energy-storing devices, was developed around 1970–1980 to store energy by using polarized electrolyte which works differently from the chemically powered traditional system. Technically, it is devices with the performance that link the gap between the traditional capacitors and ions batteries [5]. They are becoming the potential options in various fields that demand high and stable energy. They are suitable for quick storing and releasing systems [2, 6].

3 Working of Supercapacitors (SCs)

Supercapacitor stores energy in conductive materials with suitable electrolyte electrochemically by two mechanisms.

(a) On the polarized surface, adsorption (electrostatically) of charges occur. Then, the redox reactions (reversible) of surface electroactive species occur [7, 8].
(b) The redox reaction continued on the active or redox electrodes, such as hydroxides or oxides of metals and conductive polymers [8].

Both the mechanisms are associated with high reversibility and fast charging and discharging processes which make these materials completely different from the traditional battery-like electrode [8] (Fig. 1).

4 Characteristics of Supercapacitors

Without the loss of significant capacitance, supercapacitors can be charged and discharged several times very quickly, in terms of milliseconds. This will be a very important feature for a system like electric vehicles and various other electronic devices where uptake or delivery of high power, long stable cycle, and demands of variable power are required where conventional batteries have limitations [8]. Moreover, the supercapacitor also shows excellent performance at low temperatures. The supercapacitor can store energy when not in use and improve the efficiency of the power supply system. And with this ability, supercapacitor shows its potential applicability in the field of harvesting renewable energy and many modern electronics projects [8].

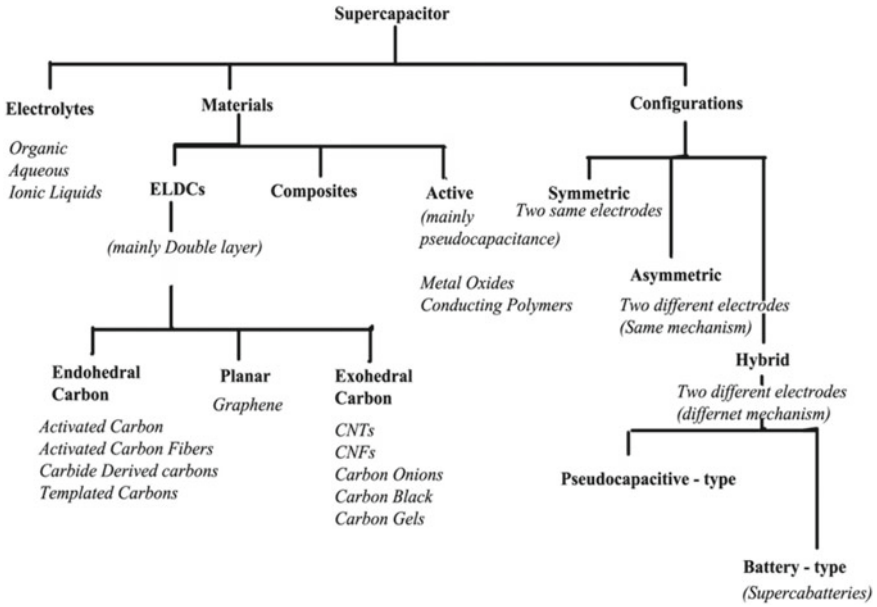

Fig. 1 Different electrolytes, materials, and configurations of supercapacitors [8]

5 Comparison of Supercapacitor and Other Energy-Storing Devices

6 Challenges of Supercapacitors

The supercapacitors show the excellent characteristics and potential of filling the gap between conventional capacitors and ion batteries. But still, many shortcomings need to be addressed before entering into the market for future needs (Table 1).

The major problem of supercapacitors being the lower energy density (<20 Wh/kg) compared to the ion batteries (30–200 Wh/kg) [5, 9, 10]. More research and development are still needed to field the gap and to overcome the difficulties facing the field of supercapacitors. Due to the lower energy density of supercapacitors, they are bulky. To make it compact, energy density needs to be high ad this can be obtained by using a suitable electrode in double-layered capacitors thereby increasing the surface area of operation or by increasing the operating voltages. To improve the capacity of storage, new electrodes of active materials and electrolytes with better electrochemical performance need to be found out and it could be a difficult task [5].

Because of the ability of supercapacitors to discharge high energy, it becomes the main area to focus the impact it will be giving on the load. Reliable designs need to be developed to study these parameters like fluctuation of load, system stability, etc. [5]. Supercapacitors have a very low voltage rating lower than 2.7 V.

Table 1 Comparison of supercapacitor and other energy-storing devices

Category	Advantages	Disadvantages
Super capacitor	It has a high density of power, cycling life is long, charging speed is fast, and can discharge high current. It shows excellent performance at low temperatures. Charging and discharging are simple [5]	It has a low density of energy [5]
Sodium-ion battery	It has high energy density and stability. Charging and discharging are fast and show no over-discharging characteristic. It has a long life cycle and is very safe. It has a very vast range of applications. It is rich in sodium and access to the required raw material is easy. Its waste is easy to recycle and is free of pollution [5]	Compared to lithium-ion batteries, it has a higher threshold and shows the worst electrochemical performance and its storage is a major concern [5]
Lithium sulfur battery	Cost is low and has a high density of energy. The toxicity level is low and environmental pollution is low [5]	Performance is poor and coulomb efficiency is also low. It has poor cyclic life and stability [5]
Lithium-ion battery	It has a huge working platform. It has a high density of energy, cycling life is long. Charging and discharging are comparatively fast but have a small self-discharge rate. It can work in large temperature range and shows good safety performance. No pollution and memory effect [5]	Cost is high. Large current cannot be discharged. Line protection is required to protect against overcharge and over discharge [5]

This left us with the only option to connect supercapacitors in series for practical applications. Overcharging has also seriously impacted the life of capacitors, which is a very important concern as many applications demand the need for charging and discharging high current [5].

7 Electrode Materials for Supercapacitors

Characteristics of supercapacitors such as capacitance and charge storage depends on the material which is used as an electrode. The capacitance depends on the effective operating area, known as electrochemically active surface area, of the electrode materials which is assessable for interaction with electrolyte [2, 11]. Largeot et al. claim that the size of the pores in the electrode material should be similar to that of

the size of the ion in the electrolyte to increase capacitance as smaller or larger pore size will reduce capacitance [2]. The pore size of the conducting electrode materials can be easily configured by deploying nanostructured materials which in turn will enhance the electrochemically active area [2, 12].

The above figure shows the effect of pore size on capacitance. The normalized capacitance increases ultimately when pore size changes from 1.1 to 0.7 and decreases on further decreasing the pore size. However, much research yet needs to be done to conclude that the porosity and capacitance have a straightforward relationship [2]. Various active materials used are based on carbon, materials based on carbon, conducting polymers, and metal oxides [2, 13–16]. Some popular electrode materials are discussed as follows:

7.1 Carbon-based Materials

It is one of the most vastly researched materials for making electrodes. It has a high surface area, excellent conductivity and capacitance, thermal and chemical stability, reliable mechanical properties, less toxic, low cost, and abundance are the major reason for the ultimate attraction of the electrode based on the carbon-based materials especially in EDLC [17, 18] (Fig. 2).

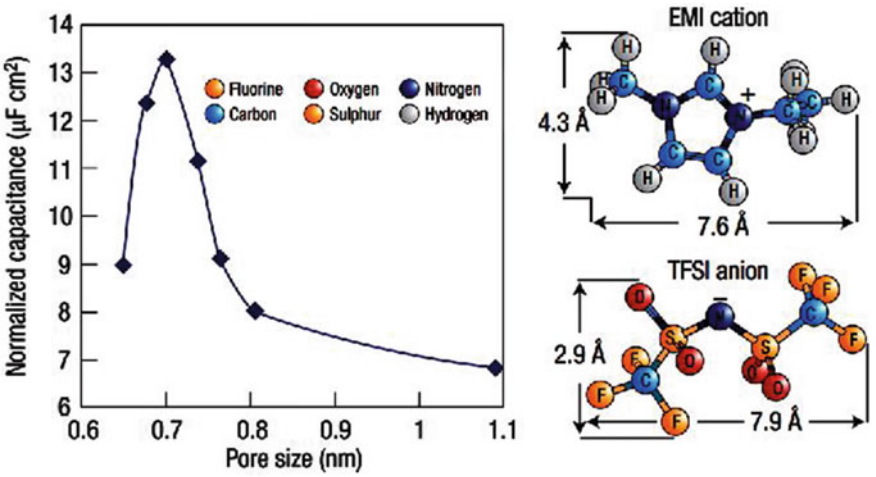

Fig. 2 Effect of pore size on capacitance. Adapted with permission from [12]. Copyright © 2008, American Chemical Society

7.2 Activated-Carbons

It is one of the most researched materials which has application in making electrodes for supercapacitors. It has shown huge potential for supercapacitors as it provides excellent surface area and electrical performance at an affordable price. It can be synthesis from biological waste which also exhibits various kinds of morphology. Their pore size is known to be tuneable.

7.3 Carbon-Nanotubes (CNTs)

It is a classic one-dimensional carbon material. They can be classified as single and multi-walled CNT and can be prepared by various techniques. They are lightweight, has good electrical conductivity, large surface area (1,600 sq.m/g), and intrinsic flexibility, making them the prominent material for supercapacitor electrode [19]. But their actual capacitance is low compared to their theoretical value as their internal resistance and micro-pores affect the performance. Also, regularly aligned carbon nanotubes perform well than the irregularly entangled carbon nanotubes in transferring ions.

7.4 Graphene

It is a structurally two-dimensioned carbon material. They can be prepared by methods like reducing graphene oxides, stripping mechanically, solvent-spalling, and CVD. CVD was a successful technique in synthesizing three-dimensional graphene structures grown on the catalytic metal foam of nickel, cobalt, etc. Graphene foam is a better candidate for preparing comparatively lightweight, flexible, highly conductive, and stable electrodes with a large surface area [20]. But it has a disadvantage when considering its typically large pores diameter. Due to excellent thermochemical properties, large surface area, high cyclic life, and processability, graphene has been widely studied to take advantage in the field of energy-storing devices [21–25].

7.5 Conducting Polymers

It is also one of the widely studied areas for preparing electrodes. It exhibits many potential features like tuneable morphology, the ability to be doped and undoped fast, etc. Due to the capabilities of reversible Faradaic redox reaction, high energy density compared to metal oxides, and lower cost of conducting polymers, several studies have been extensively carried out for supercapacitor applications. Conducting

polymers can be engineered with nano-architectures to provide higher porosity and surface area, which will increase performance. Studies have also shown that using conducting polymers, retention of capacitance increases up to 83% after a complete cycle of 15,000 [20].

7.6 Polyaniline

It is also among the notably attracted conducting polymers. It is generally synthesized chemically by polymerizing aniline in an acidic environment. It shows a huge potential in the application of energy-storing devices as it has excellent electrical activity, stability, and low cost. However, in bulk state, it is not effective due to lower surface area. Thus, polyaniline with nanostructures has much interest for supercapacitor electrodes [26, 27]. Studies have also shown that polyaniline composites with metal oxides have significantly high pseudo-capacitance.

7.7 Polypyrrole

It is a unique conducting polymer that is known to possess promising features for electrodes application. It shows high electrical conductivity, thermal stability, and high energy density. Charging and discharging are fast and the cost is low [28]. These features make polypyrrole, one of the most important conducting polymers. Its major advantages include easy processability, stability, excellent specific capacitance, high energy density, reversible electrochemical doping, etc. It can be significantly applied in the manufacturing of high-end flexible supercapacitors.

7.8 Metals Oxides

For supercapacitor electrodes, due to their mesoporous structures, metal oxides like nickel oxides, manganese dioxide, cobalt oxide, and ruthenium oxide are widely studied. The mesoporous structures provide higher surface area and uniform pore distributions [29, 30]. Metal oxides have high specific capacitance due to effective interactions of the electrolytes and electrodes. They also exhibit several properties which are exceptionally suitable for selecting materials for engineering. Being easier to prepare largely and considerably cheaper, among several solid inorganic materials, nanoparticles of magnetic metallic oxide possess attractive properties [31, 32]. For electrode application in supercapacitors, magnetic metallic oxide like perovskite-oxide and spinel-ferrites have outstanding performance due to their higher energy density, higher power, better retention of capacitance, and stable performance in the longer-term [31, 33, 34].

7.9 Transition Metal-Sulfides

Transition metal-sulfides are known for their outstanding electrochemical properties like distinct crystal lattice structures, very high conductivity and specific capacitance, excellent redox action, and lower electro-negativity [31, 35]. Owing to these properties, they are considered to be potential candidates for the application of storing energy. And it is also reported that they are far more superior than metallic oxide in terms of electrochemical properties [31, 36–38]. They show promising characters in utilizing them as electrodes in supercapacitors applications. Some notable metal-sulfides include nickel sulfide, cobalt sulfide, iron sulfide, molybdenum disulfide, tin sulfide, manganese sulfide, tungsten sulfide, etc.

7.10 Composites

Carbon-based electrode materials have lower specific capacitance compared to metal oxides and conducting polymers [39, 40]. But metal oxides and conducting polymers have comparatively low charge/discharge cycle stability. This restricts their development in supercapacitor applications. However, using composites materials, these challenges can be reduced and improve the performance of supercapacitors. Composite materials have also been shown to have higher energy density (Fig. 3).

8 Electrolytes

In energy-storing devices, electrolytes are the essential elements. It provides ionic conductivity between the electrodes in a cell [41]. Supercapacitor's performance is also predicted by it. The energy and power density of the system depends on the nature of the electrolytes used.

Important factors to consider while choosing electrolytes are:

(1) type and size of ions
(2) the materials of the electrode
(3) the concentration of ions and solvent
(4) interaction of solvent and ions
(5) the potential window
(6) less toxic
(7) relatively lower viscosity, resistivity, and volatility

Electrolytes can be broadly divided as (Table 2):

(1) liquid electrolytes (organic, aqueous, and ionic liquid)
(2) solid/quasi solid electrolytes (inorganic and organic).

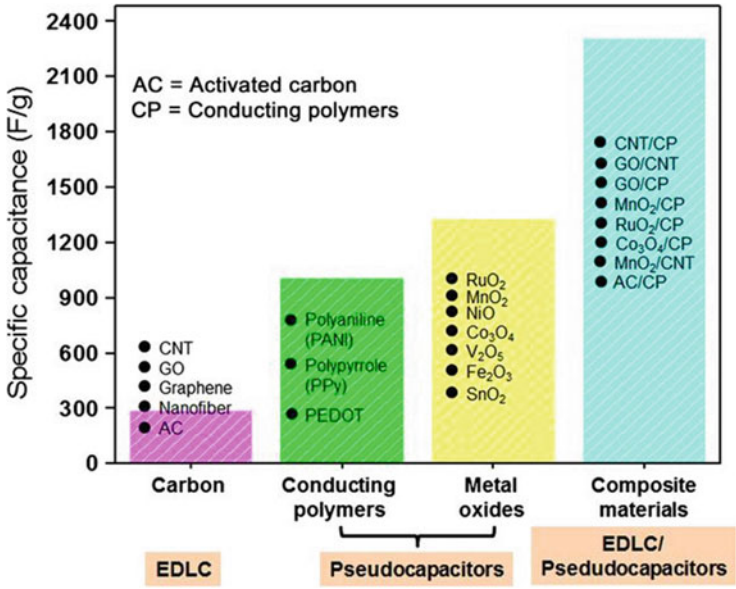

Fig. 3 Various active materials used as electrode in supercapacitor applications [14]. LICENCE by CC BY 4.0 © 2014 The Authors. Energy Science & Engineering published by the Society of Chemical Industry and John Wiley & Sons Ltd

Table 2 Specific capacity of graphene-based supercapacitors on different electrolytes

Electrolytes	Specific capacitance
Ionic liquid electrolytes	75 F/g [50]
Aqueous electrolytes	135 F/g
Organic electrolytes	99/g [51]

8.1 Aqueous Electrolytes

It can be further classified into three subtypes: acidic, alkaline, and neutral solutions. It shows good electrical conductivity better than ionic liquid and organic electrolytes and hence supercapacitors using these electrolytes will exhibit higher specific capacitance than using organic electrolytes. They are selected based on the mobility of anions and the size of hydrated cation [2]. Its limitation is the narrower potential window compared to that of organic electrolytes which exhibits a wider range.

8.2 Organic Electrolytes

Due to the low cost and high potential window in the range 2.5–2.8 V, organic electrolytes dominate the commercial market of energy-storing devices [41]. Due to a large potential window, it can store and release high energy compared to aqueous electrolytes.

8.3 Ionic Liquid Electrolytes

Ionic liquid electrolytes are pure salts in liquid form. They are known to appear to replace organic and aqueous electrolytes because of their high chemical and thermal stability, non-flammability, very low vapor pressure, and wide operating potential range; ionic liquid electrolytes show huge potential to operate at higher temperatures [2].

9 Scope of Supercapacitors in Future

Today with the advancement in electronic technology, there is a rapid advancement in many portable devices. Developing flexible, light, and small energy-storing devices with excellent electrochemical properties is the need of the future [42–44]. Micro-supercapacitor will have excellent properties like high power delivery, higher rate, and frequency response of operation [45, 46]. Hybridization of battery and supercapacitors will help in the future to solve the problem of supercapacitors having lower energy density [5]. Also, the hybrid devices have the potential to provide a long and stable performance cycle and lower cost [47–49]. Supercapacitor will become inseparable from the advancement of science and technology and the future demands. Supercapacitor development will grow rapidly in the future.

10 Conclusion

Considering the increasing needs and demand for environmentally friendly and efficient energy-storing devices, many have shown interest in the development of supercapacitor which has great potential in diverse fields. In the future, there will be a huge market for supercapacitors. However, there are many problems related to these supercapacitors which need to be addressed and resolved. Also, proper selection of materials for making electrodes and electrolytes is necessary to be able to perform well in every adverse condition. Several materials such as activated carbon, carbon nanotubes, graphene, conducting polymer, polyaniline, polypyrrole, metal oxides,

and transition metal-sulfides already show the potential for preparing electrodes. Carbon-based materials are of ultimate attraction mainly because of high surface area, excellent conductivity and capacitance, thermal and chemical stability, reliable mechanical properties, less toxic, low cost, and abundance. Intelligently selected electrolytes considering suitable characteristics regarding ions, materials for electrodes, toxicity, resistivity, volatility, etc. will result in better performance. Aqueous electrolytes show better electrical conductivity than ionic liquid and organic electrolytes. But organic electrolytes can store and release high energy, compared to aqueous electrolytes, due to the large potential window. More research is still needed to reduce the production cost, increasing energy density, and suitable electrode and electrolyte material combinations.

References

1. Chu S, Cui Y, Liu N (2017) The path towards sustainable energy. Nat Mater 16:16–22
2. Raza W, Ali F, Raza N, Luo Y, Yang J, Kumar S, Mehmood A, Kim K-H (2018) Recent advancements in supercapacitor technology. Nano Energy 52:441–473. https://doi.org/10.1016/j.nanoen.2018.08.013
3. Hollenkamp AF, Howlett PC, MacFarlane DR, Forsyth SA, Forsyth M (2009) Energy storage devices, Google Patents
4. Tasnin W, Saikia L (2018) Performance comparison of several energy storage devices in Ddregulated AGC of a multi area system incorporating geothermal power plant. IET Renew, Power Gener 12:761–772
5. Shifei, Huang, Zhu, Xianglin, Sarkar, Samrat, Zhao, Yufeng (2019) Challenges and opportunities for supercapacitors. APL Materials 7:100901. DOI: https://doi.org/10.1063/1.5116146
6. Huang J, Sumpter BG, Meunier V (2008) A universal model for nanoporous carbon supercapacitors applicable to diverse pore regimes, carbon materials, and electrolytes. Chem Eur J 14:6614–6626
7. Inagaki M, Konno H, Tanaike O (2010) Carbon materials for electrochemical capacitors. J Power Sources 195:7880–7903
8. Betrián BR (2015) Trends and research challenges in supercapacitors. Bol Grupo Espanol Cabon 37:9–13
9. Zhao Y, Ran W, He J, Song Y, Zhang C, Xiong D-B, Gao F, Wu J, Xia Y (2015) Oxygen-rich hierarchical porous carbon derived from artemia cyst shells with superior electrochemical performance. ACS Appl Mate Inter 7:1132–1139
10. Zhao Y, Zhang Z, Ren Y, Ran W, Chen X, Wu J, Gao F (2015) J Power Sources 286:1–9
11. Cai L-F, Xu J, Huang J-Y, Xu H-J, Xu F, Liang Y-R (2018) Structure control of powdery carbon aerogels and their use in high-voltage aqueous supercapacitors. Carbon 130:847
12. Largeot C, Portet C, Chmiola J, Taberna P-L, Gogotsi Y, Simon P (2008) Relation between the ion size and pore size for an electric double-layer capacitor. J Am Chem Soc 130:2730–2031
13. Hashemi M, Rahmanifar MS, El-Kady MF, Noori A, Mousavi MF, Kaner RB (2018) The use of an electrocatalytic redox electrolyte for pushing the energy density boundary of a flexible polyaniline electrode to a new limit. Nano Energy 44:489–498
14. Shown I, Ganguly A, Chen LC, Chen KH (2015) Conducting polymer-based flexible supercapacitor. Energy Sci Eng 3:2–26
15. Luo Y, Hong W, Xiao Z, Bai H (2018) A high-performance electrochemical supercapacitor based on a polyaniline/reduced graphene oxide electrode and a copper (ii) ion active electrolyte. Phys Chem Chem Phys 20:131–136

16. Liu W, Zhang S, Dar SU, Zhao Y, Akram R, Zhang X et al (2018) Polyphosphazene derived heteroatoms-doped carbon materials for supercapacitor electrodes. Carbon 129:420–427
17. Cakici M, Kakarla RR, Alonso-Marroquin F (2017) Advanced electrochemical energy storage supercapacitors based on the flexible carbon fiber fabric-coated with uniform coral-like MnO 2 structured electrode. Chem Eng J 309:151–158
18. Jayaseelan SS, Radhakrishnan S, Saravanakumar B, Seo M-K, Khil M-S, Kim HY, Jayaseelan SS (2018) Mesoporous 3D NiCo2O4/MWCNT nanocomposite aerogels prepared by a supercritical CO2 drying method for high performance hybrid supercapacitor electrodes. Colloids Surf A Physicochem Eng Asp 538:451–459
19. Koziol K, Vilatela J, Moisala A, Motta M, Cunniff P, Sennett M et al (2007) Highperformance carbon nanotube fiber. Science 318:1892–1895
20. Andres V, Kyoung Ryu Y, Alberto B, Antonio Lardron-de-Guevara, Elijah H, Jinghan Z, Jorge P, Fernando C, Javier M (2021) Recent trends in graphene supercapacitors: from large area to microsupercapacitors. RSC Sustain Energy Fuels 5:1225−1586
21. Zhang H, Chhowalla M, Liu Z (2018) 2D nanomaterials: graphene and transition metal dichalcogenides. Chem Soc Rev 47:3015–3017
22. PM (2010) Graphene-based nanomaterials and their electrochemistry. Chem Soc Rev 39:4146–4157
23. GY (2017) Graphene and polymer composites for supercapacitor applications: a review. Nanoscale Res Lett 12:387
24. Zhang H, Li C, Wang K, Sun X, Ma Y, Zhang X (2014) Recent advances in porous graphene materials for supercapacitor applications. RSC Adv 4:45862–45884
25. Yang X, Cheng C, Wang Y, Qiu L, Li D (2013) Liquid-mediated dense integration of graphene materials for compact capacitive energy storage. Science 341:534–537
26. Barbieri O, Hahn M, Herzog A, Kötz R (2005) Capacitance limits of high surface area activated carbons for double layer capacitors. Carbon 43:1303–1310
27. Li X, Yang L, Lei Y, Gu L, Xiao D (2014) Microwave-assisted chemical-vapor-induced in situ polymerization of polyaniline nanofibers on graphite electrode for highperformance supercapacitor. ACS Appl Mater Interf 6:19978–19989
28. Fan L-Z, Maier J (2006) High-performance polypyrrole electrode materials for redox supercapacitors. Electrochem Commun 8:937–940
29. Wang W, Guo J, Wang T, Shao J, Wang D, Yang Y-W (2015) Mesoporous transition metal oxides for supercapacitors. Nanomaterials 5:1667–1689
30. Zhi M, Xiang C, Li J, Li M, Wu N (2013) Nanostructured carbon–metal oxide composite electrodes for supercapacitors: a review. Nanoscale 5:72–88
31. MIA Adbel M, Ramy AF, Ahmed ES, M.Abd E, Olojede SO, Ahmed IO, Charlie F, Ala'a HAM, Awed AS, Ashour AH, David WR (2021) Advanced materials and technologies for supercapacitors used in energy conversion and storage. Environ Chem Lett 19:375–439
32. Masala O, Seshadri R (2004) Synthesis routes for large volumes of nanoparticles. Annu Rev Mater Res 34:41–81
33. Elkholy AE et al (2017) Nanostructured spinel manganese cobalt ferrite for high-performance supercapacitors. RSC Adv 7:51888–51895
34. Liang G et al (2020) Developing high-voltage spinel LiNi0.5Mn1.5O4 cathodes for high-energy-density lithium-ion batteries: current achievements and future prospects. J Mater Chem 8:15373–15398
35. Zhang Q et al (2020) Intercalation and exfoliation chemistries of transition metal dichalcogenides. J Mater Chem A 8:15417–15444
36. Geng P et al (2018) Transition metal sulfides based on graphene for electrochemical energy storage. Adv Energy Mater 8:1703259
37. Yu XY, David Lou XW (2018) Mixed metal sulfides for electrochemical energy storage and conversion. Adv Energy Mater 8:1701592
38. Benjamin Raj et al (2020) Review-futuristic direction for R&D challenges to develop 2D advanced materials based supercapacitors. J Electrochem Soc 167:136501

39. Ratha S, Marri SR, Behera J, Rout CS (2016) High-energy-density supercapacitors based on patronite/single-walled carbon nanotubes/reduced graphene oxide hybrids. Eur J Inorg Chem 2016:259–265
40. Borenstein A, Hanna O, Attias R, Luski S, Brousse T, Aurbach D (2017) Carbon-based composite materials for supercapacitor electrodes: a review. J Mater Chem A 5:12653–12672
41. Zhong C, Deng Y, Hu W, Qiao J, Zhang L, Zhang J (2015) A review of electrolyte materials and compositions for electrochemical supercapacitors. Chem Soc Rev 44:7484–7539
42. Xu Q, Wei C, Fan L, Rao W, Xu W, Liang H, Xu J (2018) Polypyrrole/titania-coated cotton fabrics for flexible supercapacitor electrodes. Appl Surf Sci 460:84–91
43. He Y, Chen W, Li X, Zhang Z, Fu J, Zhao C, Xie E (2012) Freestanding three-dimensional graphene/MnO2 composite networks as ultralight and flexible supercapacitor electrodes. ACS Nano 7:174–182
44. Shi Y, Pan L, Liu B, Wang Y, Cui Y, Bao Z, Yu G (2014) Nanostructured conductive polypyrrole hydrogels as high-performance, flexible supercapacitor electrodes. J Mater Chem A 2:6086–6091
45. Huang P, Lethien C, Pinaud S, Brousse K, Laloo R, Turq V, Respaud M, Demortiere A, Daffos B, Taberna P-L (2016) On chip and freestanding elastic carbon films for micro-supercapaccitors. Science 351:691–695
46. Beidaghi M, Gogotsi Y (2014) Capacitive energy storage in micro-scale devices: recent advances in design and fabrication of micro-supercapacitors. Energy Environ Sci 7:867–884
47. Tie D, Huang S, Wang J, Zhao Y, Ma J, Zhang J (2018) Energy Storage Mater 21:22–40. https://doi.org/doi.org/10.1016/j.ensm.2018.12.018
48. Zuo W, Li R, Zhou C, Li Y, Xia J, Liu J (2017) Battery-supercapacitor hybrid devices: recent progress and future prospects. Adv Sci 4:1600539
49. Chen Z, Xiong D-B, Zhang X, Ma H, Xia M, Zhao Y (2016) Construction of a novel hierarchical structured NH_4-Co-Ni phosphate toward an ultrastable aqueous hybrid capacitor. Nanoscale 8:6636–6645
50. Vivekchand S, Rout CS, Subrahmanyam K, Govindaraj A, Rao C (2008) Graphene based electrochemical supercapacitors. J Chem Sci 120:9–13
51. Stoller MD, Park S, Zhu Y, An J, Ruoff RS (2008) Graphene-based ultracapacitors. Nano Lett 8:3498–3502

Part II
Magnetic Nanomaterials and Nanostructured Polymers

Chapter 8
Magnetic Nanoparticles in Wastewater Treatment, Supercapacitor, and Biomedical Applications

N. Joseph Singh, Boris Wareppam, and L. Herojit Singh

1 Introduction

Nanoparticles are defined as particles having dimensions in the nanometer range (1–100). Reviews and earlier reports show that the dimensions having higher than 100 nm are considered nanoparticles. In general, the dimension of the nanoparticles can be defined as the dimension from which the particles experienced a transition in the properties from that of the bulk. NPs have a high surface area comparing to their volume, as a result of which it is highly reactive, versatile, and strong as compared to the bulk [1].

Magnetic nanoparticles (MNPs) are one of the most important, useful nanoparticles, and as a result of which these nanoparticles have become an alarming topic in modern research and applications. These nanoparticles are usually metal oxides such as iron oxides and ferrites [2]. Magnetic nanoparticles are composed of metals like cobalt, nickel, iron, and alloys [3]. These particles show strong magnetic moments in the presence of the external magnetic field. MNPs are zero-dimensional inorganic materials having metal-based configurations. Cubic iron oxides, i.e., magnetite (Fe_3O_4) and maghemite (γ-Fe_2O_3), contribute to a large extent in medical application due to their low toxicity and their metabolic pathways to take actions or chemical interactions. They have intrinsic and unique properties such as physical properties [4], chemical properties, stability [5], mechanical properties, magnetic susceptibility, biocompatibility [6], high saturation magnetization, and less toxicity [7, 8]. As a result of these exclusive properties they are used in various fields, such as industrial, environmental, analytical, and biomedical applications. MNPs, due to their distinctive physical and chemical properties, have attracted much attention particularly in biomedical applications and superior magnetism. These properties make MNPs a potential for the applications such as in MRI [9], delivery of drugs [10, 11], hyperthermia [12, 13], separation of cells [14], magnetic energy storage [15], spintronics

N. J. Singh · B. Wareppam · L. H. Singh (✉)
Department of Physics NIT Manipur, Langol, Imphal, Manipur 795004, India

B. P. Swain (ed.), *Advances in Nanostructured Materials*, Materials Horizons: From Nature to Nanomaterials, https://doi.org/10.1007/978-981-16-8391-6_8

[16], and supercapacitor. Magnetic nanoparticles are used in wastewater treatment. They are used as photocatalysts and adsorbents in waste water treatment due to their photocatalytic properties, large surface area, chemical stability, nontoxicity, and natural availability [17].

2 Properties of Magnetic Nanoparticle

The properties of magnetic nanoparticles depend upon the composition, particle size, and cation distribution over the A or B site. Also, it depends upon the particle shape. Magnetic nanoparticles with spinel structure are mostly hard magnetic material, high coercivity, moderate saturation magnetization [18], superparamagnetic, and spin canting. These properties are due to magnetization effects on the surface and the single or multi-domain effect. The features that define the properties of magnetic nanoparticles are:

(a) Finite-size effects or the single domain or multi-domain. In this condition, the particles are magnetized uniformly and all the spins are aligned unidirectionally. Superparamagnetism is the most studied finite-size effect in the small particle system. The magnetic behavior of an individual nanoparticle is dominated by the finite-size effect. With the absence of multi-domain walls, the contribution from the domain wall motion which reduces the coercitivity is eliminated.

(b) Surface effects: the breakage of symmetry of the crystal at the surface results in this effect. As the size of the nanoparticle is reduced, most of the atoms in a nanoparticle are at the surface. Since the number of surface atoms is large, surface magnetization becomes significant. A magnetic nanoparticle usually consists of a single domain particle with magnetocrystalline anisotropy. The magnetic moment orients either up or down along the easy axis. The magnetic properties will depend upon the direction of magnetic moments. The presence of defects on the surface such as vacancies (atomic), oxidation, bond dangling, and lattice disorder or strain results in disordered spins leading to surface magnetization.

2.1 Superparamagnetism

Superparamagnetism occurs in small ferromagnetic or ferromagnetic nanoparticles [19]. With the effect of temperature, the magnetization of the particle randomly flips direction. Neel relaxation time is the typical time between two flips which is given by

$$\tau = \tau_0 \exp^{(\Delta E / K_B T)}$$

where τ_0 usually ranges between 10^{-12} and 10^{-9} s [20].

In the absence of an external magnetic field, two energetically equally favorable directions are parallel to the easy axis of magnetization. The energy barrier ΔE of the size KV separates these two directions and if the thermal energy $K_{\text{B}}T$ is high, then the barrier can be overcome and the grain's magnetization changes direction. The symmetry between the two magnetizations along the easy axis is broken by the non-zero magnetic field. When magnetization points along the external magnetic field, the energy of grain are lower than when it points in the opposite direction. Energy barriers for jumping from magnetization along the external field to magnetization opposite to the external field are much bigger than the reverse.

Superparamagnetic nanoparticles have no moment when the external magnetic field is removed. The nanoparticles react similarly to a paramagnet when an external field is applied. But their magnetic susceptibility is very large compared to a paramagnet. Superparamagnetic behavior is observed below the Curie temperature.

3 Synthesis of Magnetic Nanoparticles

3.1 Magnetic Nanoparticle is Synthesized Using Different Techniques as Follows

(i) Co-precipitation method
(ii) Hydrothermal method
(iii) Sol–gel method
(iv) Auto-combustion method, etc.

Of these methods, the co-precipitation method is most favorable and extensively used. With this process, a large number of nanoparticles can be obtained. It is simple, low cost, purity of nanoparticles, and plays an important role in controlling the size of the nanoparticles. It is a low-temperature synthesis method and can be used to study the various properties of the nanoparticles by varying the following factors such as pressure, concentration, pH, stirring speed, reaction time, and nature of precursors. Some important magnetic nanoparticles synthesized using the co-precipitation method is as follows:

(a) Synthesis of magnetite (co-precipitation method): One of the easiest way and commonly used methods to synthesized magnetite is the co-precipitation method. $FeCl_2$ and $FeCl_3$ are dissolved in distilled water and heated up to ~80–100 °C with continuous stirring. A basic solution such as NaOH or NH_3 is added rapidly and a black dispersion is obtained. After stirring slowly, the dispersion is cooled down and then washed and centrifuged to obtain particles in water dispersion or dried form (Fig. 1).

(b) Synthesis of Cobalt ferrite: Using the co-precipitation method Cobalt Ferrite nanoparticles can also be easily synthesized. $CoCl_2$ (aq) and $FeCl_3$ (aq) solution with molar concentration 1:2 is prepared and the solution mixture was stirred

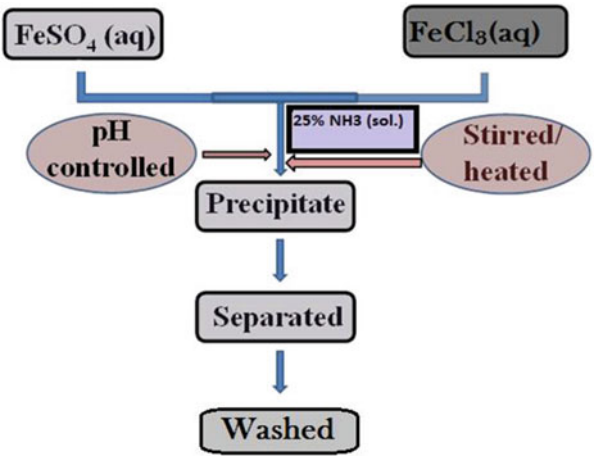

Fig. 1 Flowchart showing the synthesis of magnetite (Fe_3O_4)

magnetically for ~40–50 min at ~80–100 °C. After nucleation, $NaOH/NH_3$ solution was added under vigorous stirring. The nanoparticles were washed repeatedly with double distilled water after bringing the solution to RT. The sample was collected after centrifuging and washed. The samples are dried in the oven for further characterization (Fig. 2).

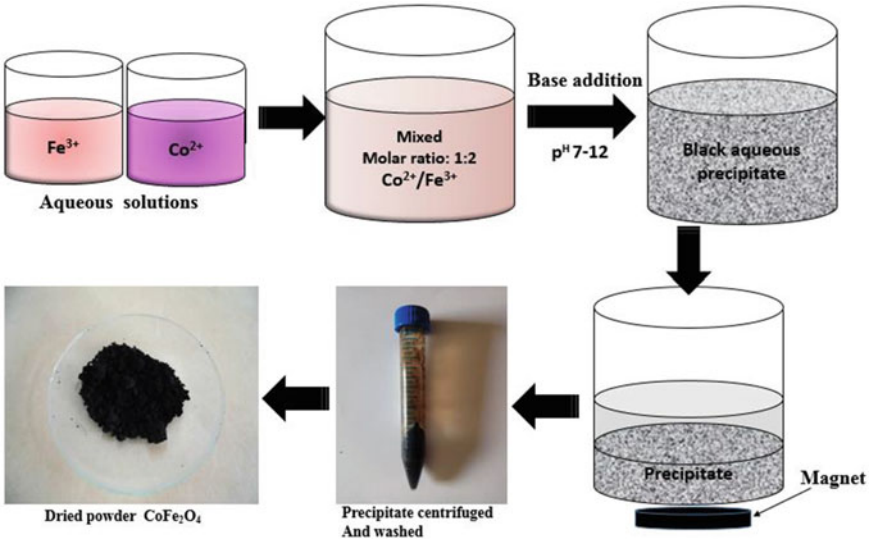

Fig. 2 Steps to synthesize cobalt ferrite nanoparticles (by co-precipitation method)

4 Some Applications of Magnetic Nanoparticles

4.1 Wastewater Treatment (Photocatalysis, Degradation, and Adsorption)

Photocatalysis: In the photocatalytic process, light is used to initiate a substance without being involved in itself and alters the rate of the chemical reaction. Photocatalyst which is usually a metal oxide is defined as a material that is capable of absorbing light enabling the production of electron–hole pairs that allow chemical transformations to break down the organic matter. In the photocatalytic process, the metal oxide activated by light generates two radicals (OH and O_2^- radicals) by oxidation of OH^{-1} anions and reduction of O_2, respectively. These radicals and anions act or react with toxic pollutants to break and transform them into lesser harmful by-products like CO_2 and H_2O.

Metal oxides have shown promising activity as photocatalysts in the removal of many toxic pollutants such as dyes, pesticides, pharmaceutical products, etc. Composites of nanoparticles show higher efficiency in removing these by-products. Some of the metal oxides and nanocomposites and their corresponding organic pollutants are shown in Table 1.

Magnetic nanoparticles such as iron oxide and cobalt ferrite are promising photocatalysts. It was reported that α-Fe_2O_3 with a low band-gap of 2.2 eV is suitable as a photocatalyst [33]. The generation of electron–hole pairs through these band-gap enables this photocatalytic activity. This iron oxide nanoparticle has been reported for photodegradation of dyes such as congo red, methylene blue, methyl blue, etc. [34] due to its catalytic and effectiveness in wastewater treatment. Magnetic nanoparticles have been used widely as photocatalysts, but due to the electron–hole recombination being very fast on the surface, the declination of activity is frequently observed. The addition or dopping of some metal on metal oxide nanoparticles can be a way to get

Table 1 List of photocatalyst and their corresponding Organic pollutants

Photocatalyst	Organic pollutants or dye	References
(a) TiO_2, (b) V_2O_5, (c) ZnO, (d) Fe_2O_3, (e) CdO, (f) Fe_3O_4, (g) CdS, and (h) Al_2O_3	Azo dye, acid orange 7, methylene blue, alizarin S, methyl red, Congo red, orange G, Imidacloprid	[21–23]
(i) TiO_2	Alizarin S, Congo red, methylene blue, Crocein orange G, methyl red	[24, 25]
(j) ZrO_2	Orange G, amido black, remazol brilliant blue R	[26]
(k) Composites of CuO-SnO_2, (l) ZrO_2-TiO_2, (m) SnO_2/TiO_2, (n) TiO_2/WO_3, (o) Fe_2O_3/SnO_2, (p) TiO_2-ZrO_2, (q) ZnO-SiO_2, and (r) CNTs-CoO-TiO_2	Acid blue 62 dye, 4-chlorophenol, rhodamine-B, methylene blue, acid blue 62, phenol, and Hg (II) reduction	[27–32]

rid of such a problem. For example, gold/iron oxide aerogels were used as photocatalysts. Under the illumination of UV light, the gold doped iron oxide degrades Blue 79 azo dye [35]. The gold particle served as the site for electron accumulation under UV light irradiation and enables the transfer of surface electrons. The better separation between electrons and holes would allow a better efficiency for oxidation and reduction reactions, thus enhancing the photocatalytic activity.

Degradation: It is a process in which the dye molecules are broken down chemically or degrade into smaller molecules with or without sunlight is called dye degradation/photocatalytic degradation. Nontoxic smaller molecules like carbon dioxide, water, and mineral by-products are the resulting products after degradation. Not all of the dye molecules are used during the dyeing process. A percentage of these dye molecules are released as wastewater from industries and factories. As most of the dye molecules are not reactive toward the light, in acidic or basic solution and oxygen, therefore, the dye molecules persist in the environment.

Heterogeneous photocatalysis is one of the modern methods widely employed for the degradation or bleaching of the dyes. The transfer of electrons from the valence band to the conduction band of a semiconductor surface is involved in this process with the illumination of the proper wavelength of light. In this process, the generated ions react with oxygen or water and produce hydroxide radicals and peroxide anions. These species have the oxidizing power to degrade or break down chemicals such as harmful dyes present in water [36]

Adsorption: It is one of the physical–chemical techniques which is most simple and economical to remove the dye and adsorbed chemicals [37]. It is employed to remove various compounds from wastewater. Adsorption is one of the best wastewater purification techniques. Adsorbents have a high internal surface area that allows the adsorption of dyes and molecules. So, the magnetic nanoparticle can be a good adsorbent due to its high surface area. Also, due to its magnetic behavior, the adsorbed molecule or dyes can be separated easily from the solution. The use of traditional methods is not efficient to decolorize the dyes from wastewater. The advantage of using this technique over others is its flexibility, simplicity, low cost, and easy operation, and lack of sensitivity to toxic pollutants is found in adsorption [38].

It is reported that the use of other particles such as active carbon has proven to be a good adsorbent and is a much-used technique because of maintenance costs and the low energy, reliability, and simplicity. An active carbon column requires a limited amount of maintenance and supervision. The effectiveness of the adsorption treatment depends on the type of substance to be removed. Substances with low water solubility and a high molecular weight are better adsorbed with active carbon. Magnetic nanoparticles such as iron oxide and their oxidized form have proven to be a good adsorbent of dyes such as methyl blue and methylene blue [39]. The addition of alkali cations in iron oxide nanoparticles was found to be effective in the adsorption and degradation of dyes than the bare iron oxide nanoparticles as shown in Fig. 3 [40].

The amount of dye adsorbed can be calculated using the following relation.

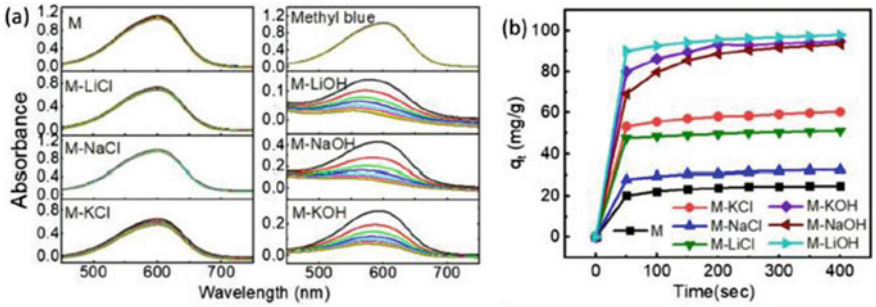

Fig. 3 **a** The UV-vis absorbance spectra of methyl blue dye in the presence of bare iron oxide nanoparticles (*M*), *M*–*X*Cl, and *M*–*X*OH. **b** The adsorption of methyl blue by bare iron oxide nanoparticles (*M*), *M*–*X*Cl, and *M*–*X*OH; $X =$ Li, Na, K [40]

$$q_t = [C_0 - C_t]\frac{V}{m},$$

where q_t is the amount of dye adsorbed at time t, C_0, and C_t is the initial and final concentration of dye at a steady time 't's in mg L^{-1}, V and m is the volume of dye in L, and the weight of the nanoparticle in g, respectively.

4.2 Biomedical Applications

(a) MNPS in drug delivery

Chemotherapies are usually practiced for cancer treatment and this method not only damages the sick cells but also the healthy cells as well [41]. So, it is important to choose and search for an alternative to getting rid of such problems. Magnetic nanoparticles can be a means to overcome this problem by carrying the healing agents to the specific target area and release the drugs with the help of an external magnetic field. When exposed to an external magnetic field the magnetic nanoparticles carry drugs to the target area and acts on it [42]. Another important property that allows the nanoparticles to be successful in adsorbing the drugs is the high surface area of the nanoparticles. With the increase in surface area, the drugs can be easily loaded to the nanoparticles and carried to the target site with the help of an external magnetic field. The magnetic nanoparticle is generally coated by a polymer such as PVA or dextran. This is done to prevent agglomeration. This facilitates the interaction of the particles with cells. The coating shields the magnetic particle from the surrounding environment [43]. The advantage of using magnetic nanoparticles over others is that these nanoparticles can respond to the external magnetic field which allows easy separation from the mixture components. Cancer treatment using magnetic albumin microspheres loaded with doxorubicin for cancer treatment was first performed in

rats. Even though noble metal coatings such as gold are also being considered, recent developmental work on carriers has focused on new polymeric or inorganic coatings on magnetite/maghemite nanoparticles [44]. The use in the surgery of eye cobalt/silica carriers has been investigated recently to repair detached retinas [45].

(b) Magnetic Hyperthermia

Another safe and easy method to replace chemotherapy and radiotherapy for cancer treatment is by using the magnetic hyperthermia method. In this method, the magnetic nanoparticles are used as heat sources [46] which raises the temperature to about 43–47 °C to heat the most sensitive cell or cancerous cell with the application of an alternating magnetic field. The temperature above 47 °C causes rapid death of tumor cells due to the high temperature. The cancerous cells have a low concentration of oxygen and nutrients which are low in pH. As a result of which these cancerous cells are sensitive to heat [47]. Through hysteresis losses, all the magnetic material generates heat with the application of the alternating magnetic field. In the magnetic hyperthermia process, the local deposition of magnetic nanoparticles generates heat due to Brownian and Neel relaxation process [48].

In 1957, Magnetic Hyperthermia Therapy was first introduced to treat cancer to the lymph nodes [49]. Attempts have already been done in the treatment of various cancerous cells of different parts of the body such as lung, breast, prostate, spine, brain, head and neck, pancreas, and liver. However, there are some disadvantages of using high temperature to heat the cancerous cell as it is difficult to maintain the tissue at a lower temperature at the same time. The lack of efficacy and techniques makes this technique unable to be established in the clinical routine. Another problem faced is the inhomogeneous distribution of heat over the tumor tissue.

(c) Magnetofaction

In this method, an externally applied magnetic field can induce transfection of magnetic nanoparticles which are associated with vector DNA into cells. This method can be achieved by coating magnetic particles with polyethyleneimine so that they become positively charged to be attracted by DNA which is negatively charged [50]. Transfection using magnetic nanoparticles enhances the gene-transfer efficiency, decreases incubation time, and improves the nucleic acid dose–response profile [51]

Krotz and co-workers have shown that by the use of magnetofaction for delivery of luciferase reporter gene to human umbilical vein endothelial cells (HUVECs) efficiency was a 360-fold increase compared to various conventional transfection systems [52]. Magnetofaction has found applications to viral and non-viral vectors for its simplicity, rapidity, and low dose saturating level transfection. Transfecting non-permissive cells, reducing incubation time, lowering vector dose are also possible by magnetic nanoparticles [53]. Comparing the toxicity and advantages of magnetofaction, the advantages of magnetofaction outweighed the increase in toxicity.

(d) Magnetic Resonance Imaging (MRI)

It was developed in 1973 and is a powerful noninvasive method that is useful in clinical medicine. It allows the visualization of the internal structure and function of the body that uses magnets radio waves and computers [54]. Magnetic nanoparticles with spinel structure can be used as MRI contrasts agents to diagnose and treat diseases. For identification of infection and inflammation, the paramagnetic behavior of nanoparticles and the local magnetic field produced by induced magnetic moments are explored to study the two basic types of MRI image namely T2 and T2* [55]. Superparamagnetic iron oxide nanoparticles coated with captopril act as a dual-mode MRI contrast agent and drug delivery systems [56]. Multifunctional polymer-based superparamagnetic iron oxide nanoparticles (bioferrofluids) are used as MRI contrast agent and their uptake in the liver is observed. It has been found that these bioferrofluids have no observed toxicity in the liver and are good T2 contrast agents. Zwitterion-coated exceedingly small SPIONS having pharmacokinetic and imaging properties which are free from Gd show a high T1 contrast power comparable to Gadolinium-based contrast agents in preclinical MRI and magnetic resonance angiography. Gadolinium-based contrasts agents have been reported to have adverse effects on the human body particularly on nephrogenic systemic fibrosis. Also, it is reported that Gd is also deposited in the human brain [57].

4.3 Supercapacitor

Over the recent years, environmentally friendly supercapacitors have gained attention due to their potential capability to deliver high specific power than the batteries and have been developed to replace non-renewable energy sources [58]. Supercapacitors also exhibit long cycle life and high charge–discharge rate, higher power density, easy operation, and reduction in weight and size [59, 60].

Magnetic nanoparticles have attracted much interest due to their potential applications in high-density storage devices, ferrofluids, microwave absorption, humidity sensor, pacemaker, photodetectors, etc. [61, 62]. These magnetic nanoparticles can be a promising electrode material for electrochemical supercapacitors. Magnetic nanoparticles with transition metal oxides with the ions and electrons in their mechanism of charge storage and make use of fast and reversible faradaic redox reactions (pseudocapacitance). The magnetic nanoparticles with their functionalized form have high specific capacitance suitable for supercapacitors. The value of specific capacitance in Fg^{-1} is shown in Table 2. Various transition metal oxides such as ZnO, NiO, Co_3O_4, IrO_2, Fe_2O_3, RuO_2, MnO_2, and V_2O_5 have been investigated as active electrode materials for energy storage and have already started to replace batteries [63–65]. The magnetic nanoparticles can be potential candidate materials as they are stable, abundant, inexpensive, and biocompatible or environmentally friendly.

Table 2 The value of specific capacitance of some magnetic nanoparticles

Samples	Specific capacitance	Reference
$CoFe_2O_4$	273 Fg^{-1} at 1 Ag^{-1}	[66]
$CoFe_2O_4$	295 Fg^{-1} at 0.5 Ag^{-1}	[67]
$CoFe_2O_4$/FeOOH composite	332.4 Fg^{-1} at 0.5 Ag^{-1}	[68]
$NiFe_2O_4$	283 Fg^{-1} at 1 Ag^{-1}	[67]
Fe_3O_4	207.7 Fg^{-1} at 0.4 Ag^{-1}	[69]
$Y3^+$ doped Fe_3O_4	138.9 Fg^{-1} at 1 Ag^{-1}	[70]
$MnFe_2O_4/MoS_2$	600–2093 Fg^{-1} at 1 Ag^{-1}	[71]

5 Summary/Conclusion

Magnetic nanoparticles such as iron oxide cobalt ferrite etc. are synthesized using different techniques such as sol–gel, hydrothermal, auto-combustion, and co-precipitation method, etc. Of these methods, the co-precipitation method is most suitable as this method is easy to synthesize and helps in large-scale production. The size of the nanoparticle can be controlled using this technique. Magnetic nanoparticles with properties such as high surface-to-volume ratio, superparamagnetic, catalytic, and biocompatible become a potential candidate for various applications. They are extensively used in wastewater treatment (photocatalysis, degradation, and adsorption), biomedical treatment, and supercapacitor. Magnetic nanoparticles such as cobalt ferrite, iron oxide, and their oxidized forms such as maghemite and hematite have been us in wastewater treatment as photocatalysts and adsorbents. They are also used in biomedical treatment as a drug carrier and magnetic hyperthermia process. Moreover, with their high specific capacitance value, these nanoparticles are used as electrodes in supercapacitors.

References

1. Issa B, Obaida IM, Albiss BA, Haik Y (2013) Magnetic nanoparticles: surface effects and properties related to biomedicine applications. Int J Mol Sci 14:21266–21305
2. Laurent S, Forge D, Port M, Roch A, Robic C, Vander Elst L, Muller RN (2008) Magnetic iron oxide nanoparticles: synthesis, stabilization, vectorization, physicochemical characterizations, and biological applications. Chem Rev 108:2064–2110
3. Govan J, Gun'ko YK (2014) Recent advances in the application of magnetic nanoparticles as a support for homogeneous catalysts. Nanomaterials 4:222–241
4. Faraji M, Yamini Y, Rezaee M (2010) Magnetic nanoparticles: synthesis, stabilization, functionalization, characterization, and applications. J Iran Chem Soc 7:1–37
5. Lu AH, Salabas EL, Schuth F (2007) Magnetic nanoparticles: synthesis, protection, functionalization, and application. Angew Chem Int Ed 46:1222
6. Mou X, Ali Z, Li S, He N (2015) Applications of magnetic nanoparticles in targeted drug delivery system. J Nanosci Nanotechnol 15(1):1533–4880

7. Nidhin M, Indumathy R, Sreeram KJ, Nair BU (2008)Synthesis of iron oxide nanoparticles of narrow size distribution on polysaccharide templates. Bull Mater Sci 3193–3196
8. Glover L, Bennett JB, Pritchett JS, Nikles SM, Ikles DE, Nikles JA, Brazel CS (2013) IEEE T Magn 49:231
9. Kim DK (2001) Characterization and MRI study of surfactant-coated superparamagnetic nanoparticles administrated into the rat brain. J Magn Magn Mater 225:256–261
10. Wu W, Wu Z, Yu T, Jiang C, Kim W-S (2015) Recent progress on magnetic iron oxide nanoparticles: synthesis, surface functional strategies and biomedical applications. Sci Technol Adv Mater 16:023501 (43pp)
11. Dorniani D, Bin Hussein MZ, Umar Kura A, Fakurazi S, Halim Shaari A, Ahmad Z (2012) Preparation of Fe_3O_4 magnetic nanoparticles coated with gallic acid for drug delivery. Int J Nanomed 7:5745–5756
12. Mahmoudi K, Bouras A, Bozec D, Ivkov R, Hadjipanayis C (2018) Magnetic hyperthermia therapy for the treatment of glioblastoma: a review of the therapy's history, efficacy, and application in humans. Int J Hyperthermia 34(8):1316–1328
13. Griffete N, Fresnais J, Espinosa A, Taverna D, Wilhelm C, Menager C (2018) Thermal polymerization on the surface of iron oxide nanoparticles mediated by magnetic hyperthermia: implications for multi-shell grafting and environmental applications. ACS Appl Nano Mater 12
14. del Campoa A, Sena T, Lellouchec J-P, Brucea IJ (2005) Multifunctional magnetite and silica–magnetite nanoparticles: synthesis, surface activation and applications in life sciences. J Magn Magn Mater 293:33–40
15. Frey NA, Peng S, Cheng K, Sun S (2009) Magnetic nanoparticles: synthesis, functionalization, and applications in bioimaging and magnetic energy storage. Chem Soc Rev 38:2532–2542
16. Singamaneni S, Bliznyuk VN, Binekc C, Tsymbalc EY (2011) Magnetic nanoparticles: recent advances in synthesis, self-assembly and applications. J Mater Chem 21:16819–16845
17. Zhang H, Zhu C, Chen Y, Yang M, Yang P, Wu X, Qi L, Meng F (2014) Enhanced photocatalytic activities of net-like hematite nanoparticle/graphene oxide composite. J Mater Chem A 4:1421–1426
18. Giri AK, Pellerin K, Pongsaksawad W, Sorescu M, Majetich S (2000) Effect of light on the magnetic properties of cobalt ferrite nanoparticles. IEEE Trans Magn 36:3029–3031
19. Benz M (2012) Superparamagnetism: theory and applications
20. Issa B, Obaidat IM, Albiss BA, Haik Y (2013) Magnetic nanoparticles: surface effects and properties related to biomedicine applications. Int J Mol Sci 14(11):21266–21305
21. Karunakaran C, Senthilvelan S (2006) Fe_2O_3-photocatalysis with sunlight and UV light: oxidation of aniline. Electrochem Commun 8:95–101
22. Khairy M, Zakaria W (2014) Effect of metal-doping of TiO_2 nanoparticles on their photocatalytic activities toward removal of organic dyes. Egypt J Pet 23:419–426
23. Kimi M, Yuliati L, Shamsuddin M (2015) Preparation of high activity Ga and Cu doped ZnS by hydrothermal method for hydrogen production under visible light irradiation. J Nanomater
24. Priya MH, Madras G (2006) Photocatalytic degradation of nitrobenzenes with combustion synthesized nano-TiO_2. J Photochem Photobiol A Chem 178:1–7
25. Reza KM, Kurny A, Gulshan F (2015) Parameters affecting the photocatalytic degradation of dyes using TiO_2: a review. Appl Water Sci 1–10
26. Karunakaran C, Senthilvelan S (2005) Photocatalysis with ZrO_2: oxidation of aniline. J Mol Catal A Chem 233:1–8
27. Xia H, Zhuang H, Zhang T, Xiao D (2008) Visible-light-activated nanocomposite photocatalyst of Fe_2O_3/SnO_2. Mater Lett 62:1126–1128
28. Xia HL, Zhuang HS, Zhang T, Xia DC (2007) Photocatalytic degradation of acid blue 62 over CuO-SnO_2 nanocomposite photocatalyst under simulated sunlight. J Environ Sci 19:1141–1145
29. Xu J, Xiao X, Stepanov AL, Ren F, Wu W, Cai G et al (2013) Efficiency enhancements in Ag nanoparticles-SiO_2-TiO_2 sandwiched structure via plasmonic effect-enhanced light capturing. Nanoscale Res Lett. https://doi.org/10.1186/1556-276X-8-73

30. Wang Y, Huang Y, Ho W, Zhang L, Zou Z, Lee S, Biomolecule-controlled hydrothermal synthesis of C-N-S-tridoped TiO_2 nanocrystalline photocatalysts for NO removal under simulated solar light irradiation. J Hazard Mater 169(1–3):77–87
31. Wu L, Yu JC, Fu X (2006) Characterization and photocatalytic mechanism of nanosized CdS coupled TiO_2 nanocrystals under visible light irradiation. J Mol Catal A Chem 244:25–32
32. Karunakaran C, Dhanalakshmi R (2008) Semiconductor-catalyzed degradation of phenols with sunlight. Sol Energy Mater Solar Cells 92:1315–1321
33. Mishra M, Chun D-M (2015) α-Fe_2O_3 as a photocatalytic material: a review. Appl Catal A Gen 498. https://doi.org/10.1016/j.apcata.2015.03.023
34. Bishnoi S, Kumar A, Selvaraj R (2018) Facile synthesis of magnetic iron oxide nanoparticles using inedible Cynometra ramiflora fruit extract waste and their photocatalytic degradation of methylene blue dye. Mater Res Bull 97:121–127
35. Wang C-T (2007) Photocatalytic activity of nanoparticle gold/iron oxide aerogels for azo dye degradation. J Non Cryst Solids 353:1126–1133
36. Viswanathan B (2018) Photocatalytic degradation of dyes: an overview. Curr Catal 7
37. Khodaie M, Ghasemi N, Moradi B, Rahimi M (2013) Removal of methylene blue from wastewater by adsorption onto $ZnCl_2$ activated corn husk carbon equilibrium studies. J Chem 383985, 6 pages. https://doi.org/10.1155/2013/383985
38. Nageeb Rashed M, El-Daim El Taher MA, Fadlalla SM (2016) Adsorption of methylene blue using modified adsorbents from drinking water treatment sludge. Water Sci Technol 74
39. Besharati N, Alizadeh N, Shariati S (2019) Removal of cationic dye methylene blue (MB) from aqueous solution by coffee and peanut husk modified with magnetite iron oxide nanoparticles. J Mex Chem Soc 62. https://doi.org/10.29356/jmcs.v62i3.433
40. Singh NJ, et al (2020) Alkali-cation-incorporated and functionalized iron oxide nanoparticles for methyl blue removal/decomposition. Nanotechnology 31:425703 (16pp)
41. Shabestari Khiabani S, Farshbaf M, Akbarzadeh A, Davaran S (2016) Magnetic nanoparticles: preparation methods, applications incancer diagnosis and cancer therapy. Artif Cells Nanomedicine Biotechnol. https://doi.org/10.3109/21691401.2016.1167704
42. Colombo M, Carregal-Romero S, Casula MF, Gutiérrez L, Morales MdP, Böhm IB, Heverhagen JT, Prosperi D, Parak WJ (2012) Biological applications of magnetic nanoparticles. Chem Soc Rev 41:4306–4334
43. Pankhurst QA, Connolly J, Jones SK, Dobson J (2003) Applications of magnetic nanoparticles in biomedicine. J Phys D Appl Phys 36:R167–R181
44. Carpenter EE (2001) Iron nanoparticles as potential magnetic carriers. J Magn Magn Mater 225:17–20
45. Rutnakornpituk M, Baranauskas V, Riffle JS, Connolly J, St Pierre TG, Dailey JP (2002) Polysiloxane fluid dispersions of cobalt nanoparticles in silica spheres for use in ophthalmic applications. Eur Cells Mater 3:102–105
46. Pankhurst QA, Connolly J, Jones SK, Dobson J (2003) Applications of magnetic nanoparticles in biomedicine. J Phys D 36:R167–R181
47. Christophi C, Winkworth A, Muralihdaran V (1999) The treatment of malignancy by hyperthermia. Surg Oncol 783–90
48. Thiesen B, Jordan A (2008) Clinical applications of magnetic nanoparticles for hyperthermia. Inf Healthc 24(6):467–474
49. Mahmoudi K, Bouras A, Bozec D, Ivkov R, Hadjipanayis C (2018) Magnetic hyperthermia therapy for the treatment of glioblastoma: a review of the therapy's history, efficacy, and application in humans. Int J Hyperth. https://doi.org/10.1080/02656736.2018.1430867
50. Gupta AK, Gupta M (2005) Synthesis and surface engineering of iron oxide nanoparticles for biomedical applications. Biomaterials 26:3995–4021
51. Gupta AK, Naregalkar RR, Vaidya VD, Gupta M Nanomedicine 2(1):23–29
52. Kroetz F, Sohn HY, Gloe T, Plank C, Pohl U (2003) J Vasc Res 40(5):425–34
53. Scherer F, Anton M, Schillinger U, Henke J, Bergemann C, Krueger A, Gaensbacher B (2002) Gene Ther 9:102–109

54. Srivastava AK, Kadayakkara DK, Bar-Shir A, Gilad AA, McMahon MT, Bulte JWM (2015) Advances in using MRI probes and sensors for in vivo cell tracking as applied to regenerative medicine. Dis Model Mech 8(4):323–336
55. Filippousi M, Angelakeris M, Katsikini M, Paloura E, Efthimiopoulos I, Wang Y, Zamboulis D, van Tendeloo G (2014) Surfactant effects on the structural and magnetic properties of iron oxide nanoparticles. J Phys Chem C 118:16209–16217
56. Pour SA, Shaterian HR (2018) Captropril-loaded superparamagnetic nanoparticles as a new dual-mode contrast agent for simultaneous in vitro/in vivo MR imaging and drug delivery system. Pharm Chem J 51:852–862
57. Wei H, Bruns OT, Kaul MG (2017) Exceedingly small iron oxide nanoparticles as positive MRI contrast agents. PNAS 114(9):2325–2330
58. Li M, Xiong Y, Liu X, Bo X, Zhang Y, Han C et al (2015) Facile synthesis of electrospun MFe_2O_4 (M = Co, Ni, Cu, Mn) spinel nanofibers with excellent electrocatalytic properties for oxygen evolution and hydrogen peroxide reduction. Nanoscale 7:8920–8930
59. Zhao X, Johnston C, Crossley A, Grant PS (2010) Printable magnetite and pyrrole treated magnetite based electrodes for supercapacitors. J Mater Chem 20:7637–7644
60. Khiew P, Ho M, Tan T, Chiu W, Shamsudin R, Abd-Hamid MA, et al (2013) Synthesis and electrochemical characterization of iron oxide/activated carbon composite electrode for symmetrical supercapacitor. Int J Chem Mol Nucl Mater Metall Eng 80:615–619
61. Jung J-S, Lim J-H, Choi K-H, Oh S-L, Kim Y-R, Lee S-H, Smith DA, Stokes KL, Malkinski L, O'Connor CJ (2005) $CoFe_2O_4$ nanostructures with high coercivity. J Appl Phys 97:10F306
62. Peng C-H, Wang H-W, Shih-Wei Kanb M-ZS, Wei YM, Chen S-YJ (2004) Magn Magn Mater 284:113
63. Qu Q, Zhang P, Wang B, Chen Y, Tian S, Wu Y, Holze R (2009) Electrochemical performance of MnO_2 nanorods in neutral aqueous electrolytes as a cathode for asymmetric supercapacitors. J Phys Chem C 113:14020–14027
64. Liu D-Q, Yu S-H, Son S-W, Joo S-K (2008) Electrochemical performance of iridium oxide thin film for supercapacitor prepared by radio frequency magnetron sputtering method. ECS Trans 103–109
65. Wee G, Soh HZ, Cheah YL, Mhaisalkar SG, Srinivasan M (2010) Synthesis and electrochemical properties of electrospun V_2O_5 nanofibers as supercapacitor electrodes. J Mater Chem 20:6720
66. Malarvizhi M, Meyvel S, Sandhiya M, Sathish M, Dakshana M, Sathya P, Thillaikkarasi D, Karthikeyan S (2021) Design and fabrication of cobalt and nickel ferrites based flexible electrodes for high-performance energy storage applications. Inorg Chem Commun 123:108344
67. Kennaz H, Harat A, Guellati O, Momodu DY, Barzegar F, Dangbegnon JK, Manyala N, Guerioune M (2018) Synthesis and electrochemical investigation of spinel cobalt ferrite magnetic nanoparticles for supercapacitor application. J Solid State Electrochem 22:835–847
68. Zhang YX, Hao XD, Diao ZP, Li J, Guan YM (2014) One-pot controllable synthesis of flower-like $CoFe_2O_4$/FeOOH nanocomposites for high-performance supercapacitors. J Mater Lett 123:229–234
69. Laheäär A, Przygocki P, Abbas Q, Béguin F (2015) Appropriate methods for evaluating the efficiency and capacitive behavior of different types of supercapacitors. Electrochem Commun 60:21–25
70. Aghazadeh M, Karimzadeh I, Maragheh MG, Ganjali MR (2018) Enhancing the supercapacitive and superparamagnetic performances of iron oxide nanoparticles through yttrium cations electro-chemical doping. Mater Res 21(5)
71. Sharifi S, Rahimi K, Yazdani A (2021) Highly improved supercapacitance properties of $MnFe_2O_4$ nanoparticles by MoS_2 nanosheets. Sci Rep 11:8378

Chapter 9
Effects of Viscosity on the Magnetic-Induced Heat Generation

Y. Haripriya Devi, L. Herojit Singh, and Boris Wareppam

1 Introduction

Magnetic nanoparticles (MNPs) occupy a major role in biomedical advances and particular magnetic hyperthermia treatment. Magnetic hyperthermia which is the induced heat generation by the magnetic nanoparticles (MNPs) under the application of an alternating magnetic field has a wide range of applications in biomedical aspects. The heat generation results from the absorption of energy from the external alternating field and its conversion into heat due to the magnetization reversal [1]. Magnetic hyperthermia has been an area of research for its high potential in cancer treatment, much better than radiotherapy and chemotherapy. It is done by injecting the magnetic nanoparticles in the affected region or at the tumor site. Under the application of the external magnetic field, there is an increase in temperature due to the heat dissipation by the MNPs which kills the tumor cells beyond a threshold temperature (42–46 °C), while the healthy cells remain unaffected. The high acidity of the tumor cells accounts for their sensitivity to high temperatures. The temperature should not be higher than 46 °C as it may result in damage to healthy cells. Moreover, there is a safety limit for the amplitude and frequency of the applied magnetic field for the treatment in the human body. This is known as the "Brezovich criterion", which states that the product of amplitude and frequency must not exceed 4.5×10^8 A m^{-1} s^{-1}. This criterion is limited by the human tolerance to external frequency. At higher values above the Brezovich limit, the eddy current that flows through the human body increases the heat of the surrounding normal tissues [2]. Further, the limit value was reexamined by taking a three-dimensional analogy to human structure [3]. The optimum limit of SAR for hyperthermia treatment should be of the order 10 kW/g [4]. MNPs in the superparamagnetic regime are suitable as the single-domain particles have no remanent magnetization and no coercive field [5]. The heat generation in magnetic hyperthermia is quantified by a parameter

Y. H. Devi · L. H. Singh (✉) · B. Wareppam
Department of Physics NIT Manipur, Langol, Imphal, Manipur 795004, India

B. P. Swain (ed.), *Advances in Nanostructured Materials*, Materials Horizons: From Nature to Nanomaterials, https://doi.org/10.1007/978-981-16-8391-6_9

known as specific absorption rate (SAR) or specific loss power (SLP). This method of cancer therapy requires a lot of improvement where efficient heat generation is of immense importance while satisfying the biocompatibility factor concomitantly. To obtain this goal, it is quite necessary to study the behavior of SAR variation with various extrinsic or rheological factors (amplitude and frequency of magnetic field, concentration, coating, viscosities) and intrinsic properties (size, size distribution, anisotropy, saturation magnetization) associated with the processor; in other words, the structural properties and environmental properties [1, 5–9]. For effective heat generation, it requires the lowest possible dose of MNPs, homogeneity in size and size distribution, less influence from the intracellular environment, and homogeneous MNPs distribution. A detailed study and analysis of the induced heat generation are required owing to high efficiency. Many researchers have been successful in reflecting the various domains responsible for high and efficient SAR. One of the domains which have comparatively less attention is the viscosity of the media in which the magnetic particles are suspended. One of the main problems or drawbacks of hyperthermia treatment is that the heating efficiency is greatly reduced by in vivo applications. The complex, heterogeneous, and dynamic nature of the biological environment authorizes the execution of magnetic hyperthermia. Thus, it has been reasonable to study the impact of viscosity in magnetic hyperthermia treatment by analyzing its effect in the heat generation process. Many studies have shown the effect of viscous solvent by dispersing the magnetic nanoparticles in different media with different viscosities. This book chapter presents the detailed effect of viscosity in relation to various parameters for efficient heat generation. The future outlook will be to obtain the range of various parameters which have high SAR value and at the same time is applicable in biological environment (Table 1).

Table 1 Heterogeneous viscosity in different biological media [6, 7]

Biological media	Viscosity in MPa s
Soft tissues	10^5
Cancer cells	Several 100 s
Lysosomes	50–90
Blood	10
Cytoplasm	4

2 Model of Heat Generation and Measurement in Magnetic Hyperthermia

2.1 Theoretical Model

The theoretical study of heat dissipation of magnetic nanoparticles in an alternating magnetic field is associated with mainly two models: the linear response theory (LRT) and the Stoner–Wohlfarth model (SWM).

i. LRT

In 2002, Rosensweig developed the theory (LRT) for heat dissipation of single-domain magnetic nanoparticles in a liquid medium (ferrofluid) for the first time. The power dissipation is given as

$$P = \pi f \mu_0 \chi_0 H_0^2 \frac{2\pi f \tau}{1 + (2\pi f \tau)^2} \tag{1}$$

where μ_0 is the permeability of free space, χ_0 is the equilibrium susceptibility, f is the frequency of the external magnetic field, H_0 is the amplitude of the magnetic field applied, and τ is the effective relaxation time.

The effective relaxation time is expressed as

$$\tau = \frac{1}{\tau_B} + \frac{1}{\tau_N} \tag{2}$$

where

$$\tau_{\mathrm{B}} = \frac{3\eta V_{\mathrm{H}}}{k_{\mathrm{B}} T} \tag{3}$$

is known as Brown relaxation time (η is the medium viscosity, k_{B} is the Boltzmann constant, V_{H} is the hydrodynamic diameter, and T is the absolute temperature in K);

$$\tau_{\mathrm{N}} = \tau_0 \exp^{KV/k_{\mathrm{B}}T} \tag{4}$$

is the Neel relaxation time (τ_0 is the attempt time, K is the anisotropy constant, and V is particle volume) [8].

The applicability of the linear response theory is restricted in the region of low magnetic field and highly anisotropic magnetic nanoparticles. LRT assumes the consistency of χ with magnetic field [9]. LRT assumes that the Neel and Brownian relaxation are independent of each other [10]. However, it may not be a good assumption as the Brownian rotation, in turn, affects the motion of magnetic moment

which influences the Neel mechanism of relaxation. The model agrees with the non-interacting superparamagnetic single-domain particles of identical shape and size [9]. The effective relaxation time often oversimplifies the physical condition as the model does not take into consideration the complex dynamics of the MNPs in solvent [9, 11].

As mentioned above, the induced heat efficiency is quantified as specific absorption rate (SAR) or specific loss power (SLP) and is given as

$$\mathrm{SAR} = \mu_0 \pi \chi'' H^2 f / \rho \tag{5}$$

ρ is the mass density of the particle and χ'' is the imaginary part of susceptibility. It may be defined as the power absorption by magnetic nanoparticles of unit mass under an applied field strength and frequency.

ii. SWM

SWM is focused on single-domain particles with the blocked magnetic moment and has no frequency limit. For single-domain particles, the magnetic anisotropy energy is given by

$$E = KV \sin^2 \varphi \tag{6}$$

where K is the anisotropy constant and φ is the angle between the induced magnetization direction and the easy anisotropy axis of the particles [12]. The hysteresis loss in SWM depends on the coercive field at $T = 0$ which is not constant with temperature [13].

iii. Viscous and Magnetic Mode Model

In 2012, Utsov et al. and Liubimov et al. proposed a generalized model of an assembly of nanoparticles in a viscous liquid using sets of stochastic equations. They studied the dynamics of two unit vectors, namely the particle director **n** and the unit magnetization vector **α**. This particular model consists of two modes depending on the amplitude of the applied external field and the effective anisotropy field, which is given as $H_\mathrm{k} = 2K/M_\mathrm{s}$, where K is the anisotropy constant of the nanoparticles and M_s is the saturation magnetization.

Viscous mode: It occurs when the applied magnetic field is smaller than the anisotropy field ($H_\mathrm{o} << H_\mathrm{k}$). In the low-frequency region, the two vectors oscillate in unison with an amplitude of $\pm H_\mathrm{o}$ with a phase difference of 90° concerning the external field. As the frequency gets higher, the two unit vectors continue oscillating in unison with reduced amplitude and the phases are further shifted. The amplitude of oscillation increases with the increase in increasing external field with particle diameter but decreases with an increase in viscosity. Hence, the area of the hysteresis loss decreases with increasing viscosity. The heat loss in viscous mode is due to the particle rotation in liquid as the magnetic vector keeps its alignment along the easy anisotropy axis.

Magnetic mode: Under the condition $H_o > H_k$, the unit vector **n** oscillates feebly, while the **α** jumps between the magnetic potential well of $\pm H_o$. In this mode, the magnetic vectors behave similarly to the assembly of immobilized nanoparticles in the solid matrix where there is a well-defined orientation. The heat loss is contributed solely by the magnetization relaxation, indicating its obvious independent nature with the viscosity (0.01–0.1 g/cm s) of the liquid. Further, the viscosity effect becomes dominant for liquid with high viscosity of 1.0 g/cm s.

Transition: The transition between these two modes occurs at a certain threshold field which increases with an increase in frequency and the liquid viscosity and may be dependent on size to some extent. The authors generalized the transition mode as $0.5H_k \leq H_o \leq H_k$.

This theoretical model has succeeded in explaining the dependence of hysteresis loss on frequency, amplitude, and viscosity although it assumes the particle diameter to be equal to the hydrodynamic diameter [11]. In the magnetic mode change in viscosity has no significant alteration in the heat generation [14].

iv. Predictive SAR Model

Tompkins et al. in 2020 proposed a model focusing on the contribution of Brownian relaxation in the heating response for IONPs (iron oxide nanoparticles) in the viscosity range of 1.024 and 17.12 MPa s based on the data studied in his paper. The model removed and isolated the contribution from Neel relaxation. They used the Reynolds number (R_e) and Prandtl number (P_r) in calculating the SAR for MNPs in a viscous fluid.

$$\mathrm{SAR} = m^{-1} k_B T f_M R_e^{\alpha} P_r^{-2} \tag{7}$$

where m is the mass of the spherical nanoparticles, k_B is the Boltzmann constant, T is the temperature of the fluid, f_M is the frequency of the induced field in Hertz, and α is the term related to the experimental data based on the sample viscosity (η) and concentration (φ) as

$$\begin{aligned}\alpha(\eta, \varphi) =& C_0 + C_1\eta + C_2\varphi + C_3\eta^2 + C_4\varphi\eta + C_5\varphi^2 + C_6\eta^3 \\ &+ C_7\eta^2\varphi + C_8\eta\varphi^2 + C_9\eta^4 + C_{10}\eta^3\varphi + C_{11}\eta^2\varphi^2\end{aligned} \tag{8}$$

C_i are the different discrete frequencies in the experiment. The author found a close fit of his simulation with the experimental data. But this simulation may not be accurate as the degree of clustering is not quantified [15].

2.2 Methods of Measurement

There are generally two types of SAR measurement, namely the calorimetric method and the magnetic measurement method. The former uses the initial temperature derivative for obtaining SAR as

$$\mathrm{SAR} = \frac{C_\mathrm{P}}{m_\mathrm{MNP}} \left| \frac{\mathrm{d}T}{\mathrm{d}t} \right|_{t=0} \tag{9}$$

C_P is the heat capacity and m_MNP is the mass of the magnetic nanoparticles.

The measurement of the evolution of temperature derivative is required to be done in completely adiabatic environmental conditions where there is no thermal loss or in thermal equilibrium and is a quite complicated task. The non-adiabatic condition requires the quantification of heat loss through conduction, convection, and radiation. Pineiro et al. propose an accurate model of non-adiabatic calorimetric measurement of superparamagnetic iron oxide nanoparticles to measure the time variation of the particles with temperature by considering the heat losses in the surrounding [16]. Secondly, the magnetometric measurement method utilizes the dynamic magnetization of the sample over a complete period [17].

$$\mathrm{SAR} = \frac{f}{c} \mu_\mathrm{o} \oint M(t).\mathrm{d}H_\mathrm{o} \tag{10}$$

In this method, the value of SAR is often determined by $\mathrm{SAR} = Af$, i.e., the product of the area under the hysteresis loop (A) and the frequency (f) of the applied alternating magnetic field. The colorimetric method is a typical one, which is limited only to the liquid samples, for induction measurement where the area of the hysteresis loop is analyzed. Determination of SAR by the inductive method has an advantage over the calorimetric method in that the former can measure the dynamic magnetization of the samples and determine the magnetic properties affecting the resultant SAR behavior.

3 Mechanism

There are three mechanisms for heat generation—hysteresis loss, Neel, and Brownian relaxation mechanism. There is another type of loss known as eddy current but the alternating field for this loss is not under the biocompatible range [9]. Based on LRT, Neel, and Brown's mechanisms mainly constitutes the heat generation in the superparamagnetic regime.

- Hysteresis loss
- Brownian relaxation
- Neel relaxation

Hysteresis loss is associated with the motion of domain walls in multi-domains and is associated with the reversal of magnetic moment in a single domain. The magnetic moments are rotated across the anisotropy energy barrier in the absence of an external field. The specific absorption rate (SAR) or specific loss power (SLP) is given by the product area under the hysteresis loop normalized by mass and the frequency of the external field. The dynamics of the hysteresis curve are controlled by three parameters: saturation magnetization, remanent magnetization, and coercivity. These parameters vary with the magnetic properties of the MNPs.

The magnetic relaxation process consists of two mechanisms: Brownian relaxation and Neel relaxation. When an applied external field is removed, the magnetic moment reverses due to thermal agitation. The energy barrier against magnetization reversal is the anisotropic energy barrier that is KV, where K is the anisotropy constant and V is the volume of the particle. This relaxation is known as Neel relaxation. Neel relaxation is the internal rotation or torque due to the magnetic interaction of the magnetic moment by flipping across the anisotropic barrier and is independent of the physical rotation. It depends on the effective anisotropy, the volume of the particle, and temperature. It will come to our knowledge after going through this chapter that the Neel relaxation is the dominant one in biological tissue (Fig. 1).

Brownian relaxation occurs due to thermally driven rotation of particles while the magnetic moment is fixed along the anisotropy axis. When an external magnetic field is applied, the magnetic dipole moment of the particles will rotate to align along the direction of the external field. It depends on hydrodynamic volume, viscosity, and temperature. Thus heat is produced by the viscous friction of the particles with the solvent [18]. According to LRT, the Brownian time is independent of field strength which is not quite so. In addition to this, Rosensweig noted that Brownian domination

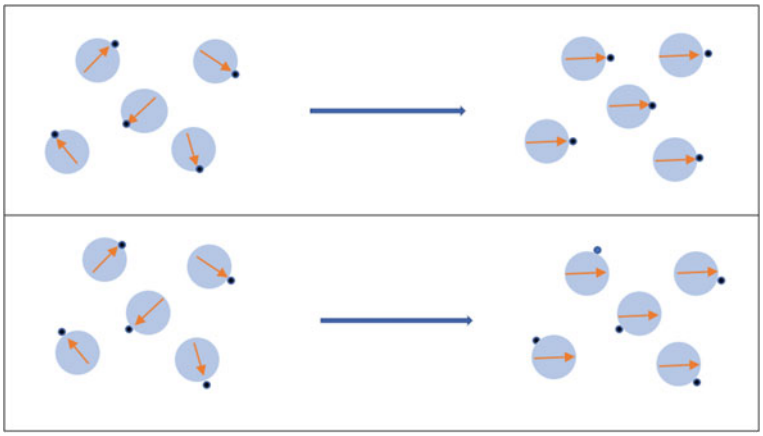

Fig. 1 Representation of Brownian relaxation (above) and Neel relaxation (below) of single-domain nanoparticles in an external magnetic field (indicated by the blue arrow). The orange arrow indicates the magnetic moment and the dark blue dots indicate the particle orientation

is necessary to achieve high heat generation [8]. Both the relaxation processes co-occur until one becomes smaller and the dominant process. And the transition in the mechanism occurs when the relaxation time is equal. The intrinsic factor and the rheological properties decide the easier pathway of relaxation between the two [19].

Recently, there was a report on the existence of a third relaxation mechanism that is faster than the above two magnetic relaxations. The third faster relaxation was observed in nanoflowers due to the disordered spin [20].

4 Effects of Viscosity

From the theoretical analysis of heat production in magnetic hyperthermia, it has become quite clear that the value of SAR is affected by the media viscosity. The viscosity drag hinders the heat loss arising from susceptibility. At 100 kHz, with increasing viscosity, the imaginary susceptibility (χ'') of cobalt ferrite nanoparticles shifts toward a lower frequency.

According to LRT, the effective relaxation time is dominated by the shorter relaxation time. Of the two mechanisms, the Brownian relaxation is affected by the solvent viscosity. Because the value of SAR depends on a wide range of factors, of which some are interdependent, such as size, size distribution, concentration, field strength and frequency, anisotropy, and particle interaction, it is quite complex to study the sole dependence of SAR on viscosity. As clearly observed in the previous section, the theoretical approach proposed by Utsov et al. shows a particular regime where the effect of viscosity is significant. The study of high viscosity regime is of utmost importance to understand the behavior of MNPs mimicking the biological media. Most of the research conducted used a solvent of different agar concentrations to obtain media of varying viscosity. Pineiro et al. displayed a 50–80% reduction in SAR at high viscosity of 200 MPa s for gel (MNPs + gelatin) as compared to the low viscosity of 2 MPa s for sol (MNPs + water) [21]. The various dependencies of viscosities on other parameters have been studied highlighting the researches.

4.1 Dipolar Interaction

Dipolar interaction has been a supporting factor in changing the SAR response. It may enhance or diminish the SAR value depending on other parameters. For example, it enhances the heating performance for soft magnetic nanoparticles [22]. The effect of viscosity regarding dipolar interaction is presented in this sub-section.

Abu-Bakr et al. used the pair approximation or the magnetic interaction between two single-domain ferromagnetic particles neglecting a third particle interaction. They found that particles in viscoelastic media have more intensified heat dissipation as compared to the ones in the rigid environment due to the rotation of particles under applied MF in the former case and the immobilized one in the latter. The difference is

attributed to the influence of magnetic interaction although the author has not made it clear in which medium the magnetic interaction prevails. Additionally, it is observed that the heat dissipation in viscous media is higher than in a solid matrix [23].

Bruvera et al. studied the heating efficiency quantifying with SAR in two conditions: ferrofluid and ferrogel. The ferrofluid provides a stable environment for the analysis of MNPs behavior, while the ferrogel consists of high viscosity and agglomeration, and immobilization of MNPs is seen as reported from the SAXS measurement. Transmission electron microscopy (TEM) measurement reported the mean interparticle distance to be larger than three diameters with the well-defined spatial distribution and results in the absence of dipolar interaction in ferrofluid. The ferrofluid shows a monotonical increase of SAR with frequency and amplitude. The ferrogel characteristics of SAR show a local frequency maximum unlike the previous case and a larger SAR value at every combination of frequency and amplitude. The difference in SAR responses is attributed to (a) the dipolar interaction driven by agglomeration in ferrogel which increases in SAR due to the compact and well-defined structural arrangement of the particles and (b) the cancellation of Brownian relaxation in ferrogel due to the fixation of MNPs reducing SAR. These two factors overall provide an increase in SAR. Considering the first factor, it is reasonable to deliver that the agglomeration resulting in dipolar interaction does not always reduce SAR, but it depends on the structural organization of the nanoparticles whether they are well defined or form into irregular clusters [24].

4.2 Aggregation and Cluster Formation

The viscosity effect cannot solely replicate the magnetic behavior of MNPs in cells or tissue. The combined effect of viscosity and particle aggregation as measured by ACS and ACM gives similar dynamic magnetic nature of the MNPs in biological cells or tissues. The increase in hydrodynamic diameter increases the aggregation of the nanoparticles which in turn influences SAR [25].

The viscosity of the aqueous media is an important factor even during the preparation as the nature of the distribution is affected. In the absence of an external magnetic field, the nanoparticles (44 nm magnetite) in the viscous media (water–agar suspension) form irregular clusters. There is chain formation of the particles in viscous media under an applied external field; chain length is inversely proportional to the viscosity of the media as the effect of the external field is hampered by high viscosity. Serantes et al. reported that the longer the chain, the greater will be the hysteresis loss and the greater the SAR [26]. Uncoated IONP of 14.42 nm means diameter dispersed in two solvents: water and ethylene glycol (WEG) and oil blend (MH) and studied the particle aggregation and clustering. DLS measurement showed the particles clustering in the solvent. The SAR value for all the 11 samples (6 in WEG and 5 in EG) decreases for all combinations of frequency and concentration. The cause of this reduction as we have already discussed is the inhibition of the Brownian mechanism with increasing viscosity. The Neel relaxation

becomes the dominant one although there may be a contribution from Brownian rotation. The author reported a decrease in Brownian relaxation frequency from 839 to 3.67 kHz when the viscosity increases from 1.024 to 234 MPa s. Specifically, the decrease in the Brownian relaxation frequency is from 839 to 50.2 kHz (94.02% reduction) for the uncapped IONPs in WEG solvent with viscosity ranging from 1.024 to 17.12 MPa s. The author also observed a smaller decrease in the Brownian frequency for the particles in MH from 5.01 to 3.67 kHz (26.74% reduction) with a high viscosity range of 171.6–234 MPa s. The author reasons the vast difference in relaxation frequency reduction about the formation of large clusters in low viscosity solvent in comparison to the high viscosity regime. The inhibition of particle movement in high viscosity regime prevents the formation of large clusters. The heating output was showing reduction with increasing output for WEG solvent, while the SAR value remains consistent with oil blend (MH). The heat generation is attributed to the combined effect of Brownian relaxation for individual and clustered particles, resulting in high SAR reduction for the WEG sample as they have a larger effective diameter than the particles sonicated in the MH sample delivering less SAR reduction in the latter. Thus, the author presented the importance of particle clustering in low viscosity solvent [15].

The threshold size of the magnetite particles comes in the range of 20–25 nm for their stability where no agglomeration is present. It was reported that the media viscosity plays a secondary role in determining the threshold diameter of the magnetic particles with anisotropy as the primary role [27].

4.3 Frequency and Amplitude of External Excitation Field

In general, the heat effect varies linearly with frequency and nonlinearly with the amplitude of the magnetic field [28]. The numerical simulation of Fokker–Planck equation done at different viscosities (obtained by adding glycerol) results in different M–H curve for the samples at low frequency and low excitation field (3.5 mT and 3 kHz) with different viscosity reflecting the influence of viscosity in the Brownian mechanism and hence the magnetization. At higher frequency and larger excitation field (20 mT and 20 kHz), the differences in the M–H curve get smaller or are almost the same. Thus, the magnetization becomes insensitive to medium viscosity (and hence the Brownian motion) at high frequency and amplitude of the excitation field reflecting the dominance of Neel magnetization. Media viscosity impacts the hysteresis loss at low field and low frequency where Brownian magnetization is dominant at low viscosity, Neel magnetization at high viscosity, and both magnetizations at intermediate viscosity [29]. 14 nm iron oxide nanocubes show sensitiveness to viscosity at low amplitude (4 kA/m) of AC field and no effect of viscosity at 24 kA/m as the dominance of magnetic relaxation is strongly dependent on external AC field [30] (Table 2).

Table 2 Brownian frequency of iron oxide dispersed in different viscosities [29]

Viscosity in MPa s	f_B in kHz at 5 mT	f_B in kHz at 20 mT
0.957	2.6	8.3
9.43	0.26	0.84
411	0.0061	0.019

4.4 Coated and Uncoated

Comparison of coated and uncoated maghemite at different viscosities: Coating of MNPs is favored in biological media accounting for the stability of the MNPs in the acidic environment. The coated samples have lesser SAR than the uncoated sample due to the hindrance of the Brownian mechanism as a result of the larger hydrodynamic size. However, the uncoated sample also shows a decrease in SAR in a medium of high viscosity due to the inhibition of Brownian motion and favoring the contribution from Neel relaxation. In low viscosity media, both the relaxation mechanism co-exists for uncoated nanoparticles, while the Neel mechanism is reported to be dominant in a high viscosity environment. Thus, the transition between the two relaxations mechanism is influenced by the dispersing media [18].

4.5 Size

The sensitivity of viscosity on heat production depends on the size; it may be the core size or the hydrodynamic size of the nanoparticles. The linear response model indicates a linear dependence of Brownian relaxation time with hydrodynamic size and an exponential increase of Neel time with the core size. Various researches done on size reported the change of SAR with viscosity for large-sized nanoparticles. This accounts for a particular threshold size beyond which the SAR value is affected by media viscosity. However, the formulation of such threshold size is complicated as there is no sole dependence of size on viscosity only. The threshold size may depend upon the anisotropy, strength, and frequency of the external field. For iron oxide nanocubes with low anisotropy, the reduction in SAR with viscosity varies monotonically with size increment [30]. Experiments performed with different sizes of 14, 18, and 22 nm conveyed that the SAR value of water (low viscosity) and agar (high viscosity) follow the same linear trend, with the field for 14 and 18 nm indicating the non-dependence of heating mechanism with viscosity and the dominance of Neel relaxation mechanism. But SAR follows a parabolic trend for 22 nm which may be due to the anisotropy field (although they may have a similar trend up to a particular amplitude but observed a large difference in SAR value at high amplitude where SAR of water being immensely higher), indicating the clear influence of viscosity [31]. The magnetic susceptibility (ACS) and magnetometry (ACM) measurements under an AC field of IONPs for two core sizes of 11 and 21 nm were studied at different viscosity. Different viscosity media were attained by the addition of glycerol (0–80%

glycerol) in aqueous media. 11 nm IONP shows no variation with viscosity increment. The hydrodynamic diameter (D_H) measured from dynamic light scattering (DLS) measurement does not show any variation with increasing viscosity of 32% glycerol content. For a core size of 21 nm, the ACM measurement displays the decrease in the area of the magnetization loop with increasing viscosity; the ACS measurement corresponds χ'' shift to the lower frequency with solvent viscosity. Hence, inference can be stated that the size around 21–22 nm is dominated by the Brownian motion [25]. According to the theory proposed by Utsov and Liubimov, the rotation of smaller particles is in magnetic mode, while bigger MNPs are associated with rotation in the viscous mode [32]. Moreover, the SAR increases with the decrease in size distribution. A polydispersity of 0.2 has 3.3 times higher SAR than the polydispersity of 0.4 under the same experimental conditions [33].

4.6 Anisotropy

According to the linear response model, the anisotropy constant of the nanoparticles has a significant impact on the SAR through the enhancement of Neel relaxation time. The power absorption in magnetic nanoparticles having high anisotropy is the result of the particle rotation under the influence of the magnetic torque due to the external or applied field. In a system of MNPs with high anisotropy, the thermal energy is not sufficient to overcome the anisotropic energy barrier, and hence the magnetic relaxation is dominated by the Brownian relaxation mechanism. According to Rosenzweig, a system of MNPs with high anisotropy and particle size will increase the Neel relaxation times exponentially, and hence the effective relaxation time is dominated by the Brownian relaxation time. Due to this dominance, the viscosity deliberately affects the healing response. The SAR decreases with the viscosity as proposed by the LRT [10]. The effect of SAR with varying viscosity is more significant in hard ferrite than soft ferrite because of the difference in anisotropy constant [34].

According to the Landau–Lipshitz–Gilbert (LLG) stochastic equation, the effect of viscosity in heat generation reduces with a smaller anisotropy constant. Cabrera et al. researched the impact of viscosity (0.9–153.5 MPa s) in the hysteresis losses at low frequency experimentally for iron oxide nanocubes (14 and 24 nm) and cobalt ferrite nanocubes (21 nm). It is important to note that the anisotropy constant of cobalt ferrite is 290 kJ/m^3 and that of iron oxide (magnetite) is -13 kJ/m^3; as a result, the value of SAR is higher in cobalt ferrite. The cobalt ferrite is more sensitive to viscosity than iron oxide. The effect of viscosity reduces with size in the case of iron oxide. The magnetic parameters such as saturation magnetization and remanent magnetization exhibit decreasing nature with increasing viscosity; the coercive field decreases for the sample with high anisotropy constant but for particles with low anisotropy constant, the coercive field is dependent on size rather than viscosity [30].

L. H. Nguyen et al. studied theoretically the variation of three types of domination (Neel, Neel–Brownian, and Brownian process) with varying viscosity and anisotropy constant (K) and also studied the behavior of the change in critical anisotropy of iron oxide nanoparticles. At first, they identified the range of K values about the dominant magnetic relaxation mechanism: $K \leq 5$ kJ/m^3 is identified as Neel dominant region; 5 kJ/m^3 $\leq K \leq$ 20 kJ/m^3 as Neel–Brownian overlap region, and $K >$ 20 kJ/m^3 as the Brownian-dominant region and deduced the critical anisotropy value (K_c) to be 20 kJ/m^3 for ferric oxide nanoparticles. The critical anisotropy constant (K_c) is the threshold value where the transition to Brownian domination occurs below which the Neel and Brownian relaxation co-exist. Secondly, he laid out the variation of K_c with viscosity ranging from 1 to 10 MPa s at different frequencies. The importance of K_c lies in the fact that the change in behavior of the SAR maximum changes significantly when the value of the anisotropy constant is less than the critical anisotropy constant. Thirdly, the author conferred the decrease in SAR maximum with increasing viscosity and the decrease becomes more pronounced with increasing anisotropy constant. provided K does not exceed K_c as the influence of viscosity lies in the Brownian-dominant region. It was also noted that the K_c value increases with frequency. Finally, he verified the above analysis with an experiment observing the reduction of SAR with increasing viscosity more significantly at high anisotropy constant [35].

4.7 Concentration

Here, we refer to the concentration of the magnetic nanoparticles dispersed in a suspension with varying viscosity. The degree of dependency of SAR on viscosity increases with MNPs concentration. At low concentration (2.5 mg/mL) of nanoparticles (22 nm), the SAR value for agar and water are comparable for a large range of magnetic field, and it is observed that SAR of agar is higher than that of water due to the susceptibility loss of non-interacting particles. At high concentrations, the SAR of water is three-fold higher than agar. The differential percentage $\left(\frac{\mathrm{SAR_{water}} - \mathrm{SAR_{agar}}}{\mathrm{SAR_{water}}} \times 100\right)$ in SAR is negligible at low concentration of IONPs but becomes significant to about 70% at high IONP concentration. At higher MNPs concentration, the hysteresis loop of MNPs in water increases while that of agar decreases and follows an elliptical structure. Moreover, the more the concentration more pronounced the elliptical shape [36] and it thereby reflects the fact that the reduction in SAR is associated with the number of interacting particles. The author also observed a more elliptical shape in agar than in water and thereby concludes the influence of viscosity in the intracellular interactions [31].

4.8 Shapes

Optimization of SAR depends on the morphology of the nanoparticles. Cuboidal-shaped nanoparticles are reported to be more efficient than nanorods or nanospheres [37]. A homogeneous nanocubes suspension does not undergo aggregation; however, the value of SAR is affected with varying viscosity [30].

Nanoflowers are packed of dense irregular aggregates of rough-surfaced iron oxide nanoparticles synthesized by the polyol method [38]. The heat generation in this case is contributed mostly by the exchange couplings of the core of the nanoparticle within the nanoflowers. Bender et al. studied the dextran-coated nanoflowers. The nanoflowers were dispersed at different solvent viscosity by adding glycerol and was observed the non-dependence of relaxation on viscosity. The relaxation time distribution according to the MRX (magnetorelaxation) data of γ-Fe_2O_3/Fe_3O_4 sample of hydrodynamic size of 54 nm displayed three peaks. Two peaks of lower relaxation time reflected the Neel domination which was in good agreement with the LRT. However, the third peak was not physically interpreted, and highlighted the possibility of a third relaxation process. This may be supported by the finite susceptibility of χ''=0.09 at high frequency of $\omega = 6.28 \times 10^6$ s^{-1} with a fast relaxation of 1.6×10^{-7} s. The disordered spins within the nanoflowers may be responsible for the fast relaxation [20].

Riahi et al. compared the effect of viscosity in dynamic magnetization for three commercially available samples of superparamagnetic iron oxide nanoparticles. The three samples are (a) γ-Fe_2O_3 (nanoflower shape, dextran coated with the size of 50 nm); (b) Fe_3O_4/γ-Fe_2O_3 (spherical, carboxydextran coated with size 45–60 nm); and (c) Fe_3O_4/γ-Fe_2O_3 (spherical, carboxydextran coated with the size of 59 nm.) The differential magnetic susceptibility $(dM/dH)_{max}$ decreases with the increase in viscosity in all the three samples as the hydrodynamic volume is affected by the media viscosity leading to extended Brownian relaxation; however, the first sample is less sensitive to viscosity which may be due to the nanoflower shape or the larger core size as seen through TEM [39].

Thus, it has come to our knowledge that the media viscosity affects heat generation due to several parameters discussed above. However, recent research has revealed the importance to study the other properties of the media such as the specific heat capacity in addition to the viscosity.

At the melting point of some solvent media such as paraffin, the viscosity reduces to a great extent at the melting temperature. It has been reported that there is a rapid nonlinear increase in the thermal response above the melting temperature of the media, not due to the change in relaxation mechanism but the reason lies in the change of specific heat capacity. Thus, this is an interesting area of research provided the melting temperature lies within the biocompatibility range for the treatment [40].

5 Summary/Conclusion

The effect of viscosity in the magnetically induced heat generation is more precisely the competition between the Neel and the Brownian relaxation. The theoretical approach of LLG delivers that the size, anisotropy, and strength of the AC field influence the viscosity effect on heat losses. The SAR reduction with increasing viscosity focuses mostly on the dominion of the Neel relaxation pathway over the Brownian one. In the solid matrix, there is no possibility of the rotation of particles, the only contribution to the heating mechanism is the response of the magnetic moments of the particles in an applied alternating field. The role of dipolar interaction depends upon other factors to define the enhancement or reduction in the healing response. There is a limited regime where there is viscosity dependence on SAR. Viscosity directs the SAR for high nanoparticles concentration with a high anisotropy constant kept in low amplitude and low frequency of the externally applied magnetic field. The influence of viscosity is restricted in the viscous mode for a large diameter range. The heterogeneous property of the intracellular environment favors the regime of magnetic nanoparticles whose dependency on viscosity is turned down as low as possible.

References

1. Serantes D, Baldomir D, Martinez-Boubeta C, Simeonidis K, Angelakeris M (2010) Influence of dipolar interactions on hyperthermia properties of ferromagnetic particles. J Appl Phys 073918:1–5
2. Tsiapla A, Kalimeri A, Maniotis N, Samaras T, Angelakeris M, Kalogirou O (2021) Mitigation of magnetic particle hyperthermia side effects by magnetic field controls. Int J Hyperth 38:511–522
3. Bellizzi G, Bucci OM, Chirico G (2016) Numerical assessment of a criterion for the optimal choice of the operative conditions in magnetic nanoparticle hyperthermia on a realistic model of the human head. Int J Hyperth 32:668–703
4. Hergt R, Dutz S (2007) Magnetic particle hyperthermia-biophysical limitations of visionary tumour therapy. J Magn Magn Mater 311:187–192
5. Galvãoa WS, Netob DMA, Freirec RM, Fechined PBA (2016) Super-paramagnetic nanoparticles with spinel structure: a review of synthesis and biomedical applications. Solid State Phenom 241:139–176
6. Vallejo-Fernandez G, Whear O, Roca AG, Hussain S, Timmis J, Patel V, O'Grady K (2013) Mechanisms of hyperthermia in magnetic nanoparticles. J Phys D Appl Phys 46:6
7. Rousseau A, Tellier M, Marin L, Garrow M, Madelaine C, Hallali N, Carrey J (2021) Influence of medium viscosity on the heating power and the high-frequency magnetic properties of nanobeads containing magnetic nanoparticles. J Magn Magn Mater 518:1–6
8. Rosensweig RE (2002) Heating magnetic fluid with alternating magnetic field. J Magn Magn Mater 252:370–374
9. Obaidat IM, Issa B, Haik Y (2015) Magnetic properties of magnetic nanoparticles for efficient hyperthermia. Nanomaterials 5:63–89
10. Torres TE, Lima Jr E, Calatayud MP (2019) The relevance of Brownian relaxation as power absorption mechanism in magnetic hyperthermia. Sci Rep 9:1–11

11. Usov NA, Liubimov BY (2012) Dynamics of magnetic nanoparticle in a viscous liquid: application to magnetic nanoparticle hyperthermia. J Appl Phys 023901:1–11
12. Çelik Ö, Fırat T (2018) Synthesis of FeCo magnetic nanoalloys and investigation of heating properties for magnetic fluid hyperthermia. J Magn Magn Mater 456:11–16
13. Lacroix LM, Bel Malaki R, Carrey J, Lachaize S, Respaud M, Goya GF, Chaudret B (2009) Magnetic hyperthermia in single-domain monodisperse FeCo nanoparticles: evidences for Stoner–Wohlfarth behavior and large losses. J Appl Phys 023911:1–4
14. Usov NA, Rytov RA, Bautin VA (2021) Properties of assembly of superparamagnetic nanoparticles in viscous liquid. Sci Rep 11:1–11
15. Tompkins J, Huitink D, Tompkins J, Huitink D (2020) Induction heating response of iron oxide nanoparticles in varyingly viscous mediums with prediction of brownian heating contribution viscous mediums with prediction of brownian heating contribution. Nanoscale Microscale Thermophys Eng 1–15
16. Teran FJ, et al (2012) Accurate determination of the specific absorption rate in superparamagnetic nanoparticles under non-adiabatic conditions. Appl Phys Lett 101
17. Hemery G, Sandre O, Ortega D, Garaio E, Plazaola F (2015) Fundamentals and advances in magnetic hyperthermia. Appl Phys Rev 2:1–35
18. Leão Â (2020) Magnetically induced heating by iron oxide nanoparticles dispersed in liquids of different viscosities. Ceram Int 46:21496–21504
19. Dutz S, Hergt R (2014) Magnetic particle hyperthermia—a promising tumour therapy ? Nanotechnology 25:1–28
20. Bender P, Fock J, Frandsen C, Hansen MF (2018) Relating magnetic properties and high hyperthermia performance of iron oxide nanoflowers. J Phys Chem C 122:3068–3077
21. Pineiro Y, Vargas-Osorio Z, Banobre-Lopez M, Kolen'Ko YV, Lopez-Quintela MA, Rivas J (2016) Relevant parameters for magnetic hyperthermia in biological applications: agglomeration, concentration, and viscosity. IEEE Trans Magn 52:1–5
22. Landi (GT) Role of dipolar interaction in magnetic hyperthermia. Phys Rev 014403:1–6
23. Abu-Bakr AF, Zubarev AY (2020) To the theory of magnetic hyperthermia in viscoelastic media: effect of interparticle interaction. Eur Phys J Spec Top 229:2981–2990
24. Bruvera IJ, Actis DG, Calatayud MP, Zélis PM (2019) Typical experiment vs. in-cell like conditions in magnetic hyperthermia: effects of media viscosity and agglomeration. J Magn Magn Mater 165563:1–7
25. Cabrera D, Coene A, Leliaert J, Arte EJ (2018) Dynamical magnetic response of iron oxide nanoparticles inside live cells. ACS Nano 12:2741–2752
26. Serantes D, Simeonidis K, Angelakeris M, Chubykalo-Fesenko O, Marciello M, Puerto Morales MD, Baldomir D, Carlos MB (2014) Multiplying magnetic hyperthermia response by nanoparticle assembling. J Phys Chem C 11:5927–5934
27. Serantes D, Baldomir D (2020) Nanoparticle size threshold for magnetic agglomeration and associated hyperthermia performance. Arxiv, pp 1–7
28. Narayanaswamy V, Sambasivam S, Saj A, Alaabed S, Issa B (2021) Role of magnetite nanoparticles size and concentration on hyperthermia under various field frequencies and strengths. Molecules 796:1–14
29. Yoshida T, Nakamura T, Higashi O, Enpuku K (2019) Effect of viscosity on the AC magnetization of magnetic nanoparticles under different AC excitation fields. J Magn Magn Mater 471:334–339
30. Cabrera D, Lak A, Yoshida T, Materia ME, Ortega D, Ludwig F, Guardia P, Sathya A, Pellegrino T, Teran FJ (2017) Unraveling viscosity effects on the hysteresis losses of magnetic nanocubes. Nanoscale 9:5094–5101
31. Salas G, Camarero J, Cabrera D (2014) Modulation of magnetic heating via dipolar magnetic interactions in monodisperse and crystalline iron oxide nanoparticles. J Phys Chem C 118:19985–19994
32. Suwa M, Uotani A, Tsukahara S (2020) Magnetic and viscous modes for physical rotation of magnetic nanoparticles in liquid under oscillating magnetic field Magnetic and viscous modes for physical rotation of magnetic nanoparticles in liquid under oscillating magnetic field. Appl Phys 262403:1–5

33. Lahiri BB, Ranoo S, Zaibudeen AW, Philip J (2017) Magnetic hyperthermia in magnetic nanoemulsions: effects of polydispersity, particle concentration and medium viscosity. J Magn Magn Mater 441:310–327
34. Phong PT, Nguyen LH, Phong LTH, Nam PH, Manh DH, Lee I-J, Phuc NX (2017) Study of specific loss power of magnetic fluids with various viscosities. J Magn Magn Mater 428:36–42
35. Nguyen LH, Phong PT, Nam PH, Manh DH (2021) The role of anisotropy in distinguishing domination of Néel or Brownian relaxation contribution to magnetic inductive heating: orientations for biomedical applications. Materials 14:11–13
36. Cabrera D, Camarero J (2015) Influence of the aggregation, concentration, and viscosity on the nanomagnetism of iron oxide nanoparticle colloids for magnetic hyperthermia. J Nano Res 17:1–6
37. Reyes-ortega F, Delgado ÁV, Iglesias GR (2021) Modulation of the magnetic hyperthermia response using different superparamagnetic iron oxide nanoparticle morphologies. Nanomaterials 11:1–14
38. Hugounenq P, Levy M, Alloyeau D, Lartigue L, Dubois E, Cabuil V, Ricolleau C, Roux S, Wilhelm C, Gazeau F, Bazzi R (2012) Iron oxide monocrystalline nanoflowers for highly efficient magnetic hyperthermia. J Phys Chem C 116:15702–15712
39. Riahi K, van de Loosdrecht MM, Alic L, ten Haken B (2020) Assessment of differential magnetic susceptibility in nanoparticles: effects of changes in viscosity and immobilisation. J Magn Magn Mater 167238:1–7
40. de Almeida AA, de Biasi E, Mansilla MV, Valdes DP, Troiani HE, Urretavizcaya G, Torres TE, Rodriguez LM, Fregenal DE, Bernardi GC, Winkler EL, Goya GF, Zysler RD, Lima Jr E (2020) Magnetic hyperthermia experiments with magnetic nanoparticles in clarified butter oil and paraffin: a thermodynamic analysis. J Phys Chem C 124:27709–27721

Chapter 10
Morphology-Controlled Synthesis and Morphology-Induce Structures of Different Nanoparticles

Heikham Farida Devi

1 Introduction

Morphology-controlled synthesis of different nanoscale materials has been motivated over the last three decades due to the acquired new specific properties at a particular shape and length scale. In this regime, the alterations in the properties of different length scales manifest themselves from various causes in various materials. This fact is evidenced by many scientific reports [1–5], driven by the enthusiasm of seeing novel surface chemistry and by the possibilities of new applications and monetary effects. Among their potential applications, the surface properties will assume the essential part in deciding the particular capacities. However, the surface phenomenon of the small size particles may no longer be stable due to their higher interfacial energy and the large surface area [6]. As a result, changes in structural morphology cause variations in the chemical behaviour of the molecular surface, opening up new possibilities for novel applications.

There has been an expeditious spreading of research into metal nanoparticles in a wide spectrum of fields like Voltaics, optoelectronics, biosensors and imaging, and so forth, because of their interesting properties, particularly optical properties, including strong plasmon absorption, enhanced Rayleigh scattering, and surface-enhanced Raman Scattering. To synthesize metal nanoparticles, researchers have employed a variety of methods, which may be classified into two categories: top-down strategy and bottom-up methodology. When it comes to gold nanoparticles that aren't spherical, the seed-mediated growth method is a straightforward and trustworthy technique to get a high output. On the other hand, the creation of gold nanorods has been seen as a result of a "zipping" exchange between the morphing specialist's faceting propensity and the development energy. The seed-mediated development system of gold nanoparticles of various forms, such as cubes, hexagons, triangles, tetrapods, and so on, was accounted for to be similar to that of gold nanorods [7]. Thus,

H. F. Devi (✉)
Department of Applied Science and Humanities, Assam University, Silchar, Assam 788011, India

B. P. Swain (ed.), *Advances in Nanostructured Materials*, Materials Horizons:
From Nature to Nanomaterials, https://doi.org/10.1007/978-981-16-8391-6_10

distinctive methods of nucleation and development of a particle, synthesis process, characterization, and properties on nanoparticles (NPs) have been described.

2 An Overview of Particle Growth and Nucleation

Generally, the tailoring of variant shape particles is occurring in the course of the precipitation method of a solid part from the solution system. The nucleation mechanism is followed by a particle development measure in the precipitation process. The nucleation and particle development processes have been concentrated from the beginning using the La Mer burst nucleation [8, 9] and then the Ostwald ripening mechanism [10] to elucidate the variations in particle sizes. However, Reiss [11] was the first to illustrate the said process, and Lifshitz–Slyozov–Wagner, LSW theory [12, 13], was the first to develop it satisfactorily. The term nucleation simply describes the process where the nuclei (seeds) behave as a template for the growing of crystal particles. Graphical representations of different types of nucleation have been shown in Fig. 1.

2.1 Primary Nucleation

Essential nucleation happens without the presence of additional crystalline substances, according to Mullin [14]. As we know that if any liquid system gets cooled, there exists a range of temperatures at which it is converted to solid. The first formed seeds or nuclei, which may be of few nanometers in size appear only when

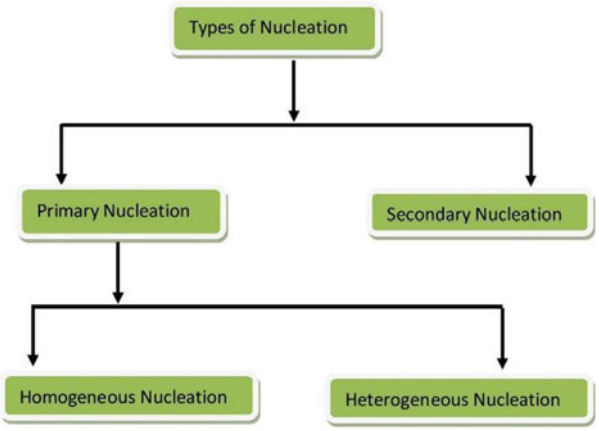

Fig. 1 Type of nucleation

the system gets supersaturated. And all crystallization processes begin in a supersaturated system when the system exhibits a metastable zone. However, nucleation will start spontaneously only when the upper limit of the metastable zone of the supersaturated system is reached. Moreover, nucleation can be enhanced by agitation, abrasion, shearing action, and alteration in pressure.

2.2 Homogeneous Nucleation

Much of the time, limited quantities of contaminations have a sensational impact on numerous crystallization processes like nucleation, crystal growth, and the obtained crystal quality [15]. Thus, the interaction of impurities and solvent at the interface highly impact the particle size, shape, and purity of the crystals. Practically, homogeneous nucleation rarely happens because the phenomenon can occur only if the solution contains no foreign particles or crystal matrix of its kind [16]. Overall, homogeneous nucleation occurs thermodynamically due to the unfavourable energy of the supersaturated system.

2.3 Heterogeneous Nucleation

Practically, heterogeneous nucleation is the one to occur readily and involves the presence of foreign particles or impurities or container walls or dislocations or grain boundaries in the crystallization system.

2.4 Secondary Nucleation

The existence of crystals and their interaction with the crystallizer environment might trigger secondary nucleation. It only happens when the nuclear seed's discontinuity is affected by fluid shear or weakening caused by interactions with the crystallizer divider, other nuclear seeds, or the stirrer.

2.5 Crystal Development

Following the nucleation course, crystal development occurs, in which the nuclear seed develops viably through the expansion of solute crystal from the supersaturated solution. The absolute particle size distribution obtained in the system is controlled by crystal growth and nucleation. Also, the purity of the product and the crystal habit is influenced by the process parameters and the rate of crystal formation.

3 Important Synthesis Techniques

The appropriate synthetic method must be chosen to acquire the desired physico-chemical characteristics for the applications. In the literature, most of the synthesized samples show irregularity with limited morphologies and polydisperse particle sizes. In terms of the accompanying viewpoint, the soft chemical synthesis way outperforms the traditional solid-state reaction technique. At first, capping agents can be easily inserted from the outer surface of the ensuing particles using a soft chemical synthesis technique. As a result, dispersing particles in either an aqueous or polar medium is suitable for preventing particle agglomeration. Secondly, reaction parameters like precursors, pH value, solvent, concentration, and reaction medium (time or temperature) may be precisely adjusted to get the desired size along with the morphology of the end products. As a result, dispersing particles in either an aqueous or polar fluid is suitable for preventing particle agglomeration. Second, reaction variables such as precursors, pH, solvent, concentration, and reaction medium (time or temperature) can be precisely adjusted to get the desired size along with the shape of the end products. Third, soft chemical synthetic strategies enable for reaction even at low temperatures; they can be used with simple apparatus, extensive production, low cost, and adaptable post-treatment of the products. As a result, soft chemical synthesis has been chosen as the most versatile method for producing surface-modified RE ion-activated phosphors, metal oxides, and other materials.

3.1 Thermal Decomposition Technique

In the whole soft chemical synthesis pathway, the thermal decomposition approach is arguably the most well-known and extensively utilized methodology for generating monodisperse, well-crystalline, and pure phase RE-activated nanoparticles. To date, it is the best technique to synthesize NPs with less than ten nanometres in size, which is efficient for biomedical applications [17, 18]. This approach is a synthetic process involving breaking down organic precursor sources in high boiling organic solvents with the assistance of surfactants and decomposing those precursors at high temperatures in the absence of air. Usually, RE organic acid salts like trifluoroacetate, oleate, acetylacetonate, and acetate are frequently used as precursors. It is essential to choose suitable organic precursors and long-chain hydrocarbon capping agents/surfactants for successful synthesis. The organic surfactant plays the following roles: (a) capping the surface of the synthesized particles to prevent agglomeration and (b) prevent the growth of the prepared particle size. In 2008, Zhang and his co-workers designed an eco-friendly methanol-assisted organic phase synthetic route to synthesize RE-activated core–shell nanostructures [19, 20]. The thermal decomposition method can be classified based on the precursors, as shown in Fig. 2.

In 2012, Zou and his co-workers have synthesized nanophosphors in ethylene glycol using polyethyleneimine as a surfactant. They obtained cubic

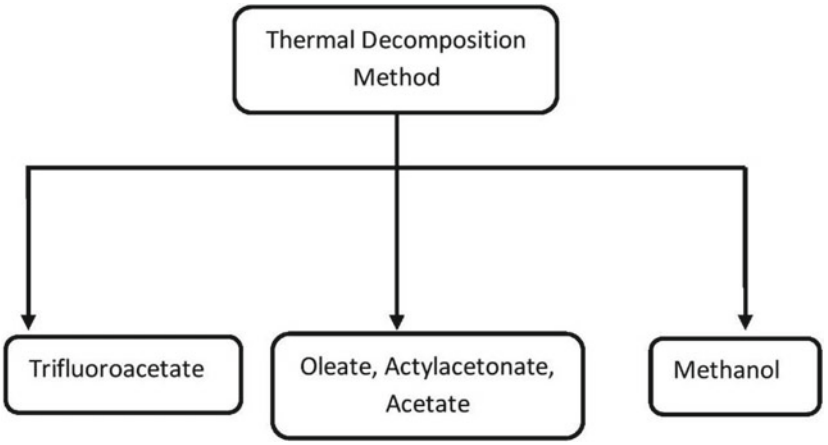

Fig. 2 Classification of the thermal decomposition method

$NaYF_4$:Yb^{3+}/Er^{3+} nano phosphors having an average mean size around 30 nm with highly crystalline in nature [21]. Because the surfactant's polar head is oriented towards the particle surface plus the hydrophobic tail is oriented towards the solvent, the surfactants changed the surface hydrophobic nature of the produced nanoparticles. This makes the particles hard to disperse in an aqueous medium and difficult for further biological functionalization. To overcome this problem, Bogdan and co-workers synthesized surfactants free $NaYF_4$:Er^{3+}/Yb^{3+} up-conversion nanophosphors following modified thermal decomposition technique and get particles with an average size around 25 nm. Using post-treatment with mineral acids, oleate surfactant was removed from the ensuing particles. The pH of the solution was therefore altered, resulting in protonation of the oleate surfactant and the release of oleic acid. Highly dispersible surfactant-free nanophosphors are showing higher up-conversion luminescence efficiency comparing to oleate capped particles. By studying different pH values solution, sample with less pH value shows positive zeta potential, indicating that the surfactant-free nanoparticle surface gets protonated and gives intense red emission [22].

Hence, the above method proves to be the most common method for synthesizing highly crystalline nanophosphors. However, some inherent problems require being paid attention to in biological applications and synthetic routes. At first, harsh synthesis conditions like high temperature, oxygen-free, and inert environment, require careful handling. Second, dangerous fluorinated and oxyfluorinated by-products are produced due to the use of expensive high boiling solvents and the presence of toxic trifluoroacetate in the reaction mixture. Third, the surfactant stabilized hydrophobic products are having limited biological applications, thus require surface-modified products for further applications. Fourth, the process is ineffective for producing RE phosphate, vanadate, and borate phosphors with an ambiguous morphology.

3.2 Solvo/Hydrothermal Method

Another well-known soft chemical synthesis process, the "solvothermal method," has been utilized to synthesize high-grade nanoparticles since the mid-1990s. This route utilizes solvents to speed up the reactions between the reactants under high pressures with elevated temperatures above its boiling point. Types of solvothermal techniques are shown in Fig. 3. An autoclave with a Teflon inner liner, a stainless steel outer shell, and a stainless steel cap must be utilized to achieve the necessary reaction conditions. The term "hydrothermal" refers to the use of water as a solvent in the synthesis route. Hydrothermal synthesis has a variety of advantages, including a low cost, environmentally acceptable solvent, ease of use, and the ability to produce huge quantities. Generally, the technique was used to make single crystals. The driving force for the formation of single crystals arises from the fact that the reacting solution has a temperature gradient between the opposite ends of the vessels. The precursor is entirely dissolved in the solvent in the hotter region. Because of the temperature difference between the two ends, the precursors that dissolve in the hotter end drop on the crystal seed, resulting in crystal formation [23].

Usually, hydrothermal synthesis is considered a single-step synthesis route. Typically, the precursors are salts of rare earth elements, like nitrates [24] and chlorides

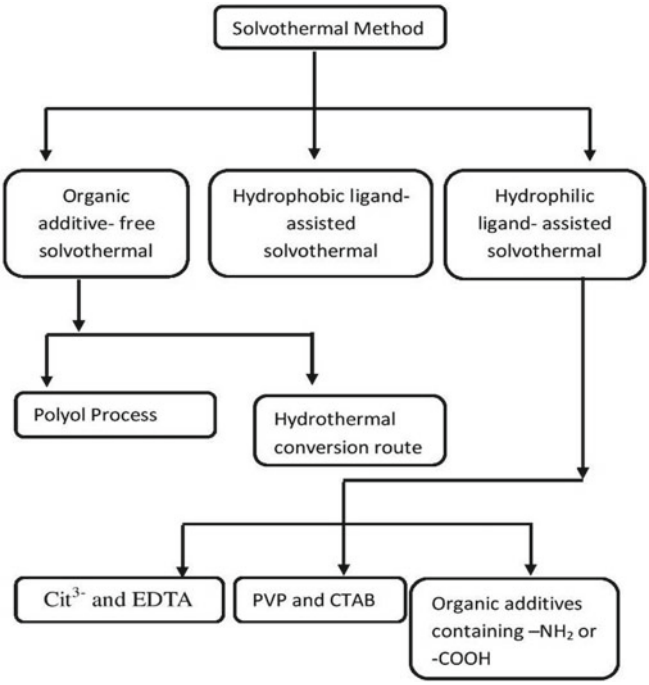

Fig. 3 Classification of solvothermal method

[25]. Because of the selective adsorption on the dissimilar facets of the produced nanocrystals, using surfactant (organic additives) can change the shape of the particles [26]. The alteration of the surface morphology of the nanomaterials can be achieved by organic additive [24, 25], assisting with hydrophilic ligand [27], and assisting with hydrophobic ligand [28]. In 2010, Wang et al. have synthesized a sequence of Ln^{3+} activated $NaYF_4$ nanoparticles, with grain sizes decreasing to ten nanometres as doping concentration increases, having cubic or hexagonal phases, and giving up-conversion emission colours ranging from green to blue [29]. The synthesis method is known as solvothermal because the solvent employed in the process is not limited to water but also includes other polar and non-polar solvents. To promote the growth mechanism of nanotube morphology, D. Chen et al. used "anhydrous alcohol as a solvent, $SnCl_2$, and thiourea as reactants and anodic aluminium oxide as a surfactant" [30]. Interestingly, many researchers have used supercritical fluids as solvents and created a variety of nanostructures, including Ag [31–33], Cu [32, 34–37], Co [38], Pt [38], GaP nanowire [39], and carbon nanotube [40].

Henceforth, solvothermal synthesis has various advantages compared to the other routes, including easily controllable morphology and size, high purity and crystallinity of the product, narrow and homogenous particle size distribution, and environmentally sustainable technique. However, there are several drawbacks, such as the high cost of autoclaves, the long duration reaction, and minimal yield.

3.3 Sol–gel Technique

The sol–gel route is essentially a polymerization reaction that involves hydrolysis, condensation, drying, and decomposition. The size of the sol particle is determined by reaction factors such as reactant composition, pH value, and reaction system temperature. The aforementioned parameters can be modified to change the size of the resultant sol particles. Another soft chemical synthesis strategy for making trivalent rare earth ion-doped metal oxide nanocrystals at low temperatures is the sol–gel method. Converting a solution to colloidal sol and then to a multiphasic gel is required for the production of organic or inorganic networks. Annealing at high temperatures is required to produce pure phase and extremely crystalline nanophosphors. All of the produced nanoparticles is made up of agglomerated irregular spherical form with a wide particle size range due to the high annealing temperature. Prasad et al. have synthesized Er^{3+} activated ZrO_2, TiO_2, and $BaTiO_3$ nanoparticles via the emulsion-based sol–gel method [41]. However, there are some inherent limitations related to the metal alkoxides and solvents used in the synthesis route due to expensive, hazardous, unavailability, and fast hydrolysis rate. However, when combined with soft lithography and electrospinning techniques, the technology is highly useful for the synthesis of inorganic compounds. Li and co-workers reported the synthesis of "1-dimensional fibre-, belt-, and tube like Ln^{3+} activated inorganic materials using the sol–gel method and electrospinning technology, where the precursor sol comprises of polymer, citric acid, and a water–ethanol solution of inorganic ions" [42]. The

polymer, specifically PVP, is utilized as a template to form one-dimensional structures and to maintain the viscosity of the precursor sol constant [43].

3.4 Microemulsion Method

The microemulsion is a thermodynamically stable medium of a two-phased inverse micelle system with an oil phase, a water phase, and a surfactant. Surfactants are employed to stabilize nanosized water droplets in the oil phase, resulting in a transparent solution. The water droplets in the system have the potential to completely dissolve the reactants, and Brownian motion ensures that the micelles in the aqueous phase are constantly swapped. The water droplets collide and coalesce after mixing two inverse microemulsions containing distinct reactants. This results in perfect nanoreactors for the production of nanoparticles, the size of which is largely determined by the water droplet's size. However, adjusting the molar ratio of water to surfactant can change the size of the water droplets (W_0). Usually, the larger value of W_0 will give large particles [43].

The microemulsion approach has proven to be one of the most frequent ways to synthesize nanoparticles. This method possesses several advantages such as being easy to prepare because of its water-soluble nature. Small nanoparticles are formed in oil due to the presence of small water droplets. Also, several water–surfactant–oil inverse systems, including water–CTABn–hexane, water–CTAB–pentanol, and water–CO-520–cyclohexane, have been employed as nanoreactors for generating nanophosphors, but the technique provides low yield with poor quality. Li et al. [44] also described a new approach for the production of nanoparticles using a conventional oil–water microemulsion system with water as the continuous phase. They also demonstrated that the process for nanoparticle growth in a regular oil–water microemulsion system differs significantly from the inverse micelle system. To produce the nanoparticles, a hexane–linoleic acid–water system has been used as a reactor with water–oil interfaces. This route is giving a high yield as compared to the traditional inverse method due to the high solubility of the precursors in the aqueous phase. The synthesis of metal atoms was described by Bönnemann et al. as a nucleation stage reduction of metal salt precursors, which can then collide with additional metal ions to create an irreversible nuclear seed of stable metal nuclei [45]. The nucleation point is where a reverse micelle collides with the arrival of new reactants due to intermicellar exchange, and this is where the growth stage begins.

3.5 Co-Precipitation Method

Because of the mild working conditions, easy procedures, and less expensive equipment, the co-precipitation method is one of the simplest approaches for the production of nanoparticles. Nanoparticles are obtained when two or more solutions containing

precursors of desired proportions are mixing under constant stirring. During this process, insoluble salt from the precursors which was used in the reaction mixture gets precipitates. The reaction process can be operated either at room temperature or at elevated temperatures. The elevated temperature might be essential to get more crystalline nanoparticles [46]. This method is benign and eco-friendly and does not produce hazardous by-products as compared to the solvothermal method [47]. Solvent, pH value, type of surfactants, ionic strength, and insoluble salts all have an impact on the generated nanomaterials (chlorides, sulphates, nitrate, etc.) size and structure.

Several trivalent rare earth ion-activated phosphates have been reported to be synthesized using the co-precipitation method. You et al. used "a water–ethanol solution to precipitate $LaPO_4$:Ln (Ln = Ce, Tb) and $LaPO_4$:Ce, Tb@$LaPO_4$ nanowires" [48]. Similarly, Ningthoujam et al. and Grzyb generated "$GdPO_4$:Yb, Tb, and YPO_4:Eu, Bi nanorods in water–glycerine solution, employing polyethylene glycol as a capping agent for YPO_4:Eu, Bi nanorods" [49, 50]. The two groups confirmed that the presence of a luminescence quencher in the form of an O–H group causes low emission intensities in the produced samples. The emission intensities rose as the crystal structure of the particles changed from hydrated hexagonal to dehydrated tetragonal following annealing at 800 °C.

Moreover, it is hard to synthesize the nanoparticles having narrow-sized distribution particles via the route as it is tough to control the kinetic factors. Separating the growth and nucleation processes is critical for controlling the particle size distribution of produced nanoparticles, which is nearly impossible in the co-precipitation approach. Surface modification of the synthesized nanoparticles is also very difficult using the precipitation route. The luminescence intensity of the samples is also weak and to enhance the emission intensity, a post-annealing method is required. But, post-annealing will decrease the hydrophilicity of the sample which is again not suitable for biomedical applications. For improving the hydrophilicity of the particles, surface modification is again essential. However, the co-precipitation method is quite useful for industrial applications because of its high productivity, inexpensive, eco-friendly, and synthetic convenience.

3.6 Sonochemical Reduction Method

Many researchers have employed the sonochemical reduction approach to fabricate metal nanoparticles. The reduction of the appropriate metal ions is required in this method. MnO^{4-}, Au^{3+}, Au^{+}, plus Pd^{2+} have been reduced sonochemically enabling the relative synthesis of size and shape-controlled metal nanostructures using this approach in the absence or presence of organic additives. Controlling the rate of reduction allows for fine-tuning of the size and shape of metal nanoparticles. K. Okitsu et al. claimed the use of citric acid as a capping agent for ensuing size-controlled gold (Au) nanoparticles [51]. Obreja et al. have performed an alcoholic reduction of platinum (Pt) nanoparticles via the sonochemical reduction method

[52]. H_2PtCl_6 was reduced in their study using ethanol, methanol, and propanol as solvents and reducing agents, as well as organic stabilizers such as chitosan, PEG, and polyethylene glycol (amide-hydroxyurethane).

3.7 Gamma Radiation

For the creation of metal nanoparticles, gamma radiation is one of the most popular methods. The approach utterly excludes the use of toxin precursors, relies on environmentally friendly solvents such as water and ethanol, keeps the reaction temperature at ambient temperature, and produces minimal waste [53]. Researchers and academicians have witnessed that the radiolytic reduction reaction to being a powerful tool to tailor monodispersed metallic clusters. The excitation and ionization of the solvent molecule occur when high-energy radiation interacts with a solution of metal ions [54].

4 Surface Chemical Modification of Nanomaterials

It is evidenced that the properties of the nanomaterials such as the solubility, reactivity, stability, melting point, and the electronic band were decided by its surface nature [55]. In addition, the surface acts as a bridging agent between particles and plays an important role in the construction of superlattices for the manufacture of novel devices. As a result, the only significant focus for new technological improvements is the chemical alteration of the particle surface. Surfactants or stabilizing agents are necessary during the nanoparticle production process to prevent particle agglomeration and precipitation. To cap the surface of the resulting particles, many organic and inorganic compounds have been used.

The interaction of particles in colloidal metallic nanomaterials is caused by weak van der Waals forces [56, 57]. Thus, overcoming this attractive force is the main target for morphology-controlled synthesis. Furthermore, several types of surfactants/capping agents can be used to counteract the attractive forces created by steric hindrance stabilization or electrostatic force stabilization. The type of metal, intended shape, and use of the resulting nanomaterials will all be determined by the nature of the capping agent. For a colloidal nanomaterial, the interface free decides its particular shape. Under equilibrium conditions, homogeneous nucleation and seed nucleation leads to the production of a spherical shape [58]. That is, the crystal shape is mostly determined by their kinetic process, in which high-surface-energy facets grow quickly and then vanish, leaving the slowest-growing facets as the final product's facets. The ultimate morphology of the material/crystal can now be regulated by adding suitable surfactants to alter the surface free energy at particular facets by tuning its crystal growth.

In addition, in the last several decades, morphology-controlled nanomaterial production has been explored in the absence of any additional organic additives [59]. The release of H^+ from the reaction medium causes the environment to become highly acidic, which may influence crystal growth rates by protonating specific facets. The fundamental driving force for modifying the pH value is to manage the surface free energy by modulating the kinetic or thermodynamic factors of the nucleation or growth stages of the crystals. The release H^+ was partially neutralized after adding NaOH to the developing suspension, modifying the surface free energy of the various aspects.

5 Growth Mechanism of Different Shape Eu^{3+} Doped Yttrium Orthophosphate Microcrystal

An easy method for tailoring different shapes of Eu^{3+} doped yttrium orthophosphate microcrystals is the Co-precipitation technique. By absorbing one or more dopant ions in its lattices, the capping agents utilized in the precipitating system, such as ethylene glycol, effectively create a potential class of hierarchical networks with controllable size. The sorption ability of metal ions is largely determined by the concentration of ethylene glycol utilized in the precipitating system. As we know that adding capping agents to the precipitating solution can change the order of interfacial energy when they interact with metal ions surfaces. This modification may increase the rates of development of particular facets of the crystals by limiting the creation of specific crystal faces [60]. We kept in mind that synthesized materials, particularly for biological purposes, should be free of harmful precursors and incorporate eco-friendly ones. As a solvent and capping agent, we are utilizing environmentally friendly ethylene glycol. Ethylene glycol has two terminal hydroxyl groups that shield the metal ions, Y^{3+}/Eu^{3+}, allowing the hydrogen ions in the molecule to be easily replaced by the metal ions, Y^{3+}, forming a complicated structure.

When the precipitation system is prolonged, yttrium orthophosphate nuclei develop swiftly into the hexagonal phase, benefiting from the OH^- group releasing from the precipitating system to the microcrystal, as seen in the case of $NaYF_4$ nuclei growth [29]. Eu^{3+} dopant ions displaced Y^{3+} sites of the host lattice, YPO_4, when they were introduced into the precipitating system. As the precipitation reaction progressed, charge balancing between the reactant molecules occurred, crystal development took over, and a mixed morphology of small agglomerated seeds and micro-dumbbells emerged. Due to the effect of the surface energy generated, the little agglomerated seeds increased in size, and the architecture of the particles altered to a dumbbell form as the reaction continued. Synthesized particles were changed into micro-rod architecture when the reaction solution got more basic as the pH value increased. That is, the crystal development mechanism and crystal structure behaviour, like degree of supersaturation, reaction–diffusion, surface energy, and so on, have an impact on the crystal growth process and final product form [61]. A

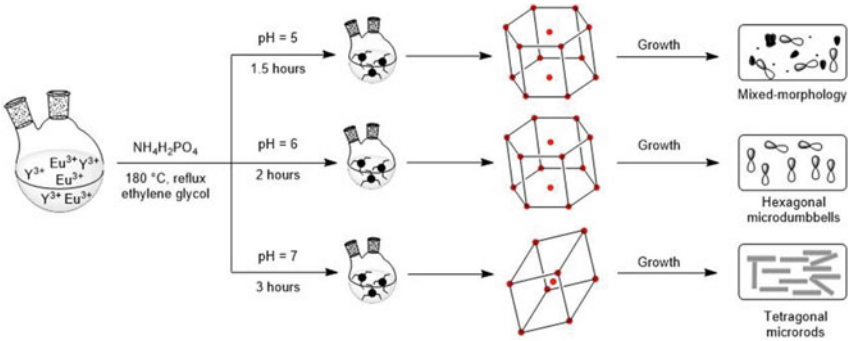

Fig. 4 Schematic illustration on the role of various pH values on the size and morphology of $YPO_4:5Eu^{3+}$

particle's development habit is linked to the relative order of the generating surface energies in a particular reaction system, according to certain research [62]. In general, crystal growth favours the perpendicular direction of the face with greater surface energy, which reduces surface energies while boosting lower surface energies in the region [63]. For micro dump bells, the surrounding edges are having higher surface energy than the central area of the crystal, so that the growth of the crystals mainly occurs on the edge of the particles. Similarly, the presence of surface energy aids in the formation of micro-rod structures, whereas edge sharpening and crystal growth rates in various edge directions are influenced substantially. Furthermore, the microparticles expand dramatically (0.6 μm in diameter and 3.5 mm in height), demonstrating that the microcrystals develop horizontally and vertically as the precipitating system ages. The ensuing red-emitting Eu^{3+} doped yttrium orthophosphate phosphor with various forms is depicted schematically in Fig. 4. When the pH value and reaction time was increased from pH 6 to pH 7 (2–3 h), a significant reduction in particle size occurred, from 5 μm in length (width = 1 μm) to 3 μm in length (width = 0.5 μm), which could be due to an increase in metal ion dissociation in the precipitating system, facilitating the formation of monodispersed micro rods.

6 Optical Properties

Strong Plasmon absorption, enhanced Rayleigh scattering, and surface-enhanced Raman scattering are all-optical phenomena seen in metal nanoparticles that are not found in bulk materials. Because electrons on the surface of the particles (d electrons in Au and Ag) can freely move through the substance. Also, plasmon absorption in metal nanoparticles is more beneficial due to their small size and non-spherical forms. Spherical gold nanoparticles, for example, contain only one Plasmon absorption peak that is independent of particle size. Gold nanorod exhibits two Plasmon absorption peaks.

Luminescence is one of the most important methods for exposing the energy structure and surface states of semiconductor nanoparticles, and it has received a lot of attention. Electrons along with holes are produced whenever a semiconductor is bombarded. If the produced electrons and holes do not recombine fast and become trapped in specific metastable states, energy is required to release them from the traps and recombine them to produce light. Photoluminescence occurs when they spontaneously recombine after some time (PL). The fluorescence mechanism in semiconductor nanoparticles is claimed to be quite complicated, with most nanoparticles exhibiting wide and Stokes shifted luminescence resulting from deep surface traps.

In our earlier publication, we have confirmed that on comparing the emission intensity of hexagonal phase $YPO_4.0.8H_2O:5Eu^{3+}$ micro-dumbbells to irregular particles, the regular h-$YPO_4.0.8H_2O:Eu^{3+}$ micro-dumbbells are anticipated to emit more, shown in Fig. 5. Furthermore, t-$YPO_4:5Eu^{3+}$ micro rods exhibit increased emission, which may be determined by the crystal growth dimension. The orientation and permittivity constants of the host materials, as well as their architectures, confirm the transient dipole field. We believe that architectural differences impacted the ionic dipole field and, as a result, the emission intensity.

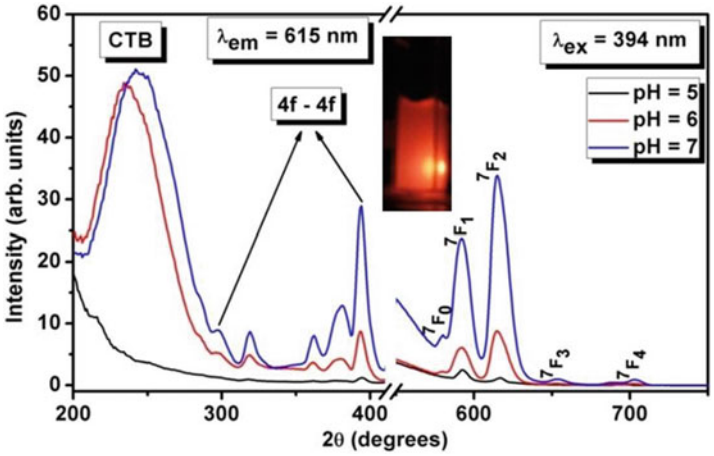

Fig. 5 Excitation and emission spectra of $YPO_4:5Eu^{3+}$ particles. The insets present a photograph of the corresponding eye-visible luminescence

7 Conclusion

In conclusion, descriptions of particle nucleation and growth have been provided. Various nanoparticle synthesis methods have been established, and they are appropriate for the production of nanomaterials of various sizes and forms. Gamma irradiation, sonochemical reduction method, thermal decomposition, sol–gel, and co-precipitation were among the methods discussed. Due to their unique characteristics, such as high plasmon absorption, increased Rayleigh scattering, and surface-enhanced Raman scattering, metal nanomaterials have potential uses in electronics, photonics, biological sensing, and imaging, and other disciplines. Thus, the preparation strategy, which includes pH adjustment based on the age of the precipitating system, might be beneficial for sustaining the development of the solution system of some biologically or technologically essential materials.

References

1. Devi HF, Singh TD (2018) Morphology control synthesis and photoluminescence of yttrium orthophosphate microstructures. Mater Lett 231:8–10
2. Devi HF, Singh MR, Singh TD (2019) Effect of glycine on the growth process of Tb^{3+} doped 2D ZnO nano/microstructures: from broom shape to star-shape flower morphology. J Mater Sci Mater Electron 30:12895–12900
3. Ung D, Tung LD, Caruntu G, Delaportas D, Alexandrou I, Prior IA, Thanh NTK (2009) Variant shape growth of nanoparticles of metallic Fe–Pt, Fe–Pd and Fe–Pt–Pd alloys. CrystEngComm 11:1309–1316
4. Kruszynska M, Borchert H, Parisi J, Kolny-Olesiak J (2010) Synthesis and shape control of $CuInS_2$ nanoparticles. J Am Chem Soc 132:15976–15986
5. Wang C, Tian W, Ding Y, Ma Y, Wang ZL, Markovic NM, Stamenkovic VR, Diamon H, Sun S (2010) Rational synthesis of heterostructured nanoparticles with morphology control. J Am Chem Soc 132:6524–6529
6. Burda C, Chen X, Narayanan R, El-Sayed MA (2005) Chemistry and properties of nanocrystals with different shapes. Chem Rev 105:1025–1102
7. Sau TK, Murphy CJ (2004) Room temperature, high-yield synthesis of multiple shapes of gold nanoparticles in aqueous solution. J Am Chem Soc 126:8648–8649
8. LaMer VK, Dinegar RH (1950) Theory, production, and mechanism of formation of monodispersed hydrosols. J Am Chem Soc 72:4847
9. LaMer VK (1952) Nucleation in phase transitions. Ind Eng Chem 44:1270
10. Ostwald WZ (1900) About the supposed isomerism of red and yellow mercury oxide and the surface tension of solid bodies. Phys Chem 34:495
11. Reiss HJ (1951) The growth of uniform colloidal dispersions. Chem Phys 19:482
12. Lifshitz I, Slyozov VJ (1961) The kinetics of precipitation from supersaturated solid solutions. Phys Chem Solids 19:35
13. Wagner C, Ber B-G (1961) Theory of the aging of precipitation through dissolving (Ostwald ripening). Phys Chem 65:581
14. Mullin JW (1997) In Mullin JW (ed) Crystallization. Butterworth-Heinemann, Boston

15. Myerson AS (1993) Handbook of industrial crystallization. Butterworth-Heinemann Ltd., Oxford
16. Mersmann A (1995) Crystallization technology handbook. M Dekker, New York
17. Chen G, Ohulchanskyy TY, Kumar R, Ågren H, Prasad PN (2010) Ultrasmall monodisperse $NaYF_4$:Yb^{3+}/Tm^{3+} nanocrystals with enhanced near-infrared to near-infrared upconversion photoluminescence. ACS Nano 4(6):3163–3168
18. Longmire M, Choyke PL, Kobayashi H (2008) Clearance properties of nano-sized particles and molecules as imaging agents: considerations and caveats. Nanomedicine 3(5):703–717
19. Li Z, Zhang Y (2015) An efficient and user-friendly method for the synthesis of hexagonal-phase $NaYF_4$:Yb, Er/Tm nanocrystals with controllable shape and upconversion fluorescence. Nanotechnology 19:345606
20. Qian HS, Zhang Y (2008) Synthesis of hexagonal-phase core-shell $NaYF_4$ nanocrystals with tunable upconversion fluorescence. Langmuir 24(21):12123–12125
21. Zou P, Hong X, Ding Y, Zhang Z, Chu X, Shaymurat T, Shao C, Liu Y (2012) Upconversion luminescence of $NaYF_4$:Yb^{3+}/Er^{3+} nanoparticles embedded into PVP nanotubes with controllable diameters. J Phys Chem C 116:5787–5791
22. Bogdan N, Vetrone F, Ozin GA, Capobianco JA (2011) Synthesis of ligand-free colloidally stable water dispersible brightly luminescent lanthanide-doped upconverting nanoparticles. Nano Lett 11:835–840
23. Demazeau G, Largeteau A (2015) Hydrothermal/solvothermal crystal growth: an old but adaptable process. Z Anorg Allg Chem 641(2):159–163
24. Zhang F, Zhao D (2009) Synthesis of uniform rare earth fluoride ($NaMF_4$) nanotubes by in situ ion exchange from their hydroxide [$M(OH)_3$] parents. ACS Nano 3(1):159–164
25. Li H, Lu Z, Cheng G, Rong K, Chen F, Chen R (2014) HEPES-involved hydrothermal synthesis of Fe_3O_4 nanoparticles and their biological application. RSC Adv 5:5059–5067
26. Huang XL, Teng X, Chen D, Tang FQ, He JQ (2010) The effect of the shape of mesoporous silica nanoparticles on cellular uptake and cell function. Biomaterials 31:438–448
27. He F, Yang P, Wang D, Niu N, Gai S, Li X (2011) Self-assembled β-$NaGdF_4$ microcrystals: hydrothermal synthesis, morphology evolution, and luminescent properties. Inorg Chem 50:4116–4124
28. Cao T, Yang Y, Gao Y, Zhou J, Li Z, Li F (2011) High-quality water-soluble and surface-functionalized upconversion nanocrystals as luminescent probes for bioimaging. Biomaterials 32:2959–2968
29. Wang F, Han Y, Lim CS, Lu Y, Wang J, Xu J, Chen H, Zhang C, Hong M, Liu X (2010) Simultaneous phase and size control of upconversion nanocrystals through lanthanide doping. Nature 463(7284):1061–1065
30. Chen D, Shen GZ, Tang KB, Liu YK, Qian YT (2003) Aligned SnS 2 nanotubes fabricated via a template-assisted solvent-relief process. Appl Phys A 77:747
31. Ji M, Chen X, Wai CM, Fulton JL (1999) Synthesizing and dispersing silver nanoparticles in a water-in-supercritical carbon dioxide microemulsion. J Am Chem Soc 121:2631
32. Ohde H, Hunt F, Wai CM (2001) Synthesis of silver and copper nanoparticles in a water-in-supercritical-carbon dioxide microemulsion. Chem Mater 13:4130
33. McLeod MC, McHenry RS, Beckman EJ, Roberts CB (2003) Synthesis and stabilization of silver metallic nanoparticles and premetallic intermediates in perfluoropolyether/CO_2 reverse micelle systems. J Phys Chem B 107:2693
34. Ziegler KJ, Doty RC, Johnston KP, Korgel BA (2001) Synthesis of organic monolayer-stabilized copper nanocrystals in supercritical water. J Am Chem Soc 123:7797
35. Cason JP, Roberts CB (2000) Reverse micelle synthesis and characterization of superparamagnetic $MnFe_2O_4$ spinel ferrite nanocrystallites. J Phys Chem B 104:1217
36. Cason JP, Miller ME, Thompson JB, Roberts CB (2001) Solvent effects on copper nanoparticle growth FFI in AOT reverse micelle systems. J Phys Chem B 105:2297
37. Cason JP, Khambaswadkar K, Roberts CB (2000) Supercritical fluid and compressed solvent effects on metallic nanoparticle synthesis in reverse micelles. Ind Eng Chem Res 39:4749

38. Sun YP, Rollins HW, Guduru R (1999) Preparations of nickel, cobalt, and iron nanoparticles through the rapid expansion of supercritical fluid solutions (RESS) and chemical reduction. Chem Mater 11:7
39. Davidson FM, Schricker AD, Wiacek RJ, Korgel BA (2004) Supercritical fluid–liquid–solid synthesis of gallium arsenide nanowires seeded by alkanethiol-stabilized gold nanocrystals. Adv Mater 16:646
40. Lee DC, Mikulec FV, Korgel BA (2004) Low-temperature growth of carbon nanotubes from the catalytic decomposition of carbon tetrachloride. J Am Chem Soc 126:4951
41. Patra A, Friend CS, Kapoor R, Prasad PN (2002) Upconversion in Er^{3+}:ZrO_2 nanocrystals. J Phys Chem B 106(8):1909–1912
42. Hou Z, Li G, Lian H, Lin J (2012) One-dimensional luminescent materials derived from the electrospinning process: preparation, characteristics, and application. J Mater Chem 22:5254–5276
43. Santa S, Tapec R, Theodoropoulou N, Dobson J, Hebard A, Tan W (2001) Synthesis and characterization of silica-coated iron oxide nanoparticles in microemulsion: the effect of nonionic surfactants. Langmuir 17(10):2900–2906
44. Ge JP, Chen W, Liu LP, Li YD (2006) Formation of disperse nanoparticles at the oil/water interface in normal microemulsions. Chem Eur J 12(25):6552–6558
45. Bönnemann H, Richards RM (2001) Nanoscopic metal particles—synthetic methods and potential applications. Carboxylates, physical basis of radiation-related technologies. Eur J Inorg Chem 10:2455–2480
46. Laurent S, Forge D, Porty M, Roch A, Robic C, Vander EL, Muller RN (2008) Magnetic iron oxide nanoparticles: synthesis, stabilization, vectorization, physicochemical characterization, and biological applications. Chem Rev 108(6):2064–2110
47. Gainer CF, Romanowski M (2014) A review of synthetic methods for the production of upconverting lanthanide nanoparticles. J Innov Opt Health Sci 7(2):1330007
48. Yang M, You H, Liu K, Zheng Y, Guo N, Zhang H (2010) Low-temperature coprecipitation synthesis and luminescent properties of $LaPO_4$:Ln^{3+}, (Ln^{3+} = Ce^{3+}, Tb^{3+}) nanowires and $LaPO_4$:Ce^{3+}, Tb^{3+}/$LaPO_4$ core/shell nanowires. Inorg Chem 49(11):4996–5002
49. Luwang MN, Ningthoujam RS, Srivastava SK, Vatsa RK (2011) Disappearance and recovery of luminescence in Bi^{3+}, Eu^{3+} codoped YPO_4 nanoparticles due to the presence of water molecules up to 800 °C. J Am Chem Soc 133(9):2998–3004
50. Grzyb T (2012) Multifunctionality of $GdPO_4$:Yb^{3+}, T^{b3+} nanocrystals—luminescence and magnetic behaviour. J Mater Chem 22:22989–22997
51. Okitsu K, Nishimura R (2010) Sonochemical reduction method for controlled synthesis of metal nanoparticles in aqueous solutions. In: Proceedings of 20th international congress on acoustics, ICA, August 2010, Sydney, Australia, pp 23–27
52. Obreja L, Foca N, Popa MI, Melnig V (2008) Alcoholic reduction platinum nanoparticles, synthesis by sonochemical method, biomaterials in biophysics. Med Phys Ecol 31–36
53. Rao YN, Banerjee D, Datta A, Das SK, Guin R, Saha A (2010) Gamma irradiation route to the synthesis of highly re-dispersible natural polymer capped silver nanoparticles. Radiat Phys Chem 79:1240–1246
54. Abidi W, Remita H (2010) Gold-based nanoparticles generated by radiolytic and photolytic methods. Recent Pat Eng 4(3):170–188
55. Alivisatos AP (1996) Perspectives on the physical chemistry of semiconductor nanocrystals. J Phys Chem 100:13226
56. Schmid G (2011) Nanoparticles: from theory to application. Wiley, Germany
57. Kunugi S, Yamaoka T (2012) Polymers in nanomedicine, vol 247. Springer Science & Business Media, Berlin, Germany
58. Sau TK, Rogach AL (2012) Complex-shaped metal nanoparticles: bottom-up syntheses and applications. Wiley, Germany
59. Fan W, Bu W, Song X, Sun S, Zhao X (2007) Selective synthesis and luminescent properties of monazite and zircon type $LaVO_4$:Ln (Ln = Eu, Sm, and Dy) nanocrystals. Cryst Growth Des 7:2361–2366

60. Tao AR, Habas S, Yang PD (2008) Shape control of colloidal metal nanocrystals. Small 4:310
61. Yang M, You H, Guo N, Huang Y, Zhengab Y, Zhang H (2010) Synthesis and luminescent properties of orderly $YPO_4:Eu^{3+}$ olivary architectures self-assembled by nanoflakes. CrystEngComm 12:4141–4145
62. Mullin JW (1971) Crystallization. Butterworths, London
63. Buckley HE (1951) Crystal growth. Wiley, New York

Chapter 11
Nanostructures in Ionic Liquid

Somas Singh Urikhinbam and Lenin S. Shagolsem

1 Introduction

Salts are generally perceived to exist in the solid state, that is, in a crystalline state at room temperature. The force that binds the ions together in salt is the strong, long-ranged Coulombic force. This results in the rise of melting points of these salts to a point that is much higher than the room temperature. The Coulombic force could be reduced by geometrically anisotropic ions, thereby lowering the melting temperature. The relatively bulky size, as well as conformational flexibility of the ions, have contributed to a substantial decrease in the melting point [1].

Liquids that contain entirely or almost entirely ions are called *ionic liquids* [2]. This description includes liquids that are traditionally known as molten salts. This molten salt, also known as fused salts, has high melting points.

The advantages of molten salts over aqueous electrolytes are mainly three-fold: high electrical conductivity, fast electrode kinetics, and wider electrochemical windows [3]. The upsides of using salts as electrolytes or reaction media in their liquid state have long been acknowledged. Although molten salts have their advantages, the high melting point of molten salts is sometimes unwelcome. If the melting point of molten salts could be lowered, this could reap many potential benefits.

Even though ionic liquids (ILs) were first reported by Gabriel [4] in 1888, Paul Walden is credited with its discovery when he reported ethyl ammonium nitrate (EAN) in 1914 [5]. EAN was the first example of protic IL with a melting point of 12 °C. Besides this discovery, ILs remained unexplored for more than 40 years. When it came to finding solutions for electroplating metals, Hurley and Weir recognized the latent advantages of lowering the melting points of the molten salts in 1951 [6]. They found that, at room temperature, 1-methyl pyridinium bromide–aluminum chloride ($[C_2py]Br - AlCl_3$) mixture in a 2:1 molarity ratio was liquid.

S. S. Urikhinbam · L. S. Shagolsem (✉)
National Institute of Technology Manipur, Langol, Imphal 795004, India

B. P. Swain (ed.), *Advances in Nanostructured Materials*, Materials Horizons:
From Nature to Nanomaterials, https://doi.org/10.1007/978-981-16-8391-6_11

In the 1980s, new researchers began to take interest in ionic liquids and thus interest in this new field began to spread slowly. During the 1990s, there was an explosion of interest, and researchers from different academic backgrounds working with ILs became aware of the work of one another. From this time onwards, the field of ionic liquid grew significantly, both in terms of the ions utilized and in terms of the applications being studied. These applications range from research labs to industries. The [NTf_2] anion is a typical example of a fluorinated anion, [6] and it has been widely employed in the battery community for many years for the same reasons it is appealing for ionic liquid electrolytes.

2 Protic and Aprotic Ionic Liquids

ILs can be formed by the transfer of a proton from a Brønsted acid, one that can donate a proton, to a Brønsted base, which can accept a proton. Such ILs are called protic ionic liquids (PILs). The degree of proton transfers to produce the salt dictates the physical characteristics of PILs, which are greatly influenced by the relative strength of the acid and base. One of the classic examples of PIL is ethyl ammonium nitrate (EAN), which is formed by the protonation of ethylamine. Since free energy change determines the amount of proton transfer to form a salt, it has a direct influence on the properties of the liquid-like vapor pressure or iconicity. Whereas, ions that do not contain transferable protons are called aprotic ionic liquid (AIL). For example, [C_2mim][BF_4], [C_4mim][NTf_2] etc.

3 Cations and Anions

Since ILs are salts in liquid form, they have cation and anion parts. Most of the room-temperature ILs have organic species as cations with alkyl chains making a tadpole-like structure while anions could be organic or inorganic species. Imidazolium, pyridinium, phosphonium, pyrrolidinium, ammonium, etc., are some examples of organic cations for ILs. While hydrazinium $\left(N_2H_5^+\right)$, sodium $\left(Na^+\right)$, tetrabromophosphite $\left(PBr_4^+\right)$ are some inorganic cations. As for the anions, they could also be inorganic–chlorine $\left(Cl^-\right)$, hexafluorophosphate $\left(PF_6^-\right)$, tetrafluoroborate $\left(BF_4^-\right)$, etc., or organic, such as bis[(trifluoromethyl)sulfonyl]imide $\left[(CF_3SO_2)_2N\right]^-$, trifluoromethyl sulfonate $[CF_3SO_3]^-$ etc. The chemical structures of some cations and anions are shown in Figs. 1 and 2. A significant characteristic of an ionic liquid is that the physical and chemical properties may be greatly affected by a change in cation or anion. The concept of 'designer solvent' introduced by Michael Freemantle [7] is built on the notion that a million combinations of cation–anion will result in ILs with unique properties. This provides a wide pool from which ILs for particular applications can be chosen.

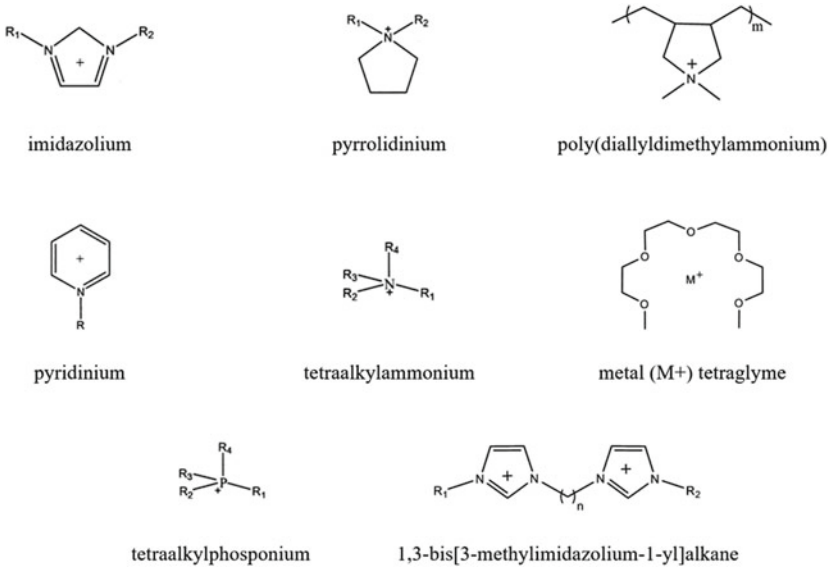

Fig. 1 Chemical structure of some cation species of Ionic Liquid. The layout of the figure was inspired by Fig. 3 in Ref. [8]

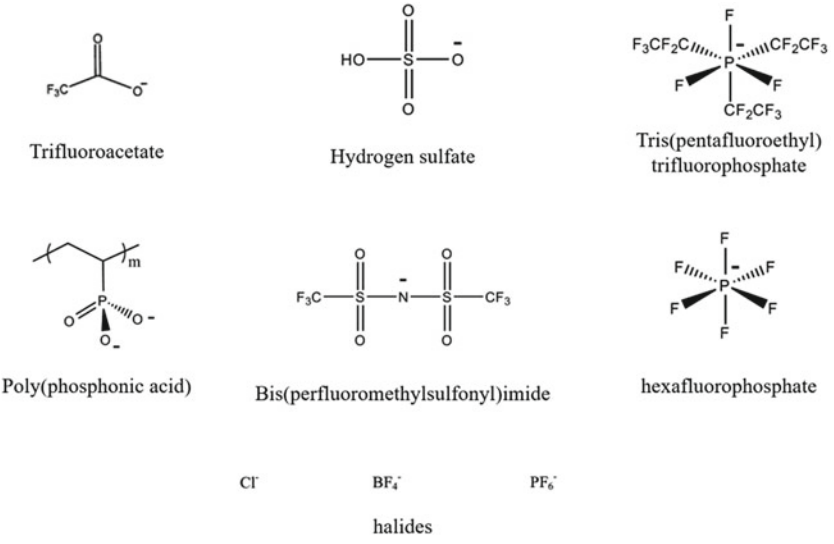

Fig. 2 Chemical structures of some anion species of Ionic Liquid. The layout of the figure was inspired by Fig. 3 in Ref. [8]

4 Some Properties of Ionic Liquids

The large variety in their properties is one of the impressive features of ILs. Some ILs are toxic while others are non-toxic. Some are acidic whereas some are basic. This difference in properties opens up numerous possibilities for independently altering the properties of cations and anions.

4.1 Melting Points

The size of anion and cation plays a major role in the ILs' melting point. With the increase in the size of cation or anion, the melting point tends to decrease. The melting point is also affected by the length of the alkyl chain linked to the cation. For example, the melting point of 1-ethyl-3-methylimidazolium chloride, $[C_2mim]Cl$ is 87 °C whereas that of $[C_2mim][AlCl_4]$ is only 7 °C. Also, $[C_4mim]Cl$ has a melting point of 65 °C, which is 20 °C lesser than that of $[C_2mim]Cl$.

The melting point could also be lowered by mixing another salt into ILs to form a eutectic mixture. For the pure $[C_2mim]Cl$, the melting point is 87 °C, but upon mixing $AlCl_3$ in the ratio 1:2 by mole, the melting point becomes—96 °C.

4.2 Liquid Range and Thermal Stability

The temperature range between the melting point (or glass transition) and boiling point (or thermal decomposition temperature) is known as the liquid range. ILs have a larger liquid range than most molecular solvents. Due to negligible vapor pressure, ILs do not boil or evaporate, rather the temperature of thermal decomposition determines the upper limit of the liquid range. ILs have high thermal stability, for example, 1-alkyl-3-methylimidazolium salts have thermal decomposition temperatures ranging from 250 °C to over 450 °C.

4.3 Vapor Pressure

The lack of measurable vapor pressure or negligible vapor pressure is the most commonly referred beneficial property of ionic liquid but the least investigated. This lack of measurable vapor pressure arises owing to the strong Coulombic interactions among the ions in the liquids. Consequently, ILs do not generally evaporate in reaction vessels and are unable to contribute to air pollution. Even so, distillation can be done on specific ILs at high temperatures and pressures. ILs with long alkyl chain imidazolium cations and $[NTf_2]^-$ anions were predicted by the Rebelo

group to be distillable at temperatures between approximate boiling and dissociation temperatures [9].

4.4 Heat Capacity and Heat Transfer

Thermal conductivity, the amount per unit time at which heat is depleted from the body, is a transport property of ILs which is important for many applications. The thermal conductivity of ILs decreases slightly with the increase in temperature but increases significantly when the ILs contain water. Thermal conductivity is not a commonly studied property of ILs, probably because it is relatively difficult to measure or predict precisely.

The heat capacity of an ionic liquid is the quantity of heat required to raise the temperature of a unit mass of the substance by 1 K. For most liquids the specific heat capacity lies in the range 1.6–2.1 $Jg^{-1}\ K^{-1}$. While those liquids containing hydrogen bond-like water have a higher value of 4.186 $Jg^{-1}\ K^{-1}$. On studying the specific heat capacity of five commonly used ILs: $[C_4mim]Cl$, $[C_4mim][PF_6]$, $[C_2mim][PF_6]$, $[C_6mim][PF_6]$ and $[C_4mim][NTf_2]$, specific heat capacity is reported to be in the range 1.17–1.80 $Jg^{-1}\ K^{-1}$ at 100 °C [10].

4.5 Viscosity

In general, the viscosity of ILs is significantly higher than that of regular organic solvents. As compared to water, its viscosity is at least 10 times higher. And the room temperature viscosity of ILs usually varies from 10 cP to more than 500 cP [11]. Vogel–Fulcher–Tammann (VFT) gives the temperature dependence of the dynamic viscosity, η. According to it, an increase in temperature rapidly decreases the viscosity of ILs. The cation size, particularly with alkyl chain length, is known to influence the viscosity linearly. Also, impurities can have certain effects on viscosity.

4.6 Density

ILs have a higher density with less bulky cations or a short alkyl chain than with bulkier cations. Its density is generally higher than water and is reported to mostly depend on the anion and cation [12–14]. Temperature changes, unlike viscosity, have a minor impact on the density of ILs.

4.7 Solubility

The broad variation of solubility and miscibility properties of ionic liquid is one of the most stimulating features of ionic liquid. They can even dissolve both ionic and covalent compounds. By designing or selecting the right ionic liquid, an extensive variety of organic/inorganic gases, liquids or gases can be dissolved. The discovery that ILs can dissolve kerogen, which is a fossilized organic material found in sedimentary rocks, while remained insoluble to other solvents, shows the dissolving power of ionic liquid [15]. This dissolving ability of ILs is attributed to its polarity and the coordination ability of its ions.

4.8 Water Stability

The stability of ILs in water varies considerably. Although many ILs are water stable, there are some exemptions. For example, ILs with $[PF_6]^-$ and $[BF_4]^-$ cations are not stable in water. ILs which are based on half aluminum, such as $[C_4mim]Cl - AlCl_3$, react strongly with moisture or water and decompose forming hydrogen halide gases and corrosive hydrohalic acid.

4.9 Conductivity

Ionic conductivity and electrochemical stability dictate the applicability of ILs for electrochemical applications. Whereas aqueous electrolytes depend on dissolved salts for their ionic conductivity, ILs possess an intrinsic ionic conductivity since they consist of ions. The conductivity of ILs will inform us of the degree of ion pairing or aggregation in the liquid since ion pairs and aggregate formations reduce the conductivity. The efficiency of ILs in an electrochemical system is determined not only by the structure but also by the dynamics of the ions. The rate of diffusion in the electrolyte influences the mobility of charge carriers. In turn, the rate of diffusion depends inversely on the viscosity of the electrolyte. As mentioned above, the viscosity of ILs reduces with the temperature rise. In ILs, the existence of both the cations and the anions affects both their viscosity and diffusion rates.

4.10 Electrochemical Potential Window

Electrochemical potential window, which is the potential range within which the electrolyte is stable, for ILs depends on various factors, mainly the cations, anions, and the purity of ILs. The oxidation limit at positive potentials is usually determined

by the stability of anion, although it is not always the case. And, the negative potential limit is determined by the stability of the cation.

5 Simulation Approaches to Understanding the Structure

Every reputable discipline of science is built on a complex web of theory and experiment, hypothesis and observation. When fresh ideas prompt new experiments and discoveries need new conceptions, great strides are accomplished. The strong relationship between measurements and thermodynamics makes it difficult to assume that our current understanding of solutions is solely empirical. The thermodynamics of ILs was assumed to be a highly theoretical study. For example, profound knowledge of thermodynamics is required to estimate the partial molar relative ionic entropy of NaCl in dilute solution. However, such weighty issues do not influence the understanding of an ion in solution, a concentrated ionic solution, or an ionic liquid.

The conceptual model of liquid must be such that highly mobile molecules interact with each other through complex intermolecular forces. Averaging of the motion of these microscopic molecules and the interactions over time gives a macroscopic overview describing the thermodynamic parameters accurately. However, there is an extreme difficulty in the successful application of such statistical mechanics' procedure designed for this purpose. In the study of ILs, the importance of computer simulation techniques resides in the capability to evaluate the movements of each molecule, the interactions among them, and the ensemble as well as time averages of the quantities. In studying the computer simulation of fluids, two main techniques have been used viz. (i) Monte Carlo (MC) simulations and (ii) Molecular Dynamics (MD) simulations.

The method of molecular dynamics uses the solution of Newton's equations of motion which is solved numerically. Newton's law, stating that the net force on a particle is equal to the rate of change of momentum of the particle, gives 3 N simultaneous second-ordered differential equation. Solving them in turn gives the positions of the N particles. Periodic boundary conditions are used to simulate a portion of the bulk fluid. Both equilibrium and time-dependent characteristics may be calculated using MD. Several properties can be swiftly calculated. Such properties include such as energy, pressure, radial distribution function, diffusion coefficient, and velocity autocorrelation function, etc.

Having stated that the structure of a fluid can be studied using computer simulation, one might wonder if there is a structure in liquid as its molecules are constantly shifting their positions. Nonetheless, the radial distribution function (RDF) can be used to describe the average positions, and the same quantity may be calculated indirectly using X-ray and neutron scattering experiments. Peaks in the RDF signify a heightened probability of finding an ion at that distance from the center ion. In the RDF, the first peak represents the nearest neighbor, and the succeeding peaks

represent the following center of masses. As a result, measuring the distance between peaks provides information on the length scales of ordering within the IL.

6 Nanostructure in Bulk Ionic Liquids

In contrast to most molecular liquids, ILs have a well-defined bulk liquid and interfacial nanostructure. The nanoscale heterogeneity observable on a length scale bigger than the ionic liquid ions are referred to as nanostructure. Strong inter-molecular interactions for instance hydrogen bonding, Coulombic interaction, electrostatic interaction, and Van der Waals forces, between charge species of ILs form distinct polar (charged) domains. The source of this nanostructure is ion amphiphilicity. Apolar moieties (usually alkyl chains) are solvo-phobically ejected from these charged areas, resulting in the formation of apolar domains. These polar and apolar regions percolate through the bulk to form a bicontinuous nanostructure. The presence of an IL bulk nanostructure was predicted by MD simulations and experimentally confirmed by radiation scattering studies for a variety of ILs [16–18].

Coulombic forces largely control the bulk amphiphilic nanostructures ejecting non-polar groups. The general arrangement of polar domains and non-polar domains is determined by simple packing constraints similar to that of surfactant self-assembly [17]. A dense H-bond network, which was originally assumed to be crucial for amphiphilic nanostructure, is no longer required, and H-bonding plays a minor role in electrostatics in PILs [20, 21].

6.1 Micelle-Like Nanostructure

Margulis suggested an inverse micelle-like structure in AILs, $[C_n min]PF_6$ [22], where spherical anions attract five or more cations in such a manner that the cation head solvates the negative charge and the alkyl tails are pushed outward, producing an interior polar region and exterior apolar region. Similarly, a micelle-like structure was also postulated by Triolo et al. [19] using XRD measurements. Greaves later reported similar findings with PILs. Small-angle X-ray scattering (SAXS), as well as wide-angle X-ray scattering (WAXS), studies for a large diversity of cation and anion combinations, were used to develop the micelle-like model in PILs. Schematic representation of $[C_n min]PF_6$ forming a micelle structure is shown in Fig. 3.

6.2 Mesoscopic Nanostructure

Studies using MD simulation suggested the formation of solvent nanostructures as a function of alkyl chain length [23–25]. With the increase in length of the chain, the

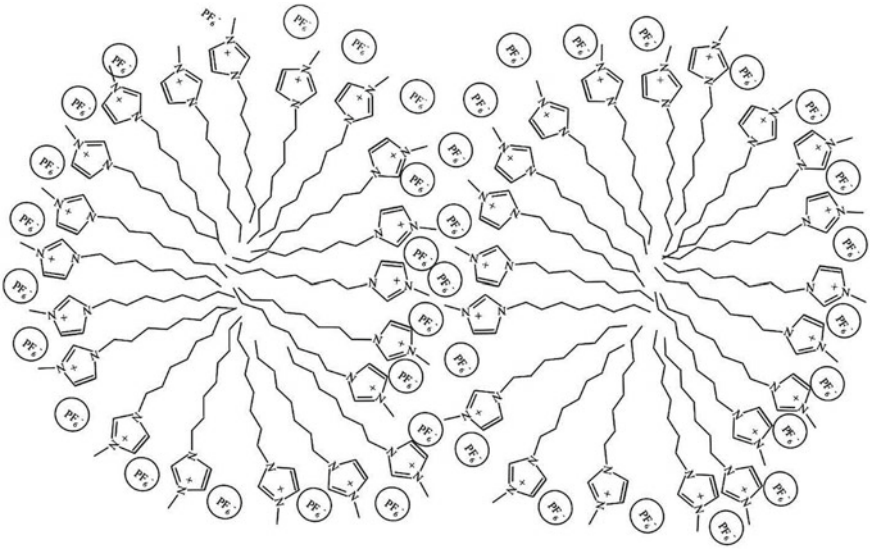

Fig. 3 Schematic representation of 3-*n*-alkyl-1-methylimidazolium-based RTILs with PF_6 anion forming a micelle-like structure. Figure reproduced with permission from Ref. [19]

formation of the heterogeneous domain by aggregation of alkyl tails together became more pronounced. Later studies by the Canongia Lopes group reinforced this model [26]. They reported the formation of a three-dimensional ionic network. Also, hydrocarbon domains can be integrated into a sponge-like, bicontinuous nanostructure by extending the chain of the alkyl group as shown in Fig. 4.

XRD findings show convincing indication of the self-assembled nanostructure, whether viewed as reflecting a micelle-like structure or bicontinuous shape. If the length of the alkyl chains is greater than 4 carbons, a well-defined peak is formed, which is an indication of amphiphilic self-assembly [17]. The main peak is located a

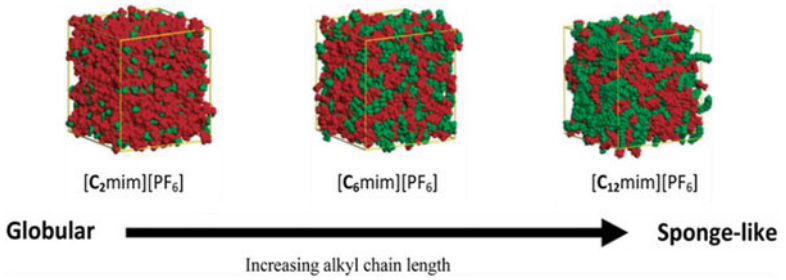

Fig. 4 Snapshot of simulation box containing [$\mathbf{C_n mim}$][$\mathbf{PF}_6$] ILs, where n = 2, 6, 12. Red region represents the polar domains while green represents nonpolar domains. Figures reproduced with permission from Ref. [26]. Copyright 2006 American Chemical Society

distance greater than the single ion or ion-pair, this validates longer-range structuring in the solvent. Scattering studies [27–29] proposed that in the bulk phase, for a chain length of the alkyl greater than or equal to 4 carbons, there exists a sponge-like nanostructure. Lower this critical chain length, globular nonpolar regions are formed.

With the abundant data from simulation studies of aprotic ILs, [20, 24, 30, 31], the formation of mesoscopic structures in ILs is confirmed. Many force fields, as well as interaction potential for simulating ionic liquid, can be cross-validated as there are several simulation studies performed [30, 32–39]. The study carried out by the Canongia Lopes group indicates that changing the geometry of the cation from that of imidazolium to tri-alkyl methyl-ammonium gives different bicontinuous nanostructures [40].

6.3 Nanostructures in IL-Solid Interface

At simple solid—ionic liquid interface: The chemistry of solid–liquid interface differs greatly from the bulk liquids as there is the change in structure and dynamics of solvent molecules at the interface, and continuum theories, which predict unstructured bulk liquid, fail. ILs show oscillatory density profiles similar to ion pair or bilayer dimensions [41–46]. Since ILs can self-assemble, the origin of their structure is different from that of solvation layers in molecular liquids. The structure of ions at the surface is best labeled as layered or lamellar-like and resembles in various ways the structure of adsorbed surfactant layers on lower length scales [47, 48].

Charged non-metal interface: Atomic force microscopy (AFM) experiments were used to study the structuring of molecular liquids perpendicular to the interface and that is adsorbed on the liquid–solid interface [49–52]. Ethyl ammonium nitrate (EAN) ionic liquid—mica interface was studied using amplitude modulation (AM–) AFM experiments. In this study, three different regimes were found: (a) a sponge-like nanostructure in bulk, (b) a layering arrangement near the interface, and (c) a worm-like arrangement at the interface with the surface. From the simple structures of mica and EAN, the above results suggested that a large number of ionic liquids will show similar patterns at the solid–liquid interface as shown in Fig. 5.

Studies from the surface force apparatus (SFA) experiments also show the occurrence of oscillatory layering of ions [54]. Amusingly, no findings of such layering were reported in a large number of SFA papers. [55–57] The reason for the absence of layering was attributed to the large Debye lengths, surface roughness, or strong repulsive force superimposed on the oscillatory forces.

Carbon interface: Graphite is known to have a smooth surface made of carbon atoms; hence its interaction with ILs is quite different from the usually studied mica or silica [58]. Even though graphite is electrically conductive, electric-field can easily enter to some distance (in Å); showing interesting surface chemistry. When single-walled carbon nanotubes are mixed with AILs, gel formation is reported: suggesting that the interactions between uncharged or charged groups of ILs are strong [59]. A structure, on which many researchers agreed upon, emerges which suggests that

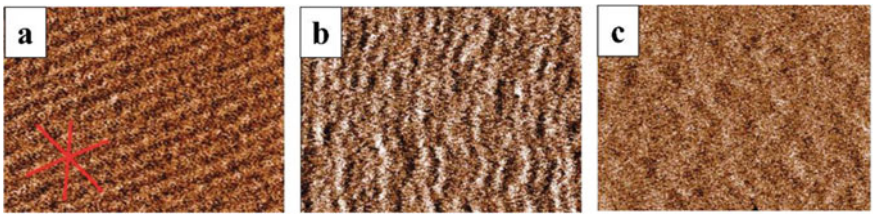

Fig. 5 AFM image of EAN—mica interface with increasing interface—tip distance from **a–c**. Shown here is **a** adsorbed the innermost layer of ions on mica, **b** wormlike structure a further away from the interface, and **c** sponge-like structure in the bulk. Reproduced with permission from ref. [53]. Copyright 2013 PCCP Owner Society

layers of ions are arranged close to the surface causing an increase in solvent density. XRR studies and electrochemical AFM [60–62] experiments at the interface support the suggested structure.

Metal interface: IL structures have been studied at the unbiased metal interface both experimentally and in theory. The presence of strong ion adsorption is evident from these studies [63, 64]. Results from AFM experiments on Au(111) surface are in agreement with the structures at other non-metallic surfaces, such as silica or mica [42]. Study of mercury—IL interface using synchrotron-based XRR data suggest the self-assembly across lateral and longitudinal direction [65]. The checkerboard pattern in the lateral direction while perpendicular to the interface, and bilayer structure were reported.

Ionic liquid films: For applications such as corrosion inhibition, catalysis, lubrication, or analytical applications, to mention some, where a tiny quantity of standalone IL is deposited over a solid to provide some functional benefits, understanding the behavior and structure of IL films are significant. The structures present at the AILs interfaces with numerous substrates including silica, [66] mica, [67], etc., were studied using several techniques used to study surfaces. Results on mica indicate that the ILs, in the micrometer scale, are patchy in lateral dimensions. Primarily, layer-by-layer development is observed for Ni(111), and at sub-monolayer coverage, a bi-layered structure is adopted by the ions.

7 Exploiting Nanostructure in Applications

Nanomaterial production is difficult owing to the unusual working situations of small length and time scales, as well as large surface-to-volume ratios. To bridge the efficiency gap, synthetic nano-reactors are being explored because of their distinct cavity or nano spaces in which reactions can occur. Although scaling of self-assembled phases forming polar or apolar domain has not been achieved, studies have been carried out for mass nanofabrication. Thus, ILs have been recommended as prospective self-assembled nano-reactors. The bicontinuous phase is formed naturally in pure

ILs and in high water content, the structure is also quite tough [68]. This suggests that IL is well suited for the nanotechnology revolution.

In several IL solvents, nanosized and microsized particles are frequently produced without aggregation. The internal structure of the ILs is responsible for the size of metal nanoparticles [69] since nucleation and development of metal nanoparticles seem to be confined in the apolar domain.

For polymers, many benefits are offered by ILs as functional additives or as a solvent for polymerization [70, 71]. Because of the solvent nanostructure, long-chain polymers as well as hydrophobic and hydrophilic monomers can be easily dissolved. Furthermore, the efficacy of ILs as additives is linked to ion amphiphilicity, indicating a direct involvement of self-assembly in structural regulation.

Electrodeposition: ILs have a large electrochemical window. And owing to this, electrodeposition of minerals like Al, Bi, Co, Cu, Ge, etc., can be easily executed. Since normal electrolytes have very small electrochemical windows and break down easily, most of the electrodepositions cannot be performed in these normal electrolytes. The ion–surface interaction strongly influences the size and morphology of the electrodeposit. If there is strong interaction, nanocrystalline deposits appear, whereas large microsized deposits appear when the interaction is weak [42].

Medicine and medical research: Medical research is one new area of ionic liquid interest. ILs have been sluggish to gain traction in the field because ionic liquid ions are thought to be poisonous and bioaccumulative. This situation began to change after the Gordon Research conference in 2014 [72]. ILs, after tuning the ion structures to match or resemble neutral molecules, began to be included in active pharmaceutical ingredients, preservatives, antibiofilm agents, prodrugs, disinfectants, etc. [73–75].

Almost half of all the medications are delivered as salts (solid). The ionic form of ionic liquid is critical to its function and also underlines its medical science heritage in many ways [76]. Till now, much of the research work has gone toward customizing the structure of the material such that it melts at a temperature below 37 °C. This allows the candidate ILs to be delivered and persist in the human body as a fluid.

Cellulose dissolution: A wide range of chemical compounds including lipids, biopolymers, and other small molecules can be extracted from various biomaterials such as lignocellulose biomass, microalgae, coal, etc., using ILs. IL anion, IL cation structures, side-chain length, functional group, and cation size have been identified as the factors that dictate the lignocellulosic biomass dissolution [77]. Cellulose is known to be amphiphilic, in the crystal hydrophobic interactions help to keep it stable in the liquid phase. [78] Every successful dissolution of cellulose in an IL occurred when one of the ions is amphiphilic. A thorough understanding of the mechanism of how ionic self-assembly facilitates biomass dissolution is essential [79]. Recently, the impact of acid hydrolysis on cellular dissolving in an ionic liquid under moderate conditions is investigated [80].

Mineral extraction: Mineral processing is a unique use of ILs for analytic separation [81]. Extracting minerals from ore requires a lot of energy and a huge amount of solvent [82]. But ILs are not possible to replace techniques like the froth floatation process due to the high cost of ILs. Even so, ILs can be used as additives to regulate the surface tension for their surfactant-like behavior. Understanding self-assembly is

anticipated to be crucial in developing future material recovery solutions using ILs. Recently, the extraction of rare earth metal ions with an undiluted hydrophobic pseudoprotic ionic liquid is studied [83]. More study on ionic liquid solvation is needed since recovery could be done simply by nucleation, aggregation, or precipitation.

Energy storage: There has been much hype for ILs for energy-based applications like batteries, fuel cells, capacitors, solar cells, thermal energy storage mediums. Surprisingly, solid ILs or quasi-solid ILs electrolytes give better results, signifying the future contribution of ionic liquid crystals or glass structures will not go unnoticed [84, 85]. A variation of an existing ionic liquid model has been studied to investigate the effect of surface transition and adsorption on ionic liquid capacitors [86]. The thermal conductivity, as well as the charge transport mechanism, is associated with degrees of ion self-assembly. Because of the reasons mentioned above, further fundamental research is needed to guide the ionic liquid design, structures created, and the general efficiency of the process.

CO_2 capture: ILs also find their way to carbon dioxide gas capture applications [87, 88]. An ion structure that reacts to CO_2 gas or one that physically dissolves CO_2 is two different scenarios reported in many studies. Chemically trapping CO_2 is encouraging because ions in ionic liquid to modified for better stoichiometries by functionalizing with amine groups. One disadvantage of this method is that it might result in a significant increase in solvent viscosity but there are ways to overcome this, for instance, selecting counter-ions such that the H-bonding network is not supported. Another intriguing option is to employ ILs containing benzimidazole, which modifies the phase from solid to liquid when carbon dioxide is dissolved. The mixture of water and ionic liquid having basic anions such as imidazolate or acetate can be used as an aqueous buffered solution in which water molecules trapped by ion pairs react with carbon dioxide reversibly to form bicarbonate species [89].

Lubrication: Owing to the strong interaction between ILs and surface, and the self-assembly capability in confined interfaces or bulk, ILs hold many advantages over conventional lubricants. This implies that under surface compression, ILs withstand being squeezed out, leading to a strong boundary coating that can withstand large pressure than a molecular lubricant of equivalent quantity [90]. Even after being dissolved in a different solvent, ILs' ability to self-assemble is preserved, this paves the road for ionic liquid additives in tribology [91, 92]. If the second solvent promotes amphiphilic self-assembly, even a 100-fold dilution will have the same effect as the pure ionic liquid to lubricate its surface. Several types of research are being carried out in this field, such as recently Mozes group explored ILs as grease base liquids at different base liquid concentrations [93]. This study suggests that ionic liquid base liquids can produce the unexpected shear thinning effect.

8 Conclusion

In summary, the ionic liquid is one of a kind liquid with huge potential for a wide variety of applications. Low vapor pressure, large electrochemical windows, the

ability to dissolve cellulose are some of the many properties that caught the attention of many researchers. Besides, by choosing the right combination of cation and anion, one can make an ionic liquid suitable to their needs. This characteristic in combination with its low melting temperature becomes the main selling point of ionic liquid. Because ILs are more complex than molecular solvents, their bulk and interfacial structure differ significantly. The ability to self-assemble is responsible for many of its unique properties and structures in bulk and at the interface. This ability is solely responsible for many of the past, current, and future interests in ionic liquid.

Nanostructures formed in ILs are due to ion amphiphilicity. Apolar species, usually alkyl chains, are solvophobic and they group forming the apolar domains, while the polar (charged) parts of the ions group together to form the polar domains. This leads to the formation of nanostructures such as micelle-like nanostructure, sponge-like bicontinuous structure, globular structure, or layering formation. These nanostructures can be exploited to be used in applications like cellular dissolution, mineral extraction, energy storage, etc. Certainly, an ion structure that reacts to CO_2 gas can be used to capture CO_2. There is an ever-increasing interest in the effect of the amphiphilic nanostructure of ILs owing to the various applications they can provide. Understanding these nanostructures from simulation as well as experimental points of view will open doors to a wide variety of applications.

References

1. Krossing I, Slattery JM, Daguenet C, Dyson PJ, Oleinikova A, Weingärtner H (2006) Why are ionic liquids liquid? A simple explanation based on lattice and solvation energies. J Am Chem Soc 128:13427–13434
2. Freemantle M (2010) An introduction to ionic liquids. The Royal Society of Chemistry, Cambridge
3. Li Q, Jensen JO, Bjerrum NJ (2009) Chemistry, electrochemistry, and electrochemical applications. In: Encyclopedia of electrochemical power sources. pp 695–708
4. Gabriel S. Ber 188:2669
5. Walden P (1914) Bull Acad Imper Sci (St Petersburg) 1800
6. Bonhote P, Dias AP, Papageorgiou N, Kalyanasundaram K, Gratzel M (1996) Hydrophobic, highly conductive ambient-temperature molten salts. Inorg Chem 35:1168–1178
7. Freemantle M (1998) Designer solvents 76:32–37
8. Hayes R, Warr GG, Atkin R (2015) Structure and nanostructure in ionic liquids. Chem Rev 115:6357–6426
9. Rebelo LPN, Canongia Lopes JN, Esperanca JMSS, Filipe E (2005) On the critical temperature, normal boiling point, and vapor pressure of ionic liquids. J Phys Chem B Lett 109:6040–6043
10. Holbrey JD, Reichert WM, Reddy RG, Rogers RD (2003) Ionic liquids as green solvents: progress and prospects; ACS symposium series. American Chemical Society, Washington, DC
11. Holbrey JD, Rogers RD (2008) In: Wasserscheid P, Welton T (eds) Ionic liquids in synthesis, vol 1. Wiley-VCH, Weinheim
12. Neves CM, Batista ML, Claudio AF, Santos LM, Marrucho IM, Freire MG, Coutinho JA (2010) Thermophysical properties and water saturation of [PF_6]-based ionic liquids. J Chem Eng Data 55:5065–5073
13. Neves CM, Carvalho PJ, Freire MG, Coutinho JA (2011) Thermophysical properties of pure and water-saturated tettradecyltrihexylphosphonium-based ionic liquids. J Chem Thermodyn 43:948–957

14. Rocha MA, Neves CM, Freire MG, Russian O, Triolo A, Coutinho JA, Santos LM (2013) Alkylimidazolium based ionic liquids: impact of cation symmetry on their nanoscale structural organization. J Phys Chem B 117:10889–10897
15. Patell Y, Seddon KR, Dutta L, Fleet A (2003) The dissolution of kerogen in ionic liquids. In: Rogers RD, Seddon KR, Volkov S (eds) Green industrial applications of ionic liquids. NATO Science Series (Series II: Mathematics, Physics and Chemistry), vol 92. Springer, Berlin
16. Hayes R, Imberti S, Warr GG, Atkin R (2011) Amphiphilicity determines nanostructure in protic ionic liquids. Phys Chem Chem Phys 13:3237–3247
17. Triolo A, Russina O, Bleif HJ, Cola ED (2007) Nanoscale segregation in room temperature ionic liquids. J Phys Chem 111:4641–4644
18. Greaves TL, Kennedy DF, Mudie ST, Drummond CJ (2010) Diversity observed in the nanostructure of protic ionic liquids. J Phys Chem B 114:10022–10031
19. Triolo A, Russina O, Fazio B, Triolo R, Cola ED (2008) Morphology of 1-alkyl-3-methylimidazolium hexafluorophosphate room temperature ionic liquids. Chem Phys Lett 457:362–365
20. Jiang W, Wang Y, Voth GA (2007) Molecular dynamics simulation of nanostructural organization in ionic liquid/water mixtures. J Phys Chem B 111:4812–4818
21. Hayes R, Imberti S, Warr GG, Atkin R (2014) Effect of cation alkyl chain length and anion type on the protic ionic liquid nanostructure. J Phys Chem C 118:13998–14008
22. Margulis CJ (2004) Computational study of imidazolium-based ionic solvents with alkyl substitutes of different lengths. Mol Phys 102:829–838
23. Wang Y, Voth GA (2005) Unique spatial heterogeneity in ionic liquids. J Am Chem Soc 127:12192–12193
24. Wang Y, Voth GA (2006) Tail aggregation and domain diffusion in ionic liquids. J Phys Chem B 110:18601–18608
25. Urahata SM, Riberio MCC (2004) Structure of ionic liquids of 1-alkyl-3-methylimidazolium cations: a systematic computer simulation study. J Chem Phys 120:1855
26. Canongia Lopes JN, Padua AA (2006) Nanostructural organization in ionic liquids. J Phys Chem B 110:3330–3335
27. Triolo A, Russina O, Fazio B, Battista G, Carewska M, Passerini S (2009) Nanoscale organization in piperidinium-based room temperature ionic liquids. J Chem Phys 130:164521
28. Bodo E, Gontrani L, Triolo A, Caminiti R (2010) Structural determination of ionic liquids with theoretical methods: C_8mimBr and C_8mimCl. Strength and weakness of current force fields. J Phys Chem Lett 1:1095–1100
29. Russina O, Triolo A, Gontrani L, Caminiti R, Xiao D, Hines Jr LG, Bartsch RA, Quitevis EL, Plechkova N, Seddon KR (2009) Morphology and intermolecular dynamics of 1-alkyl-3-methylimidazolium bis{(trifluoromethane)sulfonyl}amide ionic liquids: structural and dynamic evidence of nanoscale segregation. J Phys Condens Matter 21:424121
30. Jiang W, Yan T, Wang Y, Voth GA (2008) Molecular dynamics simulation of the energetic room temperature ionic liquid, 1-hydroxyethyl-4-amino-1,2,3-triazolium nitrate (HEATN). J Phys Chem B 112:3121–3131
31. Shimizu K, Bernardes CES, Canongia Lopes JN (2014) The complex structure of ionic liquids at an atomistic level: from "red-and-greens" to charge templates. Pure Appl Chem 86(2):119–133
32. Morrow TI, Maginn EJ (2002) Molecular dynamics study of the ionic liquid 1-n-Butyl-3-methylimidazolium hexafluorophosphate. J Phys Chem B 106:12807–12813
33. Liu Z, Huang S, Wang W (2004) A refined force field for molecular simulation of imidazolium-based ionic liquids. J Phys Chem B 108:12978–12989
34. Canongia Lopes JN, Deschamps J, Padua AAH (2004) Modeling ionic liquids using a systematic all-atom force field. J Phys Chem B 108:2038–2047
35. Margulis CJ, Stern HA, Berne BJ (2002) Computer simulation of a "green chemistry" room-temperature ionic solvent. J Phys Chem B 106:12017–12021
36. Micaelo NM, Baptista AM, Soares CM (2006) Parametrization of 1-butyl-3-methylimidazolium hexafluorophosphate/nitrate ionic liquid for the GROMOS force field. J Phys Chem B 110:14444–14451

37. Koddermann T, Reith D, Ludwig R (2013) Comparison of force fields on the basis of various model approaches—how to design the best model for the $[C_nmim][NTf_2]$ family of ionic liquids. Chem Phys Chem 14(14):3368–3374
38. Borodin O (2009) Polarizable force field development and molecular dynamics simulations of ionic liquids. J Phys Chem B 113:11463–11478
39. Chaban VV, Voroshylova IV, Kalugin ON (2011) A new force field model for the simulation of transport properties of imidazolium-based ionic liquids. Phys Chem Chem Phys 13:7910–7920
40. Shimizu K, Costa Gomes MF, Padua AAH, Rebelo LPN, Canonhia Lopes JN (2010) Three commentaries on the nano-segregated structure of ionic liquids. J Mol Struct (THEOCHEM) 946:70–76
41. Hayes R, Wakeham D, Atkin R (2012) In: Seddon KR, Plrchkova N (eds) Ionic liquids UnCOILed: critical expert overviews. Wiley, New York
42. Atkin R, Abedin SZ, Hayes R, Gasparotto LHS, Borisenko N, Endres F (2009) AFM and STM studies on the surface interaction of [BMP]TFSA and [EMIm]TFSA ionic liquids with Au(111). J Phys Chem C 113:113266
43. Hayes R, Abedin SZ, Atkin R (2009) Pronounced structure in confined aprotic room-temperature ionic liquids. J Phys Chem B Lett 113:7049–7052
44. Wakeham D, Hayes R, Warr GG, Atkin R (2009) Influence of temperature and molecular structure on ionic liquid solvation layers. J Phys Chem B 113:5961–5966
45. Horn RG, Evans DF, Ninham BW (1988) Acid–base property and pH of protic ionic liquids. J Phys Chem 92:3531
46. Mezger M, Schramm S, Schroder H, Reichart H, Deutsch M, De Souza EJ, Okasinski JS, Ocko BM, Honkimaki V, Dosch H (2009) Layering of $[BMIM]^{+-}$based ionic liquids at charged sapphire interface. J Chem Phys 131:094701
47. Atkin R, Craig VSJ, Wanless EJ, Biggs S (2003) Mechanism of cationic surfactant adsorption at the solid—aqueoup interface. Adv Colloid Interface Sci 103:219–304
48. Warr GG (2000) Surfactant adsorbed layer structure at solid/solution interfaces: impact and implications of AFM imaging studies. Curr Opin Colloid Interface Sci 5:88–94
49. Voitchovsky K (2013) Anharmonicity, solvation forces, and resolution in atomic force microscopy at the solid–liquid interface. Phys Rev E 88:022407
50. Voïtchovsky K, Kuna JJ, Contera SA, Tosatti E, Stellacci F (2010) Direct mapping of the solid-liquid adhesion energy with subnanometre resolution. Nat Nanotechnol 5:401−405
51. Ricci M, Spijker P, Voïtchovsky K (2014) Water-induced correlation between single ions imaged at the solid–liquid interface. Nat Commun 5:4400
52. Ricci M, Spijker P, Stellacci F, Molinari J-F, Voïtchovsky K (2013) Direct visualization of single ions in the stern layer of calcite. Langmuir 29:2207–2216
53. Segura JJ, Elbourne A, Wanless EJ, Warr GG, Voitchovsky K, Atkin R (2013) Adsorbed and near surface structure of ionic liquids at a solid interface. Phys Chem Chem Phys 15:3320
54. Smith AM, Lovelock KRJ, Gosvami NN, Welton T, Perkin S (2013) Quantized friction across ionic liquid thin films. Phys Chem Chem Phys 15:15317–15320
55. Min Y, Akbulut M, Sangoro JR, Kremer F, Prud'homme RK, Israelachvili JJ (2009) Measurement of forces across room temperature ionic liquids between mica surfaces. Phys Chem C 113:16445
56. Bou-Malham I, Bureau L (2010) Nanoconfined ionic liquids: effect of surface charges on flow and molecular layering. Soft Matter 6:4062
57. Gebbie MA, Valtiner M, Banquy X, Fox ET, Henderson WA, Israelachvili JN (2013) Ionic liquids behave as dilute electrolyte solutions. Proc Natl Acad Sci USA 110:9674–9679
58. Atkin R, Warr GG (2005) Self-assembly of a nonionic surfactant at the graphite/ionic liquid interface. J Am Chem Soc 127:11940–11941
59. Fukushima T, Kosaka A, Ishimura Y, Yamamoto T, Takigawa T, Ishii N, Aida T (2003) Molecular ordering of organic molten salts triggered by single-walled carbon nanotubes. Science 300:2072–2074
60. Black JM, Walters D, Labuda A, Feng G, Hillesheim PC, Dai S, Cummings PT, Kalinin SV, Proksch R, Balke N (2013) Bias-dependent molecular-level structure of electrical double layer in ionic liquid on graphite. Nano Lett 13:5954–5960

61. Li H, Wood RJ, Rutland MW, Atkin R (2014) An ionic liquid lubricant enables superlubricity to be "switched on" in situ using electrical potential. Chem Commun 50:4368–4370
62. Li H, Wood RJ, Endres F, Atkin R (2014) Influence of alkyl chain length and anion species on ionic liquid structure at the graphite interface as a function of applied potential. J Phys Condens Matter 26:284115
63. Binetti E, Panniello A, Tommasi R, Agostiano A, Fantini S, Curri ML, Striccoli M (2013) Interaction of TiO_2 Nanocrystals with imidazolium-based ionic liquids. J Phys Chem C 117:12923–12929
64. Andanson JM, Baiker AJ (2013) Interactions of 1-ethyl-3-methylimidazolium trifluoromethanesulfonate ionic liquid with alumina nanoparticles and organic solvents studied by infrared spectroscopy. Phys Chem C 117:12210–12217
65. Alam MT, Islam MM, Okajima T, Ohsaka T (2008) Ionic liquid structure dependent electrical double layer at the mercury interface. J Phys Chem C 112:2601–2606
66. Gong X, Frankert S, Wang Y, Li L (2013) Thickness-dependent molecular arrangement and topology of ultrathin ionic liquid films on a silica surface. Chem Commun 49:7803–7805
67. Spohr E (1998) Computer simulation of the structure of the electrochemical double layer. J Electroanal Chem 450:327–334
68. Hayes R, Imberti S, Warr GG, Atkin R (2012) How water dissolves in protic ionic liquids. Angew Chem Int Ed 51:7468−7471
69. Gindri IM, Frizzo CP, Bender CR, Tier AZ, Martins MAP, Villetti MA, Machado G, Rodriguez LC, Rodrigues DC (2014) Preparation of TiO_2 nanoparticles coated with ionic liquids: a supramolecular approach. ACS Appl Mater Interfaces 6:11536–11543
70. Greaves TL, Drummond C (2008) Ionic liquid as amphiphilieself-assembly media. J Chem Soc Rev 37:1709–1726
71. Lu J, Yan F, Texter J (2009) Advanced applications of ionic liquids in polymer science. Prog Polym Sci 34:431–448
72. Gordon research conference "Ionic Liquids: Solvents, Materials, or Medicines?", Newry, Maine, August, 2014
73. Ferraz R, Branco LC, Prudêncio C, Noronha JP, Petrovski Ž (2011) Ionic liquids as active pharmaceutical ingredients. ChemMedChem 6:975–985
74. Ionic Liquid Applications (2010) Pharmaceuticals, therapeutics, and biotechnology. American Chemical Society, Washington, DC
75. Cojocaru OA, Bica K, Gurau G, Narita A, McCrary PD, Shamshina JL, Barber PS, Rogers RD (2013) Prodrugionic liquids: functionalizing neutral active pharmaceutical ingredients to take advantage of the ionic liquid form. MedChemComm 4:559–563
76. Kumar V, Malhotra SV (2010) Ionic liquid applications: pharmaceuticals, therapeutics, and biotechnology, vol 1038. American Chemical Society, Washington, DC
77. Badgujar KC, Bhanage BM (2015) Factors governing dissolution process of lignocellulosic biomass in ionic liquid: current status, overview and challenges. Bioresour Technol 178:2–18
78. Medronho B, Romano A, Miguel M, Stigsson L, Lindman B (2012) Rationalizing cellulose (in)solubility: reviewing basic physicochemical aspects and role of hydrophobic interactions. Cellulose 19:581–587
79. Wang H, Gurau G, Pingali SV, O'Neill HM, Evans BR, Urban VS, Heller WT, Rogers RD (2014) Physical insight into switchgrass dissolution in ionic liquid 1-ethyl-3-methylimidazolium acetate. ACS Sustain Chem Eng 2:1264–1269
80. Acharya S, Hu Y, Abidi N (2021) Cellulose dissolution in ionic liquid under mild conditions: effect of hydrolysis and temperature. Fibers 9:5
81. Sun P, Armstrong DW (2010) Ionic liquid in analytical chemistry. Anal Chim Acta 661:1–16
82. Rao SR (2003) Surface chemistry of froth flotation, 2nd edn. Kluwer Academic/Plenium Publishers, New York
83. Matsumoto M, Yamaguchi T, Tahara Y (2020) extraction of rare earth metal ions with an undiluted hydrophobic pseudoprotic ionic liquid. Metals 10:502
84. Cooper EI, O'Sullivan EJ (1992) Proc. 8th Int. Symp. Molten Salts, vol 92-16. Electrochemical Soc., Pennington, NJ, pp 386

85. Warner IM, El-Zahab B, Siraj N (2014) perspectives on moving ionic liquid chemistry into the solid phase. Anal Chem 86:7184–7191
86. Chao H, Wang ZG (2020) Effects of surface transition and adsorption on ionic liquid capacitors. J Phys Chemm Lett 11:1767–1772
87. Cevasco G, Chiappe C (2014) Are ionic liquid a proper solution to current environmental challenges? Green Chem 16:2375–2385
88. Bates ED, Mayton RD, Ntai I, Davis JH (2002) CO_2 capture by task specific ionic liquids. J Am Chem Soc 124:926–927
89. Dupont J, Simon NM, Zanatta M, Santos FP, Corvo MC, Cabrita EJ (2017) Carbon dioxide capture by aqueous ionic liquid solutions. ChemSusChem 10
90. Perkin S, Albrecht T, Klein J (2010) Layering and shear properties of an ionic liquid, 1-ethyl-3-methylimidazolium ethylsulfate, confined to nano-films between mica surfaces. Phys Chem Chem Phys 12:1243–1247
91. Reichardt C (2007) Solvents and solvent effects: an introduction. Org Process Res Dev 11:105
92. Yang X, Meng Y, Tian Y (2014) Effect of imidazolium ionic liquid additives on lubrication performance of propylene carbonate under different electrical potentials. Tribol Lett 56:161–169
93. Mozes R, Cooper PK, Atkin R, Li H (2017) Ionic liquids as grease base liquids. Lubricants 5:31

Chapter 12
Recent Advances in Nanostructured Polymers

Thoudam Vilip Singh and Lenin S. Shagolsem

1 Introduction

Polymers are already interesting on their own. However unimaginable it may seem, our DNA and a piece of plastic are fundamentally similar to each other in the sense that they are both polymers. If we look at the molecular scale, both of them are made of repeating units called monomers. They are the fabric of the natural world. Beyond this, our lives also depend on a broad range of synthetic polymers. The discovery and the invention of polymers have revolutionized industries. On the other hand, nanotechnology has proven and still has great promise to offer countless breakthroughs that have and will change the course of technological advances in the fields of physics, chemistry, biology, materials science, and engineering. When nanotechnology combines with polymers, they can bring out superior and improved properties of matter and give opportunities to a lot of applications that are previously impossible in the bulk forms.

On the other hand, nanotechnology holds the key to solving numerous problems. For instance, the mortality rate due to infectious disease, especially in developing countries where there are inadequate vaccines, is quite high. Regarding the treatment of these infectious diseases, the use of nano-sized carriers for novel and existing drugs has great potential to prevail over many concerns like low on-target bioavailability and inadequate accumulation of the therapeutic drugs in the target site [1]. Furthermore, today we are facing extraordinary health and social crisis globally because of the coronavirus disease 2019 (COVID-19) pandemic caused by acute respiratory syndrome coronavirus-2 (SARS-CoV-2). Disinfectants and sensors based on nanotechnology for SARS-CoV-2 were reported by Talebian and coworkers [2]. Other means to fight this disease include the use of nanotechnology-incorporated surface sanitizers. Medical provisions like respiratory masks that are made efficient at the filtration of unwanted elements and that have antimicrobial properties are made

T. V. Singh (✉) · L. S. Shagolsem
National Institute of Technology Manipur, Langol, Imphal 795004, India

B. P. Swain (ed.), *Advances in Nanostructured Materials*, Materials Horizons:
From Nature to Nanomaterials, https://doi.org/10.1007/978-981-16-8391-6_12

with the use of nanofibers, and nanoparticles. Moreover, several of these nanostructured materials are based on different types of polymers. Rashidzadeh et al. reported the role of polymer-based nanotechnology in providing nano-based therapeutics in the fight against the novel coronavirus [3]. Polymer-based nanostructured materials have already been used against respiratory viruses [4–6]. Our well being is also defined by the availability of safe, clean, and adequate water. In the context of global water issues, engineered polymer-based nanomaterials can be of use in removing organic and inorganic contaminants from wastewater [7]. Although nanotechnology has endless opportunities to tackle our problems, nanosafety must be kept in mind. Recently, the toxicology and the ecotoxicology of polymeric nanoparticles were reported [8]. The same goes for its impact on the COVID-19 pandemic [9].

One of the most awe-inspiring things about human beings is their moral fiber to never stop improving the ways of their living. In this endless journey of progress and development, materials science plays a critical role. A fragment of this subject is polymer science and the concern of this chapter is a concise study of the recent progress in nanotechnology and their materials based on polymers. Polymeric substances in which the internal structures are tailored at the nanoscale are referred to as nanostructured polymers.

2 Polymer-Based Nanostructured Materials

2.1 Polymer Nanoparticles

There are colloidal solids in which sizes range from 1 to 1000 nm that can be combined with an active compound with a polymeric core. They are called *polymer nanoparticles*. Two things characterized by morphologies are taken into account when we talk of nanoparticles. They are polymer nanospheres and polymer nanocapsules. Polymer nanospheres take the form of solid spherical polymeric networks and are thus also known as matrix-type nanodevices or simply matrix systems. They are often used in drug delivery where the bioactive elements of the drugs are adsorbed on the spherical surface or kept inside the nanoparticles. On the other hand, polymer nanocapsules are characterized by the presence of solid network-like polymeric shells in which the active elements or proteins or the drugs are put inside a liquid like water or oil.

2.1.1 Polymer Nanospheres

Polymer nanospheres are small enough to pass any capillary vessels. Specific organs such as the liver, lungs, and spleen can be targeted through a variety of ways viz. nasal, oral, parenteral route. Because of these advantages, their applications include drug

delivery, theranostics, bioimaging, investigation of in vitro anti-glioma, and anti-inflammatory activities. There are, however, disadvantages of using these particles. Not only does it take skill to produce them, but they are also difficult in handling in dry or liquid forms. Moreover, there is a problem of nanospheres aggregation.

Different types of polymers are used in their synthesis and production. They include biopolymers such as chitosan, albumin, and gelatin. Homopolymers like poly(lactide) (PLA) and poly(lactide-*co*-glycolide) (PLGA) are also used. Poly(lactide)-poly(ethylene glycol) (PLA-PEG) and poly(lactide-*co*-glycolide)-poly(ethylene glycol) (PLGA-PEG) are copolymer while dextran and polyvinyl alcohol (PVA) are polymeric colloid stabilizer used in designing the polymer nanospheres. For instance, PLA and PLGA were used in making polymeric core–shell nanoparticles that can be used in drug delivery technology. Rapamycin-loaded polysorbate 80-coated PLGA nanoparticles and fenofibrate-loaded biodegradable nanoparticles were used for the study of diabetic retinopathy and ocular neovascularization [10] (Fig. 1).

Depending on the function of the nanoparticles, they are produced in different ways. One such process is called *solvent evaporation* or *extraction method* [12, 13]. Here the first step is the preparation of a suitable organic phase which takes into account a polar organic solvent to dissolve the polymer and the active substance included by dispersion or dissolution. The use of chemicals like dichloromethane and chloroform has been replaced by less toxic ethyl acetate. Next, it is in the aqueous phase in which the organic solution is emulsified with the help of a suitable emulsifying agent like polyvinyl alcohol or gelatin to form oil-in-water (O/W) emulsion. A high-speed homogenization ultrasonication is carried out to give a dispersion of nanodroplets. By constantly stirring, the solvent is evaporated at ambient temperature or evaporated slowly in reduced pressure. The result is a suspension of nanoparticles. Later on, the solidified nanoparticles are centrifuged for collection and lyophilized for long-term storage. The next process is called the *salting-out method* in which

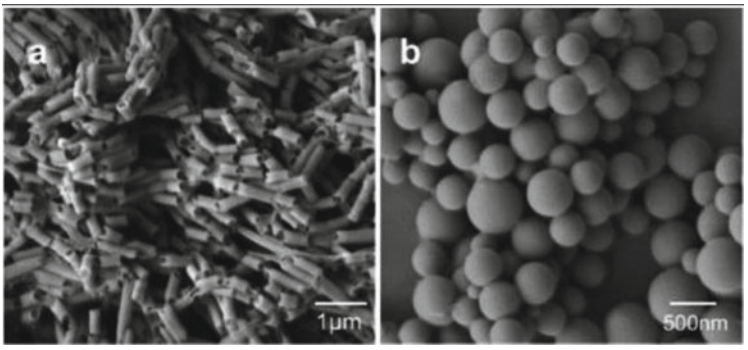

Fig. 1 Scanning electron micrographs (SEM images) of **a** poly(styrene-*b*-2-vinyl pyridine) (PS-*b*-P2VP) nano-blocks achieved by ultrasonication and **b** PS-*b*-P2VP nanospheres fabricated via swelling the nano-blocks. (With permission from Ref. [11] Copyright (2011) American Chemical Society.)

a water-miscible solvent is separated from the aqueous solution via the salting-out effect resulting in the development of polymeric nanoparticles, that is, the polymer nanospheres [14]. First, the polymer is dissolved in an appropriate organic solvent. The organic phase is dissolved in an aqueous phase consisting of a gel, the salting-out agent like electrolytes ($MgCl_2$, and $CaCl_2$), and non-electrolytes like sucrose, and a colloidal stabilizer. This is done so under intense mechanical shear at room temperature to form o/w emulsion. A suitable volume of de-ionized water is added to dilute it under mild stirring to increase the diffusion of the organic solvent into the aqueous phase. Eventually, nanospheres are fabricated whose dimension ranges from 170 to 900 nm. Lastly, the nanospheres are purified through the process of centrifugation and the salting-out agent is removed. There are other processes such as the *desolvation method* where biopolymers like albumin are used [15]. In short, a polymeric solution is created using poly(ethylene glycol) and the active ingredient is dissolved in an organic solvent like ethanol, which is added in a dropwise manner into the polymeric solution under magnetic stirring. A cross-linking agent is then added and kept for 12 h giving rise to nanosphere suspension. After this, the process of centrifugation and freeze-drying is carried out to get the desired nanospheres. *The double emulsion method* is also utilized in the synthesis of polymer nanospheres [16]. It engages in the formation of multiple emulsions. Both the polymer and the drug to be used are in an internal aqueous phase. To get a single emulsion, the aqueous solution is dispersed in the organic polymer solution which is continuously stirred. It is added dropwise into an external aqueous solution that contains surfactants. This is also carried out with continuous stirring by ultrasonication or homogenization. The result is a double emulsion. Like most other methods, the nanospheres collected are washed, and freeze-dried.

2.1.2 Polymer Nanocapsules

Polymer nanocapsules find applications in oral drug delivery, in the study of anti-cancer, anti-inflammatory, antibacterial, anti-fungal actions, in the investigation of in situ tissue regeneration and severe combined immunodeficiency diseases to mention a few. Palmarosa oil-loaded PCL and geraniol-loaded PCL nanocapsules are used as an antioxidant and an antimicrobial. There is a class of biocompatible and biodegradable synthetic polymers called Eudragit® polymers having various ratios of methacrylate and acrylate that can be used as coatings in drug delivery applications. Thyme oil-loaded Eudragit® L100-55, bergamot oil-loaded Eudragit® RS100, orange oil-loaded Eudragit® RS100 nanocapsules are also seen in antioxidant and antimicrobial applications. Ciprofloxacin-loaded PLGA and poly(ε-caprolactone) (PCL) nanocapsules are used in accelerated healing and anti-inflammatory studies. Cur-loaded PLGA, and colloidal nanocapsules have been used in investigations related to antibacterial activities and pancreatic cancer (Fig. 2).

In nanocapsules, their polymeric shells are of utmost importance as they load, protect and release the active ingredient of the drug. The stability and efficiency of the encapsulation and release are checked in creating these nanoparticles. Higher

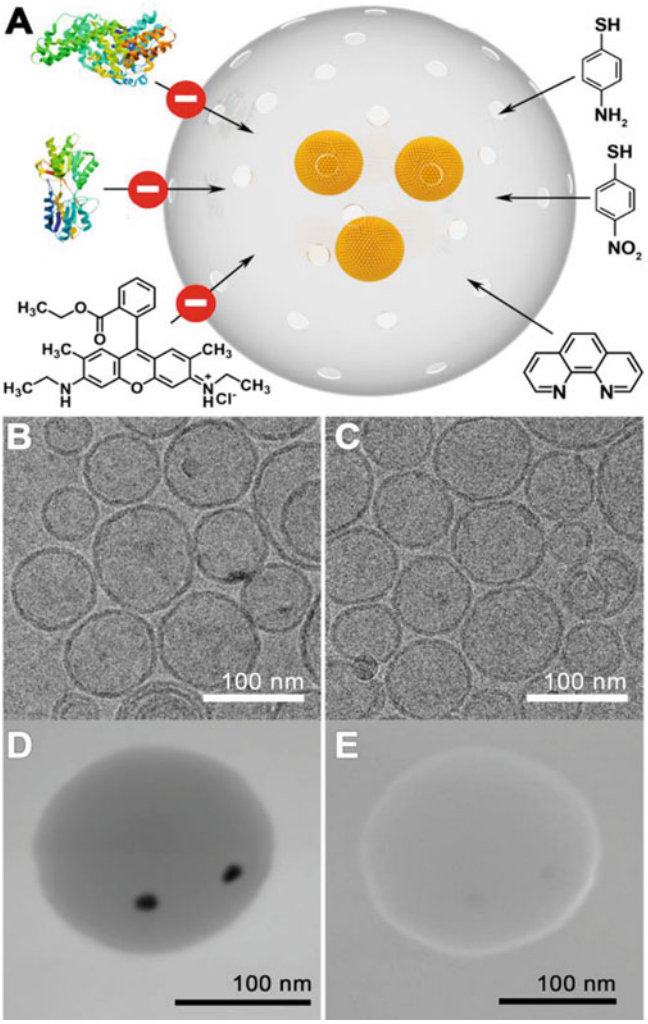

Fig. 2 **a** A representation showing that the permeation by the particles into the nanocapsules is dependent on their sizes. Cyro-transmission electron micrographs (TEM images) of vacant liposomes **b** and liposomes which are loaded with monomers before the polymerization of monomers in the hydrophobic interior of the lipid-bilayer **c**. Scanning transmission electron microscope image **d**, and scanning electron micrograph **e** of characteristic Au nanoparticles which are trapped inside a hollow polymer nanocapsule. (With permission from Ref. [17])

is the biocompatibility and biodegradability, better is the nanocapsules in a drug delivery process. Biopolymers like polysaccharides are often used in pharmaceutical applications as their biocompatibility is high and they can profit from gelation forms and mucoadhesive properties. They can form polymeric shells of nanocapsules by the Coulombic interactions of the cations and the anions that reside in

the deprotonated amino and carboxylic groups of the polysaccharides. Some of the polysaccharides used in making polymer nanocapsules are chitosan, alginate, heparin, and poly(cyclodextrin). There are also those which are based on protein like albumin. HspG41C mutant protein-based nanocapsules have been used in the study of anti-cancer activity. However, synthetic polymers like aliphatic polyesters, PEG, polyvinyl alcohol (PVA), and Eudragit® polymers are also employed in the fabrication of polymeric shells of the nanocapsules. One advantage of being synthesized is their reproducible quality, purity, and their ability to tune with different elements.

On the other hand, the core of polymer nanocapsules may be a solid or a liquid which can carry the drug or any active substance, or it can simply be hollow. For instance, the oleic core is often used owing to its ability to dissolve lipophilic drugs. Other oily cores include the copaiba oil used in PCL nanocapsules and açai oil used in anti-inflammatory desonide drug-loaded Eudragit® RL 100 nanocapsules. The core can also be in the aqueous phase to promote sustained delivery of hydrophilic molecules such as gemcitabine and hydrochloride which are hydrophilic anti-cancer drugs. One example of a core consisting of a solid-state polymeric matrix is the pectin gel core which is used in the investigation of glaucoma treatment through ocular delivery.

The polymer nanocapsules are synthesized in different ways. *Nanoprecipitation*, also known as *interfacial deposition method* or *solvent displacement method*, is one process to do so [18]. Following the displacement of the organic solvent into an aqueous phase, the interfacial deposition of the polymer takes place. This macromolecule is dissolved in a suitable solvent and the solution is put dropwise using a thin needle into an aqueous solution with constant stirring. Owing to spontaneous diffusion in that phase, polymer precipitates are created in the form of nanocapsules and nanospheres. When the active substance is in that solution, nanospheres are formed. However, the active material is dissolved in an oil, pursued by emulsification of this organic polymeric solution but before the internal phase, which has a polymer dissolved in a miscible organic solvent, is dispersed in the external phase of the emulsion. High energy instruments can be used in synthesizing nanocapsules by a method called the *nano-emulsion template method* [19]. The organic phase used in this method is emulsified with the use of a surfactant as well as under the application of steady energy processes like homogenization and sonication. In the emulsion-diffusion/evaporation process, the organic phase is emulsified in an inorganic one thereby eliminating the organic solvent by evaporation. The nanoparticles so obtained are a combination of polymer precipitation and evaporation process. In the emulsion-coacervation method which is another type of nano-emulsion template method, the polymeric shell is formed and stabilized through chemical cross-linking or physical coacervation. Another method worth mentioning for the synthesis of polymer nanocapsules is the *layer-by-layer method* where the nanocapsules consist of many layers [20]. By controlling the thickness and the composition of the polymeric shells, and by the way, the layers are ordered, this method can be applied in targeting and releasing drugs in various environments.

2.2 *Polymer Nanofibers, Nanotubes, and Nanowires*

2.2.1 Polymer Nanofibers

Polymer nanofibers are polymer-based fibres in which at least one of their dimensions has a size of 100 nm or less. They fall under a class of nanostructured polymeric materials characteristics of remarkable qualities like optical confinement, increased surface-to-volume ratio, high molecular diffusion, minute allowable bending radius, and high anisotropic electrical conductivity. There are various processing methods in the fabrication of polymer nanofibers. Some of them include electrospinning, drawing method which is also known as spinneret-based tunable engineered parameters (STEP) method, template synthesis, self-assembly, and phase separation method (Fig. 3).

In *electrospinning*, continuous polymer-based nanofibers are created from polymer melts or solutions due to the electrostatic forces [22]. It is the most frequently used process for the production of polymer nanofibers. Normally, the electrospinning system is made up of three parts. The first one is a capillary tube which consists of

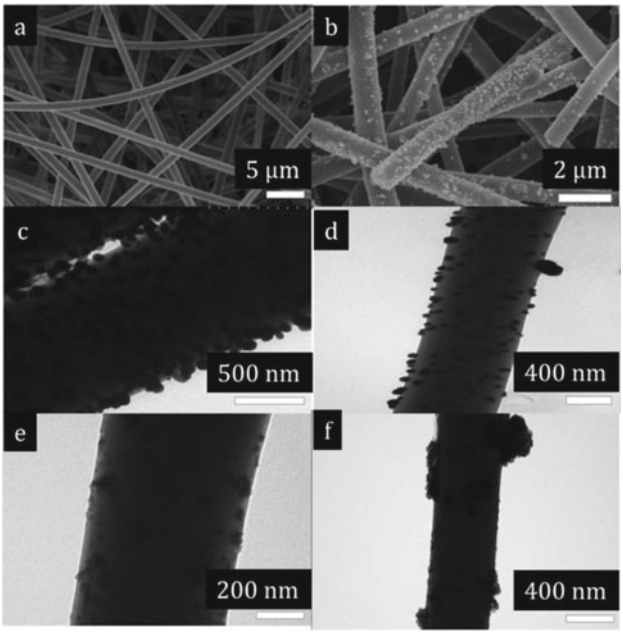

Fig. 3 Field-emission SEM image of electrospun **a** mussel-inspired copolymer nanofibers and **b** these nanofibers incorporated with Ag-nanoparticles, and high-resolution TEM micrographs of the nanofibers following incubation for **c** twenty-four hours, **d** twelve hours, and **e** six hours. **f** TEM micrographs of Ag-polydopamine-coated sample following 6 hours incubation. They could be used in wound dressing applications. (With permission from Ref. [21] Copyright (2015) American Chemical Society.)

a needle or a pipette. The second is a metal plate for collecting the nanostructured products and the third is a voltage supply that is required to generate a charged solution to jet into nanofibers. One electrode used in this setup is kept in the polymer solution while another one is fixed to the collector. Under the application of high voltage, polymer filaments are produced in the solution. When ejected out from the needle or the pipette, the solution jets evaporate only to develop into nanofibers which are collected on the metal collector. Both biopolymers and man-made polymers are utilized in the process. In applications that involve medicine, biopolymers are more commonly employed due to their biocompatibility as well as their lower immunogenicity. Some examples of these natural polymers are cellulose, collagen, casein, chitosan, chitin, gelatin silk fibron, etc. Nanofibers based on chitin/chitosan have been reported to have antibacterial and physicochemical properties and therefore are applied in tissue engineering and wound dressing applications. Those based on gelatin have good biodegradability and biocompatibility in physiological environments that they have applications in not only tissue engineering but also in scaffold wound healing. Nanofibers based on man-made polymers have their advantages too. Viscoelasticity and a high rate of degradation are just two of the many properties they exhibit. Polyglycolide (PGA), PLA, PCL, polyurethane (PU) are a few examples of synthetic polymers used in electrospinning. Nanofibers based on PLGA and poly(lactic acid) (PLLA) are biodegradable and are suitable for use in drug delivery applications. Those based on poly(lactide-*co*-caprolactone) (PLCL) are not only biodegradable but also highly elastic making them useful in the study of vascular tissue engineering.

In other types of electrospinning such as *melt electrospinning*, the molten polymers are utilized in place of polymeric solutions. Some of the polymers used in this process are polyethylene, polystyrene, poly(ethylene terephthalate), and poly(methyl methacrylate). *Solution blowing*, also known as *air-jet spinning*, is another way of producing polymer nanofibers from polymer solution with the help of high-velocity gas flow. There is another called *force-spinning* or *centrifugal spinning* in which the formation of the nanofibers is due to the centrifugal force [22].

In the STEP or *drawing process*, a micropipette is made to come in contact with the polymer solution droplet. It is then withdrawn at a constant controlled rate using a micromanipulator, thus forming nanofibers. Desired three-dimensional structures can be obtained using this technique by controlling the diameter of the nanofiber, the spacing, and the orientation of the fibrils. In *template synthesis*, nanoporous membranes or templates are used to produce hollow or solid polymer nanofibers. As the name itself suggests, in *self-assembly*, the nanofibers are spontaneously formed as a result of the self-organization of individual units. Intermolecular forces play a great role in this process. Although the nanofibers produced by self-assembly can be quite thin, the method is very time-consuming. Another time-consuming method is synthesis by *phase separation* consisting of five steps—formation of the homogenized mixture by dissolving the polymer in a solvent, gelatinization, extraction by a dissimilar solvent, freezing, and then freeze dying eventually leading to the synthesis of nanofibrous porous foam [22].

2.2.2 Polymer Nanotubes and Polymer Nanowires

Polymer nanotubes and *polymer nanowires* are one-dimensional polymer nanomaterials that have attracted many researchers and scientists owing to their remarkable properties, functions, and applications. These nanotubes are used in chemical sensors, optical sensors, biosensors, polymer light-emitting diodes, drug delivery systems, etc. On the other hand, polymer nanowires are used in sensing biomolecules, diagnostic applications, and applications regarding energy devices (Fig. 4).

Conducting polymers are those which exhibit electrical, thermal, and optical qualities close to that of metals and semiconductors, but at the same time sustain their flexibility and other common properties shown by polymers. Polypyrrole, polyaniline, and polythiophene are a few examples of polymers of this type. The template synthesis has been extensively applied in the production of one-dimensional conducting polymer structures like nanotubes and nanowires. For instance, both polymer nanowires and nanotubes are fabricated in a template created by the nanochannels found in mesoporous zeolite [24], or by the pores of a nano-porous template [25]. The hard physical

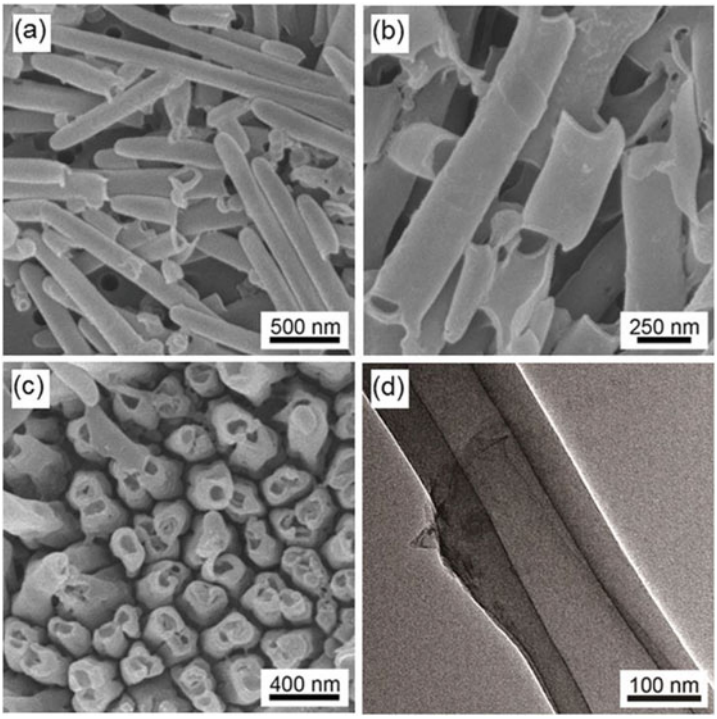

Fig. 4 Polystyrene (35 kg/mol)/poly(methyl methacrylate) (97 kg/mol) blend nanotubes: **a** and **b** side view of scanning electron micrographs **c** top-view scanning electron microscope image, and **d** transmission electron micrograph. (With permission from Ref. [23] Copyright (2015) American Chemical Society.)

template method and soft chemical template method are the two types of template methods.

In the *hard physical template method*, the lengths and diameters of these one-dimensional nanostructures can be controlled using this method. Generally, it consists of three steps. First, the nanopores of the membrane are filled with monomers. Then, these monomers are polymerized inside the nanopores and lastly, arrays of aligned polymer nanotubes and nanowires are obtained when the nanopore template is removed. Using this process, CdS-polypyrrole hetero-junction nanowires [23, 26], multisegmented Au-poly(3,4-ethylene dioxythiophene)-Au and Au-poly(3,4-ethylene dioxythiophene)-polypyrrole-Au nanowires [27, 28] are synthesized. *The soft chemical template method* or *self-assembly method* is another powerful technique to synthesize polymer nanomaterials. Surfactants, colloidal particles, aniline oligomers, surface micelles, and even DNA serve as templates. There is also a template-free method that is free of an external template and a wide range of polyaniline nanostructured materials like nanotubes [29, 30], nanofibers [31], nanowires [32], and nanotubes junctions [29] have been fabricated.

Conducting polymer nanowires can be created using *soft lithography* or *embossing* [33]. Here, a polymer film that is already flat is shaped with the help of a mold of micro-size along with the use of temperature or solvent vapors. For instance, by micro-molding in capillaries, poly(3,4-ethylenedioxythuopene) which is doped with poly(4-styrene sulfonate) has been patterned into nanowires on a glass. These nanowires are also produced by *directed electrochemical nanowires assembly* [34] and *dip-pen nanolithography* [35]. In dip-pen nanolithography, an atomic force microscope (AFM) has a tip that transfers alkane thiol to a gold surface. With this technique, one may write directly on the desired position with the AFM tip as a sort of pen. Moreover, nanowires having poly(3-hexylthiophene) with part magnetic orientation have been fabricated by utilizing a high magnetic field. In the *whisker method*, the π-conjugated polymer in a poor solvent is considered [36]. When heated and stirred till the complete dissolution of the polymer, the solution is made to cool without any disturbance. The polymer chains spontaneously self-assemble into polymer nanowires (Fig. 5).

2.3 Polymer Nanocomposites

Nanocomposites take into account nanostructured materials into a matrix of typical substance thereby enhancing the properties of that composite. However, *polymer nanocomposites* incorporate a polymer or a copolymer along with nanoparticles or nanofillers dispersed in a matrix of the polymer. These nanofillers, often called nano reinforcements, are in the range of a few nanometers and so the interfacial area per volume between the nano-element and the polymer matrix is quite large. Nanofiller reinforced composites show better toughness without sacrificing optical clarity or stiffness. Moreover, they can enhance barrier properties like thermal resistance, and can even grant electrical properties to a non-conductive polymer. Some of

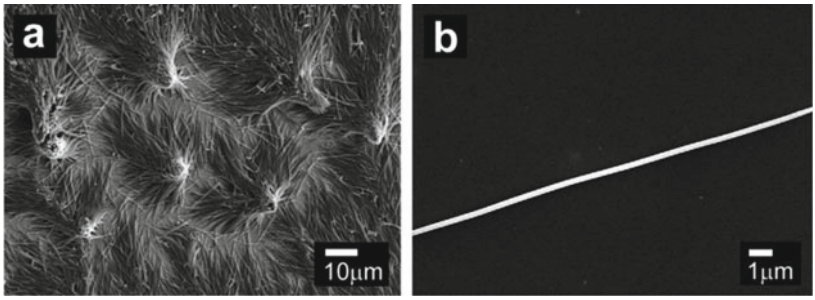

Fig. 5 Scanning electron micrograph of **a** poly(3,4-ethylene dioxythiophene) nanowires incorporated onto gold thin film **b** dispersed on a SiO_2/Si wafer (With permission from Ref. [37])

the common nanofillers are nanoclays, carbon nanoparticles like carbon nanotubes, carbon nanofibers and graphene, nano-oxides, nanocarbides, and organic nanofillers like nanocellulose and nanolignin, and some other nanoparticles like metal nanoparticles. The matrices used can be thermoplastic where nano clays, carbon nanotubes, carbon nanofibers, graphene oxides, isodimensional nanoparticles, and polysaccharide nanocrystals may be incorporated. There are also thermoset matrices and elastomeric matrices.

2.3.1 Nanofillers

The most studied nanofillers for polymer nanocomposites are the nanocatalyst which is phyllosilicates (layered silicates) resulting from minerals of natural clay. Of the four groups of phyllosilicates—montmorillonite, kaolinite, illite, and chloride, montmorillonite groups with 2:1 sheet structure are more commonly investigated. An octahedral sheet (of alumina) is kept in between 2 silica tetrahedral sheets. The tetrahedral sheet of silica comprises 2 planes of oxygen atoms closely packed or hydroxyls between which octahedrally coordinated aluminium atoms are embedded. A tactoid is the single layer formed by these three sheets. Typically there are two morphologies of clay/polymer nanocomposites called intercalated and exfoliated based on the degree of polymer penetration into the interlayer. When intercalated, there is a limited expansion of the silicate layers of less than 20–30 Å due to the penetration of the polymer chains. On the other hand, if there is delamination of the silicate tactoids separated by 80–100 Å, it is said to be exfoliated. The best combination of property improvements is seen in exfoliated nanocomposites because of the high surface area of the tactoid [38] (Fig. 6).

Composites based on carbon nanoparticles such as carbon nanotubes show that they are a type of new carbon-based substances that have a huge potential for optical and electronic nanodevices. Carbon nanotubes are one of the allotropes of graphene with lengths ranging from a few hundred nanometers to a few micrometers and can

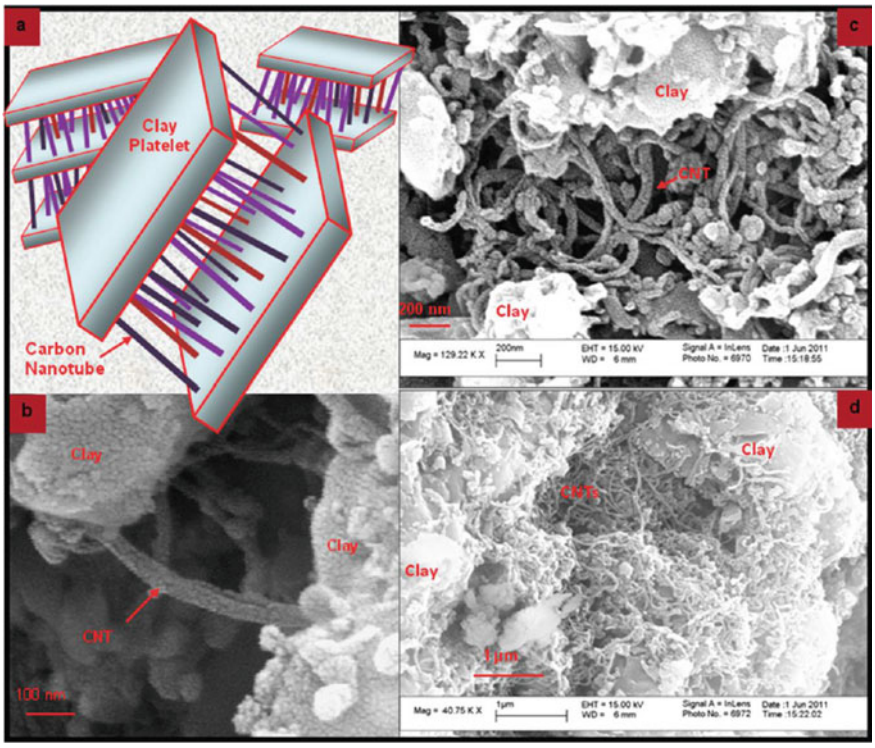

Fig. 6 **a** Schematics of montmorillonite clay-carbon nanotubes hybrid filler **b–d** SEM images of clay-carbon nanotubes structures at various magnifications. (With permission from Ref. [39] Copyright (2012) American Chemical Society.)

be imagined as a graphene sheet that is rolled up into a cylindrical form. It can have single or multiple walls. The properties of carbon nanotube-based nanocomposites show dependence on the dispersions of these nanotubes in the polymeric matrix as well as on the interfacial interactions between them. Another instance of carbon nanoparticle is carbon black which, when dispersed in a polymer matrix, exhibits enhanced mechanical and electrical properties.

Another important nanofiller is the organic nanofiller based on biopolymers. Cellulose nanocrystals are one of them and can be isolated from cellulosic fibres using acid hydrolysis. These nanomaterials, obtained by this method, have rod-like structures and show increased Young's modulus of elasticity, enhanced tensile strength, and low coefficient of thermal expansion. Owing to these qualities, cellulose nanocrystals find applications in many areas. Nanolignin and chitosan nanoparticles are also organic nanofillers that are worth mentioning.

2.3.2 Nanostructuration

In general, polymer nanocomposites are obtained in two ways. The first one is quite predominant in the nanotechnology of polymer science and is called the *top-down* approach. It is the diminution of the size of a bulk micro- or macro-material to a nanomaterial to be dispersed into the polymer matrix. The dispersion of nanoparticles like carbon nanotubes, graphenes, nanocellulose in thermosetting polymers are instances of top-down methods. There are reports of improvements in toughness on nano clay dispersion. When carbon nanotubes are used as nanofillers, not only is the toughness improved but an increase in tensile strength and wear resistance is also seen. The same nanofillers mentioned above can also be dispersed in thermoplastic matrices using top-down processes resulting in improved mechanical, gas-barrier, thermal, swelling, and flame-resistance qualities. The second approach is called *bottom-up*, and in making the polymer nanocomposites, the nanomaterials are directly produced in the polymer matrix via chemical processes. There are researches on the bottom-up process regarding block copolymer nanofabrication by phase separation. For instance, attention has been given to segmented copolymers such as thermoplastic polyurethane and thermoplastic elastomers. So, by changing the structures as well as the molecular weights of these polymer parts, the desired material can be achieved. Block polydispersity is an important aspect to be considered in this approach as it induces a shift in the order–disorder transition of the copolymer systems. These block copolymers can also serve as polymeric matrices. Peponi and coworkers [40] investigated the changes in the morphology of micelles of nanocomposite gels which was based on poly(styrene-*b*-butadiene-*b*-styrene) block copolymer and gold nanoparticles when 1 wt% gold nanoparticles were added into the gel of poly(styrene-*b*-butadiene-*b*-styrene). In the study of the assembly of silica nanospheres carried out by Zhou et al., the matrix used was of block copolymer [41].

3 Recent Advances

3.1 Drug Delivery

Drug delivery is the method or approach or technology that enables a therapeutic substance to reach its selective location to achieve its effect, without reaching or affecting other cells, tissues, and organs that are not targeted. There are, however, challenges like biological barriers [42]. Non-specific distribution and inadequate accumulation of the drug at the diseased site also contribute to these challenges. So the size, shape, surface charge, deformability, and degradability are a few parameters that have to be kept in mind while synthesizing them for different drug delivery systems. For instance, nanoparticles with an average size of 100 nm usually last longer in circulation. It has been shown that different types of sub-100 nm polymer micelles of various sizes ranging from 30 to 100 nm penetrate well within poorly permeable

tumors [43]. Nanotoxicity cannot be ignored either. Prabha and coworkers summarized the recent progress seen in the investigation of toxicity observed in polymer-based nanomaterials [44]. In the progress of drug delivery, an extensive range of polymer nanoparticles have been engaged, but some stand out better than others. Polymeric nanocapsules are extensively used in this field because of their ability to encapsulate therapeutic chemical compounds, enzymes, proteins, hormones, metabolites, genes, and so on. Docetaxel-loaded chitosan nanocapsules functionalized with monoclonal antibody Chi-Tn were recently studied as a potential targeting strategy for lung tumors [45]. Another instance of targeted drug delivery that has potential for cancer therapy is the carboxymethylcellulose-based nanocapsule prepared by sonochemical method [46]. Not only is the nanocapsule endowed with good biocompatibility, but the shells of that nanocapsule are also decorated with folic acid making the controlled release possible. In addition, the nanocapsule has favorable sizes and morphology for flowing in the blood. Zhao et al. investigated nanocapsules containing anticancer pharmaceutical drugs which could be used to target the lungs, and at the same time, these nanoparticles contained ingredients usable for synergy therapy [47]. Derivatives of poly(ethylene glycol) dimethacrylates were used in fabricating the nanocapsules. Nicolas and coworkers studied polymer-based nanocapsules for drug delivery methods that target cancer cells in the breast [48]. Neto et al. worked on the development of a new nanocapsule loaded with α-amyrin for intestinal delivery and thereby investigating the cytotoxic ability against leukemic cells [49]. Integrating three-dimensional printing technology with the use of polymeric nanocapsules, Beck and coworkers came up with a new approach to produce customized drug delivery methods [50]. In the field of drug delivery, many polymeric nanocapsules were also engaged in the study of antimicrobial effects [51], anti-melanoma activity [52], skin carcinoma [53], hair follicle targeting [54], and the like (Fig. 7).

The other type of nanoparticle—the nanosphere, is also heavy employed in the drug delivery systems. Recently, phosphazene–tannic acid nanospheres, which were not only biodegradable but also antioxidant, were used with an average size of 274 nm. These polymer nanospheres which were utilized for the release of Rhodamine 6G showed promising properties as carriers of drug [56]. Das and coworkers reported a novel drug delivery system that was pH-responsive [57]. A new aspect of cisplatin delivery was studied with the help of gluthione-responsive hydrogel and molecularly imprinted polymer nanospheres which were synthesized via precipitation polymerization process [58].

Recently, the role of polymeric nanoparticles in the delivery of drugs to the nervous system was carried out by Jörg Kreuter [59]. Such nanoparticles should be highly biocompatible and biodegradable in a matter of days. It was found that nanoparticles like doxorubicin might reduce the toxicity of drugs as well as the adverse effects owing to the alteration of body distribution. A good prospect to treat diseases related to the central nervous system like brain tumors was seen with the use of polymeric nanoparticles in the delivery system. Again the role of polymeric nanoparticles in antimicrobial therapies which might prevail over the problematic issues of usual drugs was well-reviewed by Spirescu and coworkers [60]. Polymeric micelles were studied

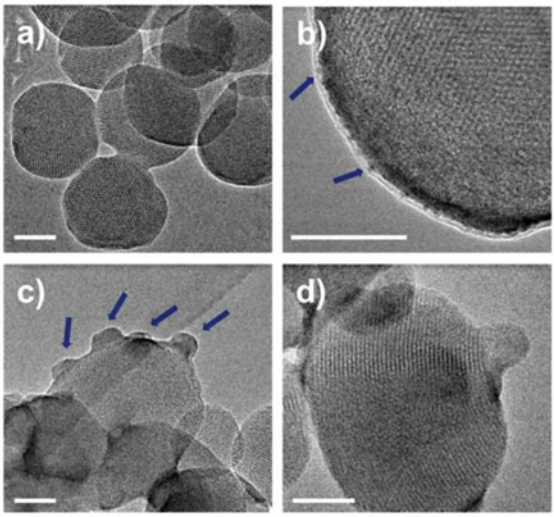

Fig. 7 Transmission electron micrographs of **a** mesoporous silica nanoparticles **b** mesoporous silica nanoparticle-collagenase **c** mesoporous silica nanoparticle-collagenase-nanocapsules. A scale of 50 nm is denoted by the white bar at the left bottom. The presence of collagenase and collagenase-nanocapsules are pointed out by the blue arrows. (With permission from Ref. [55] Copyright (2015) American Chemical Society.)

in the treatment of ocular inflammation [61], ocular infections [62], choroidal neovascularization [63], while dendrimeric nanocarriers were used for those like ocular hypertension [64]. Cyclodextrins [65] and polymeric vesicles [66] were reported for the treatment of fungal keratitis. Polymer-based nanofibers were also used in drug delivery. A promising method for the development of a fast-dissolving delivery method of drug particles exhibiting antiviral properties was studied by Celebiogle and Uyar [67]. It involved acyclovir/cyclodextrin nanofibers fabricated through electrospinning. There was another study regarding fast-dissolving electrospun nanofibers produced from jelly fig polysaccharide/pullulan [68]. These nanofibers with antibacterial properties could be potential carriers to encapsulate hydrophobic drugs in pharmaceutical delivery applications. Mitrakos et al. developed a nanocomposite-based piezoresistive pressure sensor that could be used in haptic sensing or robotic touch sensing [69].

3.2 Sensors

In simple terms, sensors are devices that detect changes in their surroundings. Various applications come under sensors for detecting a range of different gases, temperatures, light intensity, forces, etc. So, they are important to us in many ways. With the use of nanostructured polymers, researchers and scientists have been looking for

cheaper, faster, and more reliable ones. Taking the example of the pressure sensor, it is a vital element in studying applications of human motion detection, prosthetics, and robotic actions. Lee and coworkers utilized a strain sensor based on soft nanocomposites which were capable of sensing multiple points and directions [70]. Recently, a good review on conductive polymer/carbon nanotubes nanocomposites based on strain and pressure sensors was carried out [71] (Fig. 8).

Yin et al. used strain sensors based on nanocomposites for structural health monitoring of a flexible aircraft [72]. Rahman et al. fabricated nanofibers based on cellulose acetate-glycerol-conducting polymer-tungsten oxide nanoparticles which found applications in sensing H_2S gas [73]. Another sensor of NH_3 gas at room temperature by poly(3,4-ethylene dioxythiophene): poly(4-styrene sulfonate) intercalated ammonium vanadate nanofiber composites were produced via sonochemical method [74]. The high sensitivity of this composite was due to increased surface area, and p-p hetero-junctions created between poly(3,4-ethylene dioxythiophene) and poly(4-styrene sulfonate). Increased sensitivity, good flexibility, and long-term stability were some of the merits of this sensor. It also worked at room temperature. Recently, a novel

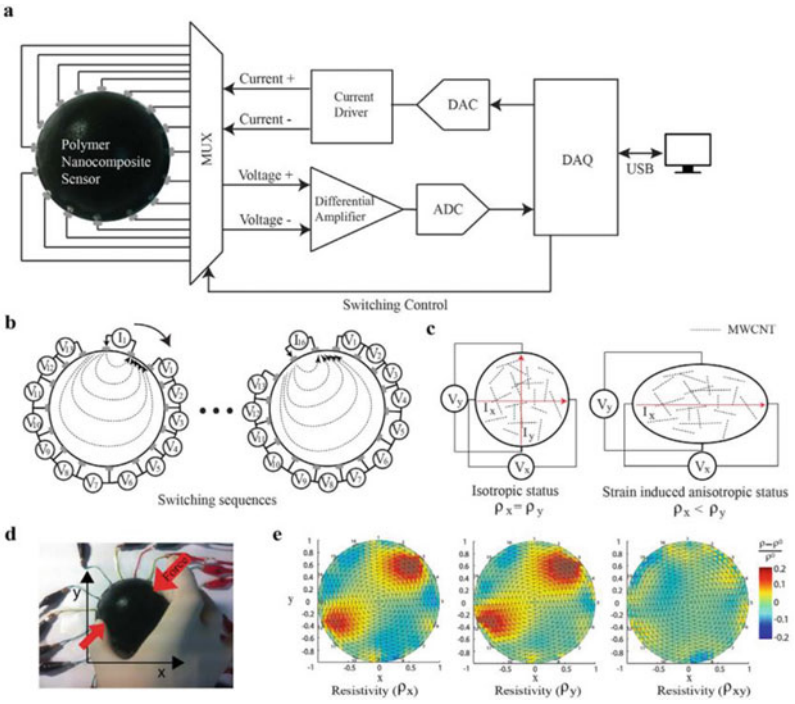

Fig. 8 A diagram of electrical impedance tomography. A schematic of **a** the hardware configurations, **b** adjacent method injecting electrical current **c** the isotropic status and strain-induced anisotropic status **d** The multiwall carbon nanotubes-silicone elastomer nanocomposites based sensor is tested using two fingers **e** Graphs of normal resistivity versus shear resistivity. (With permission from Ref. [70])

electroactive 3D gold-decorated polymer nanofiber was reported to have high sensitivity for detecting mercury [75]. There was a study on a novel sensor that could detect humidity and the sensor used sulfonated poly(ether ether ketone)/polyvinyl butyral nanocomposite nanofibers [76]. Due to exceptional humidity sensing qualities, they could be used for non-contact sensing and detection of breath. Another sensor of humidity based on poly(vinyl alcohol)/MXene nanofiber was reported that could be self-powered by a flexible molybdenum diselenide piezoelectric nanogenerator [77].

Some biosensors provide us with data by sensing biologically active elements and compounds. They can be used to detect toxic materials present in foods. Öndeș and coworkers synthesized highly stable urea biosensors with the use of poly(2-hydroxyethyl methacrylate-glycidyl methacrylate) nanoparticles [78]. They demonstrated that urea could be detected in artificial human serum. Lui et al. prepared fluorescent conjugated polymer nanoparticles to be used for the construction of a biosensor capable of detecting hydroquinone [79]. Acceptable results were attained when this biosensor was applied for the detection of hydroquinone in lake water.

3.3 Tissue Engineering

The need for organ transplantation due to injury and failures of organs is ever increasing. This is where tissue engineering comes in as an alternative method to restore the injured tissues. Tissue engineering is the technology that integrates cell biology, chemistry, and biomaterials in the creation of biology-based substitutes to fabricate, repair, maintain, and increase tissue functions. Synthetic, natural, and composite polymeric substances have been widely associated with the fabrication of nanofibers because these polymeric nanofibers possess a wide range of properties like water solubility, biodegradability, biocompatibility, conductivity, and antibacterial property. Electrospun polymeric nanofibers are used in the tissue engineering of blood vessels, neural tissues, bones, cartilages, and ligaments. Zarei et al. created and characterized polypyrrole/chitosan/collagen nanofiber scaffolds which could be employed in body parts that involve impulses [80]. These conductive scaffold nanofibers were electrospun and could be included in the family of semiconductor materials.

The formation of bones consists of a sophisticated chain of events called osteogenesis and the fabrication of bone tissues requires fulfillment of many factors such as high porosity in the biomimetic scaffolds to facilitate cell ingrowth. Maharjan and coworkers prepared chitosan hydrogels scaffolds reinforced by regenerated cellulose nanofibers [81]. There were enhancements in the mechanical properties, swelling capacity as well as water absorption making these engineered scaffolds suitable for bone tissue engineering. Oudadesse and coworkers developed a new class of biodegradable polymer/bioactive glass composites for bone regeneration methods [82] (Fig. 9).

To mimic the morphology of vascular blood vessels, there is a need for a multilayered vascular scaffold. Wu and coworkers developed a novel tri-layer tubular graft

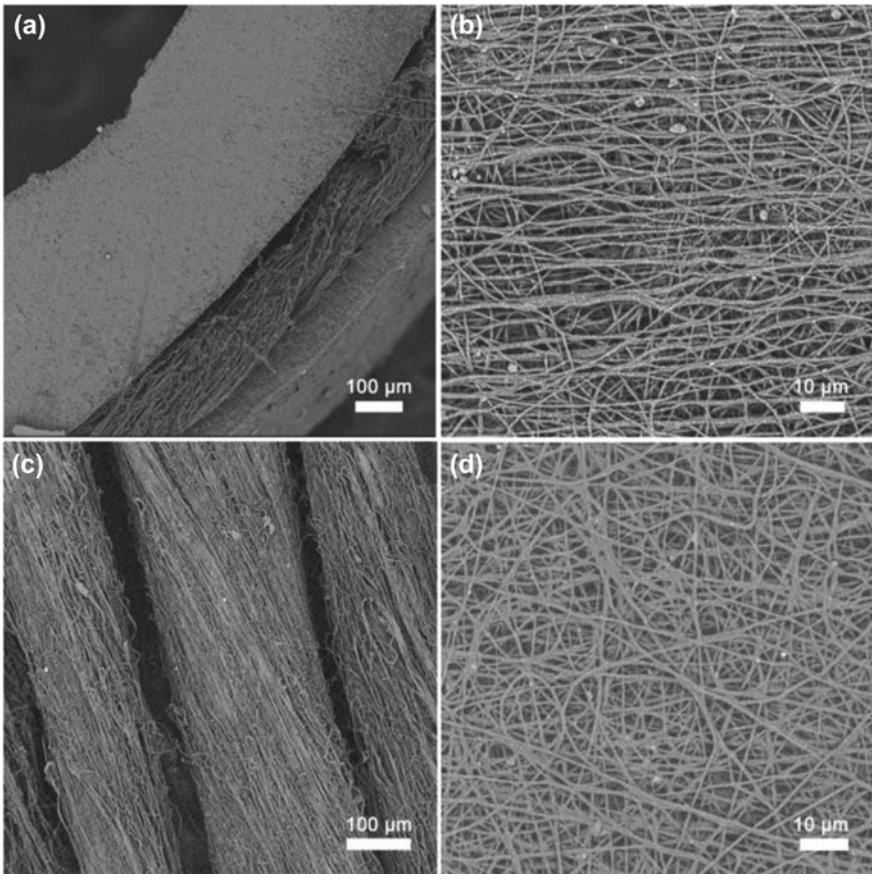

Fig. 9 Scanning electron micrographs of **a** the tri-layer tubular graft showing its cross-section **b** the aligned poly(L-lactide-*co*-caprolactone)/collagen (PLCL/COL) fibers in the inner layer **c** the poly(lactide-*co*-glycolide)/silk fibroin (PLGA/SF) yarns in the middle layer, and **d** the random PLCL/COL fibers in the outer layer. (With permission from Ref. [83])

comprising of PLCL/COL fibers and PLGA/SF yarns through a 3-step method of electrospinning [83]. When a single layer was considered, it possessed favorable tensile strength and elongation, and when the multi-layered scaffold was taken into account, it supported cell infiltration, high biocompatibility, and tissue regenerative ability. These structures are shown in Fig. 3.3. There were recent studies on vascular tissue engineering in which 3D silk fibroin microsphere-nanofiber scaffolds [84], and wet electrospun polycaprolactone/gelatin/carbon nanotubes yarns were used to form scaffolds [85]. There were also other nanostructured polymers playing important role in restoring, maintaining, and improving damaged tissues and organs. For instance, Maroufi and Ghorbani fabricated nanocomposite hydrogels of chitosan/oxidized-modified quince seed gum/curcumin-loaded in halloysite

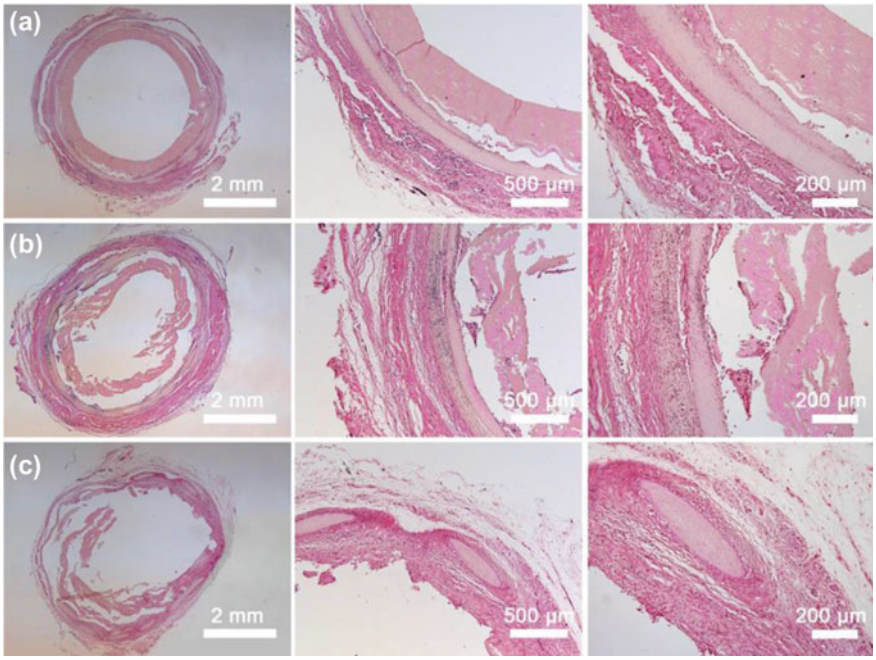

Fig. 10 Hematoxylin and eosin stain images of the grafts that were transplanted after subcutaneous embedding in mice for 14 days **a**, 42 days **b**, and 70 days **c**. (With permission from Ref. [83])

nanotubes [86]. These structures showed that the thermal stability was improved and that the rate of degradation was also enhanced (Fig. 10).

3.4 Energy Applications

There is an increasing concern about the depletion of fossil fuels. Energy demands and economic growth are of utmost importance. So, the role of polymer-based nanostructured materials in the novel creation of next-generation energy-based appliances is quite promising. The function of fuel cells is to change chemical energy into electrical one. Reza Kazemi and coworkers investigated some methods for fabricating organic–inorganic nanocomposite polymer electrolyte membranes for fuel cells through a range of processes like blending nanoparticles in a polymer matrix, and self-assembly [87]. Polymer nanocomposite membranes based on silicate were already used for these fuel cells [88]. In the present day, researchers have shown great interest in green technology. Yaqoob et al. worked on graphene/polyaniline nanocomposites anode based on cellulose to use benthic microbial fuel cells for generating energy and for applications to bioremediate harmful metals present in synthetic wastewater [89].

Another need of the hour is energy storage in portable electronic devices like cell phones and laptops, and electrical vehicles. Because nanotechnology can provide new reactions that are impossible in bulk systems and a means of shortened pathways for the transport of both charge and mass, a lot of investigations have been carried out in the past few years. Nanostructured conductive polymers were investigated for advanced energy storage and they could act as active electrode materials in supercapacitors and lithium batteries, and superior binder materials in the next-generation high-energy lithium-ion batteries [90]. In addition to all these applications, the nanostructured conducting polymers could also be used in photovoltaic and solar cells [91]. Hu et al. reported recent progress, challenges, and opportunities of polymer nanocomposite dielectrics for energy storage [92]. Graphene reinforced biopolymer nanocomposites were also used in energy storage applications [93].

Surmenev et al. studied some of the latest signs of progress regarding the use of anodic aluminium oxide templates to synthesize poly(vinylidene fluoride) or poly(vinylidene fluoride-*co*-trifluoroethylene)-based piezoelectric generators [94]. It was further reported that the piezopolymers could be used for energy harvesting, piezoelectric generators, biosensing, strain or force sensing, and smart drug delivery systems. A wavelength shifting technique called photon upconversion was enabled using nanostructured polymers that exhibited good optical quality and excellent photon upconversion efficiency of about 27% [95]. This could be applied to actuators, sensing, and solar technologies.

3.5 Filtration, Coating, and Others

The availability of clean drinking water is limited to many parts of the world, and pollution contributes a good deal to it. There are many ways to remove the pollutants present in contaminated water like electrolysis [96], electrodialysis [97], and chemical precipitation [98]. However, due to the expensive nature of the processes, it is often impossible for poor or developing countries. In methods such as chemical precipitation, there is an issue with secondary contaminants. One of the cost-effective techniques that could treat water contaminated with biological, organic, and inorganic pollutants is the adsorption method. Amari et al. studied the use of clay-polymer nanocomposites to remove organic and inorganic contaminants from wastewater [99]. Graphene reinforced biopolymer nanocomposites were also used for applications in water filtration [100].

Till today, air pollution remains a global problem that we face in our homes, workplaces, and industries. Diseases that spread through the air and volatile organic gases are unwanted in the air we breathe. Air filtration can prevent us from various health issues and provide us with good quality of life. Owing to excellent qualities like the high surface area to volume ratio, good mechanical strength, controllable diameter, and morphology, electrospun biopolymer-based nanofibers were used for air filtration [101]. Zhang and coworkers investigated anti-deformed polyacrylonitrile/polysulfone composite membranes to be used for air filtration and found that the

product demonstrated an excellent filtration efficiency of 99.992% [102]. Purwar et al. reported a promising antimicrobial air filtration mask fabricated through the electrospinning process [103]. It was made with the use of sericin/polyvinyl alcohol/clay nanofibrous mats.

Pourhashem et al. reviewed nanocomposite coatings, which were based on the use of inorganic nanofillers in the polymer matrix, that showed far better corrosion protection performance [104]. Polyvinyl chloride nanofiber nanocomposites were developed as a novel, cost-effective coating for corrosion resistance against aluminium [105]. Balakrishnan et al. studied multi-walled carbon nanotubes reinforced in a polymeric system as a coating capable of excellent sound absorption and insulation that can be used in aircraft panels [106]. The need of the hour is to move toward eco-friendly green technology. Useful applications such as drug delivery, tissue engineering, cancer therapy, biosensors, and even removal of impurities from polluted sources can be achieved with the use of biopolymer-based nanostructured materials [107] (Fig. 11).

4 Conclusion

In summary, we have discussed the most commonly used polymer-based nanostructured materials like polymer nanospheres, nanofibers, and nanocomposites, as well as their general synthesis processes. Along the way, the structures of these materials in which polymers and nanotechnology are incorporated together are seen to manifest in various ways thereby offering applications in sensors, biosensors, therapy, drug delivery, tissue engineering, energy storage, diodes, impurity removal from wastewater, corrosive coatings and a lot more. Their recent progress is also highlighted.

Today, perhaps, reaping the fruits of polymer-based nanostructured materials is the path to follow. Among the chaos and the havoc caused by the long pandemic, polymer-based nanotechnology and nanomedicine have earned their places to be in the spotlight. A vivid instance is the recently approved nanotechnology-enabled mRNA-based vaccine platform against COVID-19 [108]. Future research must be focused on the exploitation of nanotechnology-enabled methods and techniques that are sustainable, reliable, usable, and liable. What has been provided here is but the tip of an iceberg, hopefully enough to capture the essence of the importance of these materials.

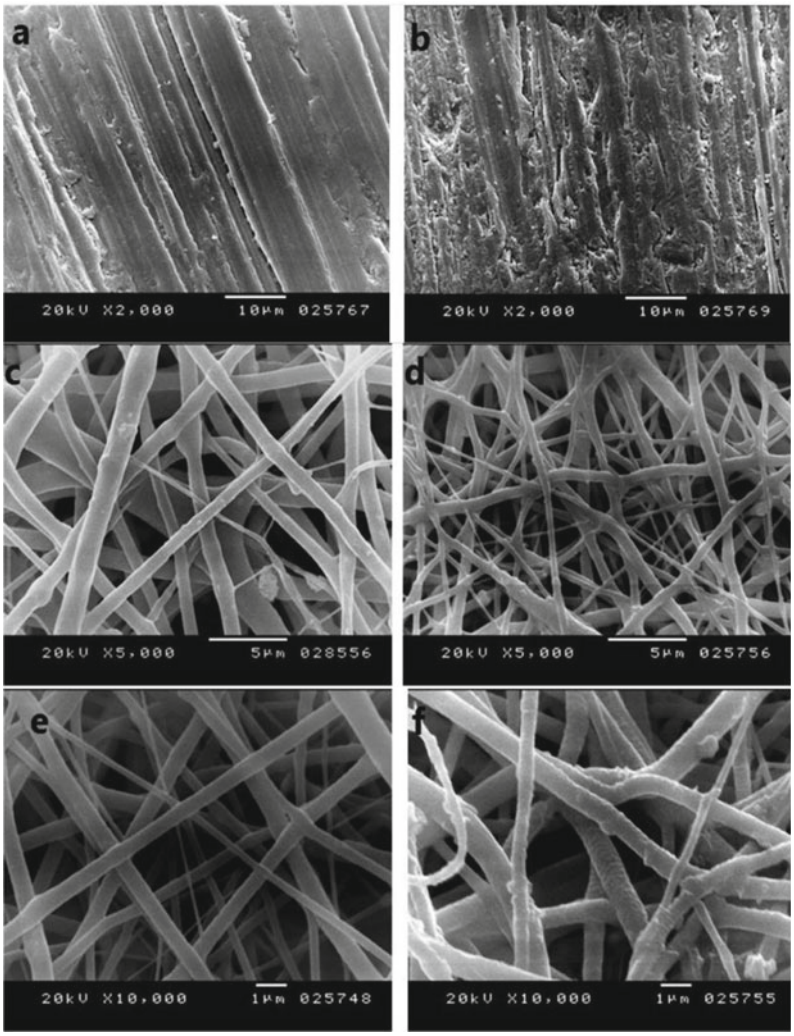

Fig. 11 Scanning electron micrographs of aluminium **a** before and **b** after immersion in 01 M HCl, PVC nanofibers coated on aluminium surface **c** before and **d** after immersion in 0.1 M HCl, PVC nanofibers embedded in situ ceria nanoparticles with concentration 3 wt% coated on aluminium surface **e** before and **f** after immersion in 0.1 M HCl. (With permission from Ref. [105])

References

1. Kirtane AR, Verma M, Karandikar P, Furin J, Langer R, Traverso G (2021) Nanotechnology approaches for global infectious diseases. Nat Nanotechnol 16:369–384
2. Talebian S, Wallace GG, Schroeder A, Stellacci F, Conde J (2020) Nanotechnology-based disinfectants and sensors for SARS-CoV-2. Nat Nanotechnol 15:618–621

3. Rashidzadeh H, Danafar H, Rahimi H, Mozafari F, Salehiabar M, Rahmati MA, Rahamooz-Haghighi S, Mousazadeh N, Mohammadi A, Ertas YN, Ramazani A, Huseynova I, Khalilov R, Davaran S, Webster TJ, Kavetskyy T, Eftekhari A, Nosrati H, Mirsaeidi M (2021) Nanotechnology against the novel coronavirus (severe acute respiratory syndrome coronavirus 2): diagnosis, treatment, therapy, and future perspectives. Nanomedicine 16
4. Lynn GM, Laga R, Darrah PA, Ishizuka AS, Balaci AJ, Dulcey AE, Pechar M, Pola R, Gerner MY, Yamamoto A, Buechler CR, Quinn KM, Selkinson MG, Vanek O, Cawood R, Hills T, Vasalatiy O, Kastenmuller K, Francica JR, Stutts L, Tom JK, Ryu KA, Esser-Kahn AP, Etrych T, Fisher KD, Seymour LW, Seder RA (2015) *In vivo* characterization of the physicochemical properties of polymer-linked TLR agonist that enhance vaccine immunogenicity. Nat Biotechnol 33:1201–1210
5. Dabaghian M, Latifi AM, Tebianian M, NajmiNejad H, Ebrahimi SM (2018) Nasal vaccination with r4M2e. HSP70c antigen encapsulated into N-trimethyl chitosan (TMC) nanoparticulate systems: preparation and immunogenicity in a mouse model. Vaccine 36:2886–2895
6. Wang Q, Zhang Y, Zou P, Wang M, Fu W, She J, Song Z, Xu J, Hung J, Wu F (2020) Self-assembly M2e-based peptide nanovaccince confers broad protection against influenza viruses. Front Microbiol 11:1961
7. Mauter MS, Zucker I, Oerreault F, Weber JR, Kim J-H, Elimelech M (2018) The role of nanotechnology in tacking global water challenges. Nat Sustain 1:166–175
8. Zielinska A, Carreiró F, Oliveira AM, Neves A, Pires B, Venkatesh DN, Durazzo A, Lucarini M, Eder P, Silva AM, Santini A, Souto EB (2020) Polymeric nanoparticles: production, characterization, toxicology and ecotoxicology. Molecules 25:3731
9. Valdiglesias V, Laffon B (2020) The impact of nanotechnology in the current universal COVID-19 crisis. Let's not forget nanosafety! Nanotoxicology 14
10. Escalona-Rayo O, Fuentes-Vázquez P, Jardon-Xicotencatl S, García-Tovar C, Mendoza-Elivira S, Quintanar-Guerrero D (2019) Rapamycin-loaded polysorbate 80-coated PLGA nanoparticles: optimization of formulation variables and *in vitro* anti-glioma assessment. J Drug Deliv Sci Technol 52:488–499
11. Mei S, Feng X, Jin Z (2011) Fabrication of nanospheres based on Rayleigh instability in capillary channels. Macromolecules 44:1615–1620
12. Viera R, Souto SB, Sanchez-Lopez E, Machado AL, Severino P, Jose S, Santini A, Fortuna A, Garcia ML, Silva AM, Souto EB (2019) Sugar-lowering drugs for type 2 diabetes mellitus and metabolic syndrome—review of classical and new compounds: part-I. Pharmaceuticals 12:152
13. Szczęch M, Szczepanowicz K (2020) Polymeric core-shell nanoparticles prepared by spontaneous emulsification solvent evaporation and functionalized by the layer-by-layer method. Nanomaterials 10:496
14. Rao JP, Geckeler KE (2011) Polymer nanoparticles: preparation techniques and size-control parameters. Prog Polym Sci 36:887–913
15. Jun JY, Nguyen HH, Paik S-Y-R, Chun HS, Kang B-C, Ko S (2011) Preparation of size-controlled bovine serum albumin (BSA) nanoparticles by a modified desolvation method. Food Chem 127:1892–1898
16. Elizabeth P-S, Maria GN-A, David L-B (2012) Pharmaceutical polymeric nanoparticles prepared by the double emulsion-solvent evaporation technique. Recent Pat Drug Deliv Formul 6:224–235
17. Jia Y, Shmakov SN, Pinkhassik E (2016) Controlled permeability in porous polymer nanocapsules enabling size- and charge-selective SERD nanoprobes. ACS Appl Mater Interfaces 8:19755–19763
18. Rivas CJM, Tarhini M, Badri W, Miladi K, Greige-Gerges H, Nazari QA, Rodriguez SAG, Roman RA, Fessi H, Elaissari A (2017) Nanoprecipitation process: from encapsulation to drug delivery. Int J Pharm 532:66–81
19. Anton N, Benoit J-P, Saulnier P (2008) Design and production of nanoparticles formulated form nano-emulsion templates—a review. J Control Release 128:185–199

20. Mora-Huertas CE, Fessi H, Elaissari A (2010) Polymer-based nanocapsules for drug delivery. Int J Pharm 385:113–142
21. GhavamiNejad A, Unnithan AR, Sasikala ARK, Samarikhalaj M, Thomas RG, Jeong YY, Nasseri S, Murugesan P, Wu D, Park CH, Kim CS (2015) Mussel-inspired electrospun nanofibers functionalized with size-controlled silver nanoparticles for wound dressing application. ACS Appl Mater Interfaces 7:12176–12183
22. Zahmatkeshan M, Adel M, Bahrami S, Esmaeili F, Rezayat SM, Saeedi Y, Mehravi B, Jameie SB, Ashtari K (2019) Polymer-based nanofibers: preparation, fabrication, and applications. In: Barhoum A, Bechelany M, Makhlouf A (eds) Handbook of nanofibers. Springer, Berlin
23. Guo YB, Zhang YJ, Liu HB, Lai SW, Li YL, Li YJ, Hu WP, Wang S, Che CM, Zhu DB (2010) Assembled organic/inorganic p–n junction interface and photovoltaic cell on a single nanowires. J Phys Chem Lett 1:327–330
24. Wu CG, Bein T (1994) Conducting carbon wires in ordered, nanometer-sized channels. Science 266:1013
25. Steinhart M, Wendoff JH, Griner A, Wehrspohn RB, Nielsch K, Schilling J, Choi J, Gösele U (2002) Polymer nanotubes by wetting of ordered porous templates. Science 296:1997
26. Guo YB, Tang QX, Liu HB, Zhang YJ, Li YL, Hu WP, Wang S, Zhu DB (2008) Light-controlled organic/inorganic p–n junction nanowires. J Am Chem Soc 130:9198–9199
27. Gence L, Faniel S, Gustin C, Melinte S, Bayot V, Callegari V, Reynes O, Demoustier-Champagne S (2007) Structural and electrical characterization of hybrid metal-polypyrrole nanowires. Phys Rev B 76:1–8
28. Callegari V, Gence L, Melinte S, Demoustier-Champagne S (2009) Electrochemically template-grown multi-segmented gold-conducting polymer nanowires with tunable electronic behavior. Chem Mater 21:4241–4247
29. Zhang LJ, Long YZ, Chen ZJ, Wan MX (2004) The effect of hydrogen bonding on self-assembled polyaniline nanostructures. Adv Funct Mater 14:693–698
30. Ding HJ, Shen YJ, Wan MX, Chen ZJ (2008) Formation mechanism of polyaniline nanotubes by a simplified template-free method. Macromol Chem Phys 209:864–871
31. Ding HJ, Wan MX, Wei Y (2007) Controlling the diameter of polyaniline nanofibers by adjusting the oxidant redox potential. Adv Mater 19:465–469
32. Ding HJ, Long YZ, Shen JY, Wan MX (2010) $Fe_2(SO_4)_3$ as a binary oxidant and dopant to thin polyaniline nanowires with high conductivity. J Phys Chem B 114:115–119
33. Tang N, Jiang Y, Qu H, Duan X (2017) Conductive polymer nanowires gas sensor fabricated by nanoscale soft lithography. Nanotechnology 28:485301
34. Wang J, Dia J, Yarlagadda T (2005) Carbon nanotubes-conducting-polymer composite nanowires. Langmuir 21:9–12
35. Basnar B, Weizmann Y, Cheglakov Z, Willner I (2006) Synthesis of nanowires using dip-pen nanolithography and biocatalyic inks. Adv Mater 18:713–718
36. Tatum WK, Luscombe CK (2018) π-conjugated polymer nanowires: advances and perspectives toward effective commercial implementation. Polym J 50:659–669
37. Long Y-Z, Li M-M, Gu C, Wan M, Duvail J-L, Lui Z, Fan Z (2011) Recent advances in synthesis, physical properties and applications of conducting polymer nanotubes and nanofibers. Prog Polym Sci 34:1415–1442
38. Peponi L, Puglia D, Torre L, Valentini L, Kenny JM (2014) Processing of nanostructured polymers and advanced polymeric based nanocomposites. Mater Sci Eng R 85:1–46
39. Tang C, Hackenberg K, Fu Q, Ajayan PM, Ardebili H (2012) High ion conducting polymer nanocomposites electrolytes using hybrid nanofillers. Nano Lett 12:1152–1156
40. Peponi L, Tercjak A, Torre L, Mondragon I, Kenny JM (2009) Nanostructured physical gel of SBS block co-polymer and Ag/DT/SBS nanocomposites. J Mater Sci 44:1287–1293
41. Zhou S, Sakamoto T, Wang J, Sugawara-Narutaki A, Shimojima A, Okubo T (2012) One-dimensional assembly of silica nanospheres: effect of nonionic block copolymers. Langmuir 28:13181–13188
42. Blanco E, Shen H, Ferrari M (2015) Principles of nanoparticle design for overcoming biological barriers to drug delivery. Nat Biotechnol 33:941–951

43. Cabral H, Matsumoto Y, Mizuno K, Chen Q, Murakami M, Kimura M, Terada Y, Kano MR, Miyazono K, Uesaka M, Nishiyama N, Kataoka K (2011) Accumulation of sub-100 nm polymeric micelles in poorly permeable tumors depends on size. Nat Nanotechnol 6:815–823
44. Prabha AS, Dorothy R, Jancirani S, Rajendran S, Singh G, Kumaran SS (2020) Recent advances in the study of toxicity of polymer-based nanomanterials. In: Rahendra S, Mukherjee A, Nguyen TA, Chandraiah G, Ritesh SK (eds) Nanotoxicity: prevention and antibacterial applications of nanomaterials. Elsevier, Amsterdam
45. Castro A, Berois N, Malanga A, Ortega C, Oppezzo P, Pristch O, Mombrú AW, Osinaga E, Pardo H (2021) Docetaxel in chitosan-based nanocapsules conjugated with an anti-Tn antigen mouse/human chimeric antibody as a promising targeting strategy of lung tumors. Int J Biol Macromol 182:806–814
46. He S, Zhong S, Meng Q, Fang Y, Dou Y, Gao Y, Cui X (2021) Sonochemical preparation of folate-decorated reductive-responsive carboxymethylcellulose-based nanocapsules for targeted drug delivery. Carbohydr Polym 266:118174
47. Zhao D, Jiang K, Wang Y, Cheng J, Mo F, Luo T, Guo Y, Zhang C, Song J (2021) Out-of-the-box nanocapsules packed with on-demand hydrophobic anticancer drugs for lung targeting, esterase triggering, and synergy therapy. Adv Healthc Mater 10
48. Nicolas S, Bolzinger MA, Jordheim LP, Chevalier Y, Fessi H, Almouazen E (2018) Polymeric nanocapsules as drug carriers for sustained anticancer activity of calcitriol in breast cancer cells. Int J Pharm 550:170–179
49. Neto SF, Prada L, Achod LDR, Torquato HFV, Lima CS, Paredes-Gamero EJ, de Moraes MOS, Lima ES, Sosa EH, de Souza TP, Amado JRR (2021) α-amyrin-loaded nanocapsules produce selective cytotoxic activity in leukemic cells. Biomed Pharmacother 139:111656–111666
50. Beck RCR, Chaves PS, Goyanes A, Vukosavljevic B, Buanz A, Windbergs M, Basit AW, Gaisford S (2017) 3D printed tablets loaded with polymeric nanocapsules: an innovative approach to produce customized drug delivery systems. Int J Pharm 528:268–279
51. Araújo RS, Garcia GM, Vilela JMC, Andrade MS, Oliveira LAM, Kano EK, Lange CC, e Brito MAVP, de Mello Brandão H, Mosqueira VCF (2019) Cloxacillin benzathine-loaded polymeric nanocapsules: physicochemical characterization, cell uptake, and intramammary antimicrobial effect. Mater Sci Eng C 104:110006
52. Ferreira LM, Cervi VF, Sari MHM, Barbieri AV, Ramos AP, Copetti PM, de Brum GF, Nascimento K, Nadal JM, Farago PV, Sagrillo MR, Nogueira CW, Cruz L (2018) Diphenyl diselenide loaded poly(ε-caprolactone) nanocapsules with selective antimelanoma activity: development and cytotoxic evaluation. Mater Sci Eng C 91:1–9
53. Venturini CG, Bruinsmann FA, Contri RV, Fonseca FN, Frank LA, D'Amore CM, Raffin RP, Buffon A, Pohlmann AR, Guterres SS (2015) Co-encapsulation of imiquimod and copaiba oil in novel nanostructured systems: promising formulations against skin carcinoma. Eur J Pharm Sci 79:36–43
54. Ushirobira CY, Afiune LAF, Pereira MN, Cunha-Filho M, Gelfuso GM, Gratieri T (2020) Dutasteride nanocapsules for hair follicle targeting: effect of chitosn-coating and physical stimulus. Int J Biol Macromol 151:56–61
55. Villegas MR, Baeza A, Vallet-Regí M (2015) Hybrid collagenase nanocapsules for enhanced nanocarrier penetration in tumoral tissues. ACS Appl Mater Interfaces 7:24075–24081
56. Onder A, Ozay H (2021) Synthesis and characterization of biodegradable and antioxidant phosphazene-tannic acid nanospheres and their utilization as drug carrier material. Mater Sci Eng C 120:111723
57. Das MP, Pandey G, Neppolian B, Das J (2021) Design of poly-L-glutamic acid embedded mesoporous bioactive glass nanospheres for pH-simulated chemotherapeutic drug delivery and antibacterial susceptibility. Colloids Surf B 202:111700
58. Loghmani MH, Shojaie AF, Hosseini SA (2021) Gluthione-responsive hydrogel and molecularly imprinted polymer nanospheres: new aspect on cisplatin delivery. J Ind Eng Chem 96:98–108
59. Kreuter J (2013) Drug delivery to the central nervous system by polymeric nanoparticles: what do we know? Adv Drug Deliv Rev

60. Spirescu VA, Chircov C, Grumezescu AM, Andronescu E (2021) Polymeric nanoparticles for antimicrobial therapies: an up-to-date overview. Polymers 13:724
61. Ryu WM, Kim S-N, Min CH, Choy YB (2019) Dry tablet formulation of PLGA nanoparticles with a preocular applicator for tropical drug delivery to the eye. Pharmaceuticals 11:651
62. Silva MM, Calado R, Marto J, Bettencourt A, Almeida AJ, Goncalves LMD (2017) Chitosan nanoparticles as a mucoadhesive drug delivery system for ocular administration. Mar Drugs 15:370
63. Xu X, Sun L, Zhou L, Cheng Y, Cao F (2020) Functional chitosan oligosaccharide nanomicelles for tropical ocular drug delivery of dexamethasone. Carbohydr Polym 227:115356
64. Lancina MG, Wang J, Williamson GS, Yang H (2018) DenTimol as a dendrimeric timolol analogue for glaucoma therapy: synthesis and preliminary efficacy and safety assessment. Mol Pharm 15:2883–2889
65. Lorenzo-Veiga B, Sigurdsson HH, Loftsson T, Alvarez-Lorenzo C (2019) Cyclodextrin-amphiphilic copolymer supramolecular assemblies for the ocular delivery of natamycin. Nanomaterials 9:745
66. Patil A, Lakhani P, Taskar P, Wu K-W, Sweeney C, Avula B, Wang Y-H, Khan IA, Majumdar S (2018) Formulation development, optimization, and *in vitro–in vivo* characterization of natamycin loaded PEGylated nano-lipid carriers for ocular applications. J Pharm Sci 107:2160–2171
67. Celebiogle A, Uyar T (2021) Electrospun formulation of acyclovir/cyclodextrin nanofibers for fast-dissolving antiviral drug delivery. Mater Sci Eng C 118:111514
68. Ponrasu T, Chen B-H, Chou T-H, Wu J-J, Chen Y-S (2021) Fast dissolving electrospun nanofibers fabricated from jelly fig polysaccharide/pullulan for drug delivery applications. Polymers 13:241
69. Mitrakos V, Hands PJW, Cummins G, Macintyre L, Denison FC, Flynn D, Desmulliez MPY (2018) Nanocomposite-based microstrctured piezoresistive pressure sensor for low-pressure measurement range. Micromachines 9:43
70. Lee H, Kwon D, Cho H, Park I, Kim J (2017) Soft nanocomposites based multi-point, multi-directional strain mapping sensor using anisotropic electrical impedance tomography. Sci Rep 7:39837
71. Kanoun O, Bouhamed A, Ramalingame R, Bautista-Quijano JR, Rajendran D, Al-Hamry A (2021) Review on conductive polymer/carbon nanotubes nanocomposites based flexible and stretchable strain and pressure sensors. Sensors 21:341
72. Yin F, Ye D, Zhu C, Qui L, Huang Y (2017) Stretchable, highly durable ternary nanocomposites strain sensor for structural health monitoring of flexible aircraft. Sensors 17:2677
73. Rahman NS, Greish YE, Mahmoud ST, Qamheih NN, El-Maghrby HF, Zeze D (2021) Fabrication and characterization of cellulose acetate-based nanofibers and nanofilms for H_2S gas sensing application. Carbohydr Polym 258:117643
74. Lee SH, Bang JH, Kim J, Park C, Choi MS, Mirzaei A, Im SS, Ahn H, Kim HW (2021) Sonochemical synthesis of PEDOT:PSS intercalated ammonium vanadate nanofiber composite for room-temperature NH_3 sensing. Sens Actuators B Chem 327:128924
75. Narouei FH, Livernois L, Andreescu D, Andreeacu S (2021) Highly sensitive mercury detection using electroactive gold-decorated polymer nanofibers. Sens Actuators B Chem 329:129267
76. Li X, Zhuang Z, Qi D, Zhao C (2021) High sensitive and fast response humidity sensor based on polymer composite nanofibers for breath monitoring and non-contact sensing. Sens Actuators B Chem 330:129239
77. Wang D, Zhang D, Li P, Yang Z, Mi Q, Yu L (2021) Electrospinning of flexible poly(vinyl alcohol)/MXene nanofiber-based humidity sensor self-powered by monolayer molybdenum diselenide piezoelectric nanogenerator. Nano Micro Lett 57
78. Öndeş B, Akpınar F, Uygun M, Muti M, Uygun DA (2021) High stability potentiometric urea biosensor based on enzyme attached nanoparticles. Microchem J 160:105667
79. Lui Y, Wang Y-M, Zhu W-Y, Zhang C-H, Tang H, Jiang J-H (2018) Conjugated polymer nanoparticles-based fluorescent biosensor for ultrasensitive detection of hydroquinone. Anal Chim Acta 1012:60–65

80. Zarei M, Samimi A, Khorram M, Abdi MM, Golestaneh SI (2021) Fabrication and characterization of conductive polypyrrole/chitosn/collagen electrospun nanofiber scaffold for tissue engineering. Int J Biol Macromol 168:175–186
81. Maharjan B, Park J, Kaliannagounder VK, Awasthi GP, Joshi MK, Park CH, Kim CS (2021) Regenerated cellulose nanofiber reinforced chitosan hydrogen scaffolds for bone tissue engineering. Carbohydr Polym 251:117023
82. Oudadesse H, Najem S, Mosbahi S, Rocton N, Refifi J, Feki HE, Lefeuvre B (2020) Development of hybrid scaffold: bioactive glass nanoparticles/chitosan for tissue engineering applications. J Biomed Mater Res A
83. Wu T, Zhang J, Wang Y, Li D, Sun B, El-Hamshary H, Yin M, Mo X (2018) Fabrication and preliminary study of a biomimetric tri-layer tubular graft based on fibers and fiber yarns for vascular tissue engineering. Mater Sci Eng C 82:121–129
84. Lui Q, Ying G, Jiang N, Yetisen AK, Yao D, Xie X, Fan Y, Lui H (2021) Three-dimensional silk fibroin microsphere-nanofiber scaffolds for vascular tissue engineering. Med Nov Technol Devices 9:100051
85. Jiang C, Wang K, Lui Y, Zhang C, Wang B (2021) Using wet electrospun PCL/gelatin/CNT yarns to fabricate textile-based scaffolds for vascular tissue engineering. ACS Biomater Sci Eng
86. Maroufi LY, Ghorbani M (2021) Injectible chitosan-quince seed gum hydrogels encapsulated with curcumin loaded-halloysite nanotubes designed for tissue engineering application. Int J Biol Macromol 177:485–494
87. Rezakazemi M, Sadrzadeh M, Mohommadi T, Matsura T (2017) Methods for preparation of organic–inorganic nanocomposite polymer electrolyte membranes for fuel cells. In: Inamuddin D, Mohommad A, Asiri A (eds) Organic–inorganic composite polymer electrolyte mambranes. Springer, Berlin
88. Miishra AK, Bose S, Kuila T, Kim NH, Lee JH (2012) Silicate-based polymer-nanocomposite membranes for polymer electrolyte membrane fuel cells. Prog Polym Sci 37:842–869
89. Yaqoob AA, Ibrahim MNM, Umar K, Bhawani SA, Khan A, Asiri AM, Khan MR, Azam M, AlAmmari AM (2021) Cellulose derived graphene/polyaniline nanocomposite anode for energy generation and bioremediation of toxic metals via benthic microbial fuel cells. Polymers 13:135
90. Shi Y, Peng L, Ding Y, Zhao Y, Yu G (2015) Nanostructured conductive polymer for advanced energy storage. Chem Soc Rev
91. Gosh S, Maiyalagan T, Basu RN (2016) Nanostructured conducting polymers for energy applications: towards a sustainable platform. Nanoscale 8:6921–6947
92. Hu H, Zhang F, Luo S, Chang W, Yue J, Wang C-H (2020) Recent advances in rational design of polymer nanocomposites dielectrics for energy storage. Nano Energy 74:104844
93. Goswami Y, Sharma S (2021) Graphener reinforced biopolymer nanocomposites inn energy storage applications. In: Sharma B, Jain P (eds) Graphene based biopolymer nanocomposites. Composites Science and Technology. Springer, Berlin
94. Surmenev RA, Chernozem RV, Pariy IO, Surmeneva MA (2021) A review on piezo- and pyroelectric responses of flexible nano- and micropatterned polymer surfaces for biomedical sensing and energy harvesting applications. Nano Energy 79:105442
95. Saenz F, Ronchi A, Mauri M, Vadrucci R, Meinardi F, Monguzzi A, Weder C (2021) Nanostructured polymers enabled stable and efficient low-power photon upconversion. Adv Funct Mater 31:2004495
96. Chebotarevaa RD, Remeza SV, Bashtana SY (2020) Water softening and disinfection using an electrolysis unit with a filtering cartridge. J Water Chem Technol 42:54–59
97. Al-Amshawee S, Yunus MYBM, Azoddein AAH, Hassell DG, Dakhil IH, Hasan HA (2020) Elecrodialysis desalination for water and wastewater: a review. Chem Eng J 380:122231
98. Verma B, Balomajumder C (2020) Hexavalent chromium reduction form real electroplating wastewater by chemical precipitation. Bull Chem Soc Ethiop 34:67–74
99. Amari A, Alzahrani FM, Katubi KM, Alsaiari NS, Tahoon MA, Rebah FB (2021) Clay-polymer nanocomposites: preparations and utilization for pollutants removal. Materials 14:1365

100. Fahim IS (2021) Graphene reinforced biopolymer nanocomposites for water filtration applications. In: Sharma B, Jain P (eds) Graphene based biopolymer nanocomposites. Composites Science and Technology, Springer, Berlin
101. Lv D, Zhu M, Jiang Z, Jiang S, Zhang Q, Xiong R, Huang C (2018) Green electrospun nanofibers and their application in air filtration. Macromol Mater Eng 1800336
102. Zhang S, Lui H, Yu J, Ding B (2016) Anti-deformed polyacrylonitrile polysulfone composite membrane with binary structures for effective air filtration. ACS Appl Mater Interfaces 8:8086–8095
103. Purwar R, Goutham KS, Srivastava CM (2016) Electrospun sericin/PVA/clay nanofibrous mats for antimicrobial air filtration mask. Fibers Polym 17:1206–1216
104. Pourhashem S, Saba F, Duan J, Rashidi A, Guan F, Nezhad EG, Hou B (2020) Polymer/inorganic nanocomposites coatings with superior corrosion protection performance: a review. J Ind Eng Chem 88:29–57
105. Gaballah S, Shehata N, Shaaban M, Nosier S, Hefnawy A, Hamed A, Samir E (2017) Corrosion inhibition of aluminium in hydrochloric acid solution using ceria doped polyvinyl chloride nanofiber. Int J Electrochem Sci 12:1094–1105
106. Balakrishnan B, Raja S, Rajagopal A (2021) Influence of MWCNT fillers on vibroacoustic characteristics of polymer nanocomposites and coated aircraft panels. Appl Acoust 172:107604
107. Singh TV, Shagolsem LS (2021) Biopolymer based nano-structured materials and their applications. In: Swain BP (eds) Nanostructured materials and their applications (Materials Horizons: Form Nature to Nanomaterials). Springer, Berlin
108. Friedrichs S, Bowman DM (2021) COVID-19 may become nanomedicine's finest hour yet. Nat Nanotechnol 16:358–364

Chapter 13
Polymer Nanocomposite Membranes for Water Remediation

Divyansh Upreti and T. Umasankar Patro

1 Introduction

Water pollution poses a serious threat to human health and ecology. The problem is more persistent especially in developing countries due to the increasing population and economic activities. As per UNICEF (United Nations Children's Fund), globally about 1800 deaths of children every day under the age of 5 and about 0.5 million diarrheal deaths per year (as per the World Health Organization) have been reported due to consumption of water from polluted sources [1]. Water can be contaminated by various industrial effluents and anthropogenic activities. The sources of contamination are often heavy metal ions, organic dyes, pharmaceutical waste, etc. Another source of water pollution emanates from the excessive use of 'biocides' or 'pesticides' in agriculture and allied food industries. Further, disposal from meat processing industries and slaughterhouses may also cause water contamination with 'zoonotic' disease-causing pathogens besides other pollutants [2]. Besides their environmental implications, heavy metal ion pollutants also cause high human mortality due to their neurotoxic and carcinogenic effects [3], which lead to diseases like Minamata, Itai-Itai, etc., [2, 3]. Similarly, organic dye pollutants from textile industries can cause serious health hazards in humans and animals [4, 5]. Therefore, a considerable research effort has been devoted to water remediation in academia as well as in various industries.

Contaminated water can be purified by various means like simple filtration, membrane filtration, adsorption, reverse osmosis, coagulation–flocculation, chemical precipitation, nanofiltration, etc. Notwithstanding the wide range of techniques, each technique has its advantages and limitations. Some may offer high throughput but less efficiency, while others may be efficient but expensive. Hence

D. Upreti · T. U. Patro (✉)
Department of Metallurgical and Materials Engineering, Polymeric Materials Laboratory, Defence Institute of Advanced Technology, Girinagar, Pune 411025, India
e-mail: umasankarp@diat.ac.in

B. P. Swain (ed.), *Advances in Nanostructured Materials*, Materials Horizons: From Nature to Nanomaterials, https://doi.org/10.1007/978-981-16-8391-6_13

sometimes more than one technique is combined for better efficacy of wastewater treatment. Among these, water remediation using porous polymeric membrane offers several advantages over other methods such as flexibility in designing pore morphology, simple filtration set-up, high efficiency, etc. However, monolithic polymeric membranes often do not offer high efficiency due to the lack of adequate functionalities, required for the complete removal of pollutants. These limitations have, to a large extent, been addressed by the advent of nanotechnology. In this context, nanomaterials offer a great promise in water remediation and wastewater treatment due to their high surface area to volume ratio, high adsorption capability, and functionality to capture various water pollutants. To utilize their effective surface area, nanoparticles (NPs) are either coated onto the polymeric membranes [6] or dispersed uniformly in the polymer matrix to prepare 'nanocomposites membranes' and these composite membranes are found to exhibit superior adsorption of heavy metal ions and dyes from wastewater than their monolithic polymer membrane counterparts [7, 8]. Several nanoparticle-embedded polymer membranes have been developed. The notable polymers used for membrane technology are poly(vinylidene fluoride) (PVDF) [9], poly(ether sulfone) (PES) [10], poly(acrylonitrile) (PAN) [11], poly(ethyleneimine) (PEI) [12], poly(vinyl alcohol) (PVA) [13], poly(ε-caprolactone) (PCL) [14], etc. These polymers offer excellent mechanical properties, polarity (PVDF in β-phase), and membrane forming ability with a tunable pore size. On the other hand, incorporation of NP not only provides an effective pathway for introducing functionality but also enhances mechanical and physical properties of the membrane [15–18]. However, the addition of nanofillers is not free from problems, particularly when carbon nanotubes (CNT) and inorganic NPs are used as fillers owing to their agglomeration tendency in the polymer matrix due to their strong interparticle van der Waals forces [19]. Hence, these nanofillers are often treated with organic surfactants [20], ionic liquids [21], or with strong acids [22] to circumvent the van der Waals forces and *vis-a-vis* to have improved adhesion with polymer matrix [23]. Different NPs or nanofillers that are generally added into polymers for achieving membrane functionality are: (i) CNT, (ii) graphene oxide (GO), (iii) carbon nanofibers (CNF) [24], (iv) metal oxide frameworks (MOF) [25], (v) metal oxide NP [26], and (vi) nanoclays [27].

In this context, the present chapter gives a concise account of the literature studies reported on water remediation using nanoparticle-incorporated polymer membranes with the focus on heavy metal ion adsorption, organic dye and pharmaceutical drug removal, and oil–water separation from contaminated water. The physicochemical (water contact angle, porosity, water flux, flux recovery rate, and fouling properties, etc.) and mechanical properties of the various membranes as a result of nanoparticle incorporation are succinctly summarized. To make this article more concise, only three different types of nanomaterials, viz., (i) carbon-based NP (CNT and GO), (ii) nanoclays (montmorillonite, laponite, and halloysite), and (iii) inorganic NP are considered. The chapter also briefly describes the structure and general properties of the polymeric membrane, and the different methods adopted for polymer membrane preparation with and without nanofillers, to give the reader a basic idea on the topic.

Structure and properties of a polymeric membrane

A polymeric membrane is essentially a porous structure with interconnected pores. The size of the pores varies from a few nanometers to several micrometers depending on the membrane type (microfiltration, ultrafiltration, or nanofiltration). There is the formation of 'finger-like pores as well [28]. The membrane should possess high separation efficiency in combination with good water permeation characteristics. The membrane should also have good fouling-resistant properties. For this, the membrane should have hydrophilic in nature. However, most of the commercial membranes made from pristine polymer monoliths are hydrophobic. Hence, various strategies have been adopted to induce hydrophilicity in polymeric membranes [29–31].

Figure 1 illustrates the typical structure and properties of a polymeric membrane, which is mainly characterized by its morphology, chemical, mechanical, adsorption properties, and water flux capability. The pore size and porosity of a membrane can be controlled by adjusting various parameters during membrane preparation. However, physical and mechanical properties depend on the polymer used for membrane fabrication. The mechanical property of the membrane also depends on the porosity and molecular weight of the polymer [32]. However, functionality and to some extent pore size determines the selectivity and separation performance of the membrane. For hot water treatment, the thermal stability of the polymer membrane is of prime importance. In various industrial applications, the contaminated water is usually treated at elevated temperatures to maintain a sustainable and energy-efficient water recycling process. Commercially available thin-film composite membranes suffer from limited thermal stability at temperatures >45 °C, resulting in a shorter working time [33]. In this context, NP has the potential to enhance the thermal stability of the membrane [34]. Another impending issue in the membrane is the trade-off between

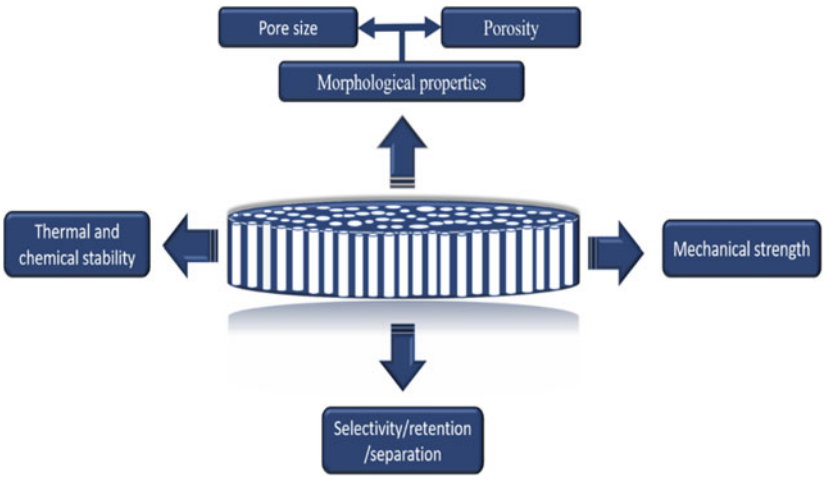

Fig. 1 Schematic representation of the flowchart indicating membrane properties

permeability and selectivity, which can be overcome by incorporating hydrophilic NP or by making them hydrophilic.

Removal of heavy metal ions from an aqueous solution not only depends on the pore size of membranes (sieving effect) but also on the functionality of the membrane. Heavy metal ions being positively charged can be bonded with the negative groups, like hydroxyl, carboxyl [35] amino groups [15, 28] present in functionalized NP, thus promoting chemisorption. The removal of heavy metal ions is attributed to the electrostatic interaction (attractive or repulsive) between charged membrane and heavy metal ions [15, 28, 35]. However, the organic dyes could be either cationic or anionic. Separation of dyes from aqueous solutions through the membrane can happen either through physisorption, electrostatic interaction (either attraction or repulsion), or to some extent sieving effect, depending on the relative size of the dye molecule and membrane pore size [36–38].

Here, we discuss some of the important properties of porous polymeric membrane.

Pore size and porosity

Pore size determination is one of the important aspects of membrane characterization, which is done by microscopy techniques and porometry measurements [39]. Porosity, P, a measure of the total void space in the membrane can be estimated by the following equation (Eq. (1)) [40]:

$$\%P = \frac{W_w - W_d}{\rho_w \times A \times D} \times 100 \tag{1}$$

where W_w = weight of wet membrane, W_d = weight of dry membrane, D = membrane thickness, A = area of the wet membrane, and ρ_w = density of water.

Water flux

Pure water flux is another important parameter that relates the structure of the membrane to its performance efficiency. It is generally defined as the volume of water passing through the membrane per unit area per unit time and per unit pressure. Water flux can be determined by the following equation (Eq. (2)) [41]:

$$J_w = \frac{Q}{A\Delta t} \tag{2}$$

where J_w is pure water flux, given in $\mathrm{Lm^{-2}\ h^{-1}}$, A is the effective area of membrane through which the filtrate passes, Q is the volume of permeate collected, and Δt is the sampling time interval.

Fouling properties

Membrane fouling is one of the common problems faced in membrane-based separation operations. Upon continuous water flux through the membrane, there is a formation of an adsorbent cake layer on the surface of the membrane, resulting in a

decline in water flux. The efficiency of a membrane in treating wastewater relies on its ability to have constant water flux while scaling up the separation process. The efficacy of a membrane can be expressed by flux recovery ratio (FRR) to quantify the fouling characteristic of a membrane and the percentage FRR can be expressed by the following equation [41]:

$$FRR(\%) = \frac{J_2}{J_1} \times 100 \tag{3}$$

where J_2 is the pure water flux (PWF) of the cleaned membrane after the operation, J_1 is pure water flux. The higher value of FRR indicates better antifouling properties.

2 Methods for Preparation of Porous Polymeric Membrane

The porous polymeric membrane can be fabricated by the following methods: (i) phase inversion technique, (ii) electrospinning, and (iii) solvent casting followed by particle leaching.

2.1 Phase Inversion Technique

The phase inversion technique can further be divided into: (i) non-solvent induced and (ii) thermal-induced phase inversion. These techniques are briefly discussed below.

Non-solvent induced phase inversion or immersion precipitation technique

Phase inversion through immersion precipitation is a commonly used membrane preparation approach. In this method, the polymer solution is cast on a suitable support and then immersed in a non-solvent-containing coagulation bath (usually water). When a homogenous polymer solution is introduced to non-solvent, due to solvent/non-solvent exchange, the polymer begins to coagulate and separates from the solution, resulting in the formation of the porous structure. This technique is first developed by Loeb and Sourirajan for making cellulose acetate porous membrane for desalination of seawater [42]. In this method, they have cast a cellulose acetate film on a solid support using the polymer solution with acetone as a solvent in the temperature range of 0–10 °C. The solvent was then allowed to evaporate for 3–4 min at the same temperature and the film was then immersed in the water bath at 0 °C to make a porous membrane. The resulting membrane showed enhanced demineralization of seawater in comparison to the existing techniques [42]. For recognizing their contribution, the method is also known as the Loeb–Sourirajan

method. This method was later termed the "phase inversion method". This process is most commonly used for making porous membranes [43–46].

The schematic of the process is shown in Fig. 2. The combination of phase separation and mass transfer decides the structure of the membrane. Further, during the process, the kinetic and thermodynamic parameters of the casting solution affect the morphology and properties of the resulting membrane. The membrane prepared by this technique creates a highly porous material (Fig. 3). When NPs are embedded

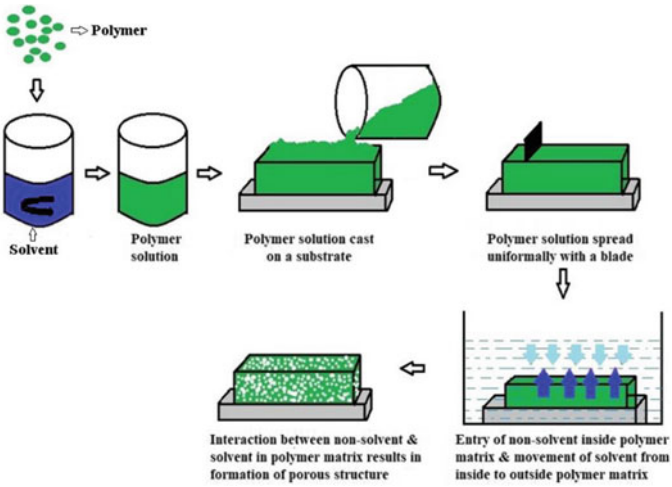

Fig. 2 Schematic diagram representing membrane fabrication via non-solvent induced phase separation technique

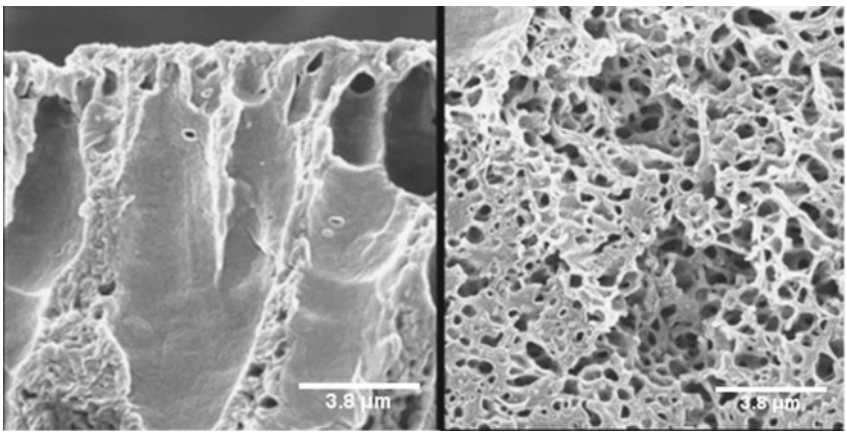

Fig. 3 Typical cross-sectional SEM images of porous PVDF membrane prepared by non-solvent-induced phase inversion or immersion precipitation technique [48]

into the polymer membrane, it significantly alters the thermodynamics (e.g., solvent–nonsolvent interaction) of the system, in turn, influencing the properties of the nanocomposite membrane [47]. However, these details are not presented in the present chapter.

The membrane structure, properties, and chemical interactions during membrane preparation by the phase inversion method depend on the choice of polymer and additives used in the casting solution [49]. The following factors control the pore size and pore structure of the membrane:

- *Polymer concentration*: The pore size and porosity of the membrane in general decrease as the polymer concentration in solvent or viscosity increases due to decreased solvent–non-solvent interaction, and as a result, flux decreases with decreasing porosity [50].
- *Solvent and non-solvent selection*: Selection of a suitable solvent and non-solvent has a profound effect on the membrane's morphology and properties. The high polymer solubility results in a high porosity [51]. Different solvents for a given polymer may result in different porous structures, due to variable densities of the solvents and their altered interaction with the polymer [52].
- *The type of additives*: Often low molecular weight molecules (e.g., poly(ethylene glycol), PEG) is added to the casting solution to speed up the precipitation process during immersion and control the solution viscosity [53–55]. Sometimes pore-forming agents, also known as, porogens, (e.g., poly(*N*-vinyl-2-pyrrolidone), PVP) are added to produce higher porosity [27].
- *Precipitation bath temperature*: By increasing the bath temperature, the membrane pore size increases [56].

Thermally induced phase inversion technique

Thermally induced phase separation (TIPS) or inversion method is a specialized method for membrane preparation, which is used for the polymer–solvent pair that does not dissolve at room temperature but dissolves at elevated temperature which is close to the melting point of the polymer and the resulting polymer solution is cast on support at high temperature. Then the temperature is reduced for demixing to occur. The solvent is then evaporated by the freeze-drying method. This method cannot be adopted for all the polymer–solvent pairs due to the problem of solvent evaporation at high temperatures, hence used for specific cases. For instance, Matsuyama et al. have prepared hydrophilic microporous membranes of ethylene/acrylic acid copolymer ionomers and PE with diphenyl ether as a solvent (B.P. ~ 260 °C) [57] via this technique. The technique produces membranes with highly porous microstructure [58, 59]. The process for producing porous membranes using this technique is shown schematically in Fig. 4.

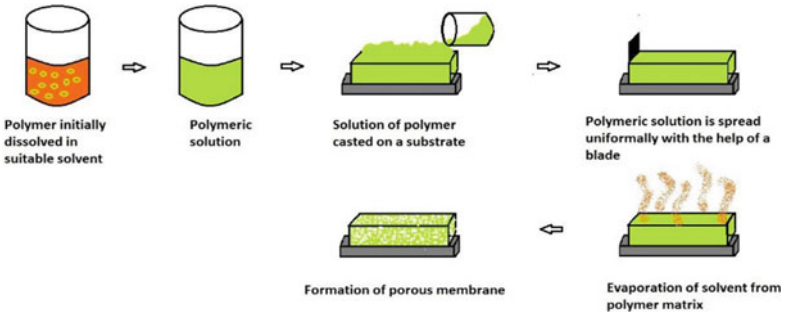

Fig. 4 Schematic illustration of membrane fabrication via thermally induced phase separation technique

2.2 Electrospinning

Electrospinning is a versatile process for making nanofibers in the size range of a few hundred nanometres to a few micrometers. In this method, a high voltage is applied to a metallic needle (electrode) connected to a syringe containing viscous polymer solution or melt. When the electrostatic force overcomes surface tension and viscosity of the polymer, a cone-shaped polymer droplet is formed at the vicinity of the syringe; this is known as the 'Taylor cone'. The cone-shaped liquid droplet is subsequently elongated to form a nanofiber jet and the fibers are ejected towards the oppositely charged electrode and simultaneously the solvent also gets evaporated [60]. A typical electrospinning setup comprises a pump, a reservoir (typically a syringe) containing polymer solution, a high voltage power source, and a collector as illustrated in Fig. 5.

The nanofibers obtained from the electrospinning technique find wide applications in biomedical scaffold [61], filtration [62], sensors [63], and energy harvesting

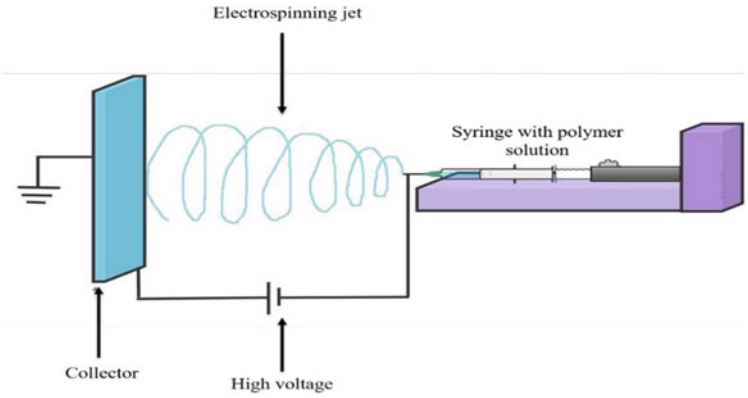

Fig. 5 Schematic representation of electrospinning setup

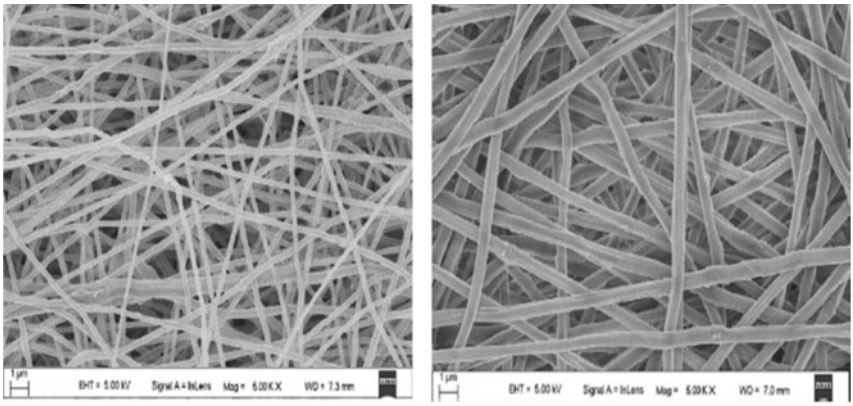

Fig. 6 SEM images of electrospun **a** PAN, **b** PAN/PEI-MWCNT nanofibers [15]

[64]. A membrane produced by electrospinning offers high porosity and surface area to volume ratio. These characteristic features of nanofiber membranes make them an attractive candidate for adsorbing heavy metal ions and organic dyes from water [65]. Nanofiller incorporation into nanofiber membrane further enhances the adsorption capability of the membrane by utilizing the effective surface area thereof [66]. Further, due to the versatility of the electrospinning process, the fiber size and morphology, and membrane porosity of the nanofiber mat can be engineered for water filtration. The polymer can be functionalized by grafting active species or by incorporating nanofillers before electrospinning. A typical scanning electron microscopy image of the electrospun nanofiber membrane of PAN/MWCNT composite is shown in Fig. 6. The images indicate that the incorporation of MWCNT-PEI into PAN nanofiber increases the fiber diameter [54].

2.3 Solution Casting Followed by Particulate Leaching

Solvent casting followed by particulate leaching is yet another process for producing porosity in polymeric membranes. In this method, the polymer is dissolved in an organic solvent with porogen like sodium chloride, sodium acetate dispersed in the solution [67, 68]. The mixture is poured into a mold or on a glass plate. As the solvent evaporates, the porogen particles are left behind in the polymer. The resulting film is immersed in a water bath which leaches out the porogen, making the structure porous. The process is schematically illustrated in Fig. 7 and a typical SEM image showing the porous nature of the membrane is also presented in Fig. 7 [69].

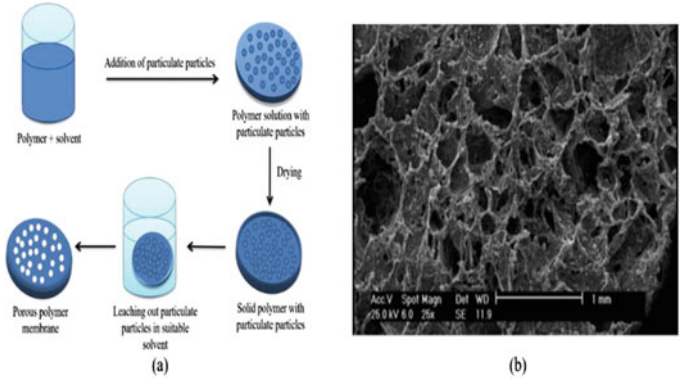

Fig. 7 A Schematic illustration of solvent casting followed by particulate leaching process (b) SEM image of a porous PCL membrane formed by solvent casting and particulate leaching [69]

Mechanisms of water remediation using polymeric membranes

Membrane filtration can be divided into three main types: (i) microfiltration, (ii) ultrafiltration, and (iii) nanofiltration, depending on their pore size [70]. The filtration efficiency also depends on the functionality and physicochemical properties of the membrane. The mechanisms which mainly govern the filtration process are the rejection of solutes, adsorption, ion exchange [71], and sieving and Donnan effects [72, 73]. Rejection is mainly governed by the surface chemistry of the membrane, for example, a hydrophilic surface would reject water-repelling substances like oil and vice versa. Adsorption depends on the functionality and available surface area of the membrane. This is the main mechanism for heavy metal ion and dye removal. Ion exchange is used mainly for heavy metal ion and salt rejection [71]. Sieving and Donnan effects are based on the size exclusion phenomenon. High molecular weight organic dyes, pharmaceutical drugs, and oligomeric pollutants can be separated by these mechanisms.

3 Nanocomposite Membranes for Water Remediation

3.1 Carbon-Based Nanocomposite Membrane for Water Remediation

Carbon-based NP may be referred to as the following materials: carbon nanotubes (CNT), graphene oxide (GO), graphene, carbon nanofibers (CNF), carbon soot, etc. Porous carbon and activated charcoal may be considered as nanostructured materials since they contain nanopores on their structure [74]. These NPs are often modified suitably and incorporated into the polymer matrix to make nanocomposite

membranes. The use of carbon-based materials has seen significant progress in fabricating polymer membranes in the past decade, which has been reviewed in the following section by taking CNT and GO as case studies.

3.1.1 CNT-Based Polymer Membranes

Since its discovery in 1991 by Iijima [75], CNTs have been used in numerous applications including energy storage [76], conducting composites [77], electromagnetic interference shielding [78], molecular electronics [79] and water filtration [80], just to name a few, due to their extraordinary electronic and thermal conductivity (200 W/m K) [81] and mechanical properties (Young's modulus, E = 270–950 GPa and strength, σ = 11–63 GPa) [82]. CNT can be best visualized into their two popular variants: (i) as a cylindrical roll of single graphene sheet into single-walled CNT (SWCNT), and (ii) multiple cylindrical rolls to make multi-walled CNT (MWCNT) as elucidated in Fig. 8. Owing to their huge surface area, ability to be chemically modified, affinity to metal ions, biocompatibility, and extraordinary mechanical properties, they are excellent candidates for adsorption of various pollutants from wastewater. However, due to their exorbitant cost and difficulty in processing, they may not be directly utilized as standalone material for water purification. Hence, CNTs are usually coated onto polymer membrane or embedded into the polymer matrix and subsequently, the CNT-incorporated polymer could be made into a nanocomposite membrane for water treatment. However, due to their inherent characteristics of agglomeration owing to the intertube van der Waals forces, it is not easy to disperse them uniformly in the polymer matrix [19]. But it is possible to introduce functional groups on CNT surface through various functionalization techniques, which help in overcoming the strong intertube van der Waals forces and facilitate uniform dispersion of CNTs in the polymer matrix to a large extent [23]. However, for most of the membrane applications, the CNT amount in the polymer

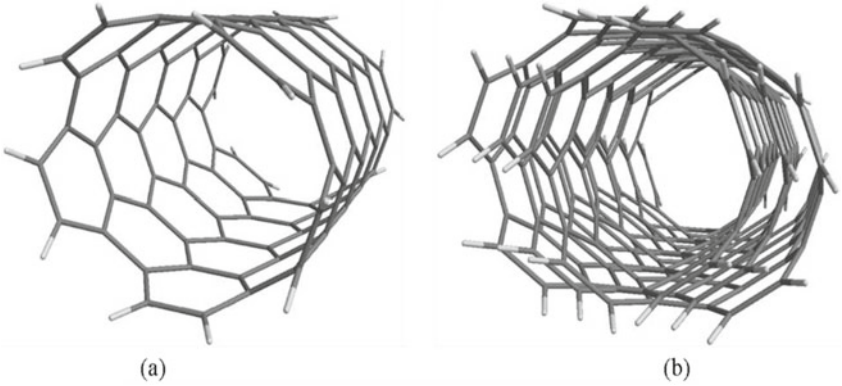

Fig. 8 Schematic representation of CNTs **a** SWCNT **b** MWCNT

is kept low, i.e., <5 wt% to mitigate the problem of agglomeration [15, 28]. Here, we review the preparation and properties of different CNT-based nanocomposite membranes through CNT functionalization and their plausible implications in water remediation. It has been observed from the literature study that MWCNTs are more widely used as modifying agents in various the polymer matrices for nanocomposite membrane fabrication than SWCNTs. This may be due to the reason that MWCNTs are easier to debundle and disperse in polymer matrix and to functionalize wide range of organic substances than SWCNTs.

Heavy metal ion removal and salt rejection

CNT-incorporated nanocomposite membranes have been found to exhibit significant improvements in heavy metal ion removal as compared to their monolithic polymer membranes. Sorption of heavy metal ions like Pb^{2+} and Cu^{2+} have been remarkably enhanced by using poly(ethyleneimine) (PEI)-modified MWCNT-incorporated PAN nanofiber mats, as reported by Deng et al. [15]. The nanofiber mats were fabricated by electrospinning followed by hot-pressing. The PEI was covalently bonded to the carboxylated-CNTs with help of 1-ethyl-3-(3-dimethyl aminopropyl)carbodiimide (EDC) and *N*-hydroxysuccinimide (NHS). The CNT-incorporated PAN membrane showed adsorption capacity of ~231 and ~108 mg/g of Pb^{2+} and Cu^{2+} ions as opposed to ~28 and ~5 mg/g of respective ions using bare PAN membrane from their aqueous solutions [15]. The resulting nanocomposite membranes with up to 3.5 wt% PEI-modified CNT displayed improved hydrophilic nature, mechanical and water flux properties [15]. In another study by Salehi et al., adsorption of Cu^{2+} ions has been significantly improved by using up to 2 wt% of NH_2-functionalized MWCNT as an additive in chitosan-PVA blends and the resulting composites were made into a membrane using the casting-evaporation method [28]. As a result, the Cu^{2+} adsorption efficiency increased from ~9.5 mg/g for the neat polymer membrane to ~18.3 mg/g for the CNT-incorporated chitosan-PVA membrane at 20 °C [28]. Moreover, with the addition of NH_2-MWCNT, the membrane showed thermodynamically more affinity to Cu^{2+} ions than the pristine polymer membrane and improved reusability [28]. Shah et al. have reported efficient removal of a series of heavy metal ions (Cr^{4+}, Pb^{2+}, Cd^{2+}, Cu^{2+}, As^{3+}) using three differently functionalized MWCNT (acid, amide, and azide) doped polysulfone (PSU) membrane, prepared by NIPS technique. Out of these, the azide-functionalized CNT-incorporated PSU membrane exhibited the best metal ion adsorption properties. The maximum adsorption efficiency reached up to ~5% for Cr^{4+} ion using 1 wt% azide-functionalized CNT-PSU membrane, as against only ~10% removal of the same ion using the bare PSU membrane. Further, CNT-embedded PSU membranes showed increased pore size and enhanced hydrophilicity [35]. Zhao et al. were able to achieve >90% salt ($ZnCl_2$, $MgCl_2$, $CuCl_2$, $CaCl_2$, $MgSO_4$, Na_2SO_4) rejection from aqueous solution using poly(dopamine) modified MWCNT (0.1 wt%) in PEI membrane [83]. In another study, Gupta et al. have found ~97, ~88, and ~94% removal of Cr^{6+}, As^{3+}, and Pb^{2+} ions, respectively, using 1% functionalized SWNT/PSU membranes, prepared by NIPS technique [84]. Shawky et al. have shown significant improvement in salt rejection by adding MWCNT into polyamide membrane, prepared by solution casting

followed by NIPS. They found NaCl rejection of >76% using the nanocomposite membrane as opposed to only ~24% rejection using pristine polyamide membrane [85].

Pharmaceutical drug and organic dye removal

Park et al. used alkylamine-grafted-MWCNTs as a functional filler in PVDF matrix and prepared a porous nanocomposite membrane by NIPS method. To improve the hydrophilicity and fouling resistance properties, the amine-MWCNT has been attached to the PVDF backbone by a complex bond formation using $CuCl_2$ as a catalyst and 4,4′-dinonyl-2,2′-dipyridyl as a ligand by atom transfer radical addition (ATRA) reaction. Consequently, the resulting membrane showed at least 2.5 times higher water flux, higher rejection of bovine serum albumin (BSA) protein (~98% against ~94% for pristine PVDF membrane), and superior foul-resistance properties than pristine PVDF membrane [86]. In another study, Masjoudi et al. immobilized an enzyme (laccase) on PVDF/MWCNT nanocomposite membrane surface by dip-coating for adsorption of two pharmaceutical model drugs: carbamazepine and diclofenac from their aqueous solutions. The membranes were prepared by the NIPS technique. They also showed that the addition of MWCNTs increased the pore size of the membrane. The efficient immobilization of laccase without losing their activity significantly was found when the PVDF/MWCNT membrane was treated with *N*-(3-dimethyl aminopropyl)-*N*′-ethyl carbodiimide hydrochloride and *N*-hydroxysuccinimide together. The removal efficiencies of carbamazepine and diclofenac drugs using enzyme-immobilized membrane were found to be ~27% in 48 h and 95% in 4 h, respectively [45]. Significant enhancement of water flux and antifouling properties have been reported by Wang et al. using sodium-lignosulfonate-modified CNT (s-CNT)-incorporated PES membranes, fabricated via NIPS technique [87]. Incorporation of s-CNT in membrane matrix resulted in increased porosity, mean pore size, hydrophilicity, and pure water flux; but BSA rejection decreased due to higher water flux. The nanocomposite membrane showed excellent antibacterial properties against *E. coli* [87].

The efficiency of organic dye removal from aqueous solutions has been significantly improved using carboxylated-MWCNT incorporated PES porous membranes, prepared by the NIPS technique [88]. The introduction of only 0.2 wt% carboxylated-MWCNT resulted in greater porosity, hydrophilicity, pure water flux, and tensile strength of the PES membrane. Further, the nanocomposite membrane exhibited significantly improved dye rejection from aqueous solution, i.e., up to 95% removal of bromothymol blue and methyl orange dyes against only 30–40% rejection by bare PES membrane [69]. CNT-incorporated PES membranes have also been able to reject high fractions of poly(ethylene glycol) (PEG) as a model pollutant from water [89]. In this study, 0.04 wt% nitrogen-doped CNT (N-CNT) in PES membrane could improve the hydrophilicity and water flux of the membrane, however, the percentage PEG rejection of the same membrane showed a decrease; while with 0.5 wt% of N-CNT, the percentage PEG rejection of the membrane was enhanced from 65% for pristine PES membrane to 77% for 0.5 wt% N-CNT loaded membrane [89]. Mousavi

et al. have demonstrated Malachite green dye rejection of ~99% from aqueous solution using a chitosan-treated CNT-coated PES nanocomposite membrane, prepared by dip-coating method [90]. The PES membrane was prepared by the NIPS method. A copolymer of polyamide and poly(ethylene oxide) (PEBA) was used as the matrix for chitosan-treated CNTs. The modified nanocomposite membranes exhibited enhanced hydrophilicity and improved pure water flux (~14 L m^{-2} h^{-1}) with 1 wt% chitosan-loaded CNTs in PEBA in comparison with pristine PES membrane [37]. Roy et al. found an order of magnitude higher water flux and comparable dye rejection (~97% rejection of Brilliant blue R and ~68% rejection of Safranin O dyes from aqueous and organic solvents) by modifying two commercially available membranes (PP and PES) with COOH-CNTs in comparison with the properties exhibited by the commercial membrane [38]. Antifouling, water, and BSA solution flux properties of polysulfone (PSU) membranes prepared by the NIPS method could be considerably enhanced by incorporating 0.25 wt% PEG-functionalized CNT [91]. The CNT-incorporated PSU membranes showed enhanced hydrophilicity, porosity, mean pore size, and FRR [91].

Oil–water separation

Polymeric porous membranes have also been employed in oil–water separation due to their tunable surface chemistry and high porosity [6]. Towards efficiently separating oil from the oil–water emulsion, Yang et al. dip-coated a commercially available PVDF membrane in 3-aminopropyltriethoxysilane (APTES)-grafted MWCNTs solution using polydopamine (PDA) as a binder to prepare a super hydrophilic membrane. The modified membrane showed hydrophilic and superoleophobic behavior with water contact angle (WCA) and oil contact angle (OCA) reaching up to ~27° and ~154°, respectively. Due to the above properties, the resulting membrane showed significant improvement in water flux (from ~328 L m^{-2} h^{-1} for the PDA-treated membrane to ~1283 L m^{-2} h^{-1} for MWCNT-treated PVDF membrane with 0.09 MPa pressure) and moderate enhancement of BSA rejection. Importantly, the CNT-modified membrane could be able to separate ~99% of diesel from various concentrations (1–8%) of diesel–water emulsions [6]. Zhao et al. found >99% separation of various oils from oil/water emulsion and 97% FRR using CNT-incorporated chitosan (CS) and tannic acid (TA) with the in situ reaction of $FeCl_3$ leading to the formation of FeOOH; they called this a 'nanohybrid membrane'. The nanohybrid membrane also showed improved water flux, foul-resistant and self-cleaning properties, and superhydrophilic and underwater superoleophobic behavior [92]. MnO_2-MWCNT decorated cellulose microfiber membrane, prepared by vacuum filtration method, displayed >99% rejection of various oils (diesel/petroleum ether/hexane/sunflower oil) from their oil–water emulsions [93]. The coated membranes also showed improved hydrophilicity and water flux. A new approach of fabricating multilayer electrospun nanofiber microporous membrane has been reported by Gu et al., wherein a thermoplastic polyurethane (TPU) nanofiber layer is sandwiched between two PVDF-CNT layers for oil–water separation [94]. Being oleophilic in nature, the CNT-embedded sandwich membranes showed superior oil–water (80–95%) separation (n-hexane, engine, sunflower seed,

and sesame seed oils from their water emulsions) than the membranes without CNT in them [94].

3.1.2 GO-Based Polymer Membranes

Graphene oxide (GO), also known as graphite oxide is a chemical derivative of graphene, prepared from graphite flakes using the popular Hummer's method [95, 96]. The strong oxidation of graphite in presence of protonated solvents leads to the introduction of functional groups like hydroxyl (–OH), alkoxy (C–O–C), carbonyl (C=O), and carboxylic acid (–COOH), etc., on the graphitic backbone. This creates significant disorderliness in the graphitic structure by remarkably altering the electronic and mechanical properties of the graphene sheets. These functional groups in GO, however, offer the opportunity to attach with a wide range of NPs and organic molecules by covalent bonds or dipolar interactions [97, 98]. The functional groups further reduce the formidable van der Waals forces between the graphitic sheets, making their dispersion facile in the polymer matrix. GO exhibits good dispersibility in aqueous and organic solvents as well as in polymer matrices [99]. The electronic conductivity of GO can be partially gained by its chemical reduction, leading to the formation of reduced GO (rGO), using various reducing agents like ascorbic acid [100], hydrazine monohydrate [101], ammonia [102], sodium borohydride [103], etc. Figure 9 schematically illustrates the structure of single-layer graphene and GO.

Heavy metal ion removal and salt rejection

Saeedi-Jurkuyeh et al. found significant enhancement of heavy metal ion removal from model aqueous solutions as well as from industrial wastewater using GO-based bilayer membrane [104]. The membrane consists of PEG (up to 8 wt%) mixed with PSU, prepared by NIPS process, and an active layer, i.e., GO (up to 0.012 wt%)-incorporated polyamide, was prepared by interfacial polymerization of 1,3-phenylenediamine/GO and trimethyl chloride on the PSU layer. The resulting bilayer membrane showed rejection of 99.9, 99.7, and 98.3% of Pb^{2+}, Cd^{2+}, and Cr^{2+} ions, which are significantly higher than their pristine membrane counterpart and also showed improved hydrophilicity, water permeability, and water flux

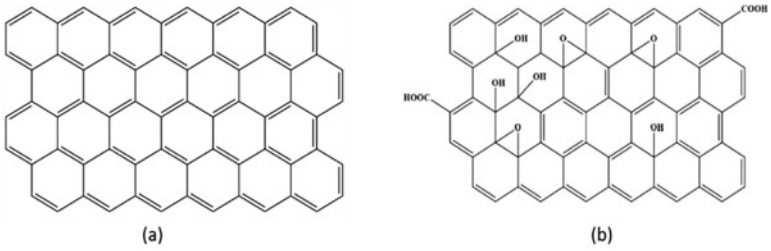

Fig. 9 Structure of **a** single-layer graphene and **b** graphene oxide

[104]. The Cs^{2+} ion can be completely removed from an aqueous solution (~99%) in the pH range of 2–12 using a composite membrane made up of a commercial PES membrane supported by PEI-treated rGO and potassium copper hexacyanoferrate [105]. Poly(acrylamide-*co*-methyl acrylate)/rGO-*g*-polyamidoxime (rGO-*g*-PAO) (up to 0.5 wt%) electrospun nanofiber membrane was used to adsorb Cu^{2+} and Cr^{4+} ions from aqueous solutions. The membrane showed improved adsorption of these ions and also exhibited efficient oil–water separation and improved water flux (~6151 L m^{-2} h^{-1}) in comparison with the membrane without rGO [106]. Poly(dopamine) (PDA)/rGO composite, coated onto a commercial cellulose acetate (CA) membrane has shown increased Cu^{2+} ion rejection (the maximum being ~100% at pH 9) and decreased flux with the increase in PDA/rGO content in the membrane [107]. Li et al. have shown ~87% Ni^{2+} ion removal from its aqueous solution using rGO and nano-MnO_2/PVDF membrane, cast by NIPS method. The nanocomposite membrane also demonstrated improved water flux, stable permeation flux, and hydrophilicity as compared to the bare PVDF membrane [108]. A marginal improvement in rejection of $MgSO_4$, NaCl, Na_2SO_4, and $MgCl_2$ salts have been observed with 0.02 g/m^2 GO-embedded poly(piperazine amide) (GO-PPA) active layer, which was rich with amine groups, prepared by interfacial polymerization of trimesoyl chloride (TMC) and piperazine (PIP) on PSU membrane, which has been prepared by NIPS method [109]. Rejection of salts like NaCl and Na_2SO_4 showed improvement by using nanocomposite membrane prepared by phosphorylated chitosan (PCS)/GO coating on PAN membrane as compared to the only PCS-coated PAN membrane [110]. Contrary to the above, nanocomposite membrane made of PES and a composite of GO and poly(sulfobetamine) (PSBA) showed lower salt rejection (Na_2SO_4, $MgCl_2$, NaCl, and $MgSO_4$) than the pristine PES membrane [111].

Organic dye removal

In Ref. [109], Lai et al. have shown remarkable rejection of organic dyes, viz., rose bengal (RB) (~100%), reactive black 5 (RB5) (~98%), methylene blue (MB) (~96%) using GO-PPA layer supported by PSU membrane. The resulting GO-embedded membranes showed improved hydrophilicity, salt solution permeability, pure water flux, and antifouling properties as compared to the membrane without GO [109]. PDA/rGO-modified CA membrane, prepared by vacuum filtration was found to exhibit ~100% rejection of methylene blue, and ~99% rejection of both congo red and rhodamine B dyes, respectively, from model aqueous solutions [107]. Though the percentage rejection for various dyes increased moderately, the flux showed a downward trend with an increase in PDA/rGO content. Further, the nanocomposite membrane was able to show ~94% FRR after washing the membrane 3 times [107]. Zhang et al. have reported ~94, ~96, and ~99% rejection of New Coccine, Ponceau S, and direct red 80 dyes using carboxyl functionalized GO (COOH-GO)/PA layer polymerized on PSU supporting layer via interfacial polymerization. However, the dye and NaCl rejections were marginally lower for GO-incorporated membranes than the membrane without GO [112]. However, the COOH-GO/PA membrane showed better water permeation and dye desalination than the only GO/PA membrane [112].

Song et al. functionalized a commercially available PAN membrane by dip-coating in phosphorylated chitosan/GO suspension and crosslinking the resulting membrane with glutaraldehyde (GA) to prepare a nanocomposite membrane. The nanocomposite membrane was able to show ~100, ~98, and ~93% rejection of direct black 38, xylenol orange, and Ponceau S dyes from their aqueous solutions, respectively. The surface modification also enhanced hydrophilicity, pure water flux, and FRR of the PAN membrane [110]. Zhu et al. have prepared a novel zwitterion polymer: poly(sulfobetamine) (PSBA) and GO composite and subsequently, the composite was used as filler in PES membrane, prepared by NIPS method. In comparison with the pristine PES membrane, the nanocomposite membrane showed higher dye rejection (~99 and ~97% of reactive black 5 and reactive red 49, respectively) and improved pure water flux, FRR, hydrophilicity, and tensile strength [111]. Cheng et al. have compared the dye rejection properties of three membranes: (i) GO, (ii) rGO and (iii) GO/polyacrylamide (PAM), prepared by vacuum filtration method. All the three membranes showed almost comparable rejection of rhodamine B dye (~99%). However, among these, GO/PAM membrane showed the highest water flux and the best hydrophilic properties [113]. In another study, a significant enhancement of water permeation (7–20 times higher) as compared to only GO on nylon membrane and comparable rejection of rhodamine B and direct red dyes (~99%) has been reported by Lu et al. using a commercial nylon microfiltration membrane dip-coated with PEI-*g*-GO or GO suspension [114]. Thermoplastic polyurethane (TPU)/GO composite electrospun nanofiber membranes showed substantially higher water flux, FRR and rejection of methylene blue (~95%) and rose Bengal (~92%) dyes as compared to the pristine TPU nanofiber membrane [115].

Antibacterial behavior and oil–water separation

Polymeric membranes which are used for water remediation should possess good antibacterial properties. GO is an excellent material for imparting antibacterial properties in polymeric membranes against various harmful pathogens [115, 116]. Sundaran et al. found that the growth of *S. Aureus* bacteria significantly inhibited on TPU/10 wt% GO electrospun nanofiber membranes, implying good antibacterial properties. They also reported that the GO-embedded TPU membranes showed good antifouling properties for oil rejection of >99% from the oil–water emulsion. However, no results on oil–water separation have been reported [115]. Ayyaru et al. have thoroughly studied the physicochemical properties of sulfonated GO (sGO)-PVDF composite membranes, prepared by NIPS technique, and compared the sGO membrane properties with that of pristine PVDF as well as with GO-PVDF membrane. They found significant improvement in hydrophilicity, pure water flux, BSA rejection, and FRR values in comparison with pristine PVDF and GO-PVDF membranes [117]. Though they have not reported any separation behavior of these membranes; however, this study is expected to imply oil–water separation as well as heavy metal ion removal [117].

The details of carbon-nanoparticle-based nanocomposite membranes including the polymer matrix, NPs used, membrane preparation method, and various membrane properties are presented in Table 1.

Table 1 Various membrane properties of carbon-based nanocomposites

Polymer	Membrane fabrication technique	Nanofiller used	Application	Membrane properties [WCA in °], [Pure Water Flux (PWF) in L m^{-2} h^{-1}], [FRR in %], [Porosity (P) in %], [Mean pore size (MPS) in nm], [Tensile strength (TS) in MPa]	Reference
PVDF	NIPS	Alkylamine grafted-MWCNTs	Antifouling membrane	Pristine membrane (PM): WCA ~ 111, P-55, MPS-260, FRR-56.7 Nanocomposite membrane (NM): WCA ~ 61, P-74, MPS-420, FRR-92.7	[86]
PAN	Electrospinning	(PEI)-modified MWCNT	Pb^{2+} (230.7 mg/g) and Cu^{2+} (107.7 mg/g) removal	PM: WCA-78, TS-0.56 ± 0.04 NM: WCA-41, TS-2,96 ± 0.2	[15]
PVA	Casting evaporation method	Alkylamine grafted-MWCNTs	Cu^{2+} (18.32 mg/g) removal	PM: P-5 NM: P-20	[28]
PVA	Casting evaporation method	Alkylamine grafted-MWCNTs	Cu^{2+} (18.32 mg/g) removal	PM: P-5 NM: P-20	[28]
PVDF	Commercial membrane	(APTES)-grafted MWCNTs/Polydopamine	Diesel separation from its water emulsion up to 99%	PM: WCA ~ 133 NM: WCA ~ 27, PWF-1282.5	[6]

(continued)

Table 1 (continued)

Polymer	Membrane fabrication technique	Nanofiller used	Application	Membrane properties [WCA in °], [Pure Water Flux (PWF) in L m^{-2} h^{-1}], [FRR in %], [Porosity (P) in %], [Mean pore size (MPS) in nm], [Tensile strength (TS) in MPa]	Reference
PVDF	NIPS	MWCNT/ laccase	Carbamazepine (27%) and diclofenac removal (95%)	PM: WCA ~ 52 NM: WCA-62	[45]
PES	NIPS	Carboxylated CNTs	95% bromophenol blue and methyl orange dye removal	PM: WCA-68, P-69 ± 3, TS-1.89 NM: WCA-55, P-76 ± 4, TS-1.94	[36]
PES	NIPS	Nitrogen doped CNT (N-CNT)	Antifouling membranes	PM: WCA-88 NM: WCA-68	[89]
PES	NIPS	Chitosan coated CNT and PEBAX®1657	(>95%) malachite green dye removal	PM: WCA ~ 56 NM: WCA ~ 33	[37]
PP/PES	Commercial membrane	Carboxylated CNTs	96.5% brilliant blue R and 67.6% Safranin O dye removal	–	[38]

(continued)

Table 1 (continued)

Polymer	Membrane fabrication technique	Nanofiller used	Application	Membrane properties [WCA in °], [Pure Water Flux (PWF) in L m^{-2} h^{-1}], [FRR in %], [Porosity (P) in %], [Mean pore size (MPS) in nm], [Tensile strength (TS) in MPa]	Reference
PSf	NIPS	PEG functionalized CNT	Antifouling membranes	PM: WCA ~ 66, P-44.56 ± 1.31, MPS-12.53, TS-16.32, FRR-57.14 NM: WCA ~ 55, P-54.44 ± 1.30, MPS-21.27, TS-10.75, FRR-80.33	[91]
Cellulose ester	Commercial membrane	CNT modified with chitosan & tannic acid	The mixture of hexadecane, pump oil, soybean oil, petroleum ether separation from its water emulsion up to 99.7%	PM: WCA ~ 87 NM: WCA ~ 24, FRR-97	[92]
PES	NIPS	Sodium lignosulfonate modified CNTs	Antifouling and anti-bacterial membranes	PM: WCA-78, PWF-1050, P-66, MPS-70.5, FRR-62 NM: WCA-57, PWF-570, P-73, MPS-86.8, FRR-94	[87]

(continued)

Table 1 (continued)

Polymer	Membrane fabrication technique	Nanofiller used	Application	Membrane properties [WCA in °], [Pure Water Flux (PWF) in L m^{-2} h^{-1}], [FRR in %], [Porosity (P) in %], [Mean pore size (MPS) in nm], [Tensile strength (TS) in MPa]	Reference
PSf	NIPS	Carboxylated CNTs	Cu^{2+}(93%), Pb^{2+}(90.1%), Cd^{2+}(78.2%), Cr^{4+}(94.2%), As^{3+}(80%) removal	PM: WCA ~ 78 NM: WCA ~ 27	[35]
Polyamide	NIPS	MWCNT	Salt (NaCl) rejection 76 ± 1.1%	PM: PWF-32 ± 0.7 NM: PWF-28 ± 0.8	[85]
PSf	NIPS	GO	Salt rejection, rose bengal, methylene blue, reactive black 5 dye rejection, antifouling properties	PM: WCA ~ 26 NM: WCA ~ 24	[109]
PAN	Electrospinning	GO	Antibacterial properties against E. coli and S. aureus	–	[116]
PSf	NIPS	GO with polyamide	Pb^{2+}(99.9%), Cd^{2+}(99.7%), Cr^{2+}(98.3%) removal	–	[104]

(continued)

Table 1 (continued)

Polymer	Membrane fabrication technique	Nanofiller used	Application	Membrane properties [WCA in °], [Pure Water Flux (PWF) in L m^{-2} h^{-1}], [FRR in %], [Porosity (P) in %], [Mean pore size (MPS) in nm], [Tensile strength (TS) in MPa]	Reference
PVDF	NIPS	Sulfonated GO	Antifouling properties	PM: WCA-78 ± 2.2, PWF-290, P-75.4 ± 2.3, MPS-60, FRR-50.3 NM: WCA-50 ± 1.2, PWF-740, P-86.7 ± 2, MPS-71, FRR-82.02	[117]
CA	Commercial membrane	rGO modified with polydopamine	Congo red, methylene blue, rhodamine B dye removal, Cu^{2+} ions removal, antifouling properties	PM: WCA-63.8, PWF-386.2 NM: WCA ~ 79, PWF-25	[107]
PSf	Commercial membrane	Carboxyl functionalized GO	New cocaine, Ponceau S, direct red 80 dyes removal, and salt (NaCl) rejection	PM: PWF-30 NM: PWF-110.4	[112]
PES	Commercial membrane	Copper ions immobilized PEI-rGO with potassium copper hexacyanoferrate	Cs^{2+} ions removal	–	[105]

(continued)

Table 1 (continued)

Polymer	Membrane fabrication technique	Nanofiller used	Application	Membrane properties [WCA in °], [Pure Water Flux (PWF) in L m^{-2} h^{-1}], [FRR in %], [Porosity (P) in %], [Mean pore size (MPS) in nm], [Tensile strength (TS) in MPa]	Reference
PAN	Commercial membrane	Phosphorylated chitosan/GO	Direct black 38, xeylenol orange, Ponceau S dye removal and salt rejection	PM: WCA ~ 53, PWF-79.2, FRR-75.4 NM: WCA ~ 42, P-78.15, FRR-99.8	[110]
Poly (acrylamide-co-methylacrylate)	Electrospinning	rGO-g-poly amidoxime	Cu^{2+}, Cr^{4+} ions removal, toluene separation from its surfactant stabilized water emulsion up to 99%	PM: PWF-93, P-62.3, TS-3.9 NM: PWF-1615, P-60.1, TS-8.0	[106]
TPU	Electrospinning	GO	Methylene blue, rose bengal dyes removal and antibacterial properties	PM: WCA ~ 116, P-52.55 ± 0.89, NM: WCA-0, PWF-17706, P-61.9 ± 1.9, FRR-99	[115]
PES	NIPS	GO-g-poly(sulfobetamine	Reactive black 5, reactive red 49 removals, and salt retention	PM: WCA-84, PWF-38.6, TS-3.2 NM: WCA ~ 55, PWF-71.7, TS-5.6, FRR-94.4	[111]
Polyacrylamide	Commercial membrane	rGO/GO	Rhodamine B dye removal	PM: WCA ~ 78, PWF-53.33 NM: WCA ~ 65, PWF-98.55	[113]

(continued)

Table 1 (continued)

Polymer	Membrane fabrication technique	Nanofiller used	Application	Membrane properties [WCA in °], [Pure Water Flux (PWF) in L m^{-2} h^{-1}], [FRR in %], [Porosity (P) in %], [Mean pore size (MPS) in nm], [Tensile strength (TS) in MPa]	Reference
Nylon	Commercial membrane	PEI-g-GO	Rhodamine B, direct red dye removal	–	[114]

3.2 *Nanoclay-Based Nanocomposite Membrane for Water Remediation*

Due to their versatile properties and ability to bind with diverse kinds of polymeric material, inorganic materials such as nanoclays have been served as functional fillers in polymeric membranes. Moreover, clays are known for their excellent adsorption properties [118]. They are mostly layered silicates and are obtained from natural sources. Their variety depends on the geographical location that they are found. Nanoclays have a general chemical formula of (Ca, Na, H) (Al, Mg, Fe, Zn)$_2$(Si, Al)$_4$O$_{10}$(OH)$_{2-x}$·xH$_2$O, where x represents water quantity [119] and typically have a smectic monoclinic structure with two Si^{4+} tetrahedral sheets sandwiching a central Al^{3+} or Mg^{2+} octahedral sheet. Most popular nanoclays used as fillers in polymer matrix are montmorillonite, hectorite, laponite, vermiculite, saponite, bentonite etc. Nanoclays have been widely acknowledged as reinforcements in the polymer matrix and found to improve the physical, chemical, thermal, and mechanical properties of polymers [120–122]. Nanoclays have also been widely used in the polymeric membrane for water remediation [123–125]. In this section, we review the use of nanoclays in the polymeric membrane as fillers and their ability to remove harmful pollutants from wastewater.

3.2.1 Montmorillonite Clay (MMT) Based Membrane

Montmorillonite (MMT) clay is a layered silicate clay with a 2:1 phyllosilicate structure. The general chemical formula of MMT is $M_x(Al_{4-x}Mg_x)Si_8O_2(OH)_4$, where M is the monovalent cation, x is the degree of isomorphic substitution, which varies from 0.5 to 1.3. Due to its hydrophilic nature, MMT does not readily disperse into polymer matrix [126]. Therefore, they are modified with organic surfactants. A wide range of organically modified MMT clays are also commercially available [127]. Numerous studies have been carried out on MMT clay-based composites in the literature, covering a wide range of properties and applications [128–130]. Therefore, the present chapter does not intend to deal with clay-based nanocomposites in general; except the ones which report the use of clay-based nanocomposites in water remediation (Fig. 10).

Heavy metal ion removal

Jacob et al. have reported a maximum of ~95% rejection of Cr^{6+} ions from their aqueous solution using the nanocomposite membrane made up of polysulfone (PSU) and 3 wt% methyl hydroxyethyl hydrogenated tallow ammonium modified MMT (mMMT) clay by NIPS method. The above membrane also showed improved antifouling properties as the FRR value (~83%) was higher in comparison with the PSU/pristine MMT (3 wt%) (~76%) and the pristine PSU (~58%) [124]. Notwithstanding the clay content, the modified clay (mMMT) showed improved water flux over the pristine MMT-PSU and pristine PSU membrane as well [124]. Shokri

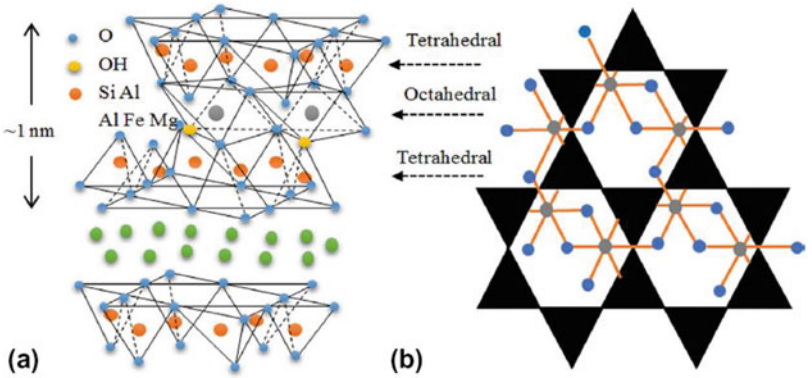

Fig. 10 Schematic representation of the structure of MMT clay **a** Side view: tetrahedrons units of MMT assembled through weak van der Waals and electrostatic forces to form the primary particles, **b** top view of MMT clay hexagonal structure of oxygen and hydroxyl ligands of the octahedral layer [131, 132]

et al. have shown ~97% rejection of Pb^{2+} ions from their aqueous solution using a composite membrane of poly(vinyl chloride) (PVC) and folic-acid-modified MMT (FA-MMT) (1 wt%), prepared by NIPS technique [133]. The membrane also retained a good rejection (~90%) of Pb^{2+} ions from the water after 5 adsorption cycles. The MMT- and FA-MMT-incorporated PVC membranes also showed improved porosity, pure water flux, hydrophilicity, FRR, and tensile strength than that of PVC [133]. Somera et al. have shown Hg^{2+} ion adsorption (~14 mg/g) from model aqueous solutions using electrospun Fe-MMT (Cloisite 24A)/PCL nanofiber membrane. However, the study has not reported the adsorption properties of Hg^{2+} ions using pristine PCL membrane [134]. PSU-lysine amino acid modified MMT (MMT-lys) (0.5–1.5 wt%) nanocomposite membranes, prepared by NIPS method, showed excellent removal of As^{5+} ion (>90%) from water, which was higher than the pristine MMT/PSU membrane (~30%) [135]. It was shown that the As^{5+} ion removal depended on the pH and initial concentration of the arsenic solution; higher concentration and lower pH facilitated As^{5+} ion removal. Further, the nanocomposite membrane using MMT-lys showed > 90% removal of As^{5+} after 5 cycles of adsorption–desorption [135].

Organic dye and pharmaceutical drug removal

Hosseini et al. have reported improved removal of a cationic dye: Basic Blue 41 (BB41) from water using MMT clay (up to 2 wt%) as an additive in the electrospun nanofibrous membrane of chitosan/PVA (20/80) blend. The dye adsorption of the nanocomposite membrane increased with an increase in pH and the maximum adsorption was obtained at pH 7. The nanocomposite membranes also displayed higher pure water flux than the pristine blend membrane [136]. Poly(4-styrene sulfonic acid-co-maleic acid) (PSSMA)-modified MMT clay has been used for salt (Na_2SO_4) rejection and pharmaceutical drug (cephalexin, amoxicillin, and ibuprofen) removal from water [123]. The nanoclays were added in PVA matrix and

a supporting membrane of PSU, fabricated via NIPS technique was dip-coated in the above composite solution followed by cross-linking with GA. Though the modified clay showed better salt rejection and drug removal than the pristine MMT clay-based membranes; however, the removal properties decreased slightly with the clay addition, regardless of their treatment; only the water flux improved marginally with clay addition [123]. Methyl dihydroxy-ethyl hydrogenated tallow ammonium-modified MMT clay (0.05–0.15 wt%) was added into PCL membrane, prepared by NIPS technique for improving the removal of Congo red dye [137]. Besides the enhanced dye removal (efficiency ~ 45%), the modified membranes showed improved tensile strength and hydrophilicity, increased porosity, and improved pure water flux than the bare PCL membrane [137]. PVDF/polyaniline (PANI) (5 wt%)/MMT (10–14 wt%) mixed matrix composite membrane prepared by NIPS technique showed removal of ~50% tetracycline from water, which is significantly higher than the removal efficient shown by the pristine PVDF (~0.3%), PVDF/PANI (2.5%) and PVDF/pristine MMT (~38%) membranes in batch experiments [138]. The above nanocomposite membrane also showed efficient desorption (~80%) in 0.05 mol/L NaOH solution and reusability up to 5 cycles without losing the efficiency significantly [138]. Wang et al. used PVP-grafted MMT clay (1–6 wt%) as a porogen additive in the PVDF matrix for preparing ultrafiltration membrane by NIPS technique. The typical morphology of the above nanocomposite membrane cross-section is shown in Fig. 11. To evaluate fouling performance of the membrane, bovine serum albumin (BSA) was taken as a model foulant. The PVP-*g*-MMT/PVDF membrane showed improved antifouling, water flux and FRR properties in comparison with the control PVDF membrane (various membrane properties are quantitatively presented in Table 2) [27]. They further predicted the potential use of this membrane in organic pollutant removal. Ferreira et al. found higher efficiency of indigo blue dye rejection (~94% at 1.5 bar pressure) with 1 wt% MMT clay than higher clay content (5 wt%) in PES and also with respect to bare PES membrane, all fabricated by NIPS technique [139].

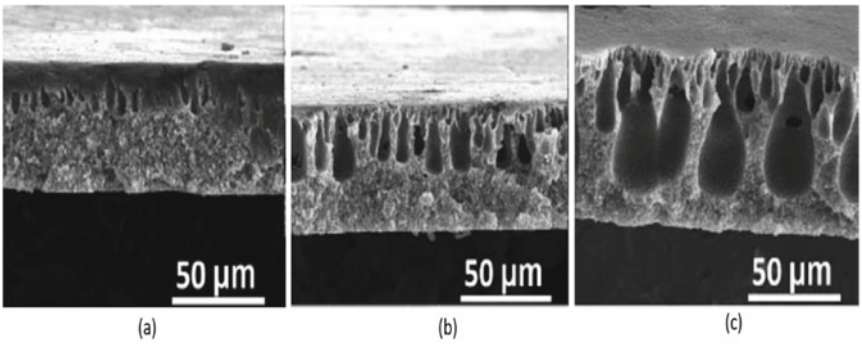

Fig. 11 Typical cross-sectional SEM images of PVDF membrane loaded with various concentrations of PVP-*g*-MMT: **a** bare PVDF membrane, PVDF membrane with **b** 1 wt%, **c** 2 wt%, PVP-*g*-MMT loading [27]

Table 2 Various membrane properties of clay-based nanocomposites

Polymer	Membrane fabrication technique	Nanofiller used	Application	Membrane properties [WCA in °], [PWF in $Lm^{-2}\ h^{-1}$], [FRR in %], [P in %], [MPS in nm], [TS in MPa]	Reference
PVA	Electrospinning	MMT	Basic blue dye (95%) removal and antifouling properties	PM: P-83, MPS-9500, TS-0.89, FRR- > 90 NM: PWF-1765, P-89, MPS-1780, TS-3.2, FRR- < 80	[136]
PSf	NIPS	MMT modified with PSSMA	Pharmaceutical drugs and salt (Na_2SO_4) removal	PM: WCA ~ 61 ± 0.22, PWF-7.5, NM: WCA-56 ± 1, PWF-14	[123]
PCL	NIPS	(Methyl dihydroxy-ethyl hydrogenated tallow ammonium) modified MMT	Congo red dye (>45%) removal	PM: WCA-85 ± 5, PWF-16.67, P-40 ± 2 NM: WCA-65 ± 5, PWF-242.42, P-59 ± 2	[137]
PVDF	NIPS	PVP-g-MMT	Antifouling properties	PM: WCA ~ 89 ± 1.8, P-55.3 ± 3.1, FRR-62 NM: WCA ~ 77 ± 1.8, P-81.3 ± 1.7, FRR- > 90	[27]

(continued)

Table 2 (continued)

Polymer	Membrane fabrication technique	Nanofiller used	Application	Membrane properties [WCA in °], [PWF in $Lm^{-2}\ h^{-1}$], [FRR in %], [P in %], [MPS in nm], [TS in MPa]	Reference
PVDF	NIPS	PANI/MMT	Tetracycline removal	PM: WCA-83, PWF-9.7 NM: WCA ~ 63, PWF-5.1	[138]
PCL	Electrospinning	Fe-MMT/cloisite 24 A	Hg^{2+} ions removal	–	[134]
PSf	NIPS	MMT modified with lysine amino acid	90% As^{5+} ions removal	PM: WCA-92 NM: WCA-82	[135]
PSf	NIPS	Methyl dihydroxyethyl hydrogenated tallow ammonium modified MMT	95% Cr^{6+} ions removal and antifouling properties	PM: FRR-58 NM: FRR-85	[124]
PVC	NIPS	MMT modified with folic acid	90% Pb^{2+} ions removal and antifouling properties	PM: WCA-72 ± 2, PWF-82, P-70 ± 1, TS-5.5 ± 0.2 NM: WCA-50 ± 1, PWF-140, P-86 ± 1, TS-9.0 ± 0.5, FRR-89.0 ± 0.7	[133]
PES	NIPS	MMT	94% indigo blue dye removal	PM: WCA ~ 43 NM: WCA ~ 24	[139]

(continued)

Table 2 (continued)

Polymer	Membrane fabrication technique	Nanofiller used	Application	Membrane properties [WCA in °], [PWF in $Lm^{-2}\ h^{-1}$], [FRR in %], [P in %], [MPS in nm], [TS in MPa]	Reference
PSf	NIPS	Mg-Fe layered double hydroxide modified MMT	Mixture of motor oil and transformer oil separation from its surfactant stabilized water emulsion up to 96% antifouling properties	–	[140]
PVA/CMC	Solvent casting	HNT	99.5% methylene blue dye removal and antibacterial properties	PM: WCA-78 NM: WCA ~ 54	[125]
PAN	Electrospinning	HNT	Vegetable oil separation from its water emulsion up to 99.5% and 31.1% Cu^{2+} ions removal	PM: PWF-81 NM: PWF-92	[141]
PVDF	NIPS	HNT functionalized with dopamine/APTES	86.5% direct red 28, 85% direct yellow 4, 93.7% direct blue 14 removal and antifouling properties	PM: WCA-79 ± 0.3, P-42.2 ± 0.7, MPA-21.8 ± 0.3, FRR-73.4 NM: WCA ~ 60 ± 0.4, P-49.9 ± 1.2, MPA-26.1 ± 0.5, FRR-89.9	[142]
PSf	Dry/wet phase inversion	HNT functionalized with tannic acid	99% reactive black 5, reactive orange 16 removal and antifouling properties	PM: PWF-18, FRR-27 NM: PWF-82, FRR-68	[143]

(continued)

Table 2 (continued)

Polymer	Membrane fabrication technique	Nanofiller used	Application	Membrane properties [WCA in °], [PWF in $Lm^{-2}\ h^{-1}$], [FRR in %], [P in %], [MPS in nm], [TS in MPa]	Reference
PEI	NIPS	Polydopamine modified HNT	79% Pb^{2+}, 73% Cd^{2+} removal and antibacterial properties	PM: WCA-79.1, PWF-149, P-36.8, FRR-26.6 NM: WCA-66.3, PWF-276, P-58.5, FRR-67.1	[144]
PVDF	NIPS	β-cyclodextrin modified HNT	88.1% direct red 88,20.9% Cu^{2+} ions removal and antifouling properties	PM: WCA-83.8, PWF-24, P-42.2 ± 0.7 NM: WCA-57.1, PWF-69.5, P-61.4 ± 2.3	[145]
PVDF	NIPS	HNT modified with 1-methyl-3-(3-triethoxysilypropyl) imdazolium chloride	Separation of diesel from its water emulsion up to 98% and antifouling properties	PM: WCA-75, P- 57.2, MPS-20, FRR-65 NM: WCA-57, P-64.5, MPS-26.1, FRR-93	[146]
PES	NIPS	HNT modified with dopamine and tannic acid	Antifouling properties	PM: WCA-62.7 ± 2.1, PWF-198.94, P-57.9 ± 2.1, MPS-35.7 ± 1.9, FRR-69 NM: WCA-45.4 ± 2.9, PWF-682.48, P-74.8 ± 2.3, MPS-46.5 ± 1.9, FRR-93	[147]
PS	Solution casting	HNT	Wastewater treatment	–	[52]

(continued)

Table 2 (continued)

Polymer	Membrane fabrication technique	Nanofiller used	Application	Membrane properties [WCA in °], [PWF in $Lm^{-2}\ h^{-1}$], [FRR in %], [P in %], [MPS in nm], [TS in MPa]	Reference
PES	NIPS	HNT-SO_3H	90% reactive black 5, reactive red 49 removal and rejection towards various salts	PM: WCA-83.5, MPS-0.71 ± 0.01 NM: WCA-58.5, MPS-0.65 ± 0.01	[148]

Oil/water separation

MMT clay has not been widely explored for oil–water separation. Nevertheless, few studies report the oil–water separation efficiency of MMT clay-loaded polymer membranes. Filho et al. used MMT (1–5 wt%)-filled polyamide 6 (PA6) membranes and explored their oil/water separation efficiency by measuring the oil present in the permeate, which was found to be ~20 mg/L versus 100 mg/L in the feed solution [149]. The hydrophilicity of the membranes improved with the clay content [149]. Makwana et al. reported higher rejection of transformer oil and motor oil from their oil–water emulsions using a hydrophilic Mg–Fe layered double hydroxide (LDH)-modified MMT (1 wt%)-filled PSU/PVP blend ultrafiltration membrane than the control PSU/PVP blend and pristine MMT-filled blend membranes [140]. The oil rejection was found to be ~87 and ~96% for transformer oil and motor oil as against ~75 and 85% for PSU/PVP blend membrane, respectively. The LDH-modified MMT clay-based nanocomposite membrane also exhibited higher water flux, BSA rejection, and FRR as compared to the pristine and unmodified MMT-filled blend membrane, indicating better antifouling properties of the former [140].

3.2.2 Halloysite Clay-Based Membrane

Halloysite clay or nanotube (HNT) is a two-layered alumina-silicate with a hollow spiral rolled sheet-like structure with chemical formula: $Al_2Si_2O_5(OH)_4{\cdot}2H_2O$. The inner cylinder core is connected to Al_2O_3 and the outer surface has properties identical to SiO_2 with an Al to Si ratio of 1. It may grow into long multi-walled tubules that roughly resemble the structure of MWCNT as shown in Fig. 12 [150]. Owing to its

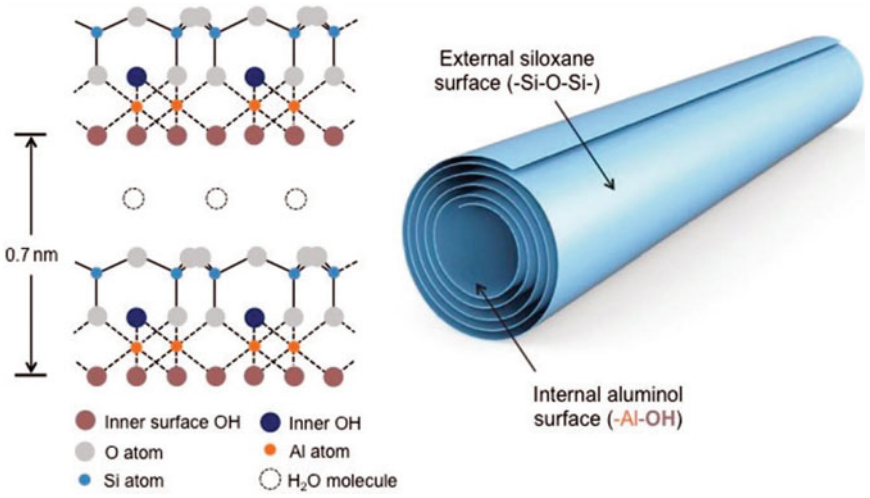

Fig. 12 Schematic elucidation of halloysite nanotube structure [152]

layered structure, the halloysite has a large specific surface area (~117 m^2/g) [151], making it a suitable candidate as an adsorbent material. Moreover, the presence of both cationic and anionic species in HNT makes it a versatile nanofiller for bonding with various ionic dyes and pollutants. Hence, HNT-based polymer nanocomposites have been extensively explored in water remediation [127–137].

Organic dye removal and antibacterial property

Radoor et al. showed improved efficiency of methylene blue (MB) adsorption from water using a novel PVA/carboxymethyl cellulose (CMC)/HNT (2–6 wt%) composite membrane, prepared by solution-cast followed by cross-linking with GA. They showed that in comparison with pristine membranes, the adsorption performance was better for nanocomposite membranes and the MB uptake increased with HNT content up to 6 wt%. However, no information was provided on whether the membrane was porous. The adsorption was also found to depend on the initial dye concentration, pH, and temperature of the solution. Further, the membrane showed antibacterial properties against *E. coli* and *S. aureus* [125]. The nanocomposite membrane of PEI filled with polydopamine (PDA)-treated HNT also showed antibacterial properties against *E. coli*, *M. smegmatis*, and *C. albicans* [144]. Zeng et al. found improved organic dye removal from aqueous solutions using dopamine-functionalized HNT using 3-aminopropyltriethoxysilane in PVDF membrane, made by NIPS method [142]. The membrane filled with the 0.36 wt% modified HNT was able to reject ~86, ~85, and ~94% of direct red 28, direct yellow 4, and direct blue 14 dyes, respectively, from water; while the rejection efficiency for the pristine PVDF membrane was ~79, ~76, and ~89% for the respective dyes. The FRR, mean pore size, hydrophilicity, and antifouling properties were also enhanced with the addition of modified HNT in the membrane [142]. In another study, Ibrahim et al. modified HNT with tannic acid and used the modified HNT as an additive in PSU membrane, made by dry/wet phase inversion technique. Using the HNT-filled PSU membrane, they found ~99 and ~95% rejection of reactive black 5 and reactive orange 16, respectively, and low rejection (<10%) of salts (Na_2SO_4, NaCl), indicating the use of the modified membrane in industrial dye purification and desalting. The modified HNT membranes also displayed improved pure water flux, FRR in comparison with pristine ones [143]. In another similar effort, high dye rejection (>90% of reactive black 5 and 80–90% of reactive red 49) with low salt rejection (<10% for $MgSO_4$, $MgCl_2$, NaCl) has been reported by Wang et al. using sulfonated HNT (HNT-SO_3H) (up to 3 wt%)-incorporated PES membrane, prepared by NIPS process. The introduction of nanofillers also led to improved water flux and PEG rejection of the PES membrane [148]. β-cyclodextrin (CD)-grafted HNT (CD-*g*-HNT) (0.09–0.36 wt%)/PVDF membranes, prepared through NIPS technique were found to efficiently adsorb organic dye (direct red 88) from aqueous solutions, as reported by Ma et al. [145]. The dye removal was ~88% for 0.36 wt% CD-*g*-HNT-loaded membrane, which is marginally higher than the virgin PVDF membrane (~85%). The nanocomposite membranes also showed superior pure water flux and antifouling properties, and reusability [145].

Oil–water separation

Makaremi et al. have explored the oil–water separation capability of HNT-incorporated PAN nanofiber membrane prepared by electrospinning [141]. Regardless of the membrane, the oil rejection efficiency was 99.5% from oil/water emulsion; however, the HNT-loaded membranes showed higher flux than the bare PAN membrane due to an increase in internal nanochannels in the former case [141]. Nanocomposite membrane of PVDF, made by NIPS method, filled with 1-methyl-3-(3-triethoxysilypropyl) imidazolium chloride-modified HNT (0.5–3 wt%) showed ~98% rejection of diesel from diesel/water emulsion, which is ~19% higher than the separation efficiency shown by the pristine PVDF membrane. The nanocomposite membrane also demonstrated improved FRR, i.e., ~93% against BSA protein, indicating better antifouling behavior, over pristine PVDF membrane [146]. PES nanocomposite membranes embedded with PDA- and TA-coated HNT (0.2 wt%) prepared by phase inversion coagulation bath containing Fe^{3+} ion, showed efficient dodecane removal from its water emulsion [147].

Heavy metal ion adsorption

PDA-coated HNT in the weight ratio of 1–4 wt% has been used as a nanofiller in PEI membrane for adsorption of Pb^{2+} and Cd^{2+} ions from aqueous solutions, reported by Hebbar et al. [144]. The membranes were cast via the NIPS technique. The nanocomposite membrane with 4 wt% modified HNT showed ~79 and ~73% removal of Pb^{2+} and Cd^{2+}, respectively, from their aqueous solutions; however, the adsorption properties for pristine PEI membrane has not been reported. The nanocomposite membranes also showed improved hydrophilicity, pure water flux, and FRR than the pristine PEI membrane [144]. Improved Cu^{2+} ion removal from water has also been shown by the nanocomposite membranes of CD-*g*-HNT/PVDF (removal of ~21% versus ~4% for pristine membrane) [145] and HNT-loaded PAN nanofiber (removal of ~31% versus 5% for pristine membrane) [141].

Purification of industrial effluents

Polymer nanocomposite filtration membranes have also been explored for the purification of actual industrial effluents. To this end, Buruga et al. attempted to purify and remediate wastewater collected from the paper and pulp industry using a nanocomposite membrane of polystyrene (PS) with 5 wt% HNT. The membrane was prepared by phase inversion method using various solvents (tetrahydrofuran and *N*-methyl-2-pyrrolidone) and anti-solvent (water, methanol, ethanol, and propanol). Using the nanocomposite membrane filtration, the water quality in terms of acceptable standard parameters (pH, hardness, conductivity, and biological oxygen demand) was found to be within the acceptable range [52].

3.2.3 Laponite-Clay-Based Membrane

Laponite is synthetic hectorite having a layered structure of sodium magnesium silicate with chemical formula: $Si_8Mg_{5.45}Li_{0.4}O_{24}Na_{0.7}$. Laponite clay is a 2-dimensional disc-like structure with an average diameter of ~25 nm and a thickness of ~1 nm. They have negatively charged faces (OH^-) and positively charged (Na^+) edges [153]. Laponite clay has been extensively used in various polymer matrices for improving mechanical, thermal, and other properties [154–156]. However, little work has been reported on laponite/polymer membranes for water treatment [157, 158].

Selim et al. have reported ~99.9% NaCl rejection from 50,000 ppm NaCl solution using a membrane fabricated by 7 wt% laponite and PVA followed by GA cross-linking. The membrane was made by the phase inversion technique. The salt rejection was higher than the pristine PVA membrane. Water flux improved from ~20 kg m^{-2} h^{-1} for the pristine membrane to ~34 kg m^{-2} h^{-1} for the 7 wt% laponite membrane. The addition of laponite further improved the hydrophilicity and swelling characteristics of the PVA membrane [157]. Laponite-clay-incorporated cellulose acetate (CA) prepared by solvent-free supercritical CO_2 phase inversion technique showed improved cell adhesion properties. However, no separation properties of the membrane are reported in this study [158].

The details of polymer, nanofillers, and their composite membrane properties and applications for some of the nanoclay-based polymer nanocomposite membranes, discussed above are presented in Table 2.

3.3 Metal Oxide-Based Nanocomposite Membranes for Wastewater Remediation

Metal oxide (MO) NPs are another class of materials, which provide a large number of functional sites and a huge surface area to volume ratio for adsorption of various water pollutants. MO NPs have also been used extensively in polymer matrix for other applications such as in biomedical scaffolds [159], sensors [160], optics [161], energy storage, anticorrosion coating [162], etc. Here we present various water remediation phenomena of some MO NP-based polymer composites.

Heavy metal ion removal and salt rejection

Ghaemi et al. have used γ-alumina NP (1 wt%)-embedded PES (20 wt%)/PVP (1 wt%) membranes for Cu^{2+} ion removal (efficiency ~ 49% after 4 cycles) from water. The membrane was prepared by NIPS method using dimethylacetamide as solvent and water as antisolvent. The nanocomposite membrane also showed improved hydrophilicity, and increased water flux and porosity [163]. Heavy metal ions such as As^{5+}, Cd^{2+}, and Pb^{2+} could be removed up to 96% and above from their respective aqueous solutions using Al–Ti_2O_6 nanoparticles (3–5 wt%)-incorporated PSU membranes, prepared by NIPS method as reported by Sunil et al. [164]. The

NP-embedded membrane also showed improved physicochemical properties like porosity, hydrophilicity, and pure water flux in comparison with the pristine PSU membranes [164]. Razmgar et al. prepared a blended composite of PVDF/PVA/Al_2O_3 membrane by NIPS method and the resulting membrane exhibited up to 90% removal of Pb^{2+} ions from water [165]. PVDF/zirconia composite membrane, prepared by solution cast method was found to show As^{5+} ion adsorption up to 21 mg/g over a wide pH range (pH 3–8) from its aqueous solutions [166]. The addition of zirconia also improved the porosity, hydrophilicity, and water flux of the PVDF membrane [166]. Alharbi et al. had prepared a nanofiber mat of PAN with TiO_2 (2–5 wt%) and ZnO (2 wt%) NP separately embedded in it. A thick layer of chitosan/PVA was developed directly over on this electrospun nanofiber mat of PAN by electrospinning. Prepared nanocomposite membrane was able to demonstrate 389 and 461 mg/g adsorption capacity toward Pb^{2+} and Cd^{2+} ions, respectively [167]. Para-amino benzoic ferroxane (PABF) NP (0.25 wt%)-incorporated PES nanofiltration membrane, prepared by phase-inversion showed improved rejection of Na_2SO_4 and NaCl salts, i.e., ~96% and ~73%, respectively, as opposed to ~61 and ~25% rejection of respective salts shown by pristine PES membrane [168]. PES membrane coated with polyamide-SiO_2 NP composites, prepared by interfacial polymerization of poly(amidoamine) (PAMAM) and TMC showed efficient salt rejection in the order of $Na_2SO_4 > MgSO_4 > MgCl_2 > NaCl$ from their respective aqueous solutions [169]. Lakhotia et al. have used modified commercially available PES membrane for salt rejection and desalination [170]. The membrane was coated with FeO NPs by interfacial polymerization of *m*-phenylenediamine (MPD) and TMC, wherein FeO NPs were dispersed in TMC solution. The FeO NP-embedded membrane exhibited improved hydrophilicity, flux and antifouling properties and also showed enhanced salt rejection (NaCl, Na_2SO_4, $C_6H_5Na_3O_7$, $MgCl_2$, and $CaCl_2$) of > 92%, which is higher than the bare PES membrane [170].

Organic dye removal

In ref [168], Moradi et al. have also shown ~99 and ~98% rejection of direct red 16 and methylene blue dyes from their aqueous solutions using 0.25 wt% PABF NP-embedded PES membrane. These values are higher than the rejection efficiency shown by the pristine PES membrane. The NP addition also improved porosity, hydrophilicity, pure water flux, FRR of the PES membrane [168]. In another study, Koulivand et al. found improved dye rejection (~98% versus ~92% for bare PES membrane) of reactive green dye using a nanocomposite membrane comprising of melamine-based dendrimer amine-treated magnetic Fe_3O_4 NPs (0.5 wt%) and PES, prepared by NIPS method [171]. The nanocomposite membrane also showed an overall enhancement of physicochemical properties, such as porosity, hydrophilicity, pure water flux, and FRR than the bare PES membrane [171]. TiO_2 NP-coated poly(lactic acid) (PLA) electrospun nanofibrous membrane, followed by functionalization with methyl trichlorosilane could be used to adsorb methylene blue dye up to ~93% from aqueous solution (dye concentration of 10 mg/L). The adsorption efficiency was found to reduce with an increase in initial dye concentration

and the modified membrane showed good reusability with ~85% of methylene blue adsorption after 9 cycles of adsorption–desorption [172].

Oil–water separation

PDA-anchored SiO_2 NP-coated PVDF membrane, prepared by NIPS method, showed improved oil–water separation efficiency than the pristine PVDF membrane due to super-hydrophilic behavior of the modified PVDF membrane [173]. The membranes also exhibited superoleophobicity in water and the oleophobicity increased with an increase in SiO_2 content, the maximum being 4.5 wt%. PVDF/PDA/SiO_2 membrane showed ~99.9% separation efficiency of the dichloroethane–water emulsion; while the pristine PVDF showed only ~70% efficiency [173]. A commercial PVDF membrane, when dip-coated in chitosan-silica NP-GA solution showed superhydrophilic and superoleophobic behavior. The modified membrane could show ~99% separation efficiency in separating gasoline from water suspension [174]. Obaid et al. have used hydrophobic PSU/1 wt% amorphous SiO_2 NPs and PSU/1 wt% GO electrospun nanofiber membranes for oil–water separation. They found enhanced separation efficiency of SiO_2 NPs in comparison with the GO-incorporated and pristine PSU membranes. The oil–water separation efficiency in terms of measured flux for SiO_2 NP-embedded membrane was found to be ~187, ~100, ~115 m^3/m^2 for hexane, gasoline, kerosene from their water emulsions, respectively [175]. TiO_2 NP-coated PLA electrospun nanofibrous membrane has also shown n-hexane separation from its water emulsion with an efficiency of ~95% [172].

General membrane properties

Bae et al. prepared different nanocomposites of PVDF, PAN, PES separately by mixing TiO_2 NPs in them, the membranes were then cast via NIPS. They also dip-coated the pristine membranes with TiO_2 NPs. Regardless of the TiO_2 incorporation method, the membranes showed decreased WCA and improved water flux. Moreover, the membranes with TiO_2 decorated on their surface showed higher flux in comparison with the NP-embedded and the bare membranes [176]. Maximous et al. reported the preparation of Al_2O_3 NP-embedded PES membrane using the NIPS method to treat activated sludge [10]. The resulting membrane exhibited improved hydrophilicity as well as flux due to the introduction of NPs, as metal oxides show good affinity to water molecules. The treated membrane had higher FRR and improved antifouling property than the raw PES membrane. The water flux increased from ~20.4 L m^{-2} bar^{-1} h^{-1} for bare membrane to ~252 L m^{-2} bar^{-1} h^{-1} for 0.05 wt% Al_2O_3-loaded PES membrane [10]. Pi et al. have coated commercially available polypropylene (PP) membrane using dopamine hydrochloride/PEI solution in tris-buffer solution. TiO_2 NPs were deposited on the resulting membrane by immersing in titanium (IV) bis-(ammonium lactate) dihydroxide (Ti-BALDH/$NH_3 \cdot H_2O$) solution [177]. As a consequence, the water flux increased from 605 ± 26 L m^{-2} h^{-1} for the pristine PP membrane to 5500 L m^{-2} h^{-1} for the PDA/PEI/TiO_2-modified PP membrane under 0.1 MPa pressure. The TiO_2 NP-incorporated membrane also showed improved antifouling properties than the pristine membrane, with FRR

increasing from 44 ± 2% for pristine to 82 ± 5% PDA/PEI/TiO_2 modified PP membrane using BSA rejection studies. Similarly, using the Lys solution, the FRR was 86 ± 3% for the TiO_2-embedded membrane as opposed to 33 ± 6% for the pristine membrane [177]. Wu et al. have prepared SiO_2 nanoparticle embedded PVDF membrane by NIPS technique. The SiO_2 NP were functionalized with a silane coupling agent: 3-(triethoxysilyl)propionitrile (TESPN) and further hydrolyzed with carboxylic groups and subsequently PEG1000 was grafted on surface of these modified NPs with the help of coupling agents such as *N*,*N*′-diiso-propylcarbodiimide (DIC) and 4-dimethylaminopyridine (DMAP). The modified membrane showed improved FRR using BSA solution, i.e., ~93.5% after 3 cycles of physical and chemical cleaning, indicating antifouling behavior of the membrane [48] (Table 3).

Other nanoparticle-based membranes for water treatment

Fang et al. decorated the internal pore walls of the PES membrane with PDA NP. These membranes were fabricated via NIPS technique and were able to show static adsorption capacity of 20.33 mg Pb/g, 17,01 mg Cd/g, and 10.42 mg Cu/g for Pb^{2+}, Cd^{2+}, and Cu^{2+}, respectively, along with properties such as decent PWF and BSA rejection (92.9%) [179]. Zhang et al. have reported simultaneous oil–water separation and catalytic reduction of 4-nitrophenol capability of superhydrophobic Au NP-embedded zeolitic imidazolate framework (ZIF-8)-incorporated PAN electrospun nanofibrous membrane. The NP-incorporated membrane was coated with tannic acid to achieve superhydrophobicity (WCA ~ 155°) [178]. The modified membrane was able to separate ~97% chloroform, ~96% n-hexane, ~97% toluene, and ~83% lubricating oil from their respective water emulsions. The modified membrane also displayed good retention of separation efficiency after 16 cycles [178].

4 Summary and Prospects

From the above discussions, it is evident that polymer nanocomposite membranes have been successfully employed in various water remediation processes. NPs have been modified with a wide range of organic moieties, surfactants, and polymers in order to improve their hydrophilicity and dispersion in the polymer matrix. Upon their incorporation into the polymer matrix, the physicochemical properties of the membrane are found to alter significantly, and the resulting membranes become more favorable for the filtration process. Nanoparticle-loaded composite membranes usually exhibit improved hydrophilicity, pure water flux, antifouling properties over their unfilled counterparts. Two membrane fabricating techniques, viz.: (i) phase inversion using solvent–non-solvent interaction and (ii) electrospinning nanofiber are widely used. Sometimes pore-forming agents, e.g., PVP are also used for increasing the porosity of the membrane prepared during the phase-inversion method. Further, in the phase inversion technique, the various parameters which influence the pore morphology are solution viscosity, solvent–non-solvent interaction, additives, precipitation time and temperature, etc. Rejection, adsorption and

Table 3 Various membrane properties of metal-oxide-incorporated polymer composites

Polymer	Membrane fabrication technique	Nanofiller used	Application	Membrane properties [Water contact angle (WCA) in °], [Pure Water Flux (PWF) in L m^{-2} h^{-1}], [Flux recovery ratio (FRR) in %], [Porosity (P) in %], [Mean pore size (MPS) in nm], [Tensile strength (TS) in MPa]	Reference
PES	NIPS	γ-alumina	49% Cu^{2+} ions removal	Pristine membrane- WCA-74.1, PWF-8.5, P-55.9 ± 3.5 Nanocomposite membrane- WCA-59.1, PWF-25.3, P-75.4 ± 2.3	[163]
PVDF	NIPS	TiO_2	Antifouling membranes	Pristine membrane- WCA-86.7, PWF-303 Nanocomposite membrane- WCA-81.1, PWF-331	[176]
PAN	NIPS	TiO_2		Pristine membrane- WCA-45.5, PWF-225 Nanocomposite membrane- WCA-43.1, PWF-233	
PSf	NIPS	TiO_2		Pristine membrane- WCA-87.6, PWF-243 Nanocomposite membrane- WCA-73.1, PWF-230	
PES	Commercial membrane	FeO	Antifouling properties and 92% salt rejection	–	[170]

(continued)

Table 3 (continued)

Polymer	Membrane fabrication technique	Nanofiller used	Application	Membrane properties [Water contact angle (WCA) in °], [Pure Water Flux (PWF) in L m^{-2} h^{-1}], [Flux recovery ratio (FRR) in %], [Porosity (P) in %], [Mean pore size (MPS) in nm], [Tensile strength (TS) in MPa]	Reference
PES	NIPS	Al_2O_3	Antifouling membranes	–	[10]
PP	Commercial membrane	TiO_2	Antifouling membranes	Pristine membrane- WCA-132, PWF-605 ± 26, FRR-44 ± 2 Nanocomposite membrane- WCA-28, PWF-5720 ± 207, FRR-82 ± 5	[177]
PES	Commercial membrane	PA-SiO_2	Desalination of oily wastewater	-	[169]
PVDF	NIPS	SiO_2 functionalized with 3-(triethoxysilyl) propionitrile	Antifouling membranes	Pristine membrane- WCA-71.3 ± 0.52, FRR-66.3 Nanocomposite membrane- WCA-76.6 ± 0.63, FRR-93.6	[48]
PSf	NIPS	Al-Ti_2O_6	96% As^{5+}, 99% Cd^{2+}, 99% Pb^{2+} ions removal	Pristine membrane- WCA-73 ± 2, Nanocomposite membrane- WCA-51 ± 1, PWF-35	[164]

(continued)

Table 3 (continued)

Polymer	Membrane fabrication technique	Nanofiller used	Application	Membrane properties [Water contact angle (WCA) in °], [Pure Water Flux (PWF) in L m^{-2} h^{-1}], [Flux recovery ratio (FRR) in %], [Porosity (P) in %], [Mean pore size (MPS) in nm], [Tensile strength (TS) in MPa]	Reference
PES	NIPS	Para-amino benzoic ferroxane nanoparticle	99% direct red 16 and methylene blue removal and salt rejection	Pristine membrane- WCA-65.4, PWF-10, P-73.6 ± 3.2, FRR-36 Nanocomposite membrane- WCA-49.34, PWF-64.2, P-86.3 ± 2.9, FRR-99	[168]
PES	NIPS	Fe_3O_4-melamine-based dendrimer amine NP	98% reactive green dye removal	Pristine membrane- WCA-74.6, PWF-75, P-69.0 ± 1.4, P-5.49, FRR-64.4 Nanocomposite membrane- WCA-37.2, PWF-185 ± 20, P-77.0 ± 1.3, P-7.44, FRR-86.4	[171]
PAN	Electrospinning	Au@ZIF-8 NP	Chloroform separation from its water emulsion up to 95–97%	–	[178]

(continued)

Table 3 (continued)

Polymer	Membrane fabrication technique	Nanofiller used	Application	Membrane properties [Water contact angle (WCA) in °], [Pure Water Flux (PWF) in L m^{-2} h^{-1}], [Flux recovery ratio (FRR) in %], [Porosity (P) in %], [Mean pore size (MPS) in nm], [Tensile strength (TS) in MPa]	Reference
PLA	Electrospinning	TiO_2	85% methylene blue dye removal and separation of toluene, carbon tetrachloride, n-hexane, petroleum ether, and soybean oil from their respective water emulsions up to >95%	–	[172]

sieving, and Donnan effects are the key mechanisms by which most of the pollutants are removed from the water. Among the carbon-based fillers, multi-walled CNTs and GO are popular additives in various polymer matrices. Among nanoclays, montmorillonite and halloysite nanotubes are widely used. The reason behind their popularity is probably because these NPs render the required functionality and ability to be modified with a wide range of functional organics and polymers. As a result, these NPs impart hydrophilicity to the membrane, which is the key property for improving the water flux and antifouling properties. Moreover, these nanofillers also improve the mechanical, thermal, and antibacterial properties of the polymeric membrane.

The polymers, which are mostly employed for membrane technology, are PVDF, PES, PSU, PEI, PAN, PVA, PCL, and cellulose acetate, etc., among others. Although, these polymers offer excellent mechanical, high thermal stability, and film-forming properties for making membranes, some of them are expensive. On the other hand, there are very few reports available on membranes using low-cost polymers and their nanocomposites, like PVC, PS, PP, etc. Therefore, future research may be focused on developing efficient and low-cost filtration membranes for large-scale water purification. Thermoplastic polyurethane (TPU) is another polymer that gives a balance between cost and performance and is less explored in membrane technology. Further, nanoparticle-filled various polymer blend composites may be explored for future research. Although a few reports can be found on blend nanocomposites, however, there is a great scope for further research. These composites offer a versatile pathway for designing functionality, improved porosity, and mechanical properties.

Though a lot of work has been carried out on nanocomposite-based membranes, however, their implications in real-life applications are still in the nascent stage. The high cost of nanofillers and processes involved are impeding factors. However, their usage is envisaged to increase in days to come due to the demand for high-performance filtration membranes owing to the stringent environmental regulations for water remediation.

Acknowledgements Divyansh Upreti would like to gratefully acknowledge the Defence Institute of Advanced Technology (DIAT), Defence Research Development Organization (DRDO) for providing his Ph.D. research scholarship. T. Umasankar Patro would like to acknowledge the financial support from DIAT during this work.

References

1. Miettinen IT (2009) Outbreaks of waterborne diseases
2. Prashanthi M, Sundaram R (2016) Integrated waste management in India. Environ Sci Eng
3. Chouhan B, Meena P, Poonar N (2016) Effect of heavy metal ions in water on human health. Int J Sci Eng Res 4:2015–2017
4. Puckett LJ (1995) Identifying the major sources of nutrient water pollution. Environ Sci Technol 29(9):408A-414A
5. Schwarzenbach RP, Egli T, Hofstetter TB, Von Gunten U, Wehrli B (2010) Global water pollution and human health. Annu Rev Environ Resour 35:109–136

6. Yang X, He Y, Zeng G, Chen X, Shi H, Qing D, Li F, Chen Q (2017) Bio-inspired method for preparation of multiwall carbon nanotubes decorated superhydrophilic poly(vinylidene fluoride) membrane for oil/water emulsion separation. Chem Eng J 321:245–256
7. Lau WJ, Ismail AF (2009) Polymeric nanofiltration membranes for textile dye wastewater treatment: preparation, performance evaluation, transport modelling, and fouling control—a review. Desalination 245:321–348
8. Wen Y, Yuan J, Ma X, Wang S, Liu Y (2019) Polymeric nanocomposite membranes for water treatment: a review. Environ Chem Lett 17:1528–1551
9. Zeng G, He Y, Zhan Y, Zhang L, Pan Y, Zhang C, Yu Z (2016) Novel polyvinylidene fluoride nanofiltration membrane blended with functionalized halloysite nanotubes for dye and heavy metal ions removal. J Hazard Mater 317:60–72
10. Maximous N, Nakhla G, Wan W, Wong K (2009) Preparation, characterization, and performance of Al_2O_3/PES membrane for wastewater filtration. J Memb Sci 341:67–75
11. Zhao R, Li X, Sun B, Shen M, Tan X, Ding Y, Jiang Z, Wang C (2015) Preparation of phosphorylated polyacrylonitrile-based nanofiber mat and its application for heavy metal ion removal. Chem Eng J 268:290–299
12. Kanagaraj P, Nagendran A, Rana D, Matsuura T, Neelakandan S (2014) Separation of macromolecular proteins and rejection of toxic heavy metal ions by PEI/cSMM blend UF membranes. Int J Biol Macromol 72:223–229
13. Mansor ES, Abdallah H, Shaban AM (2020) Fabrication of high selectivity blend membranes based on polyvinyl alcohol for crystal violet dye removal. J Environ Chem Eng 8(3):103706
14. Wang C, Yin J, Wang R, Jiao T, Huang H, Zhou J, Zhang L, Peng Q (2019) Facile preparation of self-assembled polydopamine-modified electrospun fibers for highly effective removal of organic dyes. Nanomaterials 9(1):116
15. Deng S, Liu X, Liao J, Lin H, Liu F (2019) PEI modified multiwalled carbon nanotube as a novel additive in PAN nanofiber membrane for enhanced removal of heavy metal ions. Chem Eng J 375:122086
16. Yin J, Deng B (2015) Polymer-matrix nanocomposite membranes for water treatment. J Memb Sci 479:256–275
17. Jose T, George SC, Maya MG, Maria HJ, Wilson R, Thomas S (2014) Effect of bentonite clay on the mechanical, thermal, and pervaporation performance of the poly(vinyl alcohol) nanocomposite membranes. Ind Eng Chem Res 53:16820–16831
18. Feng Y, Wang K, Davies CHJ, Wang H (2015) Carbon nanotube/alumina/polyethersulfone hybrid hollow fiber membranes with enhanced mechanical and anti-fouling properties. Nanomaterials 5:1366–1378
19. Rubel RI, Ali MH, Jafor MA, Alam MM (2019) Carbon nanotubes agglomeration in reinforced composites: a review. AIMS Mater Sci 6:756–780
20. Goh PS, Ng BC, Ismail AF, Aziz M, Sanip SM (2010) Surfactant dispersed multi-walled carbon nanotube/polyetherimide nanocomposite membrane. Solid State Sci 12:2155–2162
21. Tunckol M, Hernandez EZ, Sarasua J-R, Durand J, Serp P (2013) Polymerized ionic liquid functionalized multi-walled carbon nanotubes/polyetherimide composites. Eur Polym J 49(12):3770–3777
22. Yu H, Jin Y, Peng F, Wang H (2008) Kinetically controlled side-wall functionalization of carbon nanotubes by nitric acid oxidation. J Phys Chem C (ACS Publications) 112:6758–6763
23. Xie XL, Mai YW, Zhou XP (2005) Dispersion and alignment of carbon nanotubes in polymer matrix: a review. Mater Sci Eng R Rep 49:89–112
24. Liu T, Zhou H, Graham N, Lian Y, Yu W, Sun K (2018) The antifouling performance of an ultrafiltration membrane with pre-deposited carbon nanofiber layers for water treatment. J Memb Sci 557:87–95
25. Elrasheedy A, Nady N, Bassyouni M, El-Shazly A (2019) Metal-organic framework based polymer mixed matrix membranes: review on applications in water purification. Membranes 9(7):88
26. Ng LY, Mohammad AW, Leo CP, Hilal N (2013) Polymeric membranes incorporated with metal/metal oxide NP: a comprehensive review. Desalination 308:15–33

27. Wang P, Ma J, Wang Z, Shi F, Liu Q (2012) Enhanced separation performance of PVDF/PVP-g-MMT nanocomposite ultrafiltration membrane based on the NVP-grafted polymerization modification of montmorillonite (MMT). Langmuir 28:4776–4786
28. Salehi E, Madaeni SS, Rajabi L, Vatanpour V, Derakhshan AA, Zinadini S, Ghorabi S, Ahmadi Monfared H (2012) Novel chitosan/poly(vinyl) alcohol thin adsorptive membranes modified with amino-functionalized multi-walled carbon nanotubes for Cu(II) removal from water: preparation, characterization, adsorption kinetics and thermodynamics. Sep Purif Technol 89:309–319
29. Zhang J, Xu Z, Mai W, Min C, Zhou B, Shan M, Li Y, Yang C, Wang Z, Qian X (2013) Improved hydrophilicity, permeability, antifouling and mechanical performance of PVDF composite ultrafiltration membranes tailored by oxidized low-dimensional carbon nanomaterials. J Mater Chem A 1:3101–3111
30. Ariono D, Wardani AK (2017) Modification and applications of hydrophilic polypropylene membrane. In: IOP Conf Ser Mater Sci Eng, vol 214, pp 012014
31. Khalid A, Abdel-Karim A, Ali Atieh M, Javed S, McKay G (2018) PEG-CNTs nanocomposite PSU membranes for wastewater treatment by membrane bioreactor. Sep Purif Technol 190:165–176
32. Perego G, Cella GD, Bastioli C (1996) Effect of molecular weight and crystallinity on poly(lactic acid) mechanical properties. J Appl Polym Sci 59:37–43
33. Idris A, Mat Zain N (2006) Effect of heat treatment on the performance and structural details of polyethersulfone ultrafiltration membranes. J Teknol 44:27–40
34. Khorshidi B, Biswas I, Ghosh T, Thundat T, Sadrzadeh M (2018) Robust fabrication of thin-film polyamide-TiO_2 nanocomposite membranes with enhanced thermal stability and anti-biofouling propensity. Sci Rep 8(1):784
35. Shah P, Murthy CN (2013) Studies on the porosity control of MWCNT/polysulfone composite membrane and its effect on metal removal. J Memb Sci 437:90–98
36. Shukla AK, Alam J, Aldalbahi A (2020) A facile approach for elimination of electroneutral/anionic organic dyes from water using a developed carbon-based polymer nanocomposite membrane. Water Soil Pollut 231(3):104
37. Rahil S, Asghari M, Mohammad N (2020) Chitosan-wrapped multiwalled carbon nanotube as filler within PEBA thin-film nanocomposite (TFN) membrane to improve dye removal. Carbohydr Polym 237:116128
38. Roy S, Ntim SA, Mitra S, Sirkar KK (2011) Facile fabrication of superior nanofiltration membranes from interfacially polymerized CNT-polymer composites. J Memb Sci 375:81–87
39. Nakao SI (1994) Determination of pore size and pore size distribution. J Memb Sci 96:131–165
40. Palacio L, Prádanos P, Calvo JI, Hernández A (1999) Porosity measurements by a gas penetration method and other techniques applied to membrane characterization. Thin Solid Films 348:22–29
41. Ariono D, Aryanti PTP, Subagjo S, Wenten IG (2017) The effect of polymer concentration on flux stability of polysulfone membrane. AIP Conf Proc
42. Loeb S, Sourirajan S (1963) Sea water demineralization by means of an osmotic membrane saline water conversion—II, chapter 9. Adv Chem 8:117–132
43. Young TH, Chen LW (1995) Pore formation mechanism of membranes from phase inversion process. Desalination 103:233–247
44. Gnanasekaran G, Balaguru S, Arthanareeswaran G, Das DB (2019) Removal of hazardous material from wastewater by using a metal-organic framework (MOF) embedded polymeric membranes. Sep Sci Technol 54:434–446
45. Masjoudi M, Golgoli M, Ghobadi Nejad Z, Sadeghzadeh S, Borghei SM (2021) Pharmaceuticals removal by immobilized laccase on polyvinylidene fluoride nanocomposite with multi-walled carbon nanotubes. Chemosphere 263:1–11
46. Pang H, Chen Z, Gong H, Du M (2019) Fabrication of a superhydrophobic polyvinylidene fluoride–hexadecyltrimethoxysilane hybrid membrane for carbon dioxide absorption in a membrane contactor. J Memb Sci 595:117536

47. Guillen GR, Pan Y, Li M, Hoek EMV (2011) Preparation and characterization of membranes formed by nonsolvent induced phase separation : a review. Ind Eng Chem Res 50(7):3798–3817
48. Wu H, Mansouri J, Chen V (2013) Silica NP as carriers of antifouling ligands for PVDF ultrafiltration membranes. J Memb Sci 433:135–151
49. Strathmann H, Kock K (1997) The formation mechanism of phase inversion membranes. Desalination 21:241–255
50. Kim JF, Jung JT, Wang HH, Lee SY, Moore T, Sanguineti A, Drioli E, Lee YM (2016) Microporous PVDF membranes via thermally induced phase separation (TIPS) and stretching methods. J Memb Sci 09:94–104
51. Han MJ (1999) Effect of propionic acid in the casting solution on the characteristics of phase inversion polysulfone membranes. Desalination 121:31–38
52. Buruga K, Kalathi JT, Kim K, Ok YS, Danil B (2017) Polystyrene-halloysite nanotube membranes for water purification. J Ind Eng Chem 61:169–180
53. Kim JH, Lee KH (1998) Effect of PEG additive on membrane formation by phase inversion. J Memb Sci 138:153–163
54. Ma Y, Shi F, Ma J, Wu M, Zhang J, Gao C (2011) Effect of PEG additive on the morphology and performance of polysulfone ultrafiltration membranes. Desalination 272(1–3):51–58
55. Boom RM, Wienk IM, van den Boomgaard T, Smolders CA (1992) Microstructures in phase inversion membranes. J Membr Sci 73:277–292
56. Cheng LP (1999) Effect of temperature on the formation of microporous PVDF membranes by precipitation from 1-octanol/DMF/PVDF and water/ DMF/PVDF systems. Macromolecules 32:6668–6674
57. Matsuyama H, Berghmans S, Lloyd DR (1999) Formation of anisotropic membranes via thermally induced phase separation. Polymer 40:2289–2301
58. Su Y, Chen C, Li Y, Li J (2007) PVDF membrane formation via thermally induced phase separation. J Macromol Sci Part A Pure Appl Chem 44:99–104
59. Su Y, Chen C, Li Y, Li J (2007) Preparation of PVDF membranes via TIPS method: the effect of mixed diluents on membrane structure and mechanical property. J Macromol Sci Part A Pure Appl Chem 44:305–313
60. Feng C, Khulbe KC, Matsuura T, Tabe S, Ismail AF (2013) Preparation and characterization of electrospun nanofiber membranes and their possible applications in water treatment. Sep Purif Technol 102:118–135
61. Liao G-Y, Zhou X-P, Xie X-L, Mai Y-W (2017) Electrospun polymer scaffolds: their biomedical and mechanical properties
62. Pereao OK, Bode-Aluko C, Ndayambaje G, Fatoba O, Petrik LF (2017) Electrospinning: polymer nanofibre adsorbent applications for metal ion removal. J Polym Environ 25:1175–1189
63. Ding B, Wang M, Wang X, Yu J, Sun G (2010) Electrospun nanomaterials for ultrasensitive sensors. Mater Today 13:16–27
64. Nunes-Pereira J, Sencadas V, Correia V, Rocha JG, Lanceros-Méndez S (2013) Energy harvesting performance of piezoelectric electrospun polymer fibers and polymer/ceramic composites. Sens Actuators A Phys 196:55–62
65. Bagbi Y, Pandey A, Solanki PR (2019) Chapter-10. Electrospun nanofibrous filtration membranes for heavy metals and dye removal. In: Nanoscale materials in water purification micro and nano technologies. Elsevier, Amsterdam, pp 275–288
66. Radacsi N, Campos FD, Chisholm CRI, Giapis KP (2018) Spontaneous formation of NP on electrospun nanofibres. Nat Commun 9:3–10
67. Cannillo V, Chiellini F, Fabbri P, Sola A (2010) Production of Bioglass® 45S5—polycaprolactone composite scaffolds via salt-leaching. Compos Struct 92:1823–1832
68. Yang Q, Chen L, Shen X, Tan Z (2006) Preparation of polycaprolactone tissue engineering scaffolds by improved solvent casting/particulate leaching method. J Macromol Sci Part B Phys 45(6):1171–1181

69. Taherkhani S, Moztarzadeh F (2016) Fabrication of a poly (E-caprolactone)/starch nanocomposite scaffold with a solvent-casting/salt-leaching technique for bone tissue engineering applications. J Appl Polym Sci 43523:19–21
70. Mulder M (1991) Basic principles of membrane technology. Kluwer Academic Publishers, Alphen aan den Rijn
71. Kiefer R, Höll WH (2001) Sorption of heavy metals onto selective ion-exchange resins with aminophosphonate functional groups. Ind Eng Chem Res 40(21):4570–4576
72. Van TTT, Kumar SR, Lue SJ (2019) Separation mechanisms of binary dye mixtures using a PVDF ultrafiltration membrane: Donnan effect and intermolecular interaction. J Memb Sci 575:38–49
73. Sarkar S, Sengupta AK, Prakash P (2010) The Donnan membrane principle: opportunities for sustainable engineered processes and materials. Environ Sci Technol 44:1161–1166
74. Rivera-Utrilla J, Sánchez-Polo M, Gómez-Serrano V, Álvarez PM, Alvim-Ferraz MCM, Dias JM (2011) Activated carbon modifications to enhance its water treatment applications. An overview. J Hazard Mater 187:1–23
75. Sumiko I (1991) Helical microtubules of graphitic carbon. Nature 354:56–58
76. Kumar S, Nehra M, Kedia D, Dilbaghi N, Tankeshwar K, Kim KH (2018) Carbon nanotubes: a potential material for energy conversion and storage. Prog Energy Combust Sci 64:219–253
77. Peng C, Zhang S, Jewell D, Chen GZ (2008) Carbon nanotube and conducting polymer composites for supercapacitors. Prog Nat Sci 18:777–788
78. Al-Saleh MH, Sundararaj U (2009) Electromagnetic interference shielding mechanisms of CNT/polymer composites. Carbon 47:1738–1746
79. Avouris P (2002) Molecular electronics with carbon nanotubes. Acc Chem Res 35:1026–1034
80. Upadhyayula VKK, Deng S, Mitchell MC, Smith GB (2009) Application of carbon nanotube technology for the removal of contaminants in drinking water: a review. Sci Total Environ 408:1–13
81. Hone J, Llaguno MC, Biercuk MJ, Johnson AT, Batlogg B, Benes Z, Fischer JE (2002) Thermal properties of carbon nanotubes and nanotube-based materials. Appl Phys A Mater Sci Process 74:328–343
82. Yu MF, Lourie O, Dyer MJ, Moloni K, Kelly TF, Ruoff RS (2000) Strength and breaking mechanism of multiwalled carbon nanotubes under tensile load. Science 287:637–640
83. Zhao FY, Ji YL, Weng XD, Mi YF, Ye CC, An QF, Gao CJ (2016) High-flux positively charged nanocomposite nanofiltration membranes filled with poly(dopamine) modified multiwall carbon nanotubes. ACS Appl Mater Interfaces 8:6693–6700
84. Gupta S, Bhatiya D, Murthy CN (2015) Metal removal studies by composite membrane of polysulfone and functionalized single-walled carbon nanotubes. Sep Sci Technol 50:421–429
85. Shawky HA, Chae SR, Lin S, Wiesner MR (2011) Synthesis and characterization of a carbon nanotube/polymer nanocomposite membrane for water treatment. Desalination 272:46–50
86. Park HM, Oh H, Jee KY, Lee YT (2020) Synthesis of PVDF/MWCNT nano complex microfiltration membrane via atom transfer radical addition (ATRA) with enhanced fouling performance. Sep Purif Technol 246:116860
87. Wang W, Zhu L, Shan B, Xie C, Liu C, Cui F, Li G (2018) Preparation and characterization of SLS-CNT/PES ultrafiltration membrane with antifouling and antibacterial properties. J Memb Sci 548:459–469
88. Shukla AK, Alam J, Rahaman M, Alrehaili A, Alhoshan M, Aldalbahi A (2020) A facile approach for elimination of electroneutral/anionic organic dyes from water using a developed carbon-based polymer nanocomposite membrane. Water Air Soil Pollut 231:104
89. Phao N, Nxumalo EN, Mamba BB, Mhlanga SD (2013) A nitrogen-doped carbon nanotube enhanced polyethersulfone membrane system for water treatment. Phys Chem Earth 66:148–156
90. Mousavi SR, Asghari M, Mahmoodi NM (2020) Chitosan-wrapped multiwalled carbon nanotube as filler within PEBA thin-film nanocomposite (TFN) membrane to improve dye removal. Carbohydr Polym 237:116128

91. Khalid A, Abdel-Karim A, Ali Atieh M, Javed S, McKay G (2018) PEG-CNTs nanocomposite PSU membranes for wastewater treatment by membrane bioreactor. Sep Purif Technol 190:165–176
92. Zhao X, Cheng L, Jia N, Wang R, Liu L, Gao C (2020) Polyphenol-metal manipulated nanohybridization of CNT membranes with FeOOH nanorods for high-flux, antifouling, and self-cleaning oil/water separation. J Memb Sci 600:117857
93. Saththasivam J, Yiming W, Wang K, Jin J, Liu Z (2018) A novel architecture for carbon nanotube membranes towards fast and efficient oil/water separation. Sci Rep 8(1):7418
94. Gu J, Gu H, Zhang Q, Zhao Y, Li N, Xiong J (2018) Sandwich-structured composite fibrous membranes with the tunable porous structure for waterproof, breathable, and oil-water separation applications. J Colloid Interface Sci 514:386–395
95. Hummers WS, Offeman RE (1958) Preparation of graphitic oxide. J Am Chem Soc 80:1328
96. Choucair M, Thordarson P, Stride JA (2009) Gram-scale production of graphene-based on solvothermal synthesis and sonication. Nat Nanotechnol 4:30–33
97. He F, Fan J, Ma D, Zhang L, Leung C, Chan HL (2010) The attachment of Fe_3O_4 NP to graphene oxide by covalent bonding. Carbon 48(11):3128–3144
98. Thomas HR, Phillips DJ, Wilson NR, Gibson MI, Rourke JP (2015) One-step grafting of polymers to graphene oxide. Polym Chem 6:8270–8274
99. Konios D, Stylianakis MM, Stratakis E, Kymakis E (2014) Dispersion behavior of graphene oxide and reduced graphene oxide. J Colloid Interface Sci 430:108–112
100. Zhu X, Liu Q, Zhu X, Li C, Xu M, Liang Y (2012) Reduction of graphene oxide via ascorbic acid and its application for simultaneous detection of dopamine and ascorbic acid. Int J Electrochem Sci 7:5172–5184
101. Saini A, Kumar A, Anand VK, Sood SC (2016) Synthesis of graphene oxide using modified hummer's method and its reduction using hydrazine hydrate. Int J Eng Trends Technol 40:67–71
102. Liu C, He C, Xie T, Yang J (2015) Reduction of graphite oxide using ammonia solution and detection Cr(VI) with the graphene-modified electrode. Fullerenes Nanotub Carbon Nanostructures 23:125–130
103. Rana S, Sandhu IS, Chitkara M (2018) Exfoliation of graphene oxide via chemical reduction method. In: 2018 6th Ed Int Conf Wirel Networks Embed Syst WECON 2018—Proc, pp 54–57
104. Saeedi-Jurkuyeh A, Jafari AJ, Kalantary RR, Esrafili A (2020) A novel synthetic thin-film nanocomposite forward osmosis membrane modified by graphene oxide and polyethylene glycol for heavy metals removal from aqueous solutions. React Funct Polym 146:104287
105. Kim Y, Eom HH, Kim YK, Harbottle D, Lee JW (2020) Effective removal of cesium from wastewater via adsorptive filtration with potassium copper hexacyanoferrate-immobilized and polyethyleneimine-grafted graphene oxide. Chemosphere 250:126262
106. Wang W, Han N, Yang C, Zhang W, Miao J, Li W, Zhang X (2019) Fabrication of P(AN-MA)/rGO-g-PAO superhydrophilic nanofiber membrane for removal of heavy metal ions. J Nanosci Nanotechnol 20:1685–1696
107. Ma J, He Y, Yang S (2018) Bio-inspired method to fabricate polydopamine/reduced graphene oxide composite membranes for dyes and heavy metal ion removal. Polym Adv Technol 29(2):941–950
108. Li R, Liu L, Zhang Y, Yang F (2016) Preparation of a nano-MnO_2 surface-modified reduced graphene oxide/PVDF flat sheet membrane for adsorptive removal of aqueous Ni(II). RSC Adv 6:20542–20550
109. Lai GS, Lau WJ, Goh PS, Ismail AF, Tan YH, Chong CY, Krause-Rehberg R, Awad S (2018) Tailor-made thin film nanocomposite membrane incorporated with graphene oxide using novel interfacial polymerization technique for enhanced water separation. Chem Eng J 344:524–534
110. Song Y, Sun Y, Chen M, Huang P, Li T, Zhang X, Jiang K (2019) Efficient removal and fouling-resistant of anionic dyes by nanofiltration membrane with phosphorylated chitosan modified graphene oxide nanosheets incorporated selective layer. J Water Process Eng 34:101086

111. Zhu J, Tian M, Hou J, Wang J, Lin J, Zhang Y, Van der Bruggen B (2016) Surface zwitterionic functionalized graphene oxide for a novel loose nanofiltration membrane. J Mater Chem A 4:1980–1990
112. Zhang H, Li B, Pan J, Qi Y, Shen J, Gao C, Van der Bruggen B (2017) Carboxyl-functionalized graphene oxide polyamide nanofiltration membrane for desalination of dye solutions containing monovalent salt. J Memb Sci 528:128–137
113. Cheng M, Huang L, Wang Y, Zhao Y, Tang J, Wickramasinghe SR (2019) Synthesis of graphene oxide/polyacrylamide composite membranes for organic dyes/water separation in water purification. J Mater Sci 54:252–264
114. Lu J, Gu Y, Chen Y, Yan X, Guo Y, Lang W (2018) Ultrahigh permeability of graphene-based membranes by adjusting D-spacing with poly (ethylene imine) for the separation of dye wastewater. Sep Purif Technol 210:737–745
115. Sundaran SP, Reshmi CR, Sagitha P, Manaf O, Sujith A (2019) Multifunctional graphene oxide loaded nanofibrous membrane for removal of dyes and coliform from water. J Environ Manag 240:494–503
116. Li JH, Zhang H, Zhang W, Liu W (2019) Nanofiber membrane of graphene oxide/polyacrylonitrile with highly efficient antibacterial activity. J Biomater Sci Polym Ed 30:1620–1635
117. Ayyaru S, Ahn Y (2017) Application of sulfonic acid group functionalized graphene oxide to improve hydrophilicity, permeability, and antifouling of PVDF nanocomposite ultrafiltration membranes. J Memb Sci 525:210–219
118. Stagnaro SM, Volzone C, Huck L (2015) Nanoclay as adsorbent: evaluation for removing dyes used in the textile industry. Procedia Mater Sci 8:586–591
119. Bergaya F, Lagaly G (2013) Handbook of clay science, vol 5, 2nd edn. Newnes, London, pp 1752
120. Kahraman HT, Yar A, Avcı A, Pehlivan E (2017) Preparation of nano clay incorporated PAN fibers by electrospinning technique and its application for oil and organic solvent absorption. Sep Sci Technol 53(2):303–311
121. Lau KT, Gu C, Hui D (2006) A critical review on nanotube and nanotube/nanoclay related polymer composite materials. Compos Part B Eng 37:425–436
122. Blanton TN, Majumdar D, Melpolder SM (2000) Microstructure and physical properties of clay-polymer composites 628:1–7
123. Medhat Bojnourd F, Pakizeh M (2018) Preparation and characterization of a nanoclay/PVA/PSf nanocomposite membrane for removal of pharmaceuticals from water. Appl Clay Sci 162:326–338
124. Jacob L, Joseph S, Varghese LA (2020) Polysulfone/MMT mixed matrix membranes for hexavalent chromium removal from wastewater. Arab J Sci Eng 45:7611–7620
125. Radoor S, Karayil J, Parameswaranpillai J, Siengchin S (2020) Adsorption of methylene blue dye from aqueous solution by a novel PVA/CMC/halloysite nanoclay biocomposite: characterization, kinetics, isotherm, and antibacterial properties. J Environ Health Sci Eng 18(2):1311–1327
126. Edelman CH, Favejee L (1934) On the crystal structure of montmorillonite and halloysite
127. https://rookwood.com, https://rookwood.com. Accessed 30 June 2021
128. Vilarinho F, Vaz MF, Silva AS (2019) The use of montmorillonite (MMT) in food nanocomposites: methods of incorporation, characterization of MMT/polymer nanocomposites and main consequences in the properties. Recent Pat Food Nutr Agric 11:13–26
129. Duleba B, Spišák E, Greškovič F (2014) Mechanical properties of PA6/MMT polymer nanocomposites and prediction based on the content of nanofiller. Procedia Eng 96:75–80
130. Shuai C, Yu L, Feng P, Zhong Y, Zhao Z, Chen Z, Yang W (2020) Organic montmorillonite produced an interlayer locking effect in a polymer scaffold to enhance interfacial bonding. Mater Chem Front 4:2288–2408
131. Swearingen C, Macha S, Fitch A (2003) Leashed ferrocenes at clay surfaces: potential applications for environmental catalysis. J Mol Catal A Chem 199:149–160

132. Zhu TT, Zhou CH, Kabwe FB, Wu QQ, Li CS, Zhang JR (2019) Exfoliation of montmorillonite and related properties of clay/polymer nanocomposites. Appl Clay Sci 169:48–66
133. Shokri E, Shahed I, Hermani M, Etemadi H (2020) Applied clay science towards enhanced fouling resistance of PVC ultrafiltration membrane using modified montmorillonite with folic acid. Appl Clay Sci 200(3):105906
134. Raj Somera L, Cuazon R, Kenneth Cruz J, Joy Diaz L (2019) Kinetics and isotherms studies of the adsorption of Hg(II) onto iron modified montmorillonite/polycaprolactone nanofiber membrane. In: IOP conference series: materials science and engineering, vol 540, pp 012005
135. Shokri E, Yegani R (2017) Novel adsorptive mixed matrix membrane by incorporating modified nanoclay with amino acid for removal of arsenic from water. J Water Environ Nanotechnol 2(2):88–95
136. Abolhassan S, Vossoughi M, Mohammad N (2019) Clay-based electrospun nanofibrous membranes for colored wastewater treatment. Appl Clay Sci 168:77–86
137. Nivedita S, Joseph S (2018) Effect of unmodified and modified montmorillonite on the properties of PCL-based ultrafiltration membrane for water treatment applications. J Water Process Eng 21:61–68
138. Hieu C, Fu C, Kao D, Tuong T, Tran V, Juang R (2020) Adsorption removal of tetracycline from water using poly (vinylidene fluoride)/polyaniline-montmorillonite mixed matrix membranes. J Taiwan Inst Chem Eng 000:1–12
139. Barbosa S, Salviano AF, Sonaly S, Oliveira L, Maria E, Lira DL (2019) Treatment of effluents from the textile industry through polyethersulfone membranes. Water 11(12):2540
140. Makwana D, Polisetti V, Castaño J, Ray P, Bajaj HC (2020) Mg-Fe layered double hydroxide modified montmorillonite as hydrophilic nanofiller in polysulfone- polyvinylpyrrolidone blend ultrafiltration membranes: separation of oil-water mixture Appl Clay Sci 192:105636
141. Makaremi M, De Silva RT, Pasbakhsh P (2015) Electrospun nanofibrous membranes of polyacrylonitrile/halloysite with superior water filtration ability. J Phys Chem C 119(14):7949–7958
142. Zeng G, Ye Z, He Y, Yang X, Shi H, Ye Z, He Y, Yang X, Shi H, Feng Z (2017) Application of dopamine-modified halloysite nanotubes/PVDF blend membranes for direct dyes removal from wastewater. Chem Eng J 323:572–583
143. Ibrahim GPS, Isloor AM, Moslehyani A, Ismail AF (2017) Bio-inspired, fouling resistant, tannic acid-functionalized halloysite nanotube-reinforced polysulfone loose nanofiltration hollow fiber membranes for efficient dye and salt separation. J Water Process Eng 20:138–148
144. Hebbar RS, Isloor AM, Ananda K, Ismail AF (2016) Fabrication of polydopamine functionalized halloysite nanotube/polyetherimide membranes for heavy metal removal. J Mater Chem A 4:764
145. Ma J, He Y, Zeng G, Peng L, Sengupta A, Chen X (2018) High-flux PVDF membrane incorporated with β-cyclodextrin modified halloysite nanotubes for dye rejection and Cu(II) removal from water. Polym Adv Technol 29:2704–2714
146. Zhang L, Shu Z, Yang N, Wang B, Dou H, Zhang N (2018) Improvement in antifouling and separation performance of PVDF hybrid membrane by incorporation of room-temperature ionic liquids grafted halloysite nanotubes for oil-water separation. J Appl Polym Sci 135(21):46278
147. Bai Z, Wang L, Liu C, Yang C, Lin G, Liu S, Jia K, Liu X (2020) Interfacial coordination mediated surface segregation of halloysite nanotubes to construct a high-flux antifouling membrane for oil-water emulsion separation. J Memb Sci 620:118828
148. Wang Y, Zhu J, Dong G, Zhang Y, Guo N, Liu J (2015) Sulfonated halloysite nanotubes/polyethersulfone nanocomposite membrane for efficient dye purification. Sep Purif Technol 150:243–251
149. dos Santos Filho EA, de Medeiros KM, Araújo EM, Ferreira RDSB, Oliveira SSL, Medeiros VDN (2019) Membranes of polyamide 6/clay/salt for water/oil separation. Mater Res Express 6(10):105313
150. Joussein E, Petit S, Churchman J, Theng B, Righi D, Delvaux B (2005) Halloysite clay minerals—a review. Clay Miner 40(04):383–426

151. Yang H, Zhang Y, Ouyang J (2016) Physicochemical properties of halloysite. In: Peng Yuan AT, Faïza B (eds) Nanosized tubular clay minerals—halloysite and imogolite, ch 4, vol 7. Developments in Clay Science, Elsevier, Amsterdam, pp 67–91
152. Halloysite clay nanotubes. http://phantomplastics.com/functional-fillers/halloysite/. Accessed 30 June 2021
153. Jennings BR, Plummer H, Closs WJ, Jerrard HG (1969) Size and shape of laponite (type S) synthetic clay particles. J Colloid Interface Sci 30:134–139
154. Wheeler PA, Wang J, Baker J, Mathias LJ (2005) Synthesis and characterization of covalently functionalized laponite clay. Chem Mater 17:3012–3018
155. Patro TU, Wagner HD (2011) Layer-by-layer assembled PVA/laponite multilayer free-standing films and their mechanical and thermal properties. Nanotechnology 22:455706
156. Patro TU, Wagner HD (2016) Influence of graphene oxide incorporation and chemical cross-linking on the structure and mechanical properties of layer-by-layer assembled poly(vinyl alcohol)-laponite free-standing films. J Polym Sci Part B Polym Phys 54(22):2377–2387
157. Fozer D, Haaz E, Mizsey P (2020) Chemical engineering research and design pervaporative desalination of concentrated brine solution employing crosslinked PVA/silicate nano clay membranes. Chem Eng Res Des 155:229–238
158. Tabernero A, Cardea S, Masa R, Baldino L, del Valle EMM, Reverchon E (2019) Preparation and characterization of cellulose acetate-Laponite® composite membranes produced by supercritical phase inversion. J Supercrit Fluids 104651
159. Nikolova MP, Chavali MS (2020) Metal oxide NP as biomedical materials. Biomimetics 5(2):27
160. Kruefu V, Wisitsoraat A, Tuantranont A, Phanichphant S (2014) Gas sensing properties of conducting polymer/Au-loaded ZnO nanoparticle composite materials at room temperature. Nanoscale Res Lett 9:1–12
161. Bockstaller MR, Thomas EL (2003) Optical properties of polymer-based photonic nanocomposite materials. J Phys Chem B 107:10017–10024
162. Yang C, Wei H, Guan L, Guo J, Wang Y, Yan X, Zhang X, Wei S, Guo Z (2015) Polymer nanocomposites for energy storage, energy-saving, and anticorrosion. J Mater Chem A 3:14929–14941
163. Ghaemi N (2016) A new approach to copper ion removal from water by polymeric nanocomposite membrane embedded with γ-alumina NP. Appl Surf Sci 364:221–228
164. Sunil K, Karunakaran G, Yadav S, Padaki M, Zadorozhnyy V, Pai RK (2018) Al-Ti_2O_6 a mixed metal oxide-based composite membrane: a unique membrane for removal of heavy metals. Chem Eng J 348:678–684
165. Razmgar K, Saljoughi E, Mousavi SM (2019) Preparation and characterization of a novel hydrophilic PVDF/PVA/Al_2O_3 nanocomposite membrane for removal of As(V) from aqueous solutions. Polym Compos 40:2452–2461
166. Zheng YM, Zou SW, Nanayakkara KGN, Matsuura T, Chen JP (2011) Adsorptive removal of arsenic from aqueous solution by a PVDF/zirconia blend flat sheet membrane. J Memb Sci 374:1–11
167. Alharbi HF, Haddad MY, Aijaz MO, Assaifan AK, Karim MR (2020) Electrospun bilayer PAN/chitosan nanofiber membranes incorporated with metal oxide NP for heavy metal ion adsorption. Coatings 10(3):285
168. Moradi G, Zinadini S, Rajabi L (2020) Development of high flux nanofiltration membrane using para-amino benzoate ferroxane nanoparticle for enhanced antifouling behavior and dye removal. Process Saf Environ Prot 144:65–78
169. Jin LM, Yu SL, Shi WX, Yi XS, Sun N, Ge YL, Ma C (2012) Synthesis of a novel composite nanofiltration membrane incorporated SiO_2 NP for oily wastewater desalination. Polymer 53:5295–303
170. Lakhotia SR, Mukhopadhyay M, Kumari P (2018) Iron oxide (FeO) NP embedded thin-film nanocomposite nanofiltration (NF) membrane for water treatment. Sep Purif Technol 211:98–107

171. Koulivand H, Shahbazi A, Vatanpour V (2019) Chemical engineering research and design fabrication and characterization of a high-flux and antifouling polyethersulfone membrane for dye removal by embedding Fe_3O_4-MDA NP. Chem Eng Res Des 145:64–75
172. Zhou Z, Liu L, Yuan W (2019) A superhydrophobic poly(lactic acid) electrospun nanofibrous membrane surface-functionalized with TiO_2 NP and methyl trichlorosilane for oil/water separation and dye adsorption. New J Chem 43:15823–15831
173. Cui J, Zhou Z, Xie A, Meng M, Cui Y, Liu S, Lu J, Zhou S, Yan Y, Dong H (2019) Bio-inspired fabrication of superhydrophilic nanocomposite membrane based on surface modification of SiO_2 anchored by polydopamine towards effective oil-water emulsions separation. Sep Purif Technol 209:434–442
174. Liu J, Li P, Chen L, Feng Y, He W, Lv X (2016) Modified superhydrophilic and underwater superoleophobic PVDF membrane with ultralow oil-adhesion for highly efficient oil/water emulsion separation. Mater Lett 185:169–172
175. Khalil A, Almajid AA, Kim B, Nasser AM (2015) Effective polysulfone-amorphous SiO_2 NPs electrospun nanofiber membrane for high flux oil/water separation. Chem Eng J 279:631–638
176. Bae T, Tak T (2005) Effect of TiO_2 NP on fouling mitigation of ultrafiltration membranes for activated sludge filtration. J Membr Sci 249:1–8
177. Pi J-K, Yang H-C, Wan L-S, Wu J, Xu Z-K (2016) Polypropylene microfiltration membranes modified with TiO_2 NP for surface wettability and antifouling property. J Membr Sci 500:8–15
178. Zhang Z, Yang Y, Li C, Liu R (2019) Porous nanofibrous superhydrophobic membrane with embedded Au NP for the integration of oil/water separation and catalytic degradation. J Membr Sci 582:350–357
179. Fang X, Li J, Li X, Pan S, Zhang X, Sun X, Shen J, Han W, Wang L (2017) Internal pore decoration with polydopamine nanoparticle on polymeric ultrafiltration membrane for enhanced heavy metal removal. Chem Eng J 314:38–49

Chapter 14
Low-Dimensional Nanostructured Materials for Sustainable Generation of Water and Energy

Jackson Pame and Lenin S. Shagolsem

1 Introduction

With the advancement in science and technology and its need in every field, the requirement for more reliable, cheap, eco-friendly, and abundantly available by-products is in demand. Nanomaterials are one such material to which researchers have turned towards as an up-gradation for technological development due to their intensified properties. By definition, these are the materials whose size, in either one of the three spatial dimensions, is in the range of 1–100 nm. Different heterostructures of nanomaterials are shown in Fig. 1. Due to their small size and high surface area, they are compatible for manipulating their functionality and designing nanodevices. The origin of the research on nanoscience and nanotechnology can be traced back to 1959 [1], where a lecture by Richard Feynman addressed the approach to "manipulation and tuning the properties of materials on atomistic-scale," which was beyond the accessible length scale of the researchers at that time. However, modern nanoscience started much later. Since the properties of materials depend on the internal structure tuning the structures on the atomic level can significantly alter material properties. In this chapter, we discuss low-dimensional nanostructured materials, their applications, and the growth of enhanced properties in low dimensions.

Given the fact that the currently available natural resources are depleting at a very rapid rate due to overexploitation by humans, a sustainable resource is the need of the hour. In this regard, nanomaterials are an alternative for sustainable development and eco-friendly resources for future generations too. For example, water scarcity, which is inaccessible of clean water to the most population of the globe, overpopulation along with the exploitation of water resources in terms of domestic, industrial as well as irrigation purposes has made a dramatic increase in shortage of fresh water in many parts of the world. Although about 70% of the earth is filled with water, out of which 97% is saline water and only about 3% is freshwater distributed poorly

J. Pame · L. S. Shagolsem (✉)
National Institute of Technology Manipur, Langol, Imphal 795004, India

B. P. Swain (ed.), *Advances in Nanostructured Materials*, Materials Horizons:
From Nature to Nanomaterials, https://doi.org/10.1007/978-981-16-8391-6_14

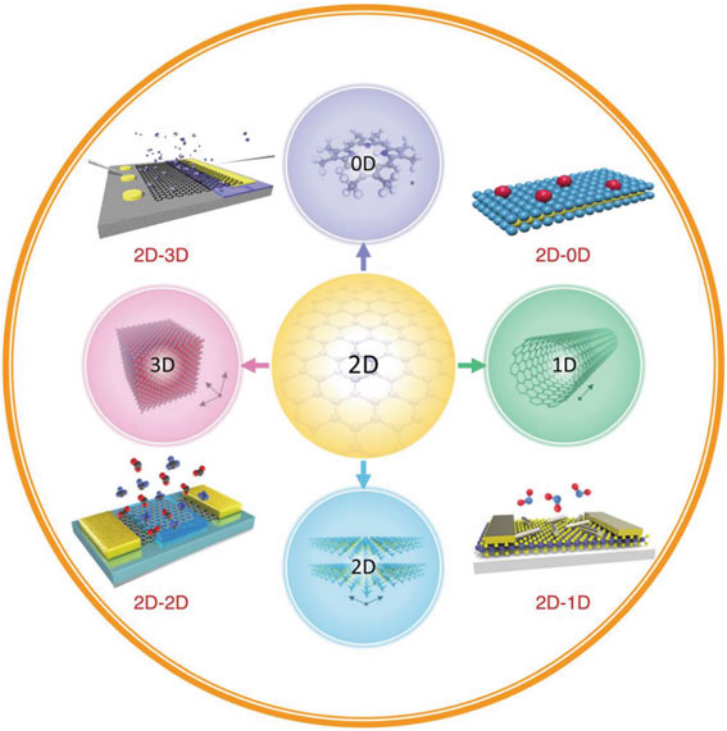

Fig. 1 Overview of nanostructured materials with different heterostructures. Adapted with permission from [2]

across the globe. Hence, desalination of water is an essential measure to overcome the demanding need for freshwater. Nanostructured materials such as zeolites, graphene, and carbon nanotubes show potential application for the demanding need for the desalination of seawater in industries. The details of which are discussed in the latter part of the chapter. More application approaches of nanostructured materials apart from desalination shall be elaborated in the chapter.

2 Low-Dimensional Nanomaterials

The dimensionality of nanomaterials can be described as zero-dimensional (0D), one-dimensional (1D), two-dimensional (2D), and three-dimensional (3D) nanomaterials based on their size, length, and thickness.

2.1 Zero-Dimensional or 0D

Zero-dimensional nanomaterials are the building blocks of all nanostructures. These are usually nanoparticles, or nanoparticles clusters, or quantum dots. Due to their high surface-to-volume ratio, high edge, and quantum confinement effect, they exhibit properties such as quantum efficiency, photoluminescence, and chemiluminescence which find applications ranging from sensors, photovoltaic, biomedicine, nanodevice, etc. Some of the well-known zero-dimensional nanostructures are graphene quantum dots, carbon quantum dots, fullerenes, inorganic quantum dots, nanoparticles, etc. For example, graphene quantum dots due to the electron confinement in all three dimensions give them high electrical and optical properties. These properties are an excellent choice for many technological advancements such as photovoltaic cells and can even be manipulated to achieve the desired properties [3]. Fullerenes too find application in solar cells and in enhancing the properties of organic photovoltaic cells due to their excellent photochemistry property [4].

2.2 One-Dimensional (1D)

Nanowire (NW), nanorod, nanofiber, carbon nanotubes, etc., are some of the most common 1D nanostructured materials. The properties of 1D nanostructures are dependent on the synthesis process, one of the most preferred methods for the production of 1D nanostructures over other physical and chemical fiber synthesis methods is Electrospinning. For example, H_2 produces electrospun nanofibers that perform better than that produced by the hydrothermal synthesis process, where the process parameter in particular calcination temperature (crystallinity) and surface area are the governing factors. The improved properties of 1D nanostructures find their usage in electronics, optoelectronics, magnetic sensor, photovoltaic, quantum computers, energy harvesting technologies, etc.

NWs have been considerably studied in recent years [5–8] due to their lower electron–hole recombination rate because of the improved electron–hole separation. These properties find application to enhance the efficiency of photoelectrochemical (PEC) technique to split water into its components, i.e., H_2 and O_2, which was tedious and costly when first demonstrated by Fujishima and Honda [9] in 1972. It has been shown that NWs yield higher PEC efficiency than those of 0D nanostructures due to their improved charged transport properties. And hence, the TiO_2 NWs were found to be much more efficient than TiO_2 nanoparticles (NPs) for H_2 generation [10].

2.3 Two-Dimensional (2D)

Research on two-dimensional (2D) nanostructured materials has been a trending interest for the advancement of low dimensional materials, which gain applications in nanostructured devices for their extraordinary and improved properties, namely electronic, magnetic, optical, catalytic, etc. Diverse methods have been employed for the evolution of the preparation of 2D nanostructured materials. However, the preparation of 2D structures like nanosheets, nanoplates, etc., remains tedious work because of complications in solution chemistry and also because of the intricate interaction between materials [11]. So far, many 2D nanostructures with diverse shapes and thicknesses have been prepared and studied both through conventional methods and also by computer simulations to understand the structure formation and to improve their properties. Graphene was the first hardest, thinnest, and lightest 2D nanostructured material produced by a human with extraordinary properties such as high thermal conductivity, high electrical property, etc. They can also be embedded in plastics to make them conductive and find applications in many industries and factories for the production of LCDs, flexible touch screen, solar cells coatings, and many more.

2D nanostructures such as nanobelts, nanosheets, nanoplates, nanolayers, nanoribbons, and nanoleaf are also found to be efficient for the H_2 production, where transfer of charge carriers to the surface occurs analogous to 1D nanostructures which helps to improve the performance.

3 Simulation Approach to Nanostructures

Simulation comes as a handy tool to overcome the drawbacks of visualizing and examining the dynamics at the atomistic or nanoscales. It is also important to test the underlying theory and to locate the required thermodynamics parameters such as the freezing or melting pressure, temperature, energy, specific heat, etc., to understand the structure formation of any materials which can be used in real experiments for verifying the developed theory. And hence act as a bridge between theory and experiments.

Computer simulation has become an integral part and is considered an interdisciplinary subject in every field of research these days mainly for the reduction in time as compared to the laboratory experiments. Since material properties depend on the microstructures, i.e., the atomic arrangement or chemical composition and the dimensions of the materials (one, two, or three dimensions). Manipulating the structures may eventually lead to the alteration of the material properties. For example, the properties of gold [12–17] drastically change when reduced to nano dimension, one such interesting change is its color from yellow to red when reduced to nano dimension. In 1995, S. Múller and M. Schwarz presented a simulation model for the first time that gives an insight into the properties of nanostructured materials such

as static structure factor and the pair correlation function through computer simulation of 3000 classical particles using Metropolis Monte Carlo algorithm in two dimensions [18].

Depending on the merits, specific to a system, molecular dynamics (MD) simulation or Monte Carlo (MC) simulation (or both MD and MC) is used to model low-dimensional systems. Through proper choice of potentials and force fields, one can reproduce the accurate behavior of an actual system. MD simulations are like real experiments in many respects. For performing real experiments, we must prepare material samples of our desired study. After which for measuring its properties, we require instruments such as a thermometer, manometer, or viscometer, etc., and measured its property of interest for a certain time interval. Now, since there is always a statistical noise in almost all measurements, hence the more we average, the more accuracy we get in our measurements. In MD simulation also similar method or approach is followed. Also, the errors encountered during computer simulation are quite similar to those of the real experiment, e.g., error/defects in sample preparation, not well equilibrated, performing wrong measurements, etc. Frenkel and Smidth [19], Gates, and Hinkley [20] investigated details of MD and MC simulation methods including applications in many systems ranging from quantum (atomic) systems to classical (mesoscale) systems.

It has been shown experimentally that the water fluxes in carbon nanotubes (CNTs) are ultrafast [21, 22]. The same result with more insight into why the ultrafast water transport inside the CNTs is also shown by Molecular Dynamics simulation [23, 24]. Firstly, the interaction of water molecules among themselves confined inside CNT is stronger than the interaction with the wall of the CNT [25]. Secondly, the water transport inside CNT also depends on the surface roughness (add friction to water flow) and the degree of hydrophobicity [21]. The friction coefficient between the walls of CNT and water molecules depends highly on the curvature of the CNTs. MD simulation results by Falk et al. [26] demonstrated that with decreasing radius of the CNT, the friction decreases and tends to vanish at a radius below 0.25 nm.

4 Applications of Low-Dimensional Nanostructured Materials

4.1 Desalination of Water

Desalination is the process of separating water from salt. The high cost in energy and infrastructure of the existing technologies has made the researchers look for new, better, low energy, and cheap byproducts that are available abundantly and are environment friendly, which is still a challenge to the present generation too. But with the beginning of nanoscience and technology, manipulation of matter for transport at nanoscales are possible and that has improved the water desalination techniques.

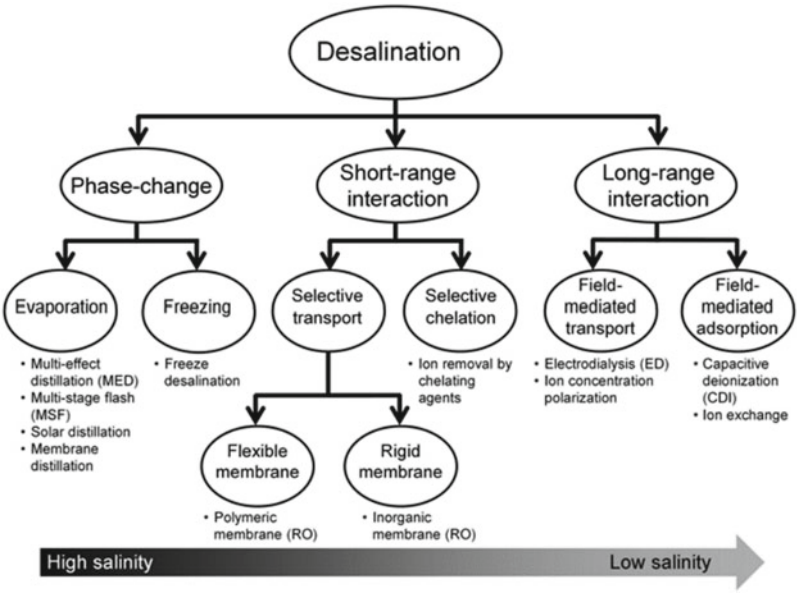

Fig. 2 Desalination techniques/mechanism and their usefulness in desalination technologies. Adapted with permission from [27]

Materials like graphene, carbon nanotubes, and zeolites show great potential for use in the transport process, e.g., it finds applications in reverse osmosis, capacitive deionization for desalination process with enhanced capacity and efficiency. We discuss below some desalination techniques using advanced nanostructured materials [27]. Figure 2 represents the schematic overview of these techniques, where three different methods are employed for converting the saline water into low salinity water and the different mechanisms involved in these processes.

The mechanism involving phase change

Desalination or the salt and water splitting process can be observed when the saline water undergoes a phase change into vapor or ice. The liquid–vapor phase transition technique is a widely used separation mechanism for desalination. Most desalination processes (e.g., solar distillation where solar thermal energy is used, membrane distillation where vapor–liquid phases are separated, humidification–dehumidification) involve evaporation of saline water to separate water from salt. As shown in Fig. 3, the saline water is heated to provide a gradient for the water to evaporate on the hydrophobic porous membrane pores, while salt compounds remain on the feed side.

One of the most preferred techniques for the desalination process is freezing, the advantage of this technique is that during the freezing transition, the salt preferred to exist in the liquid state than in the solid state, which is shown by a theoretical

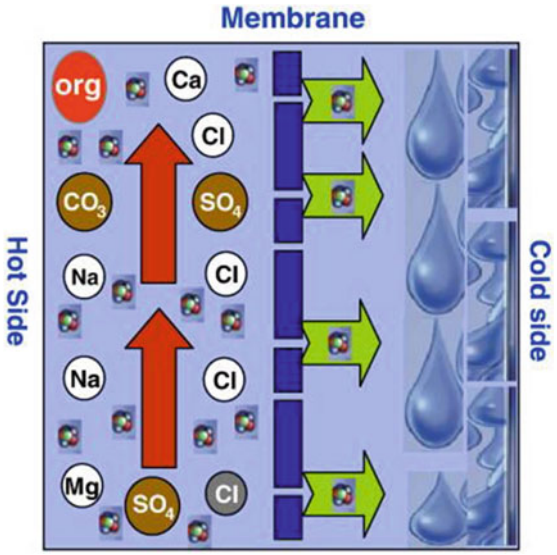

Fig. 3 Phase-change method for desalination of saline water where membrane distillation process is employed. Adapted with permission from [28]

lower energy consumption with lower heat of fusion and minimal scaling difficulties as compared to that of vaporization technique. The only disadvantage of this technique is the complex plant requirement to tackle the ice and water mixture, hence the processed water gets contaminated which has drastically hindered the wide application of this process to commercialization.

The mechanism involving short-range interactions with a selective material

This method uses transport phenomena through selective materials where short-range interactions of water molecules and ions present with third material where combine dispersion, steric, dipole, and electrostatic interactions can enhance desalination. The interactions enable desalination preferentially, either by transport of water molecules or ions present in the saline water with the desired materials or by chelation, i.e., by adsorption/absorption of ions to a chelating material, the chelating materials are usually nanostructured materials like zeolites.

Carbon nanotubes, graphene, etc. In the chelation process, selection of chelating material plays a crucial role and rely on the sorption and transport properties of material where the adsorption and absorption of molecules or ions take place on the surface of the chelating material through the nanometer pores and act as a membrane for the separation of water molecules from the salt ions.

Figure 4 represents the hybrid capacitive deionization (HCDI) technique, which consists of a sodium manganese oxide (NMO) electrode, and an anion exchange membrane, and a porous carbon electrode. As is seen in the figure once the desalination process is activated, sodium ions are held by the chemical reaction in the NMO electrode, and the chloride ions in the electric double layers are formed at the surface of the porous carbon electrode. The ability to absorb ions depends on the thickness

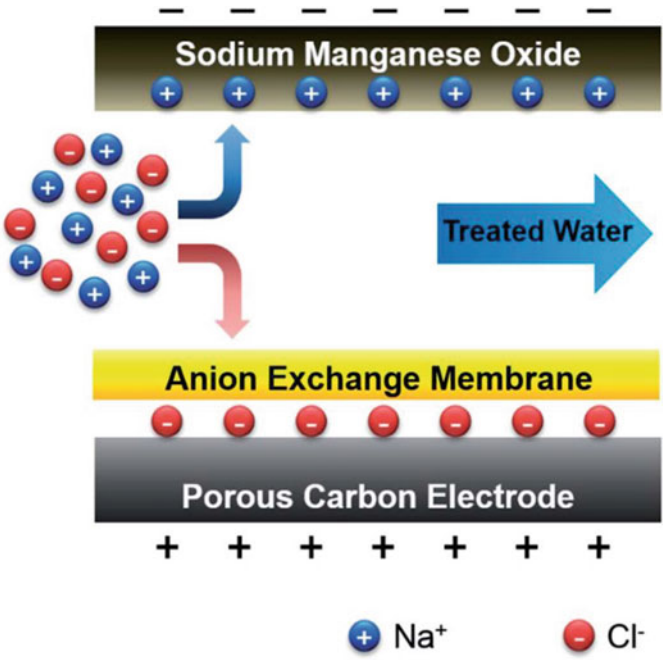

Fig. 4 Desalination by absorption of ions by HCDI method. Adapted with permission from [29]

of the electrode. It is shown that the HCDI method of desalination can remove ions rapidly and shows exceptional stability [29] in the aqueous sodium chloride solution.

Mechanisms involving long-range electrostatic interactions

In this mechanism, electrokinetics phenomena are applied, which is the advantage of the absence of net charge of water molecules and electrical charges on ions induced long-range electrostatics fields to exert force selectively on ions [30]. This enables the formation of an electric double layer (EDL) by attraction and repulsion of opposite and like charges, respectively. And hence, salt ions can be either absorbed or exported through pores of the membranes for desalination to take place.

Figure 5 shows the fabrication and manipulation of EDLs for desalination. Initially, as the starting material, anodic alumina oxide (AAO) with the pore size of about 200 nm is used (Fig. 5a1), then a 25 nm-thick aluminum (Al) layer inside AAO nanochannels was prepared by sputter deposition (Fig. 5a2) to act as an electrode, which is then coated fully to cover the electrode as well as the AAO nanochannels with 10–30 nm thick uniform HfO_2 layer by atomic layer deposition method (Fig. 5a3). When no external bias is applied, the saline water containing anions and cations pass through the nanochannels, indicating no desalination process (Fig. 5b). With the application of bias (positive or negative) on the Al electrode, extra surface charges (negative or positive) appears, that is due to surface polarization an EDL is induced on the surface of the HfO_2 layer. The EDL overlapping increases with

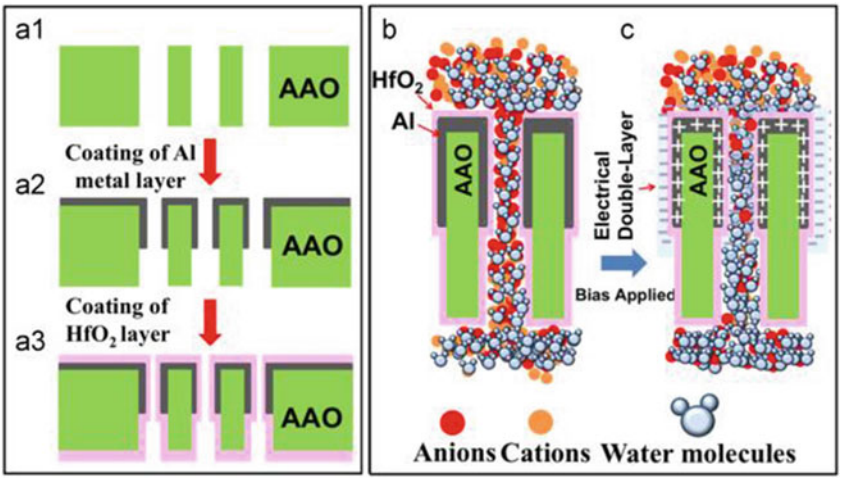

Fig. 5 Fabrication of EDL-based AAO nanochannels membranes (a1–a3) for desalination process and the manipulation of EDLs overlapping effect by controlling externally applied biases in the nanochannels. Adapted with permission from [31]

increasing bias. A unipolar channel is formed inside the AAO membrane when the EDL overlapped entirely, this action allows only the counterions to flow through the channel and results in desalination (Fig. 5c).

Reverse osmosis (RO)

The main advantage of the reverse osmosis (RO) technique for desalination of seawater over other techniques is its low-cost energy. The development in nanoscience and nanotechnology, and the understanding of membrane technology have attracted researchers to look for 2D nanostructures that have high permeabilities that can be applied for the desalination of seawater at a large scale. In RO, desalination occurred when high pressure is applied to the feedwater (seawater/saline water) to force it through a semi-permeable membrane, where the membrane allows the water molecules to flow through but restrict salt ions (see Fig. 6). For desalination in RO, the only requirement is that the applying pressure has to be always higher than the osmotic pressure of the feedwater [32–35]. To have good desalination, water flux from the membrane should be high, which requires high permeability of the membrane along with high salt rejection capabilities. Hence, the rate of water flux is greatly dependent on the membrane materials. The flux and the purity of produced water are greatly affected by biofouling or the accumulation of salt ions on the surface of the membrane and also due to degradation of the membrane. To overcome these shortcomings, appropriate designing of the system is necessary [36]. To date, the RO plants for desalination have been the most installed plants for their low energy utilization. The first commercialized RO membranes were developed in the 1960s with cellulose acetate, which offered low fluxes and also was easily degradable by biological interactions [37]. Hence, for future generations, membranes with high

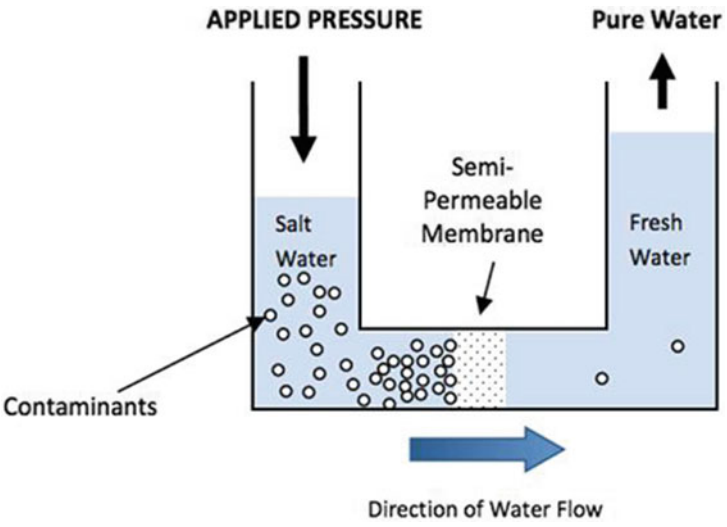

Fig. 6 Schematics of reverse osmosis process for desalination. (*Source* lenntech.com)

permeability and high salt rejection, and high durability are a must for the desalination process, which will prevent excessive use of the materials for developing the equipment and deplete the resources.

4.2 Energy Generation

With the excessive utilization of the resources, the available sources of energy are depleting at a very rapid rate. Therefore, the need for research on clean and free energy is in demand for the sustainability of the future generation [38–40]. Hydrogen (H_2) is regarded as an ideal fuel for future energy demands due to its compatibility with the environment and is considered to be sourced for clean and renewable energy resources. H_2 attracted researchers because of its fascinating features such as unlimited generation from abundant water sources on the earth. Significantly, upon combustion, it generates water as an exhaust as compared to other conventional fossil fuels.

Nanowires (NWs) exhibit significant photocatalytic activity due to improvement of electron–hole separation and lower recombination rate these characteristics are useful in hydrogen generation with relatively higher efficiencies because of the improved charge transport over 0-D nanostructures [5]. Figure 7 illustrates the production of H_2 by splitting water using nanowire while giving off oxygen as a final exhaust. Similarly, nanorods, nanotubes, etc., show enhanced properties for H_2 generation.

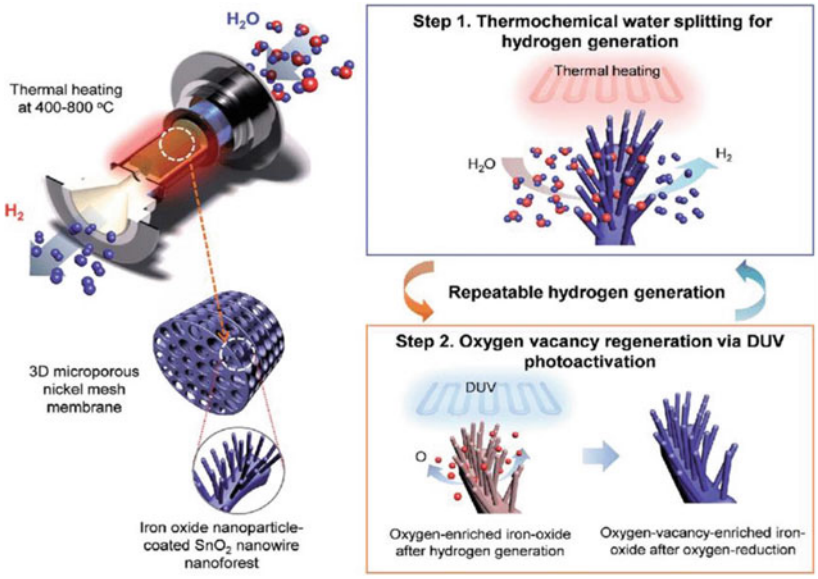

Fig. 7 (Left) hydrogen generation process on oxygen vacancy-enriched iron oxide-coated nanoforests using thermal annealing (400–800 °C). (Right) Oxygen reduction process on oxygen-enriched iron oxide nanoforests using deep ultraviolet (DUV) light exposure and low-temperature annealing (200 °C). Adapted with permission from [41]

4.3 Solar Energy Using Carbon Nanostructures

The unique and extraordinary properties of carbon nanostructures have fascinated many researchers to use them in energy generation applications [42–44]. The harvesting of photons [45–47] is important for the application in solar energy devices. Carbon nanostructures like fullerenes, CNTs, and thin films are an excellent choice for solar energy devices. These nanostructures when deposited as thin films on conducting glass surface acts as an electrode and exhibits excellent photoelectrochemical [48–51] and electrocatalytic [52] responses. Figure 8 represents the carbon nanostructured thin film image obtained from atomic force microscopy (AFM) and transmission electron microscopy (TEM). The single-wall carbon nanotubes (SWCNT) and stacked-cup carbon nanotubes (SCCNT) are the two novel classes of carbon nanostructures. SWCNT, SCCNT, and fullerene clusters are most preferable for solar energy devices because of their efficient photocurrent generation property [53] and hence have potential application to solar energy devices.

Figure 9 compares the output photocurrent of SWCNT and SCCNT to demonstrate incident photon to current conversion efficiency (IPCE) as a function of wavelength (λ). IPCE depends on the electronic properties of the materials. The IPCE of SWCNT

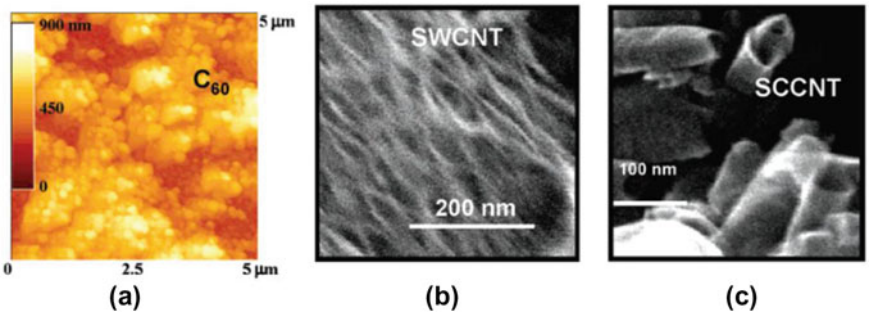

Fig. 8 AFM image of carbon nanostructured films cast on the surface of conducting glass electrodes. **a** Image of C60 cluster film, **b** film image of single-wall carbon, nanotube and **c** film image of stacked cup carbon nanotube. Adapted with permission from [53]

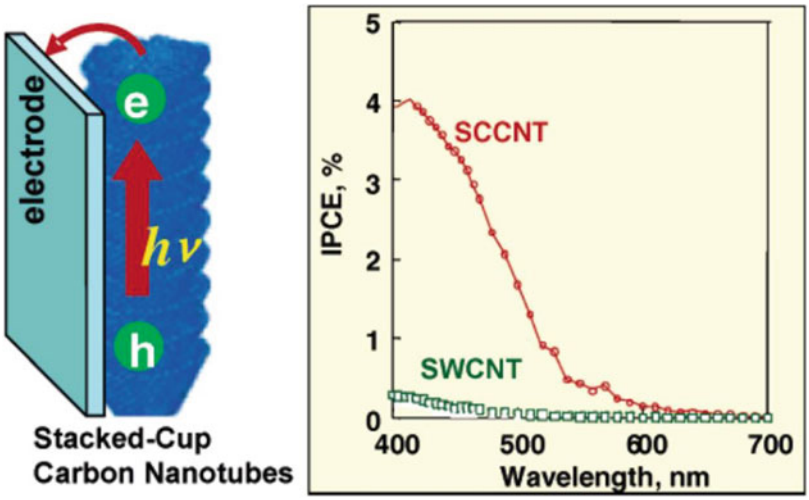

Fig. 9 The photocurrent conversion efficiency of SCCNT and SWCNT (for details see text). Adapted with permission from [53]

thin films is relatively lower than that of SCCNT, which is due to the consequence of the ultrafast recombination rate of the photogenerated charge carriers on the contrary IPCE value of SCCNT is relatively much higher and is much preferred in applications to solar cells.

5 Summary

With the advancement of nanomaterials and nanostructures, there has been immense growth and development in science and technology. These materials have shown potential applications in the development of health care, renewable energy, solar energy devices, water purification, etc., and other environment-friendly products and are considered as the raw materials for sustainable development.

Nonetheless, with such acquired knowledge, there are still many mysteries that are yet to understand, for example, the drastic change in the material properties when reduced to nano dimensions and the complex shape dependence behavior are some major issues. Fabrication of nanostructured devices on the other hand has a major issue on the device failure by increasing friction. As the device gets smaller, the interfacial area increases, which, in turn, gives rise to higher surface forces and develops friction causing wear and tear.

The increasing demand for fresh water and energy requirements too need immense research for new novel materials that are available abundantly. All these requirements need depth study and understanding before proceeding into real experiments for mass production, which is time-consuming and subject to erroneous output. Simulation comes as a tool that can predict the exact properties of the materials at different sets of thermodynamic parameters for the required need. Hence, reduce the efforts and save the erroneous experimental output.

Although humans have accomplished much progress in solving the increasing demands for energy as well as the water crisis. There is still a need for innumerable research for materials and devices, which are eco friendly, low cost, and are easily accessible to most populations of the globe which will help them in tackling their escalating requirements.

References

1. Feynman R (1959) There's plenty of room at the bottom. American Physical Society, Pasadena
2. Bag A, Lee N-E (2019) Gas sensing with heterostructures based on two-dimensional nanostructured materials: a review. J Mater Chem C 7:13367
3. Kittiratanawasin L, Hannongbua S (2016) The effect of edges and shapes on bandgap energy in graphene quantum dots. Integr Ferroelectr 175:211–219
4. Kamat PV, Haria M, Hotchandani S (2004) C60 cluster as an electron shuttle in a Ru(II)-polypyridyl sensitizer based photochemical solar cell. J Phys Chem B 108:5166–5170
5. Babu VJ, Vempati S, Uyar T, Ramakrishna S (2014) A review on 1-D and 2-D nanostructured materials for hydrogen generation. Phys Chem Chem Phys
6. Jitputti J, Suzuki Y, Yoshikawa S (2008) Synthesis of TiO_2 nanowires and their photocatalytic activity for hydrogen evolution. Catal Commun 9:1265–1271
7. Yang X, Wolcott A, Wang G, Sobo A, Fitzmorris RC, Qian F, Zhang JZ, Li Y (2009) Nitrogen-doped ZnO nanowire arrays for photoelectrochemical water splitting. Nano Lett 9:2331–2336
8. Jitputti J, Pavasupree S, Suzuki Y, Yoshikawa S (2007) Synthesis and photocatalytic activity for the water-splitting reaction of nanocrystalline mesoporous titania prepared by hydrothermal method. J Solid State Chem 180:1743–1749

9. Fujishima A, Honda K (1972) Electrochemical photolysis of water at a semiconductor electrode. Nature 238:37–38
10. Patsoura A, Kondarides DI, Verykios XE (2007) Photocatalytic degradation of organic pollutants with simultaneous production of hydrogen. Catal Today 124:94–102
11. Xu Y, Chen D, Xiuling J, Keyan X (2007) Nanosized Cu_2O/PEG400 composite hollow spheres with mesoporous shells. J Phys Chem C 111:16284–16289
12. Chen S, Ingram RS, Hostetler MJ, Pietron JJ, Murray RW, Schaaff TG, Khoury JT, Alvarez MM, Whetten RL (1998) Gold nanoelectrodes of varied size: transition to molecule-like charging. Science 280:2098–2101
13. Hicks JF, Templeton AC, Chen S, Sheran KM, Jasti R, Murray RW, Debord J, Schaaff TG, Whetten RL (1999) The monolayer thickness dependence of quantized double-layer capacitances of monolayer-protected gold clusters. Anal Chem 71:3703–3711
14. Hostetler MJ, Green SJ, Stokes JJ, Murray RW (1999) Monolayers in three dimensions: synthesis and electrochemistry of functionalized alkanethiolate-stabilized gold cluster compounds. J Am Chem Soc 118:4212–4213
15. Wood A, Giersig M, Mulvaney P (2001) Fermi level equilibration in quantum dot-metal nanojunctions. J Phys Chem B 105:8810–8815
16. Ung T, Dunstan D, Giersig M, Mulvaney P (1997) Spectroelectrochemistry of colloidal silver. Langmuir 13:1773–1782
17. Ipe BI, George TK, Barazzouk S, Hotchandani S, Kamat PV (2002) Photoinduced charge separation in a fluorophore-gold nano assembly. J Phys Chem B 106:18–21
18. Múller S, Schwarz M (1995) On the structure and stability of nanoscale materials: a two-dimensional model. Z Phys B 97:503–510
19. Frenkel D, Smith B (2002) Understanding molecular simulation—from algorithms to applications, 2nd edn
20. Gates TS, Hinkley JA (2003) Computational materials: modeling and simulation of nanostructured materials and systems
21. Vandezande P, Gevers LEM, Vankelecom IFJ (2008) Solvent resistant nanofiltration: separating on a molecular level. Chem Soc Rev 37:365–405
22. Han JY, Fu JP, Schoch RB (2008) Molecular sieving using nanofilters: past, present, and future. Lab Chip 8:23–33
23. Joseph S, Aluru NR (2008) Why are carbon nanotubes fast transporters of water? Nano Lett 8:452–458
24. Hummer G, Rasaiah JC, Noworyta JP (2001) Water conduction through the hydrophobic channel of a carbon nanotube. Nature 414:188–190
25. Kolesnikov AI, Zanotti J-M, Loong C-K, Thiyagarajan P (2003) Anomalously soft dynamics of water in a nanotube: a revelation of nanoscale confinement. Phys Rev Lett 93:035503
26. Falk K, Sedlmeier F, Joly L, Netz RR, Bocquet L (2010) Molecular origin of fast water transport in carbon nanotube membranes: superlubricity versus curvature dependent friction. Nano Lett 10:4067–73
27. Humplik T, Lee J, O'Hern SC, Fellman BA, Baig MA, Hassan SF, Atieh MA, Rahman F, Laoui T, Karnik R, Wang EN (2011) Nanostructured materials for water desalination. Nanotechnology 22:292001
28. Adham S, Hussain A, Matar JM, Dores R, Janson A (2013) Application of membrane distillation for desalting brines from thermal desalination plants. Desalination 314:101–108
29. Lee J, Kim S, Kim C, Yoon J (2014) Hybrid capacitive deionization to enhance the desalination performance of capacitive techniques. Energy Environ Sci 7:3683
30. Probstein RF (2003) Physicochemical hydrodynamics: an introduction, 2nd edn, vol xv. Wiley, Hoboken, NJ, 400
31. Lai C-C et al (2014) Desalination of saline water by nanochannel arrays through manipulation of electrical double layer. Nano Energy. https://doi.org/10.1016/j.nanoen.2014.10.039
32. Greenlee LF, Lawler DF, Freeman BD, Marrot B, Moulin P (2009) Reverse osmosis desalination: water sources, technology, and today's challenges. Water Res 43:2317–2348

33. Soltanieh M, Gill WN (1981) Review of reverse-osmosis membranes and transport models. Chem Eng Commun 12:279–363
34. Wijmans JG, Baker RW (1995) The solution–diffusion model—a review. J Membr Sci 107:1–21
35. Fritzmann C, Löwenberg J, Wintgens T, Melin T (2007) State-of-the-art of reverse osmosis desalination. Desalination 216:1–76
36. Sablani SS, Goosen MFA, Al-Belushi R, Wilf M (2001) Concentration polarization in ultrafiltration and reverse osmosis: a critical review. Desalination 141:269–289
37. Kimura S, Souriraj S (1967) Analysis of data in reverse osmosis with porous cellulose acetate membranes used. AIChE J 13:497–512
38. Dresselhaus MS, Thomas IL (2001) Alternative energy technologies. Nature 414:332–337
39. Lewis NS, Crabtree GW, Nozik AJ, Wasielewski MR, Alivisatos AP (2005) Basic energy sciences report on basic research needs for solar energy utilization. Office of Science, U.S. Department of Energy, Washington, DC
40. Crabtree GW, Dresselhaus MS, Buchanan MV (2004) The hydrogen economy. Phys Today 57:39–44
41. Lee S, Hanif Z, Seo K, Lim T, Shin H-M, Park S, Kim SH, Kwak SK, Hong S, Yoon M-H, Ju S (2016) Hydrogen production based on a photoactivated nanowire-forest. J Mater Chem A. https://doi.org/10.1039/c6ta06172a
42. Gates TS, Odegard GM, Frankland SJV, Clancy TC (2005) Computational materials: multi-scale modeling and simulation of nanostructured materials. Compos Sci Technol 65:2416–2434
43. Hammel E, Tang X, Trampert M, Schmitt T, Mauthner K, Eder A, Potschke P (2004) Carbon nanofibers for composite applications. Carbon 42:1153–1158
44. Wang J, Deo RP, Poulin P, Mangey M (2003) Carbon nanotube fiber microelectrodes. J Am Chem Soc 125:14706–14707
45. Rajesh B, Thampi KR, Bonard JM, Mathieu HJ, Xanthopoulos N, Viswanathan B (2003) Conducting polymeric nanotubules as high-performance methanol oxidation catalyst support. Chem Commun 2022–2023
46. Kamat PV (2006) Carbon nanomaterials: building blocks in energy conversion devices. Interface 15:45–47
47. Kamat PV (2006) Harvesting photons with carbon nanotubes. Nano Today 1:20–27
48. Kamat PV, Barazzouk S, Hotchandani S (2001) Nanostructured fullerene films. Adv Mater 13:1614–1617
49. Kamat PV, Barazzouk S, Hotchandani S, George Thomas K (2000) Nanostructured thin films of C60-aniline dyad clusters. Electrodeposition, charge separation, and photoelectrochemistry. Chem Euro J 6:3914–3921
50. Hasobe T, Fukuzumi S, Kamat PV (2006) Stacked-cup carbon nanotubes for photoelectrochemical solar cells. Angew Chem Int Ed 45:755–759
51. Barazzouk S, Hotchandani S, Vinodgopal K, Kamat PV (2004) Single wall carbon nanotube films for photocurrent generation. A prompt response to visible light irradiation. J Phys Chem B 108:17015–17018
52. Barazzouk S, Hotchandani S, Kamat PV (2002) Unusual electrocatalytic behavior of ferrocene bound fullerene cluster films. J Mater Chem 12:2021–2025
53. Kamat PV (2007) Meeting the clean energy demand: nanostructure architectures for solar energy conversion. J Phys Chem C 111:2834–2860

Chapter 15
X-Ray Probing for the Structural and Functional Studies of CdSe-CdS Nanoparticle for Detector Application

S. R. Patra and B. Mallick

1 Introduction

Research on the synthesis of colloidal inorganic phosphorous-based semiconductors and their nanoparticles is very much interesting and useful because of its technological importance. This advanced material is widely used in various fields. The potential application of the above materials is: fabrication of photoelectronic device [1, 2], LED [3, 4], photovoltaic device, solar cell, photo-detectors [5–13], windowless X-ray detector [14, 15], and many more. Again, quantum particles viz. quantum dots (QDs), quantum rods, etc., of such materials show very favorable optical properties as compared to their bulk size.

In principle, the element Se-doped in an organic conducting polymer has been used as a good X-ray imaging detector, because of the photoconductive nature of the solid element. Again, the selenium present in an organic conductor emitted light in the visible range when excited. In the meantime, Se is a very common trace element found in plant materials. The plant *Mimosa pudica* or touch-sensitive plant and its fibre possess electrically conducting with mechanically sensing properties. Fortunately, the element Se is present in the above fibre, hence this electrically conducting natural fibre (ECNF) acts as a good natural fluorescent material. Hence, the electro-active sensing and photo-sensing nature of ECN fibre marked it a good resource material for the fabrication of photo-detectors and organic scintillators. However, luminescent semiconductor materials viz. CdS ($E_g = 2.42$ eV) and CdSe ($E_g = 1.74$ eV) are useful for the fabrication of photo-detectors or scintillators due to their fluorescence emitting capability. The bandgap energy E_g of these materials is comparable with their absorption wavelength in the visible region, hence is suitable

S. R. Patra
School of Applied Science, KIIT University, Bhubaneswar 751024, India

B. Mallick (✉)
Institute of Physics, Bhubaneswar 751005, India
e-mail: bmallick@iopb.res.in

B. P. Swain (ed.), *Advances in Nanostructured Materials*, Materials Horizons:
From Nature to Nanomaterials, https://doi.org/10.1007/978-981-16-8391-6_15

for the fabrication of X-ray detectors [16, 17]. The efficiency of the above detector can be further enhanced by coating the ECN fibre using high photoluminescence material like CdSe-CdS nanoparticles. Hence, a thin film of CdSe-CdS quantum dots on ECN fibre is a good model for the designing of a windowless X-ray detector based on the photoluminescence principle. Designing highly responsive and sensitive windowless X-ray detectors are quite a challenging task today. An innovative approach for the designing of a windowless X-ray detector have been discussed.

2 Theory

2.1 X-Ray Theory

X-ray fibre diffraction is an important experimental technique to understand the various phases of polymer in general and fibre in particular. Broadly, polymer possesses two-phase, i.e., crystalline and amorphous structure. The crystalline phase of polymers is due to the presence of micro-para crystals and lamella thickness. Again, structure and phase investigation of the thin film of CdSe-CdS nanoparticle coated ECN fibre can be analyzed by applying the X-ray diffraction technique. Usually, the diffracted beam intensity produced by an ideal crystalline phase can be observed only when all the diffracted beams are in phase. This fulfills the condition for Bragg's diffraction. Mathematically,

$$2d \sin\theta = n\lambda \tag{1}$$

For an ideal system, the diffracted intensity for a given set of planes should be a spike at the Bragg angle θ for these planes. At a Bragg angle θ, the path difference between diffracted X-rays from two adjacent reflection planes is defined as

$$\Delta l = 2d \sin\theta = n\lambda \tag{2}$$

where d is interplanar-spacing.

If the incident beam strikes the reflection planes with a small angular deviation t from the Braggs angle, the path difference between two neighboring planes can be given by

$$\Delta l' = 2d \sin(\theta + t) \tag{3}$$

Further simplifying the Eq. (3), one can have

$$\Delta l' = 2d\ (\sin\theta \cdot \cos\ t + \cos\theta . \sin t)$$

Since t is very small, i.e., $t <<$, the value of $\cos t \approx 1$ and $\sin t \approx t$. Using these values in the above expression gives

$$\Delta l' = 2d \ \sin\theta + \ 2d \ t \ \cos\theta = n\lambda + 2d \ t \ \cos\theta \tag{4}$$

The phase difference 2ϕ due to diffraction from two neighbouring planes gives

$$2\phi = \frac{2\pi \ \Delta l'}{\lambda} = 2n\pi + \frac{4\pi \ d \ t \ \cos\theta}{\lambda} \tag{5}$$

and the effective phase difference is given by

$$2\phi = \frac{4\pi \ d \ t \cos\theta}{\lambda} \tag{6}$$

If A is the amplitude diffracted by a single lattice plane then, assuming no absorption of X-rays by the crystals, the amplitude is the same for each diffraction plane. For crystals with N layers of reflection plane, the resulting amplitude is

$$A_N = \frac{A \ \sin N\phi}{\sin\phi} \tag{7}$$

However, the scattered intensity I is defined as

$$I = AA^*, \tag{8}$$

where A^* is the complex conjugate of A.

Again, the scattered intensity at diffraction angle 2θ for N layers of reflection plane is

$$I(2\theta) = \frac{A^2 \sin^2 N\phi}{\sin^2\phi} \tag{9}$$

For diffraction angle θ, all the diffracted beams from N planes are in phase so that the scattered intensity is

$$I(2\theta) = N^2A^2 \tag{10}$$

or,

$$A^2 = \frac{I(2\theta)}{N^2}$$

Hence,

$$I(2\theta) = \frac{I(2\theta)\sin^2(N\phi)}{N^2\sin^2\phi} \tag{11}$$

$$I(2\theta) = \frac{I(2\theta)\sin^2(N\phi)}{N^2\phi^2} \tag{12}$$

when ϕ is small, $\sin\phi \approx \varphi$.

This Eq. (12) can be solved for the condition that $I = \frac{I(2\theta)}{2}$, which is satisfied when

$$N_\phi = 0.444\pi \tag{13}$$

Combining Eqs. (5) and (13), we find that the value of t as $t_{1/2}$ is given by

$$t_{1/2} = \frac{0.222\lambda}{Nd\cos\theta} \tag{14}$$

The width at half-height of the diffraction peak, i.e., full width at half maxima (FWHM), β_0 is defined as

$$\beta_0 = 4t_{1/2} = \frac{0.89\lambda}{Nd\cos\theta} \tag{15}$$

In this equation, the Scherrer shape factor k is 0.89, and crystallite size D_{hkl} is equal to Nd. This is effectively perpendicular distance through a set of N parallel planes that are d apart.

Again, the relationship between the breadth of the diffraction peak β_0 and crystal size D_{hkl} is given by the Scherrer equation

$$D_{hkl} = \frac{k\lambda}{(\beta_0 - \beta_i)\cos\theta} = \frac{k\lambda}{\beta_r\cos\theta} \tag{16}$$

where β_r is the refined line broadening, k is the shape factor, $\beta_0 (= FWHM)$ is the line broadening and β_i is the instrumental broadening. For Bragg–Brentano geometry, instrumental broadening β_i can be defined as

$$\beta_i = \frac{2\Delta\lambda}{\lambda}\tan\left(\frac{2\theta}{2}\right) + arc\ \tan\ \frac{W_R}{R_G} \tag{17}$$

where $\frac{\Delta\lambda}{\lambda}$ is the resolution of diffractometer (2.5×10^{-3}), θ is the Bragg angle, W_R is the receiving slit width, and R_G is the radius of the goniometer (say 300 mm). Again, the helix angle ψ of the fibre can be expressed as

$$\psi = \alpha\ \cos\theta \tag{18}$$

where $\alpha \left(= \frac{FWHM}{2} = \frac{\beta_0}{2}\right)$ is the average molecular disorientation or azimuth angle of the fibre.

2.2 Electrical Theory

The transport of the electric charges in a natural conducting polymer under the influence of an electric field has been investigated. Let us consider the electric field (steady) applied to the polymer is E (volt/m). The field imposes an electrostatic force F on electrons. Hence the electron would accelerate and their velocity increase with time. However, at each inelastic collision of an electron with an ion, a steady-state condition may grasp at a finite value of drift speed v. The direction of v is opposite to that of the E. The speed at the time T between collisions is aT, where $a = \frac{q\mathrm{E}}{m}$ is the acceleration. Since, the average speed can be expressed as $v = \mu\mathrm{E}$, where μ is the mobility of the electrons. The random thermal motion of the electrons affects the steady-state drift velocity by superimposing with each other. The directed flow of electrons establishes a current.

Let the ECN fibre of cross-section A and length L contain N electrons and an electron takes T second to travel the total length L(meter) of the fibre, then the total number of electrons of charge q passing through A of the polymer per unit time is $\frac{N}{T}$. The total charge passing per unit time (second) is the current I inside the fibre,

$$I = \frac{Nq}{T} = \frac{Nqv}{L} \tag{19}$$

and,

$$J = \frac{I}{A}, \tag{20}$$

where J is current density and A is the surface area of the fibre.

Using Eq. (19) in Eq. (20)

$$J = \frac{Nqv}{LA} \tag{21}$$

If $n = \frac{N}{LA}$, the electron concentration of fibre, then-current density

$$J = nqv = \rho v \tag{22}$$

where ρ is charge density, then-current density is defined by putting the value of v $(= \mu\mathrm{E})$ as

$$J = nqv = nq\mu \, \mathrm{E} = \sigma \, \mathrm{E} \tag{23}$$

where σ is the conductivity of the fibre. The electron gets energized while accelerating under the influence of the applied filled and transfer its energy to the lattice ion on collision. So, the power has degenerated within the fibre molecules. The mathematical expression for the power density becomes:

$$J \, \mathrm{E} = \sigma \, \mathrm{E}^2 \tag{24}$$

The resistance R of a wire of fibre (annular cross-section) with length l formulated as

$$R = \frac{l}{\sigma \, A} \tag{25}$$

where $R(\Omega)$, l(mm), σ $(\Omega^{-1} \cdot \mathrm{m}^{-1})$, A $(= \pi r^2)(\mathrm{mm}^2)$, and r(mm) are electrical resistance of the conductor, length of the conducting fibre, electrical conductivity, cross-sectional area, and radius of the fibre respectively. Hence, the conductivity of the fibre can be expressed as

$$\sigma = \frac{l}{R(\pi \, r^2)} \tag{26}$$

where r the radius of the fibre can be measured directly employing an optical or scanning electron microscope or indirectly by laser diffraction technique.

2.3 Quantum Theory

The physical properties such as electrical, optical, and structural of nano-phosphorous particles have differences compared to the existing natural phosphorous of the micron-scale. By changing the various parameters at the nanoscale, namely the electrical, optical, and magnetic properties of nano-dimensional phosphors or simply QDs a new phenomenon appears due to the quantum confinement effect. The bandgap propagation of QDs affects the physical significance of the material because the allowable quantum state is present in the QDs of nanoparticles. Also, different effects occur on the surface and facade due to the large surface-to-volume ratio. Nanoscale phosphor particles and their surface interface effects enhance the luminescence efficiency and reduce the scattering intensity of the emitted light photons. In terms of X-ray conversion efficiency, QD materials are also promising materials from the viewpoint of bandgap energy. Because the energy required to create an emitting single electron or single-photon hole pair is at least equal to the host bandgap in the X-ray conversion efficiency of phosphorous materials is higher for small bandgap

materials than the large bandgap. The bandgap is dependent on the particle size in nano-dimensional phosphors or QDs. By manipulating the structural orientations, the bandgap of nano-dimensional phosphors can be tuned to produce QD materials with a smaller bandgap. In a small bandgap, each X-ray photon generates more electron–hole pairs from the nano-dimensional phosphors or QDs, compared to conventional phosphors. Although the X-ray-induced excitation mechanism in QD material is still not very clear, charge carrier multiplication has been observed particularly using UV radiation. The quantum gain Q_{gain} of the phosphor is given by [18]

$$G_{quantum} = \frac{E_\gamma \; f_{eh} \; f_{QE}}{\eta \; E_g} \tag{27}$$

where the symbol $E_\gamma \; (= h\gamma)$, f_{eh}, f_{QE}, η, and E_g are used for the energy of X-ray photon, fraction of electrons and holes that undergo recombination at active luminescent centers, the quantum efficiency of photon generation from excited centers, inefficiency parameter ($\eta \geq 1$, the energy loss of the scattered phonon), and bandgap energy respectively.

3 Experimental

The complete experimental work consists of several important steps, starting from the extraction of ECN fibre for the substrate to the fabrication of an X-ray sensing detector based on a photoluminescence mechanism. Broadly the material processing steps are as follows.

3.1 Processing of ECN Fibre

The electro conducting natural (ECN) fibre, whose main constituent is cellulose was extracted from the stem of the *Mimosa pudica* plant followed by the chemical treatment method by keeping the stem in 10% NaOH solution for 1 week [19]. Again, the ECN fibre sample was collected from the treated stem by cleaning the pulps and washing the same with tape water several times until the sample reaches the form of neutrality. In the next stage, cellulosic-ECN fibre was obtained by sun-drying the above samples and cut into the required length for a particular experiment purpose.

3.2 Synthesis of CdSe-CdS Nanoparticle

The nano-dimensional phosphor and high-luminescence CdSe-CdS QDs were synthesized by the hot-injection technique. By mixing in a triple-necked flask with 0.195 g cadmium oxide (CdO, 99.998%, Puratronic, Alfa Aesar), 2.1 g oleic acid (OA, 90%, Sigma-Aldrich), and 3 g trioctyphosphine oxide (TOPO, 98%, Alfa-Aesar) CdSe/CdS core QDs particles were formed. At a temperature of about 120 °C, the reaction mixture was heated and then placed with nitrogen. Then the reaction temperature was raised to 330 °C. Then the solution lost color, during which time 1.8 mL of trioctyphosphine (TOP, 97%, vapour) was injected. A volume of 1.8 mL of a solution consisting of 86 nmol of CdSe core and 0.12 g of sulfur was pumped into TOP after temperature recovery. The reaction was quenched by a sudden drop in temperature with a water shower, retarded by infusion of 10 mL of toluene in 3 min. Centrifuged at 3000 rpm for 12 min and dispersed in toluene, the nanocrystals were purified by including isopropanol and methanol. The top of the nanocrystals was cleared with the inclusion of isopropanol and methanol [18–21].

3.3 Luminescent QDs Thin Film Coating

The colloidal solution of QDs of CdSe-CdS was coated on the ECN fibre as a form of thin film by the chemical dipping technique. Every single filament of the ECN fibre surface was coated individually. Extra care was taken for the uniform distribution of luminescent QDs on the surface of each filament. These coated filaments were dried properly in a clean environment.

3.4 Fabrication of CdSe-CdS Coated ENC Fibre Plate

A rectangular shape 3 mm PVC sheet of area 20×15 mm^2 was taken initially to fabricate the frame of the sensing plate. Keeping a margin of 5 mm from three sides except for one side in length-wise direction, and a slot of 10×10 mm^2 was taken out by vanishing a margin from the preferred site. A slot with a C-shaped slot with three sides was fabricated and properly cleaned using alcohol. Then the PVC frame was dried. The single filament of virgin ECN fibre was carefully mounted on the above frame using conducting silver paint. Again, the CdSe-CdS coated single filaments as defined in the above Sect. 3.3. were carefully mounted on the second C-frame with the help of conducting silver paint as earlier. Again, both the ends of the filament on the frame (lengthwise arrangement of filament) in each plate were clamped with copper tape for tight binding and further electrical circuit connection.

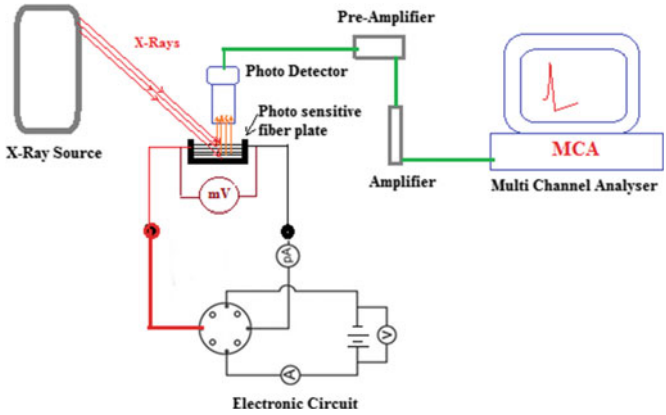

Fig. 1 Schematic arrangement of in-situ X-ray-induced electrical (V ~ I) sensing experiment

3.5 X-Ray-Induced-Sensing Arrangement

X-ray-induced electrical sensing of the sensor plate was carried out in environmental conditions at room temperature. The sensor plate was vertically arranged to strike the $MoK_{\alpha 1}$ (17.48 keV) X-ray photon perpendicular to the plane of the sensor plate. Again, both virgin ECN fibre and CdSe-CdS NPs coated ECN fibre plates arranged to allow the incident X-ray beam at an angle rather than 90° and shown in Fig. 1. The schematic arrangement of the in-situ irradiation caused variation in current was measured by changing the applied voltage. A simple electronic circuit consists of a pico-Ammeter, millivoltmeter, commutator, etc., was attached to the sensor plate to observe the current, voltage, and forward-reverse biasing effect respectively.

3.6 Characterization

Structural characterization of ECN fibre plate and CdSe-CdS NPs coated ECN fibre plate was carried out using a fine focus $CuK_{\alpha 1}$ line applying X-ray diffraction technique. However, the X-ray-induced electrical effect, i.e., V ~ I characteristics due to irradiation was performed using high flux $MoK_{\alpha 1}$ X-ray beam and a simple electronic circuit.

4 Results and Discussion

4.1 X-Ray Diffraction Analysis

X-ray diffraction pattern of virgin ECN fibre plate was taken applying $CuK_{\alpha 1}$ characteristic line ($\lambda = 1.54046$ Å) from a Bruker D8 Advance (USA) X-ray diffractometer operated at 40 kV and 40 mA. The scan speed and step size is chosen are 0.005°/s and 0.01°. The fibre diffraction pattern possesses a cellulose-II structure and is shown in Fig. 2a. since the main component of natural fibre is cellulose ($C_6H_{10}O_5$).The structure of ECN fibre is monoclinic with a = 8.02 Å, b = 7.90 Å, c = 10.30 Å and the angle $\gamma = 83.3°$ [19]. The most intense (100%) reflection of the ECN fibre is found along with the (002) plan with a d-value of 3.881 Å. The fibre shows a high order of % crystallinity, i.e., %C (=(1-A) × 100) around 59% [19]. Various structural parameters of the ECN fibre are tabulated in Table 1. The full width at half maximum(FWHM), i.e., β_o of individual reflection as defined in Eq. (15) is recorded in the table. The micro-crystallite size of cellulose of each reflection was calculated by subtracting the instrumental broadening β_i from the width of the line broadening β_o. The smallest value of crystallite size D_{hkl} $(= \frac{k\lambda}{(\beta_0 - \beta_i)\cos\theta})$ is found

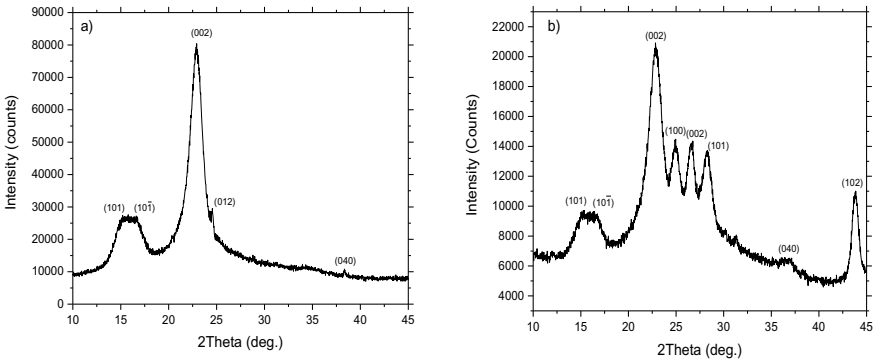

Fig. 2 X-ray fibre diffraction pattern of **a** virgin ECN fibre, and **b** thin film of CdSe-CdS nanoparticle coated ECN fibre

Table 1 X-ray structural parameters of ECN fibre

2θ (deg.)	*hkl*	I_{int}(counts)	d_{hkl}(Å)	β_o(deg.)	β_r(deg.)	D_{hkl}(Å)
15.59	101	4061	5.679	2.44	2.40	33.4
17.25	10$\bar{1}$	63,391	5.136	3.14	3.08	26.1
22.90	002	160,650	3.881	1.55	1.51	53.7
25.13	012	–	3.541	3.03	2.99	27.2
42.02	040	–	2.148	2.20	2.16	39.4

Table 2 Orientation of virgin ECN fibre

hkl	2θ (deg.)	β_r(deg.)	α (deg.)	ψ(deg.)
101	15.59	2.40	1.20	1.209
$10\bar{1}$	17.25	3.08	1.54	1.442
002	22.90	1.51	0.76	0.760
012	25.13	2.99	1.50	1.479
040	42.02	2.16	1.08	1.027

along ($10\bar{1}$) direction, and the largest size is along (002). The instrumental broadening β_i is already defined in Eq. (17). Again, the average angle of macromolecular disorientation α (=$\beta_0/2$) or azimuth angle of ECN fibre was found to be small. The helix angle ψ was computed using the relation $\psi = \alpha \cos\theta$ obtained from the uni-axial spiral orientation condition ($0° < \psi < 90°$) and tabulated in Table 2. The small value ψ indicates, the fibre having a very high order of orientation, which is a good sign for electrical conductance.

Similarly, the X-ray diffraction pattern of CdSe-CdS NPs coated ECN fibre was taken by fixing the same experimental parameters. Polycrystalline diffraction phases are shown in Fig. 2b is observed due to the presence of CdSe-CdS and cellulose materials. In this case, the maximum peak intensity was found in the case of cellulose (002). However, several well-resolved and sharp CdSe-CdS planes viz. (100), (002), (101), and (102) were observed. Among these planes, CdSe-CdS plan (002) possesses the highest intensity with a d-value of 3.353 Å. Other structural parameters are given in Table 3. The small value of α and ψ given in Table 4 indicates that the CdSe-CdS coated ECN fibre possesses high orientation even after coating the materials. In the case of ECN fibre, the orientation of crystallographic planes is enhanced after coating CdSe-CdS NPs materials as compared to virgin fibre. Since, lower the value of ψ, the orientation of fibre becomes higher. This improvement in orientation may be due to an increase of atomic density by inserting nanoparticles of CdSe-CdS on

Table 3 X-ray structural parameters of CdSe-CdS coated ECN fibre nanoparticle

Material phase	2θ (deg.)	*hkl*	I_{int}(counts)	d_{hkl}(Å)	β_o(deg.)	β_r(deg.)	D_{hkl}(Å)	$\overline{D}$(Å)
$C_6H_{10}O_5$	5.14	101	4151	5.847	1.80	1.76	45.66	
	16.64	$10\bar{1}$	4469	5.323	1.51	1.51	55.17	
	22.85	002	41,762	3.890	1.80	1.80	46.06	
CdSe-CdS	24.98	100	1686	3.562	0.85	0.85	100.57	124
	26.57	002	12,021	3.353	1.17	1.17	72.29	
	28.28	101	5161	3.153	1.06	1.06	80.33	
	39.14	042	–	2.300	2.77	2.77	30.89	
	43.80	101	3453	2.065	0.76	0.76	153.08	

Table 4 Orientation of CdSe-CdS nanoparticle coated ECN fibre

Material phase	*hkl*	2θ (deg.)	β_r(deg.)	α (deg.)	ψ(deg.)
$[C_6H_{10}O_5]$	101	15.14	1.76	0.88	0.892
	$10\bar{1}$	16.64	1.51	0.76	0.742
	002	22.85	1.80	0.90	0.882
[CdSe-CdS]	100	24.98	0.85	0.43	0.414
	002	26.57	1.17	0.59	0.832
	101	28.28	1.06	0.53	0.513
	042	39.14	2.77	1.39	1.304
	102	43.80	0.76	0.38	0.352

the crystal lattice of fibre. The crystallite size D_{hkl} of each plane was calculated by applying refined line width β_r.

The largest crystallite size was found out to be 153 Å along (101) direction and the smallest D_{hkl} (=31 Å) is found along (042) direction. Since, the experimentally observed line broadening β_o as defined in Eq. (16) is the sum of instrumental broadening β_i, small crystallite size broadening, and strain broadening β_s, so the estimated crystallite size D_{hkl} even after using refined width cannot be free from the lattice strain. However, average crystallite size $\overline{D}$ and lattice strain δ in the nano-system can be estimated by applying the Williamson-Hall relation, i.e.,

$$\beta_r \cos\theta = \frac{k\lambda}{\overline{D}} + 4\,\delta \sin\theta,$$

as plotted in Fig. 3. In this plot, the slope of the line gives the average lattice strain δ, and the y-intercept $\frac{k\lambda}{\overline{D}}$, gives out the value of average crystallite size $\overline{D}$ by applying

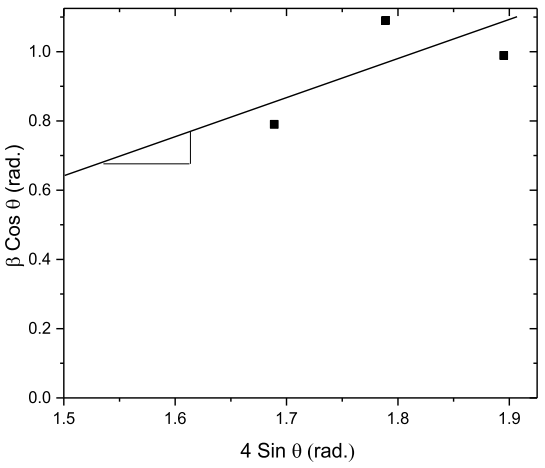

Fig. 3 Williamson-Hall plot of CdSe-CdS nanoparticle

the value of shape factor k (= 0.89), wavelength (=1.54046 Å) and by equating with the value of y-intercept. Hence, the average crystallite size $\overline{D}$ of the CdSe-CdS nanoparticle was estimated to be 12 nm (=124 Å).

4.2 X-Ray-Induced Sensing Analysis

The electrical characteristics of single-filament of ECN fibre have been studied at low bias voltage ranging from 10 to 36 V. The filament start conducting at a voltage around 10 V. The V ~ I characteristics plot of the single-virgin fibre is shown in Fig. 4a. The plot shows that the current is linearly increases with applied voltage up to 36 V confirms a good Ohmic contact. Similarly, the V ~ I plot of CdSe-CdS NPs coated single-filament is shown in Fig. 4b, shows an enhancement of current concerning applied voltage. The enhancement of current for voltage in the case of CdSe-CdS coated single-filament becomes twice as compared to the uncoated filament.

The slope $\frac{\Delta I}{\Delta V}$ of the virgin (Fig. 4a) and CdSe-CdS coated single fibre was calculated to be 6.91×10^{-9} A/V and 1.29×10^{-8} A/V respectively. Hence, the resistance of the filament R, which is the inverse of the slope calculated above. The resistance of both the single filaments was found out to be 1.45×10^{8} Ω and 7.81×10^{7} Ω respectively. Using the above value of R in the expression for conductivity σ, as defined in Eq. (26), obtained for both the filament was found out to be 0.37 $\Omega^{-1} \cdot \mathrm{m}^{-1}$ and 0.69 $\Omega^{-1} \cdot \mathrm{m}^{-1}$respectively. This shows that the sample conductivity increases because of the coating of quantum particles. However, the average diameter of the ECN filament was found out to be 15.4 μm, using the relation $D = \frac{m\lambda L}{w}$, where m is the order of diffraction, λ is the wavelength of laser light, L is the perpendicular distance between sample (filament) and screen, and w is the fringe width. In this investigation, it is concluded that the Ohmic contact of the sample is excellent and the current expanding linearly with the applied voltage.

In-situ V ~ I characteristics curve of the virgin ECN fibre plate was carried out with and without X-ray irradiation and shown in Fig. 5. The plate shows diode characteristics with a barrier voltage of about +10 V.In a forward bias, the current increases linearly with voltage up to +15 V. The forward saturation was observed at a voltage +20 V. Again, the reverse barrier voltage was observed at −10 V and attains reverse saturation at about −20 V. It is observed that there is not much variation in both the data points, i.e., when X-ray is on or X-ray is off. The variation of current with voltage is noted in Table 5. However, in both cases, a steady saturation was observed in a range from ±20 to ±40 V.

Similarly, *In-situ* analysis of V ~ I characteristics of the CdSe-CdS coated ECN fibre plate was carried out with and without X-ray irradiation and shown in Fig. 6. The data points are tabulated in Table 6. The plot shows comparable diode characteristics as in the case of virgin ECN fibre. In his case, the current to voltage ratio was found to be improved as compared to the virgin ECN fibre plat. However, in the forward bias, an avalanche current situation was observed after +20 V in the case of X-ray irradiation. This indicates that the sensor plat having a good response to the

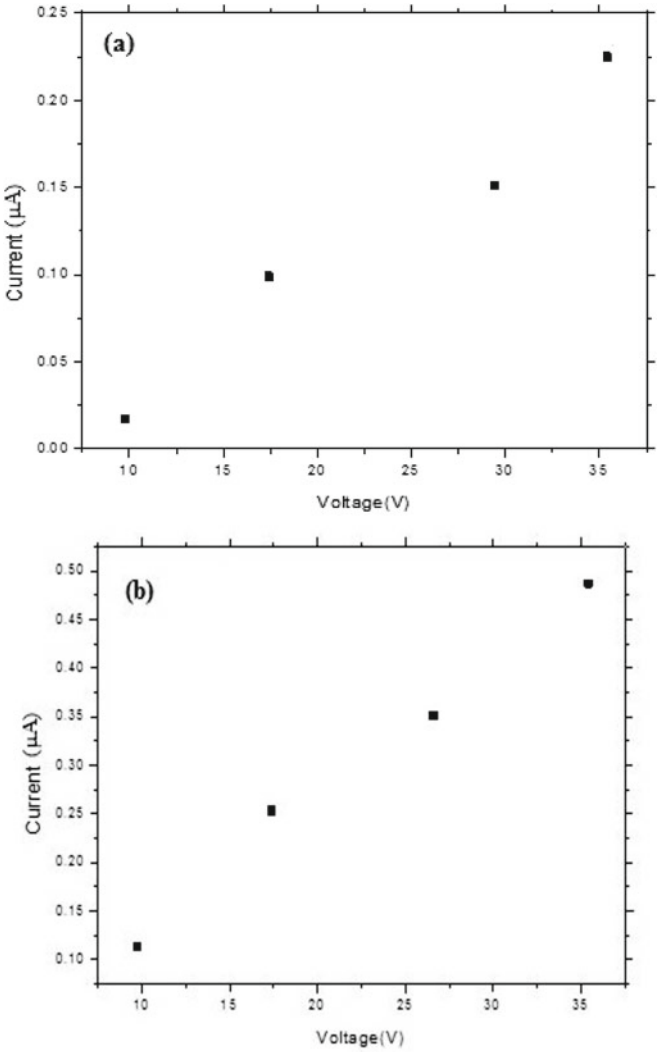

Fig. 4 Electrical voltage ~ current (V ~ I) characteristics of single ECN fibre: **a** virgin and **b** CdSe-CdS NPs coated

X-ray signal. In the case of reverse bias voltage around −20 V, a similar avalanche current situation was observed. It has been noticed that the avalanche current in the case of non-induced X-rays is more as compared to X-ray-induced data. This loss of current converts into photo-luminescence light by interacting with nano-phosphorous material coated on the surface of the filament. This gives a good sign to fabricate the windowless X-ray detector for the observation of low-energy X-rays [22–26].

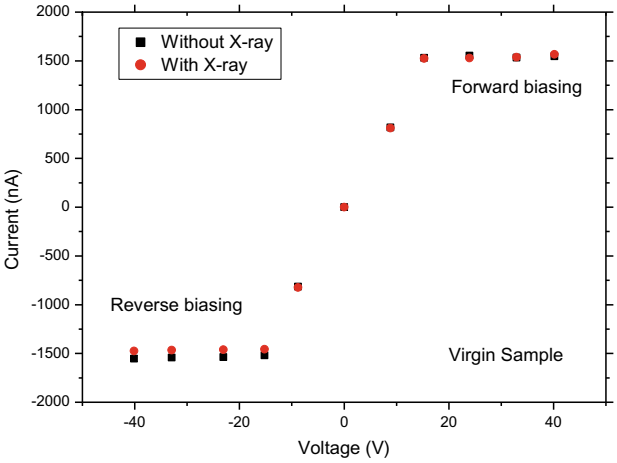

Fig. 5 X-ray-induced V ~ I characteristics of virgin ECN fibre with and without X-rays

Table 5 X-ray-induced electrical (V ~ I) sensing of virgin ECN fibre with and without X-rays

Voltage (V)	Current (nA)		$\lvert\Delta I\rvert$(nA)
	Without X-ray irradiation	With X-ray irradiation	
+40.18	+1574	+1567	07
+32.95	+1553	+1538	15
+23.96	+1543	+1528	15
+15.27	+1531	+1524	07
+8.84	+817	+811	06
0	0	0	0
−8.80	−815	−823	08
−15.20	−1520	−1456	64
−23.08	−1537	−1461	76
−32.92	−1543	−1466	77
−40.11	−1553	−1476	77

5 Conclusion

X-ray sensor plate was designed using NPs of photoluminescence CdSe-CdS solids coated over single-filament of electro conducting natural (ECN) fibre. The CdSe-CdS nanoparticle was synthesized by the hot injection cum short time processing technique. The structure of the above quantum particle was analyzed using the X-ray diffraction technique applying using $CuK_{\alpha 1}$(8 keV) X-ray line. The small value of the helix angle ψ indicates, the fibre having a very high order of orientation, which is a good sign for electrical conductance. The sensing plate made up of the ENC fibres

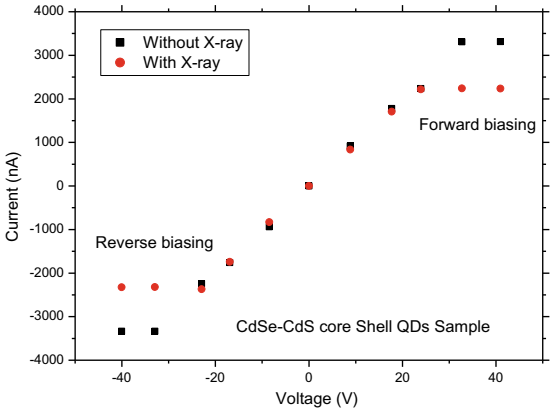

Fig. 6 X-ray-induced V ~ I characteristics of CdSe-CdS nanoparticle coated ECN fibre with and without X-rays

Table 6 X-ray-induced electrical (V ~ I) sensing of CdSe-CdS nanoparticle coated ECN fibre with and without X-rays

Voltage (V)	Current (nA)		$\lvert\Delta I\rvert$(nA)
	Without X-ray irradiation	With X-ray irradiation	
+40.97	+3314	+2237	1077
+32.71	+3307	+2228	1079
+23.96	+2236	+2217	19
+17.71	+1776	+1705	71
+8.84	+918	+834	84
0	0	0	0
−8.45	−939	−830	109
−16.93	−1760	−1743	17
−22.95	−2243	−2370	127
−32.95	−3334	−2320	1014
−40.05	−3336	−2327	1009

coated with a thin film of NPs were arranged in a 10 × 10 mm^2 active area. *In-situ* X-ray-induced electrical (V ~ I) characteristics of the sensing plate were carried out using MoK$_{\alpha 1}$ (17 keV) characteristics line. It has been noticed that the avalanche current in the case of non-induced X-rays is more as compared to X-ray-induced data. This loss of current converts into photo-luminescence light by interacting with nano-phosphorous material coated on the surface of the filament. The present study is very interesting and useful for future development of the windowless X-ray detector for low energy X-rays detection purposes.

References

1. Cotta MA (2020) A new era of metal-organic framework nano-materials and applications. ACS Appl Nano Mater 3:4917–6126
2. Reshma VG, Mohanan PV (2019) Quantum dots: applications and safety consequences. J Lumin 205:287–298
3. Yanbin Z, Fengjuan Z, Hongzhe W, Lei W, Fangfang W, Qingli L, Huaibin S, Lin S (2019) High-efficiency CdSe/CdS nanotod-based red light –emitting diodes. Opt Express 27:7935–7944
4. Sadeghi S, Sadeghi SK, Abkenar CW, Ow-Yang, Nizamoglu S (2019) Efficient white LEDs using liquid-state magic-sized CdSe quantum dots. Sci Rep 9:1–7
5. Clément L, Bertille M, Nicolas G, Charlie G, Junling Q, Audrey C, Sébastien R, Sandrine I, Mathieu GS, Benoit D, Emmanuel LCL (2019) A colloidal quantum dot infrared photodetector and its use for intraband detection. Nat Commun 10:1–10
6. Shihab BH, Michael S, Ayaskanta S, Dong-KK (2019) Colloidal quantum dots for thermal infrared sensing and imaging. Nano Converg 6:1–22
7. Surana K, Salisu IT, Mehra RM, Bhattacharya B (2019) Organic polymer and perovskite CdSe–CdS QDs hybrid thin film: a new model for the direct detection of light elements. Opt Mater 93:135–140
8. Rossinelli AA, Riedinger A, Gallego PM, Knüsel PN, Antolinez FV, Norris DJ (2017) High-temperature growth of thick-shell CdSe/CdS core/shell nanoplatelets. Chem Comm 53:9938–9941
9. Peng X, Schlamp MC, Kadavanich A, Alivisatos AP (1997) Epitaxial growth of highly luminescent CdSe/CdS core/shell nanocrystals with photo-stability and electronic accessibility. J Am Chem Soc 119:7019–7029
10. Peng X, Manna L, Yang WD, Wickham J, Scher E, Kadavanich A, Alivisatos AP (2000) Shape control of CdSe nanocrystals. Nature 404:59–61
11. Kaur M, Sharma A, Olutas M, Erdem O, Kumar A, Sharma M, Demir HV (2018) Cd-free Cu-doped ZnInS/ZnS core/shell nanocrystals: controlled synthesis and photophysical properties. Nanoscale Res Lett 13:182
12. Sharma J, Singh R, Kumar A, Singh T, Agrawal P, Thakur A (2018) Size-controlled synthesis of nanocrystalline CdSe thin films by inert gas condensation. Appl Nanosci 8:359–367
13. Kaur M, Singh P, Kaur G, Kaur M, Sharma J, Kumar M, Sharma M, Kumar A (2019) Development of colloidal semiconductor nanocrystals: synthesis, properties and their outlook for light emitting diodes (LEDs). Int J Emerg Technol 10:16–35
14. Patra SR, Pattojoshi P, Mishra SC, Mallick B (2019) Enhancing Photoluminescence potential of conducting natural fiber using CdSe/CdS Dot-in-Rods. Indian J Phys 93:1413–1418
15. Patra SR, Sinha SP, Mishra SC, Mallick B (2014) X-Ray fibre diffraction analysis of 6MV photon-induced Mimosa pudica. Adv Sci Lett 20:733–736
16. Nam et al (2004) US2004\0200972 A1
17. Létant SE, Wang TF (2006) Semiconductor quantum dot scintillation under γ-ray irradiation. Nano Lett 6:2877–2880
18. Carbone L, Nobile C, De Giorgi M, Sala FD, Morello G, Pompa P, Hytch M, E, Fiore A, Franchini IR, Nadasan M, Silvestre L, Kudera S, Cingolani R, Krahne R, Manna L (2007) Synthesis and micrometer-scale assembly of colloidal CdSe/CdS nanorods prepared by a seeded growth approach. Nano Lett 7:2942–2950
19. Patra SR, Pattojoshi P, Mishra SC, Mallick B (2017) Structural investigation of Mimosa pudica Linn fibre. Indian J Phys 91:377–382
20. Chen Y, Vela J, Htoon H, Casson JL, Werder DJ, Bussian DA, Klimov VI, Hollingsworth JAJ(2008) 'Giant' multishell CdSe nanocrystal quantum dots with suppressed blinking: novel fluorescent probes for real-time detection of single-molecule events. Am Chem Soc 130:5026–5027
21. Gomes R, Aubert T, Cirillo M, Emplit P, Biermann A, Lange H, Thomsen C, Brainis E, Hens Z (2014) "Flash" synthesis of CdSe/CdS core-shell quantum dots. Chem Mater 26:1154–1160

22. Patra SR, Mallick B (2018) Investigation of high-energy X-ray photon-induced effect on an electrically-conducting natural fiber (Mimosa pudica L.). Int J Plast Technol 22:115–121
23. Patra SR, Samal SK, Mallick B (2017) Fabrication of windowless X-ray detector based on CdSe-CdS core-shell QDs. Sens Lett 15:398–401
24. Patra SR, Pattojoshi P, Samal SK, Mishra SC, Mallick B (2017) Electron microscopy analysis of CdSe-CdS quantum dot-in-rods coated Mimosa pudica fiber. Nano Hybrids Compos 12:79–87
25. Patra SR, Mallick B (2020) Effect of nanostructure CdSe/CdS Dot-in-Rods coated on flexible cellulosic fiber substrates to improve Photoluminescence potential of conducting fibre. Sens Lett 18:216–221
26. Patra SR, Mallick B (2020) Structure and luminescence properties of CdSe/CdS-cellulose nanocomposites. J Mater Sci Mater Electron 31:14101–14107

Part III
Ferroelectric Nanomaterials

Chapter 16
Magnetism in Nanostructured Spinel Ferrites with Recent Advances in Processing, Characterization, and Applications

Elangbam Chitra Devi and Shougaijam Dorendrajit Singh

1 Introduction

Spinel ferrites have received appreciable attention as an important magnetic material. They have been extensively explored for different applications in different domains of basic and applied sciences because of their certain desirable properties such as magnetic properties, electrical properties, optical properties, thermal and chemical stability. Their potential applications are also expanding to new areas like biomedical applications [1, 2], wastewater treatment [3], sensor technology [4], etc. with the progress in nanoscience and nanotechnology. Based on the Scopus database, research works on spinel ferrites were found to be reported since 1956 along with an exponential increase in the last 20 years which can be seen from Fig. 1.

Also according to the Scopus database, research works on spinel ferrites are found to be investigated in different subject areas which can be seen from Fig. 2. A major contribution comes from Material Sciences followed by Physics and Astronomy, Engineering, Chemistry, Chemical Engineering and a minor contribution from other fields. Although they possess certain desirable properties, most of their applications are found to have relied on their magnetic properties. Their properties are usually tuned by using different strategies such as composition variation, processing conditions, controlling morphologies, reducing size, adopting different preparation methods. This signifies a need for a clear understanding of factors affecting their properties and hence a precise control of their properties and for subjecting to certain applications. New preparation methods with the advancement of nanotechnologies lead toward the production of spinel ferrites into different morphologies with unique magnetic properties. Spinel ferrites of different morphologies such as nanospheres, microspheres, nanofibres, nanorods, nanowires, nanocomposites, core–shell structures were found to be reported by many researchers. Such a wide variety of spinel ferrites were found to be fabricated by different routes of synthesis methods such as

E. C. Devi (✉) · S. D. Singh
Department of Physics, Manipur University, Canchipur, Imphal, Manipur 795003, India

B. P. Swain (ed.), *Advances in Nanostructured Materials*, Materials Horizons:
From Nature to Nanomaterials, https://doi.org/10.1007/978-981-16-8391-6_16

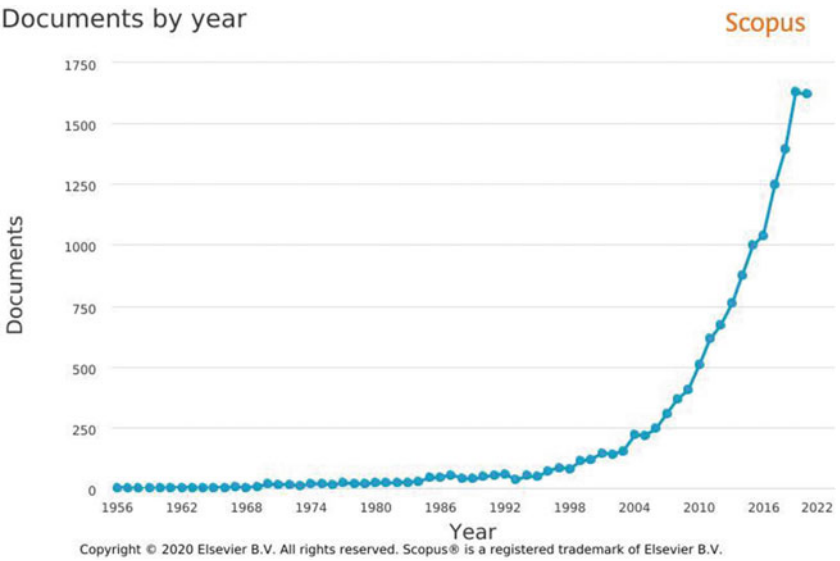

Fig. 1 Publications on spinel ferrites since 1956 based on Scopus database, searched by using keyword "spinel ferrites" on 13th October 2020

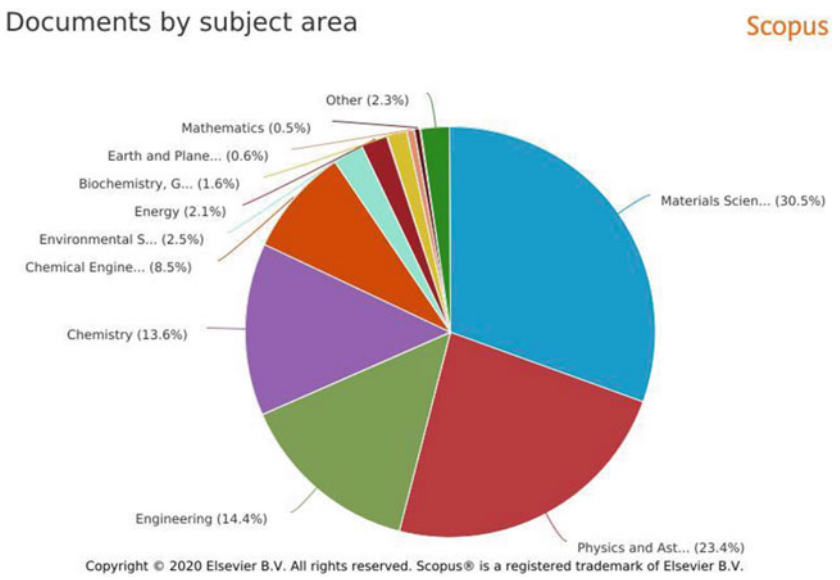

Fig. 2 Percentage of published articles on spinel ferrites contributed from different branches of Science and Engineering based on Scopus database, extracted on 13th October 2020

co-precipitation, hydrothermal, sol–gel, electrospinning, thermal treatment method, etc. Also, emerging research on multifunctional materials consisting of a combination of magnetic spinel ferrites and other material like a luminescent material is found to be reported [5, 6]. The use of microstructural characterization techniques like SEM and TEM effectively provides their morphology which also helps in understanding their associated magnetic properties and hence further tailoring of their properties. This chapter gives a compilation report on research work conducted on nanostructured spinel ferrites, fundamental concepts of their magnetic properties, effects of processing conditions, composition, and morphologies thereby emphasizing their importance and emerging applications.

2 Magnetism in Spinel Ferrites

The unit cell of spinel ferrite (as shown in Fig. 3.) is made up of 8 formula units of AB_2O_4 formed by 32 anions and 24 cations. Nearly cubic close packing of anions offers 64 tetrahedral sites and 32 octahedral sites also called A-sites and B-sites respectively. Only 1/8th of tetrahedral sites and 1/2 of octahedral sites are occupied by cations. The spinel structure is categorized in the space group Fd3m.

The Bravia lattice is a face-centered cubic with a basis formed by two formula units ($2\,AB_2O_4$) [7]. According to the site occupancy of the cations, they are classified as normal, inverse, and mixed spinels. In a normal spinel, divalent ions take A-sites while trivalent ions take B-sites. In the case of inverse spinels, divalent ions take B-sites and trivalent ions are equally distributed between A and B-sites. Spinels having cation distribution between these two extremes are known as mixed spinels.

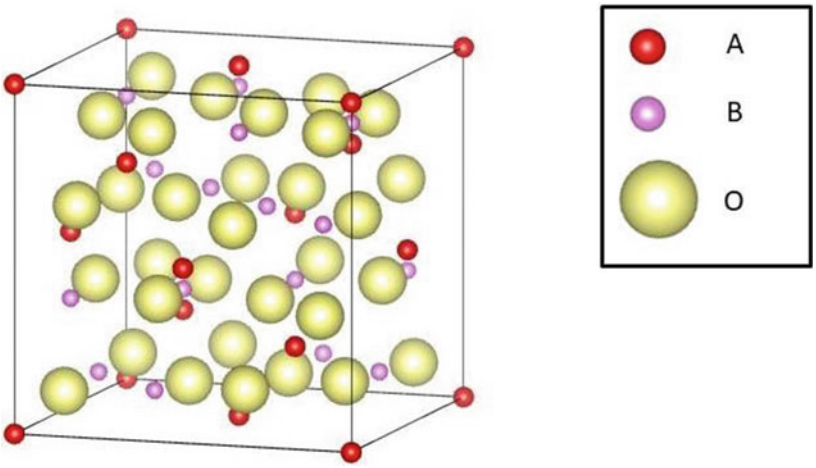

Fig. 3 Spinel structure generated using Vesta

Cation distribution in the spinels is dependent on factors such as temperature, cationic radii, cationic charge, crystal field effects, electrostatic contribution to lattice energy [7]. Cation distribution in spinels is not unique and for any composition of spinel, cation distribution has resulted from an equilibrium of oxygen positional parameter, inversion degree, and lattice constant.

Spinel ferrites have magnetic properties which are found to be greatly dependent on the constituent cations as well as their occupancy in A and B-sites. Using this fact or simply taking into account the magnetic moments associated with the cations and their preference for a specific site, the magnetic properties of spinel ferrites are usually tailored. A variety of spinel ferrites composed of transition metals and rare-earth elements of different compositions are found to be reported, some of which are listed in Table 1. The magnetism in spinel ferrites is found to be originated from the negative interaction or exchange force between the moments of the two cations on different interstitial sites which depends on the distances between the metal–oxygen-metal ions and the angle between them [8]. In general, the interaction is found to be greatest for an angle of 180° and the shortest inter-ionic distance. Three types of interactions are possible namely A-B, B-B, and A-A. Owing to preferable bond angles and lengths in the case of A-B interaction, it is the dominant exchange interaction among the three possible interactions. But, in the case of A-A and B-B interactions, the distances between the oxygen and metal ions are much large and the angle between the metal and oxygen ions are too small. Thus, the magnetic interaction in spinel ferrites, in general, comprises of strong A-B interaction with much weaker B-B interaction and most unfavorable A-A interaction. Neel first explained the ferrimagnetism of ferrites by considering the main negative interaction occurring between A and B-sites and thus developed the theory of ferrimagnetism [8].

3 Materials and Method

Table 1 represents an overview of some of the research works reported in spinel ferrites prepared through different methods and processing conditions giving rise to different sizes and morphologies and their associated magnetic properties. From the table, it can be found that a wide variety of methods are found to be adopted for different types of spinel ferrites ranging from a low-temperature method such as simple co-precipitation methods to conventional methods including high-temperature heat treatments. Desirable magnetic properties are found to be tuned by using a particular synthesis method or processing conditions. Apart from these, composition variation is another factor used for tailoring their properties. Table 1 elucidates that for the varying composition of spinel ferrites and their processing conditions, the important magnetic parameters like saturation magnetization, coercivity, and retentivity values are different. Spinel ferrites of different morphologies ranging from simple spherical nanoparticles to complex structures are found to be reported. Yuan et al. [9] reported studies on $CoFe_2O_4$ microspheres which are composed of assemblies of nanoparticles of $CoFe_2O_4$ of average sizes of 8 nm

Table 1 Spinel ferrites were prepared using different methods under different processing conditions

Composition	Preparation method	Processing condition	Size and Morphology	M_s (emu/g)	H_c (Oe)	References
$Cd_xCo_{1-x}Zr_{0.05}Fe_{1.95}O_4$ x = 0 to 0.30, step size of 0.05	Pechini method	Calcined at 700 °C in air for 1 h	32–40 nm Spherical	57.33–67.89	1120–1500	[25]
$CoLn_{0.12}Fe_{1.88}O_4$ Ln = Ce, Eu, Sm, Dy, Gd, Er	Micelles method	–	~20 nm	65–85	7256–12,112	[26]
$CoFe_2O_4$ encapsulated in mesoporous silica matrices and $CoFe_2O_4$ nanowires	Chemical method	–	2.5–9 nm Encapsulated structures and nanowires	31.9–53.6	–	[27]
$Cd_{0.5-}Ni_xCo_{0.5}Fe_2O_4$	Auto-combustion method	–	7.2–12.9 nm Spherical	33.785–51.311	300–657	[28]
$CoFe_2O_4$ $CoFe_2O_4/SiO_2$	Hydrothermal and sol–gel method	Heated at 1000 °C for 96 h	16 nm and 17 nm Rounded polyhedral morphology	80,2–86.8	–	[29]
$Mn_{0.5}Co_{0,5}Fe_2O_4$	High energy ball milling	100, 200, 300, 400, 500 °C at argon atmosphere	7–11 nm Spherical	29.8–51.0	–	[30]
$CoFe_2O_4$	Solvothermal method		2–15 nm Spherical	256–506	–	[31]
$Co_{1-x}Zn_xFe_2O_4$	Auto-combustion method	Calcined at 800 °C for 3 h Sintered at 1300 °C for 12 h in air	Spherical			[32]

(continued)

Table 1 (continued)

Composition	Preparation method	Processing condition	Size and Morphology	M_s (emu/g)	H_c (Oe)	References
$CoFe_2O_4$	Coprecipitation method	Annealed at 300, 1000, 1300 °C	10 nm Spherical	45–85	1000–5000	[33]
$Co_{0.4+x}Zn_{0.6-x}Fe_2O_4$ and $Co_{0.4+x}Zn_{0.5-x}Li_{0.1}Fe_2O_4$	Sol–gel auto-combustion method	–	13–34 nm Platelets shaped	59.06–148.70 and 56.98–123.32	16–2560 and 114–1476	[34]
$Zn_xCo_{1-x}Fe_2O_4$	Sol–gel method	Annealed at 500 oC and 900 °C for 2 h in air	15–46 nm Spherical	53–116	–	[35]
$Co_{0.5-x}Zn_{0.5}Ni_xFe_2O_4$ x = 0.05 to 0.25, in 0.05 step size	Auto-combustion method	Annealed at 1000 °C for 4 h	34.54- 37.56 nm Spherical	35.3–65.68	–	[36]
$ZnFe_2O_4$	Co-precipitation method	–	5–11 nm Spherical	3–7.3	–	[37]
$ZnFe_2O_4$	Co-precipitation method	–	9.8–13.4 nm	37.6–52.9	–	[38]
$ZnFe_2O_4$ Dispersed in silica aerogel matrix	Chemical method	Heated at 450, 750, 900 °C for 1 h and 750 °C for 6 h	4.2–11.1 nm Dispersed in silica matrix	6.3–9.2	444–786	[39]
$Ni_xMn_{1-x}Fe_2O_4$ x = 0 to 1.0, step size of 0.2	Microwave-assisted combustion method	–	16–19 nm Spherical	35.42–66.93	60.23–111.42	[40]
Fe_3O_4	Colloidal nanocrystal synthesis	–	12 nm Slightly elongated spherical shaped	51	~ 0	[41]

(continued)

Table 1 (continued)

Composition	Preparation method	Processing condition	Size and Morphology	M_s (emu/g)	H_c (Oe)	References
Fe_3O_4	Oxidation reaction method	–	9.6–287 nm Cubic and spherical	54.7–84.7	0–190	[42]
$CaFe_2O_4$	Sol–gel method	–	7.6 nm	27.78–29.92	0–150	[43]
$CaFe_2O_4$	Sol–gel method	Heated at1000 °C for 12 h	6–10 nm	13.2–15.3	–	[44]
$Zn_{1-x}Ni_xFe_2O_4$ x = 0 to 1.0, in 0.2step size	Combustion method	–	30–42 nm	36.77–59.93	24.4–138.7	[45]
$Mn_{0.5}Zn_{0.25}Fe_2O_4$	Co-precipitation method	–	19 nm Spherical	18.4	~ 0	[46]
$Co_{1-x}Zn_xFe_2O_4$	Sol–gel auto-combustion method	–	22.9–34.9 nm Agglomerated, complex grain arrangement	21.8–67.8	175–786	[47]
$Cu_{1-x}Zn_xFe_2O_4$ x = 0 to 0.75, step size of 0.25	Novel nanocasting route	-	6.5–8.3 nm	18–52	40–380	[48]
$NiFe_2O_4$	Microwave-assisted combustion method	Heated for 8 h at 300, 400, 500, 600, 700, 800 °C	3.88–85.16 nm Nearly cubic	1.73–39.39	23–180	[49]
$CuCe_xFe_{2-x}O_4$	Co-precipitation method	Calcined at 600 °C for 6 h, sintered at 950 °C for 6 h	Agglomerated nanoparticles	16.39–37.79	61.26–257.08	[50]

(continued)

Table 1 (continued)

Composition	Preparation method	Processing condition	Size and Morphology	M_s (emu/g)	H_c (Oe)	References
$Cu_xCr_xFe_{2-x}O_4$ x = 0 to 0.5, step size of 0.05	Citrate precursor method Annealed at 600 °C for 2 h	–	23–42 nm Agglomerated nano-structure	17.22–35.32	125–209	[51]
$NiFe_2O_4$	Thermal treatment method	Calcined for 3 h at 623, 673, 723, 823 K	10–51 nm Spherical	0.6–29.05	51–150	[52]
$NiFe_2O_4$	Microwave-assisted combustion method	–	34.7–42 nm Regular and irregular polyhedrons	48.75–60.87	112.62–177.55	[53]
$Zn_xNi_{1-x}Fe_2O_4$	PEG assisted hydrothermal method	–	9.1–27.0 nm Irregular polygonal and regular nanospheres	3.09–80.24	–	[54]
$NiFe_2O_4$	Hydrothermal method	–	51.23 nm Rod-like platelet	16.10		[55]
$Ni_{1-x}Mg_xFe_2O_4$	Co-precipitation method	Annealed at 900 °C	30–40 nm Agglomerated spherical, irregular structured nanoparticles	10.03–28.82	82.85–186.22	[56]
$Zn_{1-x}Mg_xFe_2O_4$ x = 0–1.0, step size of 0.2	Co-precipitation method	Annealed at 900 °C for 5 h in air	21–188 nm Agglomerated nanoparticles	1–34	85–101	[57]

(continued)

Table 1 (continued)

Composition	Preparation method	Processing condition	Size and Morphology	M_s (emu/g)	H_c (Oe)	References
$MgFe_2O_4$	Hydrothermal method	–	8.935 nm Spherical shaped and chain liked clusters	4	–	[58]
$Ni_{0.7-x}Zn_{0.3}M_xFe_2O_4$ $M = Co^{2+}, Mn^{2+}, Cu^{2+}$ $x = 0, 0.1, 0.3, 0.5, 0.7$	Citrate method	–	25.75–54.84 nm Agglomerated nanoparticles with different shapes and sizes	51.3–66.4	76–477	[59]
$CoCr_xFe_{2-x}O_4$ $x = 0–1.0$, step size of 0.25	PVA assisted sol–gel method	Calcined at 350, 500, 700, 1000 °C for 4 h	7–49 nm Cubic like grains	7–78	13–1411	[60]
$Mg_{1-x}Zn_xFe_2O_4$ $x = 0, 0.05, 0.10, 0.15$	Electrospining method	Calcined at 550 °C for 2 h in air	Nanofibers of average diameter 100–350 nm	20.25–29.76	90–96	[61]
$Co_{1-x}Cu_xCe_{0.05}Fe_{1.95}O_4$ $x = 0–1.0$, step size of 0.25	Sol–gel method	Sintered at 700 °C for 5 h	31.25–84.69 nm Nanoparticles with varying shapes	14.13–29.81	240.5–315.89	[62]
$Mg_{0.5}Zn_{0.5-x}Co_xFe_2O_4$ $x = 0$ to 0.500, step size of 0.125	Co-precipitation method	–	36.17–70.13 nm	36.18–59.41	0–883.40	[63]

(continued)

Table 1 (continued)

Composition	Preparation method	Processing condition	Size and Morphology	M_s (emu/g)	H_c (Oe)	References
$NiDy_xFe_{2-x}O_4$	Auto-combustion method	Annealed for 2 at 800 °C h, sintered for 3 h at 1200 °C	39–52 nm Polygonal shaped grains with non-uniform size distribution	43.75–50.07	27.37–58.41	[64]
$NiFe_2O_4$, $Ni_{0.9}Cd_{0.1}Fe_2O_4$, $Ni_{0.9}Sr_{0.1}Fe_2O_4$, $Ni_{0.9}Cd_{0.05}Sr_{0.05}Fe_2O_4$	Auto-combustion method	Calcined at 800 °C for 6 h and sintered at 850 °C for 8 h	26–37 nm	18.34–34.79	183.5–218.59	[65]
$Co_{0.7}Zn_{0.3}Sm_yFe_{2-y}O_4$ x = 0 to 0.04, step size of 0.01	Auto-combustion method	Sintered for 4 h at 450 °C	22–47 nm Closely packed spherical shaped fine grains	7.78–96.83	274–481	[66]
$CuPr_xFe_{2-x}O_4$ x = 0 to 1.0, step size of 0.25	Sol–gel method	Sintered at 750 °C for 6 h	62.31–84.05 nm Agglomerated nanoparticles with irregular shapes	30.37–42.22	295.29–773.82	[67]
$CoY_xFe_{2-x}O_4$ x = 0, 0.1, 0.15, 0.2, 0.3	Auto-ignition method	Sintered at 800 °C for 2 h	37–43 nm Nearly spherical shaped nanoparticles	35.63–72.19	346–684	[68]
$Ni_xCu_{0.1}Zn_{0.9-x}Fe_2O_4$	Co-precipitation method	Heated for 2 h at 800 °C	21.3–23.5 nm Nearly spherical and uniform sized nanoparticles	23.87–38.36	24.09–64.99	[69]

(continued)

Table 1 (continued)

Composition	Preparation method	Processing condition	Size and Morphology	M_s (emu/g)	H_c (Oe)	References
$CoFe_2O_4$	Mechanical milling	Calcined at 1000 °C for 2 h	28–324 nm Agglomerated and irregular shapes	48–78	650–2092	[70]
$CoCe_xDy_xFe_{2-2x}O_4$ x = 0 to 0.05, in 0.01step size	Auto-combustion method	Calcined for 4 h at 400 °C in air	Agglomerated nanoparticles	52–84	245–976	[71]
$CoFe_2O_4$	Reverse co-precipitation method Magnetic field assisted	–	22.44–26.96 nm Agglomerated nanoparticles	54.24–61.22	339.25–385.2	[72]
$Co_xNi_{1-x}Fe_2O_4$ x = 0 to 1.0 in 0.2step size	Sol–gel auto-combustion method	Pre-heated for 1 h at 500 °C and calcined for 2 h at 1200 °C in air	36–58 nm Roughly spherical and beveled edges cubes	50–93	50–650	[73]
$Co_{1-x}Mn_xFe_2O_4$ x = 0, 0.05, 0.10, 0.15, 0.20, 0.25, 0.30	Auto-combustion method	Annealed at 1000 °C for 12 h	22–30 nm	52.55–68.94	604–1592	[74]
$Mn_{1-x}Zn_xFe_2O_4$ x = 0 to 0.5, in 0.1step size	Co-precipitation method	–	10.66–25.96 nm	37.05–58.66	12.59–74.55	[75]
$Mn_{1-x}Ni_xFe_2O_4$ x = 0.1 to 0.5, in 0.1step size	Co-precipitation method	–	21.16–26.38 nm	23.09–60.90	87.616–123.32	[76]

(continued)

Table 1 (continued)

Composition	Preparation method	Processing condition	Size and Morphology	M_s (emu/g)	H_c (Oe)	References
$MnFe_{2-x}La_xO_4$ and $MnFe_{2-x}Gd_xO_4$ x = 0.02 to 0.10, step size of 0.02	Co-precipitation method	–	26.84–32.86 nm ($MnFe_{2-x}La_xO_4$) 26.07–30.88 nm ($MnFe_{2-x}Gd_xO_4$)	50.36–69.1 and 44.10–60.4	107.54–126.69 ($MnFe_{2-x}La_xO_4$) and 100.36–155.08 ($MnFe_{2-x}Gd_xO_4$)	[77]
$NiFe_{2-x}Cr_xO_4$ x = 0 to 1.0, in 0.2 step size	Co-precipitation method	Heated at 837 K for 6 h	20–30 nm	10.18–53.38	16–320	[78]
$Co_{0.7}Zn_{0.3}Tm_xFe_{2-x}O_4$ x = 0 to 0.04, step size of 0.01	Sonochemical method	–	7.37–9.66 nm Agglomerated grains	20.2–28.9	15.5–19.1	[79]

shown in Fig. 4. The microspheres of $CoFe_2O_4$ were prepared using the solvothermal method at different reaction times resulting in the average size distribution of 200 to 330 nm along with transformation from spherical to octahedral shapes. In their studies, 220 nm-sized $CoFe_2O_4$ microspheres composed of 8 nm nanoparticles were found to exhibit superparamagnetism. Li et al. [10] described the preparation of monodispersed $CoFe_2O_4$ nanoparticles using the hydrothermal method (as shown in Fig. 5.). The prepared nanoparticles were nearly spherical shaped with a mean size of 5.5 nm and were found to exhibit superparamagnetism at room temperature. Yang

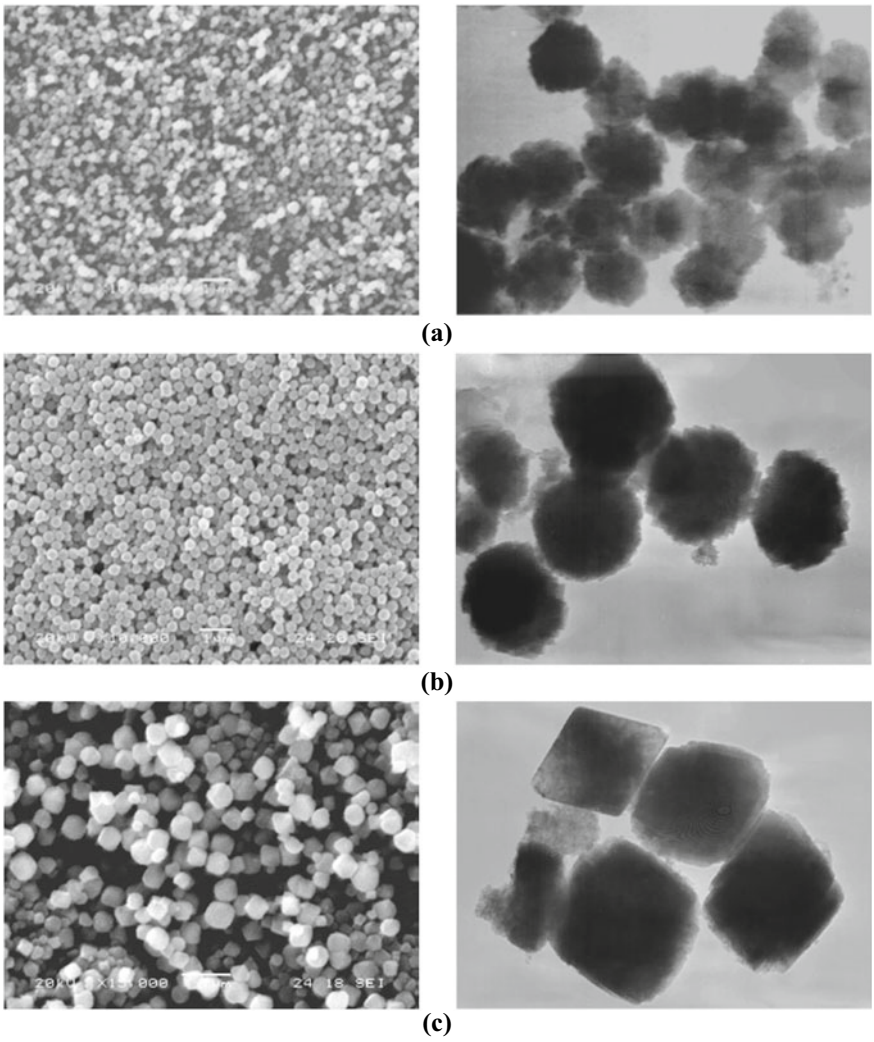

Fig. 4 SEM (left) and TEM (right) images of $CoFe_2O_4$ microspheres prepared using solvothermal method at different reaction time of **a** 12 h, **b** 24 h, **c** 36 h [9]

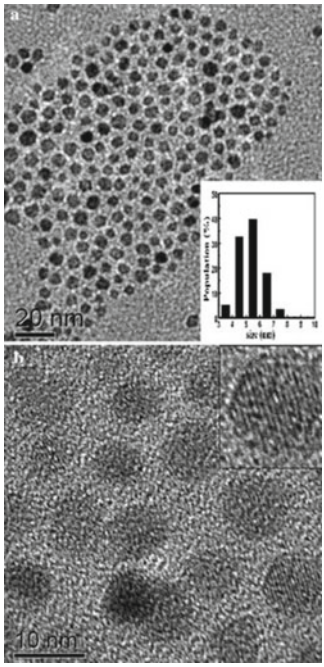

Fig. 5 TEM images of monodispersed $CoFe_2O_4$ nanoparticles prepared using hydrothermal method [10]

et al. [11] fabricated nanorods of Fe_3O_4 which are shown in Fig. 6 and investigated for hyperthermia applications. Gao et al. [12] reported studies on the directional dependency of nanowire arrays of $ZnFe_2O_4$ having about 16 nm diameter ordered in anodic aluminum oxide (AAO) templates that were prepared using the electrodeposition method (shown in Fig. 7). Maensiri et al. [13] reported studies on nanofibres of $MgFe_2O_4$/polyvinyl pyrrolidone (PVP) composites fabricated by the method of electrospinning. Their study shows that the morphology of the nanofibres greatly depends on the calcination temperature. The structural transformation (which is shown in Figs. 8. and 9) from smooth and uniform cross-section nanofibres to a structure of packed crystallites of about 10–20 nm for 700 °C and 25–80 nm for 800 °C calcined samples. Along with the increase in crystallinity, saturation magnetization values

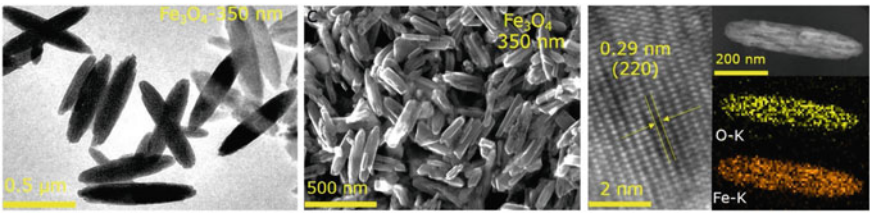

Fig. 6 Images of Fe_3O_4 nanorods prepared using hydrothermal method, TEM (left), SEM (middle), HRTEM (right), adapted from [11]

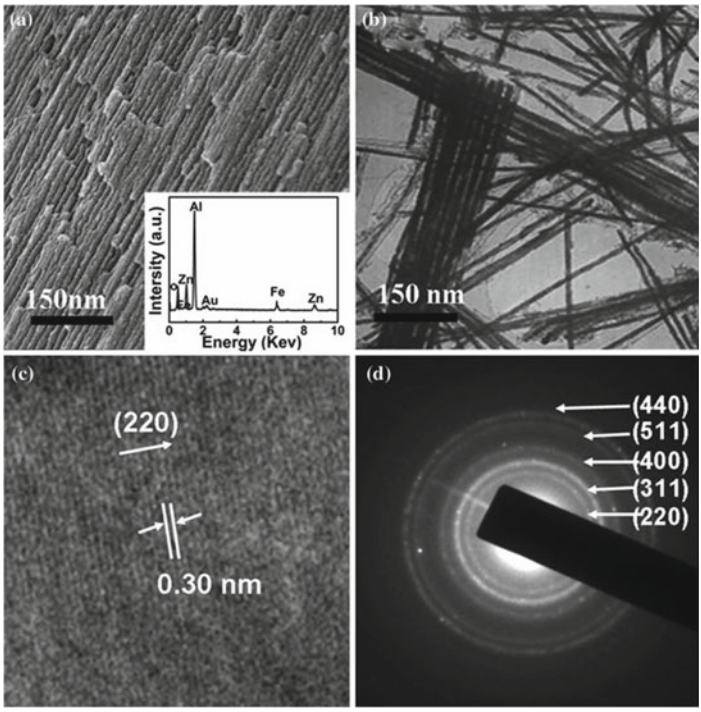

Fig. 7 $ZnFe_2O_4$ nanowires arrays in AAO templates prepared using electrodeposition method **a** SEM, **b** TEM, **c** HRTEM **d** SAED pattern [12]

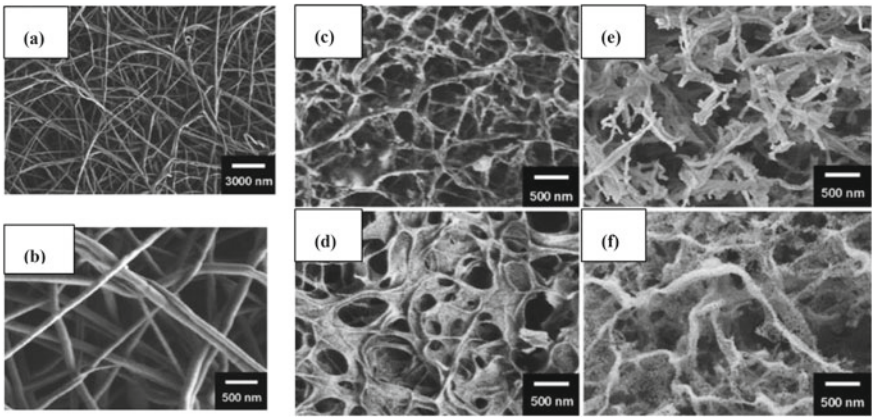

Fig. 8 SEM images of as-spun (**a**), **b** $MgFe_2O_4$/PVP composites and calcined for 2 h in air at **c** 500 °C, **d** 600 °C, **e** 700 °C and **f** 800 °C, adapted from [13]

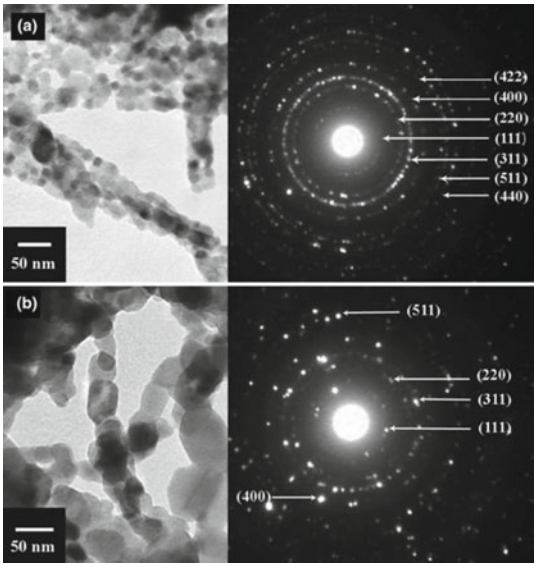

Fig. 9 TEM images and SAED pattern of $MgFe_2O_4$/PVP composites calcined at **a** 700 °C and **b** 800 °C for 2 h in air [13]

were also found to be enhanced with increasing calcination temperature. In addition to these, different structures namely coaxial nanobelts, Janus nanofibres, hollow nanofibers, sandwiched structures, nanorattles, microspheres, core–shell structures formed with other kinds of materials are also found to be reported which are being discussed in Sect. 6.

4 Characterization of Magnetic Properties

4.1 Fundamentals of Magnetization

The fascinating and versatile applications of magnetic materials are based on their magnetization curves or hysteresis loops. Applications of magnetic materials are determined using the knowledge of how they respond to a magnetic field which is represented by their hysteresis loops. It gives information about how magnetic materials take their path when they are subjected to a magnetic field. Magnetic materials are categorized based upon the characteristics of their magnetization curves or hysteresis loops. For instance, a paramagnetic material possesses a weak positive magnetization, showing a linear response when a field is applied. While ferromagnetic and ferrimagnetic types of materials show a non-linear S-shaped magnetization curve with a hysteresis loop. When a magnetic field is applied to ferromagnetic or ferrimagnetic materials, their magnetization increases until it reaches a maximum called saturation magnetization. But when the field is decreased from the saturation region it doesn't return in the same path, rather takes up a new path

retaining some magnetization even after complete removal of the applied field which is termed as retentivity. A field applied in opposite direction can remove the retentivity and is known as coercivity. With the further increase in the applied magnetic field along opposite direction, again saturation will be attained and after increasing the magnetic field along the original direction up to saturation, a complete hysteresis loop is formed. Based upon the coercivity and retentivity, they are categorized as hard and soft magnetic materials. A soft magnetic material refers to those having small values of coercivity and retentivity that are easy to magnetize and demagnetize while hard magnetic materials have the opposite case. Soft magnetic materials are thus found to be used in electromagnets, recording heads, transformer cores, etc. While hard magnetic materials are used in making permanent magnets, memory devices, loudspeakers, etc. [8, 14, 15].

4.2 Theoretical Models

The phenomenon of hysteresis is understood due to the existence of spontaneously magnetized small regions called magnetic domains in ferromagnetic and ferrimagnetic materials [8]. In a demagnetized state, domains are randomly oriented such that the specimen as a whole has zero magnetization but when a magnetic field is applied, they get aligned along the field direction and hence, a net magnetization. The process of magnetization varies in different regions consisting of three main different regions. Starting from the beginning, the 1st region with only reversible magnetization, the 2nd region with an additional non-reversible magnetization, and the 3rd region with reversible magnetization. The magnetization process takes place in two ways, one by magnetic domain wall motion that is the growth of favorably aligned domains at the cost of unfavorably aligned domains and the other by rotation of magnetic domains in the direction of the field applied. At the low field, magnetic domain wall motion dominates while at high field domain rotation dominates and the existence of both in between the two regions. Especially, the high field region of magnetization curves is studied by different forms of the law of approach to saturation. A model represents how basically the magnetization varies with the applied field which is usually expressed proportionally to magnetic field raised with different powers and their combinations [16, 17]. Their dependency and the constant associated with the different field terms give information on their magnetic microstructures, the directional dependency of magnetic properties or magnetic anisotropy, magnetic moments, etc. Increasing research work on tracing the magnetization curves using different models are found to be reported in different types of magnetic materials in different forms, shapes, dimensions for detailed information such as magnetic microstructures, anisotropies, magnetic moments which are intrinsically associated with them [17].

5 Magnetism in Spinel Ferrite Nanoparticles and Their Applications

Magnetic materials had become an indispensable one that covers a wide spectrum of applications like electronic devices, industrial applications, power supply, and storage devices, etc. [14, 15]. In addition, the emergence of nanoscience and nanotechnologies opens up entirely new scientific opportunities. Owing to its interdisciplinary nature, many applications are being extended to different areas like remedies to environmental problems and biomedical applications. It is found that magnetization curves or loops are also dependent on the size of the materials resulting in variation in the models in comparison with their bulk forms. It has been found that in the nano regime, the magnetic materials possess the characteristics of single domain nature which results in the phenomena of superparamagnetism and such materials are termed as superparamagnetic materials [8, 18]. Their behavior is similar to the paramagnetic material that is ideally no retentivity and no coercivity but possesses a much higher magnetization. These are reflected in their magnetization curves and detailed information on their magnetic microstructures can be traced by using suitable models like the Langevin function [19]. Their interesting and spectacular properties lead to new applications such as hyperthermia for cancer treatment, targeted drug delivery, biosensing, enhanced magnetic resonance imaging, etc. thereby widening up the applications of the magnetic materials. For instance, Yang et al. [11] demonstrated the applicability of Fe_3O_4 nanorods for use as magnetic hyperthermia agents. Nanorods of Fe_3O_4 were prepared by hydrothermal method using graphene oxide for avoiding aggregation at different reaction times and post-annealing. Spinel ferrites are also becoming an important candidate for a solution to environmental pollutions. Adsorption based on magnetic separation is desirable because of its effectiveness, low cost, and simple operation process, and hence nanosized spinel ferrites are becoming suitable candidates for adsorption.

Gao et al. [20] investigated the experiment on hollow α-Fe_2O_3 nanofibers for use as a dye adsorbent. In their studies, hollow α-Fe_2O_3 nanofibers were synthesized using a nanofiber template of polyvinyl alcohol by hydrothermal method with calcination. Their studies reported that the α-Fe_2O_3 nanofibers exhibited efficient adsorption of methyl orange present in water along with good magnetic response performance. Zhao et al. [21] studied the adsorption capability of Gd doped Co-ferrites for Congo- red for varying composition of Gd^{3+}. Due to the great surface-to-volume ratio, nano-sized particles exhibit enhanced photocatalytic activity. Ali and Mostafa [22] investigated the photocatalytic activity of Mn-ferrites, Mn-Zn-ferrites, and Mn-Cd-ferrites in reduction of Cr(VI) to Cr(III). Madhubala et al. [23] studied the photocatalytic degradation of dye like methylene blue using Mn-Ni ferrites of 15–20 nm crystallites. Ahalya et al. [24] reported the applicability of Mn-Co-ferrites as adsorbents of Cr(VI). Their results showed the effective adsorption of the heavy metal using spinel ferrites as well as the possibility of reuse of the adsorbent and the heavy metal. Moreover, by combining their properties with other materials in desirable morphologies, new applications in different areas have been reported which are

being discussed in Sect. 6. Better understanding leads to the development of new tricks in expanding their applications. Thus, it can be said that the scenario for the application of magnetic materials is expanding because of more understanding of their behavior.

6 Hybrid-Structured with Other Materials and Their Applications

Apart from the above-discussed applications, magnetic materials are also becoming an important component in multifunctional materials. As magnetic materials can be simply controlled with a magnetic field applied externally, they are also used as an important component in multifunctional materials, vehicles for drug delivery in specific sites inside the human body, and many others. Bifunctional magnetic and luminescent materials are reported to be investigated in biomedical applications such as transporters for drug delivery, agents for MRI, hyperthermia, etc. using simultaneously the magnetic and the luminescent property as the control and tracking respectively. A core–shell structured material comprising of a magnetic core with a luminescent shell occupies an important place in such a class of hybrid-structured materials. For instance, Sun et al. [80] reported multifunctional properties of CdTe quantum dots linked with silica-coated Fe_3O_4 nanoparticles having superparamagnetic properties and their potential applications as immune-labeling with fluorescent imaging of tumor cells. By integrating the magnetic and fluorescent properties into single nanostructured composites their potential applicability as simultaneous targeted drug delivery and bioimaging were investigated. Their studies found that the prepared nanocomposites can be magnetically guided for the delivery of drugs and at the same time their fluorescent property enabled the optical imaging of the nanocomposites and hence with the feasibility of their optical tracing. Atabaev et al. [81] reported fabrication and characterization of bifunctional composites comprising of magnetic Fe_3O_4 particles coated with luminescent Y_2O_3:Tb^{3+} shell. The average size of about 306 to 330 nm magnetic core covered with a phosphor shell of a thickness of about 25 nm was found to exhibit desirable magnetic and luminescent properties suggesting ease for magnetic targeting and separation as well which may find applications in biomedical and bioanalytical applications. Liu et al. [5] investigated bifunctional properties of core–shell Fe_3O_4-CdSe nanoparticles prepared by a polyol process. Magnetic Fe_3O_4 core of about 10 nm diameter covered with CdSe luminescent shell of about 2 nm thicknesses. Sun et al. [82] reported the fabrication of hybrid materials consisting of Fe_3O_4 nanoparticles encapsulated with SiO_2 and functionalized by YVO_4:Eu^{3+} phosphors. The prepared nanocomposites were found to exhibit good ferrimagnetic behavior with a strong red emission. Shi et al. [6] prepared and investigated bifunctional properties of Fe_3O_4@C/YVO_4:Sm^{3+} microspheres synthesized by hydrothermal combined with the sol–gel method. In their work, the carbon layer was used to protect Fe_3O_4 particles from oxidation and

protect the lanthanide-based luminescent shell from quenching of luminescence due to Fe_3O_4. Strong red–orange emission and good ferrimagnetic behavior were observed in their composites. Zhang et al. [83] conducted the studies on nanorattles composed of SiO_2 coated Fe_3O_4 covered with luminescent shells of α-NaYF/Yb, Er which was fabricated using an ion-exchange route for application in targeted chemotherapy. The mesoporous composites were found to possess both upconversion luminescent and magnetic properties along with a high capacity for loading drugs, low cytotoxicity, and excellent cell imaging properties. Yang et al. [84] also reported similar sandwich structured materials having magnetic, mesoporous and luminescent properties. Microspheres of Fe_3O_4 encapsulated with silica and functionalized through YVO_4:Eu^{3+} phosphor deposition which was prepared using a combination of hydrothermal and sol–gel method with heat treatment. The resulted composites were found to possess ordered hexagonal mesoporous, good luminescent properties and high magnetization values and were proposed for using as potential candidates for drug delivery system.

Also, core–shell structures with Fe_3O_4 as cores and other luminescent shells such as YVO_4:Eu^{3+} [85] and Gd_2O_3:Eu^{3+} composites [86] having good magnetic and luminescent properties are also reported. Apart from the core–shell structures, other forms of composites are also found. For instance, Huarac et al. [87] prepared the composites of magnetic Fe_2O_3 and luminescent ZnS: Mn nanoparticles prepared by the co-precipitation method. Highly crystalline two phases were found to coexist in XRD studies and the clusters of nanoparticles of Fe_3O_4 and ZnS: Mn existed side by side from HRTEM studies. In addition to these, nanofibre composites of different types such as core–shell nanofibers, nanobelts, Janus nanofibres are also reported. For instance, using the electrospinning method, flexible hollow nanofibers of Fe_3O_4/$Eu(BA)_3$ phen/PVP [88] and core–shell nanofibres composites of Fe_3O_4/PVP@$NaYF_4$:Yb^{3+}, Er^{3+}/PVP [89] having bifunctional properties were fabricated. Xue et al. [90] reported the fabrication of coaxial nanobelts with tunable bifunctional properties of magnetic and luminescent properties. The composites were composed of the magnetic core of $CoFe_2O_4$/polymethyl methacrylate (PMMA) and photoluminescent shells of [$Tb(BA)_3$(phen) + $Eu(BA)_3$ (phen)]/PMMA synthesized by the electrospinning method. Zhou et al. [91] investigated bifunctional magnetic and luminescent properties of double-stranded nanofibers called Janus nanofibers fabricated by the electrospinning method. A Janus nanofiber is composed of side-by-side assembled two strands of nanofibers, one possessing magnetic properties and the other one having luminescent properties. It was found that they have superior luminescent and magnetic properties owing to their special nanostructures and tunable colors based on their composition. Their work demonstrated an approach for the preparation of composites of controlled and tunable luminescent properties, expected to find applications in magnetic nano-bio-label and anti-counterfeit materials, etc. Thus, nanocomposites having combined properties such as magnetically responsive and luminescent properties with different morphologies were proposed to find applications in biomedical applications like drug delivery, targeting on specific sites, bio-separation, and diagnostic applications.

7 Conclusion

To conclude, it can be summarized that the ever-increasing research work on spinel ferrites and their applications in different fields can be observed with the exposure of nanoscience. A variety of compositions of spinel ferrites in different morphologies were fabricated and investigated through different experimental approaches of nanotechnology. Spinel ferrites of different types, compositions, and their composites of different morphologies were found to be fabricated by different routes of synthesis such as co-precipitation, auto combustion, sol–gel, thermal decomposition, microemulsion, hydrothermal, solvothermal method, and electrospinning method. In addition to their composition, their properties also depend on a particular method, specific processing conditions, and morphologies. Spinel ferrites of desirable nanostructured morphologies have been able to realize using advanced techniques in fabrication and microscopy at nano levels. These advanced nanostructured materials on the other hand lead toward new emerging applications which extend to many multidisciplinary areas such as dye degradation, adsorption of heavy metals, drug delivery, hyperthermia applications. Nanoscience and nanotechnology also lead toward the development of hybrid-structured materials possessing bifunctional properties. As a magnetic component in bifunctional materials, Fe_3O_4 has been reported to be successfully used by many researchers. So, it is desirable to extend the investigation also to other varieties of spinel ferrites. Moreover, the development of advanced bifunctional materials could lead toward device miniaturization, designing of cost-effective and energy-efficient devices, etc. The combination of magnetic materials with other different properties will open up new exciting applications in addition to the improvement in the existing applications.

Acknowledgements The author Elangbam Chitra Devi expresses her gratitude to the UGC, New Delhi, India for the award of UGC-DSKPDF (F. 4-2/2006(BSR)/PH/18-19/0090).

References

1. Amiri M, Salavati-niasari M, Akbari A (2019) Magnetic nanocarriers: evolution of spinel ferrites for medical applications. Adv Colloid Interface Sci 265:29–44
2. Kefeni KK, Msagati TAM, Ti T, Mamba BB (2020) Spinel ferrite nanoparticles and nanocomposites for biomedical applications and their toxicity. Mater Sci Eng C 107:110314
3. Reddy DHK, Yun YS (2016) Spinel ferrite magnetic adsorbents: alternative future materials for water purification. Coord Chem Rev 315:90–111
4. Wu K, Li J, Zhang C (2019) Zinc ferrite based gas sensors: a review. Ceram Int 45: 11143–11157
5. Liu H, Wu J, Min JH, Lee JH, Kim YK (2019) Synthesis and characterization of magnetic-luminescent Fe3O4–CdSe core-shell nanocrystals. Electron Mater Lett 15:102–110
6. Shi J, Tong L, Ren X, Li Q, Ding H, Yang H (2013) Bifunctional Fe3O4@C/YVO4:Sm3+ composites with the core-shell structure. Mater Chem Phys 139:73–78
7. Sickafus KE, Wills JM, Grimes NW (1999) Structure of spinel. J Am Ceram Soc 82:3279–3292
8. Cullity BD, Graham CD (2011) Introduction to magnetic materials. Wiley, Hoboken, New Jersey
9. Yuan HL, Wang YQ, Zhou SM, Liu LS, Chen XL, Lou SY, Yuan RJ, Hao YM, Li N (2010) Low-Temperature preparation of superparamagnetic CoFe 2O 4 microspheres with high saturation magnetization. Nanoscale Res Lett 5:1817–1821
10. Li XH, Xu CL, Han XH, Qiao L, Wang T, Li FS (2010) Synthesis and magnetic properties of nearly monodisperse CoFe2O4 nanoparticles through a simple hydrothermal condition. Nanoscale Res Lett 5:1039–1044
11. Yang Y, Huang M, Qian J, Gao D, Liang X (2020) Tunable Fe3O4 nanorods for enhanced magnetic hyperthermia performance. Sci Rep 10:1–7
12. Gao D, Shi Z, Xu Y, Zhang J, Yang G, Zhang J, Wang X, Xue D (2010) Synthesis, magnetic anisotropy and optical properties of preferred oriented zinc ferrite nanowire arrays. Nanoscale Res Lett 5:1289–1294
13. Maensiri S, Sangmanee M, Wiengmoon A (2009) Magnesium ferrite (MgFe2O4) nanostructures fabricated by electrospinning. Nanoscale Res Lett 4:221–228
14. Goldman A (2006) Modern ferrite technology. Springer, USA
15. Chikazumi S (1997) Physics of ferromagnetism. Oxford University Press, New York
16. Devi EC, Soibam I (2019) Law of approach to saturation in Mn–Zn ferrite nanoparticles. J Supercond Nov Magn 32:1293–1298
17. Devi EC, Singh SD (2021) Tracing the magnetization curves: a review on their importance strategy, and outcomes. J Supercond Novel Magn 34:15–25
18. Bedanta S, Kleemann W (2009) Supermagnetism. J Phys D Appl Phys 42:013001
19. Devi EC, Singh SD (2021) Manifestation of magnetic characteristics of zinc ferrite nanoparticles using the Langevin function. J Supercond Nov Magn 34:617–622
20. Gao Q, Luo J, Wang X, Gao C, Ge M (2015) Novel hollow α-Fe2O3 nanofibers via electrospinning for dye adsorption. Nanoscale Res Lett 10:1–8
21. Zhao X, Wang W, Zhang Y, Wu S, Li F, Liu JP (2014) Synthesis and characterization of gadolinium doped cobalt ferrite nanoparticles with enhanced adsorption capability for Congo Red. Chem Eng J 250:164–174
22. Othman AI, Mostafa AG (2015) Photocatalytic reduction of chromate oxyanions on MMnFe2O4 (M=Zn, Cd) nanoparticles. Mater Sci Semicond Process 33:189–198
23. Madhubala G, Manikandan A, Arul AS, Ramar P (2016) Photocatalytic degradation of methylene blue dye and magneto-optical studies of magnetically recyclable spinel NixMn1-xFe2O4 (x = 0.0–1.0) nanoparticles. J Mol Struct 1113: 79–87
24. Ahalya K, Suriyanarayanan N, Ranjithkumar V (2014) Effect of cobalt substitution on structural and magnetic properties and chromium adsorption of manganese ferrite nanoparticles. J Magn Magn Mater 372:208–213
25. Motavallian P, Abasht B, Mirzaee O, Abdollah-Pour H (2019) Correlation between structural and magnetic properties of substituted (Cd, Zr) cobalt ferrite nanoparticles. Chin J Phys 57:6–13

26. Kahn ML, Zhang ZJ (2001) Synthesis and magnetic properties of CoFe2O4 spinel ferrite nanoparticles doped with lanthanide ions. Appl Phys Lett 78:3651–3653
27. Virumbrales M, Blanco-Gutiérrez V, Delgado-Cabello A, Sáez-Puche R, Torralvo MJ (2018) Superparamagnetism in CoFe2O4 nanoparticles: an example of a collective magnetic behavior dependent on the medium. J Alloys Compd 767:559–566
28. Coutinho DM, Verenkar VMS (2019) Spin canting and surface spin disorder in Ni substituted Co-Cd ferrite nanoparticles synthesized by fuel deficient combustion method. J Alloys Compd 782:392–403
29. Blanco-Gutiérrez V, Climent-Pascual E, Sáez-Puche R, Torralvo-Fernández MJ (2016) Temperature dependence of superparamagnetism in CoFe2O4 nanoparticles and CoFe2O4/SiO2 nanocomposites. Phys Chem Chem Phys 18:9186–9193
30. Moyo HMIAT (2013) The influence of annealing temperature on the magnetic properties of Mn 0.5 Co 0.5 Fe2O4 Nanoferrites synthesized via mechanical milling method. J Supercond Novel Magn 26:1361–1367
31. Vázquez-Vázquez C, López-Quintela MA, Buján-Núñez MC, Rivas J (2011) Finite size and surface effects on the magnetic properties of cobalt ferrite nanoparticles. J Nanoparticle Res 13:1663–1676
32. Nlebedim IC, Vinitha M, Praveen PJ, Das D, Jiles DC (2013) Temperature dependence of the structural, magnetic, and magnetostrictive properties of zinc-substituted cobalt ferrite. J Appl Phys 113:193904
33. Liu BH, Ding J (2006) Strain-induced high coercivity in CoFe2 O4 powders. Appl Phys Lett 88:042506
34. Lal G, Punia K, Dolia SN, Alvi PA, Choudhary BL, Kumar S (2020) Structural, cation distribution, optical and magnetic properties of quaternary Co0.4+xZn0.6-xFe2O4 (x = 0.0, 0.1 and 0.2) and Li doped quinary Co0.4+xZn0.5-xLi0.1Fe2O4 (x = 0.0, 0.05 and 0.1) nanoferrites. J Alloys Compd 828:154388
35. Chithra M, Anumol CN, Sahu B, Sahoo SC (2017) Structural and magnetic properties of ZnXCo1−XFe2O4 nanoparticles: nonsaturation of magnetization. J Magn Magn Mater 424:174–184
36. Prasad BBVSV, Ramesh KV, Srinivas A (2018) Structural and soft magnetic properties of nickel-substituted Co-Zn nanoferrites. J Supercond Nov Magn 31:3223–3237
37. Mendonça EC, Jesus CBR, Folly WSD, Meneses CT, Duque JGS (2013) Size effects on the magnetic properties of ZnFe2O4 nanoparticles. J Supercond Nov Magn 26:2329–2331
38. Choi EJ, Ahn Y, Hahn EJ (2008) Size dependence of the magnetic properties in superparamagnetic zinc-ferrite nanoparticles. J Korean Phys Soc 53:2090–2094
39. Thomas JJ, Shinde AB, Krishna PSR, Kalarikkal N (2013) Temperature-dependent neutron diffraction and Mössbauer studies in zinc ferrite nanoparticles. Mater Res Bull 48:1506–1511
40. Madhubala G, Manikandan A, Arul Antony S, Ramar P (2016) Photocatalytic degradation of methylene blue dye and magneto-optical studies of magnetically recyclable spinel NixMn1-xFe2O4(x = 0.0–1.0) nanoparticles. J Mol Struct 1113:79–87
41. Manohar A, Krishnamoorthi C (2017) Low Curie-transition temperature and superparamagnetic nature of Fe3O4 nanoparticles prepared by colloidal nanocrystal synthesis. Mater Chem Phys 192:235–243
42. Li Q, Kartikowati CW, Horie S, Ogi T, Iwaki T, Okuyama K (2017) Correlation between particle size/domain structure and magnetic properties of highly crystalline Fe3O4 nanoparticles. Sci Rep 7:9894
43. Lal G, Punia K, Dolia SN, Alvi PA, Dalela S, Kumar S (2019) Rietveld refinement, Raman, optical, dielectric, Mössbauer and magnetic characterization of superparamagnetic fcc-CaFe2O4 nanoparticles. Ceram Int 45:5837–5847
44. Samariya A, Dolia SN, Prasad AS, Sharma PK, Pareek SP, Dhawan MS, Kumar S (2013) Size dependent structural and magnetic behaviour of CaFe2O 4. Curr Appl Phys 13:830–835
45. El-fadl AA, Hassan AM, Mahmoud MH, Tatarchuk T, Yaremiy IP, Gismelssed AM, Ahmed MA (2019) Nanoparticles synthesized by microwave combustion method. J Magn Magn Mater 471:192–199

46. Debnath S, Deb K, Saha B, Das R (2019) X-ray diffraction analysis for the determination of elastic properties of zinc-doped manganese spinel ferrite nanocrystals (Mn0.75Zn0.25Fe2O4), along with the determination of ionic radii, bond lengths, and hopping lengths. J Phys Chem Solids 134:105–114
47. Barrera G, Coisson M, Celegato F, Raghuvanshi S, Mazaleyrat F, Kane SN, Tiberto P (2018) Cation distribution effect on static and dynamic magnetic properties of Co1-xZnxFe2O4 ferrite powders. J Magn Magn Mater 456:372–380
48. Najmoddin N, Beitollahi A, Kavas H, Majid MS, Rezaie H, Åkerman J, Toprak MS (2014) XRD cation distribution and magnetic properties of mesoporous Zn-substituted CuFe2O4. Ceram Int 40:3619–3625
49. Karcıoḡlu KZ, Boncukcuoḡlu R, Karakaş IH, Ertuḡrul M (2015) The effects of heat treatment on the synthesis of nickel ferrite (NiFe2O4) nanoparticles using the microwave assisted combustion method. J Magn Magn Mater 374:298–306
50. Roman T, Pui A, Lukacs AV, Cimpoesu N, Lupescu S, Iulian A, Kordatos K, Ntziouni A, Postolache P, Zaharia M, Stanciu S, Mito L (2019) Structural changes of cerium doped copper ferrites during sintering process and magneto-electrical properties assessment. Ceram Int 45:17243–17251
51. Heiba ZK, Maher A, Bakr M (2017) Structural analysis and magnetic properties of biphasic chromium-substituted copper ferrites. J Mol Struct 1147:668–675
52. Goodarz M, Saion EB, Abbastabar H, Hashim M, Halim A (2011) Simple preparation and characterization of nickel ferrite nanocrystals by a thermal treatment method. Powder Technol 212:80–88
53. Kooti M, Sedeh AN (2013) Synthesis and characterization of NiFe2O4 magnetic nanoparticles by combustion method. J Mater Sci Technol 29:34–38
54. Kavas H, Baykal A, Toprak MS, Köseoğlu Y, Sertkol M, Aktaş B (2009) Cation distribution and magnetic properties of Zn doped NiFe2O4 nanoparticles synthesized by PEG-assisted hydrothermal route. J Alloys Compd 479:49–55
55. Amiri M, Pardakhti A, Ahmadi-zeidabadi M, Akbari A (2018) Colloids and surfaces B: biointerfaces magnetic nickel ferrite nanoparticles: green synthesis by Urtica and therapeutic effect of frequency magnetic field on creating cytotoxic response in neural cell lines. Colloids Surf B Biointerfaces 172:244–253
56. Moradmard H, Shayesteh SF, Tohidi P, Abbas Z, Khaleghi M (2015) Structural, magnetic and dielectric properties of magnesium doped nickel ferrite nanoparticles. J Alloys Compd 650:116–122
57. Nadeem K, Rahman S, Mumtaz M (2015) Effect of annealing on properties of Mg doped Zn-ferrite nanoparticles. Prog Nat Sci Mater Int 25:111–116
58. Meidanchi A, Motamed A (2020) Preparation, characterization and in vitro evaluation of magnesium ferrite superparamagnetic nanoparticles as a novel radiosensitizer of breast cancer cells. Ceram Int 46:17577–17583
59. Abu-Elsaad NI, Nawara AS, Mazen SA (2020) Synthesis, structural characterization, and magnetic properties of Ni–Zn nanoferrites substituted with different metal ions (Mn2+, Co2+, and Cu2+). J Phys Chem Solids 146:109620
60. Nikmanesh H, Eshraghi M, Karimi S (2019) Cation distribution, magnetic and structural properties of CoCrxFe2-xO4: effect of calcination temperature and chromium substitution. J Magn Magn Mater 471:294–303
61. Ghazi N, Mahmoudi CH, Ghodsi FE (2018) Rietveld refinement, morphology analysis, optical and magnetic properties of magnesium-zinc ferrite nanofibers. J Magn Magn Mater 468:132–140
62. Akhtar MN, Khan AA, Akhtar MN, Ahmad M, Khan MA (2019) Structural rietveld refinement, morphological and magnetic features of Cu doped Co–]Ce nanocrystalline ferrites for high frequency applications. Phys B Condens Matter 561:121–131
63. Sharma R, Thakur P, Kumar M, Thakur N, Negi NS, Sharma P, Sharma V (2016) Improvement in magnetic behaviour of cobalt doped magnesium zinc nano-ferrites via co-precipitation route. J Alloys Compd 684:569–581

64. Chauhan L, Singh N, Dhar A, Kumar H, Kumar S, Sreenivas K (2017) Structural and electrical properties of Dy3+ substituted NiFe2O4 ceramics prepared from powders derived by combustion method. Ceram Int 53:8378–8390
65. Tiwari R, De M, Tewari HS, Ghoshal SK (2020) Structural and magnetic properties of tailored NiFe2O4 nanostructures synthesized using auto-combustion method. Results Phys 16:102916
66. Mugutkar AB, Gore SK, Tumberphale UB, Jadhav VV, Mane RS, Patange SM, Shirsath SE, Jadhav SS (2020) Role of composition and grain size in controlling the structure sensitive magnetic properties of Sm3+ substituted nanocrystalline Co-Zn ferrites. J Rare Earths 38:1069–1075
67. Akhtar MN, Babar M, Qamar S, Rehman Z, Khan MA (2019) Structural Rietveld refinement and magnetic features of prosademium (Pr) doped Cu nanocrystalline spinel ferrites. Ceram Int 45:10187–10195
68. Chakrabarty S, Dutta A, Pal M (2018) Effect of yttrium doping on structure, magnetic and electrical properties of nanocrystalline cobalt ferrite. J Magn Magn Mater 461:69–75
69. Ramakrishna KS, Srinivas C, Meena SS, Tirupanyam BV, Bhatt P, Yusuf SM, Prajapat CL, Potukuchi DM, Sastry DL (2017) Investigation of cation distribution and magnetocrystalline anisotropy of NixCu0.1Zn0.9−xFe2O4 nanoferrites: role of constant mole percent of Cu2+ dopant in place of Zn2+. Ceram Int 43:7984–7991
70. Mahdikhah V, Ataie A, Babaei A, Sheibani S, Yang CWO, Abkenar SK (2019) Control of structural and magnetic characteristics of cobalt ferrite by post-calcination mechanical milling. J Phys Chem Solids 134:286–294
71. Hashim M, Raghasudha M, Meena SS, Shah J, Shirsath SE, Kumar S, Ravinder D, Bhatt P, Alimuddin KR, Kotnala RK (2018) Influence of rare earth ion doping (Ce and Dy) on electrical and magnetic properties of cobalt ferrites. J Magn Magn Mater 449:319–327
72. Samadi MS, Shokrollahi H, Zamanian A (2018) The magnetic-field-assisted synthesis of the Co-ferrite nanoparticles via reverse co-precipitation and their magnetic and structural properties. Mater Chem Phys 215:355–359
73. Torkian S, Ghasemi A, Shoja RR (2017) Cation distribution and magnetic analysis of wideband microwave absorptive CoxNi1−xFe2O4 ferrites. Ceram Int 43:6987–6995
74. Yadav SP, Shinde SS, Bhatt P, Meena SS, Rajpure KY (2015) Distribution of cations in Co1-xMnxFe2O4 using XRD, magnetization and Mössbauer spectroscopy. J Alloys Compd 646:550–556
75. Devi EC, Soibam I (2017) Effect of Zn doping on the structural, electrical and magnetic properties of MnFe2O4 nanoparticles. Indian J Phys 91:861–867
76. Devi EC, Soibam I (2019) Magnetic properties and law of approach to saturation in Mn-Ni mixed nanoferrites. J Alloys Compd 772:920–924
77. Devi EC, Soibam I (2019) Tuning the magnetic properties of a ferrimagnet. J Magn Magn Mater 469:587–592
78. Patange SM, Shirsath SE, Jadhav SS, Jadhav KM (2012) Cation distribution study of nanocrystalline NiFe 2-xCrxO4 ferrite by XRD, magnetization and Mössbauer spectroscopy. Phys Status Solidi Appl Mater Sci 209:347–352
79. Almessiere MA, Slimani Y, Kurtan U, Guner S, Sertkol M, Shirsath SE, Akhtar S, Baykal A, Ercan I (2019) Structural, magnetic, optical properties and cation distribution of nanosized Co0.7Zn0.3TmxFe2−xO4 ($0.0 \leq x \leq 0.04$) spinel ferrites synthesized by ultrasonic irradiation. Ultrason Sonochem 58:104638
80. Sun P, Zhang H, Liu C, Fang J, Wang M, Chen J, Zhang J, Mao C, Xu S (2010) Preparation and characterization of Fe3O4/CdTe magnetic/fluorescent nanocomposites and their applications in immuno-labeling and fluorescent imaging of cancer cells. Langmuir 26:1278–1284
81. Atabaev TS, Kim HK, Hwang YH (2013) Fabrication of bifunctional core-shell Fe3O4 particles coated with ultrathin phosphor layer. Nanoscale Res Lett 8:357
82. Sun Z, Liu D, Tong L, Shi J, Yang X, Yu L, Tao Y, Yang H (2011) Synthesis and properties of magnetic and luminescent Fe3O 4/SiO2/YVO4:Eu3+ nanocomposites. Solid State Sci 13:361–365

83. Zhang F, Braun GB, Pallaoro A, Zhang Y, Shi Y, Cui D, Moskovits M, Zhao D, Stucky GD (2012) Mesoporous multifunctional upconversion luminescent and magnetic "Nanorattle" materials for targeted chemotherapy. Nano Lett 12:61–67
84. Yang P, Quan Z, Hou Z, Li C, Kang X, Cheng Z, Lin J (2009) A magnetic, luminescent and mesoporous core-shell structured composite material as drug carrier. Biomaterials 30:4786–4795
85. Peng H, Liu G, Dong X, Wang J, Xu J, Yu W (2011) Preparation and characteristics of Fe3O4@YVO 4:Eu3+ bifunctional magnetic-luminescent nanocomposites. J Alloys Compd 509:6930–6934
86. Peng H, Cui B, Li L, Wang Y (2012) A simple approach for the synthesis of bifunctional Fe 3O 4@Gd 2O 3: Eu 3+ core-shell nanocomposites. J Alloys Compd 531:30–33
87. Beltran-Huarac J, Guinel MJF, Weiner BR, Morell G (2013) Bifunctional Fe3O4/ZnS: Mn composite nanoparticles. Mater Lett 98:108–111
88. Yu W, Ma Q, Li X, Dong X, Wang J, Liu G (2014) One-pot coaxial electrospinning fabrication and properties of magnetic-luminescent bifunctional flexible hollow nanofibers. Mater Lett 120:126–129
89. Ma Q, Wang J, Dong X, Yu W, Liu G (2014) Electrospinning fabrication and characterization of magnetic-upconversion fluorescent bifunctional core-shell nanofibers. J Nanoparticle Res 16:2239
90. Xue H, Sun X, Bi J, Wang T, Han J, Ma Q, Han L, Dong X (2015) Facile electrospinning construction and characteristics of coaxial nanobelts with simultaneously tunable magnetism and color-tuned photoluminescence bifunctionality. J Mater Sci Mater Electron 26:8774–8783
91. Zhou X, Ma Q, Yu W, Wang T, Dong X, Wang J, Liu G (2015) Magnetism and white-light-emission bifunctionality simultaneously assembled into flexible Janus nanofiber via electrospinning. J Mater Sci 50:7884–7895

Chapter 17
Lead-Free Piezoelectric Nanostructures and Their Applications

Huidrom Surjalata Devi and Mamata Maisnam

1 Introduction

When mechanical stress is applied to some materials, they produced electricity. This is referred to as the piezoelectric effect. This stress can be generated by striking or bending the material just enough to deform the crystal lattice without breaking it. The phenomenon often occurs in the opposite direction, with the substance mildly deforming when a small electric current is applied. Piezoelectricity was found more than a century ago and has many uses today. It is used in electronic clocks, gas ovens, inkjet printers, and a variety of other devices. It is also used in scientific instruments, such as microscopes, that require extremely precise movements. The highest piezoelectric mechanical responses now exist in lead-based perovskite materials, such as $Pb(Zr, Ti)O_3$ (PZT). Lead found in cosmetics, paints, or soldering materials has been eliminated in commercial products via a growing legislative and moral campaign. There is also a need for more eco-friendly lead-free nanomaterials owing to the lack of acceptable substitutes for lead toxicity and anticipated further restrictions on the use of lead-based piezoelectric nanofillers. This study trend has also developed into nanoscience and nanotechnology, because of the breakthroughs.

In the present chapter, recent progress and development on the synthesis and application of the lead-free piezoelectric nanostructure either in individual particles or hybrid composite materials are discussed. The material presented in this chapter gives an in-depth look into lead-free piezoelectric nanostructures and associated energy harvesting systems.

H. S. Devi (✉) · M. Maisnam
Department of Physics, National Institute of Technology Manipur, Imphal, Manipur 795004, India

B. P. Swain (ed.), *Advances in Nanostructured Materials*, Materials Horizons:
From Nature to Nanomaterials, https://doi.org/10.1007/978-981-16-8391-6_17

2 Origin of the Piezoelectric Effect

Pierre and Jacques Curie discovered piezoelectric materials in 1880. Hundreds of piezoelectric materials are naturally occurring. Piezoelectric materials such as quartz, Rochelle salts, topaz, and cane sugar are naturally occurring ones. It is critical to understand the crystal structures of piezoelectric materials as well as the physics underlying how the piezopotential is formed in piezoelectric materials. When we apply mechanical pressure, they become polarized, and when we provide voltage, the material deforms. However, only specific materials have this feature. The crystal structure must have no center of symmetry to demonstrate this characteristic. Figure 1 shows an example of a hexagonal crystal structure developing piezopotential under mechanical stress. As shown in Fig. 1a, when we draw a line in any direction, the charge that remains there is not equal to the charge that remains in the opposite direction to the line at equal distance. It is important to note, however, that before any mechanical stress is applied to deform the structure, the net positive charge center, and the negative charge center, coincide with each other. The net charge center of the positive and negative charges is located at point "O." When mechanical stress is applied along the Y-axis, the negative charge center and the positive charge center no longer coincide due to the change in the respective positions of the positive and negative charges along the deformed direction, resulting in a polarization along the direction of the applied force. When the force is applied along the X-axis, the polarization is along the Y-axis, as shown in Fig. 1c. Therefore, it is possible to produce polarization in another direction when the applied force is in another direction. The linear relation between the applied stress, Tj, and polarization, Pi, is given as

$$P_i = d_{ij} T_j \tag{1}$$

where d_{ij} is the piezoelectric coefficient, "i" and "j"s represent the directions. Similarly, when we apply an electric field E_i, the deformation produced in the material

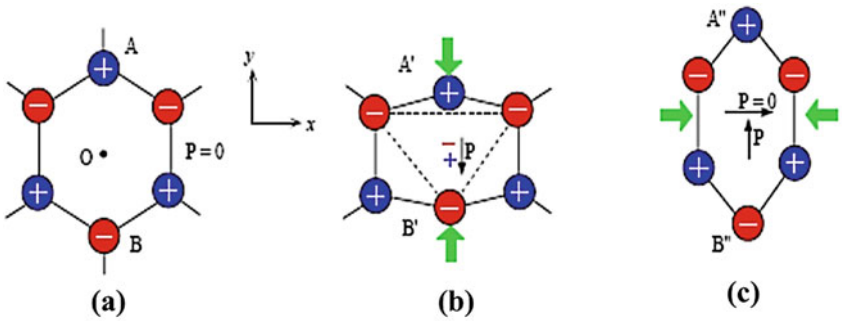

Fig. 1 A hexagonal crystal structure in three different states—**a** with no stress **b** stress on Y-axis, and **c** stress on X-axis. Due to the stress applied either in Y-axis or X-axis, polarization is developed. Reproduced from [1], copyright © Creative Commons Attribution License 4.0

S_j is related as

$$S_j = d_{ij} E_i \tag{2}$$

The maximum piezoelectric coefficient (d = 480 pm/V) is found in lead zirconate titanate (PZT). However, as it contains Pb^+, which is toxic to the environment, researchers have been looking for many lead-free piezoceramics, which include $BaTiO_3$, $BaNiTiO_3$, $KNaNbO_3$ (KNN), etc.

3 Lead-Free Piezoelectric Materials

The zero-dimensional, one-dimensional, and two-dimensional piezoelectric nanostructures are classified according to their configuration and dimensions [2]. The categories of piezoelectric nanostructure are as follows: nanoparticles, nanocubes, nanowires, nanorods, nanofibers, and nanotubes are in OD PNs; 1D piezoelectric nanostructures comprise nanowires, nanorods, nanofibers, and nanotubes; and 2D PNs include nanoplates and nanofilms.

According to the arrangement of the crystal lattice, the lead-free piezoelectric nanostructures may be roughly categorized into two main categories: (i) perovskite structure and (ii) wurtzite structure. However, there is recent progress in 2D structural material-based piezoelectric nanostructure whose crystal structure is quite different from both perovskite and wurtzite structures. In the subsequent section, the above three categories of piezoelectric nanostructures are discussed.

3.1 Perovskite Structure Piezoelectric Nanostructures

A perovskite is any substance that has a crystal structure that is comparable to the mineral perovskite, which is composed of calcium titanium oxide ($CaTiO_3$). The most common perovskite structure is the ABX_3 formula. A and B are two distinct cations, while X is an anion (most often an oxygen atom). The illustration Fig. 2a shows a lattice with the A-site ions located at the vertices, while the B-site ions are placed in the center of the lattice, and the oxygen ions are placed at the facial or face centers. Due to the crystalline structure of a perovskite exhibiting perfect cubic symmetry, piezoelectricity is not seen, however, deformed structures with non-cubic symmetries may possess piezoelectric property. When considering the structures of perovskite crystals in Fig. 2b, they may move their B-site ions from the cubic body center, which results in a non-centrosymmetric form. Without this deformation, the piezoelectric property cannot be found. In comparison to the research on other perovskite materials, the work on perovskite oxides (ABO_3) is greatly progressed.

ABO_3 is classified into three types: $A^IB^VO_3$, $A^{II}B^{IV}O_3$, and $A^{III}B^{III}O_3$. The valence state of the respective cations is represented by the superscript Roman

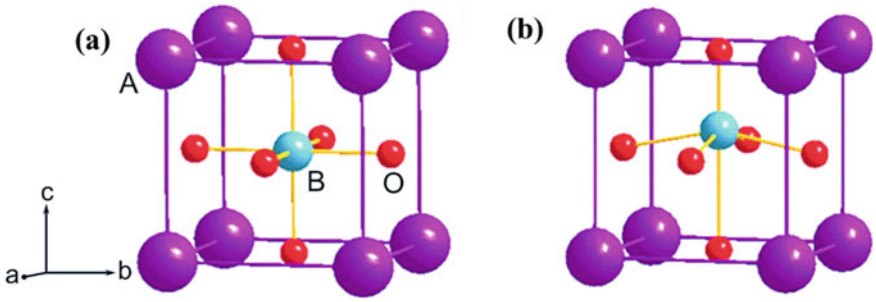

Fig. 2 ABO_3 perovskite structure in **a** cubic and **b** tetragonal phases with polarization variations shown in stereoscopic detail. Reproduced with permission [3], copyright © 2016, Elsevier Ltd

numerals. One of the many promising and environmentally friendly lead-free piezoelectric ceramic materials that can be found inside the $A^{I}B^{V}O_3$ perovskite system is (K, Na)NbO_3. And among the members of the $A^{II}B^{IV}O_3$ group, $BaTiO_3$ is the most important material. It is also commonly utilized in constructing multilayer supercapacitors due to its excellent dielectric property. Other things being equal, group $A^{III}B^{III}O_3$ members include materials like BFO, which are widely regarded multiferroics capable of providing lead-free piezoelectricity in high-temperature applications. The scanning electron microscopy images shown in Fig. 3 reveal the nanorod and nanocube structure of $NaNbO_3$ which was prepared by the hydrothermal method [4].

3.2 Wurtzite Structure Piezoelectric Nanostructures

ZnO, GaN, InN, and ZnS are some of the wurtzite structure piezoelectric materials. Among them, ZnO is the widely used piezoelectric material. The piezoelectric property in the wurtzite structure originates from their non-centrosymmetric structure in the crystal structure. Considering the structure illustrated in Fig. 4, where Zn^{2+} and O^{-2} are stacked one on top of the other. When presented in their intact form, the cation and anion charge centers coincide with one another. When an external force is applied to it, the structure will distort (either compressed or elongated). An electric dipole forms and a piezopotential is generated because the charge centers of the cations and anions are maintained apart.

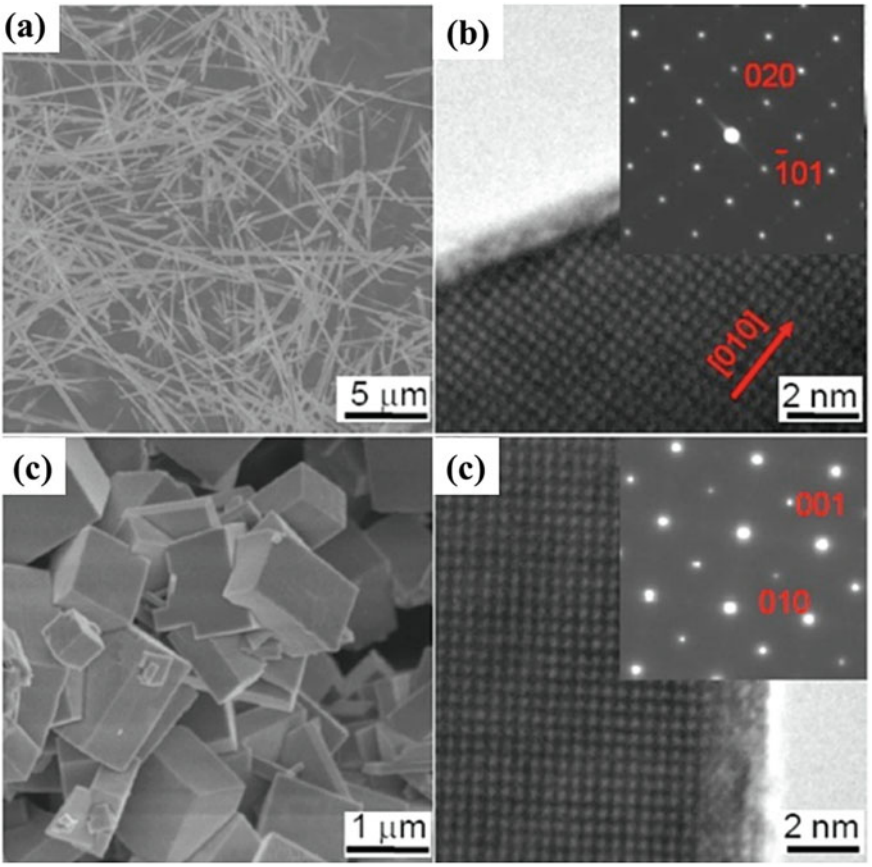

Fig. 3 SEM and TEM images of **a–b** $NaNbO_3$ nanorods and **c–d** $NaNbO_3$ nanocubes. Reproduced with permission [4], copyright © 2011, American Chemical Society

3.3 2-D Piezoelectric Nanostructure

Two-dimensional monolayer transition metal dichalcogenides (TMDCs) and modified graphene are the three generalized piezoelectric 2D nanomaterials. Crystallographic sheets in the in-plane direction (i.e., 2D crystallographic sheets that are non-centrosymmetric and lack inversion symmetry) make 2D piezoelectric materials possible.

Duerloo et al. [6] have shown that monolayer h-BN, MoS_2, $MoSe_2$, $MoTe_2$, WS_2, WSe_2, and WTe_2 have high piezoelectric coupling based on their density functional theory calculations (Fig. 5).

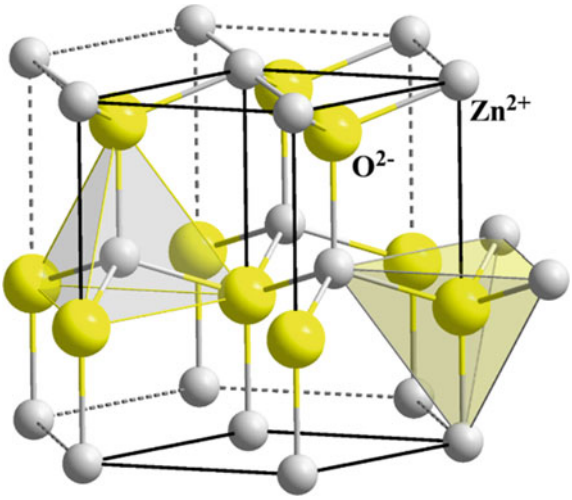

Fig. 4 **a** The Wurtzite structure of ZnO. Reproduced from [5], copyright © public domain

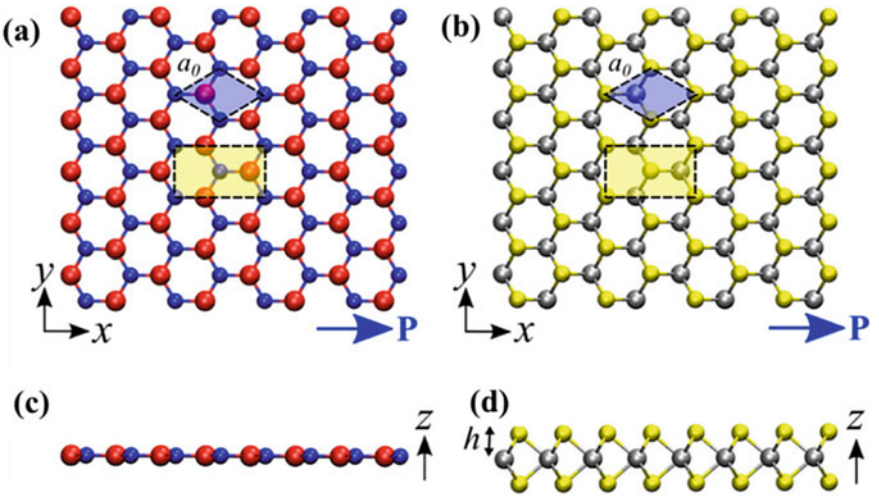

Fig. 5 **a** Boron nitride (h-BN) and **b** trigonal prismatic molybdenum disulfide monolayer top view geometry, where red-, blue-, silver-, and yellow-colored balls represent B, N, Mo, and S atoms, respectively. **c** A view from the side of the atomically thin h-BN monolayer. **d** Out-of-plane structure of the 2H-MoS_2 monolayer as seen from the side. Reproduced with permission [6], copyright © 2012, American Chemical Society

4 Preparation of Piezoelectric Nanostructures

The techniques for nanostructure synthesis may be categorized as "top-down" and "bottom-up." Top-down methods, which include nanolithography, etching, milling, and probe-based technologies, are more often used in downsizing large structures.

Although synthesis of nanostructures by means of a top-down approach, such as lithography, may synthesize them to the specified size and reproduce it many times, their high cost and application to certain materials limit their usage. On the other hand, in terms of diversity of materials, cost, and high-volume manufacture, a process of chemical synthesis may give an alternative approach to making piezoelectric nanostructures. Several manufacturing techniques have been proposed for nanoparticles with piezoelectric properties, including, for example, hydrothermal, solid-state reaction, sol–gel, electrospinning, molten salt reaction. The adjustment of reaction parameters differs based on the conventional manufacturing methods. The nanostructure size is subject to change depending on reaction time, temperature, raw ingredients, pH value, and template type. Some of the important methods which are commonly employed for the synthesis of the lead-free piezoelectric nanostructures are discussed in the consequent subsections.

4.1 Hydrothermal Method

The hydrothermal method is a process for creating nanostructured materials in which an aqueous solution is utilized as a reaction system that is enclosed inside a vessel to generate high temperature and high pressure. Materials can dissolve and then crystallize, which is impossible at normal temperatures and pressures. The primary processes of crystalline development include the processes in which the reactants are first dissolved into the aqueous solution to produce either ions or molecular groups; the second stage entails transporting these ions or molecules to an area of the solution with lower temperature. Because the ions/molecules move to the colder zone, the solution becomes supersaturated, resulting in the production of seed crystals [7]. As a result, the reaction system is experiencing adsorption, decomposition, and desorption activities all at the same time. Finally, the dissolved substances solidify. The temperature and pressure inside the reaction system have a large influence on the morphology of the crystallized materials. For the experimental synthesis of nanostructured materials, the solution is placed in a Teflon beaker and sealed inside a stainless-steel jacket (autoclave), as shown in Fig. 6, to contain the high pressure generated during the reaction. To maintain the temperature, the entire system is placed inside an oven.

Using the hydrothermal method, various lead-free piezoelectric nanostructures can be synthesized. It can even be used to grow vertically oriented nanostructures. One of the most commonly used materials which can be easily grown using the hydrothermal method is ZnO. Xu et al. [9] have shown that ZnO NW arrays may grow on any substrate so long as the surface is flat (polymer, glass, semiconductor, metal, and more). Zinc nitrate and hexamethylenetetramine (HMTA) were combined at a ratio of one-to-one. This is an inventive, low-cost, time-efficient, and scalable way for synthesizing ZnO NW arrays for a variety of purposes, including field emission, vertical field-effect transistor arrays, nanogenerators, and nano piezotronics. In a work by L. Vayssieres, he demonstrated the growth of ZnO nanorod arrays from zinc nitrate hexahydrate ($Zn(NO_3)_2.6H_2O$) and methenamine ($C_6H_{12}N_4$) [10]. He has

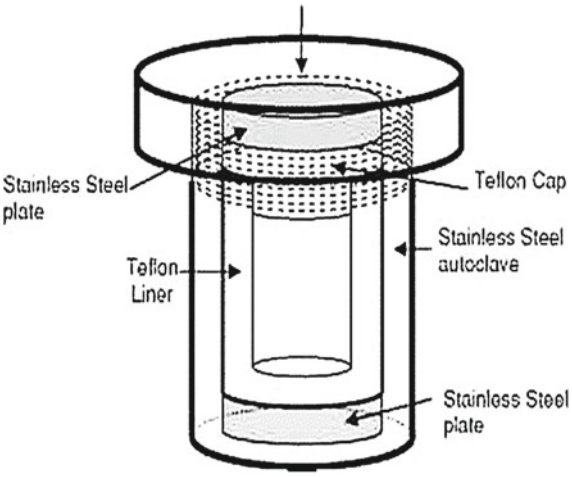

Fig. 6 An illustrative schematic design of an autoclave lined with Teflon for use in the hydrothermal technique. Reproduced from [8]

shown that a non-template, non-surfactant aqueous synthesis of advanced metal oxide thin films is capable of producing films with controlled complexity and cheap cost at large scales, as well as at low temperatures. Figure 7 shows ZnO nanorods grown over a plastic substrate which was synthesized from $Zn(NO_3)_2$ aqueous solution using hydrothermal-electrochemical method [11].

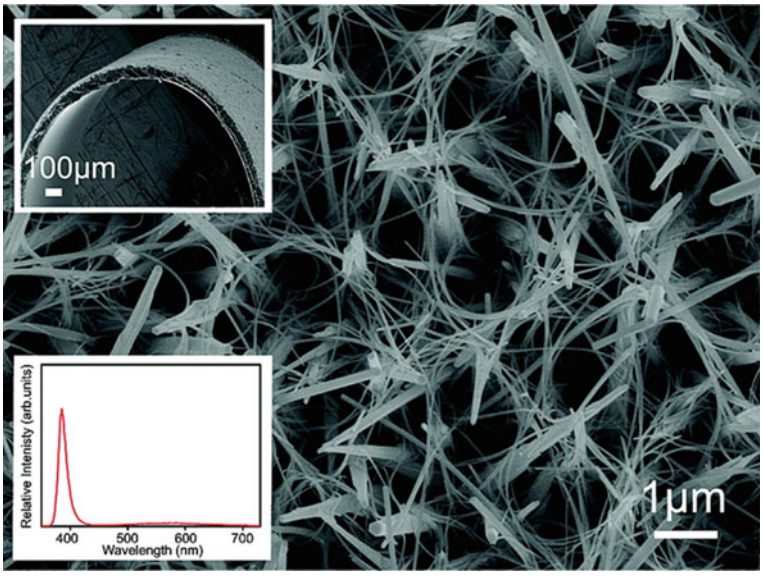

Fig. 7 ZnO nanorods synthesized by hydrothermal-electrochemical method, which are grown over a flexible substrate as shown in the upper inset. The lower inset shows the photoluminescence emission spectra. Reproduced with permission [11], copyright © 2009, American Chemical Society

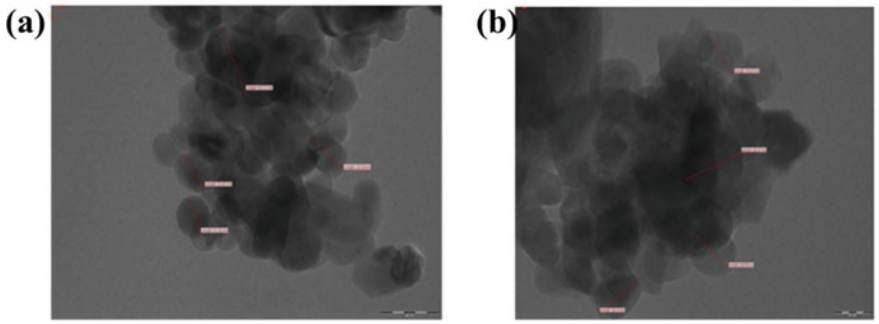

Fig. 8 TEM pictures of **a** pure ZnO and **b** ZnO which is doped with 15% manganese. Reproduced with permission [12], copyright © 2016, Elsevier Ltd

4.2 Sol–Gel Method

Sol–gel polymerization is the method by which a molecular precursor undergoes polycondensation processes in a liquid. After the solution of precursors is hydrolyzed, a colloidal suspension is formed, which is subsequently made into a gel by aggregation. Crystallization processes need calcination at high temperatures.

The $Zn_{1-x}Mn_xO$ (x = 0.00, 0.05, 0.10, and 0.15) has been fabricated by Mote et al. [12]. Zinc acetate dihydrate, Manganese acetate, and analytical reagent grade N-dimethylformamide (DMF) were used in the absence of any further treatment to form the precursor materials. Figure 8a, b illustrates the synthesis of the generated pure ZnO, as well as a doped form with Mn.

4.3 Solid-State Method

Ferroelectric powders with excellent particle shapes can be synthesized via solid-state reaction pathways from oxides and carbonates. Solid-state reaction synthesis has the added benefit of being both cost-effective and simple to implement. As a result, this approach is particularly attractive for technical applications. The solid-state reaction technique is a method of high-temperature synthesis. At room temperature, the solids do not naturally react with each other and must be heated to a considerably higher temperature. The feasibility and pace of the solid-state reaction are determined by various elements, including reaction circumstances, reactant structural features, solid surface area, reactivity, and thermodynamic free energy. The initial components in a typical synthesis technique are oxide precursors. Using an agate mortar and pestle, the needed amount of chemicals is weighed and pounded to a fine powder. During the mixing process, the reaction begins spontaneously, accompanied by the production of heat and water vapour. Acetone, ethanol or water, etc. are sometimes used as a mixing

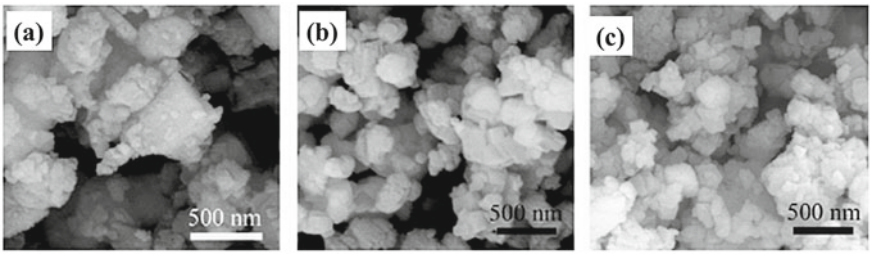

Fig. 9 FESEM images of $(K_{0.44+x}Na_{0.52}Li_{0.04})(Nb_{0.86}Ta_{0.10}Sb_{0.04})O_3$ powders: **a** x = − 0.06, **b** x = 0.00 and **c** x = 0.04. Reproduced with permission [13], copyright © 2010, Elsevier Ltd

medium to achieve a uniform mixture. The ground sample is put in alumina/platinum crucibles and heated to a high temperature for a specific amount of time.

Following a solid-state reaction approach, Rubio-Marcos et al. [13] synthesized (K,Na,Li)(Nb,Ta,Sb)O_3. Before combining the components, the separate carbonate and oxide raw materials were milled to improve particle size. The fabricated nanoparticle is of size ranging from 50 to 200 nm. Figure 9a–c shows the synthesized modified KNN powders. Amirkhanlou et al. [14] synthesized nanocrystalline/nanoparticle ZnO utilizing a high-intensity ball milling technique. As a starting material, commercially obtainable ZnO powder particles with a purity of 99.9% and an average particle size of roughly 8 mm were employed. A high-energy planetary ball mill equipment was used for ball milling at various milling periods. They even got ZnO powder particles with crystallite sizes of 15 nm and particle sizes of around 60 nm.

4.4 Molten Salt Reaction

One such prospective technology that can be extensively applied by researchers in various domains is the molten salt synthesis (MSS) technique. This is only one of several innovative and cutting-edge technologies that might benefit researchers in a wide range of disciplines. To make sure the combination reaches the melting point of the salt, a low-melting-point salt is added to the reactants. In other words, the solvent is molten salt.

To date, the gram-scale and environmentally friendly molten salt synthesis approach with repeatable shape control and no surfactant use have allowed for the simple and efficient fabrication of several oxides, such as niobates, titanates, ferrites, and cobalt oxide nanostructures, among others.

Xue et al. [15] synthesized $BaTiO_3$ powders using the molten salt synthesis technique. They have shown that the molar ratio of NaCl to KCl, as well as the calcination temperature, impact the particle size of $BaTiO_3$. Figure 10 shows the synthesized $BaTiO_3$, which is found to have a melting point of about 620 °C. $0.948K_{0.5}Na_{0.5}NbO_3$–$0.052LiSbO_3$ powder and $NaNbO_3$ were also synthesized by

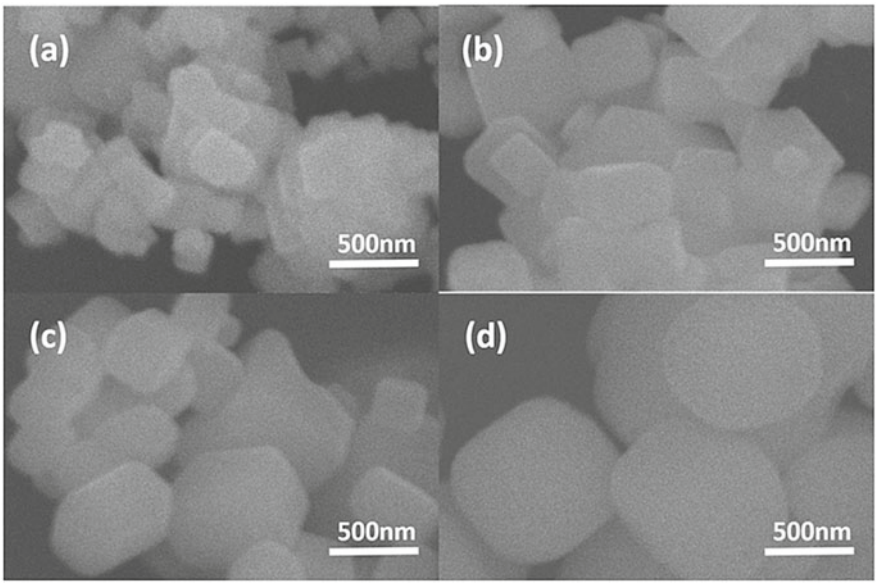

Fig. 10 SEM images of $BaTiO_3$ nanostructures prepared molten salt synthesis technique which is calcined at different temperatures **a** 700 °C, **b** 800 °C, **c** 900 °C, and **d** 1000 °C. Reproduced with permission [15], copyright © 2017, Elsevier Ltd

the molten salt reaction technique in the respective works by Phatungthane et al. [16] and Ge et al. [17].

5 Applications

Piezoelectric nanostructures have become rather popular for sensing and harvesting energy. The benefit of piezoelectric devices over other mechanical energy harvesting devices is that the other devices are incompatible with changes in humidity and are subject to mechanical abrasion, as well as an encapsulating issue. This explains why there has been an increased interest in piezoelectric energy harvesters over the past decade, which are capable of harvesting mechanical energy and transforming it into electrical energy output. When they initially discovered that ZnO nanowires could generate energy, Professor Zhong Lin Wang and his research group came up with the name nanogenerator to describe the concept [18]. Vertically aligned ZnO nanowires were grown on an α-Al_2O_3 substrate. To undertake atomic force microscopy (AFM) measurements on the ZnO nanowires, a conducting AFM tip was brought into close contact with the nanowires and so imposing a mechanical pressure on the wires. Since crystal structure deformation results in piezopotential development, the ZnO structure undergoes a mechanical deformation that is detected by a conducting AFM

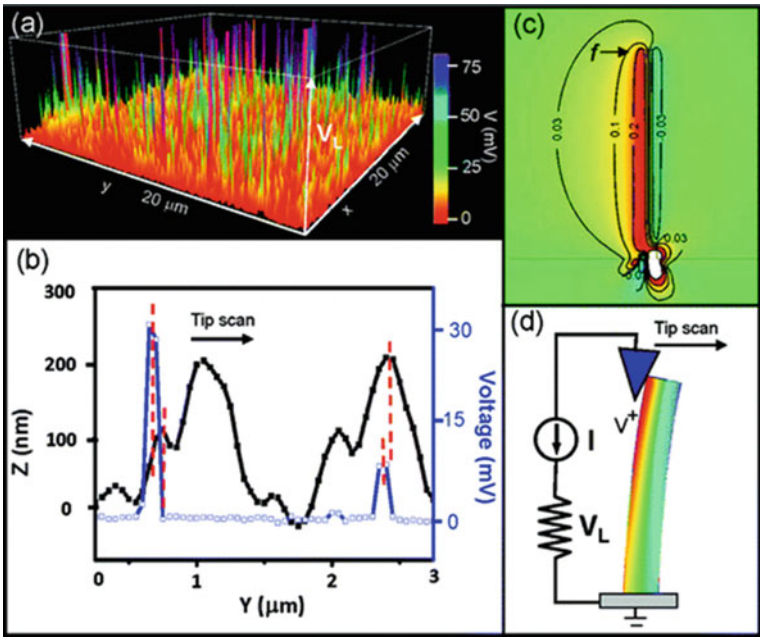

Fig. 11 **a** The 3D plot of voltage measured from the piezoelectric nanogenerator of ZnO nanorod arrays, **b** Height and voltage measured at different points along with a line scan of 3 μm length, **c** Calculated piezopotential when ZnO nanorod is deformed by using AFM tip and **d** schematic of the experimental setup where AFM tip used to impart pressure on ZnO while the voltage dropped across a load resistance is measured. Reproduced with permission [19], copyright © 2009, American Chemical Society

tip. Figure 11 shows a similar work, where the p-type ZnO nanorods were deformed by using a conducting AFM tip and measured the output potential across a load resistance [19].

Afterward, there has been lots of progress in designing and improving the efficiency of the piezoelectric nanogenerator [20–22]. The piezoelectric nanostructures are grown over a substrate or it is mixed into a polymer matrix to make the piezoelectric nanogenerator. Seol et al. [23] demonstrated a piezoelectric nanogenerator fabricated from the vertically grown $BaTiO_3$ nanorods which are densely packed and they called it a "nanoforest." To create tightly packed vertical nanowires and nanovoids, they employed a metal-assisted chemical etching procedure known as mac-etch.

In a recent work by P-Che Lee et al. [24] developed a porous ZnO film that shows much enhanced piezoelectric output and demonstrated its application as a force sensor. By annealing a sputtered ZnO thin film (650–950 °C), they produced a porous ZnO structure. It is possible to boost the output voltage of primitive PENG (up to 3 mV) by 7.5 times by using a porous ZnO thin sheet (0.4 mV). ZnO thin-film pores boost the sensor's piezotronic sensor sensitivity by 6.9 times. Sometimes multiple

steps required fabrication processes are employed to fabricate multiple devices at once, which will give combined output from individual units. Zhu et al. [25] used a scalable sweeping printing approach to transfer vertically produced ZnO nanowires to generate horizontally aligned arrays. To link all the horizontally aligned nanowires of ZnO, Au was placed parallel to the wires, and when bent, a circuit voltage of 2.03 V and a power density of ~11 mW/cm^3. Figure 12 shows the procedures used in fabricating the gadget.

Aleman et al. [26] demonstrated a piezoelectric nanogenerator which was made up of a sandwich structure of Ti–$BaTiO_3$–graphite–Ti encased in polydimethylsiloxane. Several works on other lead-free piezoelectric nanostructures $NaNbO_3$, [4] $ZnSnO_3$, [27–29], GaN, [30–32], etc. have been developed.

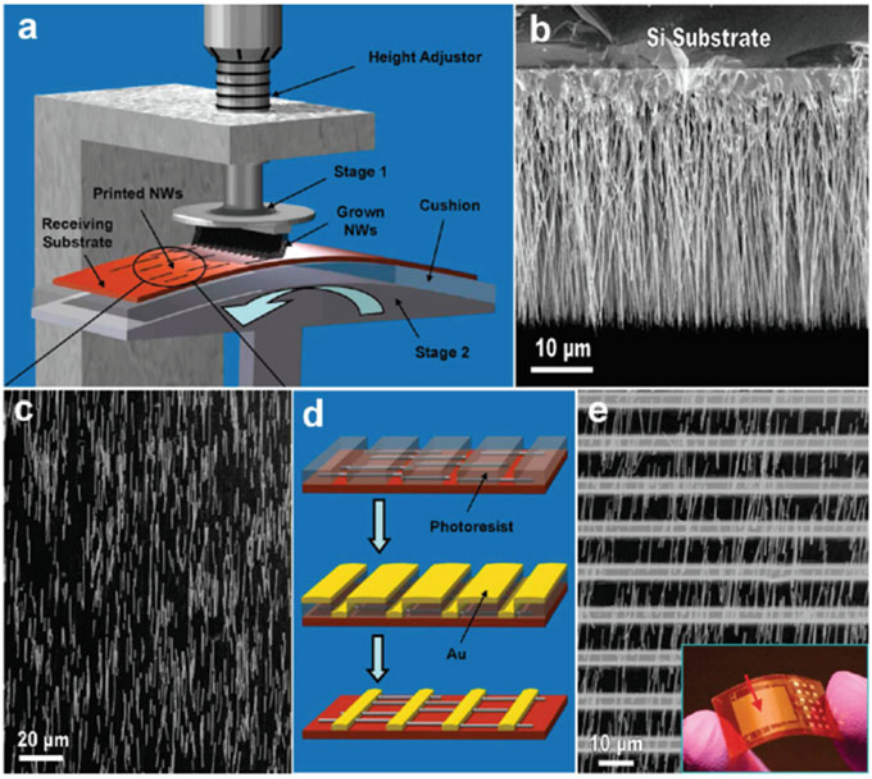

Fig. 12 **a** Experimental setup where a sweeping printing device is used to transfer the vertically grown ZnO nanowires to a flexible substrate, **b** SEM images of as-grown vertically aligned ZnO nanorods, **c** SEM images of the ZnO after being transferred to the substrate (**c**) steps showing how the parallel strips of Au electrodes were bonded to the ZnO nanowires and **d** SEM images of the Au electrodes bonded to the ZnO nanowires while the inset of the figure shows the photographic image of the actual fabricated device. Reproduced with permission [25], copyright © 2010, American Chemical Society

6 Summary and Outlooks

In this chapter, we have covered a brief introduction to the principles of piezoelectric materials, different lead-free piezoelectric nanostructures, their synthesis processes, and their applications on energy harvesting devices. People's interest in this material class has only increased because new applications have emerged and their present device performance has improved. However, it is important to further carry research on cost-effective synthesis techniques of the lead-free piezoelectric nanostructure, and their large-scale production. Till now, the theoretical understanding of the change in the piezoelectric property of the lead-free piezoelectric nanostructures is not fully understood, which can be a good research area in the future.

References

1. Ajienka ADI (2011) Application of piezoelectric energy generated from quartz plus semi-precious metals on wax deposition control. J Pet Gas Eng 5:93–98
2. Zhang Y, Kim H, Wang Q, Jo W, Kingon AI, Kim SH, Jeong CK (2020) Progress in lead-free piezoelectric nanofiller materials and related composite nanogenerator devices. Nanoscale Adv 2:3131–3149
3. Cheng LQ, Li JF (2016) A review on one-dimensional perovskite nanocrystals for piezoelectric applications. J Materiomics 2(1):25–36
4. Jung JH, Lee M, Hong J Il, Ding Y, Chen CY, Chou LJ, Wang ZL (2011) Lead-free NaNbO3 nanowires for a high output piezoelectric nanogenerator. ACS Nano 5:10041–10046
5. File: Wurtzite polyhedra.png—Wikimedia commons. https://commons.wikimedia.org/wiki/File:Wurtzite_polyhedra.png
6. Duero KAN, Ong MT, Reed EJ (2012) Intrinsic piezoelectricity in two-dimensional materials. J Phys Chem Lett 3:2871–2876
7. Yang G, Park SJ (2019) Conventional and microwave hydrothermal synthesis and application of functional materials: a review. Materials 12(7):1177
8. Solution phase methods based on hydrothermal synthesis—nanoscale materials. https://www.texaspowerfulsmart.com/nanoscale-materials/solution-phase-methods-based-on-hydrothermal-synthesis.html
9. Xu S, Lao C, Weintraub B, Wang ZL (2008) Density-controlled growth of aligned ZnO nanowire arrays by seedless chemical approach on smooth surfaces. J Mater Res 23:2072–2077
10. Vayssieres L (2003) Growth of arrayed nanorods and nanowires of ZnO from aqueous solutions. Adv Mater 15:464–466
11. Park SK, Park JH, Ko KY, Yoon S, Chu KS (2009) Hydrothermal—electrochemical synthesis of ZnO nanorods. Cryst Growth Des 9:3615–3620
12. Mote VD, Purushotham Y, Dole BN (2016) Structural, morphological, physical and dielectric properties of Mn-doped ZnO nanocrystals synthesized by sol-gel method. Mater Des 96:99–105
13. Rubio-Marcos F, Romero JJ, Martín-Gonzalez MS, Fernández JF (2010) Effect of stoichiometry and milling processes in the synthesis and the piezoelectric properties of modified KNN nanoparticles by solid-state reaction. J Eur Ceram Soc 30:2763–2771
14. Amirkhanlou S, Ketabchi M, Parvin N (2012) Nanocrystalline/nanoparticle ZnO synthesized by high energy ball milling process. Mater Lett 86:122–124
15. Xue P, Hu Y, Xia W, Wu H, Zhu X (2017) Molten-salt synthesis of BaTiO3 powders and their atomic-scale structural characterization. J Alloys Compd 695:2870–2877
16. Phatungthane T, Samran B, Rujijanagul G (2017) Synthesis of modified K0.5Na0.5NbO3 powder by molten-salt technique. Key Eng Mater 728:160–165

17. Ge H, Hou Y, Xia C, Zhu M, Wang H, Yan H (2011) Preparation and piezoelectricity of NaNbO3 high-density ceramics by molten salt synthesis. J Am Ceram Soc 94:4329–4334
18. Wang ZL, Song J (2006) Piezoelectric nanogenerators based on zinc oxide nanowire arrays. Science (80–.) 312:242–246
19. Lu MP, Song J, Lu MY, Chen MT, Gao Y, Chen LJ, Wang ZL (2009) Piezoelectric nanogenerator using p-type ZnO nanowire arrays. Nano Lett 9:1223–1227
20. Hasan MR, Baek SH, Seong KS, Kim JH, Park IK (2015) Hierarchical ZnO nanorods on Si micropillar arrays for performance enhancement of piezoelectric nanogenerators. ACS Appl Mater Interfaces 7:5768–5774
21. Wang ZL, Yang R, Zhou J, Qin Y, Xu C, Hu Y, Xu S (2010) Lateral nanowire/nanobelt based nanogenerators, piezotronics, and piezo-phototronics. Mater Sci Eng R Rep 70:320–329
22. Lee J-H, Yoon H-J, Kim TY, Gupta MK, Lee JH, Seung W, Ryu H, Kim S-W (2015) Micropatterned P(VDF-TrFE) film-based piezoelectric nanogenerators for highly sensitive self-powered pressure sensors. Adv Funct Mater 25:3203–3209
23. Seol ML, Choi JM, Kim JY, Ahn JH, Moon D Il, Choi YK (2013) Piezoelectric nanogenerator with a nanoforest structure. Nano Energy 2:1142–1148
24. Kim HG, Kim EH, Kim SS (2021) Growth of ZnO nanorods on ito film for piezoelectric nanogenerators. Materials (Basel) 14
25. Zhu G, Yang R, Wang S, Wang ZL (2010) Flexible high-output nanogenerator based on lateral ZnO nanowire array. Nano Lett 10:3151–3155
26. Aleman CKA, Narvaez JAB, Lopez GDB, Mercado CC (2020) Array pattern effects on the voltage output of vertically aligned BaTiO 3 nanotubular flexible piezoelectric nanogenerator. MRS Commun 10:500–505
27. Rovisco A, Dos Santos A, Cramer T, Martins J, Branquinho R, Águas H, Fraboni B, Fortunato E, Martins R, Igreja R, Barquinha P (2020) Piezoelectricity enhancement of nanogenerators based on PDMS and ZnSnO3 nanowires through microstructuration. ACS Appl Mater Interfaces 12:18421–18430
28. Guo R, Guo Y, Duan H, Li H, Liu H (2017) Synthesis of orthorhombic perovskite-type ZnSnO3 single-crystal nanoplates and their application in energy harvesting. ACS Appl Mater Interfaces 9:8271–8279
29. Paria S, Ojha S, Karan SK, Si SK, Bera R, Das AK, Maitra A, Halder L, De A, Khatua BB (2020) Approach for enhancement in output performance of randomly oriented ZnSnO3 nanorod-based piezoelectric nanogenerator via p-n heterojunction and surface passivation layer. ACS Appl Electron Mater 2:2565–2578
30. Fu J, Zong H, Hu X, Zhang H (2019) Study on ultra-high sensitivity piezoelectric effect of GaN micro/nanocolumns. Nano Converg 6:1–10
31. Johar MA, Waseem A, Hassan MA, Bagal IV, Abdullah A, Ha JS, Ryu SW (2020) Highly durable piezoelectric nanogenerator by heteroepitaxy of GaN nanowires on Cu foil for enhanced output using ambient actuation sources. Adv Energy Mater 10:2002608
32. Waseem A, Johar MA, Hassan MA, Bagal IV, Abdullah A, Ha JS, Lee JK, Ryu SW (2021) Flexible self-powered piezoelectric pressure sensor based on GaN/p-GaN coaxial nanowires. J Alloys Compd 872:159661

Chapter 18
Lead-Free Ferroelectrics: Barium Titanate Based Ceramics: Past, Present, and Future

Devidas Gulwade

1 Introduction

The ferroelectric era began in the early twentieth century after the existence of permanent electric dipoles was postulated, followed by the experimental discovery in sodium potassium tartrate [1, 2]. Sodium potassium tartrate, also termed as Rochelle salt, had been discovered by Elie Seignette at La Rochelle, France, 200 years before the discovery of ferroelectricity [3]. The pyroelectric and piezoelectric effects in Rochelle salt were studied prior to the discovery of ferroelectricity. This was the first material exhibiting a switching of polarization in an applied electric field. The systematic study of the properties of Rochelle salt and its analogy with the ferromagnetic materials established the term "ferroelectric" for the observed set of properties. Following the discovery of ferroelectricity in Rochelle salt, the first formulation of ferroelectric theory took a long time due to the difficulty in appreciating the loss of ferroelectricity upon departure from stoichiometry. Rochelle salt exhibits a complicated structure with 120 atoms in the unit cell and even today it is one of the most complicated structures in the ferroelectric family. Potassium dihydrogen phosphate (KDP), the second ferroelectric material took over a decade to be discovered. As a consequence, it was thought that ferroelectricity as being a rare phenomenon and raised confusion about the necessity of the presence of an O–H bond for ferroelectricity.

The ferroelectricity in $BaTiO_3$ (BT) was discovered in simultaneous independent studies [4–6]. Cross et al. [7] have reviewed initial progress in research in ferroelectric. The simplicity of the perovskite structure, the chemical and mechanical stability, ease of synthesis, and ferroelectricity at room temperature made BT the most widely explored ferroelectric material. The simpler crystallographic structure offered an

D. Gulwade (✉)
Vivekanand Education Society's College of Arts, Science, and Commerce, Sindhi Society, Chembur, Mumbai, India
e-mail: devidas.gulwade@ves.ac.in

B. P. Swain (ed.), *Advances in Nanostructured Materials*, Materials Horizons: From Nature to Nanomaterials, https://doi.org/10.1007/978-981-16-8391-6_18

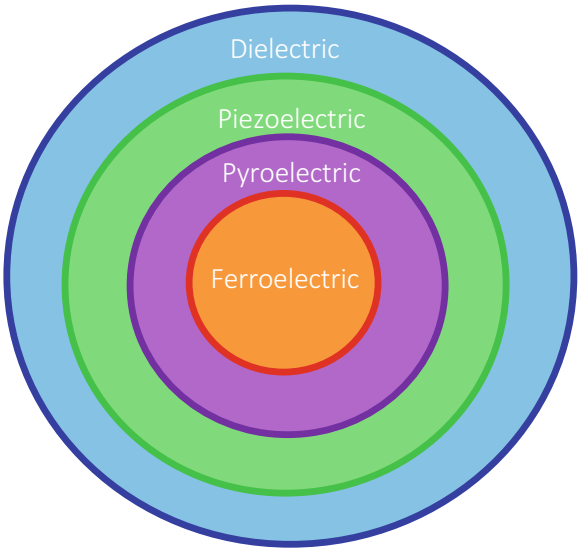

Fig. 1 Subsets of dielectric materials

opportunity for better insights into the origin of ferroelectricity. The discovery of the ferroelectric perovskites was followed by the investigation of various ferroelectric materials and they attracted the attention of researchers for their potential use in pyroelectric detectors, memories, capacitors, transducers, thermistors, electro-optic modulators, etc.

In total 32 point groups, 11 exhibit center of symmetry, i.e., net electric dipole moment cannot exist in it. Out of the remaining non-centrosymmetric 21 classes, 20 may exhibit piezoelectric effect, the change in polarization with applied stress. Further, a subgroup of piezoelectric materials exhibits spontaneous polarization which changes with temperature change, termed the pyroelectric effect. Ferroelectrics are the subgroup of the pyroelectric class, having two states of polarization that can be switched from one state to another in the presence of an electric field (see Fig. 1).

2 Structure, Synthesis, and Transitions in BT

In the perovskite ABO_3 structure, A cations are in 12-fold coordination while B cations are in sixfold coordination. The structure is depicted in Fig. 2; in the cubic form, the B cation at the centre of the cube is surrounded by oxygen octahedra, formed by oxygen ions at face-centered positions and A cations at the corner positions. The parent member of the family is the mineral perovskite, namely, $CaTiO_3$, and other important members are $BaTiO_3$, $PbTiO_3$, $SrTiO_3$, $BaZrO_3$, and $PbZrO_3$. Barium titanate is the first perovskite established as a ferroelectric [5]. Thereafter, BT received the attention of different research groups and was followed by series of investigations

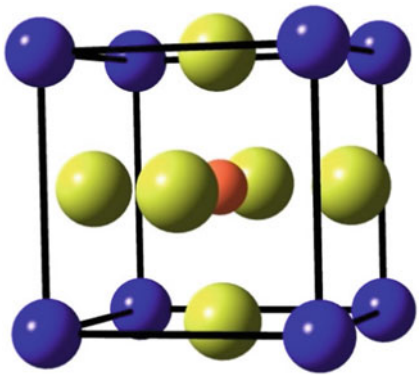

Fig. 2 Crystal structure of perovskite BT

on crystal structure [8–10], crystallographic transitions, the phenomenology of phase transition [11], and domain structure [12–14].

Following a debate, in the beginning, the consistent work of Kaenzig et al. [15, 16] Magaw et al. [8], and Evans et al. [17, 18] established the existence of tetragonal structure at room temperature; the crystal structure, fractional coordinates, and thermal parameters of the ions were reported. However, there was little confidence in the values of thermal factors and the atomic shifts, as it was affected by many factors including systematic errors such as extinction, absorption, and incorrect scaling [19]. Also, the wide variation in the scattering factors of barium and oxygen for X-rays and a slight distortion from the cubic phase added difficulties in establishing a unique solution of the structure. The neutron data has been of great use for such critical analysis, as scattering is less sensitive to angle and atomic number. Further, single-crystal neutron diffraction data have been used to confirm the atomic shift and temperature factors; the shifts in atomic parameters are predicted unambiguously [20].

The fractional coordinates of atoms in the tetragonal structure for BT are provided in Table 1, to exhibit changes in the structure as compared to the cubic phase. The tetragonal phase is slightly elongated in the z-direction as compared to the cubic phase; the lattice parameter "c" is more than "a" by 1 percent for BT at room temperature. A parameter z in Table 1 is a small deviation in positions of atoms compared with the body centre and phase centre symmetric positions of atoms in the cubic phase. The relative shift of Ti and O leads to spontaneous polarization, as a result of a small separation between positive and negative charge centres.

Table 1 Fractional coordinates in tetragonal structure

Ion	Fractional coordinate
Ba	(0,0,0)
Ti	(0.5,0.5,0.5 + z_{Ti})
O	O1: (0.5, 0.5, z_{O1})
	O2: (0,0.5,0.5 + z_{O2}), (0.5, 0,0.5 + z_{O2})

On cooling, at ~134 °C, the cubic unit cell of $BaTiO_3$ elongates along an edge resulting in a tetragonal structure. The high-temperature centrosymmetric cubic phase changes to a non-centrosymmetric phase and the net polarization sets in, resulting in a ferroelectric phase. Further, at about 0 °C the cube elongates along the face diagonal resulting in an orthorhombic structure. Thereafter, at around −90 °C, the elongation along a body diagonal results in a rhombohedral phase [21]. The change in lattice parameters as a function of temperature above room temperature is exhibited in Fig. 3. The crystallographic transition from tetragonal to cubic phase is depicted at 125 °C. The lattice parameters of the tetragonal phase at room temperature are a = b = 3.99 and c = 4.03 Å. The tetragonal splitting in XRD peaks cannot be observed as the c/a ratio is very close to 1; the tetragonal peaks are observed as a shoulder to the main peak rather than as two well-resolved peaks. Also, the splitting is influenced by grain size and strain effects. Raman spectroscopy is another technique to confirm the transition temperature and the presence of the tetragonal phase. The Raman spectra for pure BT at room temperature as well as a function of temperatures are studied [22, 23]. Raman spectra for pure BT are depicted in Fig. 4. The tetragonal phase depicts two additional bands as compared to the cubic phase at ~340 and 750 cm^{-1}. The intensity of the bands corresponding to the tetragonal phase decreases with an increase in temperature and disappears above ~134 °C. The disappearance of the additional bands corroborates with the dielectric measurement and a corresponding change in lattice parameters in pure BT.

BT also exhibits a hexagonal phase that is non-ferroelectric. In the tetragonal phase, all octahedra are corner sharing. However, in the hexagonal polymorph, two-thirds of the octahedra share a face, i.e., Ti is closely placed to each other and their repulsion does not permit ferroelectricity. The electromechanical coupling in the corner-sharing octahedra in the tetragonal phase leads to interaction between vibrating dipoles. The interaction enforces displacement in the Ti position. The comparison between these two polymorphs indicates the vital role of the position

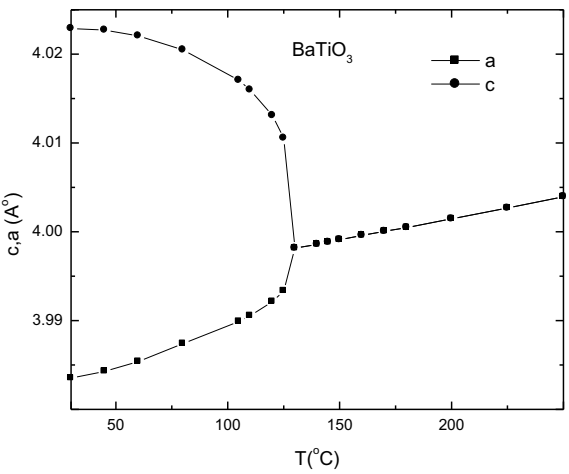

Fig. 3 Change in lattice parameters as a function of temperature

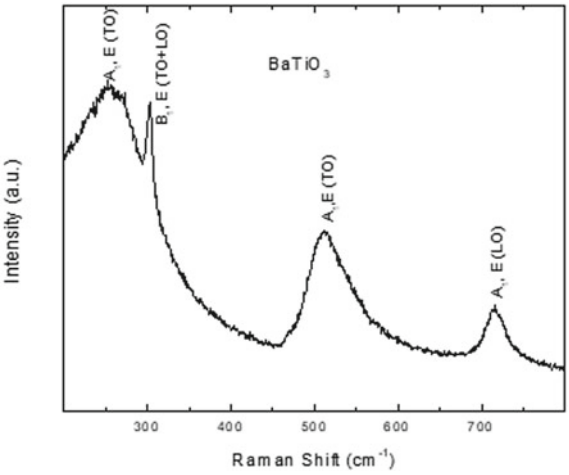

Fig. 4 Raman spectra of BT at room temperature

of Ti in ferroelectricity [24]. The shielding of Ti^{4+} ion in the oxygen cage, shape of oxygen octahedra, and space available to Ti play a key role in ferroelectricity.

Regarding tetragonal to cubic transition, the displacive transition and the Ti rattling concept were prevalent in the beginning [25, 26]. Cochran et al. [27] opposed the Ti rattling concept, with a view that lattice phonon modes should be taken under consideration. If covalency or polarizability are not accounted for, then the short-range forces would be sufficient to keep $BaTiO_3$ in the cubic phase [28]. Below Tc, induced dipoles overcome thermal agitations and the Ti ions are locked in an acentric position displaced toward one of its six oxygen neighbors. Ab-initio calculations depict the existence of covalence between Ti and O and reveal that the effective charge is different from nominal charges for Ti^{4+} and O^{2-} [29–32].

The pure compound has been studied with different synthesis routes in ceramic as well as single crystal form. The widely explored methods for synthesizing BT are solid-state reaction, sol–gel, Pechini process, coprecipitation, and hydrothermal [33–35]. In ceramic form, along with the one-to-one Ba:Ti ratio in BT, the impurity compounds corresponding to other Ba:Ti ratios are observed along with BT, namely, $BaTi_2O_5$, $BaTi_4O_9$, $Ba_2Ti_3O_3$, $BaTi_3O_7$, Ba_2TiO_4 [36, 37]. The formation of the impurity phases at the initial stage of calcination, the reaction between BaO and TiO_2 to form BT does not occur in a single step. Initially part of reactants reacts with each other leading to the partial formation of BT. Further, unreacted $BaCO_3$ reacts with $BaTiO_3$ with a formation of Ba_2TiO_4 [38, 39]. Thereafter, this is converted to $BaTiO_3$ by a reaction with TiO_2. The ferroelectric and piezoelectric properties of $BaTiO_3$ vary with the synthesis route, grain size, stoichiometry.

Research in ferroelectrics was always intending to either understand the basic phenomenology of the ferroelectric transition or to modify properties of the host material for different applications. Many of the doped $BaTiO_3$ family of materials exhibit diffused phase transition rather than a steep transition as in the case of pure $BaTiO_3$. Materials exhibiting a high dielectric constant as well as a lower temperature coefficient of dielectric constant in the temperature range of interest are useful for various Electronic industry standards (EIS) capacitors.

3 Modified Curie–Weiss Law

The tetragonal to cubic transition at 120 °C is accompanied by a steep change in the dielectric constant in BT. Various doping schemes have been adopted to modify the properties of pure $BaTiO_3$. Many dopants change the transition temperature and/or the shape of the transition, namely, the ε versus T plot. A large number of doped compositions exhibit a broad peak in ε versus T plot, diffused phase transition accompanied by a deviation from Curie–Weiss (CW) law, and enhanced frequency dispersion. The CW law and modified CW law are provided in Eqs. 1 and 2.

$$\varepsilon = \frac{C_o}{T - T_o} \tag{1}$$

where T_o is Curie temperature, C_o is Curie Weiss constant, and ε is the dielectric constant.

The behavior in the case of doped BT having diffused phase transition is governed by a modified CW law (Eq. 2) [40].

$$\frac{1}{\varepsilon} - \frac{1}{\varepsilon_{\max}} = \frac{(T - T_{\max})^{\gamma}}{C} \tag{2}$$

where C and γ are constants and ε_{max} is the maximum dielectric constant attained at a temperature T_{max} in ε versus temperature plot.

Typical deviation from linear behavior of CW law is depicted in Fig. 5 [41]. The temperature from which it exhibits deviation from linearity is termed as $T_{dev.}$ The difference between T_{dev} and T_{max} depicts the extent of diffuseness of the transition. The value of γ may be obtained from a graph between log $(1/\varepsilon\text{-}1/\varepsilon_{max})$ and log $(T\text{-}T_{max})$. The value varies from 1 to 2. In the limiting case for classical ferroelectric material, $\gamma = 1$ and Eq. 2 reduces to Eq. 1. The value of γ governs the diffuseness of the transition. The properties of pure perovskites are modified with the dopants resulting in a relaxor or diffuse phase transition. The properties of $BaTiO_3$ are enhanced by different dopants. The widely explored dopants are La, Sn, Sr, Zr, Al, Ga, and Pb. Many of these doped materials exhibit a diffuse phase transition.

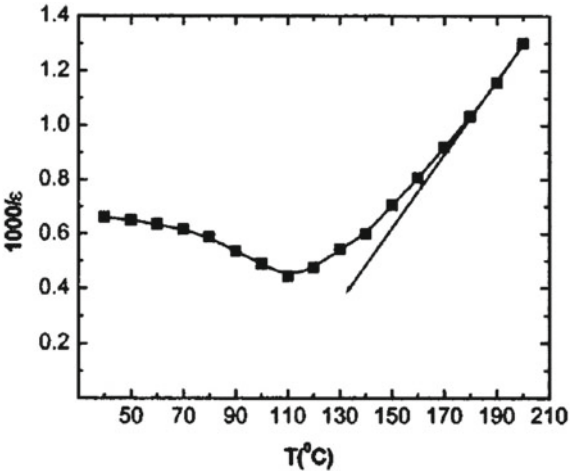

Fig. 5 1000/Ɛ as a function of Temperature for doped BT [41]

4 Grain Size Effect on Ferroelectric Properties

The microstructure influences the ferroelectric properties. Therefore, the various methodologies for synthesis, sintering, and schemes of doping are employed to manipulate microstructure and thereby the properties of $BaTiO_3$. The densification and grain growth mechanism in doped, as well as pure $BaTiO^3$ has been thoroughly investigated [42]. The liquid phase sintering in pure $BaTiO_3$ takes place at 1325 °C. The densification is also followed by an anomalous grain growth resulting in large rounded grains. The anomalous grain growth occurs due to the formation of twins or liquid phase sintering [43, 44]. The combined effect of mutually interlinked parameters such as anomalous grains coalesces of pores and closure of pores leads to de-densification. However, limiting the densification temperature effectively helps to maintain the final grain size for the desired use of material. The conventional sintering consists of a higher grain size over 34 μm with few grains more than 100 μm [45]. Advanced techniques such as hot isostatic pressing [46], spark plasma sintering [47], microwave sintering result in a finer control on grain size [48]. The samples prepared using hydrothermal synthesis or wet chemical synthesis and sintered using spark plasma sintering result in above 95% density having grain size ranging from 0.06 to 0.5 μm [49]. A higher dielectric constant is observed for the 0.5 μm relative to the 0.06 μm grain size. Martirena et. al. [50] have depicted an increase in the diffuseness and decrease in the transition temperature with the decrease in grain size. The transition temperature distribution model has been proposed to explain the observed diffuseness, namely, that different regions exhibit different transition temperatures resulting in the broad rounded peak as a combined effect. The increase in the permittivity for the finer grain size is the effect of the unrelieved stress in the finer grain size as compared to the coarse grain size or based on reduction in the frequency of the 90° domains [51, 52]. Independent studies consisting of different microstructure and grain size distribution on account of different synthesis routes used in investigations

corroborates with the trends discussed above [46, 53–55]. Raman spectra studies of BT of different grain size depicts decrease in tetragonality with the decrease in the grain size corroborating with XRD investigations [23]. These trends are also confirmed using high-resolution synchrotron radiation investigation [56]. The transition temperature decreases with the decrease in grain size corroborating with a corresponding change in tetragonality. The trend observed in BT corroborates with the grain size dependence in other materials such as $PbTiO_3$ [57]. The effects of grain size dependence on transition temperature may be compared with the external hydrostatic pressure as the transition temperature decreases with the increase in external pressure. Also, the finer grains lead to unrelieved stress during phase transformation.

Kinoshita et al. [58] have established that there is no change in the dielectric constant in the paraelectric region. However, the dielectric constant in the ferroelectric region increases with a decrease in the grain size, i.e., effectively due to an increased diffuseness of the transition. The transition temperature, the C-W constant, and the dielectric constant in the paraelectric region are observed to be independent of the grain size. This behavior depicts that the differences observed in the ferroelectric region are borne out of the internal stresses that develop in the ferroelectric tetragonal phase during transformation. There are varied reports about the dependence of grain size on the nature of transition and dielectric constant. However, it has been established that below a critical grain size, ferroelectricity disappears and the structure becomes cubic. The range of this critical size is disputed in the literature as different processing and techniques to interpret the absence/presence of ferroelectricity have been used. The XRD peaks get broader with the decrease in grain size and below some threshold, and the tetragonal splitting appears merged. However, the Raman investigations exhibit the presence of tetragonal phase even for the finer grain size [59]. There is a phenomenological difference between the different techniques; XRD provides an average picture, while the Raman spectroscopy is sensitive to the Ti shift at the unit cell level. Therefore, a faint presence of tetragonal bands in Raman spectra does not necessarily imply a cooperative domain structure.

5 Properties of Doped $BaTiO_3$

The different dopants bring about different effects on the properties and transitions of BT. In general, the effect of the dopant ion on the host lattice is explained based on thumb rules like tolerance factor or the space available for the Ti on the octahedral site. However, the effects cannot be explained by such a simple size rule and there exist many exceptions to it [60]. The effect of few important dopants on the properties of $BaTiO_3$ is discussed below.

5.1 Sn Doping

Sn-doped BT has been investigated by Smolenskii et al. [61] in the early years following the discovery of $BaTiO_3$. The broadening of the transition as a function of dopant concentration is observed and it enhances the dielectric constant at room temperature. The tetragonality(c/a) decreases with an increase in dopant concentration and the structure becomes cubic for 13 m% Sn at room temperature [62]. Therefore, the transition temperature decreases with an increase in Sn dopant concentration; it may be attributed to the lower size of Sn relative to that for the host Ti. Also, the non-ferroelectric Sn on the active Ti site disturbs the long-range order leading to an increase in the diffuseness of the transition, termed as the ferroelectric dilution effect. The increased frequency dispersion observed for higher dopant concentration is explained based on the size and polarization relaxation of the polar nano-regions (PNR). The size and relaxation frequency of PNR governs enhanced change in dielectric constant as a function of frequency [63]. The diffuse transition is also explained based on different phase transition temperatures in different regions of crystal on account of internal stresses and composition fluctuations [64]. The composition fluctuation or inhomogeneity is the difference in the dopant concentration inside the synthesized material. In other words, the observed diffuse transition may be attributed to an unequal spread of Sn in the different regions. Further, the Burns temperature, the maximum temperature at which the polar nano-regions are observed above $T_{max,}$ is found to increase in the compositions exhibiting a diffuse phase transition [65].

5.2 Sr Doping

Strontium titanate exhibits a perovskite structure and is cubic at room temperature. Strontium titanate and BT exhibit a solid solution over the entire composition range. The family of compounds, $Ba_{1-x}Sr_xTiO_3$ having strontium titanate and BT as end members, is termed as BST. The tetragonality decreases with an increase in strontium doping concentration [66–69]. In BST, the three transitions of BT, namely, tetragonal to cubic transition (T_{t-c}), orthorhombic to tetragonal (T_{o-t}), and rhombohedral to orthorhombic (T_{r-o}) decrease at the rate of 3, 2.3, and 1.0 °C/mol, respectively [70]. The effect of Pb and Ca on the three transitions is quite different from that of Sr dopant [21]. The effect of different dopants on transitions of BT cannot be explained or generalized based on simple cation size consideration. The addition of Sr impurity in Barium titanate leads to the formation of local polar clusters that become a precursor for a cubic to tetragonal transition. The existence of both the phases around $T_{max.}$ results in a diffuse phase transition [71]. The phase transformations in BST are also studied using Raman spectroscopy [72, 73]. The change in lattice parameters and dielectric constant for $Ba_{1-x}Sr_xTiO_3$ ($x = 0, 0.1, 0.2$ and 0.25) compositions is depicted in Fig. 6 and high temperature Raman spectra is exhibited in Fig. 7 for $x = 0.25$ composition. It depicts

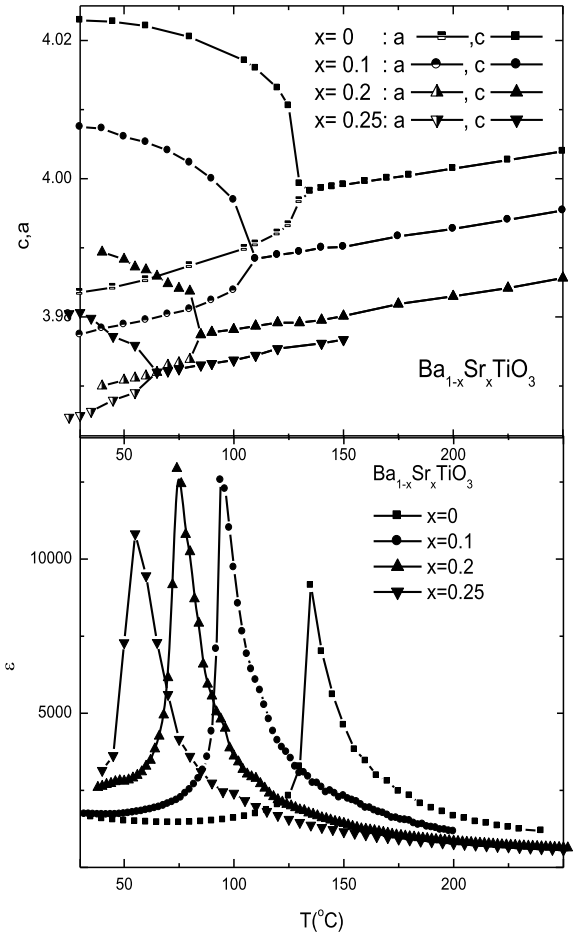

Fig. 6 Lattice parameters (**a**) and dielectric constant (**b**) as a function of temperature for $Ba_{1-x}Sr_xTiO_3$

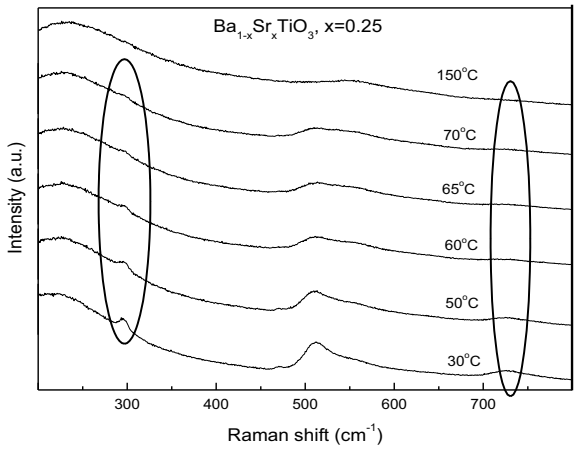

Fig. 7 Raman spectra at different temperature for $Ba_{1-x}Sr_xTiO_3$, $x = 0.25$

that the diffuseness of the transition increases with an increase in dopant concentration. Also, it exhibits that T_{max} and crystallographic transition temperature observed in high-temperature Raman spectra are different. The dielectric constant increases with the increases in Sr dopant concentration and exhibits a maximum for composition and decreases thereafter [74, 75]. The diffuse nature of the transition observed in BST is attributed to inter and intragranular strain and compositional inhomogeneity [76]. Differences in the ferroelectric properties of the solid solution vary with a change in sintering temperature may be attributed to varied microstructure [77, 78]. Magnesium and Manganese additives are added for grain growth inhibition and for trapping electrons, respectively, to improve and optimize the overall performance of BST [79]. Further, the focus is toward growing thin films and BST is continually being explored for use in next-generation memory applications [80–82]. Many aspects relating to ferroelectric thin films such as degradation and loss mechanisms in BST need through investigations [83].

5.3 *La Doping*

Lanthanum doping results in a remarkable enhancement of the properties of $BaTiO_3$. In the $Ba_{1-x}La_xTi_{1-x/4}O_3$ (BLT) family of compounds, the transition temperature decreases with an increase in the concentration of doping. The decrease in T_c corroborates with a corresponding decrease in the tetragonal distortion [84]. The decrease in tetragonality is depicted in XRD as well as Raman spectroscopy. The Raman spectra for different compositions are depicted in Fig. 8. The decrease in intensity of the tetragonal band at ~340 cm^{-1} depicts a decrease in tetragonality with an increase in dopant concentration. The possible defects in La-doped BT are provided in Eqs. 3–5 [85, 86]. The defect model depends on dopant concentration as well as the processing

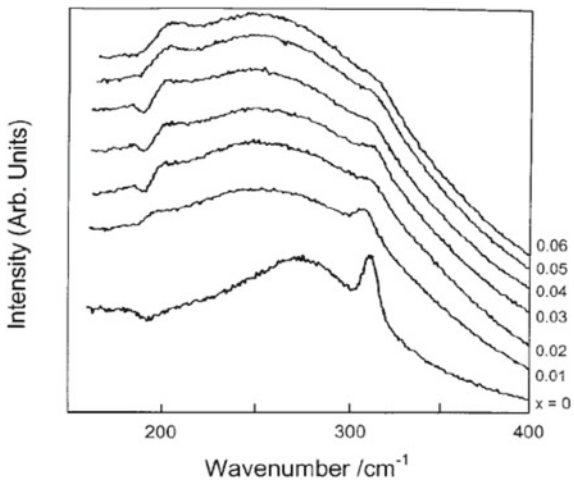

Fig. 8 Raman spectra for $Ba_{1-x}La_xTi_{1-x/4}O_3$ compositions [84]

of compounds. The lower concentration of La doping results in semiconducting properties as the effect of the electronic charges created by the excess positive charge due to La^{3+} dopant at Ba^{2+} site (Eq. 3). At higher La concentration, Ti vacancy defects (see Eq. (4) predominates resulting in higher resistivity [84, 87].

$$Ba_{Ba}^{x} \rightarrow La_{Ba}^{\cdot} + e^{\mathrm{I}} \tag{3}$$

$$Ba_{Ba}^{x} + Ti_{Ti}^{x} + 4La_{Ba}^{\cdot} + V_{Ti}^{||||} \tag{4}$$

$$3Ba_{Ba}^{x} \rightarrow 2La_{Ba}^{\cdot} + V_{Ba}^{||} \tag{5}$$

The extent of diffuseness of transition increases with an increase in dopant concentration. The compositions with higher La dopant concentration exhibit deviation from the C-W law. Transition temperatures $T_{t\text{-}c}$ and $T_{o\text{-}t}$ decreases with the different rates with an increase in dopant concentration. Eventually, due to the difference in the rate of change of transition temperature, both transitions overlap and a broad transition is observed for around 8 m/o La. The effect of overlap of transition temperature is called as pinching effect and results in board Ɛ versus T peak. The Dielectric constant as a function of temperature for $Ba_{1\text{-}x}La_xTi_{1\text{-}x/4}O_3$ compositions is depicted in Fig. 9. In general, the B site dopant at ferroelectric active Ti octahedral results in a diffuse phase transition. However, the enhancement in diffuseness observed in La doping on A-site is analogous to that of the B-site dopant effect. The effect of La alters the Ti ordering by creating Ti vacancies and leads to interesting ferroelectric properties exhibiting high dielectric constant and diffuseness.

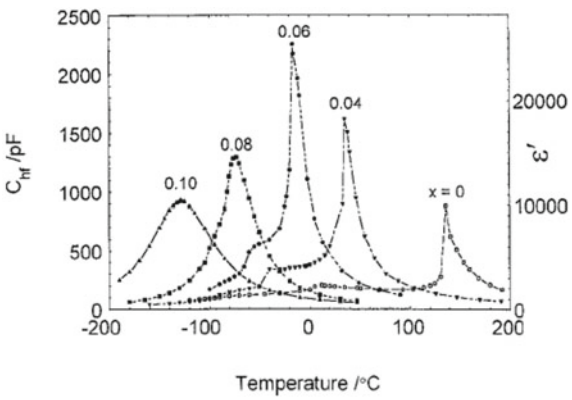

Fig. 9 Dielectric constant as a function of temperature for $Ba_{1\text{-}x}La_xTi_{1\text{-}x/4}O_3$ compositions [84]

5.4 Ce, Zr, and Other Widely Investigated Dopant Effects

Cerium exists in 3+ and 4+ states and can substitute for Barium as well as Titanium sites. Further, this substitution as an effect of different processing routes results in varied defect mechanisms and properties of compound [88, 89]. For a ceramic fired in the air, Ce is incorporated at Ba site under reducing atmosphere [89]. The ionic radii of Ce^{4+} in VII and XII coordination are 0.87 and 1.14 Å, respectively. On the other hand, the ionic radii for Ce^{3+} are 1.01 and 1.34 Å [90]. The ionic radii depict that Ce^{4+} will be favored on the Ti site and Ce^{3+} on the Ba site. The donor charge Ce^{3+} at the Ba^{2+} site results in an excess positive charge and is compensated by the electronic defects at lower dopant concentrations. However, at higher dopant concentrations, Ti vacancies are favored. An increase in Ce dopant concentration results in decreases in tetragonality and results in a relaxor behavior [91–94]. The three transitions of BT changes with the different rates as a function of dopant concentration and results in merging of these transitions resulting in diffuse phase transition [91]. Observed relaxor behavior is a result of the incorporation of non-ferroelectric Ce at Ti site leading to dilution of ferroelectric ordering and existence of core–shell structure [95].

The Zr doping on the Ti site results in a change in transition temperature to a larger extent relative to Ce^{4+}. The pinching effect results in a broad transition at around 20 m/o Zr [96]. The core–shell structure in Zr-doped $BaTiO_3$ has been established using energy dispersive spectroscopy [97]. A similar behavior, namely, increased diffuseness of the transition with increase in dopant concentration is also observed for Hf-doped BT [98]. The relaxor characteristics increase with an increase in dopant concentration. The dielectric constant as a function of temperature for Hf-doped BT is exhibited in Fig. 10 [99]. Compositions of the type $Ba_{1-x}(Sm_{0.5}Na_{0.5})_xTiO_3$ exhibit relaxor type behavior. The Sm- and Na-doped $BaTiO_3$ is tetragonal at room temperature up to $x = 0.4$ and transforms to cubic with a further increase in dopant concentration. The initial increase in the dopant concentration (up to $x = 0.3$) increases relaxor characteristics due to the random distribution of Sm and Na. However, further, an increase in dopant concentration results in a classical ferroelectric transition [100].

The trivalent yttrium ion is a preferred dopant for the Ti site but a low solid solubility up to 1.5 m% on the Ba site is observed [101]. The transition temperature in Y doping decreases at a higher rate than those observed for Zr or Ce doping. Nb^{5+} and Ta^{5+} substitute at Ti site and results in vacancies at A and/or B sites. Similar to Y, Zr, Ce, the doping of Nb, Ta, Nd, Bi results in a lowering of the transition temperature, and the increase in diffuseness of the transition is observed. The switchover from the classical ferroelectric to the enhanced diffuse transition accompanied by the frequency dispersion in Bi-doped $BaTiO_3$ compositions is observed [102]. However, in Nd doping, the relaxor behavior is not observed but the high variation in dielectric constant with frequencies suggests the formation of free charges, i.e., interfacial polarization at grain boundaries [103].

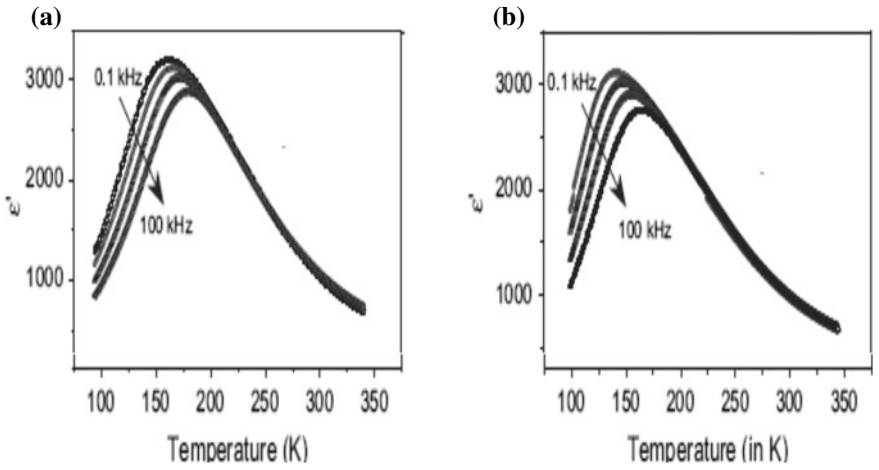

Fig. 10 Dielectric constant as a function of temperature for 20 m% (**a**) and 22 m% (**b**) Hf-doped $BaTiO_3$ [99]

5.5 A and B Site Co-doping

As discussed above, La and Ce are the widely investigated dopants. Further, the combination of these two dopants results in remarkable characteristics that may be tailored by either dopant concentration [104]. In the co-doped material, a higher change in transition temperature with La dopant (−34 to −38 °C/mol) is observed relative to in La-doped $BaTiO_3$. Also, the rate of decrease of transition temperature with Ce concentration in a co-doped is −7 °C/mol; higher than the value of −3 °C/mol observed in only Ce-doped $BaTiO_3$. Either dopant results in an increase in the extent of diffuseness and the transition temperature is affected largely by La dopant concentration. The change in dielectric constant as a function of temperature for constant Ce is exhibited in Fig. 11.

La- and Ce-doped $BaTiO_3$ compositions exhibit highly diffuse phase transition as a result of Ti vacancies formed because of excess positive charge due to La dopant at the host Ba ion. These compositions are potential materials for X7R and Y5V EIA class-2 capacitors. Thin-film Ca- and Zr-doped BT (BCT-BZT) leads to enhanced dielectric properties using strain engineering by using the suitable substrate. Pulsed laser depositions (PLD) and RF sputtering are widely used methods for the study of BT-based thin films [105]. Recent studies on the thin film of BT using PLD deposition have established temperature-independent dielectric responses and large piezoelectric responses [106].

In the family of compounds of type BT-$KNbO_3$ and BT-$NaNbO_3$, a broad transition is observed exhibiting enhanced frequency dispersion and departure from C-W law. The behavior is a result of nanoscale compositional inhomogeneity [107, 108]. This effect is similar to the explanation provided in well-known lead-based material, La- and Zr-doped $PbTiO_3$ (PLZT) [109, 110].

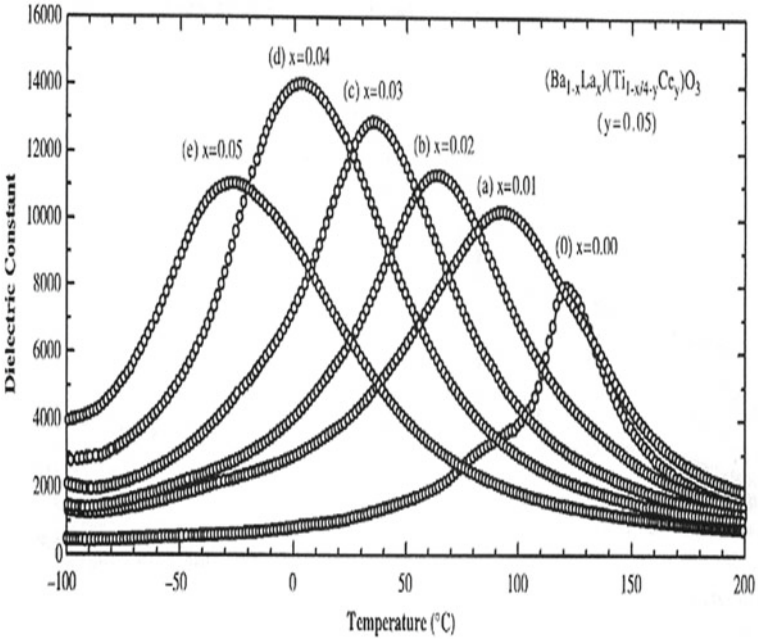

Fig. 11 Dielectric constant as a function of temperature for La- and Ce-doped $BaTiO_3$ [104]

The La and Al/Ga co-doped BT systems exhibit deviation from C-W law and diffuse phase transition [111, 112]. For the higher doping concentration, the constant γ, in modified CW law approaches 1.8. Using high-temperature XRD and Raman spectroscopy it has been established that the tetragonal phase exists well above T_{max}. In pure $BaTiO_3$ the crystallographic transition from tetragonal to cubic and T_{max} coincides. However, the difference between the T_{max} and the crystallographic transition temperature observed in HTXRD increases with an increase in diffuseness of transition. The temperature where deviation from CW law sets in (T_{dev}) is related to the formation of polar nanodomains (see Fig. 5). The temperature difference between T_{dev} and T_{max} is directly related to extent of diffuseness of the transition.

In past the piezoelectric applications were dominated by lead-based materials. However, recent work in Zr- and Ca-doped BT compounds has depicted that BT-based systems are also suitable for piezoelectric applications [113, 114]. Subsequent work has led to confidence in the use of BT-based ceramics for piezoelectric applications and further investigations [115]. Morphological phase boundary (MPB) consisting of lower symmetry Monoclinic phase in PMN-$PbTiO_3$ and PZT-$PbTiO_3$ compounds is well established. This existence of MPB results in a high piezoelectric response [116, 117]. A similar phenomenon called a Thermotropic or Morphotropic Phase Boundary consisting of intermediate phases of intrinsic monoclinic symmetry

has been observed in BT-based ceramics, resulting in enhanced properties [118]. In a system, (1-x)$Ba(Ti_{0.8}Zr_{0.2})O_3$-x$(Ba_{1-y}Ca_y)TiO_3$ existence of morphotropic phase boundary over a temperature range near transition has led to enhanced dielectric and piezoelectric properties [119].

6 Summary and Prospects

The perovskite family being of great interest for various applications, various methodologies of doping have been adopted to enhance the properties of pure $BaTiO_3$. The few widely explored dopants are Sr, Sn, La, Ce, and Zr. A majority of these dopants exhibit a diffuse phase transition and/or relaxor-type behavior. Various explanations have been provided in the literature to explain the observed behavior. In the case of doped BT, the pinching effect in few dopants results in a broad diffuse transition. The dopant causes loss of long-range ordering by diluting the ferroelectric characteristics and by impurity induced clusters [120, 121]. Also, the behaviour may be explained based on the formation of the core–shell structure consisting of compositional inhomogeneity, inhomogeneous strain, and the formation of PNR. Thereafter, the dynamics of PNR give rise to enhanced frequency dispersion and a broad transition. The co-existence of both ferroelectric and paraelectric phase over a wide range of temperature around transition temperature leads to broad Ɛ versus T transition.

Piezoelectric applications were limited to lead-containing materials such as $PbZr_{1-x}Ti_xO_3$ (PZT) and $PbMg_{1/3}Nb_{2/3}O_3$(PMN), and BT was believed to be no match. However, emerging research led to confidence in the development of BT-based materials as lead-free piezo material. Recently, tape casting studies of BT are explored and effects of microstructure, texture are explored for various capacitor applications. Textured ceramics using templated grain growth resulted in enhancement of properties [122]. In-depth texture, grain boundaries, and microstructure may lead to new paths in this area. Also, morphotropic phase boundary has resulted in enhanced piezoelectric properties in BT-based systems. These emerging areas in BT-based materials have developed a new recipe to tailor enhanced properties, suitable for piezoelectric applications. Further research may lead to the development of BT-based materials having comparable or even superior properties to lead-based ceramics.

References

1. Valasek J (1920) Piezoelectric and allied phenomena in Rochelle salt. Phys Rev 15:537–538
2. Valasek J (1921) Piezo-electric and allied phenomena in rochelle salt. Phys Rev 17:475–481
3. Mason WP (1971) Fifty years of ferroelectricity. J Acoust Soc Am 50:1281–1298
4. Gray B (1946) Transducers and method of making the same. U.S. Patent No 2 486 560
5. Hippel AV, Breckenridge RG, Chesley FG, Tisza L (1946) High dielectric constant ceramics. Ind Eng Chem 38:1097–1109

6. Ogawa S (1946) On polymorphic change of $BaTiO_3$. J Phys Soc Jpn 1:32–33
7. Cross LE, Newnham RE (1987) History of ferroelectrics. Ceram Civiliz 111:289–345. Am Ceram Soc Inc.
8. Megaw H (1945) Crystal structure of barium titanate. Nature 55:484–485
9. Merz W (1956) Switching time in ferroelectric BaTiO3 and its dependence on crystal thickness. J Appl Phys 27:938–943
10. Fraser BC, Danner H, Pepinski R (1955) Single-crystal neutron analysis of tetragonal $BaTiO_3$. Phys Rev 100:745–746
11. Devonshire AF (1949) Theory of barium Titanate. Part I. Philos Mag 40:1040–1063
12. Matthias B, Hipple AV (1948) Domain structure and dielectric response of barium titanate single crystals. Phys Rev 73:1378–1384
13. Blattner H, Kaenzig W, Merz W (1949) Production and investigation of BaTiO3 single crystals. Helv Phys Acta 22:35–65
14. Merz W (1952) Domain properties in $BaTiO_3$. Phys Rev 88:421–422; Merz W (1954) Domain formation and domain wall motions in ferroelectric $BaTiO_3$ single crystals. Phys Rev 95:690–698
15. Kaenzig W (1951) X-ray studies on the seignette electricity of barium titanate. Helv Phys Acta 24:175–216
16. Kaenzig W (1950) Atomic positions and vibrations in the ferroelectric $BaTiO_3$ lattice. Phys Rev 80:94–95
17. Evans HT (1951) The crystal structure of tetragonal barium titanate. Acta Cryst 4:377–377
18. Evans HT (1961) An X-ray diffraction study of tetragonal barium titanate. Acta Cryst 14:1019–1026
19. Megaw H (1962) Refinement of the structure of $BaTiO_3$ and other ferroelectrics. Acta Cryst 15:972–973
20. Frazer BC, Danner HR, Pepinsky R (1955) Single-crystal neutron analysis of tetragonal $BaTiO_3$. Phy Rev 100:745–746
21. Jaffe B, Cook WR, Jaffe H (1971) Piezoelectric ceramics. Academic Press Inc., London
22. Lu SW, Lee BI, Wang ZL, Samuels WD (2000) Hydrothermal synthesis and structural characterization of $BaTiO_3$ nanocrystals. J Cryst Growth 29:269–276
23. Deng X, Wang X, Wen H, Kang A, Gui Z, Li L (2006) Phase transitions in nanocrystalline barium titanate ceramics prepared by spark plasma sintering. J Am Ceram Soc 89:1059–1064
24. Hipple AV (1950) Ferroelectricity, domain structure, and phase transitions of barium titanate. Rev Mod Phys 22:221–237
25. Slater JC (1950) The Lorentz correction in barium titanate. Phys Rev 78:748–761
26. Mathiss B, Hipple AV (1948) Domain structure and dielectric response of barium titanate single crystals. Phys Rev 73:1378–1384
27. Cochran W (1960) Crystal stability and the theory of ferroelectricity. Adv Phys 9:387–423
28. Cohen RE, Krakauer H (1990) Lattice dynamics and origin of ferroelectricity in $BaTiO_3$: linearized-augmented-plane-wave total-energy calculations. Phys Rev B 42:6416–6423
29. Cohen RE (1992) Origin of ferroelectricity in perovskite oxides. Nature 358:136–138
30. Ghosez P, Cokayayne E, Waghmare UV, Rabe KM (1999) Lattice dynamics of $BaTiO_3$, $PbTiO_3$, and $PbZrO_3$: a comparative first-principles study. Phys Rev B 60:836–843
31. Ghosez P, Michenaud JP, Gonze X (1998) Dynamical atomic charges: the case of ABO_3 compounds. Phys Rev B 58:6224–6240
32. Gonze X, Lee C (1997) Dynamical matrices, Born effective charges, dielectric permittivity tensors, and interatomic force constants from density-functional perturbation theory. Phys Rev B 55:10355–10368
33. Klein L, Aparicio M, Jitianu A (eds) (2016) Handbook of sol-gel science and technology. Springer. Online. ISBN 978-3-319-19454-7
34. Wei LS, Lee BI, Wang L, Samuels WD (2000) Hydrothermal synthesis and structural characterization of $BaTiO_3$ nanocrystals. J Cryst Growth 219:269–276
35. Yamamura H, Watanabe A, Shirasaki S, Moriyashi Y, Tanada M (1985) Preparation of barium titanate by oxalate method in ethanol solution. Ceram Int 11:17–22

36. Rase DE, Roy R (1955) Phase equilibria in the system $BaTiO_3$-SiO_2. J Am Ceram Soc 38:389–395
37. Statton WO (1951) The phase diagram of the BaO–TiO_2 system. J Chem Phys 19:33–40
38. Beauger A, Muion JC, Niepce JC (1983) Synthesis reaction of metatitanate $BaTiO_3$ Part 1 Effect of the gaseous atmosphere upon the thermal evolution of the system $BaCO_3$-TiO_2. J Mater Sci 18:3441–3446
39. Beauger A, Muion JC, Niepce JC (1983) Synthesis reaction of metatitanate $BaTiO_3$ Part 2 Study of solid-solid reaction interfaces. J Mater Sci 18:3543–3550
40. Uchino K, Nomura S (1982) Critical exponents of the dielectric constants in diffused-phase-transition crystals. Ferroelectr 44:55–61
41. Bobade SM, Gulwade DD, Kulkarni AR, Gopalan P (2005) Dielectric properties of A- and B-site-doped $BaTiO_3$: La- and Al-doped solid solutions. J App Phys97:074105
42. Drofenik M, Popovic A, Kolar D (1984) Grain growth and related effects in doped $BaTiO_3$. Am Ceram Soc Bull 63:702–704
43. Kastner G, Wagner R, Hilarius V (1994) Nucleation of twins by grain coalescence during the sintering of $BaTiO_3$ ceramics. Philos Mag A 69:1051–1071
44. Demartin M, Herard C, Carry C, Lemaıtre J (1997) Dedensification and anomalous grain growth during sintering of undoped barium titanate. J Am Ceram Soc 80:1079–1084
45. Veneva AK, Muklich F (2002) Orientation imaging microscopy applied to BaTiO3 ceramics. Cryst Eng 5:235–242
46. Arlt G, Hennings D, With GD (1985) Dielectric properties of fine-grained barium titanate ceramics. J Appl Phys 58:1619–1625
47. Takeuchi T, Capiglia C, Balakrishnan N, Takeda Y, Kageyama H (2002) Preparation OF fine-grained $BaTiO_3$ ceramics by spark plasma sintering. J Mater Res 17:575–581
48. Agrawal DK (1998) Microwave processing of ceramics. Curr Opin Solid State Mater Sci 3:480–485
49. Fukai K, Hidaka K, Aoki M, Abe K (1990) Preparation and properties of uniform fine perovskite powders by hydrothermal synthesis. Ceram Int 16:285–290
50. Martirena HT, Burfoot JC (1974) Grain-size effects on properties of some ferroelectric ceramics. J Phys C Solid state Phys 7:3182–3192
51. Buessem WR, Cross LE, Goswami AK (1966) Phenomenological theory of high permittivity in fine-grained barium titanate. J Am Ceram Soc 49:33–36
52. Buessem WR, Cross LE, Goswami AK (1966) Effect of two-dimensional pressure on the permittivity of fine- and coarse-grained barium titanate. J Am Ceram Soc 49:36–39
53. Uchino K, Sadananga E, Hirose T (1989) Dependence of the crystal structure on particle size in barium titanate. J Am Ceram Soc 72:1555–1558
54. Buscaglia V, Buscaglia MT, Viviani M, Mitoseriu L, Nanni P, Trefiletti V, Piaggio P, Gregora I, Ostapchuk T, Pokorny J, Petzelt J (2006) Grain size and grain boundary-related effects on the properties of nanocrystalline barium titanate ceramics. J Europ Ceram Soc 26:2889–2898
55. Zhao Z, Buscaglia V, Vivaiani M, Buscalia MT, Mitoseriu L, Testino A, Nygren M, Johnsson M, Nainni P (2004) Grain-size effects on the ferroelectric behavior of dense nanocrystalline $BaTiO_3$ ceramics. Phys Rev B 70:024107
56. Yashima M, Hoshina T, Ishimura D, Kobayashi S, Nakamura W, Tsurumi T, Wada S (2005) Size effect on the crystal structure of barium titanate nanoparticles. J Appl Phys 98:014313
57. Ishiwaka K, Yoshikawa K, Okada N (1988) Size effect on the ferroelectric phase transition in $PbTiO_3$ ultrafine particles. Phys Rev B 37:5852–5855
58. Kinoshita K, Yamaji A (1976) Grain-size effects on dielectric properties in barium titanate ceramics. J Appl Phys 47:371–373
59. Frey MJ, Payne DA (1996) Grain-size effect on structure and phase transformations for barium titanate. Phys Rev B 54:3158–3168
60. West AR, Adams TB, Morrison FD, Sinclair DC (2004) Novel high capacitance materials: BaTiO3: La and CaCu3Ti4O12. J Euro Ceram Soc 24:1439–1448
61. Smolensky GA, Isupov VA (1954) Segnetoelektricheskie svoistva tverdykh Rastovorov stannata Bariya V titanate Bariya. Zh Tech Fiz 24:1375–1386

62. Markovic S, Mitric M, Cvjeticanin N, Uskokovic D (2007) Preparation and properties of $BaTi_{1-x}Sn_xO_3$ multilayered ceramics. J Euro Ceram Soc. 27:505–509
63. Xiaoyong W, Yujun F, Xi Y (2003) Dielectric relaxation behavior in barium stannate titanate ferroelectric ceramics with diffused phase transition. App Phys Lett 83:2031–2033
64. Bokov AA, Ye ZG (2006) Recent progress in relaxor ferroelectrics with perovskite structure. J Mater Sci 41:31–52
65. Muellera V, Jagerb L, Beigea H, Abichtb HP, Muller T (2004) Thermal expansion in the Burns-phase of barium titanate stannate. Solid State Comm 129:757–760
66. Suasmoro S, Pratapa S, Hartanto D, Setyoko D, Dani UM (2000) The characterization of mixed titanate $Ba_{1-x}Sr_xTiO_3$ phase formation from oxalate coprecipitated precursor. J Euro Ceram Soc 20:349–314
67. Hilton AD, Ricketts BW (1996) Dielectric properties of $Ba_{1-x}Sr_xTiO_3$ ceramics. J Phys D Appl Phys 29:1321–1325
68. Kuo SYWF, Liao WY, Hsieh (2001) Structural ordering transition and repulsion of the giant LO-TO splitting in polycrystalline $Ba_xSr_{1-x}TiO_3$. Phys Rev B 64:224103
69. Bethe K, Welz F (1971) Preparation and properties of (Ba, Sr)TiO_3 single crystals. Mat Res Bull 6:209–217
70. Zhou L, Vilarinho PM, Baptista JL (1999) Dependence of the structural and dielectric properties of $Ba_{1-x}Sr_xTiO_3$ ceramic solid solutions on raw material processing. J Euro Ceram Soc 19:2015–2020
71. Singh N, Singh AP, Prasad CD, Pandey D (1996) Diffuse ferroelectric transition and relaxational dipolar freezing in: III. Role of order parameter fluctuations. J Phys Condens Matter 8:7813–7827
72. Tenne DA, Soukiassian A, Xi XX, Choosuwan H, Guo R, Bhalla AS (2004) Lattice dynamics in $Ba_xSr_{1-x}TiO_3$ single crystals: a Raman study. Phy Rev B 70:174342
73. Pasha UM, Zheng H, Thakur OP, Feteira A, Whittle KR (2007) In situ Raman spectroscopy of A-site doped barium titanate. Appl Phys Lett 91:062908
74. Lemanov VV, Smirnova EP, Syrnikov PP, Tarakanov EA (1996) Phase transitions and glasslike behavior in $Sr_{1-x}Ba_xTiO_3$. Phy Rev B 54:3151–3157
75. Tiwari VS, Singh N, Pandey D (1995) Diffuse ferroelectric transition and relaxational dipolar freezing in (Ba,Sr)TiO_3. J Phys Condens Matter 7:1441–1460
76. Syamaprasad U, Galgali RK, Mohanty BC (1998) Dielectric properties of the $Ba_{1-x}Sr_xTiO_3$ system. Mater Lett 7:197–200
77. Jeon JH (2004) Effect of $SrTiO_3$ concentration and sintering temperature on microstructure and dielectric constant of $Ba_{1-x}Sr_xTiO_3$. J Euro Ceram Soc 24:1045–1048
78. Hirbebecq V, Huber C, Maglione M, Anonietti M, Elissalde C (2004) Dielectric properties of pure (BaSr)TiO_3 and composites with different grain sizes ranging from the nanometer to the micrometer. Adv Funct Mater 14:899–904
79. Chiou BS, Liou JW (1997) Dielectric characteristics of doped $Ba_{1-x}Sr_xTiO_3$ at the paraelectric state. Mater Chem Phys 51:59–63
80. Tao K, Hao Z, Xu B, Chen B, Miao J, Yang H, Zhao BR (2003) Ferroelectric properties of (Ba, Sr)Ti_O3 thin films grown on $YB_a2C_u3_O7$ layers. J Appl Phys 94:4042–4046
81. Wang RV, McIntyre PC (2003) Point defect distributions and their electrical effects on (Ba,Sr)TiO_3/Pt thin films. J Appl Phys 94:1926–1933; Cole MW, Nothwang WD, Hubbard C, Ngo E, Ervin M (2003) Low dielectric loss and enhanced tunability of $Ba_{0.6}Sr_{0.4}TiO_3$ based thin films via material compositional design and optimized film processing methods. J Appl Phys 93:9218–9225; Kim WJ, Wu HD, Chang W, Qadri SB, Pond JM, Kirchoefer SW, Chrisey DB, Horwitz JS (2000) Microwave dielectric properties of strained ($Ba_{0.4}$ $Sr_{0.6}$)TiO_3 thin films. J Appl Phys 88:5448–5451; Jin HZ, Zhu J (2002) Size effect and fatigue mechanism in ferroelectric thin films. J Appl Phys 92:4594–4598
82. Pontesa FM, Longoa E, Leitea ER, Varelab JA (2001) Study of the dielectric and ferroelectric properties of chemically processed $Ba_xSr_{1-x}TiO_3$ thin films. Thin Solid Films 386:91–98
83. Kingon AI, Marla JP, Streiffer SK (2000) Alternative dielectrics to silicon dioxide for memory and logic devices. Nature 406:1032–1038

84. Morrison FD, Sinclair DC, West AR (1999) Electrical and structural characteristics of lanthanum-doped barium titanate ceramics. J App Phys 86:6355–6366
85. Morrison FD, Coats AM, Sinclair DC, West AR (2001) Charge compensation mechanisms in La-doped BaTiO3. J Electroceram 6:219–232
86. Morrison FD, Sinclair DC, West AR (2001) An alternative explanation for the origin of the resistivity anomaly in La-doped $BaTiO_3$. J Am Ceram Soc 84:474–476
87. Morrison FD, Sinclair DC, Skakle JMS, West AR (1998) Novel doping mechanism for very-high-permittivity barium titanate ceramics. J Am Ceram Soc 81:1957–1960
88. Makovec D, Kolar D (1997) Internal oxidation of Ce3+-BaTiO3 solid solutions. J Am Ceram Soc 80:45–52
89. Markovec D, Samardzija Z, Kolar D (1996) Solid solubility of cerium in BaTiO3. J Solid State Chem 123:30–38
90. Shannon RD (1976) Revised effective ionic radii and systematic studies of interatomic distances in halides and chalcogenides. Acta Crystal A 32:751–767
91. Chen A, Zhi Y, Zhi J, Vilarinho PM, Baptista JL (1997) Synthesis and characterization of $Ba(Ti_{1-x}Ce_x)O_3$ ceramics. J Euro Ceram Soc 17:1217–1221
92. Chen A, Zhi J, Zhi Y (2002) Ferroelectric relaxor $Ba(Ti,Ce)O_3$. J Phys Condens Matter 14:8901–8912
93. Yu Z, Ang C, Jing Z, Viarinho PM, Baptista JL (1997) Dielectric properties of $Ba(Ti, Ce)_O3$ from 1^02 to 1^05 Hz in the temperature range 85–700 K. J Phys Condens Matter 9:3081–3088
94. Hennings DFK, Schreinemacher B, Schreinemacher H (1994) High-permittivity dielectric ceramics with high endurance. J Euro Ceram Soc 13:81–88
95. Park Y, Kimb HG (1997) The microstructure analysis of cerium-modified barium titanate having core-shell structured grains. Ceram Int 23:329–336
96. Hennings D, Schnell A, Simon G (1982) Diffuse ferroelectric phase transitions in $Ba(Ti_{1-y}Zr_y)O_3$ ceramics. J Am Ceram Soc 65:539–544
97. Lu HY, Bow JS, Deng WH (1990) Core-shell structures in ZrO_2-modified $BaTiO_3$ ceramic. J Am Ceram Soc 73:3562–3568
98. Payane W, Tennery V (1965) Dielectric and structural investigations of the system $BaTiO_3$-$BaHfO_3$. J Am Ceram Soc 48:413–417
99. Anwar S, Sagdeo PR, Lalla NP (2007) Study of the relaxor behavior in $BaTi_{1-x}Hf_xO_3$ ($0.20 \leq x \leq 0.30$) ceramics. Solid state Sci 9:1054–1060
100. Abdelmoula N, Chaabane H, Khemakhem H, Muhll RVD, Simon A (2006) Relaxor or classical ferroelectric behavior in A-site substituted perovskite type $Ba_{1-x}(Sm_{0.5}Na_{0.5})xTiO_3$. Solid State Sci 8:880–887
101. Zhi J, Chen A, Zhi Y, Vilarinhi PM, Baptista JL (1999) Incorporation of yttrium in barium titanate ceramics. J Am Ceram Soc 82:1345–1348
102. Bahri F, Khemakhem H, Simon A, Mühll RVD, Ravez J (2003) Dielectric and pyroelectric studies on the $Ba_{1-3a}Bi_{2a}TiO_3$ classical and relaxor ferroelectric ceramics. Solid State Sci 5:1235–1238
103. Yao Z, Liu H, Liu Y, Wu Z, Shen Z, Liu Y, Cao M (2008) Structure and dielectric behavior of Nd-doped $BaTiO_3$ perovskites. Mat Chem Phys 109:475–481
104. Lu DY, Toda M, Sugano M (2006) High-permittivity double rare-earth-doped barium titanate ceramics with diffuse phase transition. J Am Cearm Soc 31:3112–3123
105. Wang TH, Hsu PC, Korytov M, Genoe J, Merckling C (2020) Polarization control of epitaxial barium titanate ($BaTiO_3$) grown by pulsed-laser deposition on a MBE-$SrTiO_3$/Si(001) pseudo-substrate. J Appl Phys 128:104104
106. Everhardt AS, Denneulin T, Grunebohm A, Shao YT, Ondrejkovic P, Zhou S, Domingo N, Catalan G, Hlinka J, Zuo JM, Matzen S, Noheda B (2020) Temperature-independent giant dielectric response in transitional $BaTiO_3$ thin films. Appl Phys Rev 7:011402
107. Ravez J, Simon A (1998) Relaxor ferroelectricity in ceramics with composition $Ba_{1-x}K_x(Ti_{1-x}Nb_x)O_3$. Mat Lett 36:81–84
108. Bahari F, Khamakhem H, Garagouri M, Simon A, Muhll RV, Ravez J (2003) Dielectric and Raman studies on the solid solution $(1–x)BaTiO_3/xNaNbO_3$ ceramics. Solid State Sci 5:1445–1450

109. Dai X, Xu Z, Li J, Viehland D (1996) Effects of lanthanum modification on rhombohedral $Pb(Zr_{1-x}Ti_x)O_3$ ceramics: Part I. Transformation from normal to relaxor ferroelectric behaviors. J Mat Res 11:618–625; Dai X, Xu Z, Li J, Viehland D (1996) Effects of lanthanum modification on rhombohedral $Pb(Zr_{1-x}Ti_x)O_3$ ceramics: Part II. Relaxor behavior versus enhanced antiferroelectric stability. J Mat Res 11:626–638
110. Gupta SM, Li JF (1998) Coexistence of relaxor and normal ferroelectric phases in morphotropic phase boundary compositions of lanthanum-modified lead zirconate titanate. J Am Ceram Soc 81:557–564
111. Gulwade DD, Bobade SM, Kulkarni AR, Gopalan P (2005) Dielectric properties of A- and B-site-doped $BaTiO_3$.: La- and Ga-doped solid solutions. J Appl Phys 97:074106
112. Gulwade DD, Gopalan P (2009) Study of diffuse phase transition in $BaTiO_3$-$LaAlO_3$. J Alloys Compd 481:316–319; Gulwade DD, Gopalan P (2008) Diffuse phase transition in La and Ga doped barium titanate. Solid State Comm 146:340–344
113. Liu W, Ren X (2009) Large piezoelectric effect in Pb-free ceramics. Phys Rev Lett 103:257602
114. Rodel J, Webber KG, Dittmer R, Jo W, Kimura M, Damjanovic D (2015) Transferring lead-free piezoelectric ceramics into application. J Eur Ceram Soc 35:1659–1681
115. Acosta M, Novak N, Rojas V, Patel S, Vaish R, Koruza J, Rossetti GA, Rödel J (2017) $BaTiO_3$-based piezoelectrics: fundamentals, current status, and perspectives. Appl Phys Rev 4:041305
116. Noheda B, Gonzalo JA, Cross LE, Guo R, Park SE, Cox DE, Shirane G (2000) Tetragonal-to-monoclinic phase transition in a ferroelectric perovskite: the structure of $PbZr_{0.52}Ti_{0.48}O_3$. Phys Rev B 61:8687–8695; Noheda B, Cox DE, Shirane G, Park S-E, Cross LE, Zhong Z (2001) Polarization rotation via a monoclinic phase in the piezoelectric 92% $PbZn_{1/3}Nb_{2/3}O_3$–8% $PbTiO_3$. Phys Rev Lett 86:3891–3894
117. Guo R, Cross LE, Park SE, Noheda B, Cox DE, Shirane G (2000) Origin of the high piezoelectric response in $PbZr_{1-x}Ti_xO_3$. Phys Rev Lett 84:5423–5426
118. Lummen TA, Gu Y, Wang J, Lei S, Xue F, Kumar A, Barnes AT, Barnes E, Denev S, Belianinov A, Holt M, Morozovska AN, Kalinin SV, Chen LQ, Gopalan V (2014) Thermotropic phase boundaries in classic ferroelectrics. Nat Commun 5:3172
119. Zhou C, Ke X, Yao Y, Yang S, Ji Y, Liu W, Yang Y, Zhang L, Hao Y, Ren S, Zhang L, Ren X (2018) Evolution from successive phase transitions to "morphotropic phase boundary" in $BaTiO_3$ based ferroelectrics. Appl Phys Lett 112:182903
120. Ravez J, Simon A (2001) Some solid state chemistry aspects of lead-free relaxor ferroelectrics. J Solid State Chem 162:260–265
121. Simon A, Ravez J, Maglione M (2004) The crossover from a ferroelectric to a relaxor state in lead-free solid solutions. J Phys Condens Matter 16:963–970
122. Messing GL, McKinstry ST, Sabolsky EM, Duran C, Kwon S, Brahmaroutu B, Park P, Yilmaz H, Rehrig PW, Eitel KB, Suvaci E, Seabaugh M, Oh KS (2004) Templated grain growth of textured piezoelectric ceramics. Crit Rev Solid State Mat Sci 29:45–96

Chapter 19
Recent Advances on Ferrites Nanomaterial's as Photocatalyst for Environment

Promod Kumar, Gajendra Kumar Inwati, Mohan Chandra Mathpal, Jero Maze, and H. C. Swart

1 Introduction

Ferrite materials have been widely implemented toward the incremental development in catalytic invention and technologies. Number of research findings were published based on unsupported and modified ferrites to achieve their expected results in the treatment of environmental pollutants such as organic dyes, inorganic heavy ions, microbes [1, 2]. The extraordinary multifunctional personalities of ferrites including superparamagnetic, no-toxicity, and chemical stability offered multiple uses among the reported metal-oxides [3, 4]. The appropriate bandgap (≈2.2 eV) with the required band position encouraged it as a potential nanocatalyst particularly for breaking the molecular structures in organic dyes and heavy metal adsorption [4, 5]. In general, the physicochemical and catalytic processing of the ferrites (magnetite (Fe_3O_4)/maghemite (Fe_2O_3) could be manipulated by applying different magnetic fields [3, 6]. It is well known that ferrite materials have strong magnetic configurations including their thermal stability, mechanical strength with lower toxicity [7, 8], used in multifunctional optoelectronics, catalysis applications. Apart from, the simplest cost-effective preparation and environmentally friendly behavior of these ferrites are genuine reasons to employ them as the strongest tools to overcome the many environmental problems mainly photo-assisted pollutant purifications, remedial biodegradations [1, 9, 10]. The degradation of hazardous pollutants such as inorganic and organic contents, releasing from textile and pharmaceutical industries, is a serious issue for healthy water management and developments [11, 12]. To resolve such environmental objects several researchers have put their efforts toward developing hybrid ferrite nanomaterials as advanced technology especially

P. Kumar (✉) · G. K. Inwati · H. C. Swart (✉)
Department of Physics, University of the Free State, Bloemfontein 9300, ZA, South Africa
e-mail: SwartHC@ufs.ac.za

M. C. Mathpal · J. Maze
Instituto de Física, Pontificia Universidad Católica de Chile, Casilla 306, Santiago, Chile

B. P. Swain (ed.), *Advances in Nanostructured Materials*, Materials Horizons: From Nature to Nanomaterials, https://doi.org/10.1007/978-981-16-8391-6_19

for biodegradations, and photochemical catalysis. Hence, ferrite materials are been explored as a much suitable candidate for improving the catalytic actions under light stimulated reactions. The decomposition of the hazardous pollutant was efficiently triggered by the change in band gap energy and surface modifications in ferrites [13, 14]. Recently, extensive invention in designing and fabrication of modified ferrite structure have been processed to develop the hybrid ferrites for the increased photocatalytic action and optimal processing. The electronic bands were optimized by introducing heteroatom dopants/localized centers into the ferrite semiconductors. The dopant centers promotes to the Photoelectochemical (PEC) performance by increasing conductance and recombination rate. Several noble metal (Au, Pt, Ag, and Pd) ions [11, 13, 15, 16] including another metal cations such as Ti, Sn, Tb, Ru, Al, Mn, Co, etc., have been doped to adjust the electronic and physical properties toward catalysis movements. In an example, Jang et al. [13] obtained an optimum photocurrent density for the 50% Ag–50%Fe hematite co-doped with 2% Sn because of improved electrical conductivity which was comparably higher than Ag-Fe binary hematite. The photocatalytic redox reaction were well triggered by the Wei et al. [16] by inserting Pd metals on Fe_2O_3 which promote to the electron–hole transfer and separations phenomenon. The redox based concept was explained in order to respond the catalytic reduction and oxidation, takes place on Pd and Fe_2O_3 part of Pd-Fe_2O_3.

In a typical photocatalytic process, the photocatalyst typically uses photon energy to carry out the oxidation and reduction reaction. When semiconductor nanomaterials are irradiated by the light energy, which has energy greater or equal to the band-gap of the semiconductor, then the electron is promoted from its valence band to the conduction band and leaving holes in the valence band [17–20]. It is well known that the photogenerated electron and hoes both react with O_2 and H_2O (or OH^-) to form the superoxide radicals such as $O_2^{\bullet-}$ and $OH^{\cdot}$, as shown in Fig. 1, respectively.

These superoxide radicals can be widely used for the degradation of the organic pollutant into CO_2, H_2O, and other inorganic oxides.

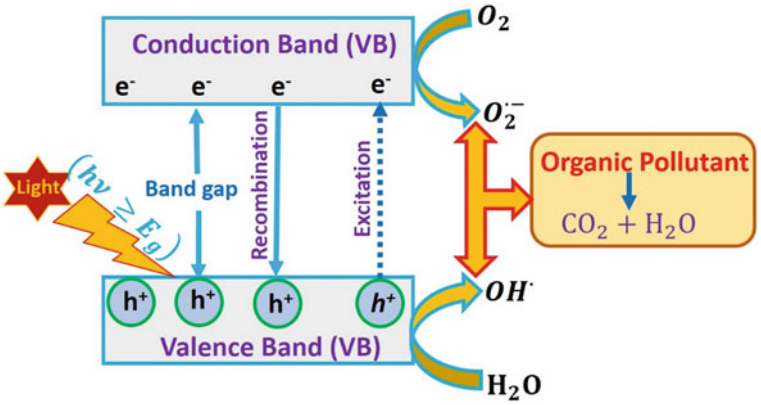

Fig. 1 The basic mechanism of photocatalysis

The mechanism of photocatalysis is shown in the below equations [18].

$$\text{Photocatalyst} + h\nu \rightarrow e^- + h^+ \, (I) \tag{1}$$

$$H_2O + h^+ \rightarrow OH + H^+ \, (II) \tag{2}$$

$$O_2 + e^- \rightarrow O_2^- \, (III) \tag{3}$$

The $OH^{\cdot}$ and $O_2^{\cdot -}$ both ions are produced by the redox reactions of the dye molecules and produce smaller compounds and this leads to the degradation of the dye. The superoxide anion radicals are formed when it reacts with H^+ ions to form more $OH^{\cdot}$ radicals.

$$OH + Dye \rightarrow dye(Oxidation) \tag{4}$$

$$e^- + dye \rightarrow dye(reduction) \tag{5}$$

Photocatalysis of dye molecules is not possible without dissolving oxygen and H_2O molecules as they produce the $OH^{\cdot}$ radicals [18].

The basic principle of the photocatalysis mechanism is shown in Fig. 1. When electromagnetic radiation is incident on a semiconductor, then electrons and holes are formed. It has been observed that the different types of the semiconductors exhibited the photosensitivity properties which are widely studied for the photocatalytic application. After selecting suitable photocatalysts, the band-gap energy of the semiconducting nanomaterial's generally decided the wavelength of the light, which can be absorbed by the semiconductor materials. It is also noticed that the bandgap is inversely proportional to the wavelength of light $\left(E(eV) = \frac{hc}{\lambda} = \frac{1240}{\lambda(nm)}\right)$, where E is known as the bandgap energy in eV [21].

Figure 2 shows the absorbance spectrum of the total energy from the solar energy spectrum, which arrives at the earth's surface in the form of ultraviolet (UV), visible, and infrared (IR) radiation. It can be observed from the solar spectrum that the visible region only absorbs 46% of the light energy from the Sun, while the UV region only absorbs 5% of the light energy from the Sun, and the Remaining 49% of the light energy is absorbed only by the Infrared region of the spectrum [20].

But, the main problem is that most semiconductors such as ZnO, ZnS, CdS, and TiO_2 have a wide band-gap that absorbs only 4–5% of photon energy in the UV-region from the Sun [18].

The other issue is the fast recombination rate of the electron and hole, which reduces the efficiency of the photocatalyst [22, 23]. Various photocatalysts have wide band gaps of more than 3.1 eV, capable of absorbing small amounts of sunlight. It is therefore necessary to use the visible solar energy, which normally falls on the earth's surface, which is about 10, 000 times higher than the current annual energy consumption [24]. Therefore, semiconducting nanomaterials with a bandgap

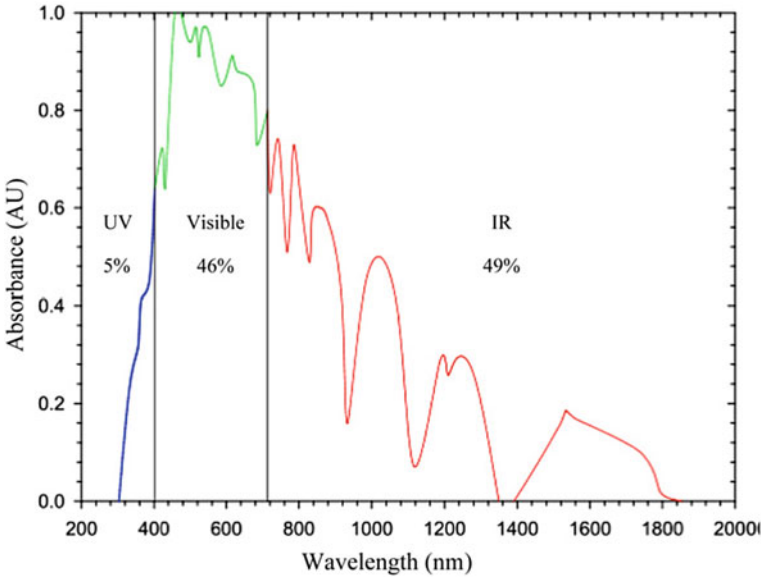

Fig. 2 Solar energy spectrum. Reproduced with permission from Ref. [20], copyright elsevier

of 3.1 eV be essential for an effective photocatalyst to absorb solar energy [21]. It has been widely accepted that TiO2 is one of the prominent photocatalysts used by the researcher from the last decades due to its wide bandgap (3.03 eV rutile and 3.18 eV anatase) and can therefore absorb only a small portion of the light energy of sunlight.

Therefore, ferrite materials combined with other photocatalysts such as TiO_2 showed enhanced photocatalytic activities. When ferrite nanomaterials are combined with TiO_2, it shows higher efficiency of the photocatalysts than pure TiO_2 nanomaterials. Because, the ferrite nanomaterials combined with TiO_2 nanoparticles produces a synergistic effect, showing enhanced photocatalytic activities, resulting in higher degradation of the pollutant contaminations. Hence the ferrite materials combined with TiO_2 become more effective under visible light irradiation, as TiO_2 is only effective only under UV light [20].

The other materials such as ZnO, Ag, $Ag3VO_4$, multicarbon nanotubes, WO_3, etc., [20] combined with ferrite materials show similar effects and enhance the photocatalytic activity. The composites of ferrite with other materials showed the enhanced photocatalytic by absorbing the visible light and found promising results for the degradation of contaminants in water.

The main aim of the combined photocatalysts is to reduce the recombination rate of the electron–hole pairs. Because the combined photocatalysts have different bandgap positions, resulting effectively more separation of the electron–hole pairs, which is the basic requirement for enhancing the photocatalytic activities.

The main objective of this chapter is to explore the ferrite nanomaterials and their potential for the degradation of the contaminants in aqueous environments. The

synthesis process, optical properties such as bandgap, steps to increase the photocatalytic efficiency of ferrites, and their potential to degrade the contaminants, such as organic compounds including dyes, inorganic compounds, and bacteria are discussed.

2 Experimental Technique

Various chemical and physical technologies were processed to fabricate and alter the structural surface of the ferrite crystal structure. Many researchers are trying to develop an economical cheap and ecofriendly approach to design pure as well as hybrid ferrite materials over the last few years. Based on easy handling and processing in chemical reactivity, different methods such as sol–gel, hydrothermal, co-precipitations, combustions, and sonochemical were employed. It has been studied, the ferrite materials are very sensitive and modulated by several factors including synthesis approaches, experimental parameters, and chemical environments. Here, we gathered literature-based experimental findings especially for the morphological and electrical changes in ferrites for catalytic selectivity and functionalities. In a sequence, the synthetic approaches are explained as follow.

2.1 Sol–Gel Synthesis

Controlled morphology with clear distribution in particles was obtained by the simple sol–gel techniques particularly for ferric and super ferromagnetic semiconductors. It is used to obtain crystalline phases with uniform sizes of the final product. The method involved optimum temperature for regular growth in nucleation and particle structures mediated by the required stabilizing agents depend upon morphologies and surface modifications. Tang et al. [25] were formed magnetite thin films using the same route associated with thermal annealing at 300 °C while the higher temperature (350 °C), produced the hematite phase of ferrites. So the experimental conditions strongly affect the magnetism of the ferrites and hence the synthesis process moderates in the case of magnetic nanoparticle formations. In this sol–gel, iron-oxides were mainly produced using ferric nitrate as a precursor and ethylene glycol (polyol) as reducing and capping both. It is also noted that the nitrate phase was found chemically favorable in sol–gel synthesis due to its easy solubility and ionic dissociation in solvents [26].

2.2 Co-precipitation

On this route, the shape, size, and composition of the synthesized ferrites can be changed by regulating the stoichiometric ratios of Fe(II) and Fe(III) salts, pH of the

used solution with the reaction time. The controlled geometry of the magnetic materials could be oriented under the influence of pH media mainly acidic environment and its ionic strength, offering a good dispersion and stability for a narrow-sized ferrite particle. A lot of procedures were reported based upon chemical precipitation of the products surrounded by the stabilizers such as PVP, surfactants (cationic, anionic), and other organic stabilizing agents. Organic ligands or polymeric structures generally assist in the particle size and their clustering during the reaction which helps to restrict the dimensional growth of particles [27, 28]. After separating the final product, it can be stored in the alkaline or acidic medium as a dispersed phase for a long duration. However, for the oxidation variation in Fe(II) and Fe(III) state of hematite and magnetite, the followed route is adopted as very feasible by facing the experimental challenges. It has been considered as a most effective technique over reported approaches due to its simplest processing, less space for performing experiments, lower cost, and larger yield.

2.3 Hydrothermal Synthesis

To date, hydrothermal is successfully adopted to manufacture the metamaterials including metallic nanoparticles, metal-oxide (semiconductors), clusters, etc. This method involves polyol, alcohols, and water as an essential solvent either in an individual or in a mixed phase. The precursor salts are used to dissolve in preferred solvents at a fixed amount and then transferred into Teflon coated stainless still for the reaction at higher temperature and pressure. Under hydrothermal, growth of the particles takes place very slow for the specific morphology of the particles on optimized experimental parameters. Li and coworkers employed hydrothermal methods for the uniform distribution of the single crystalline ferrite microspheres [29]. A colloidal mixture of $FeCl_3$, polyol, and sodium acetate was prepared and kept in an inert Teflon-lined autoclave at fixed reaction parameters (8–72 h at 200 °C). The ferrite materials were prepared by followed hydrothermal to amend the magnetic properties of the magnetite and hematite both. Often, a longer aging time is used to carry the synthesis procedure to regulate the chemical kinetics and the growth mechanism with the comparison of other methods.

2.4 Temperature-Induced Decompositions

For yielding solid crystalline semiconducting materials, thermal decompositions have been preferred by the researchers and scientists as it does not require aqueous media during synthesis. The magnetic nanocrystal and oxides are essentially prepared in terms of tunable magnetic, optical, and surface properties by using temperature tempted reactions. Usually, the organometallic slats such as metal bonded acetylacetonates along with surface directing agents are used to dissociate at a higher

temperature. The applied reaction temperature, time, and ratio of the precursors are the decisive factors to achieve an expected structure of ferrites. It is known, the fundamental characteristics of the metal oxides are manipulated due to the intrinsic imperfection of crystals which depends on synthesis procedures. Monodisperse iron nanoparticles were synthesized by Hyeon et al. [30] using Fe (III) chloride and sodium oleate as starting materials and dissociates in an ionic form at different temperatures ranged from 240 to 320 °C. The change in temperature with respect to aging time triggers the chemical and physical properties of the magnetic nanostructures. The obtained magnetic particles were found to be dispersed and stable in an organic medium like toluene and hexane. Hence, this technique is performed to produce ferrite materials with a structured shape and magnetic potential, used for various optoelectronic, biomedical, and environmental applications. Besides that, the biological method has been used as an alternative way to form iron oxides. Essentially, the microbes, algae, and plant extract utilized in the synthesis procedure, due to the presence of reducing agents such as ascorbic acids, citric acids, and organic polyols [31, 32]. Green synthesis of the ferrite substances is also appreciated among chemical components and manufacturing strategies due to non-toxic contents and natural abundance.

2.5 UV–Vis Spectrophotometer: Optical Bandgap Study

UV–Vis spectrophotometer is one of the simplest techniques for evaluating the optical response of the pure and doped ferrites nanosystem. Easy handling and processing of this technique is been significantly performed among the various instruments in academic research and developments. To find out the electronic band positions in modified ferrite systems, the spectral absorption phenomenon was utilized where the observed spectra respond according to the modified band gap values. However, the targeted band gap alteration can be made during the synthesis procedure under certain experimental parameters. But, the separation between conduction band (CB) and valence band (VB) could be identified in terms of bandgap energies (E_g) using some theoretical model such as Tauc plots $(\alpha h\nu)^2 = A\ (h\nu - Eg)$, and Kubelka–Munk $(\alpha = (1 - R)^2/R2)$ function for the direct band. Where, α denote the absorption coefficient, A is the constant, $h\nu$ is photon energy, E_g is bandgap energy, and R stands for reflectance. The relation between photon energy ($h\nu$) and wavelength (λ) of the incident light is used to calculate the energy gap between CB and VB. F. Al-Mokdad and colleagues, [33] engineered E_g values for the pure and Mo-doped $MnFe_2O_4$ ferrites using co-precipitation and studied its E_g values by applying the Tauc formula for all samples. A decreased order in E_g values was observed from 2.12 to 1.81 eV due to the decreased values (8.451(Å) to 8.395 (Å) of the lattice parameters in Mo-$MnFe_2O_4$ crystals. Notably, the ionic radii of the doping ions, concentrations, and the applied temperature affect the E_g values by creating the defect points/imperfections in the bulk or and surface on host semiconductors [34, 35].

A descending order in E_g values was obtained by Ni-doped hematite nanoparticles. The different amounts (2–8% of Ni) were introduced in Fe_2O_3 structures and calculated their band gaps which varied from 2.02 to 1.18 eV [36]. The partial substitution of Ni ions into the hematite matrix caused the change in unit cell volume and packed density of Fe_2O_3 semiconductor.

3 Steps to Increase the Photocatalytic Efficiency of Ferrites

Fundamentals of dopant ions and their influence toward better catalytic uses have been studied in detail by several chemists and engineers. The surface selectivity and the chemical reactivity of the doped catalysts are essentially tuned by the insertion of wanted elements into the semiconducting materials (ferrites). The current progress in material designing and its advanced functionalization invited to researchers for expressing the elementary concepts based upon defects chemistry. Various metal ions in the periodic table, expressed their electrochemical affinity while doping with the ferrite structures due to appropriate ionic radii and overlapping in electronic bands. However, as it was reported that the ferrites having a bandgap from 2.0 to 2.2 eV which could be modified via ionic doping for the expected applications like removal of dye pollutants, antimicrobial, and drug-resistant bacteria. We are going to report some fundamentals concerning defects formation and its reasonable findings for the betterment of photocatalyst appliances. The factors affecting the activities of the catalysts could be understood by given facts.

3.1 Dopant Types and Rational Stoichiometric

Typically, alkali, transitional, and lanthanide ions are been selected for the rational doping in semiconducting host materials. The available electrons in valance orbitals likewise s, p, d, and f make them more favorable to interact with the atomic orbitals of the metal oxides. Detailed theoretical and experimental reports were studied for the orbital coupling between dopant and the central metal atom in metal oxides. The choice of dopants depends on near similarities in ionic radii of doped ions and the host metals, which allow forming a thermodynamically stable complex after doping. To produce p-type ZnO semiconductors, noble metals such as Ag, Cu, and Au were doped with ZnO by Yanfa Yan and groups, [37] and theoretically calculated their transition energies to systemized complex formations using density functional theory (DFT). It has been observed that the mismatch level in ionization energies and the participating ionic orbitals determine the interstitial and substitutional doping inside the host structures. For example, group-I ions (La, Na) form shallow acceptor levels in T_d geometries followed by interstitial sites but it also creates donor levels followed by interstitial sites when the Fermi level is closed to valence bond maxima. Considering

group-IB elements, Ag was found to be anticipated for producing p-type ZnO structures due to the formations of shallower accepter levels [37]. Though, transitional Co ions were introduced inside the α-Fe_2O_3 ferrites to obtain controlled crystalline structures which determine the catalytic proportion for Co-doped α-Fe_2O_3. The 4% stoichiometric doping of Co was found to be more effective for the dye degradation as compared to 2% of Co-α-Fe_2O_3 [3]. A fixed quantity of the dopant is detected as ideal concentration for the efficient catalysts in spinel ferrites while the extra ions of the dopant possess heavy obstructions on the open surfaces and become the reason for aggregations or agglomeration, decreasing the activity during photocatalysis. Therefore, the types, stoichiometric ratios with experimental conditions are the key features to insert the dopant into the ferrites crystal lattice which direct the catalytic performance in several applications.

3.2 Tunable Bands Position

As known, the structural, optical, and surface modification of the semiconducting materials fundamentally depend on bandgap values which could be altered by introducing the ionic centers into the lattice of metal-oxide crystals. The ferrite materials are been fabricated and explored due to strong magnetic and electronic magnitude especially for light-based catalytic propagation in physicochemical systems. The separation of CB and VB in iron oxides was already tailored by the doping of various ions through the specific fabrication methods and the set parameters during synthesis. The doped ions can be introduced as interstitial or substitutional sites depending on ionic radii and participating valence orbitals of the doped atoms. The change in bandgap is caused by the generation of the lots of defects levels likewise oxygen vacancies, metal interstitials (M_i), oxygen interstitials (O_i), on the surface as well as bulk in ferrites. These imperfections mainly influence the perfect lattice orientation of the host structures in terms of distorted geometry of the octahedral or tetrahedral coordination and thus the electronic structure changes, respectively. Some major outcomes were reflected to explain the doping concept in semiconductors including crystal field theory (CFT) and discrete energy states for the bands. In this conception, CFT is supportive to evaluate a shifting in band gaps for the metal oxides. The transitional iron (Fe) metals have their variable oxidation states, Fe (II) and Fe (III) boded with the negative oxides ions. Thus, the ferrite complex shows tetrahedral (Td) or/and octahedral (Oh) geometries with the attached ligands in coordination compounds. When the dopant ion interacts with the surface of the ferrite it induces an observable transition of (Fe)-d-orbitals by splitting into t_{2g} and E_g energy states. It is noted that the E_g orbital consists of the σ antibonding energy states while the t_{2g} is composed of π antibonding states. It is also noteworthy to observe that the VB consists of the O 2p orbitals in iron oxides, having pπ excited levels (on the top of VB) [35]. The doped ions create surface and intrinsic defects (oxygen vacancies). Consequentially, integration in defects levels (deep levels) onto the band often

decreases the band gap values in the semiconductors. In spinel ferrites, the variation in oxidation states of Fe (II&III) possess a substantial change in magnetic and oxidation behavior and these belongings could be programmed for the biomedical and ROS formations, respectively. The dopant ions modified the volume density in perfect octahedral and tetrahedral orientation in spinel ferrites, resulting in a change in magnetic and catalytic strength. It is also been evaluated that the overlapping of s-p/p-d/or f-d atomic orbitals between the dopant and ferrites, changed the band positions by creating donor or acceptor levels near the VB and CB. And, this has been acknowledged as a genuine reason for bandgap alteration for ferrites and several metal-oxides.

Gajendra et al. [38] reported a defects level formation and its role to manipulate the band gap values which respond differently in photoluminescence in the case of pure and Rb-doped ZnO as shown in Fig. 3a. In another study, Lalit and co-

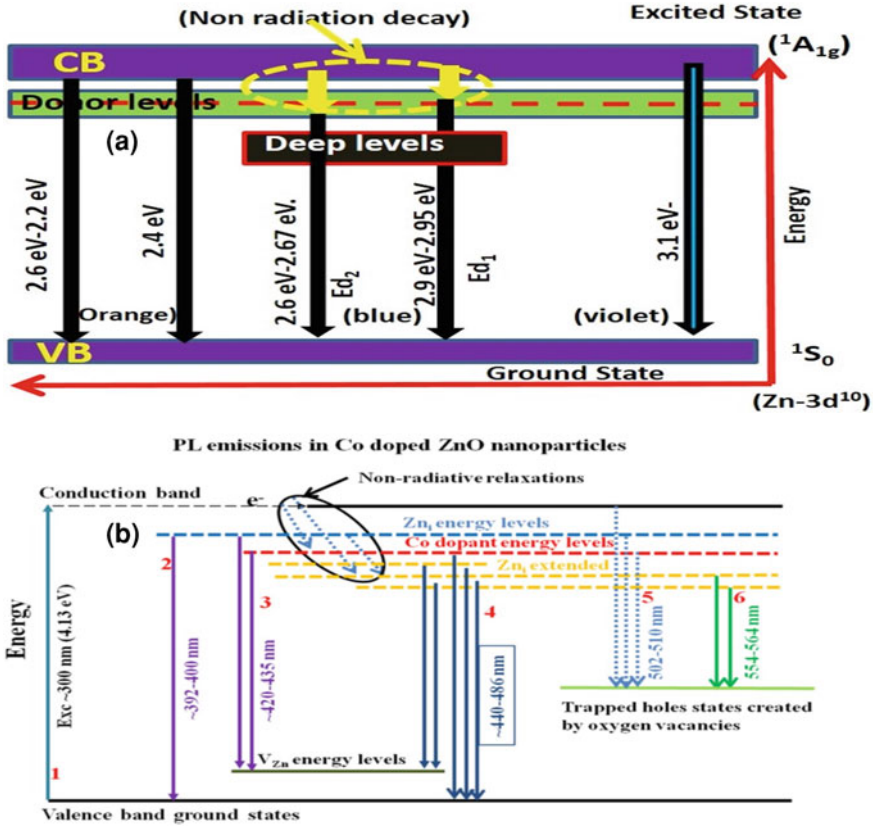

Fig. 3 Defects level in doped semiconducting materials: **a** Rb-doped ZnO nanostructures, Reproduced with permission from Ref. [38], copyright elsevier, **b** Co-doped ZnO band gaps, Reproduced with permission from Ref. [39], copyright elsevier

authors[39] have proposed an energy level band scheme for the Co-doped metal oxides by showing its multi-step emission spectra corresponding to different bandgap values as shown in Fig. 3b. So, the understanding of defects/imperfections has value in the solid crystal formations and alteration in their physicochemical properties, used in optoelectronic systems, and integrated devices.

3.3 Surface Morphology

The surface morphology of nanomaterials plays an important role in improving the photocatalytic performance of ferrite materials [17]. It was further observed that the photocatalytic activity of semiconducting photocatalysts increases with an increase in their specific surface area, resulting in a decrease in the size of their particles. It is well known that the small particle's size has a larger surface area and the higher the photocatalytic performance was achieved [40]. Because good photocatalysts have high adsorption of pollutants due to their higher surface area, which is widely used for efficient pollutant degradation in wastewater treatment [18, 41].

Therefore we can say that the specific surface area plays an important role in the degradation of the organic pollutant and improves the photocatalytic efficiency of the semiconducting nanomaterial. Because when the pollutants are very close to the surface of the photocatalytic materials, they can be easily changed by the active radicals by photocatalytic semiconducting materials during the reaction and easily enhance the photocatalytic efficiency [42–45].

Zhang et al. [46] synthesized the bismuth ferrite nanomaterial using the hydrothermal method and studied the photocatalytic activities of the synthesized bismuth ferrite nanomaterial, which usually depends on the surface morphology of the crystals under the influence of UV–Vis light. The photocatalytic activity of the bismuth ferrites increases from sheets to cube under visible light irradiation. The tunable morphology of bismuth ferrites was achieved due to the concentration effect of hydroxide.

Wang et al. [47] also synthesized $BiFeO_3$ nanomaterials using a sol–gel technique and showed that both the morphology as well as the specific surface area have a good impact on the photocatalytic activities of the synthesized nanomaterial under visible light irradiation. Their studies showed that the photocatalytic activities of $BiFeO_3$ nanoparticles were found to be much higher than that of the $BiFeO_3$ bulk. Zhu et al. [48] synthesized hexagonal-shaped bismuth ferrite nanomaterials with diameters of 10–50 nm using the hydrothermal method. Their study showed that the photocatalytic activities of hexagonal-shaped bismuth ferrite nanomaterials were found to be significantly better than that of the spherical-shaped perovskite bismuth ferrite-based materials.

Pan Xiong et al. [49] synthesized CdS−MFe2O4 (M = Zn, Co) nanomaterials using the hydrothermal method. Their study showed that the CdS − MFe2O4 (M = Zn, Co) nanomaterials showed higher photocatalytic activity and photostability than pure CdS toward the degradation of two dyes such as b RhB and 4-CP under

visible-light irradiation. The photocatalytic performance of the synthesized materials increases significantly due to their higher surface area as well as the synergic effect of CdS and $ZnFe_2O_4$(or $CoFe_2O_4$), which can lead to greater absorption and more efficient charge separation in the visible-light region. Similarly, the crystallinity of the nanoparticles improves the photocatalytic activities as well as the charge transport properties of the materials. The crystallinity of the synthesized nanoparticles can be achieved under the influence of thermal treatments at higher temperature, however, it can also increase the size of the nanomaterial. It has thus been demonstrated that the fabrication techniques should be well organized by optimizing the specific surface area of the nanomaterials without affecting the crystallinity.

3.4 Effect of Hetero-junction

The main purpose of the photocatalyst is to initiate or enhance the redox reaction in the presence of the irradiating semiconductor nanomaterial according to the law of semiconducting photocatalyst. When the electromagnetic radiation is incident by semiconducting photocatalysts whose energy must be equal to or greater than the bandgap energy of the semiconductor catalysts to complete the redox reactions. The electron-holes are formed at the surface of the semiconductor nanomaterials and recombine with each other. The recombination of the electron-holes dissipates the input energy in the form of light or heat. Crystalline defects and electron–hole recombination are often facilitated through scavenging. Therefore, the good crystallinity of the nanomaterials can reduce the trapping points as well the recombination sites, resulting in the increased formation of the photo-generated charge carriers for a favorable reaction. It is also well known that the recombination cannot authorize for the preferable photo-catalytic performance. Hence, a suitable method is applied to increase the efficiency of the photocatalytic in which a semiconductor heterojunction is formed with another semiconductor [18, 50, 51]. When these different semiconductors combine between two components with different bandgaps, it results in an interfacial band arrangement is known as a heterojunction. Hence, a Schottky barrier is formed at the semiconductor heterojunctions, which reduces the recombination rate of the photogenerated electron, and electron-holes, which improves the photocatalytic activities [52, 53].

Zhang et al. [54] synthesized $BiFeO_3/Bi_2Fe_4O_9$ heterojunction nanofibers using an electrospinning technique followed by a facile wet chemical process. Their result showed that the band-gap energy calculated from UV–visible were found to be at 2.15 and 1.96 eV for $BiFeO_3$ and $Bi_2Fe_4O_9$, respectively, and conduction band positions of $BiFeO_3$ and $Bi_2Fe_4O_9$ was observed at 0.43 eV and −0.77 eV, respectively. The valence bands (VBs) of $BiFeO_3$ and $Bi_2Fe_4O_9$ were observed at 2.58 and 1.19 eV according to their XPS-based results, respectively. A heterojunction is formed by the combination of BiFeO3 and $Bi_2Fe_4O_9$, respectively. When visible light is incident on both $BiFeO_3$ and $Bi_2Fe_4O_9$, both have different photo-absorption ranges as shown in Fig. 4.

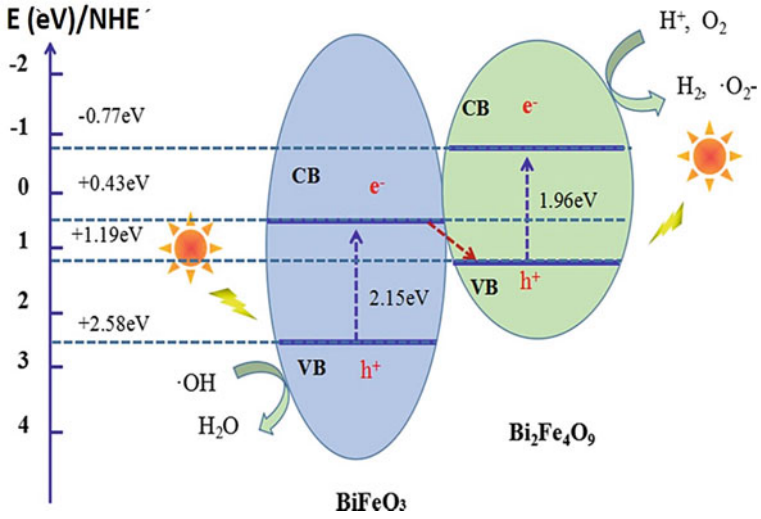

Fig. 4 Schematic illustration for the electron–hole transport at the interface of the $BiFeO_3/Bi_2Fe_4O_9$ heterojunction nanofibers, Reproduced with permission from Ref. [54], copyright ACS

The conduction band position of $BiFeO_3$ was observed at 0.43 eV, which indicates the poor reduction of H^+ into H_2. On the other hand side, the conduction band position of $Bi_2Fe_4O_9$ was observed at −0.77 eV, as a result of which the photoactive electrons in the $Bi_2Fe_4O_9$ CB show a stronger reducing ability to split water than pure $BiFeO_3$. In this case, the photogenerated electrons in the conduction band of BiFeO3 move to the valence band of $Bi_2Fe_4O_9$ and are associated with the holes in its valence band. This type of charge transfer process eventually increases the separation of electron/hole pairs and suppresses their recombination, thus leading to enhanced photodegradation performance and higher H_2 evolution performance of BiFeO3/Bi2Fe4O9 samples under visible-light irradiation.

4 Ferrites for Photocatalytic Applications

On photocatalysis, ferrite catalyst excited by the certain frequency of the electromagnetic radiations especially in UV and visible regions. Usually, semiconducting materials have been promoted for photon-stimulated catalysis due to their optimum bandgap energies, which require fixed excitation energy to produce the electron–hole pairs. Recent advances in hybrid ferrites and their wider applications have opened multidisciplinary scientific research and academic knowledge for multifunctional applications owing to their characteristic superparamagnetic and physicochemical functionalities [4, 55]. In this regard, ferrites stand out among various metal oxides having their optical band gap energy ranging from 2.0 to 2.2 eV which is found to be a

favorable band position for the harvesting of visible light (up to ≈600 nm) in the solar spectrum. For the photo-generated charges, it is very compulsory to apply excitation energy that must be equal to or more than the bandgap energy of ferrites (semiconductors), resulting from the fast creations of electrons and holes on conduction band (CB) and valence band (VB), respectively. The excited charges subsequently initiate the process to generate reactive oxygen species (ROS) such as OH*, O_2* and O_2H* radicals on the ferrite surfaces. The ROS chemistry on the surface is mostly accepted for the photocatalytic degradation of pollutants and antimicrobial damages in waste.

4.1 Ferrites Spinel Towards Photocatalytic Degradation of Pollutants (Dyes)

The delayed rate in charge recombination rate and fast production in reactive ROS constituents are mostly studied for the better photocatalytic degradation of aromatic dyes, adsorption of toxic elements, from the environmental pollutants. For investing the photoconductive and photothermal applications of ferrites, Noshan Nazar et al. [1] successfully produced iron-oxides using pomegranate seed extract under green synthesis and obtained around 96% efficiency for the textile dye degradation. The adjusted narrow bandgap of the prepared ferrites was found to be much suitable for the harvesting of UV light during the degradation process. Also, different morphology of the ferrite materials was achieved by Manjula Shenoy and their group, [56] using the simplest hydrothermal process. In this case, hexagonal ferrites were found more efficient for the methylene blue (MB) degradation as compared to the oval and aggregated iron oxides. The photo persuaded dissociation of dye was carried out using different nanostructures of ferrites such as nanoparticles, nanoclusters, and nano-thin film. Ferric oxide (α-Fe_2O_3) thin films were developed to engineer the bag gap values by Mahadik [12] and their colleagues. The spray pyrolysis technique was employed to fabricate the ferrite thin films and used to dissociate heterocyclic organic contaminants mainly Rhodamine B on solar illumination. It has been reported, the chemical reduction of Fe^{3+} to Fe^{2+} take place on the catalyst surface by the constant illumination of solar energy and the reduced iron ions speedily degrade to hydrogen peroxides followed by chemical reduction, resulting in an increased population of hydroxyl radicals on catalyst surface as shown in Fig. 5.

Spherical iron oxide (α-Fe_2O_3) nanoparticles were prepared by Abdelmajid Lassoued et al. at low temperature by chemical precipitation and then annealed at different temperatures (600–800 °C) to alter the morphological, optical, magnetic, and photocatalytic functionalities [57]. Around 2.1 eV, bandgap values were obtained for the bare sample and the bandgap varied with the calcination temperatures along with magnetic properties. It is observed that the optimum calcination at 700 °C showed a better band gap value including higher magnetism for the methylene blue dye (MB) degradation. Looking toward dimensional confinement, one dimensional (1D) hematite (α-Fe_2O_3) nanorod along with α–FeOOH magnetic rods were formed

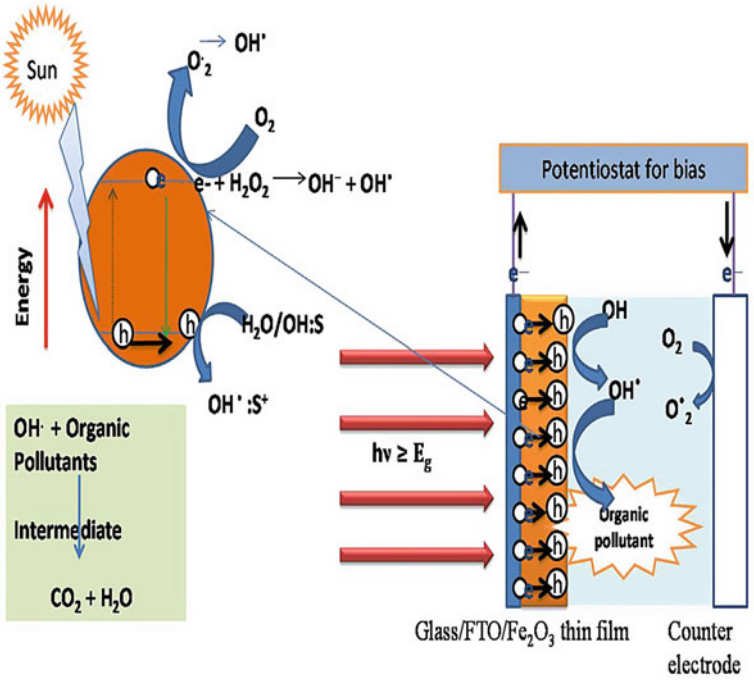

Fig. 5 Photoelectrochemical degradation scheme by α-Fe_2O_3 photoelectrode, (S: organic pollutant and S^+: intermediate), Reproduced with permission from Ref. [12], copyright elsevier

by Xuemei Zhou and coworkers [58] via thermal dehydration. In this study, a synergetic role of elemental compositions, sizes and the defected local structures were proposed for the efficient decomposition of Rhodamine B dye with the comparison of α-FeOOH composites. The nanoscale hematite particles were found to be more active than the micro-sized for the catalysis reaction due to their confinement effect and higher surface area. Further, an 83 and 95% reduction of phenol red and crystal yellow were observed on sunlight and fluorescent light, respectively by Nathan et al. from the biosynthesized hematite nanoparticles [59]. The higher amount of the catalyst decreased the degradation power of organic molecules may be due to the blockage in active sites of ferrite surfaces.

However, pure ferrites showed speedy charge recombination and a low lifetime excited state during catalysis and such practical factors make them limited for several catalytic procedures. In alternate, heterogeneous magnetic nanoparticles are structurally engineered to attain controlled optical, magnetic, and electronic properties using different synthetic routes [60, 61]. Various desired elements such as noble metals, rare earth ions, and dimensional confined thin films were impregnated with the magnetic nanoparticles particularly for enhanced photocatalysis of dye degradations, heavy metal extractions, adsorptions, and purifications [8, 55, 62]. These transitional, lanthanides, or thin films and their compositional ratios play an intense

stroke to adjust the recombination rate of electron–hole pairs during photo-mediated catalysis of ferrites. Numbers of articles are available based on catalytic work function especially for modified magnetic nanoparticles including their optoelectronic and photocatalytic properties in the last few decades [8, 55, 63]. Here, we focused on the fundamental characteristics of the ferrites toward catalytic applications induced by solar energy by considering much-appreciated examples. However, metal-doped magnetic nanoparticles (heterogeneous photocatalysis) have been recognized as a reliable material owing to their easy recyclability, durability, high efficiency, and low-cost tendency [61]. For an efficient nanocatalyst, the recombination rate must be longer so that the light-induced free electrons and holes could involve in radical formations on the catalyst surface. It is studied that the doped iron oxides showed a higher catalytic rate as compared to pure ferrites due to electronic change in bandgap energies and surface modifications. To increase recombination time, modified nanostructures of the ferrites are in higher demand for dye degradation, water splitting, and wastewater decontaminations. In particular, silver (Ag), gold (Au), platinum (Pt), and palladium (Pd) are considered as the most suitable elements due to their unusual plasmonic, and catalytic functionalities [4, 55, 63, 64]. These noble metals felicitate a high performance in photocatalysis by absorbing a wider range of sunlight due to their large surface area, surface plasmon resonance (SPR), and quantum confinement effect. For the doped metal ions in semiconductors, mainly two conditions are studied based on Fermi level energies; Fermi level energy can be lower or higher than the conduction band (CB) of the semiconducting materials (ferrites). In both situations, doped ions are helpful to regulate the catalytic activities under photoirradiation in the UV–Vis region. The photoexcited free electrons of the metal ions can be easily transferred to the CB of ferrites and effectively contribute to stimulating the redox reaction by delaying in recombination speed of electron-holes combines [36].

For instance, Eman Alzahrani designed rectangular and squares-shaped Ag-Fe_3O_4 nanostructures under coprecipitation to catalyze the eosin Y dye contents on UV irradiations [65]. Comparably, higher degradation performance (90.12%) of eosin Y was obtained using Ag-Fe_2O_3 nanoparticles over pure Fe_3O_4 (40%) due to the involvement of noble Ag as shown in Fig. 6, respectively. The doped Ag ions adapt to the free electrons on the surface and regulate the recombination process between electrons and holes which determine the photocatalytic efficiency. Generally, noble metal does not affect by the dye effluents or pollutants while the ferrites can be easily separated due to stronger magnetic behavior, and thus the catalyst could be reused for further catalytic applications. The chemical stability and recyclability are the key parameters to reuse the catalyst and with this point of view, modified iron oxides have proven their superior personalities correspond to other metal oxides in photocatalysis. In the above case, it was found that there was no significant loss in catalytic progress in Ag-Fe_3O_4 and therefore, it reused three times more for the photocatalysis cycle [65]. This is because of inertness in physicochemical properties of noble metals and the easier segregation of the ferrite materials under magnetic field [63, 64].

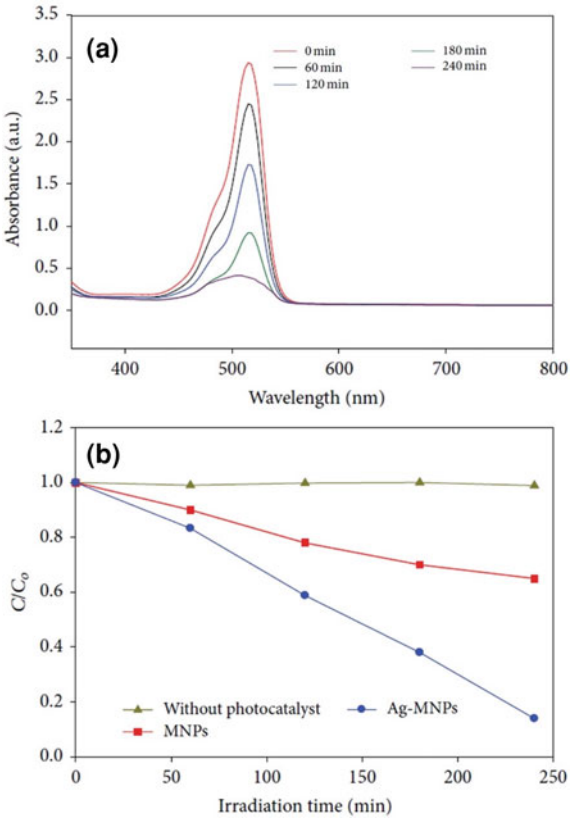

Fig. 6 Degradation of eosin Y using Ag-Fe_3O_4, and **b** Degradation rate concerning irradiation time [65], open access

In addition, defects harmony of the ferrites has been explored to understand the bandgap alteration and surface changes for the progressive enactment in photocatalysis. Moreover, doped and co-doped nanostructures of the magnetic materials are been implemented for the expected outcomes in the catalysis-based chemical reactions [5, 36]. For example, the bandgap of Fe_2O_3 nanoparticles was attuned by the Abdelmajid Lassoued and group by the doping of Ni ions at different stoichiometric amounts. The Ni-doped Fe_2O_3 nanostructures showed an effective decolorization of methylene blue (MB) over pure Fe_2O_3 [36]. The modified bandgap of hematite supports the late recombination for electron–hole charges on visible light. Doped Ni ions increase the electron transport properties, resulting in improved photocatalytic activity of ferrite materials. It has become a fundamental observation to determine the electron transport properties of photocatalyst by performing the photoelectrochemical (PEC) measurements [36]. PEC results determine the charge recombination frequency for the semiconducting materials during catalytic functions. Normally, the doped ions help to increase the electron transport nature of semiconductors due to the formations of defects on the surfaces, interfering in the recombination of delocalized electrons at band positions. It is known, catalytic work of the catalyst boosts up by

having a large surface area with confined particle sizes. But the paradigm has changed over the years that is catalyst must have specific active surface sites for the adsorption and or absorption phenomenon for the estimated photocatalysis. By the doping of metal ions, surface sites and the bandgap energies could be structurally moderate in ferrite substances to tackle the catalytic mechanism. The doped materials may have different morphologies (active faces) due to the change in surface energy caused by doped ions. The role of different morphologies with their different exposed surface sites was studied by Amoresi et al. for CeO_2 semiconductor in order to achieve enhanced photocatalytic efficiency [66]. The rod, rod/cube, bean, and hexagon-like morphologies were developed with the different coordinated planes and then used to decompose the micropollutants. Theoretically, it was observed that the exposed surfaces have the different electrostatic potential of exposed surfaces, which actively involve damaging the antibiotic and dye components in micropollutants. Also, the defects and imperfections affect the band energies and the surface geometry of the semiconductors. In this context, Promod Kumar et al. observed a significant interference in electron–hole recombination by the doping of rare Rb ions in ZnO crystals [67] and evaluated increased electron transport properties, delayed the charge recombination for photocatalytic performances. Overall, the ionic vacancies, interstitials, and/or surface defects interrupt the charge carrier transportation inside the semiconductors by forming impurity bands. Although, the point defects such as oxygen vacancies are most commonly performed as a central player in ferrites or iron oxide-based research. The reported studies revealed that the superconductivity of the magnetic oxides can be improved by creating dopant centers in magnetic oxides, employed in catalytic, ionic conductivity, and energy harvesting aspects. Consequently, defect concepts in ferrite reflects a deeper understanding towards experimental and theoretical evaluations in oxide-based technology. Moreover, Mahadik et al. [63] have fabricated an Au-doped Fe_3O_4 photocatalyst (thin films) using spray pyrolysis for the photoelectrocatalytic degradation of salicylic acids as shown in Fig. 7, respectively.

The results showed about 45% more degradation efficiency for the 2% of Au-Fe3O4 nanomaterials as compared to undoped Fe_3O_4 [63]. The Au (III) helps to absorb a large amount of the incident light in the visible region on the Fe_3O_4 surface and it allows direct electrons scavenging by the Au nanoparticles. This determines a rapid production of the exciting radicals, resulting from a fast redox in organic and inorganic pollutants. The durability and the chemical stability increase, especially by the contribution of noble metals and that, is why such plasmon-based ferrites are highly used in heavy metal removal, and dye degradations.

Yat Li et al. [2] fabricated Ti-doped Fe_2O_3 films employing deposition-annealing technique using iron (III) chloride as Fe precursor. The photoelectrochemical activity of the designed catalyst was enhanced by optimizing Ti and Fe concentrations and certain stoichiometric ratios were shown an improved conversion efficiency in photon energy to the photocurrent. The higher photocurrent was assigned to the higher donor density with reduced charge recombination due to inserted Ti dopant in Fe_2O_3 crystals which are strongly used in photoexcited water oxidation reactions.

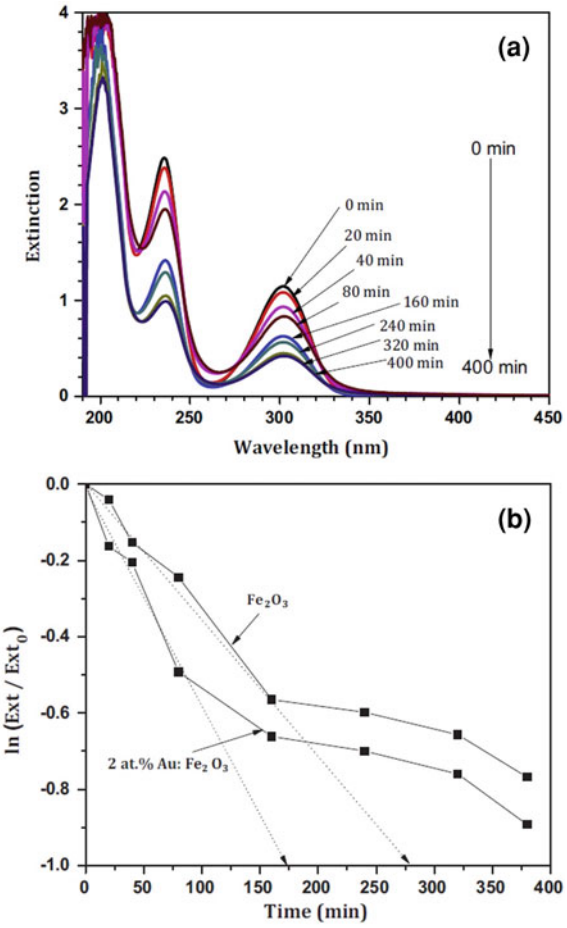

Fig. 7 Excitation spectra for salicylic acid decomposition, and **b** Kinetics plot for pure and 2% Au: Fe_2O_3 thin films. Reproduced with permission from Ref. [63], copyright elsevier

In a strategical study of enhanced photocatalysis, Co-doped Fe_2O_3 magnetic nanoparticles were used to catalyze the MB dye on UV-light [3]. Rhombohedral Co-Fe_2O_3 nanostructures were used to degrade the heterocyclic organic compounds. It is proposed, the cationic components of the MB dye interact with the negative surface of the catalyst via electrostatic adsorption and dissociate to the aromatic molecules into possible derivatives. The doping of Co helps to increase the combining effect between electron–hole species, resulting from the enhanced photocatalytic elimination (92%) of dye contents at 4% of Co concentration as compared to 2% of Co dopant as shown in Fig. 8.

Similarly, transitional metals such as Co and Mn-doped Fe_3O_4 nanostructures were made on microwave-assisted co-precipitation by A. Wahab et al., to fragment the synthetic MB dye on continuous irradiation of visible light [8]. Both the transitional metals were found highly effective toward bandgap engineering in Fe_3O_4 solids due to dopant effects. The optical and magnetic behavior were upgraded in order to improve

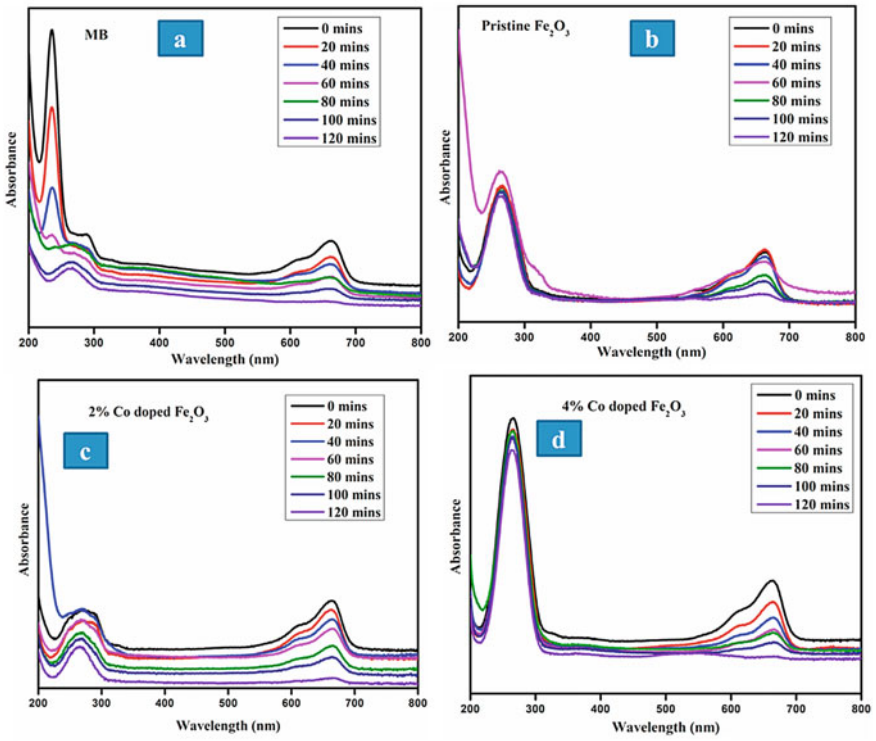

Fig. 8 UV–Vis spectra for **a** pure MB solution, **b** pure Fe_3O_4-MB solution, **c** 2% Co-Fe_3O_4 and 4% Co-Fe_3O_4 , Reproduced with permission from Ref. [3], copyright elsevier

the catalytic quality of the magnetic nanocatalysts for wastewater treatment. It has been studied that the doped ions create possible trapping levels or and deep levels at the bottom of CB in iron oxides. These levels capture the free electrons, generated from photo-induced dissociation of electron-holes and become the reason for longer charge separations. A simple co-precipitation method was performed to moderate the electronic and structural features of the iron oxide (Fe_2O_3) nanostructures by Sivaranjani et al. [68]. It was seen that the doped iron oxides showed considerably higher photocatalytic action against MB dye. Zn ion was aimed to introduce in Fe_2O_3 lattice in the form of interstitial dopant centers because of almost similar valence properties. The band edges shift in Fe_2O_3 crystal and the photosensitization reaction takes place for the MB dissociation on visible light. It is also considered that the oxidation of Zn takes place at a higher concentration of dopants along with Fe^{3+} to Fe^{2+} reduction, which may simultaneously accelerate the rapid formation of hydroxyl radicals by the decomposition of H_2O_2 on light illumination.

Recently, 2D materials such as graphene, carbon nanotube (CNT), carbon nitride, and boron nitrite have gained considerable attention for the best utilization of solar

power in energy conversion integrated circuits. Various techniques such as photovoltaics, and photocatalysis have grown as advanced tools for renewable energy. Many optoelectronic devices and sensors are constructed based upon solar energy conversion efficiency to resolve the energy shortage in recent progress in sustainable energy. Therefore, researchers have targeted the new class of metamaterials for the designing and development of multicomponent microsystems. Particularly, iron-oxides (magnetic nanomaterials) are integrated with the carbonaceous 2D materials (graphene, CNT) to manufacture the hybrid catalysts in chemical industries and laboratories [69, 70]. To discharge the industrial contaminants containing toxic metal ions, heterocyclic organics, and microorganisms, these supported magnetic materials are used on a large scale where the 2D components retain the chemical stability and longer durability. At present, numerous research groups have published their work based on the utmost decomposition of aromatic complexes especially thiazine minerals, which caused lung infections, hyperhidrosis, and mental problems. Therefore, this topic is highly focused on advanced research and development in photocatalysis. Singh et al. have studied a remarkable enhancement in photocatalytic systems using metal oxide catalysts associated with graphene materials owing to its large surface space and recycling personalities [71]. It is demonstrated, the graphene sheets bonded with ferrites possess open active surfaces which means larger atomic centers for stimulating the redox mechanism during photocatalysis. The honeycomb structure of the graphene referred to a higher mechanical strength, and flexibility to carry the amazing catalytic impacts of the ferrite composites. Likewise, fascinated RGO@α-Fe_2O_3 nanocomposites were found more competent against individual reduced graphene oxides (RGO) and α-Fe_2O_3. The functionalized RGO@α-Fe_2O_3 materials due to enlarged robust faces, providing numerous oxygen vacancies which play an imperative character for delaying in charge recombination. By using this RGO@α-Fe_2O_3 catalyst, around 99% degradation of MB dye was claimed by Kasimayan Uma and colleagues [70] on visible region. Notably, 2.5 and 0.7 times more photodegraded efficiency was verified as compared to pure RGO and α-Fe_2O_3 nanostructures and the reusability along with stability confirmed by the recycling process.

In another class of carbonaceous sheets, [72] CNT has been admired for the removal of phenol from contaminant water using modified ferrites loaded with CNT. The adsorption of phenolic substance was analyzed using the Freundlich model, which suggested a strong impact on the adsorption tendency of phenolic ions on the impregnated CNT-Fe_2O_3 surfaces. Analogous to graphene, hexagonal boron nitride (h-BN) also possesses phenomenal physicochemical and adsorption features toward organic dyes, and inorganic pollutants eliminations. Due to rapid solution processibility, active surface area, and high polarity of B-N bond, h-BN (called white graphene) has preferred to serve as catalysts for pollutant removal from the environmental waste [73]. Besides that, pure HB also has the same bond length as the graphene with similar honeycomb structures which behave as an insulator (5–6 eV bandgap) [74]. For the tunable optical and electronic properties of these 2D-supported ferrite materials were used for a longer charge separation mechanism, resulting from charge transportation ability during the photocatalytic process. Light-driven photocatalytic removal of dye molecules was carried out by the Manjula R. Shenoy et al.

[75] employing ά-Fe_2O_3/h-BN composites. The chemical kinetical and mechanism exhibited around 91% decay of MB dye where 5% decay in case of h-BN combined with the ά-Fe_2O_3. The recycling study was also done for the reuse of catalysts which proved that the functionalized ferrite materials are highly suitable for large-scale mineralization in waste water. Carbon nitride (C_3N_4) has also attracted huge consideration owing to its appropriate band gap value (2.7–2.8 eV) along with thermochemical stability, and non-toxicity [76]. Boron-doped C_3N_4 supported $NiFe_2O_4$ nanocomposite were explored towards the enhanced performance of photo-driven decomposition of MB under visible illumination where B-doped C_3N_4 were synthesized by thermal condensation and Ni loaded Fe_2O_4 prepared by the economical sol–gel method by Surabhi kamal and group [76]. The higher degradation (98%) of MB was achieved using C_3N_4/$NiFe_2O_4$ nanomaterials as compared to pure B-doped C_3N_4 and $NiFe_2O_4$ as shown in Fig. 9, respectively. Alteration in the bandgap of C_3N_4/$NiFe_2O_4$ (2.05 eV) structures and its response to absorbing visible light,

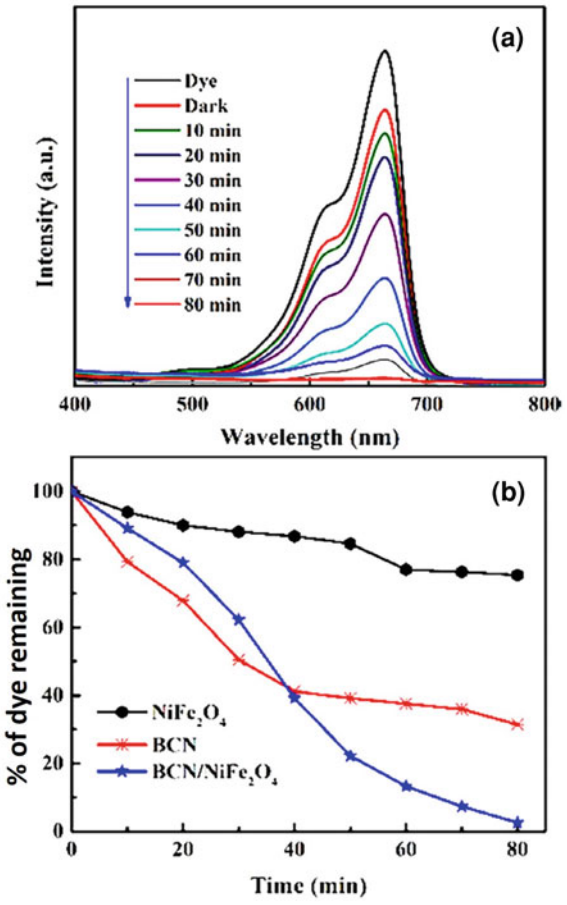

Fig. 9 Photocatalysis degradation of MB using B-doped C_3N_4/$NiFe_2O_4$, and **b** plot of time versus % of dye remained [76], open access

allowed them to improve the catalytic action than the pure C_3N_4 (2.65 eV) and $NiFe_2O_4$ (2.38 eV). These electronic band positions were found to be responsible for the almost complete decomposition of heterocyclic organic structures from the environmental pollutants.

4.2 Photocatalytic Antibacterial Enhancement in Ferrites

The killing factor in antimicrobial agents was improved and implemented in biomedical sectors over the past few years. The development and success in cost-effective medicines and chemicals have attracted extensive interest in formulating biocompatible antibiotic carriers in pharmaceutical industries and laboratories at large scale. The advanced metamaterials with their exceptional functionalities assembled and extremely processed in the field of photo-based antimicrobial research and innovations. However, ferrites have shown their potentials in biomedical fields due to unique magnetic and electronic properties, allowed them as the strongest candidates for the diagnosis of diseases, drug carrier, and deliveries, over the studied metal oxides [77]. Numbers of experimental and theoretical database studies are addressed for the antibacterial aspects of ferrite substances. Besides, the role of light has been directed for the rapid formation of the ROS species on the ferrite surfaces to raise the separation period between electrons and holes. Wider applications of ferrites have been published for the antibacterial performances induced by UV light. In this section, we will cover some of the ferrite-based antimicrobial findings to conceptualize the ROS generations and delayed recombination process on illuminated light. Therefore, various spinel ferrites were formed at the micro and nanoscales like Ag-$CuFe_2O_4$@WO_3 nanocomposite were synthesized by Mohammad et al. [78] and found its light-driven antibacterial mechanism. The formation of ROS radicals exist a vital character to increase the recombination time in ferrites and enhance the antibacterial activity. The bonded metal ions initiate to form multiple bands into the ferrites which delayed the recombination, already discussed in the above sections. The relation between ROS production and late recombination is the widely accepted reasons for the gathered photocatalytic research. Hence, the role of light found to be necessary for catalyzing the ferrites and for producing active ROS which participate to damage the antibacterial cell. In a mechanism, the free radical ions insert into the bacteria membranes which caused a disturbance in metabolic processes. The damage in cell lines caused leakage of cytoplasm in bacteria and such abnormal media destroy the organelles eventually, restricting the normal growth in cells. Jesudoss et al. [79] deduced a systematic cell killing mechanism on light illumination using ferrites $Mn_{1-x}Ni_xFe_2O_4$ nanocomposites against Gram-positive and negative bacteria as shown in Fig. 10, respectively.

For more clearance, ferrite nanosystems [79] were used for the antibacterial studies against the Gram-positive (*Staphylococcus aureus and Bacillus subtilis*) and Gram-negative (*Pseudomonas aeruginosa and Escherichia coli*) species. They revealed the role of excited free electrons and holes as reducing and oxidizing

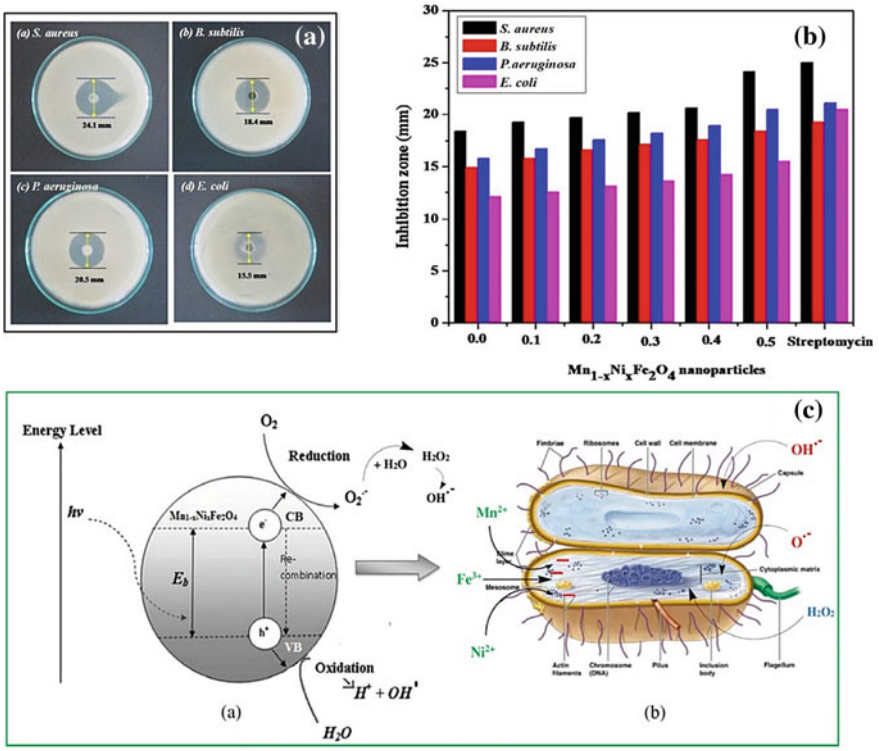

Fig. 10 **A** Zone of inhibition observed by $Mn0.5Ni0.5Fe_2O_4$ nanoparticles against the different bacterial strains; **B** Inhibitory zone w.r.t. the standard streptomycin toward bacteria; **C**: (a) Systematic antibacterial process for the $Mn_{1-x}Ni_xFe_2O_4$ magnetic nanoparticles, (b) inhibition activity of bacterial growth by the nanoparticles, Reproduced with permission from Ref. [79], copyright elsevier

agents. The free electrons interact with the oxygen molecules at the top of CB and produce superoxide anion ($O_2^{-\bullet}$) by reduction which degrade water and produces toxic hydrogen peroxide (H_2O_2) whereas holes generate active hydroxyl ions (OH^*) via oxidation reactions. These radicals are highly pressed to improve photocatalytic antibacterial studies in the case of ferrites and their derivatives. Overall, the spinel ferrites shown their remarkable photo tempted biomedical applications such as bioimaging cancer therapy, diabetes medicine, and developments in vaccines.

5 Conclusion and Future Perspective

This chapter gives a comprehensive overview of the synthesis techniques of ferrite nanomaterials with their potential applications in photocatalysis such as the degradation of organic contaminants. In the present scenario, the various techniques are

discussed for the synthesis of the ferrite nanomaterials with their tunable shape and size properties, which ultimately influence the photocatalytic activities. Ferrite nanomaterials and ferrite nanocomposites are known as a promising new class of photocatalytic materials and were found a suitable candidate for the photocatalysts to address many global environmental problems such as organic contaminants, removal of heavy metal toxic ions, and antimicrobial applications. Two different semiconductors combine between two components with different band-gaps under visible region response, which results in an interfacial band arrangement as known as a heterojunction. Hence, a Schottky barrier formed at the semiconductor heterojunctions which reduced the recombination rate of the photogenerated electron, and electron-holes pairs, which improve the photocatalytic activities.

Therefore, the photocatalytic activity of ferrite-based heterojunction materials is enhanced, due to the delay in the charge recombination rate, extended light adsorption, enhanced light absorption efficiency, enhanced charge separation efficiency, and transport properties. There are various factors such as electron–hole pair dissociation, recombination rate, temperature, pH, catalytic structure, and intensity of incident light which are responsible for the photocatalytic activities of ferrite nanomaterials. Thus the ferrite nanomaterial's with its excellent chemical stability, which shows the ability to treat wastewater and other industrial effluents. Thus we can say that in the future, notable efforts should be made for the commercialization of ferrite nanomaterials doped with other semiconducting or plasmonic nanoparticles for practical use in industries for wastewater treatment.

The photocatalytic activity of ferrite nanomaterials and ferrite nanocomposites for the degradation of other pollutants such as antibiotics, pesticides, and other organic pollutants should remain an area of scientific interest until exciting results are acquired.

Acknowledgements The authors (Prof. HC Swart and Dr. Promod Kumar) acknowledge the support provided by the South African Research Chairs Initiative of the Department of Science and Technology (DST) (84415) and the University of the Free State for taking a keen interest in research and extending financial support for carrying out the research work. Dr. Mohan C. Mathpal greatly acknowledges the funding from the FONDECYT program (N ° 3190316) to support the research activity. J.R.M and M.C. acknowledge support from ANID Fondequip EQM140168.

References

1. Bibi I, Nazar N, Ata S, Sultan M, Ali A, Abbas A, Jilani K, Kamal S, Sarim FM, Khan MI, Jalal F, Iqbal M (2019) Green synthesis of iron oxide nanoparticles using pomegranate seeds extract and photocatalytic activity evaluation for the degradation of textile dye. J Mater Res Technol 8:6115–6124
2. Wang G, Ling Y, Wheeler DA, George KEN, Horsley K, Heske C, Zhang JZ, Li Y (2011) Facile synthesis of highly photoactive α-Fe2O 3-based films for water oxidation. Nano Lett 11:3503–3509
3. Keerthana SP, Yuvakkumar R, Ravi G, Kumar P, Elshikh MS, Alkhamis HH, Alrefaei AF, Velauthapillai D (2021) A strategy to enhance the photocatalytic efficiency of α-Fe2O3. Chemosphere 270:129498
4. Mahmoud MHH, Ismail AA, Sanad MMS (2012) Developing a cost-effective synthesis of active iron oxide doped titania photocatalysts loaded with palladium, platinum, or silver nanoparticles. Chem Eng J 187:96–103
5. Guo X, Wang L, Tan Y (2015) Hematite nanorods Co-doped with Ru cations with different valence states as high-performance photoanodes for water splitting. Nano Energy 16:320–328
6. Zhang X, Li H, Wang S, Fan FRF, Bard AJ (2014) Improvement of hematite as photocatalyst by doping with tantalum. J Phys Chem C 118:16842–16850
7. Wang D, Astruc D (2014) Fast-growing field of magnetically recyclable nanocatalysts. Chem Rev 114:6949–6985
8. Wahab A, Imran M, Ikram M, Naz M, Aqeel M, Rafiq A, Majeed H, Ali S (2019) Dye degradation property of cobalt and manganese doped iron oxide nanoparticles. Appl Nanosci 9:1823–1832
9. Zhang Z, Hossain MF, Miyazaki T, Takahashi T (2010) Gas-phase photocatalytic activity of ultrathin pt layer coated on α-Fe2O3 films under visible light illumination. Environ Sci Technol 44:4741–4746
10. Cong Y, Chen M, Xu T, Zhang Y, Wang Q (2014) Tantalum and aluminum co-doped iron oxide as a robust photocatalyst for water oxidation. Appl Catal B Environ 147:733–740
11. Zhang J, Liu X, Wang L, Yang T, Guo X, Wu S, Wang S, Zhang S (2011) Au-functionalized hematite hybrid nanospindles: general synthesis, gas sensing and catalytic properties. J Phys Chem C 115:5352–5357
12. Mahadik MA, Shinde SS, Rajpure KY, Bhosale CH (2013) Photocatalytic oxidation of Rhodamine B with ferric oxide thin films under solar illumination. Mater Res Bull 48:4058–4065
13. Jang JS, Yoon KY, Xiao Y, Fan FRF, Bard AJ (2009) Development of a potential Fe2O3-based photocatalyst thin film for water oxidation by scanning electrochemical microscopy: effects of Ag-Fe2O3 nanocomposite and Sn doping. Chem Mater 21:4803–4810
14. Liu J, Cai YY, Tian ZF, Ruan GS, Ye YX, Liang CH, Shao GS (2014) Highly oriented Ge-doped hematite nanosheet arrays for photoelectrochemical water oxidation. Nano Energy 9:282–290
15. Hu Y, Kleiman-shwarsctein A, Forman AJ, Hazen D, Park J, Mcfarland EW, Barbara S, Barbara S (2008) Pt-doped α-Fe2O3 thin films active for photoelectrochemical water splitting. Chem Mater 20:3803–3805
16. Wei Y, Han S, Walker DA, Warren SC, Grzybowski BA (2012) Enhanced photocatalytic activity of hybrid Fe2O3-Pd nanoparticulate catalysts. Chem Sci 3:1090–1094
17. Xu H, Li BO, Li P (2018) Morphology dependent photocatalytic efficacy of zinc ferrite probed for methyl orange degradation. J Serb Chem Soc 83:1261–1271
18. Irfan S, Zhuanghao Z, Li F, Chen Y, Liang G, Luo J, Ping F (2019) Critical review: Bismuth ferrite as an emerging visible light active nanostructured photocatalyst. J Mater Res Technol 8:6375–6389
19. Kelebogile O,. Masunga N, Kuvarega A, Ti T, Mamba BB, Kefeni KK (2020) Cobalt ferrite nanoparticles and nanocomposites: photocatalytic , antimicrobial activity and toxicity in water treatment. Mater Sci Semicond Process 123:105523

20. Casbeer E, Sharma VK, Li X (2012) Synthesis and photocatalytic activity of ferrites under visible light: a review. Sep Purif Technol 87:1–14
21. Shun Li YW, Lin Y-H, Zhang B-P, Nan C-W (2009) Photocatalytic and magnetic behaviors observed in nanostructured BiFeO3 particles. J Appl Phys 105:056105–3
22. Herrmann J (1999) Heterogeneous photocatalysis: fundamentals and applications to the removal of various types of aqueous pollutants. Catal Today 53:115–129
23. Rajeshwar K, Osugi ME, Chanmanee W, Chenthamarakshan CR (2008) Journal of photochemistry and photobiology C: photochemistry reviews heterogeneous photocatalytic treatment of organic dyes in air and aqueous media. J Photochem Photobiol C Photochem Rev 9:171–192
24. Kitano M, Hara M (2010) Heterogeneous photocatalytic cleavage of water. J Mater Chem 20:627–641
25. Tang NJ, Zhong W, Jiang HY, Wu XL, Liu W, Du YW (2004) Nanostructured magnetite (Fe3O4) thin films prepared by sol-gel method. J Magn Magn Mater 282:92–95
26. Da Costa GM, De Grave E, De Bakker PMA, Vandenberghe RE (1994) Synthesis and characterization of some iron oxides by sol-gel method. J Solid State Chem 113:405–412
27. De Freitas JC, Branco RM, Lisboa IGO, Da Costa TP, Campos MGN, Júnior MJ, Marques RFC (2015) Magnetic nanoparticles obtained by homogeneous coprecipitation sonochemically assisted. Mater Res 18:220–224
28. Lu AH, Salabas EL, Schüth F (2007) Magnetic nanoparticles: synthesis, protection, functionalization, and application. Angew Chemie Int Ed 46:1222–1244
29. Deng H, Li X, Peng Q, Wang X, Chen J, Li Y (2005) Monodisperse magnetic single-crystal ferrite microspheres. Angew Chemie Int Ed 44:2782–2785
30. Park J, An K, Hwang Y, Park JEG, Noh HJ, Kim JY, Park JH, Hwang NM, Hyeon T (2004) Ultra-large-scale syntheses of monodisperse nanocrystals. Nat Mater 3:891–895
31. Makarov VV, Makarova SS, Love AJ, Sinitsyna OV, Dudnik AO, Yaminsky IV, Taliansky ME, Kalinina NO (2014) Biosynthesis of stable iron oxide nanoparticles in aqueous extracts of hordeum vulgare and rumex acetosa plants. Langmuir 30:5982–5988
32. Singh OV (2015) Bio-nanoparticles: biosynthesis and sustainable biotechnological implications. Wiley-Blackwell, pp 1–375
33. Al-Mokdad F, Hassan RS, Awad R (2019) Physical and dielectric properties of MnFe2O4 doped by Mo. Curr Nanomater 4:125–136
34. Arfan M, Nawaid D, Shahid T, Iqbal Z, Majeed Y, Akram I, Bagheri R, Song Z, Zeb A (2019) Tailoring of nanostructures: Al doped CuO synthesized by composite-hydroxide-mediated approach. Results Phys 13:102187
35. Iqbal M, Ali A, Shahzad K, Farhat A, Rana M, Khan J, Khan K (2019) Synthesis and characterization of transition metals doped CuO nanostructure and their application in hybrid bulk heterojunction solar cells. SN Appl Sci 1:647–648
36. Lassoued A, Lassoued MS, García-Granda S, Dkhil B, Ammar S, Gadri A (2018) Synthesis and characterization of Ni-doped α-Fe2O3 nanoparticles through co-precipitation method with enhanced photocatalytic activities. J Mater Sci Mater Electron 29:5726–5737
37. Yan Y, Al-Jassim MM, Wei S-H (2006) Doping of ZnO by group-IB elements. Appl Phys Lett 181912:87–90
38. Kumar G, Kumar P, Roos WD, Swart HC (2020) Colloids and surfaces B: biointerfaces thermally induced structural metamorphosis of ZnO: Rb nanostructures for antibacterial impacts. Colloids Surf B Biointerfaces 188:110821
39. Gaur LK, Gairola P, Gairola SP, Mathpal MC, Kumar P, Kumar S, Kushavah D, Agrahari V, Aragon FFH, Soler MAG, Swart HC (2021) Cobalt doping induced shape transformation and its effect on luminescence in zinc oxide rod-like nanostructures. J Alloys Compd 868:159189
40. Huang C, Zhang X, Zhang H, Zhang W, Lan C, Li M (2020) Enhanced photoelectrocatalytic performance from size effects in pure and La—doped—BiFeO3 nanoparticles. Appl Phys A 126:273–279
41. Keterew K, Mamba BB (2020) Photocatalytic application of spinel ferrite nanoparticles and nanocomposites in wastewater treatment. Rev Sustain Mater Technol 23:e00140

42. Ruan Q, Zhang W (2009) Tunable morphology of Bi2Fe4O9 crystals for photocatalytic oxidation. J Phys Chem 113:4168–4173
43. Fei L, Yuan J, Hu Y, Wu C, Wang J, Wang Y (2011) Visible light responsive perovskite BiFeO 3 pills and rods with dominant 111 c facets. Cryst Growth Des 11:1049–1053
44. Zhang Q, Sando D, Nagarajan V (2016) Chemical route derived bismuth ferrite thin films and nanomaterials. J Mater Chem C 4:4092–4124
45. Han L, Zhou X, Wan L, Deng Y, Zhan S (2014) Synthesis of ZnFe2O4 nanoplates by succinic acid-assisted hydrothermal route and their photocatalytic degradation of rhodamine B under visible light. J Environ Chem Eng 2:123–130
46. Zhang X, Lv J, Bourgeois L, Cui J, Wu Y (2011) Formation and photocatalytic properties of bismuth ferrite submicrocrystals with tunable morphologies. New J Chem 35:937–941
47. Wang X, Lin Y, Zhang ZC, Bian JY (2011) Photocatalytic activities of multiferroic bismuth ferrite nanoparticles prepared by glycol-based sol–gel process. J Sol-Gel Sci Technol 60:1–5
48. Zhu X, Hang Q, Xing Z et al (2011) Microwave hydrothermal synthesis, structural characterization, and visible-light photocatalytic activities of single-crystalline bismuth ferric nanocrystals. J Am Ceram Soc 94:2688–2693
49. Xiong P, Zhu J, Wang X (2013) Cadmium sulfide−ferrite nanocomposite as a magnetically recyclable photocatalyst with enhanced visible-light-driven photocatalytic activity and photostability. Ind Eng Chem Res 52:17126–17133
50. Sobahi TR, Amin MS (2021) Synthesis of ZnO/ZnFe2O4/Pt nanoparticles heterojunction photocatalysts with superior photocatalytic activity. Ceram Int 46:3558–3564
51. Zheng F, Shen M, Guo R, Fang L, Dong W (2011) Magnetically separable BiFeO3 nanoparticles with a g-Fe2O3 parasitic phase: controlled fabrication and enhanced visible-light photocatalytic activity. J Mater Chem 21:18645–18652
52. Thongam DD, Chaturvedi H (2021) Advances in nanomaterials for heterogeneous photocatalysis. Nano Express 2:012005
53. Dutta V, Sharma S, Raizada P (2019) Review on augmentation in photocatalytic activity of CoFe2O4 via heterojunction formation for photocatalysis of organic pollutants in water. J Saudi Chem Soc 23:1119–1136
54. Zhang T, Shen Y, Qiu Y, Liu Y, Xiong R, Shi J, Wei J (2017) Facial synthesis and photoreaction mechanism of BiFeO3/Bi2Fe4O9 heterojunction nano fibers. ACS Sustain Chem Eng 5:4630–4636
55. Marimuthu S, Antonisamy AJ, Malayandi S, Rajendran K, Tsai PC, Pugazhendhi A, Ponnusamy VK (2020) Silver nanoparticles in dye effluent treatment: a review on synthesis, treatment methods, mechanisms, photocatalytic degradation, toxic effects and mitigation of toxicity. J Photochem Photobiol B Biol 205:111823
56. Shenoy MR, Ayyasamy S, Reddy MVRV, Kadarkarai G, Suryakanth J, Tamilarasan S, Thangavelu S, Jeyaramane AC (2020) The effect of morphology-dependent surface charges of iron oxide on the visible light photocatalytic degradation of methylene blue dye. J Mater Sci Mater Electron 31:17703–17717
57. Lassoued A, Lassoued MS, Dkhil B, Ammar S, Gadri A (2018) Photocatalytic degradation of methylene blue dye by iron oxide (α-Fe2O3) nanoparticles under visible irradiation. J Mater Sci Mater Electron 29:8142–8152
58. Zhou X, Yang H, Wang C, Mao X, Wang Y, Yang Y, Liu G (2010) Visible light induced photocatalytic degradation of rhodamine B on one-dimensional iron oxide particles. J Phys Chem C 114:17051–17061
59. Nathan VK, Ammini P, Vijayan J (2019) Photocatalytic degradation of synthetic dyes using iron (III) oxide nanoparticles (Fe(2)O(3)-Nps) synthesised using Rhizophora mucronata Lam. IET Nanobiotechnol 13:120–123
60. Reveendran R, Khadar MA (2018) Structural, optical and electrical properties of Cu doped α-Fe2O3 nanoparticles. Mater Chem Phys 219:142–154
61. Suresh R, Giribabu K, Manigandan R, Mangalaraja RV, Solorza JY, Stephen A, Narayanan V (2017) Synthesis of Co2+-doped Fe2O3 photocatalyst for degradation of pararosaniline dye. Solid State Sci 68:39–46

62. Muraro PCL, Mortari SR, Vizzotto BS, Chuy G, dos Santos C, Brum LFW, da Silva WL (2020) Iron oxide nanocatalyst with titanium and silver nanoparticles: Synthesis, characterization and photocatalytic activity on the degradation of Rhodamine B dye. Sci Rep 10:1–9
63. Mahadik MA, Shinde SS, Kumbhar SS, Pathan HM, Rajpure KY, Bhosale CH (2015) Enhanced photocatalytic activity of sprayed Au doped ferric oxide thin films for salicylic acid degradation in aqueous medium. J Photochem Photobiol B Biol 142:43–50
64. Liu H, Tian K, Ning J, Zhong Y, Zhang Z, Hu Y (2019) One-Step solvothermal formation of pt nanoparticles decorated Pt 2+-doped α-Fe2O3 nanoplates with enhanced photocatalytic O2 evolution. ACS Catal 9:1211–1219
65. Alzahrani E (2015) Photodegradation of eosin y using silver-doped magnetic nanoparticles. Int J Anal Chem 2015:1–11
66. Amoresi RAC, Oliveira RC, Marana NL, De Almeida PB, Prata PS, Zaghete MA, Longo E, Sambrano JR, Simões AZ (2019) CeO2 nanoparticle morphologies and their corresponding crystalline planes for the photocatalytic degradation of organic pollutants. ACS Appl Nano Mater 2:6513–6526
67. Kumar P, Kumar A, Ahmad M, Kazim S (2020) Optical and photocatalytic properties of Rb doped ZnO nanoparticles. Appl Surf Sci 514:145930
68. Sivaranjani R, Thayumanavan A, Sriram S (2019) Photocatalytic activity of Zn-doped Fe2O3 nanoparticles: a combined experimental and theoretical study. Bull Mater Sci 42:185
69. Bharath G, Anwer S, Mangalaraja RV, Alhseinat E, Banat F, Ponpandian N (2018) Sunlight-Induced photochemical synthesis of Au nanodots on α-Fe2O3@Reduced graphene oxide nanocomposite and their enhanced heterogeneous catalytic properties. Sci Rep 8:1–14
70. Uma K, Chong S, Mohan SC, Jothivenkatachalam K, Thomas C, Yang K, Lin J (2020) Multi-functional RGO-supported α-Fe_2O_3 nanocomposites for high-performance pseudocapacitors and visible light–driven photocatalytic applications. Ionics 26:3491–3500
71. Singh N, Prakash J, Gupta RK (2017) Design and engineering of high-performance photocatalytic systems based on metal oxide-graphene-noble metal nanocomposites. Mol Syst Des Eng 2:422–439
72. Asmaly HA, Abussaud B, Ihsanullah, Saleh TA, Gupta VK, Atieh MA (2015) Ferric oxide nanoparticles decorated carbon nanotubes and carbon nanofibers: from synthesis to enhanced removal of phenol. J Saudi Chem Soc 19:511–520
73. Hassan MIJ, Haider MIJ, Hamid AU, Ikram ISM, Qumar ARU (2020) 2D chemically exfoliated hexagonal boron nitride (hBN) nanosheets doped with Ni: synthesis, properties and catalytic application for the treatment of industrial wastewater. Appl Nanosci 10:3525–3538
74. Wang N, Yang G, Wang H, Sun R, Wong CP (2018) Visible light-responsive photocatalytic activity of boron nitride incorporated composites. Front Chem 6:1–12
75. Shenoy MR, Ayyasamy S, Bhojan V, Swaminathan R (2021) Visible light sensitive hexagonal boron nitride (hBN) decorated Fe2O3 photocatalyst for the degradation of methylene blue. J Mater Sci Mater Electron 32:4766–4783
76. Kamal S, Balu S, Palanisamy S, Uma K, Velusamy V, Yang TCK (2019) Results in physics synthesis of boron doped C3N4/NiFe2O4 nanocomposite: an enhanced visible light photocatalyst for the degradation of methylene blue. Results Phys 12:1238–1244
77. Lam SM, Sin JC, Mohamed AR (2020) Magnetic-based photocatalyst for antibacterial application and catalytic performance. In: Inamuddin, Asiri A, Lichtfouse E (eds) Nanophotocatalysis and environmental applications. environmental chemistry for a sustainable world, vol 30. Springer, Cham. https://doi.org/10.1007/978-3-030-12619-3_8
78. Sayadi MH, AhmadpourN, Homaeigohar S (2021) Photocatalytic and antibacterial properties of Ag-$CuFe_2O_4$@WO_3 magnetic nanocomposite. Nanomaterials 11:298–19
79. Jesudoss SK, Vijaya JJ, Kennedy LJ, Rajan PI, Al-lohedan HA, Jothiramalingam R, Kaviyarasu K, Bououdina M (2016) J Photochem Photobiol B Biol 165:121–132

Chapter 20
Polycrystalline Alkali Niobate Piezoelectric Ceramics Sintered by Microwave Technique

Irom Monika Aniz and Mamata Maisnam

1 Introduction

Piezoelectricity comes from the Greek word piezo meaning pressure. It is an effect that arises due to specific microscopic structures in crystalline solid. Piezoelectric phenomena convert mechanical energy into electrical energy and vice versa which originated due to the induced displacement of ionic charges within the crystal structure. Piezoelectricity occurs in crystals where the unit cell does not have a center of symmetry. When no external stress is applied, the crystal exhibits asymmetrical charge distribution and zero net electric dipole moment. On application of external stress, the initial symmetry is disrupted and an intrinsic electric field develops due to charge displacement and the development of polarization out of the displaced charges. Since piezoelectric materials produce internal electric potential under the application of an external force or vice versa, they are often referred to as smart materials and occupy vital roles in our day-to-day life in different ways. Various naturally occurring crystals like quartz, sucrose, Rochelle salt, Topaz, Tourmaline exhibit piezoelectricity. However, recent modern devices attempt to use polycrystalline ceramics, which are fabricated easily and shaped at a low cost. Some piezoelectric ceramics materials such as barium titanates, lead zirconate titanates (PZTs), bismuth sodium titanates, alkali niobates, etc. show piezoelectric phenomena and among them, PZT is most widely used for its high-performance characteristics. For decades, PZT ceramics have dominated the technological industries and market due to their magnificent and outstanding piezoelectric properties. However, its main component: lead oxide (almost 60%), is highly toxic leading to extreme environmental concerns. Piezoelectric ceramics generally have the perovskite ABO_3 structure. The perovskite structure undergoes many phase transitions such as cubic, tetragonal, rhombohedral, orthorhombic, monoclinic, etc., beyond the Curie point. Below

I. M. Aniz (✉) · M. Maisnam
Department of Physics, National Institute of Technology Manipur, Langol, Imphal 795004, India

B. P. Swain (ed.), *Advances in Nanostructured Materials*, Materials Horizons:
From Nature to Nanomaterials, https://doi.org/10.1007/978-981-16-8391-6_20

the Curie point, different regions called domains containing spontaneous polarization constitute the crystal that orients themselves in different directions, and these regions are separated by walls called domain walls. Piezoceramics do not show spontaneous polarization and piezoelectricity because the ceramics are composed of randomly oriented domains in different directions, resulting in the cancellation of spontaneous polarization and net-zero polarization. To exhibit piezoelectricity, methods such as "poling" may be adopted by applying a static electric field to polarize the domains. If the polarization changes its direction with the application of electric fields a phenomenon known as ferroelectricity develops in the materials. The electric field required to reorient back the polarized domains is called the coercive field involving domain wall motion. Technically important physical parameters for piezoelectric materials includes relative permittivity, dielectric constant, piezoelectric coupling factors to name a few and thorough studies of these properties are essential to understand the piezoelectricity showing materials [1–3].

2 Potassium SodiumNiobate (KNN)

The general formula of alkali niobates is $ANbO_3$ where A is alkali metal. Potassium Niobate ($KNbO_3$) is ferroelectric having orthorhombic symmetry and sodium Niobate ($NaNbO_3$) is the anti-ferroelectric having orthorhombic symmetry. A specific composite compound comprising of $KNbO_3$ and $NaNbO_3$ as constituents have been developed as what is known as potassium sodium niobate, with compositional formula $K_xNa_yNbO_3$ (KNN), where x and y may be equal or may differ. This material family emerged as promising candidates for substitutes of lead-based ceramics owing to its high Curie temperature ~420 °C and comparable piezoelectric performance as that of the PZT family. Tailoring varieties of KNN have been in progress with an effort to achieve the higher piezoelectric properties in these perovskite-structured ferroelectrics. Potassium Sodium Niobates (KNNs) being a ferroelectric system with highly complex perovskite structured (ABO_3) body-centered cubic lattice where A denotes the lattice point at the corner of the cube which is occupied by K or Na, Nb occupies the B sites lattice points at the center and O occupies the face-centered position of the BCC lattice system. An illustration of the structure of KNN at room temperature is shown in Fig. 1. The perovskite-type ABO_3 unit cells show monoclinic symmetry even though the structure of KNN is orthorhombic at room temperature. It also shows the lattice parameters $a_m = c_m > b_m$, where b_m is perpendicular to a_m/c_m plane, and angle β is closer to 90°. The projection of the subcell along the axis b_m is shown in Fig. 1. As the a_m axis equals the c_m axis in length, diagonals are linked by dashed from rectangle as in the figure which is the projection of the unit cell of KNN along the b_m axis. [2].

In the early 1950s, potassium niobate and sodium niobate were found to exhibit ferroelectric properties. The phase diagram of $KNbO_3$ and $NaNbO_3$ was first reported in 1971 by Jaffe, which is shown in Fig. 2 [2]. The labels F and P in the diagram indicate the ferroelectric (F) phases and paraelectric (P) phases respectively, while

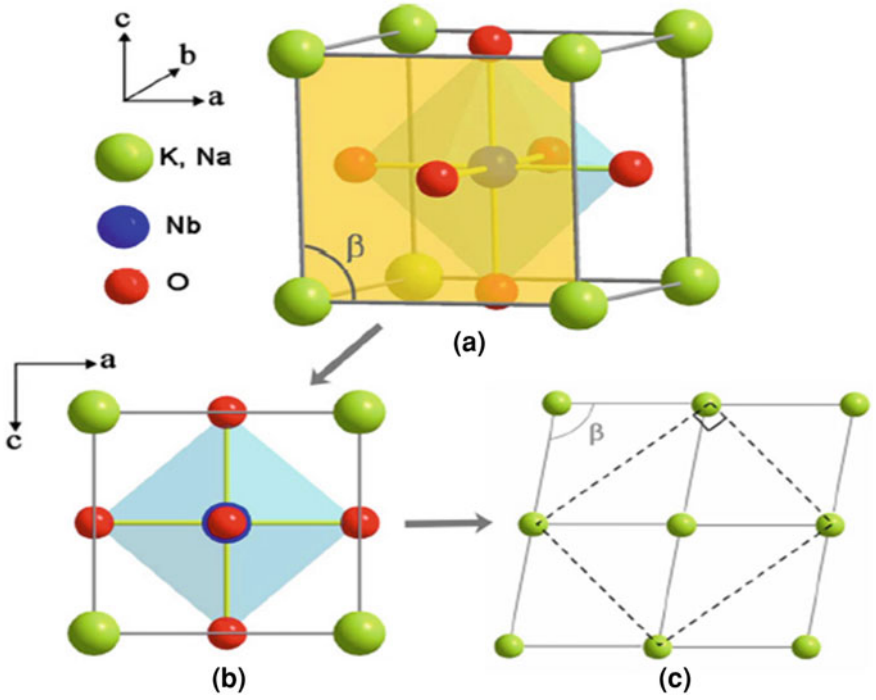

Fig. 1 Cell structure of KNN [2]

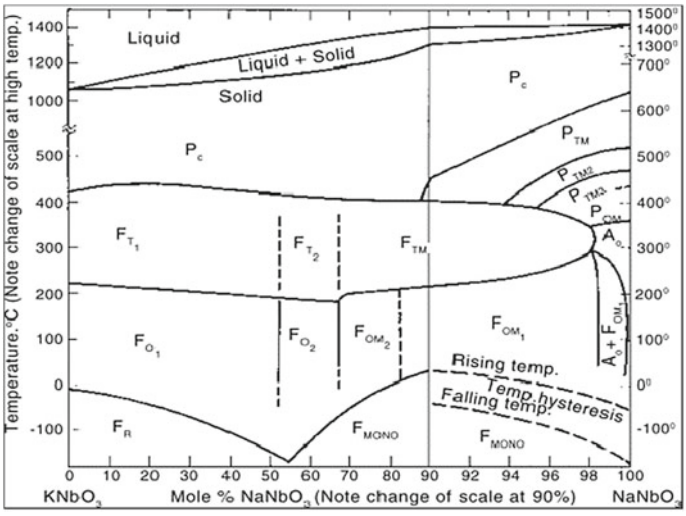

Fig. 2 Phase diagram of $KNbO_3$-$NaNbO_3$ solid solutions [2]

the subscripts O, T, M, C indicate whether they are orthorhombic (O), tetragonal (T), monoclinic (M), or cubic (C), respectively. The region in the phase diagram where there is a sudden change of structure indicates the morphotropic phase boundary (MPB) and generally shows enhanced dielectric and piezoelectric properties. For KNN, the MPB is found in between orthorhombic and tetragonal phases. The MPB further exhibits two distinct orthorhombic phases at lower temperatures and two tetragonal phases at higher temperatures. Solid solutions $KNbO_3$ and $NaNbO_3$ with perovskite structures have distinct symmetries depending on the compositions. Generally, pure $KNbO_3$ has different polymorphisms: a low temperature (lesser than −10 °C) rhombohedral phase, a room temperature orthorhombic phase, and a high-temperature tetragonal phase (225–435 °C) and cubic phase (>435 °C). Contrastingly, $NaNbO_3$ shows seven polymorphic phases at different temperatures. At room temperature, $NaNbO_3$ is known to be orthorhombic and antiferroelectric. An oxygen octahedral tilting can further complexify the $NaNbO_3$ structure. Even 2% of K due to its relatively smaller size can change the structure of $NaNbO_3$ toward that of $KNbO_3$, which can then alter the piezoelectric performance. Many reports referred to the compositions around the $K_{0.5}Na_{0.5}NbO_3$ in recent decades. Some reports showed enhancement of the dielectric and piezoelectric properties in the vicinity of $K_{0.5}Na_{0.5}NbO_3$ composition even with dopping. Shifting of the phases is possible by varying the chemical compositions and doping in the KNN systems. Besides change of temperature plays a significant role in the phase shift of KNN systems. For example, at a temperature above ~200 °C, the orthorhombic phase of KNN changes into the tetragonal phase which then becomes cubic at temperature ~420 °C. The different phases correspondingly interfere with the piezoelectric behavior of these systems [4].

3 Sintering

Sintering is a common technique adopted for fabricating many functional ceramics with nearly accurate phases and structures. It is divided into three stages that overlap considerably, depending on the sintering kinetics, grains growth, size, and shape of the grains, pores development, and finally, densification close to the required dimension of the product. In the initial stage of the process, the particles become connected neck to neck, decrease the surface roughness, and form a porous powder of the compound particles with almost 60–70% densification. In the intervening stage, the grain grows rapidly due to the increase in densification rate. The densification rate then decreases in the final stage followed by the isolated pores either shrinking or merging. The grain growth dominates in the final stage depending on the mobility and interaction of pores/grain boundary. If this mobility increased in an uncontrolled fashion, abnormal grain growth occurs which inhibits proper densification [5].

3.1 Sintering of KNN Ceramics

KNN is a well-known candidate among lead-free piezoceramics. In general, for densification, sintering is done in two ways: normal sintering and spark plasma sintering. Normal sintering is the oldest conventional way of fabrication technique and is still more preferably used due to its significant advantages in shaping. Because of the volatilization problem of the alkali elements in KNN which is temperature-dependent, there is always deterioration in the density, phase, and mechanical strength of the KNN ceramics. Loss of stoichiometry due to volatilization of alkali elements and hence compositional variation is almost preventable even at a higher sintering temperature (greater than the melting point of KNN ~ 1200 °C). The volatilization of from many studies, it is verified that density dominantly influences the piezoelectric performance, and enhancement in densification is almost the result of the sufficient sintering temperature which is generally high for the ceramics. The piezoelectric coefficient of KNN is mainly dependent on the polymorphic phase transition temperature. However, a loss of A-site elements due to the requirement of high sintering temperature may lead to a shift in transition temperature and consequently degrades piezoelectric coefficient values despite attempts to increase the density. Grain growth processes are also influenced by sintering conditions. At low sintering temperatures, a homogeneous microstructure develops with quadrant grain shape powders in the size range of 500 nm to 1 μm. At the higher temperature of sintering, the grain coalescence appears between some grains meanwhile the others retain their original shape and size. Formation of the liquid phase may occur if the sintering temperature becomes higher and may result in the secondary phase. To achieve high density without liquid phase formation, solid-state sintering of KNN could be achieved with proper modification and elaborately controlled sintering procedures. The addition of sintering aids in the sintering of KNN ceramics minimizes the effect of abnormal grain growth by decreasing sintering temperatures. The commonly used sintering aids in this system are ZnO, CuO, LiF, MnO_2, Li_2O, Na_2O, etc. Spark plasma sintering (SPS) is one ideal tool for sintering highly volatile KNN ceramics. This sintering technique enhances piezoelectric and electrical properties more than normal sintering. It can improve mechanical properties with the improvement of densification and fine-grained microstructures. Many researchers have adopted these techniques for better properties of KNN ceramics. But, SPS is not suitable for industrial-scale for its high processing cost compared to normal sintering [6].

4 Characterizations

Characterization is one important step during the whole procedure of making a unique material. There are many techniques and instruments to characterize the yielded samples. For the piezoelectric materials, some important techniques for characterization include the structural properties, microstructural properties, and electrical

properties like dielectric constant, dielectric loss, and A.C conductivity. A brief theoretical background of these techniques is discussed below.

4.1 Structural Studies

X-ray diffraction experiment was first performed by Max. V. Laue in 1912. With his observation, Laue explained the crystalline nature of solids and proved that X-Rays behave like waves which he was later awarded the Nobel Prize in 1914. Thus, Laue suggested X-rays can be used as a tool for investigating the structure of crystals. This technique provides a piece of good information on phase information, crystal structure analysis, quantitative analysis, particle size, strain measurements, error locating, etc., of any kind of material.

In this method, a beam of monochromatic light, often K_α radiation, of X-rays are made to strike on the finely powdered sample. It is known that polycrystalline material consists of a large number of crystallites that are randomly oriented in all possible orientations. When an X-ray's beam is incident on the sample containing a large number of randomly oriented planes of crystallites, all possible interatomic planes with each diffraction angle, θ will be detected by the beam. Thus, diffraction peaks from differently oriented planes will be produced based on Bragg's condition of X-ray diffraction and established a relationship between the diffraction and structural properties. The Bragg condition of diffraction is given in the form of an equation known as Bragg's equation which is expressed as,

$$\lambda = 2d\sin\theta \tag{1}$$

where λ is the wavelength of the incident X-ray beam, d is the lattice spacing, and θ is the angle at which X-ray beam incidents on the crystal planes. As the relation suggests X-rays will be diffracted selectively only from those planes with respective directions given by θ, in which Bragg's law is satisfied. The direction of diffraction provides the interplanar spacing, d for a set of crystal planes (h k l). As the values of d area geometric function of the size and shape of the unit cell of crystal, the XRD technique can determine the type and dimension of crystal system to which they belong. By knowing the values of (h k l) corresponding to specific diffraction maximum and corresponding "d" values, the value of lattice constants or dimensions of the crystalline substance can be easily determined. The lattice parameter which can be obtained for different systems corresponding to the specific plane (hkl) are as follows;

For a cubic system:

$$1/d^2 = \left(h^2 + k^2 + l^2\right)/a^2 \tag{2}$$

For an orthorhombic system:

$$1/d^2 = h^2/a^2 + k^2/b^2 + l^2/c^2 \tag{3}$$

For a tetragonal system:

$$1/d^2 = \left(h^2 + k^2\right)/a^2 + l^2/c^2 \tag{4}$$

The crystalline size of the sample can be determined using the XRD data from the Scherrer formula given as

$$D = 0.9\lambda/\beta\cos\theta \tag{5}$$

where β is the full width at half the maximum of the diffraction peak.

The bulk density or experimental density for all the samples can be determined by the Archimedes principle. Using this principle, the experimental density can be calculated by measuring the weight and volume of the sample in air and water medium. By the given formula, we can obtain the bulk density as

$$d_{exp} = w_a/(w_a + w_w) \tag{6}$$

The porosity of a material is defined by the relative volume of pores present in the material. We can evaluate the porosity of the prepared sample as [7]

$$p = \frac{dx - dexp}{dx} \times 100 \tag{7}$$

4.2 Dielectric Measurements

Piezoelectric materials show dielectric phenomena which is the ability of the material to be polarized by an external electric field involving the arrangement of electrically charges species present in the material in space and thus acquiring electrical moment. Therefore the value of the dimensionless parameter known as relative permittivity or the dielectric constant is an extremely important parameter. It is a measure of polarization of the dielectrics and the ability to form a capacitance. Both polarization and electrical conduction phenomena are closely related as both phenomena are governed by the displacement of the charged species in the dielectrics. Different types of polarization such as electronic, ionic, and dipole polarization can occur involving specific charged species brought into motion not leaving their confined position, however, the electrical conduction caused the drift motion of the free charge species through the entire material from one electrode to the other. However, the conductivity of the material strongly influences the dielectric phenomena. In addition, the dielectric constant of a material is dependent on many changeable external factors

such as frequency of the applied field, temperature, pressure, humidity, etc. We determine the dielectric constant after measuring the capacitance as

$$\varepsilon' = \mathrm{Cd}/\varepsilon_o \mathrm{A} \tag{8}$$

where C, d, and A are the capacitance, thickness, and area of the sample respectively, $\varepsilon_o = 8.854 \times 10^{-14}$ F cm^{-1} is the permittivity of the free space. An application of an external electric field on a dielectric or conductor material is mostly accompanied by dissipation of electrical energy transformed generally into heat energy. The amount of power loss under the action of an applied electrical field is commonly measured by the parameter of what is known as dielectric loss and this parameter is important for that measured under the alternating applied field for dielectrics. Under this condition, the dielectric loss is measured from a quantity referred to as dielectric loss angle which describes the difference in the phase angle, "δ" between the applied field and the current through the dielectric. More descriptively, the tangent of this angle "tanδ" defines the dielectric loss dissipated. The dielectric loss grows with this angle and the reciprocal of the tangent of dielectric loss angle determines the quality factor of the dielectrics whose value is orders of tens of thousandths for good dielectrics. The electrical permittivity of dielectrics being associated always with a loss component can always be expressed as a complex quantity as $\tan\delta = \varepsilon' + i\varepsilon''$ where the real part ε' is the real permittivity of the material and the imaginary part, ε'' gives the dissipative part. The tangent of dielectric loss is also defined as

$$\tan\delta = \varepsilon''/\varepsilon'. \tag{9}$$

The value of dielectric loss varies inversely with the frequency of the applied field but increases with the increase of temperature. Other factors that influence the dielectric loss significantly are electrical conductivity, humidity, applied voltage, etc., to name a few.

Dielectric polarization in ceramics arises from the four polarization mechanisms: electronic, ionic, dipole polarization, and interfacial or space charge polarization. In electronic polarization, the center of the electron cloud around the atom separates the center of its nucleus by applying an electric field. Ionic polarization happens in solids with ionic bonding which automatically have dipoles but which get canceled due to the symmetry of the crystals. Under the application of an external field, the ions are displaced from their equilibrium positions which induce a net dipole moment. For dipole polarization, the molecular dipoles which are otherwise randomly distributed due to thermal energy become oriented along the applied field. Lastly, in interfacial or space charge polarization the charges become aligned with the applied field due to the limited movement of charges. Dipolar polarization and interfacial polarization are temperature-dependent and they occur at a low frequency while the atomic and ionic polarization is temperature and frequency-dependent and they occur at high frequency. These dielectric properties are dependent on many factors such as chemical composition, microstructure, methods of preparation, sintering temperature, and

sintering atmosphere [8]. The other electrical property of importance for dielectric materials is the a. c. conductivity which is the response of charge carriers under an applied a. c. field. The a. c. conductivity of a sample depends on the dielectric constant and dielectric loss as,

$$\sigma = \omega \varepsilon' \varepsilon_o \tan\delta \tag{10}$$

where ω is the angular frequency of the applied field [6].

5 Effect of Metal Oxides on the Preparation of KNN

The preparation and fabrication of advanced ceramics are the most crucial part of producing the materials efficiently. There are many techniques available to synthesis the materials. Some of the existing conventional methods are optimized, and some new techniques are being developed. Most piezoelectric materials synthesis is preferred in the conventional ceramic processing routes such as mechano-chemical, wet chemical, sol–gel, precursor, etc. High-energy ball milling produces fine homogeneous powders simply and effectively before sintering. There are many types of mills such as planetary, vibratory, rod, tumbler, etc. They change the reactivity of milled powder or induce chemical reactions during milling, and modify the conditions in which chemical reactions typically occur during synthesis. Sometimes phase transformations are indued due to milling among materials of similar composition.

Preparation of KNN faced difficulties mainly due to the volatility of alkali metals at high temperatures, difficulty in processing, sintering, and full densification. Adding metal oxide as a sintering aid like CuO, ZnO, MnO_2, etc., during processing efforts to diminish these drawbacks. Such additives influence the properties such as densification, grain size growth, phase formation, etc. Of these, MnO_2 has shown to promote the sintering process and suppress abnormal grain growth. Generally, piezoelectric performance is better when the leakage current in the material is relatively small. Larger leakage currents have an adverse effect on the polarization process, making it unsuitable for industrial applications. Lead-based ceramics are also usually doped with manganese, in an attempt to improve the mechanical quality factor (Qm) and reduce dielectric losses ($tan\ \delta$). The Mn^{2+}cation enters the solid solution creating oxygen vacancies and hardens the ferroelectric properties, enhancing the mechanical factor. Thus, MnO_2 added KNN piezoceramics have encouraging prospects in improving the performance of piezoelectric ceramics [9].

6 Experimental Methods

MnO_2 oxide added potassium sodium niobate electroceramics with compositional formula $K_{0.5}Na_{0.5}NbO_3$ + (x)MnO_2, where x = 0wt%, 5wt%, 10wt%, 15wt%, 20wt%, and 25wt%) were synthesized by ceramic route using high energy ball milling and microwave sintering technique. High purity AR grade starting chemicals (HIMEDIA) such as K_2CO_3 (98.0%), $NaCO_3$ (99.8%), and Nb_2O_5 (99.9%) were used and weighed in stoichiometry ratio for the composition $K_{0.5}Na_{0.5}NbO_3$. The powders were milled for 5 h to obtain a fine and homogeneous mixture of the compounds. The milled powders were calcined or pre-sintered at 850 °C for 20 min using the microwave sintering technique. The calcined powders were added with different amounts of MnO_2 as mentioned above and then milled again for 5 h in the high-energy ball milling. 2 wt. % of polyvinyl alcohol (PVA) was added as a binder, grounded in an agate mortar until we get a smooth free flow powder and pressed into pellets using an 8 mm diameter pellet die, the thickness of about 1–2 mm and giving a pressure of 5 N for 4 min using a hydraulic press (VB Ceramics make). A different set of pellets were then sintered at 950 °C for 10 min, 1000 °C for 10 min, 1000 °C for 20 min, and 1050 °C for 10 min by microwave sintering technique. The sintered pellets were polished on both the flat faces to get smooth, flat, and even surfaces free from any secondary oxide layers on the pellet faces and further cleaned thoroughly using acetone to be used for further characterizations. X-ray diffraction (XRD) using D8 Advance Eco Bruker Diffractometerwas done to study the structural properties of the samples. For measuring electrical properties, electrical contacts were made using silver paste on both the flat surfaces of the pellets and heated at 200 °C for 30 min. The electrical properties such as capacitance, dielectric loss, a. c. conductivity were measured with the variation of frequency in the range 1 kHz–5 MHz at room temperature using an Impedance Analyzer (Keysight E4990A) on the unpoled samples. From the measured capacitance, the dielectric constant was calculated using the formula given by Eq. (8) and the dimensions of the pellets. The a. c. conductivity was measured using Eq. (10). The dielectric loss was directly measured using the analyzer. The temperature variation of the electrical parameters was determined using the same Analyzer interfaced to a temperature chamber and PC in the range of 30–250 °C.

7 Results and Discussions

Figure 3 shows the XRD diffraction patterns of the samples sintered at 950 and 1000 °C for 10 min. The sample does not show proper and clear phase formation indicating insufficient sintering conditions applied. The tetragonal phases, however, started showing at sintering temperature 1000 °C for 10 min, in the 15wt%, 20wt%, and 25wt% MnO_2 added sample with crystallite size are 28.19 nm, 28.11 nm, and 28.13 nm, respectively. Also, peak intensity increased for increased the addition of

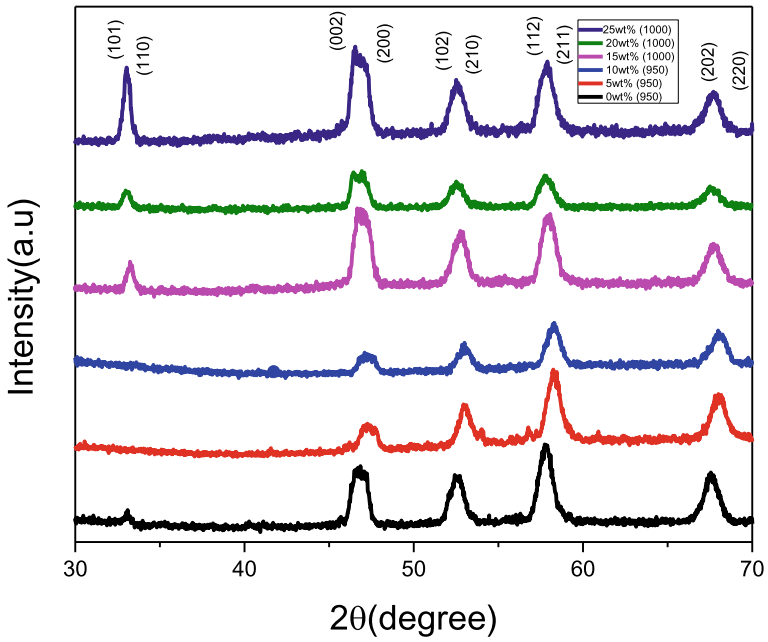

Fig. 3 XRD patterns of KNN and KNN with weight% of $Mn0_2$ sintered at 950 and 1000 °C for 10 min

MnO_2 content as shown in Fig. 3. The conditions may be further imposed with the sintering conditions either by increasing the sintering time or the sintering temperature without forgetting the fact that higher sintering time and longer duel time may invoke volatilization of the alkali components in the KNN. Therefore a study has been done on the sintering conditions, i.e., 1000 °C for 20 min and 1050 °C for 10 min for this present chapter. XRD patterns for KNN ceramics which are sintered at 1000 °C for 20 min and 1050 °C for 10 min are shown in Figs. 4 and 5, respectively. In all the patterns, it is observed that there is the formation of the perovskite tetragonal phase with P4mm symmetry. The XRD patterns do not show any extra peak out of impurities.

The unit cell parameters obtained from XRD data for these samples are given in Tables 1 and 2, respectively, and they are found to be obtained in the desired range for the observed symmetry. From the figure, it is observed that sample sintered without MnO2 tetragonality improves at higher temperature though with lesser time as indicated by the peak at $2\theta \sim 45°$. The peals for a tetragonal phase have been indexed in the figures. The crystallite size as calculated from the XRD data using Scherrer's formula is tabulated in Tables 1 and 2 and ranged from 27.8 to 31.7 nm. Microwave sintering due to its short but efficient sintering process, the nanocrystallite samples could be obtained in the tetrahedral phase. This sintering does not allow exaggerated growth of the crystallite size and correspondingly the grain size. The table further showed that MnO_2 addition till 20wt % does not show a significant

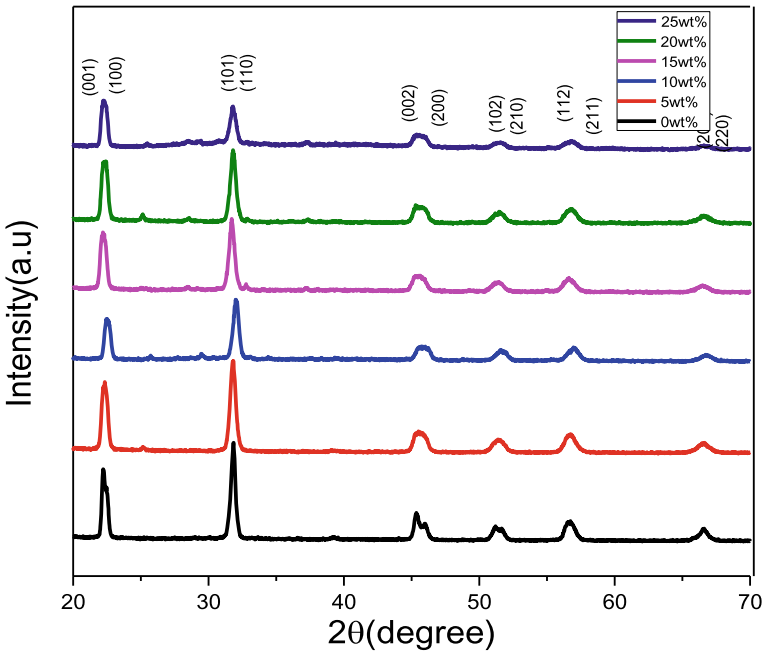

Fig. 4 XRD patterns for KNN and KNN with weight % of MnO_2 sintered at 1000 °C for 20 min

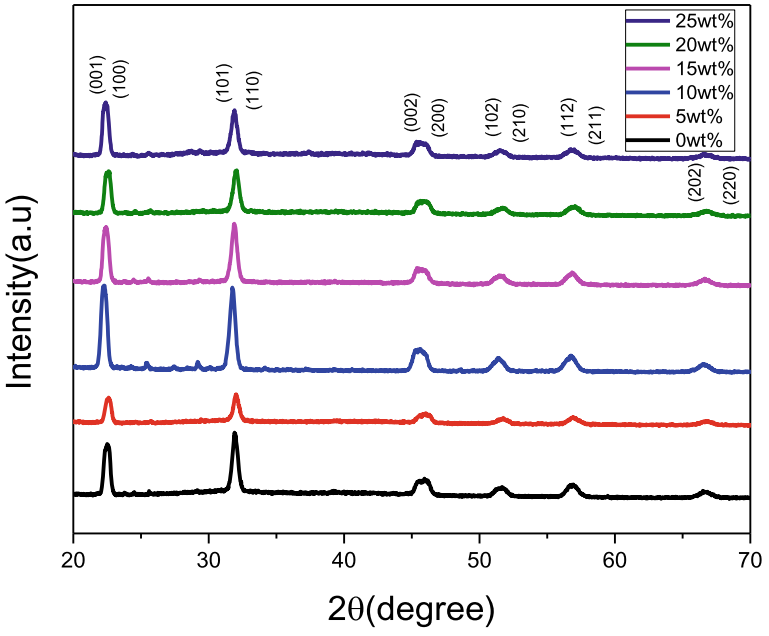

Fig. 5 XRD patterns of KNN and KNN with weight % of MnO_2 sintered at 1050 °C for 10 min

Table 1 Structural parameters for the KNN and KNN with a weight percentage of MnO_2 sintered at 1000 °C for 20 min

Sample (wt%)	a(Å)	c(Å)	Cell volume $(Å)^3$	Crystalline size D (nm)
0	3.994	3.949	62.723	29.82
5	3.979	3.995	63.272	29.83
10	3.961	3.952	62.041	27.86
15	4.005	3.551	56.967	28.88
20	3.994	4.004	63.871	29.95
25	3.994	3.997	63.760	29.95

Table 2 Structural parameters of KNN and KNN with a weight percentage of MnO_2 sintered at 1050 °C for 10 min

Sample (wt%)	a (Å)	c (Å)	Cell volume $(Å)^3$	Crystalline size D (nm)
0	3.882	3.951	60.708	29.90
5	3.933	3.943	61.017	29.50
10	3.993	3.886	61.963	32.33
15	3.960	3.968	62.240	27.88
20	3.960	3.953	62.012	27.86
25	3.932	3.993	61.741	31.78

change of the lattice "a" and "c" constant in both the sintering conditions while at 25wt% the parameter size slightly showed an increase. The change can also be significantly observed in the unit cell volume tabulated in the tables which may be indicative of intrusion of Mn into the structures due to the high concentration of the addition of MnO_2. The right shifting of the peaks for reduced cell volume and a left shift for increased cell volume as seen from the figures also supports the values tabulated in the tables. The increase of crystallite size with an increase of sintering temperature is evident for the same samples. However, since there is a play of the sintering temperature and time significant difference could not be observed in these sintering conditions.

Figures 6 and 7 show the room temperature frequency changes of the dielectric constant measured on electrode pellets of the KNN ceramics series sintered at 1000 °C for 20 min and 1050 °C for 10 min. The variation is dispersive where the dielectric constant value is higher in low frequencies and decreased in the increasing frequencies. As we know that dielectric behavior of polycrystalline ceramics is contributed by four different polarization mechanisms viz space-charge, dipolar, ionic, and electronic. The high value of the dielectric constant at lower frequencies shows the dominant contribution from space charge polarization. When an alternating field is applied, the conduction charges accumulated on the grain boundaries lead to an induced space charge polarization with the production of large capacitance. At higher frequencies, the charge accumulation and polarization produced are reduced which results from

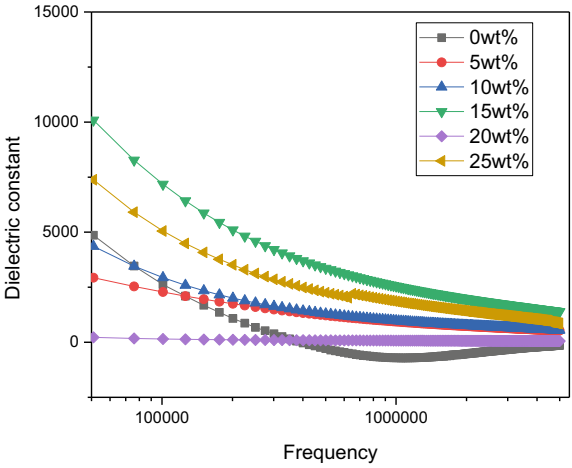

Fig. 6 Change in dielectric constant with the frequency of KNN ceramics sintered at 1000 °C for 20 min

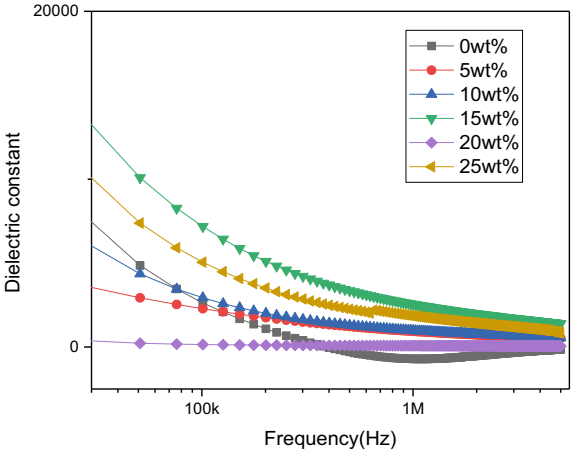

Fig.7 Change of dielectric constant with the frequency of KNN ceramics sintered at 1050 °C for 10 min

the fast charge exchanges. At much higher frequencies, the charge exchange could not follow the frequencies of the applied electric field where polarization stops, and hence dielectric constant remains nearly constant. From both figures, it is observed that the increased addition of MnO_2 improves dielectric constant values at both sintering temperatures.

Figures 8 and 9 show the change of dielectric loss with the frequency which decreases with the increase of the frequency which showed similar behavior to frequency variation with dielectric constant and followed the Koops' phenomenological model [9]. The dielectric loss is a contribution of conduction loss due to ions migration, ions jumps, ions polarization, and vibration loss. Dielectric losses dispersion exhibit resonance when the frequency of electron exchanges between the ions producing polarization equals the frequency of the applied electric field. In both

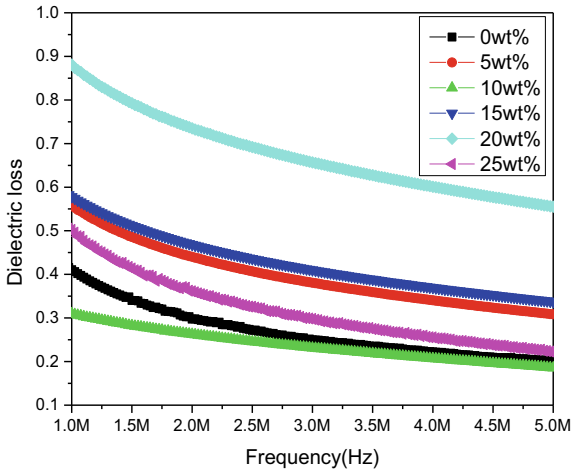

Fig. 8 Change of dielectric loss with the frequency of KNN ceramics sintered at 1000 °C for 20 min

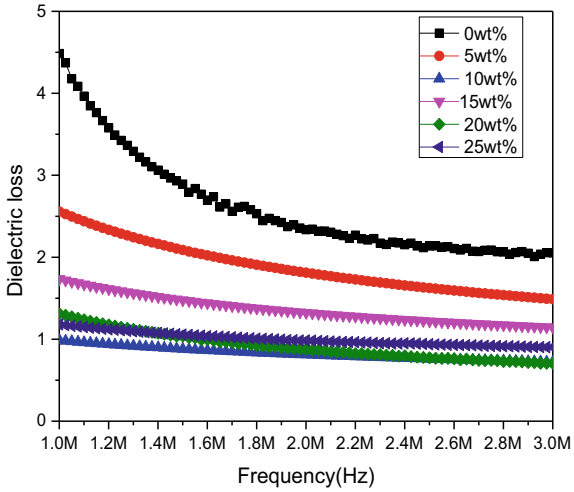

Fig. 9 Change of dielectric loss with the frequency of KNN ceramics sintered at 1050 °C for 10 min

figures, dielectric loss shows no resonance phenomena in the measured frequency range. For both sintering temperatures, it is observed that the dielectric loss decrease with the increased addition of MnO_2, and at 10 wt % of MnO_2, the dielectric constant shows the minimum.

The change of a.c conductivity with frequency for different sintering temperature are shown in Figs. 10 and 11. It is observed that the a.c conductivity at lower frequencies remains constant as it is independent of frequency. But as the increase of frequencies, the value increases linearly until at a certain frequency, then the value rises steeply with a frequency. According to Koop's Model and Maxwell–Wagner

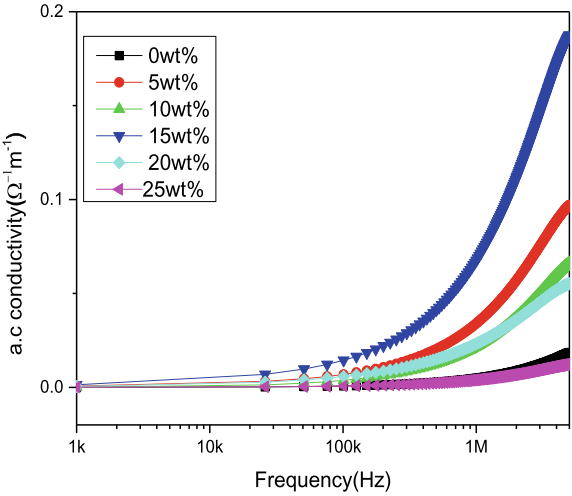

Fig. 10 Change of a.c conductivity with the frequency of KNN ceramics sintered at 1000 °C for 20 min

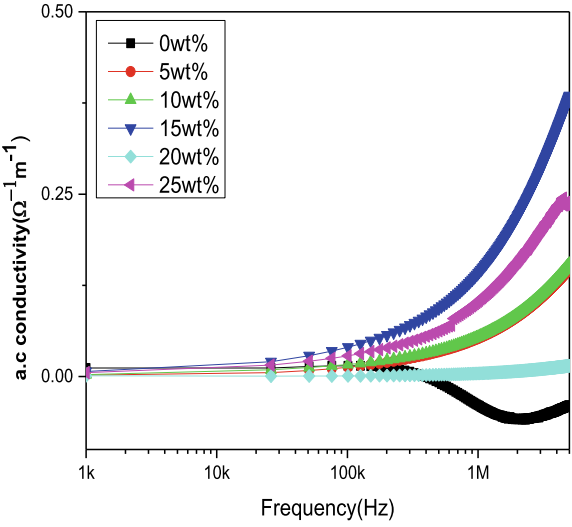

Fig. 11 Change of a.c conductivity with frequency for KNN ceramics sintered at 1050 °C for 10 min

Theory, the charge exchange is less at lower frequencies due to the activeness of insulating grain boundaries and less in charge hopping, and at higher frequencies, more activeness of conducting grain boundaries leads to enhancement of charge hopping.

Figures 12 and 13 show the variation of dielectric constant with temperature at different frequencies for the sintering temperatures for the two series. In both the figures, the dielectric constant initially decreased until certain temperatures beyond which it increased with the increase of temperature, the increase becoming steeper at higher temperatures. The strongly localized charge carriers are activated thermally with the increase of temperature and their drift mobility increased the charge

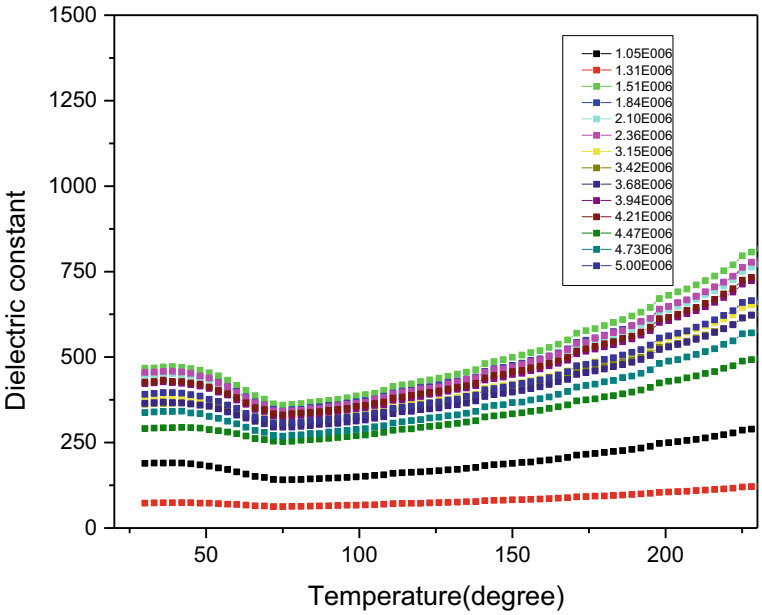

Fig. 12 Variation of dielectric constant with the temperature of 25% weight of MnO_2 in KNN ceramics sintered at 1000 °C for 20 min

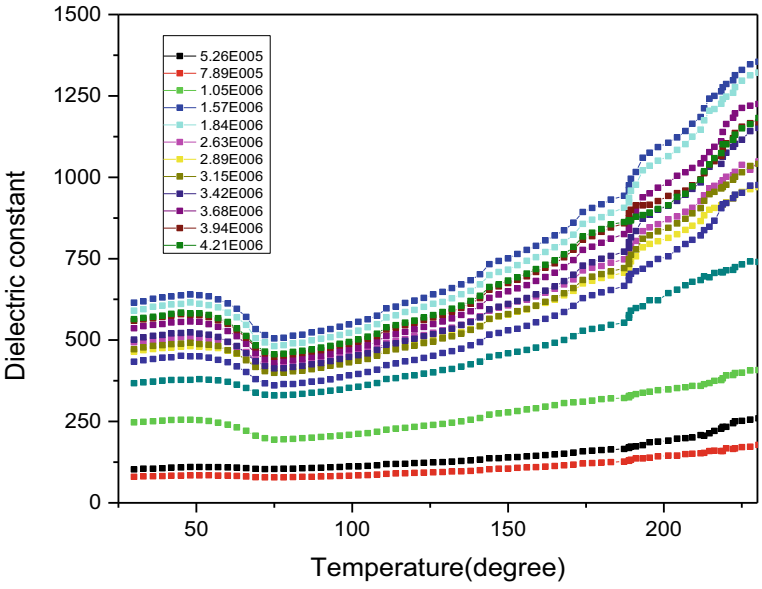

Fig. 13 Variation of dielectric constant with temperature 25% weight of MnO_2 in KNN ceramics sintered at 1050 °C for 10 min

exchanges which results in increased dielectric constant. If the temperature exceeds the Curie temperature, the dielectric constant of a ferroelectric material should strictly obey the Curie–Weiss law. KNN ceramics generally show two dielectric anomalies with the increase of temperature. The first anomalies being the depolarization temperatures which correspond to the transition of the ferroelectric state to the antiferroelectric state while the second anomalies which occur at many high temperatures correspond to the antiferroelectric state to paraelectric state. In the measured temperature range, the dielectric constant does not show any dielectric anomalies until the temperature of 200 °C.

Figures 14 and 15 show the change of dielectric loss with the change of temperature for KNN ceramics at different frequencies for the sintering temperatures 1000 °C and 1050 °C, respectively. They showed a similar trend with the changing temperature which rises with the increase of temperature at all the measured frequencies. The measured temperature range does not show any phase transition for these compositions.

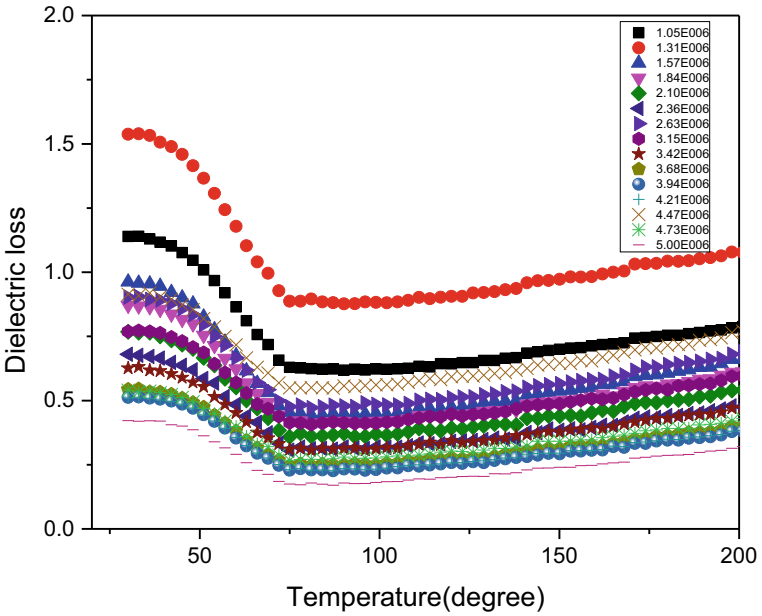

Fig. 14 Change of dielectric loss with the change of temperature of 25% weight of MnO_2 in KNN ceramics sintered at 1000 °C for 20 min

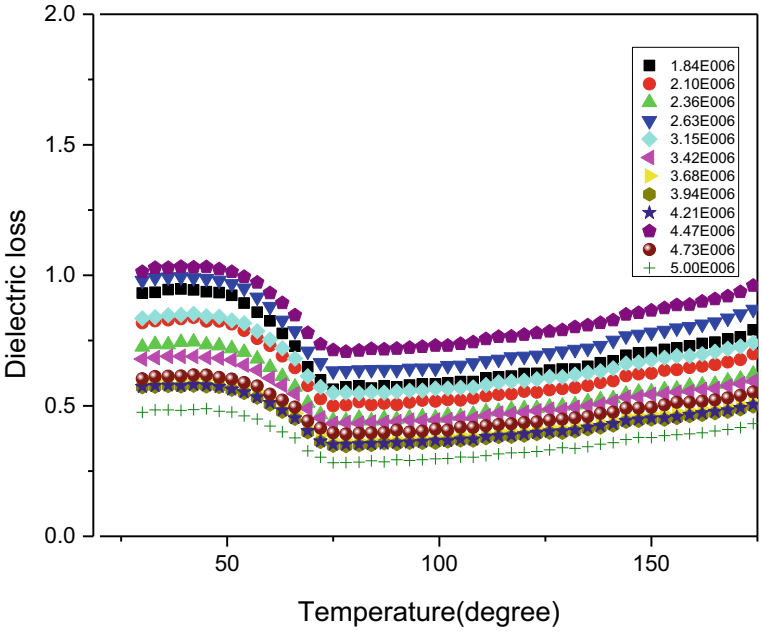

Fig. 15 Change of dielectric loss with the change of temperature of 25% weight of MnO_2 in KNN ceramics sintered at 1050 °C for 10 min

8 Conclusion

Piezoelectric ceramics potassium sodium niobate with compositional formula $K_{0.5}Na_{0.5}NbO_3$ were prepared by adding different amounts (x) of MnO_2 (x = 0wt%, 5wt%, 10wt%, 15wt%, 20wt%, and 25wt%) via ceramic technique using high energy ball milling and microwave sintering technique. The samples were studied by sintering at different temperatures viz. 950 °C for 10 min, 1000 °C for 10 min, 1000 °C for 20 min, and 1050 °C for 10 min. The samples showed the formation of a tetragonal phase whose crystallite size ranges from 29 to 32 nm those sintered at 1000 °C for 20 min and 1050 °C for 10 min. These samples do not show much change in the unit cell dimensions except for higher MnO2 (25wt%). The addition of MnO2 has been found to improve the dielectric properties. The dielectric constant does not show any phase change until 200 °C.

References

1. Cady WG (1946) Piezoelectricity. McGraw-Hill, New York
2. Jaffe H (1958) Piezoelectric ceramics. J Am Cerami 41:494–498
3. Panda PK, Sahoo B (2015) PZT to lead-free piezoceramics: a review. Ferroelectrics 474:128–143

4. Li JF, Wang K, Zhu FY, Cheng LQ, Yao FZ (2013) (K, Na) NbO 3-based lead-free piezoceramics: fundamental aspects, processing technologies, and remaining challenges. J Am Cerami Soc 96(12):3677–3696
5. German RM (1996) Sintering Theory and practice. Wiley, New York, NY, USA
6. Wang K, Li JF (2012) (K, Na) NbO 3-based lead-free piezoceramics: phase transition, sintering and property enhancement. J Ad Ceramic 1:24–37
7. Levy RA (1968) Principles of solid state
8. Hench LL, West JK (1985) Principles of electronic ceramics
9. Smeltere I, Antonova M, Kalvane A, Grigs O, Livinsh M (2011) The effect of dopants on sintering and microstructure of lead-free KNN ceramics. Mater Sci 17:62–64

Chapter 21
Electrical Characterization of Sol–GelDerived Nanostructured Li–Ni–Co Ferrites

Nandeibam Nilima, Sumitra Phanjoubam, and Mamata Maisnam

1 Introduction

Over the last few decades there is a rise in the continuous demand, interests and importance of the newly emerged advanced materials for use in different purposes. Researchers have been engaged in the search of new and more advanced materials for the development of the society. Ferrites have emerged as important magnetic materials [1] and research activities in the field of ferrites material have been developed when Snoek [2] and Neel [3] in 1948 gave the theoretical interpretation for the magnetic properties of ferrites. Spinel lithium based ferrites are found useful in many modern electronic devices because of the particular interesting properties like rectangular hysteresis loop, good value saturation magnetization and high resistivity. The Curie temperature of lithium ferrite is known to be the highest among spinel ferrites [4]. The properties of ferrites are found to depend on many factors such as preparation method, nature and amount of substituent, sintering temperature and conditions [5]. Wide range of ferrites with varied properties can be synthesized by varying the above factors. Usually there are two methods for ferrites preparation, viz. conventional solid-state method and non-conventional chemical method. Conventional solid-state method, though simple, has certain disadvantages. The process of prolong grinding and milling of the precursor often leads to loss of some of the constituent materials, and also impurity pick-ups and the preparation of Li ferrites by this method requires high temperature to sinter the prepared sample [6]. Therefore, nowadays, much attention has been given to the non-conventional chemical method which offers better option to produce Li ferrites at low temperature [6].

N. Nilima (✉)
Department of Physics, Oriental College (Autonomous), Takyel, Imphal 795001, India

S. Phanjoubam
Department of Physics, Manipur University, Canchipur, Imphal 795003, India

M. Maisnam
Department of Physics, National Institute of Technology, Manipur, Langol, Imphal 795004, India

B. P. Swain (ed.), *Advances in Nanostructured Materials*, Materials Horizons:
From Nature to Nanomaterials, https://doi.org/10.1007/978-981-16-8391-6_21

Sol–gel method is preferred because this method is simple, economical, easy and less time consuming [7]. In this method the mixing of constituent cations is done at the atomic level in the solution state, thus producing more refined finished products with high sinterability at low temperature. Sintering at low temperature is especially advantageous for the preparation of lithium-based ferrites as lithium and oxygen are volatile at high temperature [7, 8].

Ferrites are ferrimagnetic compound of iron oxide and some other metal oxides. They appear to be dark grey or black in color, very hard and brittle and they are ceramic in nature [9]. They crystallize into the cubic spinel structure which is derived from that of the mineral spinel $MgAl_2O_4$. Thus the spinel ferrites have the general formula MFe_2O_4, where M is one of the divalent ions of the metallic elements like Cu^{2+}, Zn^{2+}, Cd^{2+}, Ni^{2+}, Co^{2+}, Fe^{2+}, Mg^{2+}, Ca^{2+}, Mn^{2+} or a combination of these ions having average valency of two such as combination of Li^{1+} and Fe^{3+} which can behave as a divalent ion in lithium ferrite, viz, $(Li_{0.5}Fe_{0.5})\ Fe_2O_4$ or generally written as $Li_{0.5}Fe_{2.5}O_4$ [9]. The ferric ion in the chemical formula MFe_2O_4, can be partly or completely substituted by different ions such as Al^{3+}, Cr^{3+}, Ga^{3+} or Ti^{4+} resulting to various ferrites with varied properties.

The structure and crystal chemistry of spinel ferrites have been extensively dealt by Gorter [10], Hafner [11] and Blasse [12]. The unit cell of spinel structure is shown in Fig. 1. The crystal structure is made up of the closest possible packing of oxygen ions and they form an f.c.c. lattice leaving two kinds of interstitial sites, the tetrahedral or the A-site (Fig. 1a) surrounded by or coordinated with four nearest neighboring oxygen ions and the octahedral or the B-sites (Fig. 1b) coordinated by six nearest neighboring oxygen ions.

The unit cell of a spinel lattice contains eight molecules of MFe_2O_4, having 32 oxygen ions forming a cubic closed packed structure, 8—divalent ions and 16—trivalent ions as shown in Fig. 1c. This close packed f.c.c. structure contains 64 tetrahedral and 32 octahedral sites [9]. Of these only 8 tetrahedral and 16 octahedral sites are occupied by the metal ions in order to maintain the charge neutrality [9]. A schematic diagram showing location of the oxygen and the metal ions in two adjacent octants of a spinel ferrite can be seen from Fig. 1d.

George et al. [13] prepared fine particles of lithium ferrites using sol–gel method. They found that certain parameters like grain size, saturation magnetization, dielectric constant and A.C. conductivity were sensitively influenced by sintering temperature. Their investigation showed that as-prepared sample possesses largest value of saturation magnetization which may be due to the ultra fine nature of the particles of the sample [13]. Besides substituent like Co, Zn, Cr, Ni, Al, Mn, Cu, Sb, Mg, Zr, etc. also significantly influenced the various properties of ferrites [14]. Addition of divalent zinc ion in lithium ferrites is very effective in lowering magnetic anisotropy and improvement of microstructure. Reports showed that Zn-substituted Li ferrites are useful in microwave devices [14]. Li–Ti–Zn ferrites can be used for microwave frequency applications [15]. Mazen et al. [16] had studied the frequency and temperature variation of A.C. conductivity of Li–Ge ferrites synthesized by ceramic method. The studies showed an abrupt increase in A.C. conductivity at lower temperature while the increase is slower at higher temperature. They concluded that the behavior

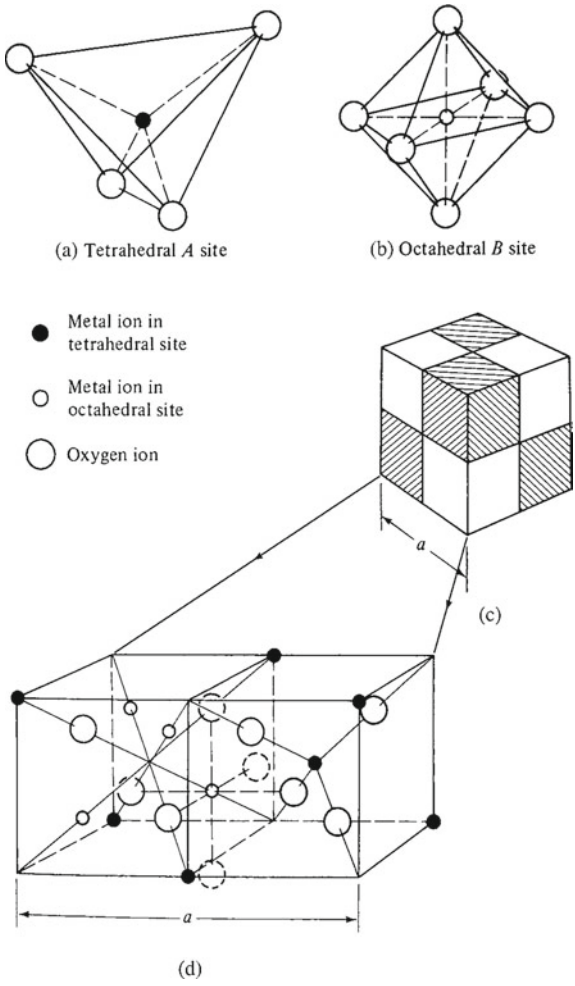

Fig. 1 Structure of spinel ferrite

of the A.C. conductivity is due to the hopping of electrons having energies near the Fermi level [16]. Substitution of small amount of Ni^{2+} is found to enhance the squareness and remanence ratio. It also improves the electrical resistivity as well as shows good hysteresis properties [14]. Li–Ni ferrites are useful in many electromagnetic devices such as currency counting machine, energy meter and D.C.–D.C. converter [17]. Kuroda et. al [18] studied low noise memory core obtained from Li–Ni ferrites. The beneficial effect on the properties of lithium ferrites brought by the addition of Co^{2+} ions includes effectiveness in increasing power handling capacity, coercivity and broadening spin wave, linewidths, improving density and magnetization as well as increase temperature stability. The presence of Co^{2+} ions in B-sites of the lithium ferrites can compensate the negative value of magnetostriction constant [14]. Watawe et. al [19] studied the dependence of dielectric properties of Li–Co ferrites

prepared by standard ceramic method on composition, frequency and temperature. The compositional dependence of dielectric constant showed an inverse trend with D.C. resistivity.

2 Electrical Properties of Spinel Ferrites

It is important to discuss the electrical properties of ferrites as they are important in high-frequency application. The response of dielectric properties is important for designing devices like cores of inductors, transformer and directional couplers [20]. Hilpert [21] was the first person to realize that ferrites might be more useful than magnetite (Fe_3O_4) as magnetic core materials because of their higher resistivity. At room temperature the values range from 5×10^{-3} Ω-cm to over 10^{11} Ω-cm and such high resistivity reduces the eddy current losses, resonance losses and relaxation losses. Many factors like composition, condition of preparation and synthesis method control the resistivity of these materials [9].

Extensive investigations have been done to explain the origin of electrical conductivity. Many models have been forwarded like band polaron model, phonon induced tunnel and a few models based on the fact that ferrites are ferromagnetic materials and their electrical properties are influenced by magnetic properties [22]. The most extensively accepted model is the electron hopping model given by Verwey [23]. According to Verwey Model the electrical conduction in ferrites is the result of exchange or hopping of electron between Fe^{2+} and Fe^{3+} ions distributed randomly at the B-sites [9, 23]. The formation of Fe^{2+} ions can be controlled by controlling the nature and amount of the substituent, processing methods and conditions and microstructure [9]. The dielectric behavior of polycrystalline ferrites can be understood from the inhomogeneity model or the two-layer model proposed by Maxwell [24] and Wagner [25] in agreement with the model given by Koops [26]. The composition and electrical properties of the grain boundaries are completely different from those of the conducting grains. The heterogeneous structure of ferrites can be represented by parallel R–C combination which is again connected in series as shown in Fig. 2.

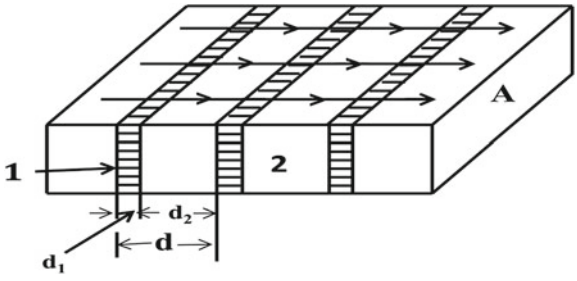

Fig. 2 Model of inhomogeneous dielectric material. Conducting grains (Region 2) are separated by poorly conducting layers (Region 1)

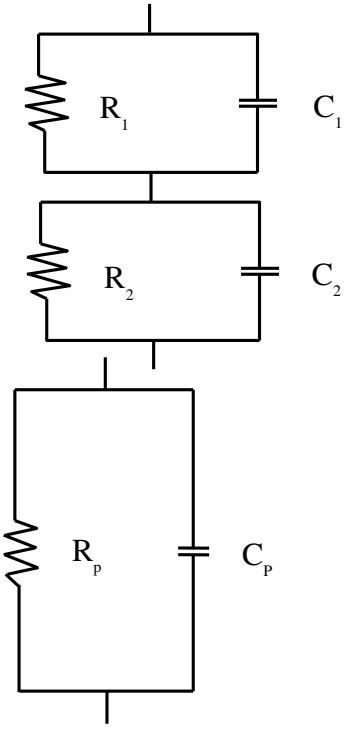

Fig. 3 Equivalent circuit for the dielectric properties of ferrites

Suppose R_1, C_1 and R_2, C_2 represent the resistance, capacitance of grain boundary and grains, respectively, and R_P and C_P the equivalent resistance and the capacitance of the parallel combination (Fig. 3). Therefore, the impedance of the equivalent circuit is given by Eq. (1), where A is the cross section and d is the thickness of the sample, ρ and ε' are the resistivity and relative dielectric constant of the ferrite material and ε_o is the permittivity of free space [11].

$$\frac{1}{Z} = \frac{1}{R_p} + jwC_p \tag{1}$$

where

$$R_p = \frac{\rho d}{A} \text{ and } C_p = \frac{\varepsilon A}{d} = \frac{\varepsilon_o \varepsilon' A}{d}$$

As the dielectric constant is not loss free, it can be written in the form of complex equation, i.e.,

$$\varepsilon = \varepsilon' - i\varepsilon'' \tag{2}$$

where ε' and ε'' are the real part and imaginary part of the dielectric constant [16]. The dielectric loss factor or loss angle or loss tangent is given by the Eq. (3)

$$\tan\delta = \frac{\varepsilon''}{\varepsilon'} \tag{3}$$

The behavior of charge carriers under the influence of A.C. field, their mobility and the mechanism of conduction can be understood from the investigation of A.C. conductivity behavior.

3 Electrical Studies of Nanostructured Li–Ni–Co Ferrites

Li–Ni–Co ferrites chemical formula $Li_{0.45-0.5x}Ni_{0.1}Co_xFe_{2.45-0.5x}O_4$, where x ranges from 0.00 to 0.10 in steps of 0.02 were successfully prepared by the chemical sol–gel method [27]. Stiochiometric amount of starting materials, i.e., lithium nitrate, cobalt nitrate, nickel nitrate and iron nitrate were taken and dissolved in ethylene glycol in the molar ratio 3:1 at 40 °C to form a homogeneous clear solution [7]. The temperature was increased to 80 °C and kept for around 20 min to change the clear solution to a wet gel. Further, the temperature was raised to 130 °C, at which the gel gets dried and led to self ignition giving rise to a highly voluminous fluffy product [7]. The final product so obtained is the as-prepared Li–Ni–Co ferrites. The as-prepared ferrite powder was grounded to fine powder and mixed with a small amount of PVA (3% by weight) [7] which acts as a binder and pressed in the form of pellets by using a load of 100 kg/cm^2 for 5 min. The prepared samples were conventionally sintered at 900 °C for 4 h in air and subsequently furnace cooled [7]. These sintered samples were then polished and cleaned for use in various electrical measurements. Electrical contacts were made on both the flat surfaces of the pellets using silver coating. The resistance of all the samples was taken using two-probe method. The dielectric measurements were carried out on these electroded pellets using an Agilent HP 4284 A LCR meter from 100 Hz to 1 MHz.

XRD pattern confirmed the Spinel structure of all the prepared samples and it is shown in Fig. 4. Compositional variation of D.C. resistivity is shown in Fig. 5. D.C. resistivity was found to increase with the increase of Co^{2+} content and such behavior can be understood from Verwey mechanism of electron hopping and cation distribution. It is already explained that electron hopping takes place between Fe^{2+} and Fe^{3+} ions distributed randomly at the B-sites of ferrite lattice [5]. During the process of sintering partial evaporation of lithium and oxygen at the ferrites surfaces may have formed Fe^{2+} ions preferentially at the B-sites [8]. As Fe^{2+} ions do not exist at the A sites, A–A hopping is neglected. A–B hopping is also neglected because the distance between the metal ions at A-site and B-site is greater than that between the metal ions at B-sites. The main mode of conduction is hence B–B electron exchange between Fe^{2+} and Fe^{3+} ions [5]. The cation distribution for the ferrites system has been well established from the site preferences of the substituted ions. Ni^{2+} ions

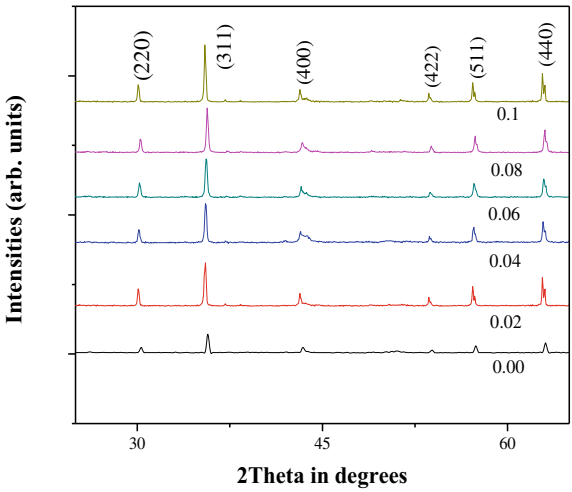

Fig. 4 XRD patterns for $Li_{0.45-0.5x}Ni_{0.1}Co_xFe_{2.45-0.s5x}O_4$ nanoferrite [7]

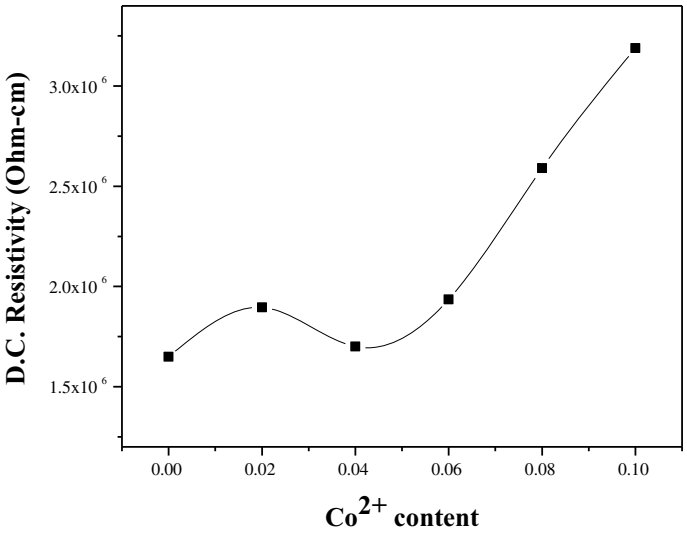

Fig. 5 Variation of room temperature D.C. resistivity with Co^{2+} content for $Li_{0.45-0.5x}Ni_{0.1}Co_xFe_{2.45-0.5x}O_4$ nanoferrite

have strong preference for the B-sites. Low concentration of Co^{2+} ions are reported to occupy the B-sites, while, for higher concentration, some of the ions start to migrate to A-sites also [7]. As the Co^{2+} ions content, $x \leq 0.1$, the cation distribution [7, 12] of the present series may be represented as

$$(Fe)\left[Li_{0.45-0.5x}Ni_{0.1}Co_xFe_{1.45-0.5x}\right]O_4,$$

where parenthesis and square brackets represent tetrahedral A-site and octahedral B-site, respectively [7]. It is seen that the concentration of Ni^{2+} is constant in the composition. From the cationic distribution it is clear that increase in the concentration of Co^{2+} ions reduces the amount of Li^{1+} and Fe^{3+} in the ferrites [27], thereby decreasing the probability of formation of Fe^{2+} ions. Therefore, the exchange of electron between Fe^{2+} and Fe^{3+} ions is reduced resulting in an enhancement in the resistivity [28].

Frequency variation of dielectric constant in the range 100 Hz–1 MHz is shown in Fig. 6. The curve shows the normal dispersive dielectric behavior of spinel ferrites. The dielectric constant is considerably high at low frequencies thereafter the values decrease abruptly with increasing frequency. At higher frequencies the values become nearly constant and such behavior can be understood from exchange of electron between Fe^{2+} and Fe^{3+} ions and space charge polarization along with Koop's model [26]. Under the application of an external applied field the electrons through hopping reach the highly resistive grain boundaries and they start to accumulate resulting in the pilling up of the charges at the grain boundaries and hence producing large polarization [5]. With the increase of applied field, the electronic exchange is not able to follow the applied field. Accordingly, the probability of electrons accumulating at the grain boundaries are decreased thereby reducing the space charge polarization and hence the dielectric constant decreased [8].

Dielectric constant as a function of composition at the frequency 10 kHz is depicted in Fig. 7. The dielectric constant is found to decrease with Co^{2+} substitution. As explained above, substitution of Co^{2+} ions reduces the amount of Fe^{3+} ions and formation of Fe^{2+} ions and hence the hopping probability of electron between Fe^{2+}

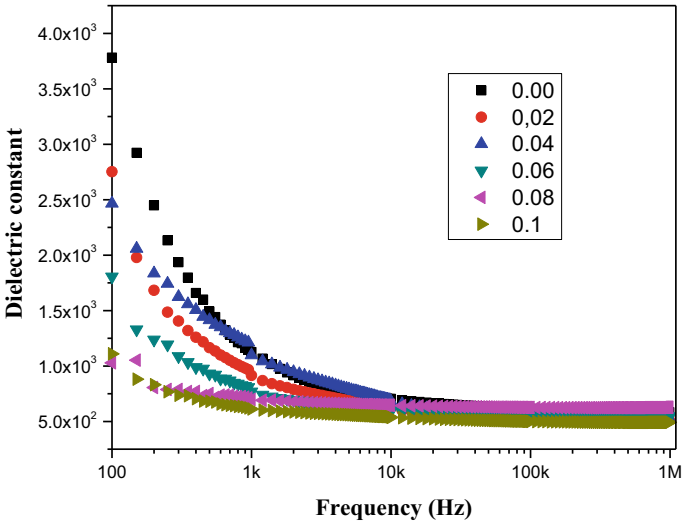

Fig. 6 Frequency dependence of dielectric constant for $Li_{0.45-0.5x}Ni_{0.1}Co_xFe_{2.45-0.5x}O_4$ nanoferrite [5]

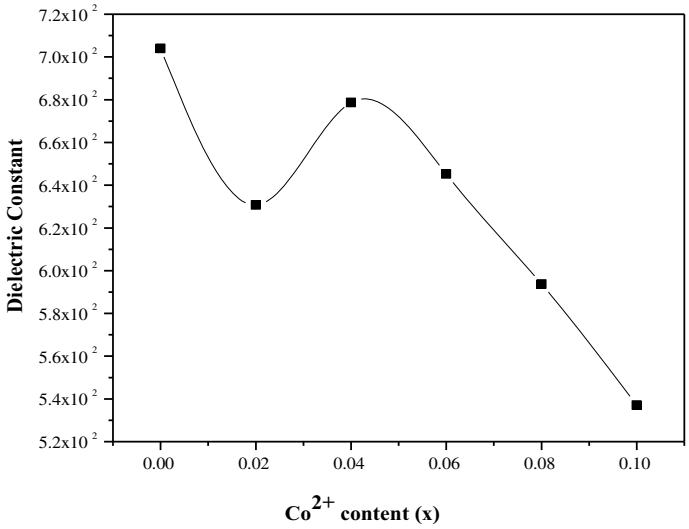

Fig. 7 Variation of room temperature dielectric constant with Co^{2+} content at 10 kHz for $Li_{0.45-0.5x}Ni_{0.1}Co_xFe_{2.45-0.5x}O_4$ nanoferrite

and Fe^{3+} ions at the B-sites. Thus creation of space charge polarization decreased with the Co^{2+} substitution and hence the dielectric constant.

Figure 8 shows the frequency variation of dielectric loss. The dielectric loss also

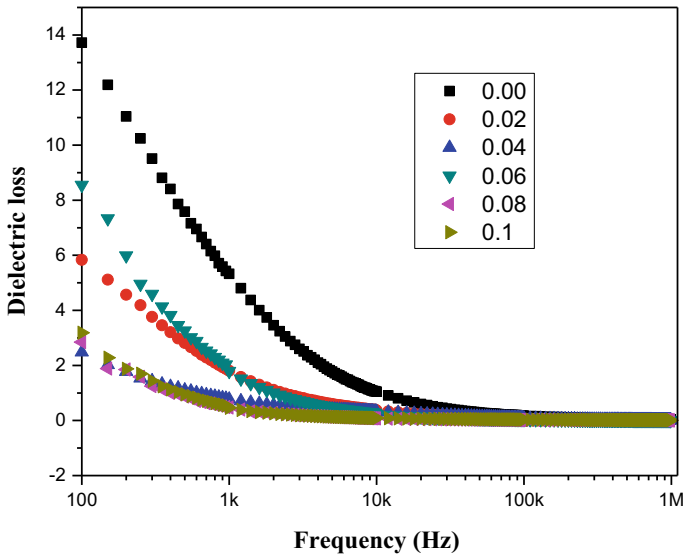

Fig. 8 Frequency dependence of dielectric loss for $Li_{0.45-0.5x}Ni_{0.1}Co_xFe_{2.45-0.5x}O_4$ nanoferrite [5]

shows dispersion with frequency for all the samples. This behavior can be explained by the relation given in Eq. 4 where the dielectric loss varies inversely with the angular frequency of the applied field and the resistivity of the material

$$tan\delta = \frac{1}{\omega\epsilon'\rho} \tag{4}$$

where tan δ is the dielectric loss, ω the angular frequency of the applied field, and ρ, the resistivity of the material. This is in agreement with the explanation given by the Koop's phenomenological model. It is reported that the dielectric loss is contributed by the presence of impurities and structural inhomogeneity in the ferrites [5].

Frequency dependence of A. C. conductivity in the range 100 Hz–1 MHz is shown in Fig. 9. At low frequencies the values of A.C. conductivity increases slowly but above a certain frequency it increases rapidly. According to Maxwell–Wagner [24, 25] in agreement with the Koop's phenomenological model [26], ferrites can be assumed to be compacted as a multilayer capacitor in which the grains and grain boundaries have different properties and the impedance of this model being given by

$$Z^{-1} = R^{-1} + j(2\pi f C)$$

where f is the frequency and R and C are the parallel equivalent resistance and capacitance of the material, respectively. Conduction mechanism in ferrites is attributed

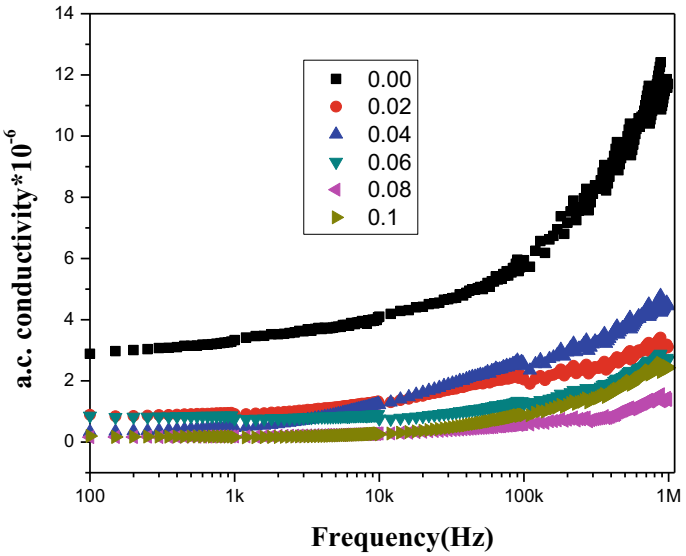

Fig. 9 Frequency dependence of A.C. conductivity for $Li_{0.45-0.5x}Ni_{0.1}Co_xFe_{2.45-0.5x}O_4$ nanoferrite [5]

to exchange of electrons between Fe^{2+} and Fe^{3+} ions at the B-sites. The poorly conducting grain boundaries are more active at low frequencies and this reduces the hopping of electron between Fe^{2+} and Fe^{3+} ions and hence the observed low value of A. C. conductivity is expected. As the frequency is increased the grain boundaries become less active and conducting grains become more active thereby increasing the hopping of electron and hence a gradual increase in the conductivity has been observed [16]. The value of A. C. conductivity is found to decrease with the increase in Co^{2+} content and this may be attributed to the reduction of formation of Fe^{2+} ions in the composition with Co^{2+} substitution which may have restricted the hopping of electron.

4 Conclusion

Lithium-based ferrites are found to be important from application point of view. Lithium ferrites substituted with Ni^{2+} and Co^{2+} having the compositional formula $Li_{0.45-0.5x}Ni_{0.1}Co_xFe_{2.45-0.5x}O_4$ were successfully prepared by sol–gel method. Co^{2+} substitution has been found to enhance the value of D.C. resistivity. Enhancement in D.C. resistivity lowered the dielectric constant and dielectric loss values. Ferrites with low dielectric loss are preferred for high-frequency applications as low dielectric loss increases the penetration depth of electromagnetic waves and reduces skin effect. A.C. conductivity of all the samples has been found to increase with the increase in frequency.

References

1. El Hiti MA (1996) AC electrical conductivity of Ni-Mg ferrites. J Phys D Appl Phys 29:501–505
2. Snoek JL (1946) Non-metallic magnetic materials for high frequencies Phil. Tech Rev 8:353–360
3. Neel L (1948) Magnetic properties of ferrites: ferrimagnetism and antiferromagnetism. Ann Phys 12(3):137–198
4. Maisnam M, Phanjoubam S (2014) Structural and electrical properties of V_2O_5 added Li–Mn–Ti ferrites. Modern Phys Lett B 28(8):1450065
5. Nilima N, Maisnam M, Phanjoubam S (2015) Structural and electrical properties of Sol-gel prepared Li-Ni-Co nanoferrites sintered at reduced temperature. Int J Eng Innov Res 4:415–418
6. Maisnam M, Nilima N, Victory M, Phanjoubam S (2016) Low dielectric loss in nano-Li-ferrite spinels prepared by sol–gel auto-combustion technique. Bull Mater Sci 39(1):249–254
7. Nilima N, Maisnam M, Phanjoubam S (2017) Structural and magnetic properties of nanostructured Li-Ni-Co ferrite prepared by sol-gel method. Int J Mod Phys B 31:1750083
8. Maisnam M, Phanjoubam S, Sharma HNK, Thakur OP, Devi LR, Prakash C (2003) Dielectric properties of vanadium substituted lithium zinc titanium ferrites. Int J Mod Phys B 17:3881–3887
9. Swain BP (ed) (2021) Nanostructured materials and their applications. Springer Science and Business Media LLC, Singapore
10. Gorter EW (1954) Saturation magnetization and crystal chemistry of ferrimagnetic oxides. Philips Res Rep Einthoven 9:295–443

11. Hafner S (1960) Schweiz, Min, Petrogr.: Metalloxyde mit Spinellstructur, Mitt, vol 40, pp 207
12. Blasse G (1964) Crystal chemistry and some magnetic properties of mixed metal oxides with spinel structure. Philips Research Laboratories
13. George M, Nair SS, John AM, Joy PA, Anantharaman MR (2006) Structural, magnetic and electrical properties of the sol-gel prepared $Li_{0.5}Fe_{2.5}O_4$ fine particles. J Phys D Appl Phys 39:900–910
14. Baba PD, Argentina GM, Courtney WE, Dionne GF, Temme DH (1972) Fabrication and properties of microwave lithium ferrites. IEEE Trans Magn 8:83–94
15. Shivaji C (2008) Structural, electrical and magnetic investigations on lithium antimony ferrites substituted with Zn^{2+} and Ti^{4+}. PhD thesis, Manipur University, pp 14
16. Mazen SA, Zaki HM (1995) AC conductivity of Li-Ge ferrite. J Phys D Appl Phys 20:609–613
17. Joshi NC, Verma A, Kumar N, Kumar S, Islam OB (2007) Nickel-substituted lithium-zinc-manganese ferrite for the suppression of radiated emission noise. Def Sci J 57:471–480
18. Kuroda C, Kawashima T (1969) Temperature–stable Low noise ferrite memory cores. IEEE Trans Mag Mater 5(3):192–196
19. Watawe SC, Sarwada BD, Bellad SS, Sutar SD, Chongule BK (2000) Microstructure, frequency and temperature-dependent dielectric properties of cobalt-substituted lithium ferrites. J Magn Magn Mater 214:55–60
20. Shivaji C (2008) Structural, electrical and magnetic investigations on lithium antimony ferrites substituted with Zn^{2+} and Ti^{4+}. PhD thesis, Manipur University, pp 99
21. Hilpert S (1909) Correspondence as to structure and origin in magnetic properties of ferrite and iron oxide. Ber Dtsch Chem Ges 42:2248–2261
22. Shivaji C (2008) Structural, electrical and magnetic investigations on lithium antimony ferrites substituted with Zn^{2+} and Ti^{4+}. PhD thesis, Manipur University, pp 31
23. Verwey EJW, Haayman PW, Romeijn FC (1947) Physical properties and cation arrangement of oxides with spinel structures. J Chem Phys 15:181–187
24. Maxwell JC (1873) Electricity and Magnetism, Oxford University Press, London, vol. 1, section 328
25. Wagner KW (1913) The theory of incomplete dielectrics. Ann Phys 40:817–855
26. Koops CG (1951) On the dispersion of resistivity and dielectric constant of some semiconductors at audiofrequencies. Phys Rev 83:121–124
27. Nilima N, Maisnam M, Phanjoubam S (2019) Enhanced structural and magnetic properties of microwave sintered Li–Ni–Co ferrites prepared by sol–gel method. Chin Phys B 28(2): 026101(1–5)
28. Maisnam M (2006) Structural, electrical and magnetic studies of Li-Zn-Ti ferrites substituted with V^{5+} and Li-Ni-Mn ferrites substituted with $Co^{2+"}$. PhD thesis, Manipur University, pp 100